Evaluation multi-échelle de toxines de venins comme agents antinociceptifs potentiels

Tânia C. Gonçalves

NNT : 2018SACLS587

Evaluation multi-échelle de toxines de venins comme agents antinociceptifs potentiels

Thèse de doctorat de l'Université Paris-Saclay
préparée à l'Université Paris-Sud

École doctorale n°569
Innovation thérapeutique : du fondamental à l'appliqué (ITFA)
Spécialité de doctorat: Sciences pharmacologiques

Thèse présentée et soutenue à Gif-sur-Yvette, le 19 décembre 2018, par

Tânia Cristina Gonçalves

Composition du Jury :

Hervé Daniel Professeur, Université Paris-Sud (Neuro-PSI)	Président
Eric Lingueglia Directeur de recherche, Université Côte d'Azur (IPMC)	Rapporteur
Christian Legros Professeur, Université d'Angers (Institut MITOVASC)	Rapporteur
Michel De Waard Directeur de recherche, Université de Nantes (Institut du thorax)	Examinateur
Evelyne Benoit Chargée de recherche, Université Paris-Saclay (CNRS/CEA)	Examinateur
Michel Partiseti Chercheur, SANOFI R & D (IDD-HCB)	Examinateur
Denis Servent Chercheur, Université Paris-Saclay (CEA)	Directeur de thèse

Thèse de doctorat

A mon petit champion,

Université Paris-Saclay
Espace Technologique / Immeuble Discovery
Route de l'Orme aux Merisiers RD 128 / 91190 Saint-Aubin, France

Cette thèse CIFRE n° 2015_0278, financée en partie par l'Association Nationale de la Recherche et de la Technologie (ANRT), a été réalisée en collaboration entre l'équipe "High Content Biology" de Michel Partiseti (Département "Integrated Drug Discovery", SANOFI R&D, Vitry-sur-Seine) et l'équipe "Toxines, récepteurs et canaux ioniques" de Denis Servent (Service d'Ingénierie moléculaire des protéines, Institut des Sciences du vivant Frédéric Joliot, CEA de Saclay).

Remerciements

Je voudrais tout d'abord remercier le Dr Michel Partiseti ainsi que le Dr Denis Servent de m'avoir choisie pour réaliser cette thèse CIFRE et de m'avoir donné cette opportunité au sein de leurs équipes respectives. Je voudrais aussi remercier les membres du jury d'avoir accepté d'évaluer ce travail. Je remercie le Dr Eric Lingueglia et le Dr Christian Legros d'avoir accepté d'être rapporteurs. Je remercie également le Dr Hervé Daniel et le Dr Michel De Waard d'avoir accepté de faire partie du jury.

Un merci au Dr Denis Servent, en tant que directeur de thèse, pour sa disponibilité, sa bienveillance, ses conseils ainsi que ses relectures constructives, pour tout le temps consacré à orienter ou recadrer certains aspects ainsi que pour son expertise en toxines peptidiques.

Je voudrais remercier aussi le Dr Michel Partiseti, en tant que co-encadrant, pour son œil critique sur le déroulement du projet, bien que par moment un peu dur. Je voudrais aussi remercier sa vision de la recherche innovatrice, non conformiste, sa volonté de simplifier les démarches administratives quand elles semblent vraiment inutiles et sa prise de position concernant ma place au sein du laboratoire.

Je voudrais remercier principalement le Dr Evelyne Benoit, en tant que co-encadrante, pour avoir été un guide tout au long de ces 3 années. Son dévouement aux étudiants est sans faille et sans limite ainsi que sa volonté de bien faire (à partir de 5h du matin, une possibilité pour l'étudiant insomniaque de la contacter si besoin). Merci pour l'expertise en électrophysiologie, pour avoir su me transmettre d'une façon limpide toutes les méthodologies d'analyses, de présentations et d'écriture. J'ai beaucoup appris…

Merci aussi à Rémy Béroud, président directeur général de SMARTOX, et Michel De Waard, co-fondateur de cette même société, d'avoir toujours été présents pour discuter de l'avancement du projet toxines-canaux sodium dans le cadre de la déconvolution des venins, ainsi que Patrick Jimonet de SANOFI qui a supervisé la mise en place du contrat entre SANOFI et SMARTOX.

<u>Du côté de SANOFI :</u>

Je voudrais tout d'abord remercier Rachid Boukaiba pour son accueil chaleureux au sein du laboratoire dès les premiers jours et son aide au quotidien en ce qui concerne les procédures internes à SANOFI ainsi que pour son implication dans le projet $Na_V1.7$-toxines, au même titre que Sophie Fouconnier. Ensuite, je voudrais remercier le Dr Jean-Marie Chambard et Laetitia Lucarain pour le travail

qu'ils ont abattu avant mon arrivée au laboratoire concernant la déconvolution de venins sur le même projet, ainsi que le Dr Andrees Bohme, Brigitte Schombert et Camille Sanson pour leur implication dans la partie "sureté pharmacologique au niveau cardiaque". Je voudrais aussi remercier Cathy Cojean pour son aide dans la génération de lignées stables directement liées à mon projet de thèse.

Je voudrais aussi mentionner Philippe Boudeau, dernier "patch-clampeur" du laboratoire, qui a su me transmettre beaucoup de son savoir sur la technique mais aussi sur l'entreprise, avec ses nombreuses anecdotes qui reflétaient bien l'évolution de celle-ci au fil du temps. Une petite attention particulière à Anne-Julie Chevrel, super camarade de bureau, toujours souriante et serviable. Sans oublier le Dr Pascal Roux, Eric Tagat et Sylvie Houtmann avec qui j'ai eu moins d'échanges sur le plan professionnel, mais qui étaient toujours très agréables à la pause-café. Au Dr Ouassila Habi, je voudrais juste dire "Ne change pas, la recherche pour avancer à besoin de jeunes personnes ultra-dynamiques et volontaires comme toi".

Au Dr Bruno Biton ainsi qu'à Pauline Cervello qui ont mis à disposition une partie de leur temps pour la transmission du savoir-faire concernant la culture des neurones des ganglions de la racine dorsale de souris.

Au Dr Veronique Ballet ainsi qu'à Thierry Carriot et Céline Chantoiseau pour m'avoir si gentiment accueillie dans leur laboratoire et m'avoir transmis toutes les informations nécessaires à l'avancement de mon projet concernant l'évaluation de la sécurité pharmacologique sur le système cardiovasculaire grâce aux expériences sur les fibres de Purkinje et le cœur isolé de lapin.

Au Dr Jean-Michel Itier ainsi qu'àe Sandra Viale de s'être investis dans une partie de mon projet et m'avoir fourni des cardiomyocytes dérivées de cellules souches pluripotentes induites humaines. Je voudrais aussi souligner leur bonne volonté à partager avec moi leurs connaissances et leur savoir-faire en la matière.

Sans oublier de remercier le Dr Isabel Lefèvre pour la relecture de tous les manuscrits inclus dans cette thèse.

Un grand merci au Dr Rosalia Arrebola, responsable du laboratoire de « Simple Management », complémentaire d'"High Content Biology" de Michel Partiseti, de s'être souciée de moi sur le plan professionnel mais aussi personnel pendant tout le déroulement de ma thèse.

<u>Du côté du CEA :</u>

Je voudrais remercier le Dr Jordi Molgó pour son savoir, sa gentillesse, sa disponibilité et sa promptitude à répondre à tout type de question de façon claire et précise ainsi que pour l'aide fournie pour la préparation et l'enregistrement des hémi-diaphragmes de souris. Merci aussi au Dr Muriel Amar pour son introduction au patch clamp manuel ainsi que pour les échanges que l'on a eu au laboratoire.

Au Dr Gilles Mourier et à Margot Vanden Driessche pour leur aide en synthèse peptidique ainsi qu'au Dr Lidia Ciccone d'avoir toujours répondu gentiment à mes questions, même les plus basiques, concernant l'étude ou la génération des structures 3D des toxines peptidiques.

Au Dr Nicolas Gilles, avec qui j'ai travaillé sur une des toxines antidouleur, au Dr Pascal Kessler, pour son humour décalé, au Dr Philippe Robin, pour sa gentillesse, et au Dr Romulo Araoz, pour sa convivialité quand il s'agit de nous préparer un apéro typiquement chilien.

Un petit clin d'œil à Christelle Carvalho, à Justyna Cyolek, au Dr Daad Saraf, au Dr Marcela Silva, à Manon Lancien, à Julia Boeri, à Fanny Noirmain, à Minh-Tuyet Nguyen, au Dr Pavel Shpak, au Dr Sarah Brégant et au dernier arrivé, le Dr Nicolo Tonali qui ont su égayer, évidemment par des discussions purement scientifiques, mes pauses cafés au quotidien. Sans oublier Evelyne Rabouille et Alexandra Aleixo, pour leur sourire et les aides précieuses pour tout ce qui concerne les procédures administratives.

<u>Du côté des étudiants (BTS, Licence, Master et Doctorat) :</u>

Je voudrais mentionner tous les stagiaires que j'ai vus défiler à SANOFI (Shanon Abergel, Pauline Ferlan, Manon Sirvin, Lise Bettoun, Eva Kirasic, Laura Chladni, Charlotte Saint-Omer et Julie Somkhit) mais aussi au CEA (Alexandre Sampaio, Amandine Gaudin, Claire Lamoise, Pierre-Emmanuel Girault-Sotias, Sarah Nadif, Hugo Dosquet, Steven Ascoët, Florian Blondel et Mickaël Susset) et qui, chacun par nos échanges, m'ont beaucoup apporté et permis de tenir le rythme assez mouvementé de ces trois dernières années.

Une mention spéciale à mes "frères de combat", Marc Ravatin, doctorant à SANOFI, ainsi que Steve Reynaud, doctorant au CEA, à qui je souhaite la meilleure réussite possible pour la suite de leur thèse. Je voudrais aussi mentionner la doctorante, à ce jour, déjà docteur, avec qui j'ai partagé le bureau pendant un peu plus de 2 ans, Laura Droctové, et qui a toujours eu les mots tout en douceur pour me rassurer à chaque fois qu'un obstacle pointait son nez. Merci à Nassim Mahtal, Aurélien Azam et Livia Tepshi, les doctorants du sous-sol, maintenant docteurs, toujours souriants et sympathiques ainsi que Monika Kaminska et Héloïse Cahuzac, les doctorantes du premier étage, avec qui j'ai partagé mes dernières angoisses et à qui je souhaite la meilleure continuation.

<u>Du côté de ma famille :</u>

Finalement, je voudrais dire un grand merci à ma famille, surtout à mes grands-parents qui ont participé à mon éducation étant jeune, à mes parents et mon frère qui, malgré leur méconnaissance concernant ce que je fais, me soutiennent et m'aident au quotidien, à mon fils pour sa patience, et enfin à mon conjoint qui me porte depuis le début dans la réalisation de ce projet.

Table des matières

Liste des abréviations

4-AP :	4-aminopyridine
AID :	Domaine d'interaction à la sous-unité α1 ("α1-subunit Interacting Domain")
AINS :	Anti-inflammatoires non-stéroïdiens
AMM :	Autorisation de mise sur le marché
ASIC :	Canal senseur de protons ["Acid-Sensing (proton-gated) Ion Channel"]
CAM:	Protéines d'adhésion cellulaire ("Cell-Adhesion Molecules")
Canal CatSper :	"Cation channel of Sperm"
Canal Ca_V :	Canal calcium dépendant du potentiel
Canal CNG :	"Cyclic Nucleotide-Gated channel"
Canal HCN :	"Hyperpolarisation-activated, Cyclic Nucleotide-gated channel"
Canal K_{2P} :	Canal à domaine deux P ("Two P domain channel")
Canal Kir :	Canal potassium à rectification entrante
Canal K_V :	Canal potassium dépendant du potentiel
Canal Na_V :	Canal sodium dépendant du potentiel
Canal SOC:	"Store-Operated Calcium channel
Canal TRP :	"Transient Receptor Potential channel"
CHO :	"Chinese hamster ovary"
CiPA :	"Comprehensive *in vitro* Proarrhythmia Assay"
Cryo-ME :	Cryo-microscopie électronique
CssII :	Toxine II du scorpion *Centruroides suffusus suffusus*
CTD :	Partie C-terminale ("Carboxy-Terminal Domain")
CyrTx-1a :	Cyriotoxine-1a
D :	Domaine
DRG :	Ganglion de la racine dorsale ("Dorsal root ganglion")
EC_{50} :	Concentration effective produisant 50% de l'effet
EF :	Main EF ("EF hand")
ENaC :	Canal sodium des cellules épithéliales ["Epithelial sodium (Na) Channel"]
ES :	Erreur standard
ESM :	Erreur standard de la moyenne
FDA :	"Food and Drug Administration"
GABA :	Acide γ-aminobutyrique
GPI :	Glycophosphatidylinositol
HEK :	"Human embryonic kidney"
hiPSC-CM :	Cardiomyocyte dérivé de cellules souches pluripotentes humaines
HMM :	Hidden Markov Model
HPLC :	Chromatographie en phase liquide haute pression (le terme "à haute performance" est aussi fréquemment utilisé)

HVA :	Canaux à haut seuil d'activation ("High Voltage Activated")
HwTx-IV :	Huwentoxine-IV
Ig :	Immunoglobuline
i.m. :	Intramusculaire
i.p. :	Intrapéritonéal
i.pl. :	Intrapleural
IASP :	Association internationale pour l'étude de la douleur (International Association for the Study of Pain)
IC_{50} :	Concentration inhibant de 50% la réponse
ICK :	Nœud de cystines inhibiteur ("Inhibitor cystine knot")
IFM :	Isoleucine-Phénylalanine-Méthionine
Ig :	Immunoglobuline
IP3 :	Inositol trisphosphate
IVA :	Canaux à seuil d'activation intermédiaire ("Intermediate Voltage Activated")
JzTx :	Jinghaotoxine
k_g :	Pente de la courbe de la conductance en fonction du potentiel de membrane
k_h :	Pente de la courbe d'inactivation stationnaire en fonction du potentiel de membrane
LqhIII :	Toxine III du scorpion *Leiurus quinquestriatus hebraeus*
LVA :	Canaux à bas seuil d'activation ("Low Voltage Activated")
MAPS :	Balayage positionnel multi-attributs ("Multi Attribute Positional Scan")
MS/MS :	Masse en tandem
NALCN :	Canal sodium de fuite ("Sodium Leak Channel")
NaSpTx-1 :	Famille 1 des toxines d'araignées inhibant les canaux Na_V
NaSpTx-2 :	Famille 2 des toxines d'araignées inhibant les canaux Na_V
NaSpTx-3 :	Famille 3 des toxines d'araignées inhibant les canaux Na_V
OAIP :	Peptide insecticide actif par voie orale ("Orally active insecticidal peptide")
OD1 :	Toxine 1 du scorpion *Odonthobuthus doriae*
OMS :	Organisation mondiale de la Santé
p :	Bras long du chromosome
PA :	Potentiel d'action
PD :	Pore du canal ("Pore Domain")
PDB :	Base de données des protéines ("Protein data bank")
PecTx-1a :	Poécitoxine-1a
PhlTx-1 :	Phlotoxine-1
PKA :	Phosphokinase A
PKC :	Phosphokinase C
ProTx-II :	Protoxine-II
q :	Bras court du chromosome
SFETD :	Société française d'étude et de traitement de la douleur
SNC :	Système nerveux central
SNP :	Système nerveux périphérique

STX :	Saxitoxine
TEA :	Tétraéthylammonium
TPC :	Canal à deux pores ("Two-Pore Channel")
TTX :	Tétrodotoxine
TTX-R :	Résistant à la tétrodotoxine
TTX-S :	Sensible à la tétrodotoxine
U2OS :	"Human bone osteosarcoma epithelium"
$V_{P50\%}$:	Potentiel correspondant à une diminution de 50% de l'inactivation stationnaire
VSD :	Domaine senseur du potentiel membranaire ("Voltage Sensing Domain")
$V_{T50\%}$:	Potentiel correspondant à une diminution de 50% de la conductance
ZAC :	Canal activable par le zinc ("Zinc-Activated Channel")

Acides aminés essentiels

Ala (A) :	Alanine	Leu (L) :	Leucine
Arg (R) :	Arginine	Lys (K) :	Lysine
Asn (N) :	Asparagine	Met (M) :	Méthionine
Asp (D) :	Aspartate	Phe (F) :	Phénilalanine
Cys (C) :	Cystéine	Pro (P) :	Proline
Gln (Q) :	Glutamine	Ser (S) :	Sérine
Glu (E) :	Glutamate	Thr (T) :	Thréonine
Gly (G) :	Glycine	Trp (W) :	Tryptophane
His (H) :	Histidine	Tyr (Y) :	Tyrosine
Ile (I) :	Isoleucine	Val (V) :	Valine

Acides aminés non naturels

1-Nal :	1-naphthylalanine

Préambule

Les travaux de recherche de ma thèse concernent l'évaluation multi-échelle de toxines de venins comme agents antinociceptifs potentiels. Ils ont été effectués dans le cadre d'une convention CIFRE associant l'équipe de Michel Partiseti (SANOFI) et celle de Denis Servent (CEA) pour lesquelles l'exploitation des venins comme source d'agents thérapeutiques potentiels est un sujet d'intérêt.

En effet, en décembre 2013, le groupe SANOFI a signé un partenariat de recherche avec Smartox Biotechnology, un partenariat rendu officiel le 6 février 2014 avec cette biotech grenobloise, spécialiste de l'exploitation des venins d'animaux, qui maîtrise la purification, le séquençage et la synthèse des peptides composant ces mélanges complexes. De son côté, l'équipe "High Content Biology" de Michel Partiseti (Département "Integrated Drug Discovery", SANOFI R&D, Vitry-sur-Seine) est experte dans le criblage à haut débit de librairie de ligands, comme des fractions et sous-fractions de venins, pour en extraire des molécules naturelles d'intérêt afin d'en évaluer les propriétés thérapeutiques. Quant aux axes de recherches développés par l'équipe "Toxines, récepteurs et canaux ioniques" de Denis Servent (Service d'Ingénierie moléculaire des protéines, Institut des sciences du vivant Frédéric Joliot, CEA de Saclay), ils visent, d'une part, à identifier de nouvelles toxines aux propriétés originales et, d'autre part, à caractériser fonctionnellement (par des approches multi-échelles in vitro, ex vivo et in vivo) et structuralement leur interaction avec les récepteurs et canaux ioniques, à modifier ces propriétés fonctionnelles par ingénierie et à exploiter ces ligands en tant qu'outils d'étude du fonctionnement de leurs cibles moléculaires ou pour leurs potentialités thérapeutiques.

Ce mémoire de thèse est organisé en trois parties:

La première partie, introductive, est un état des connaissances actuelles (i) *sur les canaux ioniques (sodium, potassium et calcium), dépendants du potentiel de membrane, et des canalopathies associées,* (ii) *sur l'utilisation des toxines en tant que thérapeutiques, en mettant plus particulièrement en évidence les peptides de venin d'animaux potentiellement antalgiques, et* (iii) *sur la physiopathologie de la nociception. Cette partie se termine par une revue publiée sur le sujet dans "Frontiers in Pharmacology".*

La seconde partie, intitulée "Résultats et Discussion", est structurée en 5 sous-parties portant sur les données obtenues suite au criblage à haut débit de deux banques de venins qui a permis l'identification et la caractérisation, par des approches fonctionnelles multi-échelles, de peptides dérivés de venins et ayant des propriétés potentiellement antinociceptives. Elles sont présentées sous

forme d'articles publiés ou en révision dans des journaux à comité de lecture, d'articles en préparation et de résultats non publiés.

La troisième et dernière partie de ce mémoire est consacrée aux conclusions générales et aux perspectives découlant du travail réalisé au cours de cette thèse.

Partie 1

INTRODUCTION

1.1. Canaux cationiques dépendants du potentiel

Actuellement, 2880 cibles moléculaires humaines ont été identifiées dont les principales classes sont les enzymes (1201, soit 42%), les transporteurs (509, soit 18%) et les récepteurs couplés aux protéines G (399, soit 14%). Parmi ces classes, les enzymes et les récepteurs couplés aux protéines G représentent 77% des cibles thérapeutiques actuelles. Les canaux ioniques, quant à eux, ne constituent que 7% des cibles thérapeutiques actuelles mais 10% des cibles moléculaires humaines (Figure 1-1).

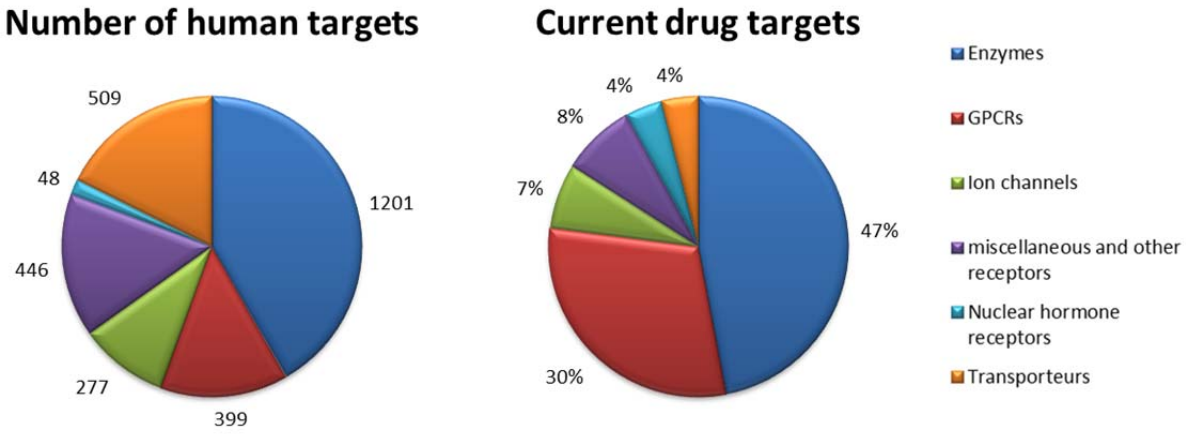

Figure 1-1. Nombre de chaque classe de cibles moléculaires humaines et la part de chacune d'entre elle dans le panel thérapeutique actuel. Adapté de Harding et al. (2018) et de Hopkins & Groom (2002).

Parmi les canaux ioniques se trouvent les canaux activables par un ligand (81, soit 29%), par le potentiel de membrane (144, soit 52%) et les autres canaux ioniques (52, soit 19%). Les canaux activables par un ligand comprennent, notamment, les récepteurs sérotoninergiques (5-HT_3), de l'acide γ-aminobutyrique de type A ($GABA_A$), glycinergiques, ionotropiques du glutamate, purinergiques (P2X) et nicotiniques de l'acétylcholine ainsi que certains canaux de la famille ENaC [pour "epithelial sodium (Na) channel"] tels que les canaux sodium activés par le FMRFamide. Les autres canaux ioniques incluent, notamment, d'autres canaux de la famille ENaC tels que les canaux senseurs de protons [ASIC pour "acid-sensing (proton-gated) ion channel"], les canaux chimiosensoriels répondant au sel ou encore les canaux mécanosensoriels responsables de la sensation tactile, les aquaporines, les connexines/pannexines, certains canaux chlore, les canaux SOC (pour "store-operated calcium"), les canaux Piezo et le canal sodium de fuite (NACLN ou "sodium leak channel"). Finalement, 8 groupes de canaux ioniques dépendants du potentiel sont dénombrés: les canaux calcium CatSper (pour "cation channel of sperm") et les canaux à deux pores (TPC pour "two-pore channel"), les canaux régulés par les nucléotides cycliques (comprenant les canaux CNG pour

"cyclic nucleotide-gated" et les canaux HCN pour "hyperpolarisation-activated, cyclic nucleotide-gated"), les canaux potassium [dont ceux activés par le calcium ou le sodium, ceux à rectification entrante, ceux à domaine deux P ("two P domain" ou K_{2P}) et ceux dépendants du potentiel], les canaux TRP (pour "transient receptor potential channels") ainsi que les canaux chlore (CIC-x), calcium, proton et sodium dépendants du potentiel (Alexander et al., 2017; Figure 1-2).

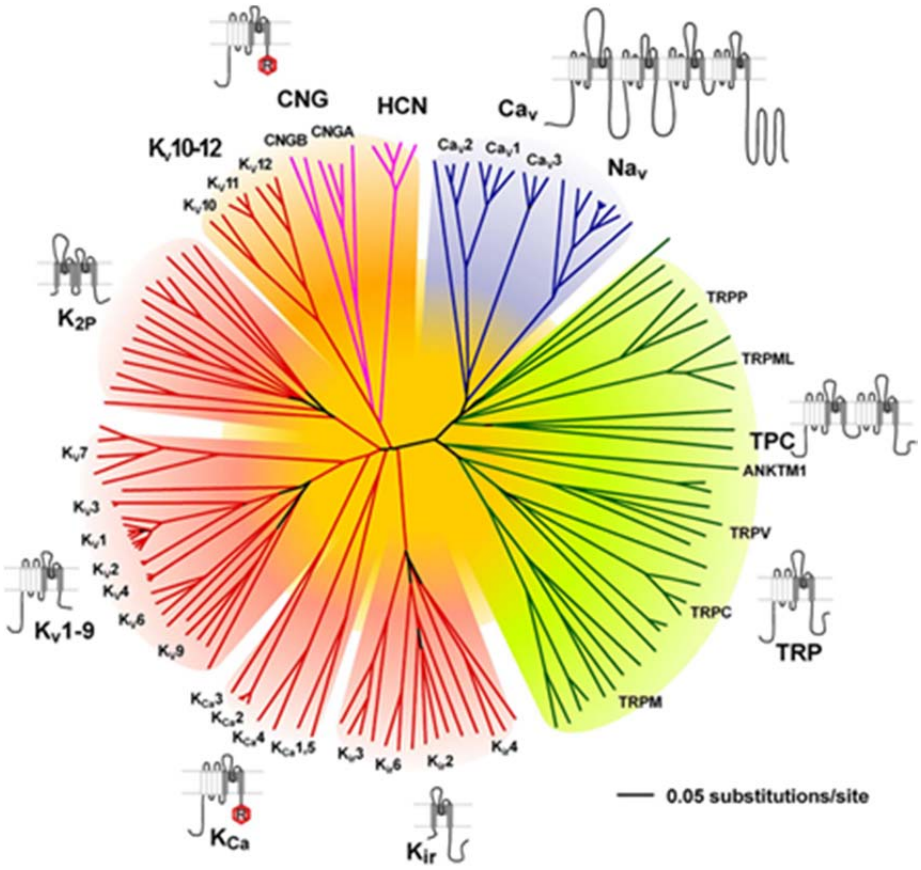

Figure 1-2. Représentation des relations entre les séquences d'acides aminés du pore formant le canal de la superfamille des canaux ioniques dépendants du potentiel de membrane (Yu & Catterall, 2004).

Les canaux cationiques (sodium, potassium et calcium) dépendants du potentiel (respectivement Na_V, K_V et Ca_V) sont des protéines transmembranaires qui confèrent aux cellules nerveuses la propriété d'excitabilité en participant à la génération et à la propagation du potentiel d'action (canaux Na_V et K_V) pour permettre *in fine* la libération des neurotransmetteurs (canaux Ca_V). Ces canaux, ou du moins certains d'entre eux, interviennent également dans la genèse des contractions musculaires, la fréquence des battements cardiaques, la sécrétion, la balance eau/électrolyte, la réponse immunitaire, la prolifération cellulaire…. Ils peuvent se trouver dans les trois états conformationnels principaux suivants (à l'exception de certains canaux K_V): l'état fermé (non conducteur), l'état activé (conducteur) et l'état inactivé (non conducteur), selon le sous-type de canal ionique considéré et en fonction du temps et du potentiel appliqué à la membrane plasmique (Figure

1-3A). La sous-unité principale, qui constitue le pore ionique du canal (sous-unité α), est souvent associée à des sous-unités auxiliaires qui en modifient les propriétés biophysiques et pharmacologiques (sous-unités β, δ, γ). Des modifications post-traductionnelles sur une des sous-unités constituant le canal ionique peuvent également contribuer à la modulation des propriétés fonctionnelles du pore. Au cours de ces dernières années, l'obtention de la structure tridimensionnelle des canaux ioniques, grâce à la cristallographie et à la cryo-microscopie électronique (Cryo-ME), a permis de mieux comprendre leur fonctionnement, les différences structurales associées à leurs différents états, ainsi que le mode d'interaction entre la sous-unité principale et les sous-unités auxiliaires (Figure 1-3B) (Payandeh et al., 2011; Payandeh & Minor, 2015; Wu et al., 2016; Shen et al., 2017; Yan et al., 2017; Matthies et al., 2018; Pan et al., 2018).

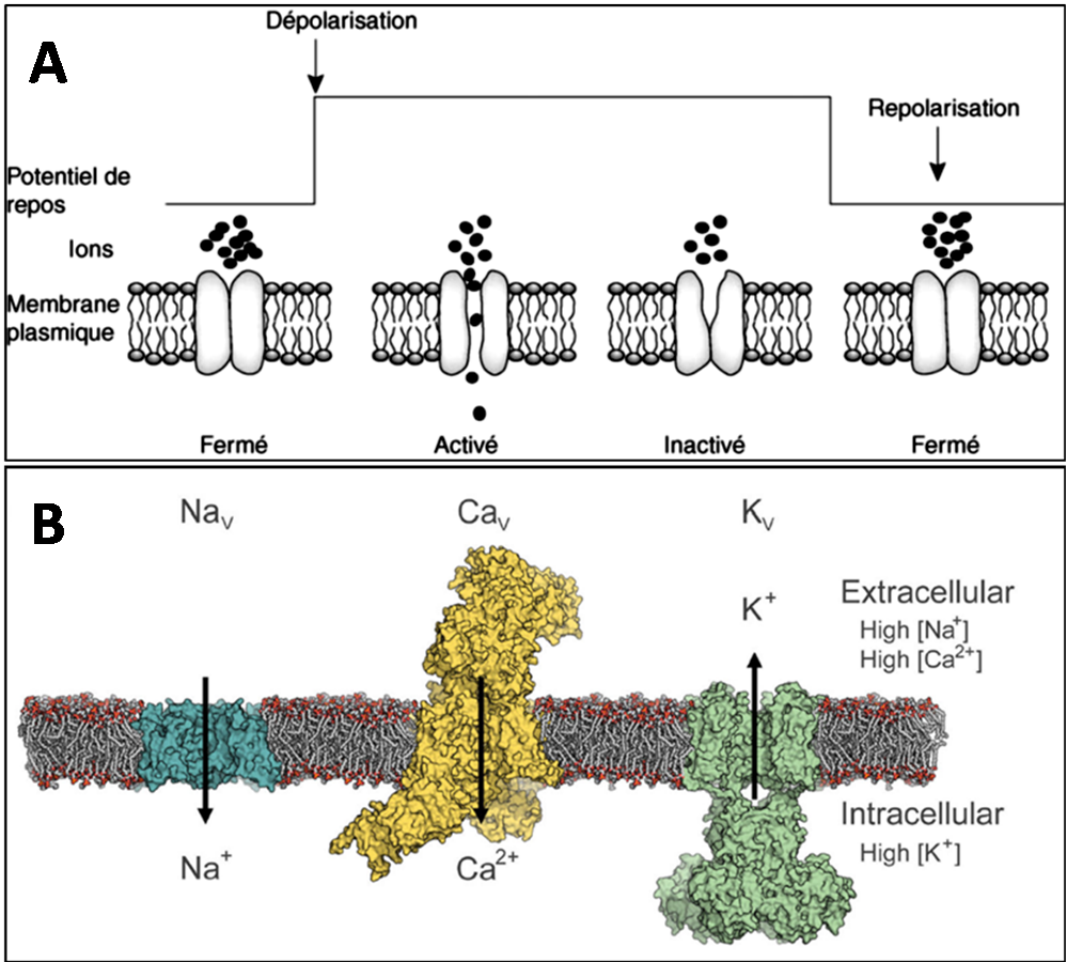

Figure 1-3. Bases chimiques de la signalisation électrique et propriétés d'ouverture et de fermeture des canaux cationiques dépendants du potentiel. (**A**) Principaux états biophysiques (fermé, activé et inactivé) des canaux ioniques en fonction du temps et du potentiel appliqué à la membrane plasmique. D'après Bourdain et al. (2005). (**B**) Représentation des canaux cationiques (Na_V, Ca_V et K_V) au niveau de la membrane lipidique, avec un milieu extracellulaire hautement concentré en ions sodium et calcium alors que le milieu intracellulaire est concentré en ions potassium. De la gauche vers la droite, le canal bactérien Na_VAb, le sous-type Ca_V1.1 de canal calcium de mammifère complexé à ses sous-unités auxiliaires, et la chimère de mammifère K_V1.2/2.1 complexée aux sous-unités β intracellulaires. D'après Catterall et al. (2017).

1.1.1. Canaux sodium

Les canaux Na_V sont composés d'une sous-unité α principale d'environ 220-260 kDa, liée de façon covalente ou non à des sous-unités β auxiliaires avoisinant les 33-36 kDa (stœchiométrie α/β non encore élucidée) (Isom et al., 2001; Catterall et al., 2007; Namadurai et al., 2015).

La sous-unité α est constituée de 4 domaines (DI-DIV) regroupant chacun 6 segments transmembranaires dont les 4 premiers (S1-S4) forment le domaine senseur du potentiel (VSD pour "Voltage Sensing Domain"). Le segment 4 chargé positivement (par la présence d'arginines) est le principal composant du VSD et les deux derniers (S5-S6), reliés par la boucle P, forment le pore du canal (PD pour "Pore Domain") (Figure 1-4A).

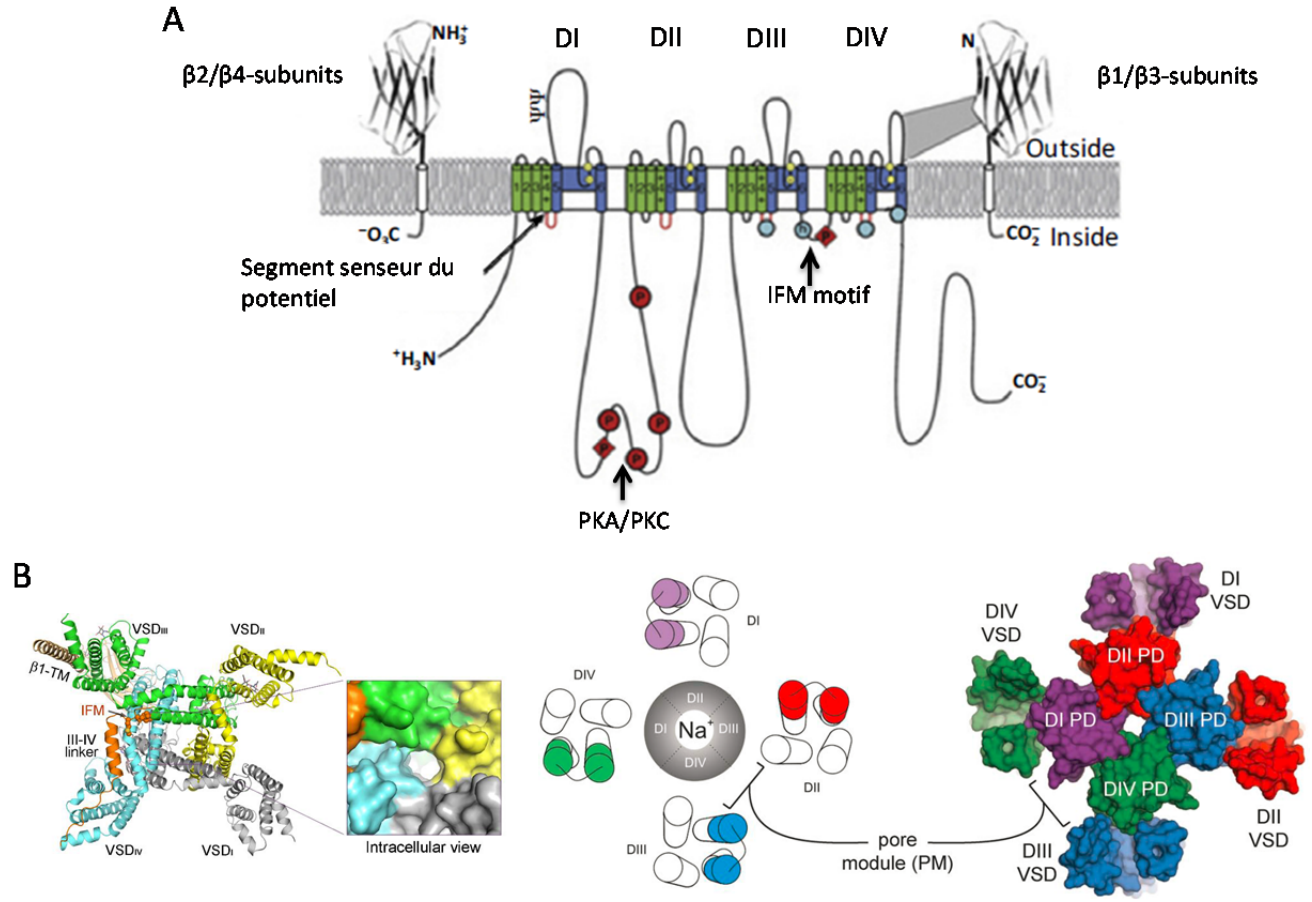

Figure 1-4. Structure architecturale des canaux Na_V (d'après Catterall & Swanson, 2015; Ahern et al., 2016; Tibbs et al., 2016; Pan et al., 2018). (**A**) Organisation transmembranaire du canal sodium avec la sous-unité α au centre constituée de 4 domaines transmembranaires (DI à DIV) à 6 segments entourée par les sous-unités β auxiliaires se liant soit par des ponts disulfures (matérialisés par le rectangle gris, β1 ou β3) ou bien soit des liaisons hydrogènes (β2 ou β4). Le segment 4 par la présence d'arginine (R) est le segment senseur du potentiel, en bleu le segment S5-S6 constitue le pore module. Le motif IFM permet l'inactivation rapide du courant en se fixant sur les points gris bleutés adjacents. Ces canaux sont phosphorylés par des PKA et PKC. (**B**) À gauche, structure obtenue en Cryo-ME (3,2 Å de résolution) du complexe musculaire humain $Na_V1.4/β1$. Au milieu, vue schématique du dessus du canal Na_V eucaryotes dont la boucle extracellulaire S3b-S4 des parties VSD est colorée différemment en fonction du domaine. Les ions sodium passent par le pore, module formé par les parties PD de chaque domaine. À droite, vue supérieure du canal Na_VAb coloré de façon à mettre en évidence l'arrangement décalé, dit "domain-swapped", des parties VSD de chaque domaine par rapport à leur partie PD pour tous les canaux ioniques dépendants du potentiel.

Tableau 1-1. Matrice d'identité en pourcentage des sous-unités α des sous-types de Na_V humains. Les alignements de séquence multiple de haute qualité ont été réalisés grâce à CLUSTAL Oméga, version 1.2.3 (version Web).

Subtypes	$hNa_V1.1$	$hNa_V1.2$	$hNa_V1.3$	$hNa_V1.4$	$hNa_V1.5$	$hNa_V1.6$	$hNa_V1.7$	$hNa_V1.8$	$hNa_V1.9$	hNa_V1
$hNa_V1.1$	100.00	86.65	83.23	61.50	59.53	74.12	75.88	53.57	44.56	
$hNa_V1.2$	86.65	100.00	87.02	63.02	60.46	74.89	77.11	54.22	45.35	
$hNa_V1.3$	83.23	87.02	100.00	62.28	60.57	73.44	75.22	54.01	45.39	
$hNa_V1.4$	61.50	63.02	62.28	100.00	58.02	60.32	60.33	52.58	46.53	
$hNa_V1.5$	59.53	60.46	60.57	58.02	100.00	59.39	58.39	60.93	48.07	31.69
$hNa_V1.6$	74.12	74.89	73.44	60.32	59.39	100.00	69.69	53.51	44.90	
$hNa_V1.7$	75.88	77.11	75.22	60.33	58.39	69.69	100.00	53.54	45.92	
$hNa_V1.8$	53.57	54.22	54.01	52.58	60.93	53.51	53.54	100.00	48.44	
$hNa_V1.9$	44.56	45.35	45.39	46.53	48.07	44.90	45.92	48.44	100.00	

UniprotKB entry identifier (UEI) - Human (homo sapiens)

UEI	P35498	Q99250	Q9NY46	P35499	Q14524	Q9UQD0	Q15858	Q9Y5Y9	Q9UI33
Gene	SCN1A	SCN2A	SCN3A	SCN4A	SCN5A	SCN8A (MED)	SCN9A	SCN10A	SCN11A
Protein	hNav1.1	hNav1.2	hNav1.3	hNav1.4	hNav1.5	hNav1.6	hNav1.7	hNav1.8	hNav1.9

Au niveau de la structure tridimensionnelle, la partie VSD est positionnée en décalage par rapport à la partie PD d'un même domaine ("domain-swapped arrangement") (Figure 1-4B). En fonction du temps et du potentiel de membrane, les canaux Na_V peuvent être successivement dans les 3 états fonctionnels suivants: *(i)* l'état de repos (état fermé), *(ii)* l'état activé (état ouvert) et *(iii)* l'état inactivé (état fermé). L'inactivation du canal est due à une boucle intracellulaire, nommée "la boucle d'inactivation" ou "IFM" (pour "isoleucine-phénylalanine-méthionine"), située entre DIII et DIV qui bouche le pore (Figure 1-4A).

Il existe 9 sous-unités α1 à l'origine de 9 sous-types de canaux sodium ($Na_V1.1$-1.9) classés par leur sensibilité à la tétrodotoxine (TTX), une toxine extraite de certaines espèces de poissons, les tétrodons. Un dixième leur est associé, le canal Na_X qui, comme le canal sodium de fuite (NALCN pour "sodium leak channel"), n'est cependant pas dépendant du potentiel mais de la concentration d'ions sodium (Hiyama et al., 2002; Snutch & Monteil, 2007). Les gènes codant pour la sous-unité α des sous-types $Na_V1.1$-1.3 et 1.7 de canaux sodium sensibles à la tétrodotoxine (TTX-S) sont localisés sur le bras long du chromosome 2 (2q23-24 plus précisément) d'où leur fort pourcentage d'identité (75,22% à 87,02% d'identité de séquence entre eux). Le gène codant pour la sous-unité α des sous-types $Na_V1.4$ et $Na_V1.6$ de canaux sodium TTX-S sont localisés sur le bras long du chromosome 17 (17q23-25) et 12 (12q13), respectivement, avec un pourcentage d'identité moyen (60,33% et 74,90% avec les gènes des Na_V du chromosomes 2) alors que les gènes codant pour la sous-unité α des sous-types $Na_V1.5$ et $Na_V1.8$-1.9 de canaux sodium résistants à la tétrodotoxine (TTX-R) sont localisés sur le bras court du chromosome 3 (3p21-24) d'où un pauvre pourcentage d'identité (44,56% et 60,57% avec les gènes des Na_V du chromosomes 2) (Tableau 1-1). Il est à noter que des différences existent

sur le pourcentage d'identité des séquences citées ci-après et ceux de la littérature due à des versions de Clustal différentes. La version Clustal oméga étant plus récente, elle est plus rapide et en constante évolution. Elle peut aligner des centaines de milliers de séquences en quelques heures et possède une plus grande précision en raison de l'utilisation de méthodes d'alignements progressifs simples améliorées par le modèle probabiliste de Markov caché (HMM pour "Hidden Markov Model"). La version plus classique du logiciel, ClustalW, utilise la consistance des séquences par des méthodes basées sur les matrices (Catterall et al., 2005a).

Les sous-types de canaux sodium ont des profils d'expression tissulaire bien établis au niveau des cellules excitables musculaires et neuronales mais aussi des sites d'expression moins canoniques (Goldin, 2001; Trimmer & Rhodes, 2004; Brackenbury et al., 2012; Black & Waxman, 2013).

Le **$Na_V1.1$**, codé par le gène SCN1A, est exprimé au niveau du système nerveux central (SNC) et périphérique (SNP) ainsi qu'au niveau des kératinocytes et des cellules cancéreuses de l'ovaire.

Le **$Na_V1.2$**, codé par le gène SCN2A, est exprimé au niveau du SNC et SNP ainsi qu'au niveau des fibroblastes, des cellules β des îlots de Langerhans, des odontoblastes, des ostéoblastes et des cellules cancéreuses (du cervix utérin, du mésothéliome, de l'ovaire, de la prostate).

Le **$Na_V1.3$**, codé par le gène SCN3A, est la forme fœtale des sous-unités α qui est exprimé au niveau du SNC et SNP en cas de lésion. Il est aussi retrouvé au niveau des fibroblastes, des cellules β des îlots de Langerhans et des cellules cancéreuses (de l'ovaire, de la prostate, du cancer du poumon à petite cellules).

Le **$Na_V1.4$**, codé par le gène SCN4A, est exprimé au niveau du tissu musculaire squelettique, ainsi qu'au niveau des cellules endothéliales, des globules rouges et des cellules cancéreuses (du cervix utérin, de l'ovaire et de la prostate).

Le **$Na_V1.5$**, codé par le gène SCN5A, est exprimé au niveau du tissu musculaire lisse cardiaque et squelettique fœtal ou dénervé ainsi qu'au niveau des cellules endothéliales, des globules rouges et des cellules cancéreuses (du cancer du sein, du colon, du lymphome, et du neuroblastome dont c'est le sous-type majoritaire, du cancer du poumon à petites cellules ou non à petites cellules et du cancer de l'ovaire).

Le **$Na_V1.6$**, codé par le gène SCN8A, est exprimé au niveau du SNC et SNP ainsi qu'au niveau des fibroblastes, kératinocytes, macrophages, cellules endothéliales, et des cellules cancéreuses (du cancer du sein, du cervix utérin, du lymphome, du mélanome, du mésothéliome, du cancer du poumon non à petites cellules, du cancer de la prostate, du cancer du poumon à petites cellules).

Le **$Na_V1.7$**, codé par le gène SCN9A, est exprimé au niveau du SNC et SNP ainsi qu'au niveau du tissu musculaire lisse, de la prostate, des progéniteurs érythroïdes, des fibroblastes, des cellules immunitaires et des cellules cancéreuses (du cancer du sein, du cervix utérin, du lymphome, du mésothéliome, du cancer du poumon non à petites cellules, du cancer de l'ovaire et du cancer de la prostate pour lequel le sous-type $Na_V1.7$ est la forme prédominante).

Le **$Na_V1.8$**, codé par le gène SCN10A, est exprimé au niveau du SNC et du SNP, ainsi qu'au niveau des cellules endothéliales, des fibroblastes, des kératinocytes et des lymphocytes T.

Le **$Na_V1.9$**, codé par le gène SCN11A, est exprimé au niveau du SNC et SNP ainsi qu'au niveau des cellules endothéliales, des fibroblastes et des lymphocytes T mais aussi au niveau des cellules cancéreuses (de lymphome et du cancer du poumon à petites cellules).

Le **Na_X**, codé par le gène SCN7A, est un sous-type de canal sodium qui n'est pas dépendant du potentiel mais de la concentration extracellulaire de sodium (Hiyama et al., 2002). Il est exprimé au niveau du SNC et SNP ainsi qu'au niveau du poumon, de l'utérus et du cœur.

Les canaux Na_V sont sélectifs aux ions sodium mais aussi aux ions lithium. Les sous-types TTX-S ont des cinétiques d'activation et d'inactivation relativement rapides comparées à celles des sous-types TTX-R. De plus, les cinétiques d'activation et d'inactivation du sous-type TTX-R $Na_V1.9$ sont particulièrement lentes comparées à celles des deux autres sous-types TTX-R $Na_V1.5$ et 1.8. La dépendance vis-à-vis du potentiel de l'activation des sous-types TTX-S est similaire à celle du sous-type TTX-R $Na_V1.5$ mais est déplacée vers des potentiels plus négatifs d'environ 15-30 mV comparée à celle du sous-type $Na_V1.8$, et plus positifs d'environ 10-25 mV comparée à celle du sous-type $Na_V1.9$. En revanche, la dépendance vis-à-vis du potentiel de l'inactivation des sous-types TTX-S est déplacée vers des potentiels plus positifs d'environ 10-20 mV comparée à celle du sous-type $Na_V1.5$, et plus négatifs d'environ 15-30 mV comparée à celles des sous-types $Na_V1.8$ et 1.9 (Figure 1-5a; Deuis et al., 2017; Inserra et al., 2017). De ce fait, la superposition des courbes d'activation et d'inactivation en fonction du potentiel des sous-types TTX-R laisse apparaitre une "fenêtre de courant" à des potentiels physiologiques (entre -70 et -40 mV) pour lesquels le courant est persistant, ce qui permet à la membrane d'atteindre la valeur "seuil" de déclenchement des potentiels d'action qui apparaissent donc de façon spontanée, comme cela est le cas au niveau cardiaque pour le sous-type $Na_V1.5$ et au niveau neuronal pour le sous-type $Na_V1.8$ (Figure 1-5b et c).

Les sous-unités β auxiliaires sont des protéines transmembranaires, membres de la famille des protéines d'adhésion cellulaire (CAM pour "cell-adhesion molecules") ayant un domaine extracellulaire de type immunoglobuline (Ig) et permettant, comme les protéines propres à cette

famille, l'interaction cellule-cellule (Figure 1-4a; Barbosa et al., 2015). Elles sont au nombre de 4. Les sous-unités β1 et β3, codées par les gènes SCN1B et SNC3B respectivement, se lient de façon covalente et les sous-unités β2 et β4, codées par les gènes SCN2B et SNC4B, se lient par des liaisons hydrogènes.

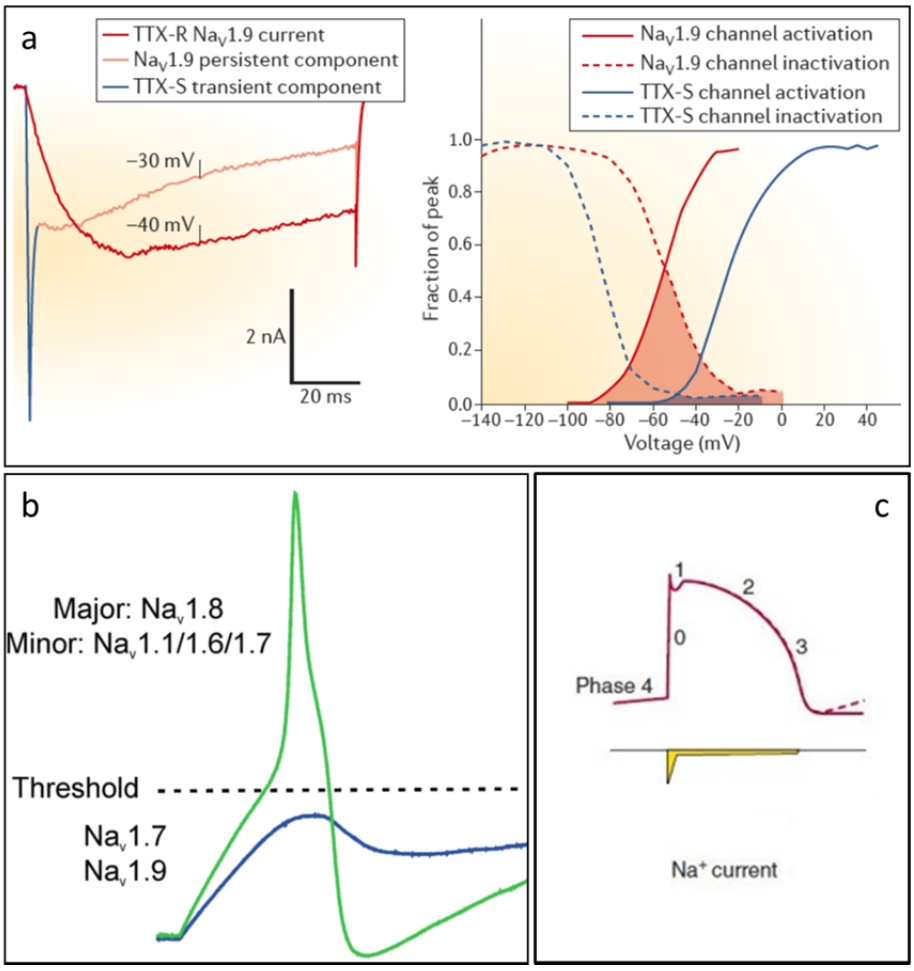

Figure 1-5. Propriétés biophysiques et implication dans la genèse du potentiel d'action neuronal ou cardiaque des différents sous-types de canaux sodium. (**a, gauche**) Courant sodium persistant TTX-R médié par le sous-type Na$_V$1.9 et, à des fins de comparaison, le courant sodium TTX-S médié par les sous-types Na$_V$1.6 et/ou Na$_V$1.7, enregistrés à partir des petits neurones de ganglions de la racine dorsale (DRG) d'une souris knock-out pour le gène codant le sous-type Na$_V$1.8 (absence du courant TTX-R lent médié par ce sous-type). Les courants ont été enregistrés au cours d'impulsions dépolarisantes de 100 ms à -30 ou -40 mV à partir d'un potentiel de maintien de −120 mV. Il est à noter l'activation et l'inactivation rapide du courant TTX-S par rapport à l'activation lente et l'inactivation très lente du Na$_V$1.9. (**a, droite**) Le sous-type Na$_V$1.9 s'active à des valeurs de potentiel plus négatives et s'inactive à des valeurs de potentiels plus positives que les sous-types TTX-S. En conséquence, il existe un "courant de fenêtre" persistant, médié par le sous-type Na$_V$1.9, dans la gamme de potentiels proche du potentiel membranaire de repos des neurones (−70 à −40 mV). D'après Dib-Hajj et al. (2015). (**b**) Sous-types de canaux Na$_V$ impliqués dans le potentiel d'action (PA) neuronal sain. Les sous-types Na$_V$1.7 et 1.9 seraient des canaux sodium de "seuil" qui mèneraient le potentiel de repos au potentiel "seuil" avant que le sous-type Na$_V$1.8 ne permette le dépassement de cette valeur "seuil" et l'apparition d'un PA, les sous-types Na$_V$1.1, 1.6 et 1.7 ne jouant qu'un rôle mineur dans le PA. En cas de lésion, le sous-type Na$_V$1.3 prend le relais aux deux niveaux (d'après Rush et al., 2007). (**c**) Potentiel d'action cardiaque ventriculaire composé de 5 phases mettant en jeu le courant I_{Na+}, médié par le sous-type Na$_V$1.5, contribuant principalement à la phase 0 et, en ne s'inactivant pas complètement, participant à maintenir le "plateau" (phase 2) du potentiel d'action avec le sous-type Ca$_V$1.2 de canal calcium (adapté de Nerbonne & Kass, 2005).

Excepté le SCN1B qui est localisé sur le chromosome 19, les autres le sont sur le chromosome 11. Ces unités β ont un grand impact sur les sous-unités α puisqu'elles favorisent leur expression, leur localisation subcellulaire et leur déplacement membranaire, et modulent fortement leurs propriétés biophysiques, *i.e.* cinétiques et dépendance vis-à-vis du potentiel de l'activation et de l'inactivation des canaux sodium, et pharmacologiques (Xie et al., 2016).

Tout comme les sous-unités α, les sous-unités β sont hautement exprimées de façon variable selon le type cellulaire au niveau du SNC, SNP ainsi qu'au niveau des muscles squelettiques et cardiaques mais aussi au niveau de cellules non-excitables comme les astrocytes, la glie radiale, les cellules vasculaires endothéliales et les cellules cancéreuses (du cancer du sein, du cervix utérin, du cancer du poumon non à petites cellules, de la prostate) (Brackenbury & Isom, 2011; Brackenbury et al., 2012; Winters et al., 2017). Par exemple, au niveau des neurones des ganglions de la racine dorsale (DRG pour "dorsal root ganglia"), l'expression des 4 sous-unités β est variable et modulera donc le message différemment (Lopez-Santiago et al., 2006; Ho et al., 2012) (Figure 1-6).

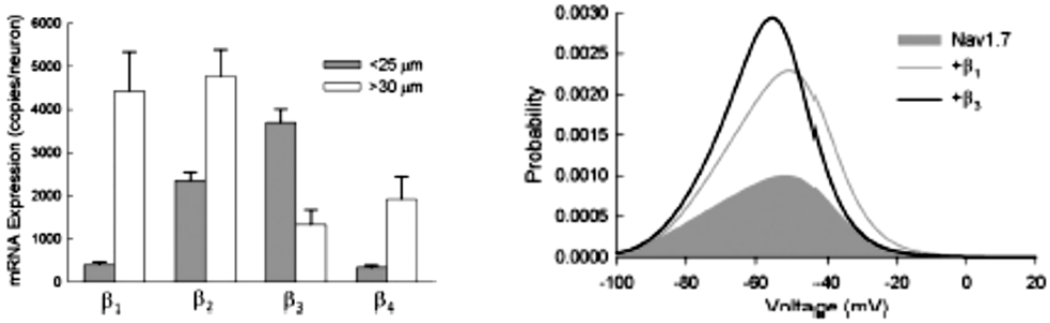

Figure 1-6. Influence des sous-unités β hautement exprimés au niveau des petits ou grands neurones de DRG sur le courant $Na_V1.7$. À gauche, taux d'expression des ARN messagers des 4 sous-unités β en fonction de la taille des neurones extraits des DRG et à droite, probabilité de courant $Na_V1.7$ spontané et persistant en fonction du potentiel imposé en la présence ou non des sous-unités β1 ou β3 (Ho et al., 2012).

Les sous-unités α de canaux sodium impliquées dans la douleur sont $Na_V1.1$, 1.3, 1.6, 1.7 et Na_X (Gonçalves et al., 2018a). Concernant les sous-unités β, malgré la forte expression des sous-unités β2 et β3, il semblerait que la sous-unité β4 par son association à $Na_V1.6$ jouerait un rôle crucial dans l'apparition des courants résurgents et serait donc plus impliquée dans la douleur pathologique chronique (Barbosa et al., 2015).

1.1.2. Canaux potassium

Les canaux K_V sont composés d'un tétramère de 4 sous-unités α associées à des sous-unités β, le ratio étant variable.

Les sous-unités α d'environ 50 à 135 kDa, formant le pore, s'assemblent en homotétramère (sous-types identiques) ou hétérotétramère (sous-types non identiques) et ressemblent chacune à un domaine du canal Na_V, regroupant 6 segments transmembranaires hydrophobes reliés entre eux par des boucles intra- et extracellulaires dont les 4 premiers (S1-S4) forment le VSD et sont senseurs du potentiel membranaire alors que les deux derniers (S5-S6), reliés par la boucle P, forment le pore du canal (Figure 1-7). Les segments du VSD sont arrangés en décalage par rapport aux segments du pore ("domain-swapped arrangement") comme décrit pour tous les canaux ioniques (Catterall et al., 2017). L'activation du canal est assurée par le segment 4 du VSD, chargé positivement, des 4 sous-unités α (par la présence d'arginines). La tétramérisation des 4 sous-unités α est consolidée par l'association de sous-unités β à leur partie N-terminale, ce qui modifie les propriétés du canal (Bahring et al., 2001). Il y a donc une grande diversité de complexes moléculaires ayant des propriétés biophysiques et pharmacologiques différentes.

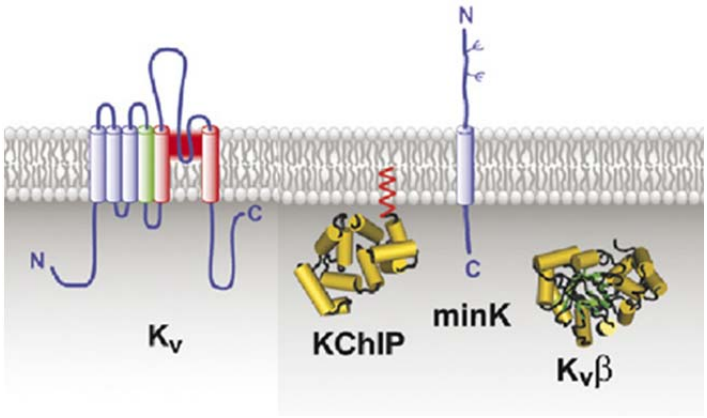

Figure 1-7. Les sous-unités des canaux potassium dépendants du potentiel (Catterall et al., 2007). Le monomère α du canal K_V et les trois types de sous-unités β ($K_V\beta$, KChIp, minK). Les cylindres correspondent aux hélices α transmembranaires; en rouge, les segments S5-S6; en vert le segment S4; en bleu, les segments S1-S3). Les glycosylations protéiques sont annotées avec la lettre grecque suivante: ψ.

C'est une famille de 40 membres, classés en 12 sous-familles (K_V1.x-K_V12.x), qui représente plus de 25% de la superfamille des canaux ioniques dépendants du potentiel (Catterall et al., 2007; Wulff et al., 2009; Alexander et al., 2017). La localisation chromosomique du gène qui encode chacune de ces 40 sous-unités ainsi que leur pattern d'expression témoignent d'une hétérogénéité des sous-unités α (Tableau 1-2). D'un point de vue électrophysiologique, on peut les classer aussi en 6 groupes, les canaux à rectification retardée qui s'inactivent lentement ou pas du tout (K_V1.1-3, K_V1.5-8, K_V2, K_V3;1-2, K_V7.1-5, K_V10.1), les canaux potassium de type A qui s'inactivent rapidement (K_V1.4, K_V3.3-4, K_V4.1-3), les canaux à rectification sortante (K_V10.2), les canaux à rectification entrante (K_V11.1-3), les canaux s'activant lentement (K_V12.1-3) et les canaux « silencieux » (K_V5.1, K_V6.1-4, K_V8.1-2, K_V9.1-3). Ils sont impliqués dans la repolarisation de la membrane lors d'un potentiel d'action (Figure 1-8).

D'un point de vue pharmacologique, des substances inhibent les canaux potassium telles que l'ion tétraéthylammonium (TEA), la 4-aminopyridine (4-AP) ou encore certaines dendrotoxines. D'autres, telles que la régitabine (K_V7.1), l'activent.

Tableau 1-2. Site d'expression, nom et localisation chromosomique du gène des 40 sous-unités α des canaux potassium dépendants du potentiel. Adapté de Wulff et al. (2009).

Protein	Gene	Gene location	Expression
K_V1.1	KCNA1	12p13	CNS (medulla, pons, cerebellum, midbrain, hippocampus, auditory nuclei), Node of Ranvier Kidney
K_V1.2	KCNA2	1p13	CNS (pons, medulla, cerebellum, hippocampus, thalamus, cerebral cortex), spinal cord
K_V1.3	KCNA3	1p13	T and B cells, macrophages, microglia, osteoclasts, platelets, CNS (prominent in olfactory bulb), testis
K_V1.4	KCNA4	11p14	CNS (olfactory bulb, corpus striatum, hippocampus), heart, skeletal and smooth muscle, pancreatic islets
K_V1.5	KCNA5	12p13	cardiac myocytes (IKur), CNS (hippocampus, cortex, pituitary), microglia, Schwann cells, macrophages vascular smooth muscle
K_V1.6	KCNA6	12p13	Spinal cord, CNS, oligodendrocyte progenitor cells, astrocytes, pulmonary artery smooth muscle
K_V1.7	KCNA7	19p13	Heart, skeletal muscle, liver, lung, placenta, CNS
K_V1.8	KCNA10	1p13	Kidney, CNS, heart, skeletal muscle
K_V2.1	KCNB1	20q13	CNS (cerebral cortex, hippocampus, cerebellum), pancreatic beta cells, insulinomas, gastric cancer cell
K_V2.2	KCNB2	8q21	CNS (olfactory bulb, cortex, hippocampus, cerebellum), pancreatic delta cells
K_V3.1	KCNC1	11p15	CNS (cerebellum, substantia nigra, cortical and hippocampal interneurons, inferior colliculi, cochlear and vestibular nuclei), skeletal muscle, mouse CD8+T cells
K_V3.2	KCNC2	12q21	CNS (fast spiking GABAergic interneurons), pancreatic islets, Renshaw cells (spinal interneurons), pancreatic beta cells
K_V3.3	KCNC3	19q13	CNS (brainstem, cerebellum, forebrain, Purkinje cells, motorneurons, auditory brainstem)
K_V3.4	KCNC4	1p13	CNS (brainstem, hippocampal granule cells), skeletal muscle
K_V4.1	KCND1	Xp11	CNS, heart, liver, kidney, thyroid gland, pancreas
K_V4.2	KCND2	7q31	CNS (cerebellum, hippocampus, thalamus, forebrain, dorsal horn neurons), heart [rodents]
K_V4.3	KCND3	1p13	Heart, CNS (cortex, cerebellum), atrial and ventricular myocytes (Ito) smooth muscle
K_V5.1	KCNF1	2p25	-
K_V6.1	KCNG1	20q13	-
K_V6.2	KCNG2	18q23	-
K_V6.3	KCNG3	2p21	-
K_V6.4	KCNG4	16q24	-
K_V7.1	KCNQ1	11p15	Heart, ear, skeletal muscle, liver, epithelia in kidney, lung, gastrointestinal tract
K_V7.2	KCNQ2	20q13	CNS (hippocampus, cortex, thalamus, cerebellum, brain stem, nodes of Ranvier); sympathetic and dorsal root ganglia
K_V7.3	KCNQ3	8q24	CNS (hippocampus, cortex, thalamus, cerebellum, brain stem), nodes of Ranvier; sympathetic and dorsal root ganglia
K_V7.4	KCNQ4	1p34	Outer hair cells and neurons of auditory system, vascular smooth muscle
K_V7.5	KCNQ5	6q13	CNS (hippocampus, cortex, thalamus), skeletal muscle, vascular smooth muscle
K_V8.1	KCNV1	8q23	-
K_V8.2	KCNV2	9p24	-
K_V9.1	KCNS1	20q13	-
K_V9.2	KCNS2	8q22	-
K_V9.3	KCNS3	2p24	-
K_V10.1	KCNH1, eag-1	1q32	CNS
K_V10.2	KCNH5, eag-2	14q23	CNS, muscle, heart, placenta, lung, liver, kidney, pancreas
K_V11.1	KCNH2, erg-1, HERG	7q36	Heart, CNS, endocrine cells, lymphocytes
K_V11.2	KCNH6, erg-2	17q23	CNS, endocrine cells
K_V11.3	KCNH7, erg-3	2q24	CNS
K_V12.1	KCNH8, elk-1	3p24	CNS
K_V12.2	KCNH3, elk-2	12q13	CNS
K_V12.3	KCNH4, elk-3	17q21	CNS

Les complexes moléculaires de sous-unités α peuvent également être associés à divers types de sous-unités auxiliaires β (K_Vβ1-3, KChIp1-4, minK1-5), ce qui permet de modifier leurs propriétés. De

plus, la sous-unité β1 des canaux Na_V peut aussi moduler les propriétés biophysiques des sous-types K_V1.1, 1.2, 1.3, 1.6, 4.2 et 7.2 (Nguyen et al., 2012; Marionneau et al., 2012).

Tout comme les sous-unités β des canaux calcium, les sous-unités auxiliaires Kvβ (≈40-45 kDa) des canaux potassium sont cytoplasmiques mais avec une séquence en acide aminés et une structure complétement différentes. Les sous-unités auxiliaires KChIp (≈30 kDa), sont membres de la famille des protéines régulatrices calciques neuronales, comme la calmoduline, et ont quatre motifs main EF ("EF hand").

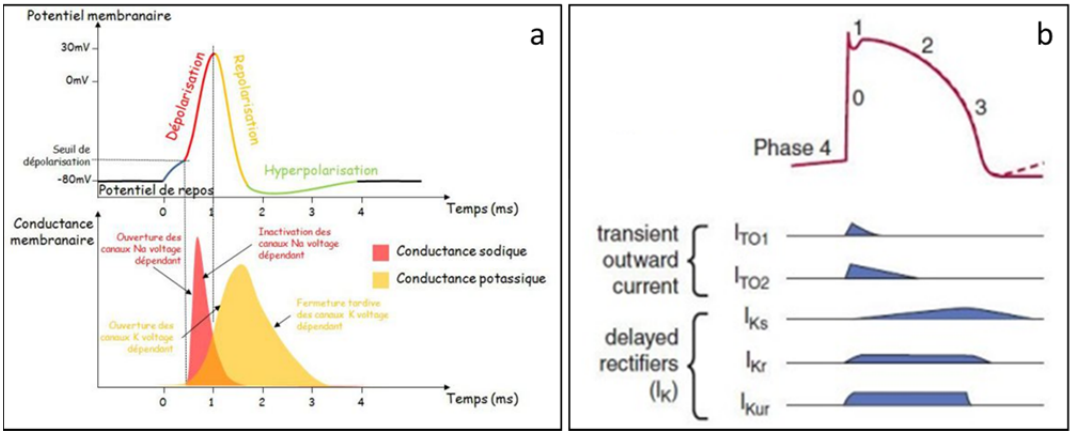

Figure 1-8. Rôle des canaux potassium dépendants du potentiel. (**a**) Potentiel d'action (PA) axonal. La conductance potassium est responsable de la repolarisation et de l'hyperpolarisation du PA avec la fermeture des canaux Na_V. (http://ressources.unisciel.fr/physiologie/co/grain3b_1.html). (**b**) PA cardiaque ventriculaire. La conductance potassium générée par les courants I_{TO1} (K_V4.3) et I_{TO2} (K_V1.4), I_{Ks} (K_V7.1), I_{Kr} (K_V11.1), I_{Kur} (K_V1.5) permet de rythmer correctement la repolarisation du PA cardiaque (adapté de Nerbonne et Kass, 2005).

Les sous-unités auxiliaires minK (≈11-23 kDa) sont des glycoprotéines avec un seul segment transmembranaire (Figure 1-7). Les sous-unités auxiliaires K_Vβ1-3, codées par les gènes KCNAB1-3, sont localisées sur les chromosomes 3q25, 1p36 et 17p13 respectivement. Les sous-unités auxiliaires KChIp1-4, codées par les gènes KCNIP1-4, sont localisées sur les chromosomes 5q35, 10q24, 2q11 et 4p15, respectivement. Quant aux sous-unités auxiliaires minK1-5 codées par les gènes KCNE1-5, elles sont localisées sur les chromosomes 21q22, 21q22, 11q13, 2q36 et Xq23, respectivement. Des mutations de cette sous-unité seraient à l'origine d'arythmies cardiaques graves telles que certaines formes du syndrome du QT long. Concernant leur fonctions respectives, l'association des sous-unités auxiliaires K_Vβ aux sous-types Kv1 conduit à la formation d'un second tétramère symétrique qui joue le rôle de porte d'inactivation au niveau de la face intracellulaire du canal. L'association des sous-unités auxiliaires KChIp aux sous-types K_V4 résulte en une augmentation de leur expression au niveau de la membrane cellulaire et en une altération de leurs propriétés fonctionnelles. Quant aux sous-unités auxiliaires minK, ce sont des régulateurs fonctionnels importants des sous-types K_V7, mais aussi K_V3, K_V4, K_V10 et K_V11.

Les sous-types de canaux K_V impliqués dans la douleur sont les sous-types $K_V1.4$, $K_V3.4$ et K_V4, mais aussi les sous-types $K_V9.1$/$K_V2.1$, K_V7 et $K_V1.2$ dans le cadre de douleur due à des neuropathies traumatiques (Wang et al., 2017b; Zemel et al., 2018).

1.1.3. Canaux calcium

Les canaux Ca_V sont constitués de 5 sous-unités avec un ratio stœchiométrique: une sous-unité α1 (190 kDa), une glycoprotéine composée d'un dimère de deux sous-unités α2 et δ reliées par des ponts disulfures (170 kDa), une sous-unité β intracellulaire (55 kDa) et une sous-unité de glycoprotéine γ transmembranaire (33 kDa) (Figure 1-9).

La sous-unité α1 des canaux Ca_V s'organise comme la sous-unité α1 des canaux Na_V, soit 4 domaines divisés en 6 segments transmembranaires dont les 4 premiers (S1-S4) forment le VSD et les deux derniers (S5-S6), reliés par la boucle P, forment le pore du canal. L'arrangement des 2 parties de chaque domaine est en décalage. Cependant, elle possède une partie C-terminale beaucoup plus longue que celle des canaux sodium dont la fonction reste inconnue et dont des variants d'épissage existent (Figure 1-2). Il en existe 10, divisées en trois superfamilles de canaux calcium, les canaux à haut seuil d'activation (HVA) Ca_V1 de type L ("long lasting"), les canaux Ca_V2 neuronaux à seuil intermédiaire d'activation (IVA) de types N, P/Q et R et les canaux à bas seuil d'activation (LVA) Ca_V3 de type T (pour "transient" ou "tiny") (Lory et al., 2006; Catterall et al., 2011; Zamponi et al., 2015).

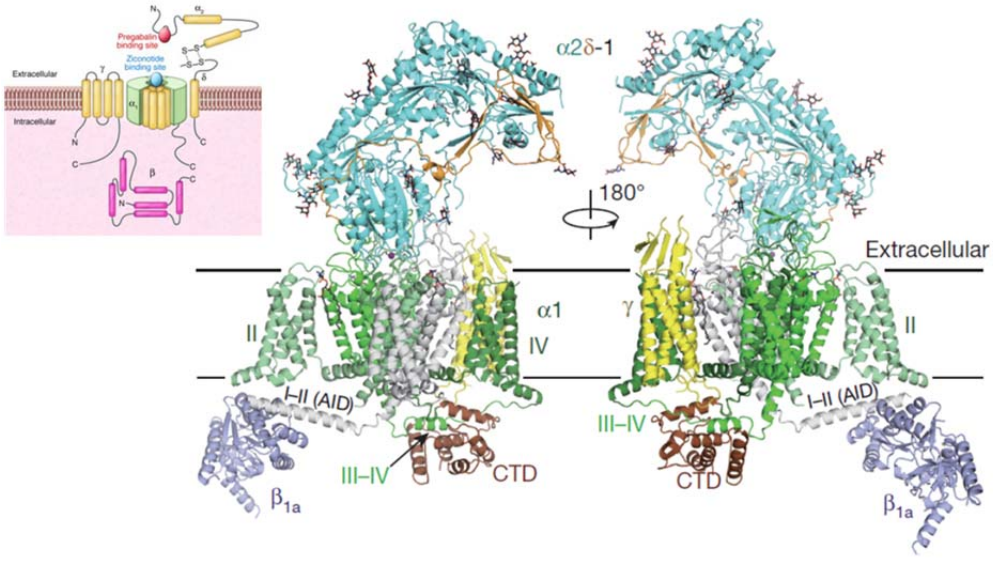

Figure 1-9. Structure globale du sous-type $Ca_V1.1$ de canal calcium de lapin associé à ses 4 sous-unités auxiliaires à une résolution de 3.6 Å (Cryo-ME). Les groupements glycosyl sont indiqués en bâtonnets noirs sur la sous-unité α2δ. La partie C-terminale (CTD pour "carboxy-terminal domain") forme un domaine globulaire avec la boucle DIII-DIV, la sous-unité β1a interagit avec le domaine d'interaction à la sous-unité α1 (AID pour "α1-subunit Interacting Domain") qui est une extension du S6 du DI (Wu et al., 2016). Dans le coin en haut à gauche, une représentation schématique de la structure où sont mentionnés les sites de fixation du ziconotide et du prégabaline.

En plus du classement par leur fonction, les différents sous-types de canaux calcium peuvent être aussi classés en fonction de l'homologie de leur séquence. Il existe 4 sous-types appartenant à la superfamille Ca_V1, $Ca_V1.1$-1.4 codés par des gènes localisés sur les chromosomes 1q32, 12p13, 3p14 et Xp11 respectivement, partageant un fort pourcentage d'identité entre eux (entre 54,51 et 63,66%). Les membres de la superfamille Ca_V2, $Ca_V2.1$-2.3 codés par des gènes localisés sur les chromosomes 19p13, 9p34 et 1q25-q31 respectivement, partagent un fort pourcentage d'identité entre eux (entre 53,97 et 59,43%). Ceux de la superfamille Ca_V3, $Ca_V3.1$-3.3 codés par des gènes localisés sur les chromosomes 17p22, 16p13 et 22q11 respectivement, présentent un pourcentage d'identité entre eux permettant de les classer ensemble (entre 48,60 et 51,08%). Les superfamilles Ca_V1 et Ca_V2 partagent environ 30% d'identité de séquence alors que la superfamille Ca_V3 possède environ 20% d'identité de séquence avec les deux autres superfamilles, tout comme les canaux Ca_V comparés aux canaux Na_V quelle que soit la superfamille étudiée (Tableau 1-3).

Tableau 1-3. Matrice d'identité en pourcentage des sous-unités α des sous-types de Ca_V humain. Les alignements de séquence multiple de haute qualité ont été réalisés grâce à CLUSTAL Oméga, version 1.2.3 (version Web). Les traits noirs délimitent les 3 superfamilles de canaux Ca_V.

Subtypes	hCav1.1	hCav1.2	hCav1.3	hCav1.4	hCav2.1	hCav2.2	hCav2.3	hCav3.1	hCav3.2	hCav3.3	hCav1, hCav2, hCav3
hCav1.1	100.00	54.99	55.08	54.51	31.31	32.85	32.57	19.77	20.28	21.55	
hCav1.2	54.99	100.00	63.66	55.02	31.82	33.31	32.54	19.75	19.26	20.85	
hCav1.3	55.08	63.66	100.00	59.95	32.03	33.36	31.83	19.88	20.17	20.22	
hCav1.4	54.51	55.02	59.95	100.00	30.83	34.47	32.45	20.78	20.54	21.90	
hCav2.1	31.31	31.82	32.03	30.83	100.00	59.43	53.97	19.81	18.54	19.83	7.54
hCav2.2	32.85	33.31	33.36	34.47	59.43	100.00	54.33	21.15	20.32	21.13	
hCav2.3	32.57	32.54	31.83	32.45	53.97	54.33	100.00	20.01	20.12	20.23	
hCav3.1	19.77	19.75	19.88	20.78	19.81	21.15	20.01	100.00	51.22	48.60	
hCav3.2	20.28	19.26	20.17	20.54	18.54	20.32	20.12	51.22	100.00	51.08	
hCav3.3	21.55	20.85	20.22	21.90	19.83	21.13	20.23	48.60	51.08	100.00	

UniprotKB entry identifier (UEI) - Human (homo sapiens)

UEI	Q13698	Q13936	Q01668	O60840	O00555	Q00975	Q15878	O43497	O95180	Q9P0X4
Gene	CACNA1S	CACNA1C	CACNA1D	CACNA1F	CACNA1A	CACNA1B	CACNA1E	CACNA1G	CACNA1H	CACNA1I
Protein	hCav1.1	hCav1.2	hCav1.3	hCav1.4	hCav2.1	hCav2.2	hCav2.3	hCav3.1	hCav3.2	hCav3.3

Les sous-types de canaux calcium ont des profils d'expression tissulaire bien établis au niveau des cellules excitables musculaires et neuronales et une pharmacologie moléculaire bien définie (Catterall et al., 2005b; 2011; Sousa et al., 2013; Zamponi et al.,2015).

Le **$Ca_V1.1$**, de type L, codé par le gène CACNA1S, est exprimé au niveau du muscle squelettique et des tubules transverses plus particulièrement.

Le **$Ca_V1.2$**, de type L, codé par le gène CACNA1C, est exprimé au niveau des cardiomyocytes, des muscles lisses intestinaux et de la vessie, des cellules endocriniennes, des corps cellulaires de certains neurones ainsi qu'au niveau des dendrites proximales dans le SNC.

Le **$Ca_V1.3$**, de type L, codé par le gène CACNA1D, est exprimé au niveau des cellules endocriniennes, des corps cellulaires de certains neurones ainsi qu'au niveau des dendrites dans le SNC, au niveau des cardiomyocytes atriales et des cellules "pacemaker" et au niveau des cellulaires

ciliées cochléaires et vestibulaires.

Le **Ca_V1.4**, de type L, codé par le gène CACNA1F, s'exprime au niveau des bâtonnets rétiniens et des cellules bipolaires, de la moelle épinière, de la glande surrénale et des mastocytes.

Le **Ca_V2.1**, de type P/Q, codé par le gène CACNA1A, s'exprime au niveau des dendrites et des terminaisons des neurones et des cellules neuroendocriniennes.

Le **Ca_V2.2**, de type N, codé par le gène CACNA1B, s'exprime au niveau des dendrites et des terminaisons des neurones et des cellules neuroendocriniennes.

Le **Ca_V2.3**, de type R, codé par le gène CACNA1E, s'exprime au niveau des dendrites et des corps cellulaires des neurones et des cardiomyocytes.

Le **Ca_V3.1**, de type T, codé par le gène CACNA1G, s'exprime au niveau des dendrites et des corps cellulaires des neurones du cervelet et du thalamus, ainsi que des cardiomyocytes et des muscles lisses.

Le **Ca_V3.2**, de type T, codé par le gène CACNA1H, s'exprime au niveau des dendrites et des corps cellulaires des neurones, des cardiomyocytes et des muscles lisses, du foie, du rein, du poumon et du pancréas.

Le **Ca_V3.3**, de type T, codé par le gène CACNA1I, s'exprime au niveau des dendrites et des corps cellulaires des neurones.

Les membres de la superfamille Ca_V1 (type L) initient la contraction, la sécrétion, la régulation de l'expression des gènes, l'intégration des entrées synaptiques dans les neurones et la transmission synaptique dans les cellules sensorielles spécialisées. Les membres de la superfamille Ca_V2 (types P/Q, N et R) sont principalement responsables de l'initiation de la transmission synaptique. Les membres de la superfamille Ca_V3 (type T) sont importants pour le déclenchement répétitif des potentiels d'action dans les cellules rythmiques telles que les cardiomyocytes et les neurones du thalamus (Figure 1-10; Catterall et al., 2011).

Sur le plan pharmacologique, des petites molécules, telles que les dihydropyridines, ont permis d'identifier les membres de la superfamille Ca_V1 dans des systèmes natifs. De même, des toxines peptidiques de venins d'animaux, telles que l'ω-agatoxine IVA, l'ω-conotoxine GVIA et l'ω-théraphotoxine-Hg1a (SNX-482), ont permis d'identifier chaque sous-type de canaux Ca_V2. Concernant les membres de la superfamille Ca_V3, il n'y a pas vraiment de bloqueurs sélectifs qui ont permis leur découverte mais il existe des antagonistes tels que le mibéfradile et le pimozide (Tableau 1-4; Catterall et al., 2005b; Sousa et al., 2013).

Bien que la sous-unité α1 soit responsable des principales caractéristiques électrophysiologiques et pharmacologiques, les sous-unités auxiliaires α2δ, β et γ modulent les propriétés d'ouverture et de fermeture du canal.

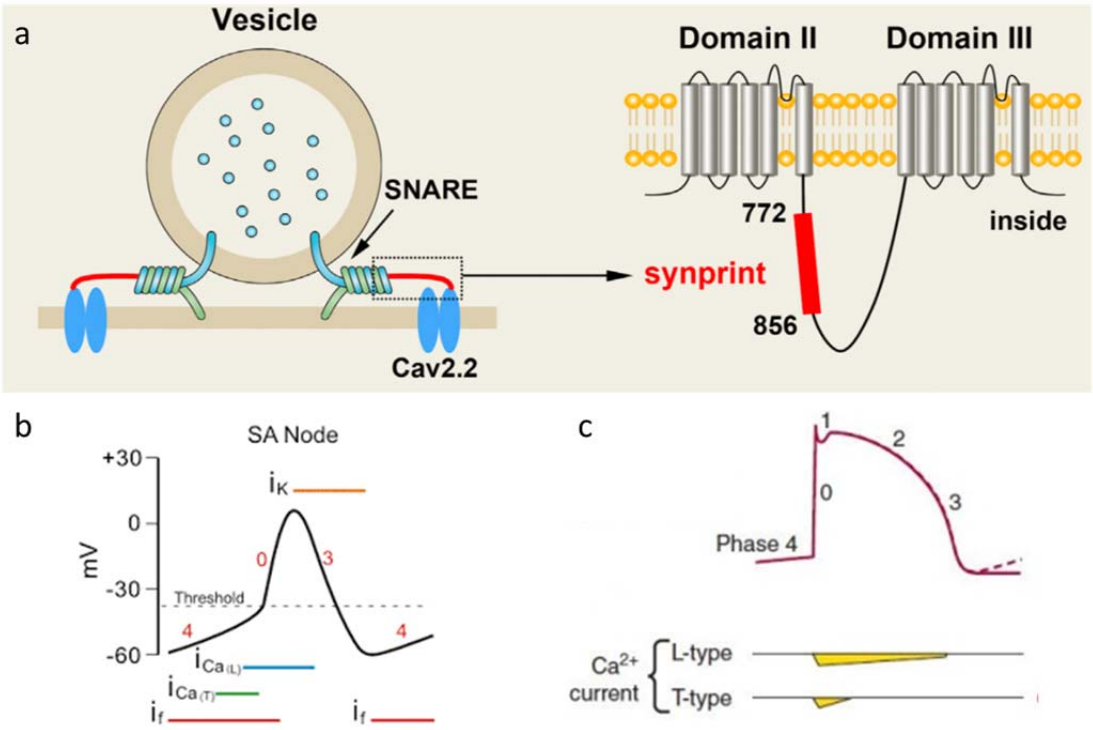

Figure 1-10. Exemple de certaines fonctions des trois superfamilles de canaux calcium Ca_V. (**a**) Rôle des $Ca_V2.2$ dans la transmission synaptique. La région correspondant aux acides aminés 772-856 du sous-type $Ca_V2.2$, nommée "synprint" permet l'arrimage des vésicules à la membrane (Chai et al., 2017).(**b**) Au niveau du nœud sino-atrial, les canaux Ca_V1 et Ca_V3 sont mis en jeu dans la genèse du potentiel d'action (PA) sinusal. La phase ascendante 0 du PA met principalement en jeu les canaux Ca_V1. Les canaux Ca_V3 et Na_V avec l'aide des canaux HCN (responsables du courant I_f) permettent au potentiel d'arriver au potentiel "seuil". Les canaux potassium sont responsables de la phase de repolarisation du PA (https://www.cvphysiology.com/textbook). (**c**) Le PA cardiaque met en jeu le sous-type de canaux Ca_V1 et Ca_V3. Les canaux Ca_V1, qui s'inactivent plus lentement que les canaux Ca_V3, sont responsables du plateau du PA cardiaque (phase2). Les canaux Ca_V3, par leurs propriétés d'activation à des valeurs de potentiel plus négatives, permettent le déclenchement de celui-ci (phase 0-1). Adapté de Nerbonne et Kass (2005).

Quatre gènes CACNA2D1-4 principalement, localisés sur les sites chromosomiques 7q21, 3p21, 3p21-p14 et 12p13 codent respectivement pour les sous-unités auxiliaires α2δ-1, 2, 3 et 4 qui s'expriment de façon ubiquitaire dans les cellules, qu'elles soient excitables (musculaires et neuronales) ou non. On retrouve plus particulièrement dans les neurones les sous-types α2δ-2 et α2δ-3, le sous-type α2δ-4 étant exprimé plutôt au niveau des neurones rétiniens. La sous-unité α2 est une glycoprotéine extracellulaire et extrinsèque à la membrane attachée par des ponts disulfures à celle-ci par la sous-unité δ qui est ancrée à la membrane par un GPI (glycophosphatidylinositol). C'est sur les sous-types de cette sous-unité α2δ-1 et α2δ-2 que se fixent les anti-épileptiques gabapentine et prégabaline pour traiter les douleurs neuropathiques et certaines formes d'épilepsie. Des effets anxiolytiques et antipyrétiques dans un modèle rongeur sont aussi décrits (Field et al.,

2006; Lotarski et al., 2011, Lotarski et al., 2014).

Tableau 1-4. Caractéristiques physiologiques et pharmacologiques des canaux Ca_V. Adapté de Sousa et al. (2013). DHP: Dihydropyridine, PHA: Phénylalkylamine, BTZ: Benzithiazépine, Ni^{2+}:Nickel, Zn^{2+}:Zinc.

	Ca_v subtype	Current type	Antagonist class/Name
HVA	$Ca_v1.1$	L	DHP, PHA, BTZ
HVA	$Ca_v1.2$	L	DHP, PHA, BTZ
HVA	$Ca_v1.3$	L	DHP, PHA, BTZ
HVA	$Ca_v1.4$	L	DHP, PHA, BTZ
IVA	$Ca_v2.1$	P/Q	ω-agatoxin IVA
IVA	$Ca_v2.2$	N	ω-conotoxin CVID, GVIA MVIIA
IVA	$Ca_v2.3$	R	ω-theraphotoxin-Hg1a (SNX-482)
LVA	$Ca_v3.1$	T	Pimozide, mibefradil, TTA-P2, Ni^{2+}, Zn^{2+}
LVA	$Ca_v3.2$	T	Kurtoxin, pimopzide, mibefradil, Z123212, TTA-P2, Ni^{2+}, Zn^{2+}
LVA	$Ca_v3.3$	T	Pimozide, TTA-P2, Zn^{2+} Ni^{2+}, mibefradil

Des mutations humaines sur α2δ-1 sont associées à des troubles cardiaques, incluant le syndrome Brugada et le syndrome du QT court (Templin et al., 2011; Bourdin et al., 2015). Un expression augmentée est observée dans les neurones de DRG lésés ou dans un modèle rongeur de douleur neuropathique, diminuant les effets des antagonistes des $Ca_V2.2$ (Luo et al., 2001; Luo et al., 2002). Il existe 4 sous-types de sous-unités β codés par 4 gènes situés sur les sites chromosomiques 17q12, 10p12, 12q13 et 2q23. Ce sont des sous-unités cytoplasmiques constituées d'hélices alpha qui se fixent sur la partie proximale de la boucle intracellulaire reliant le DI et le DII, sur une région de 18 acides aminés nommée AID (pour "α1-interaction domain"), domaine d'interaction avec la sous-unité α1. Elles s'expriment de façon ubiquitaire et agit plutôt comme une chaperonne qui permet le bon repliement de la sous-unité α1 et la protège ainsi de la dégradation en favorisant son arrimage à la membrane. L'interruption de l'interaction entre la sous-unité β et α1 serait une bonne approche thérapeutique dans certaines conditions, par exemple de douleurs chroniques (Young et al., 1998). Des mutations de la sous-unité auxiliaire β seraient liées à des formes d'épilepsie et de dysfonctions cardiaques. La sous-unité γ est une glycoprotéine avec 4 segments transmembranaires, mise en évidence initialement sur le muscle squelettique, cependant des sous-types ont été récemment trouvés au niveau du cerveau. Sur un plan pharmacologique, la sous-unité γ n'a pas été clairement étudiée. Il semblerait que contrairement aux sous-unités auxiliaires α2δ et β qui ont des effets synergétiques positifs sur la densité de courant des différents canaux calciques, la sous-unité γ aurait des effets négatifs sur le courant calcium (Sousa et al., 2013).

Les sous-unités α1 des canaux calcium dépendants du potentiel, impliquées dans la douleur sont $Ca_V2.2$, $Ca_V3.2$; les sous-unités auxiliaires α2δ-1 et β le sont aussi (Saegusa et al., 2001; Sousa et al., 2013; François et al., 2014; Sekiguchi et al., 2018).

1.1.4. Canalopathies

Des mutations au niveau des canaux ioniques dépendants du potentiel sont souvent à l'origine de beaucoup de maladies génétiques que l'on nomme communément "canalopathies". Parmi ces canalopathies, beaucoup d'entre elles sont aussi référencées par Orphanet en Europe pour être associées à des maladies rares, maladies définies par son homogénéité clinique, indépendamment de son étiologie ou du nombre de gènes impliqués dont la prévalence (nombre de malades à un instant précis t) est inférieure à 1 personnes sur 2000 selon la commission européenne (http://europa.eu/rapid/press-release_IP-97-480_fr.htm). Cette prévalence des maladies rares est définie par chaque nation. Par exemple, aux USA, elle tombe à 1/1500 selon *rare Disease Act of 2002*.

Sous la forme de tableaux sont présentées les canalopathies et maladies orphelines humaines associées à chaque sous-type de canaux Na_V, K_V et Ca_V (Tableaux 1-5 à 1-10). Elles sont liées au site d'expression de chaque sous-type de canal ionique étudié, et sont résumées ci-dessous.

- ✓ Canalopathies affectant le SNC qui s'exprime par différentes formes d'épilepsie, d'ataxies, de migraines ainsi que les troubles neurodéveloppementaux (une multitude de mutations peuvent être mises en cause touchant les $Na_V1.1$-3, $Na_V1.6$-8, les $K_V2.1$, $K_V3.1$, $K_V3.3$, $K_V4.2$-3, $K_V7.2$-3, $K_V7.5$ et $K_V10.1$ ainsi que les $Ca_V2.1$, $Ca_V3.1$-2).
- ✓ Canalopathies affectant le SNP plus particulièrement le système sensoriel qui traite le message douloureux (un nombre non négligeable de mutations touchant principalement $Na_V1.7$-9).
- ✓ Canalopathies affectant les tissus musculaires squelettiques (les mutations touchent principalement $Na_V1.4$, $Ca_V1.1$ et $Ca_V2.2$).
- ✓ Canalopathies affectant les tissus cardiaques (les mutations touchent $Na_V1.5$, $K_V1.5$, $K_V4.3$, $K_V7.1$, $K_V11.1$, $Ca_V1.2$ et $Ca_V1.3$).
- ✓ Canalopathies affectant le système visuel ($K_V8.2$, $Ca_V1.4$).
- ✓ Canalopathies affectant le système auditif ($K_V7.4$).

Ce résumé met en évidence le rôle important joué par ces sous-types de canaux ioniques dans chacun des systèmes physiologiques où ils sont exprimés. D'un point de vue moins réducteur, des canalopathies acquises apparaissent par exemple suite à l'exposition aux xénobiotiques, substances étrangères au corps humain et le polluant (Imbrici et al., 2018).

Tableau 1-5. Canalopathies associées aux sous-types Na_V. Les informations ont été extraites de la base de données "UniprotKB".

$Na_V1.1$	Generalized epilepsy with febrile seizures plus 2 (GEFS+2) Epileptic encephalopathy, early infantile, 6 (EIEE6) Intractable childhood epilepsy with generalized tonic-clonic seizures (ICEGTC) Migraine, familial hemiplegic, 3 (FHM3) Febrile seizures, familial, 3A (FEB3A) Neurodevelopmental disorders (autism)
$Na_V1.2$	Epileptic encephalopathy, early infantile, 11 (EIEE11) Seizures, benign familial infantile, 3 (BFIS3) Autism spectrum disorder (ASD)
$Na_V1.3$	Epilepsy, familial focal, with variable foci 4 (FFEVF4) Epileptic encephalopathy, early infantile, 62 (EIEE62)
$Na_V1.4$	Paramyotonia congenita of von Eulenburg (PMC) Periodic paralysis hypokalemic 2 (HOKPP2) Periodic paralysis hyperkalemic (HYPP) Periodic paralysis normokalemic (NKPP) Myotonia SCN4A-related (MYOSCN4A)
$Na_V1.5$	Progressive familial heart block 1A (PFHB1A) Long QT syndrome 3 (LQT3) Brugada syndrome 1 (BRGDA1) Sick sinus syndrome 1 (SSS1) Familial paroxysmal ventricular fibrillation 1 (VF1) Sudden infant death syndrome (SIDS) Atrial standstill 1 (ATRST1) Cardiomyopathy, dilated 1E (CMD1E) Atrial fibrillation, familial, 10 (ATFB10)
$Na_V1.6$	Cognitive impairment with or without cerebellar ataxia (CIAT) Epileptic encephalopathy, early infantile, 13 (EIEE13) Seizures, benign familial infantile, 5 (BFIS5)
$Na_V1.7$	Primary erythermalgia (PERYTHM) Indifference to pain, congenital, autosomal recessive (CIP) Paroxysmal extreme pain disorder (PEPD) Generalized epilepsy with febrile seizures plus 7 (GEFS+7) Febrile seizures, familial, 3B (FEB3B)
$Na_V1.8$	Episodic pain syndrome, familial, 2 (FEPS2)
$Na_V1.9$	Neuropathy, hereditary sensory and autonomic, 7 (HSAN7) Episodic pain syndrome, familial, 3 (FEPS3)

Tableau 1-6. Maladies orphelines associées aux sous-types Na_V. Les informations ont été extraites de la base de données "Orphanet".

$Na_V1.1$	Dravet syndrome Familial or sporadic hemiplegic migraine Generalized epilepsy with febrile seizures-plus Lennox-Gastaut syndrome Malignant migrating partial seizures of infancy
$Na_V1.2$	Benign familial infantile epilepsy Benign familial neonatal-infantile seizures Dravet syndrome Early infantile epileptic encephalopathy Generalized epilepsy with febrile seizures-plus West syndrome
$Na_V1.3$	-
$Na_V1.4$	Acetazolamide-responsive myotonia Hyperkalemic periodic paralysis Hypokalemic periodic paralysis Myotonia fluctuans Myotonia permanens Paramyotonia congenita of Von Eulenburg Postsynaptic congenital myasthenic syndromes
$Na_V1.5$	Atrial stand still Brugada syndrome Familial atrial fibrillation Familial isolated dilated cardiomyopathy Familial progressive cardiac conduction defect Familial sick sinus syndrome Idiopathic ventricular fibrillation, not Brugada type Romano-Ward syndrome
$Na_V1.6$	Early infantile epileptic encephalopathy
$Na_V1.7$	Channelopathy-associated congenital insensitivity to pain Dravet syndrome Erythromelalgia Generalized epilepsy with febrile seizures-plus Hereditary sensory and autonomic neuropathy type 2 Paroxysmal extreme pain disorder Primary erythermalgia Sodium channelopathy-related small fiber neuropathy
$Na_V1.8$	Channelopathy-associated congenital insensitivity to pain Paroxysmal extreme pain disorder Primary erythermalgia Sodium channelopathy-related small fiber neuropathy
$Na_V1.9$	Channelopathy-associated congenital insensitivity to pain Familial episodic pain syndrome with predominantly lower limb involvement Hereditary sensory and autonomic neuropathy type 7 Paroxysmal extreme pain disorder Primary erythermalgia Sodium channelopathy-related small fiber neuropathy

Tableau 1-7. Canalopathies associées aux sous-types K_V. Les informations ont été extraites de la base de données "UniprotKB".

K_V1.1	Episodic ataxia 1 (EA1) Myokymia isolated 1 (MK1)
K_V1.2	Epileptic encephalopathy, early infantile, 32 (EIEE32)
K_V1.3	-
K_V1.4	-
K_V1.5	Atrial fibrillation, familial, 7 (ATFB7)
K_V1.6	-
K_V1.7	-
K_V1.8	-
K_V2.1	Epileptic encephalopathy, early infantile, 26 (EIEE26)
K_V2.2	-
K_V3.1	Epilepsy, progressive myoclonic 7 (EPM7)
K_V3.2	-
K_V3.3	Spinocerebellar ataxia 13 (SCA13)
K_V3.4	-
K_V4.1	-
K_V4.2	Temporal lobe epilepsy ASD and epilepsy
K_V4.3	Spinocerebellar ataxia 19 (SCA19) Brugada syndrome 9 (BRGDA9)
K_V5.1	-
K_V6.1	-
K_V6.2	-
K_V6.3	-
K_V6.4	-
K_V7.1	Long QT syndrome 1 (LQT1) Jervell and Lange-Nielsen syndrome 1 (JLNS1) Atrial fibrillation, familial, 3 (ATFB3) Short QT syndrome 2 (SQT2) Diabetes mellitus, non-insulin-dependent (NIDDM)
K_V7.2	Seizures, benign familial neonatal 1 (BFNS1) Epileptic encephalopathy, early infantile, 7 (EIEE7)
K_V7.3	Seizures, benign familial neonatal 2 (BFNS2)
K_V7.4	Deafness, autosomal dominant, 2A (DFNA2A)
K_V7.5	Mental retardation, autosomal dominant 46 (MRD46)
K_V8.1	-
K_V8.2	Cone dystrophy retinal 3B (RCD3B)
K_V9.1	-
K_V9.2	-
K_V9.3	-
K_V10.1	Temple-Baraitser syndrome (TMBTS) Zimmermann-Laband syndrome 1 (ZLS1)
K_V10.2	-
K_V11.1	Long QT syndrome 2 (LQT2) Short QT syndrome 1 (SQT1)
K_V11.2	-
K_V11.3	-
K_V12.1	-
K_V12.2	-
K_V12.3	-

Tableau 1-8. Maladies orphelines associées aux sous-types K_V. Les informations ont été extraites de la base de données "Orphanet".

K_V1.1	Episodic ataxia type 1 Hereditary continuous muscle fiber activity Isolated autosomal dominant hypomagnesemia, Glaudemans type
K_V1.2	-
K_V1.3	-
K_V1.4	-
K_V1.5	Familial atrial fibrillation
K_V1.6	-
K_V1.7	-
K_V1.8	-
K_V2.1	Early infantile epileptic encephalopathy
K_V2.2	-
K_V3.1	-
K_V3.2	-
K_V3.3	Spinocerebellar ataxia type 13
K_V3.4	-
K_V4.1	-
K_V4.2	Temporal lobe epilepsy ASD and epilepsy
K_V4.3	Brugada syndrome Spinocerebellar ataxia type 19/22
K_V5.1	-
K_V6.1	-
K_V6.2	-
K_V6.3	-
K_V6.4	-
K_V7.1	Familial atrial fibrillation Familial short QT syndrome Jervell and Lange-Nielsen syndrome Romano-Ward syndrome
K_V7.2	Benign familial infantile epilepsy Benign familial neonatal seizures Benign familial neonatal-infantile seizures Early infantile epileptic encephalopathy
K_V7.3	Benign familial infantile epilepsy Benign familial neonatal seizures Juvenile myoclonic epilepsy
K_V7.4	Autosomal dominant non-syndromic sensorineural deafness type DFNA
K_V7.5	-
K_V8.1	-
K_V8.2	Cone dystrophy with supernormal rod response
K_V9.1	-
K_V9.2	-
K_V9.3	-
K_V10.1	-
K_V10.2	-
K_V11.1	Familial short QT syndrome Romano-Ward syndrome
K_V11.2	-
K_V11.3	-
K_V12.1	-
K_V12.2	-
K_V12.3	-

Tableau 1-9. Canalopathies associées aux sous-types Ca_V. Les informations ont été extraites de la base de données "UniprotKB".

$Ca_V1.1$	Periodic paralysis hypokalemic 1 (HOKPP1) Malignant hyperthermia 5 (MHS5) Thyrotoxic periodic paralysis 1 (TTPP1)
$Ca_V1.2$	Timothy syndrome (TS) Brugada syndrome 3 (BRGDA3)
$Ca_V1.3$	Sinoatrial node dysfunction and deafness (SANDD) Primary aldosteronism, seizures, and neurologic abnormalities (PASNA)
$Ca_V1.4$	Night blindness, congenital stationary, 2A (CSNB2A) Cone-rod dystrophy, X-linked 3 (CORDX3) Aaland island eye disease (AIED)
$Ca_V2.1$	Spinocerebellar ataxia 6 (SCA6) Migraine, familial hemiplegic, 1 (FHM1) Episodic ataxia 2 (EA2) Epileptic encephalopathy, early infantile, 42 (EIEE42)
$Ca_V2.2$	Dystonia 23 (DYT23)
$Ca_V2.3$	-
$Ca_V3.1$	Spinocerebellar ataxia 42 (SCA42)
$Ca_V3.2$	Epilepsy, idiopathic generalized 6 (EIG6) Epilepsy, childhood absence 6 (ECA6) Hyperaldosteronism, familial, 4 (HALD4)
$Ca_V3.3$	-

Tableau 1-10. Maladies orphelines associées aux sous-types Ca_V. Les informations ont été extraites de la base de données "Orphanet".

$Ca_V1.1$	Hypokalemic periodic paralysis Malignant hyperthermia Periodic paralysis with transient compartment-like syndrome Thyrotoxic periodic paralysis
$Ca_V1.2$	Brugada syndrome Timothy syndrome
$Ca_V1.3$	Aldosterone-producing adenoma Aldosterone-producing adenoma with seizures and neurological abnormalities Sinoatrial node dysfunction and deafness
$Ca_V1.4$	Aland Islands eye disease Cone rod dystrophy Congenital stationary night blindness
$Ca_V2.1$	Alternating hemiplegia of childhood Benign paroxysmal torticollis of infancy Familial or sporadic hemiplegic migraine Familial paroxysmal ataxia Spinocerebellar ataxia type 6
$Ca_V2.2$	-
$Ca_V2.3$	-
$Ca_V3.1$	-
$Ca_V3.2$	Childhood absence epilepsy
$Ca_V3.3$	-

1.2. Toxines

Une toxine peut-être définie comme un poison, une substance telle qu'une petite molécule organique, un peptide ou une protéine, produit par l'activité métabolique d'un organisme vivant (bactérie, champignon vénéneux, plantes, algues, animaux venimeux), hautement toxique pour un ou plusieurs autres organismes vivants. On parle aussi de "biotoxines" car elles sont extraites d'organismes vivants. Selon la spécificité d'action, il y a des neurotoxines, myotoxines, des hémotoxines, des cytotoxines, des dermatotoxines, des hépatotoxines et des néphrotoxines. Ce n'est pas la substance qui est toxique mais la dose qui est ingérée ou injectée à l'organisme cible, d'où l'idée d'utiliser ces toxines comme médicaments dans une fenêtre thérapeutique non toxique.

Une partie non négligeable (11%) des médicaments, considérés comme basiques, essentiels à la pharmacopée par l'Organisation Mondiale de la Santé (OMS) et actuellement sur le marché, sont extraits des plantes et décrits comme plus efficaces et plus surs pour l'être humain (Veeresham, 2012). Les métabolites secondaires des plantes, aussi nommés "toxines", font déjà partie de la pharmacopée. On retrouve, par exemple, les hétérosides cardiotoniques (digitaline, ouabaïne) qui ont des effets tonicardiaques comme leur nom l'indique, les alcaloïdes tropaniques (atropine, hyoscyamine, scopolamine) qui provoquent des effets musculaires relaxants, les opioïdes (morphine, codéine, thébaïne, narcotine) et la capsaïcine associés à des effets antalgiques, le quinquina et l'artémisinine à des effets antipaludiques, les dérivés de la cocaïne (xylocaïne, novocaïne…) induisant des effets anesthésiques et la vinblastine et le paclitaxel des effets antitumoraux (Sevenet, 2006; Veeresham, 2012). Explorer d'autres sources de molécules à potentiel thérapeutique pourrait permettre de mettre en évidence d'autres classes de molécules avec des activités nouvelles. C'est dans ce cadre que l'étude des venins d'animaux, source d'une immense diversité de toxines pouvant élargir potentiellement le panel thérapeutique actuel, devient opportune.

1.2.1. Toxines et canaux ioniques

Le venin est défini comme "une sécrétion, produite dans une glande spécialisée chez un animal et délivrée à une proie à l'aide d'un appareil inoculateur (crochet, harpon, dard…), qui contient des molécules qui perturbent les processus physiologiques normaux dans la victime de manière à faciliter l'alimentation ou la défense de l'animal producteur de venin". Les serpents, araignées, scorpions, cônes marins et anémones de mer représentent la majorité des organismes venimeux étudiés jusqu'à présent. D'autres (tels que les oursins, étoiles de mers, fourmis, centipèdes, abeilles, guêpes, moustiques, tiques, lézards…) ont été plus négligés. Cependant, chaque venin est unique de par la diversité des molécules qui le constituent et de par l'expression de ces molécules selon les saisons,

l'étape du développement de l'animal et le but à atteindre, *i.e.* prédation ou défense (Dutertre et al., 2014; Santana et al., 2017; Tobassum et al., 2018). Il ne faut donc pas négliger une espèce venimeuse par rapport à une autre car chacune présente un venin qui lui est propre.

Le venin est composé de sels inorganiques, de petites molécules organiques, ainsi que de protéines à haute masse moléculaire incluant les enzymes. Cependant, les peptides riches en cystéines (< 10 kDa) et les polypeptides (> 10 kDa) sont la classe de molécules les plus abondantes dans ces sécrétions venimeuses (King et al., 2008; Fry et al., 2009; Pennington et al., 2018). Parmi les différents composés des venins d'animaux, les peptides riches en cystéines se sont révélées être des ligands puissants des canaux Na_V, K_V et Ca_V. Les toxines peptidiques inhibant/modulant ces canaux sont principalement extraites de cônes, d'anémones de mer, d'araignées, de scorpions, de serpents (Figure 1-11; Gilchrist et al., 2014; Gandini et al., 2015; Norton & Chandy, 2017). Ces peptides sont de puissants outils permettant d'étudier les différents sous-types d'une même famille de canaux ioniques ayant des fonctions proches, des patterns d'expression proches et partageant un fort pourcentage d'identité de séquence. Par exemple, l'étude de certains sous-types ou certaines superfamilles de canaux calcium a été permise par la découverte de toxines peptidiques très sélectives d'un sous-type ou d'une superfamille donné (Tableau 1-11). Concernant les toxines peptidiques ciblant les canaux K_V ou Ca_V, certaines d'entre elles sont devenues des médicaments, comme par exemple l'ω-conotoxine-MVIIA (Prialt), antalgique dans le traitement de douleurs chroniques rebelles, ou sont en cours d'évaluation en phase clinique de phases I-II, comme la ShK-186 (Dalazatide) ainsi que d'autres analogues de la ShK (ShK-170 ou ShK-192) comme immunomodulateurs dans le traitement de maladies auto-immunes telles que la sclérose en plaques ou l'arthrite rhumatoïde. On remarque cependant une absence de représentation des toxines peptidiques ciblant les canaux Na_V (Tableau 1-12).

1.2.2. Toxines - Na_V - Modulations des propriétés biophysiques

Malgré l'absence de molécules peptidiques dérivées de venin ciblant les canaux Na_V sur le marché ou tout du moins en phase clinique, la mise en évidence de cette catégorie de molécules représente un axe de recherche important. Tout d'abord, les canaux Na_V représentent une cible thérapeutique de choix puisque de nombreux anti-arythmiques cardiaques de classe I (tels que la méxilitine, la flécaïne), anti-épileptiques (tels que le carbamazépine, l'oxcarbazépine), analgésiques locaux (tels que la lidocaïne) sont déjà sur le marché et ciblent spécifiquement ces canaux. De plus, la plupart des toxines dérivées des venins ciblent les canaux Na_V du fait de leur importance dans l'initiation du potentiel d'action (Kalia et al., 2015). Au niveau de ces canaux, elles se fixent sur

différents sites associés à des modifications de leurs propriétés biophysiques (de Lera Ruiz & Kraus, 2015; Israel et al., 2017).

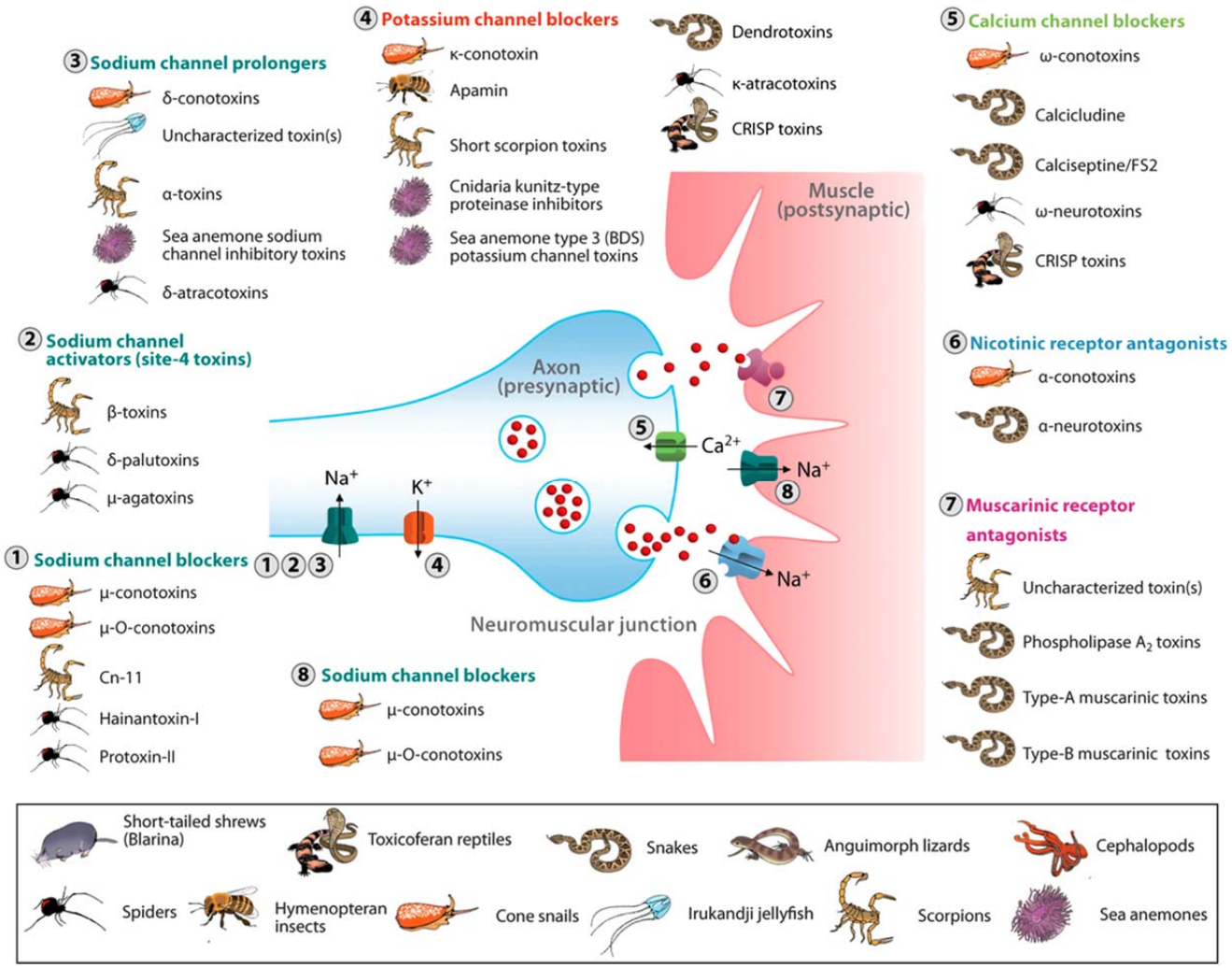

Figure 1-11. Convergence observée de l'action des neurotoxines extraites de différentes espèces animales (Fry et al., 2009). Les principales cibles sont les canaux sodium, potassium et calcium dépendants du potentiel, ainsi que les récepteurs nicotiniques et muscariniques de l'acétylcholine.

Tableau 1-11. Exemples de toxines peptidiques ciblant les canaux Ca_V selon le type de famille (Gandini et al., 2015).

Selectivity	Toxin	Lenght	Source	Concentration
L-type	Calciseptine	60 aa	*Dendroaspis polylepis polylepis*	100 nM-2 μM
	FS-2	60 aa	*Dendroaspis polylepis polylepis*	100 nM-2 μM
	Calcicludine	60 aa	*Dendroaspis angusticeps*	1-10 nM
P/Q-type	ω-Agatoxin IVA	48 aa	*Agelenopsis aperta*	20 nM-1 μM
	ω-Agatoxin IVB	48 aa	*Agelenopsis aperta*	100-800 nM
P/Q & N-type	ω-Grammotoxin SIA	36 aa	*Grammostola spatulata*	50 -500 nM
	ω-PnTx3-3	34 aa	*Phoneutrica nigriventer*	60-100 nM
	Phonetoxin IIA	76 aa	*Phoneutrica nigriventer*	60-100 nM
N-type	ω-Conotoxin GVIA	27 aa	*Conus geographus*	100 nM-1 μM
	ω-Conotoxin MVIIA	25 aa	*Conus magus*	100 nM-2 μM
	ω-Conotoxin MVIIC	26 aa	*Conus magus*	50 nM-1 μM
	ω-Conotoxin CVID	27 aa	*Conus catus*	10-100 nM
R-type	SNX482	41 aa	*Hysterocrates gigas*	10-100 nM
T-type	Kurtoxin	63 aa	*Parabuthus transvaalicus*	50 -500 nM
	ProTx-I	35 aa	*Thrixopelma pruriens*	10-100 nM
	ProTx-II	30 aa	*Thrixopelma pruriens*	10-500 nM

Le préfixe grec utilisé pour nommer les toxines ciblant les canaux Na_V donne déjà une indication sur les effets attendus de chacune d'entre elle: α, pour les toxines de scorpions ralentissant et inhibant une partie de l'inactivation et affectant la dépendance vis-à-vis du potentiel de la courbe d'inactivation; β, pour les toxines affectant la dépendance vis-à-vis du potentiel de la courbe d'activation; δ, pour les toxines ralentissant et inhibant une partie de l'inactivation; μ, pour les toxines bloquant le pore du canal (King et al., 2008).

Tableau 1-12. Pharmacologie des composés dérivés de venins d'animaux sélectionnés. Adapté de King et al. (2011).

Protein or derivative	Source of venom protein	Molecular target	Indication	FDA approval	Company
Captopril‡ (Capoten®)	Pit viper (snake)	ACE	Hypertension	1981	Bristol-Myers Squibb
Eptifibatide§ (Integrilin®)	Pygmy rattlesnake	$\alpha_{IIb}\beta_3$ integrin receptor	Acute coronary syndromes	1998	Merck
Tirofiban¶ (Aggrastat®)	Saw-scaled viper (snake)	$\alpha_{IIb}\beta_3$ integrin receptor	Acute coronary syndromes	1999	Iroko Cardio and Merck (USA only)
Bivalirudin# (Angiomax®)	Medicinal leech	Thrombin	Coagulation during surgery	2000	The Medicines Co.
Ziconitide** (Prialt®)	Cone snail	$Ca_V2.2$ channel	Chronic pain	2004	Azur Pharma and Eisai (Europe)
Exenatide (Byetta®)	Lizard (Gila monster)	GLP-1 receptor‡‡	Type 2 diabetes	2005	Amylin and Eli Lilly
Batroxobin (Baquting)	Lancehead snake	Fibrinogen	Perioperative bleeding	Outside USA§§	Nuokang Biopharma

Protein or derivative	Source of venom protein	Molecular target	Indication	Trial Phase	Company
Xen2174 (χ-CTX MrIA)	Cone snail	Norepinephrine transporter	Postoperative pain	II	Xenome Ltd
BAY86-7548 (bombesin)‡	Fire-bellied toad	Gastrin-releasing peptide receptor	Prostate cancer imaging	I	Bayer
CNSB004 (Leconotide)§	Cone snail	$Ca_V2.2$ channel	Neuropathic pain	I	Relevare Pharmaceuticals
ShK-192	Sea anemone	$K_V1.3$ channel	Autoimmune disease	I (first quarter 2012)	Airmid
Tumor Paint (chlorotoxin)¶	Deathstalker scorpion	Annexin A2	Tumor marker for surgery	I	TransMolecular
Cenderitide (CD-NP)#	Eastern green mamba (snake)	Natriuretic peptide receptor	Congestive heart failure	II	Nile Therapeutics
RPI-MN (α-cobrotoxin)**	Cobra (snake)	nAChR	HIV	I	ReceptoPharm
RPI-78M (α-cobratoxin)‡‡	Cobra (snake)	nAChR	Multiple sclerosis	I	ReceptoPharm
Agkistrodon§§ (agkisacutacin)	Sharp-nosed viper	Fibrin(ogen)	Perioperative bleeding	III	China Nuokang Bio-Pharmaceutical
Desmoteplase (rDSPAα1)¶¶	Common vampire bat	Plasminogen	Acute ischemic stroke	III	H. Lundbeck A/S

Le **site 1** est formé par les quatre boucles P constituant le pore du canal [plus particulièrement, le filtre de sélectivité formé par les acides aminés D, E, K, A, et le vestibule extracellulaire (Penzotti et al., 1998). Il représente le site de fixation des toxines telles que la TTX, la saxitoxine (STX) et les μ-conotoxines dont le principal effet est l'obstruction du pore et, en conséquence, une inhibition du courant sodium en fonction du temps et du potentiel (Figures 1-12 et 1-13).

Le **site 2** est constitué par le segment S6 des domaines DI et DIV. Il permet la fixation des toxines telles que la batrachotoxine, la vératridine et l'antillatoxine qui entrainent une inhibition de l'inactivation (courant sodium maintenu en fonction du temps tout au long de l'impulsion dépolarisante) (Figure 1-12).

Le **site 3** est formé par la boucle reliant les segments S3-S4 du domaine DIV. Il représente le site de fixation des toxines α de scorpion qui ralentissent ou inhibent une partie de l'inactivation en empêchant le mouvement vers l'extérieur du segment S4, sans modifier la cinétique d'activation, et affectent la dépendance vis-à-vis du potentiel de la courbe d'inactivation avec des effets mineurs sur la dépendance vis-à-vis du potentiel de la courbe d'activation (Figures 1-12 et 1-13). Des toxines d'autres espèces (anémones de mer, cônes, araignées et serpents) présentent les mêmes effets sur le canal sodium. Cependant, le site de fixation n'est pas toujours le même.

Le **site 4** est formé des boucles extracellulaires reliant les segments S1-S2 et S3-S4 du domaine DII (Figure 1-12). Il représente le site de fixation des toxines β de scorpions et de certaines toxines d'araignées. Les toxines β de scorpions provoquent généralement un déplacement de la courbe d'activation vers des valeurs de potentiel plus négatives, ce qui résulte en une augmentation du pic de courant (Figure 1-13, exemple de la Css-IV). Les toxines d'araignées, quant à elles, produisent un déplacement de la courbe d'activation vers des valeurs de potentiel plus positives, ce qui provoque une diminution du pic du courant (Figure 1-13, exemple de la protoxine-II) mais ce n'est pas une caractéristique générale des théraphotoxines se fixant sur le site 4 (exemple de l'huwentoxine-IV).

Le **site 5** est formé du segment S6 du domaine DI et du segment S5 du domaine DIV. Il constitue le site de fixation des ciguatoxines et des brévétoxines qui ralentissent ou inhibent une partie de l'inactivation des canaux sodium (Figure 1-12).

Le **site 6** est formé du segment S4 du domaine DIV et représente le site de fixation des μO- et δ-conotoxines dont le principal effet est de bloquer les domaines senseurs du potentiel à l'état fermé sans affecter la dépendance du courant vis-à-vis du potentiel, ce qui se traduit par une diminution du pic du courant (Figures 1-12 et 1-13). Certaines toxines d'araignées présentent les mêmes effets sans que leur site de fixation ne soit connu.

Le **site des anesthésiques locaux** est formé des portions intracellulaires du segment 6 des domaines DI, DIII et DIV du pore ouvert (Figure 1-12). C'est aussi le site de fixation principal de toutes les molécules citées précédemment et déjà sur le marché (telles que les anti-arythmiques, les antiépileptiques…). D'autres molécules, telles que la benzocaïne et la phénytoïne, peuvent inhiber le canal sodium en atteignant la cavité centrale du pore fermé *via* ses fenestrations latérales (Payandeh et al., 2011). L'action de l'ensemble de ces molécules dépend de l'état du canal et donc de sa fréquence d'ouverture et de fermeture.

Le **site 8, site des petites molécules des compagnies pharmaceutiques Icagen et Pfizer**, est beaucoup moins communément admis par la communauté scientifique. Il est dû à la découverte récente de cette classe de molécules dans le cadre de la recherche de nouvelles molécules antidouleur (McCormack et al., 2013; Sun et al., 2014) et est formé par des portions intracellulaires des segments 2 et 3 du domaine DIV (Figure 1-12). D'autres auteurs définissent le site 8 comme étant le segment 5 du domaine DII, cible de la conotoxine GVIIJ (Gajewiak et al., 2014).

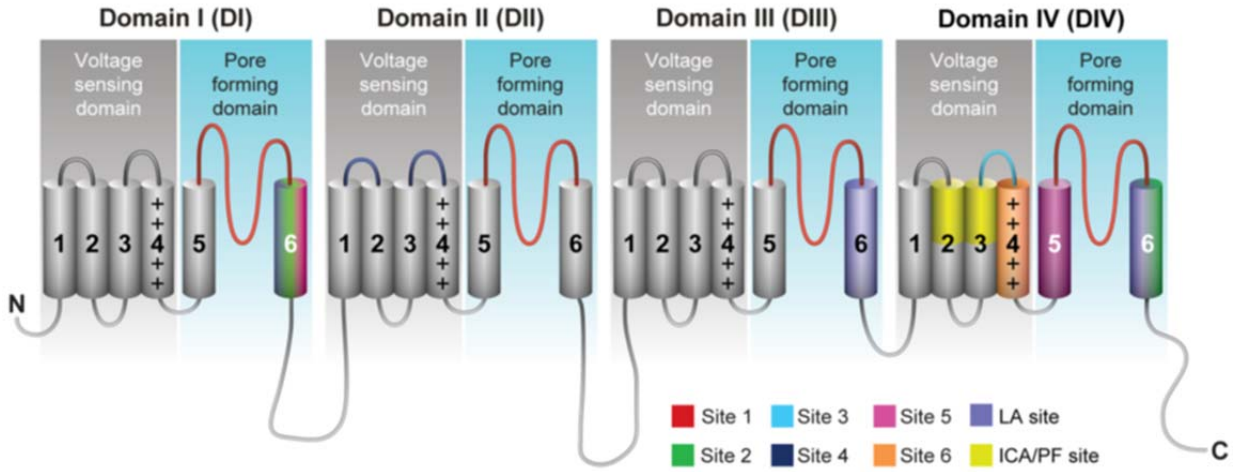

Figure 1-12. Sites de fixation des différents types de toxines sur les canaux Na_V (Ahern et al., 2016). Outre les 6 sites identifiés pour les toxines (site 1-6), les sites de liaison des anesthésiques locaux (site AL) et des petites molécules d'Icagen et de Pfizer (site ICA/PF) sont aussi indiqués.

Parfois, il n'y a pas de corrélation entre les effets électrophysiologiques observés sur le courant sodium et le site de fixation défini après mutagénèse du canal, ce dernier prenant souvent le dessus lors de la classification du site de fixation d'une toxine donnée.

1.2.3. Toxines – Canaux Na_V – Douleur

Les toxines activatrices ou inhibitrices de canaux Na_V sont retrouvées dans les venins de toutes les espèces (araignées, guêpes, serpents, scorpions, cônes de mer, anémones de mer…). Elles sont utiles lorsque l'animal veut atteindre son but de prédation ou de défense en produisant, parmi les

premiers symptômes, la douleur chez la proie ou le prédateur. Cependant, il est admis que les toxines qui induisent la douleur sont mieux adaptées à des fins défensives alors que celles qui produisent une paralysie sont souvent supposées avoir évolué spécifiquement à des fins de prédation. En effet, certains des venins les plus douloureux, comme celui de l'abeille, de la guêpe, du poisson-pierre ou d'ornithorynque, ne sont utilisés qu'à des fins défensives ou de compétition (Jami et al., 2017).

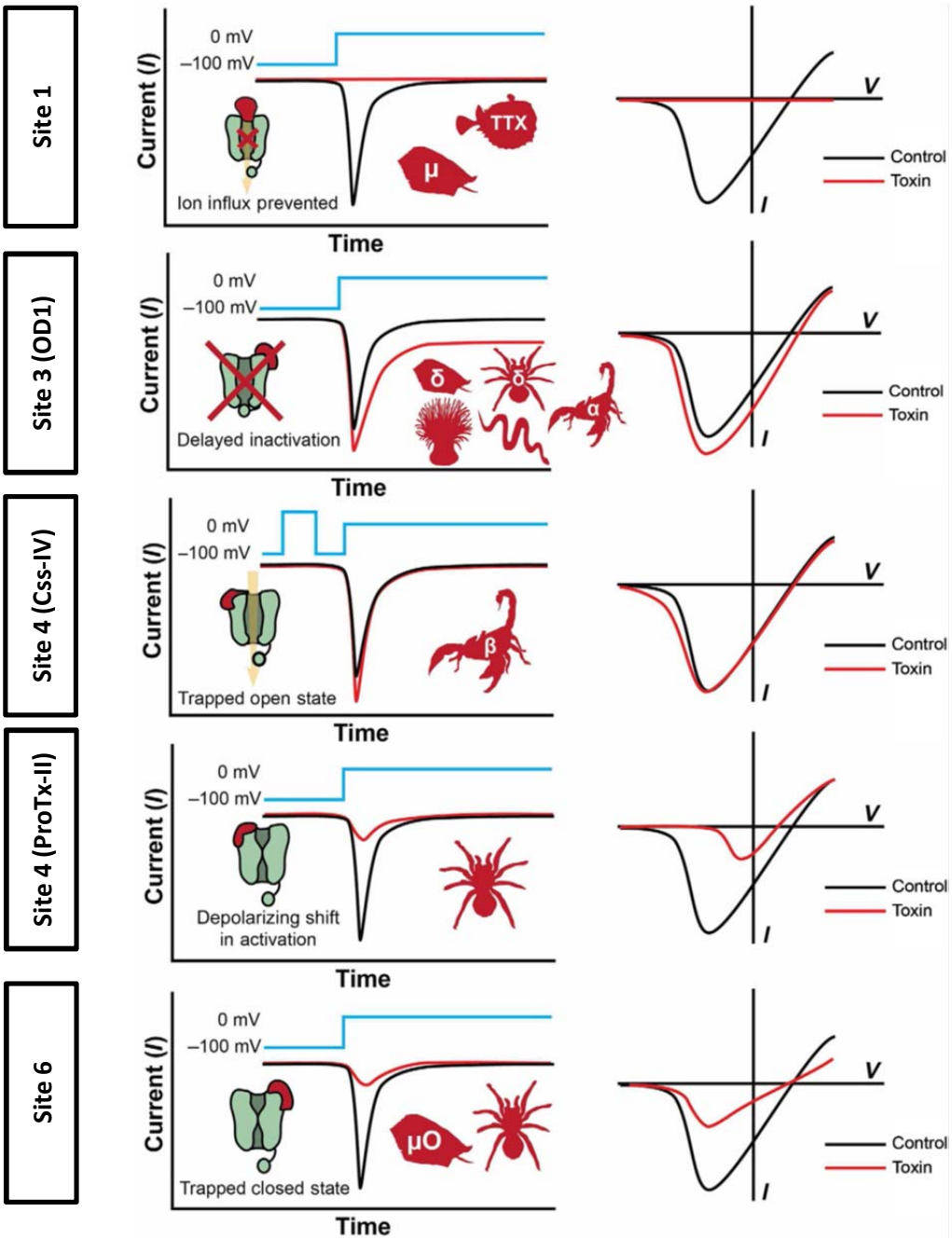

Figure 1-13. Représentations schématiques des effets des toxines sur le courant sodium. Tracés de courant en fonction du temps (à gauche) et courbes courant–potentiel (I–V, à droite). Effets représentatifs d'une concentration maximale de toxine. Adapté d'Israel et al. (2017).

Les toxines activatrices de canaux Na_V (tout comme la vératridine) sont des outils pharmacologiques précieux qui peuvent être employées, par exemple, lors de criblages à haut débit

de molécules inhibitrices de ces canaux, basés sur l'utilisation de sondes fluorescentes (Klint et al., 2015). Cependant, Il y a deux inconvénients principaux à ces criblages basés sur les sondes fluorescentes: l'inefficacité des toxines activatrices sur un sous-type donné de canaux Na_V (exemple du sous-type $hNa_V1.8$ résistant à la vératridine) et l'échec de la mise en évidence de l'effet d'une molécule criblée à cause d'une compétition sur le site de fixation (Deuis et al., 2016a). Ces toxines activatrices ont également permis de décortiquer le rôle joué par chaque sous-type de Na_V dans la transmission du message douloureux comme, par exemple, le sous-type $Na_V1.1$ dont le rôle a été mis en évidence par la toxine Hm1a qui inhibe de façon sélective l'inactivation de ce sous-type (Osteen et al., 2016). Celles du sous-type $Na_V1.7$, cible d'intérêt pour traiter la douleur, ont permis de créer des modèles pour évaluer l'effet antalgique des toxines inhibant ce sous-type (Deuis et al., 2016b; Cardoso et al., 2017; Deuis et al., 2017; Sousa et al., 2017; Rahnama et al., 2017). Le modèle le plus couramment utilisé est le modèle rongeur de douleur induite par l'OD1, une toxine α de scorpion ayant des effets mixtes α/β (Meng et al., 2015). Selon le sous-type Na_V étudié en rapport avec la douleur, il existe un panel non négligeable de toxines activatrices de ces sous-types, avec une sélectivité plus ou moins importante (Tableau 1-13; Jami et al., 2017).

Tableau 1-13. Exemples des principales toxines produisant la douleur *via* l'activation de certains sous-types de canaux Na_V (Jami et al., 2017).

Venom Peptide	Species	Pharmacological Target(s)	Pain Phenotype (Route)
δ-theraphotoxin-Hm1a	*Heteroscodra maculata*	$Na_V1.1$	Spontaneous pain (i.pl.), mechanical allodynia (i.pl.)
OD1	*Odontobuthus doriae*	$Na_V1.7$	Spontaneous pain (i.pl.)
Cn2	*Centruroides noxius*	$Na_V1.6$	Spontaneous pain (i.pl.), mechanical allodynia (i.pl.)
δ-conotoxin SuVIA	*Conus suturatus*	$Na_V1.3$, $Na_V1.4$, $Na_V1.6$, $Na_V1.7$	Spontaneous pain (i.pl.)
α-scorpion toxin CvIV4	*Centruroides vittatus*	$Na_V1.2$, $Na_V1.3$, $Na_V1.4$, $Na_V1.7$	Spontaneous pain (i.pl.)

Les toxines inhibitrices de canaux Na_V, en rapport avec la douleur, ont été très étudiées principalement pour les développer comme nouvelles classes de traitement antalgique avec moins d'effets secondaires que les opioïdes utilisés dans le cadre de douleurs chroniques récidivantes. Tous les sous-types de canaux Na_V présents sur les premiers neurones senseurs de la douleur, et transmettant le message au SNC, sont potentiellement des cibles antinociceptives intéressantes. Dans ce sens, le sous-type le plus criblé est le $Na_V1.7$ et les toxines les plus étudiées sont celles d'araignées ayant un réarrangement des ponts disulfures sous forme de nœud de cystines inhibiteur (ICK pour "inhibitor cystine knot") (Figure 1-14; Vetter et al., 2017), comme cela est développé dans la Publication n°1.

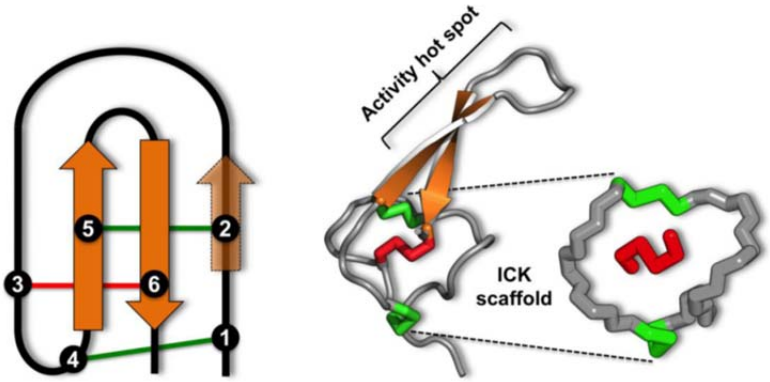

Figure 1-14. Toxines d'araignées à trois ponts disulfures réarrangés en structure ICK (Saez et al., 2010). La connectivité des ponts disulfures est CI-CIV, CII-CV, CIII-CVI. Exemple de l'ω-héxatoxine-Hv1a, une toxine d'araignée de 37 acides aminés.

1.3. Nociception

La douleur a été définie officiellement par l'association internationale pour l'étude de la douleur (IASP pour "International Association for the Study of Pain") en 1979 comme "une expérience sensorielle et émotionnelle désagréable, associée à une lésion tissulaire réelle ou potentielle, ou décrite dans ces termes". La douleur est une sensation subjective, très difficile à quantifier et à qualifier autant par le patient que par les professionnels de la santé, surtout qu'elle n'est pas toujours associée à une lésion.

1.3.1. Catégories de douleurs et épidémiologie

Il existe deux catégories de douleur selon la durée: *(1)* les douleurs aiguës, souvent intenses et brèves, servant de signal d'alarme permettant de maintenir l'intégrité du corps et *(2)* les douleurs chroniques, aussi nommées douleurs pathologiques, récurrentes maintenues depuis plus de trois mois, qui deviennent une maladie à part entière (Figure 1-15).

Figure 1-15. Les différentes étapes de la douleur chronique (Crofford et al., 2015). De gauche à droite, portrait des émotions négatives et de l'aspect intrusif de la douleur. La composante émotionnelle empêche les professionnels d'évaluer objectivement la douleur chronique et les symptômes somatiques associés qui peuvent-être prédits par des facteurs déterminés lors d'études épidémiologiques telles que des traumatismes ou abus subits dans l'enfance, une éducation pauvre, un isolement social, de la dépression et de l'anxiété.

Il existe trois catégories de douleur selon le processus physiopathologique mis en jeu. Les douleurs inflammatoires, les douleurs neuropathiques et les douleurs mixtes. Il y a donc une lésion due à une dérégulation des phénomènes inflammatoires et/ou une atteinte du SNC ou du SNP. Les douleurs neuropathiques entrainent souvent un trouble de la sensibilité locale (hypoesthésie ou anesthésie complète au toucher ou à la piqûre) associé à des allodynies ou des hyperesthésies (Figure 1-16). Il existe une quatrième catégorie dont les processus physiopathologiques sont encore mal connus, les douleurs dysfonctionnelles. Celles-ci ne sont dues à aucun des deux systèmes précédemment décrits, une altération des systèmes centraux modulateurs de la douleur en étant probablement la cause.

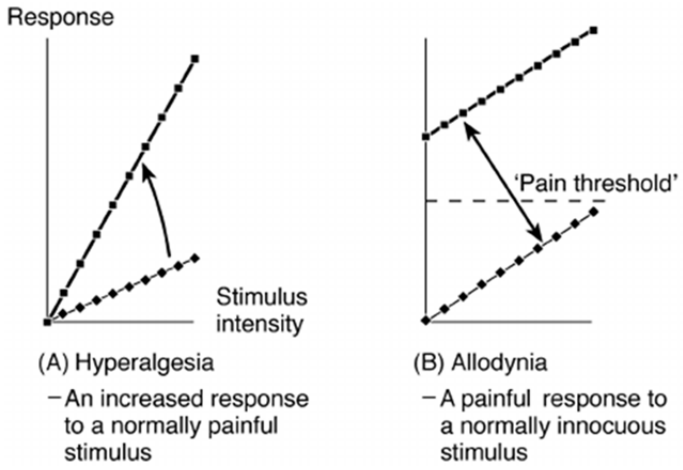

Figure 1-16. Zoom sur deux manifestations cliniques de la douleur (Bridges et al., 2001; Rostaing-Rigattieri & Guerin, 2014). (**A**) L'hyperalgie est une réponse exagérée à un stimulus qui normalement est douloureux (**B**) L'allodynie est une douleur causée par un stimulus qui normalement ne produit pas de douleur. Elle peut être tactile ou mécanique à l'effleurement cutané (allodynie dite "dynamique") ou à la pression (allodynie dite "statique") ou encore thermique, à la chaleur non nociceptive (< 42 °C) ou au froid non nociceptif (> 10 °C).

Le trajet de l'information douloureuse (que l'on nomme "nociception") est largement décrit dans la Publication n°1 (cf. "Primary sensory neurons as front door for pain"). Bien qu'une personne sur dix souffre de douleur dans le monde, d'après l'IASP (Goldberg and McGee, 2011), une étude réalisée en France a permis de montrer que les douleurs chroniques touchent 20% des français dont ¼ ayant des douleurs neuropathiques avec une fréquence accrue chez les femmes, les personnes de 50-64 ans, les travailleurs manuels et les patients habitant en zone rurale (Bouhassira et al., 2008). La douleur chronique/pathologique est souvent accompagnée d'émotions négatives déclenchant une dépression (anxiété et pensées suicidaires). Elle altère inévitablement la qualité de vie entraînant souvent des arrêts de travail. La prise en charge de celle-ci a un coût socio-économique important d'où la nécessité de trouver des solutions globales à la maitrise de la sensation douloureuse.

1.3.2. Arsenal thérapeutique

Des traitements non pharmacologiques existent tels que l'acuponcture, la relaxation, la sophrologie ou la stimulation électronique médullaire. Cependant, les traitements pharmacologiques sont le plus utilisés au quotidien. Les douleurs inflammatoires, tout comme les douleurs aiguës, sont aujourd'hui bien prises en charge grâce au paracétamol, à l'aspirine, aux anti-inflammatoires non-stéroïdiens (AINS) ou encore à la morphine et ses dérivés pour les douleurs les plus rebelles. Ceci étant, les effets secondaires sont non négligeables (troubles gastriques et rénaux, tolérance et dépendance à la morphine…), surtout s'il s'agit d'une utilisation prolongée, voire chronique. Bien que les douleurs neuropathiques répondent à certains opioïdes, les traitements les plus adéquates sont les antidépresseurs et les anti-épileptiques, qui présentent moins d'effets indésirables.

Trois paliers d'antalgiques, devant être prescrits en fonction de l'intensité de la douleur, ont été établis à la disposition des médecins par l'OMS et l'IASP. Cependant, l'IASP préconise, d'emblée, la prescription d'opioïdes pour toute douleur d'intensité supérieure à 6/10 sur l'échelle visuelle analogique (Tableau 1-14).

✓ Les antalgiques du Palier I, pour les douleurs légères et modérées: l'aspirine, le paracétamol et les anti-inflammatoires non stéroïdiens, comme par exemple l'ibuprofène. Ils sont parfois appelés "antalgiques périphériques" ou "non morphiniques" et ont la puissance antalgique la plus faible.

✓ Les antalgiques du Palier II, pour les douleurs plus importantes: la codéine, la nalbuphine, le tramadol ou des associations de médicaments de Paliers 1 et 2. Ils sont dits "centraux" ou "morphiniques faibles" car ils sont actifs sur la perception de la douleur au niveau cérébral.

✓ Les antalgiques du Palier III, pour les douleurs très intenses: la morphine. Malgré des réticences à prescrire la morphine qui ont longtemps empêché les médecins de calmer les douleurs les plus fortes, il a été prouvé que ce composé ne rend pas toxicomane quand il est utilisé pour traiter la douleur de façon contrôlée. La morphine peut être donnée en sirop, en comprimé ou par injection. Dans certains cas, une pompe d'analgésie contrôlée permet au patient de s'administrer lui-même la quantité dont il a besoin (selon un maximum fixé par le médecin).

Cependant, seulement la moitié de patients sous traitement ressentent un soulagement de la douleur chronique et plus de 70% ne sont pas correctement traités, d'où la nécessité de trouver d'autres solutions d'après les spécialistes de la Société française d'étude et de traitement de la douleur (SFETD).

Tableau 1-14. Famille d'antalgiques (Palier I à III) à prescrire selon l'intensité de la douleur (de faible à sévère).

Famille	Dénomination Commune Internationale (DCI)
Palier I Antalgiques non opioïdes	Paracétamol Acide acétylsalicylique Ibuprofène Kétoprofène Néfopam
Palier II Antalgiques opioïdes faibles	Codéine Codéine + Paracétamol Tramadol Tramadol + Paracétamol
Palier III Antalgiques opioïdes	Morphine Fentanyl Oxycodone Buprénorphine Nalbuphine

Par conséquent, l'arsenal thérapeutique doit être élargi *(i)* en étudiant et élucidant davantage les mécanismes d'action des traitements existants, *(ii)* en en améliorant leur spécificité en favorisant, par exemple, une voie de signalisation intracellulaire (Manglik et al., 2016; Villanueva, 2017), *(iii)* en les rendant plus puissants et mieux tolérés par couplage à une deuxième molécule procurant des effets antidouleur potentiels synergiques (Emery et al., 2016; Deuis et al., 2017), ou *(iv)* en réfléchissant à la voie d'administration de molécules déjà connues afin d'optimiser leur pouvoir antalgique (Hagen et al., 2017; Mattei et al., 2018).

Cet arsenal peut-être aussi élargi en cherchant de nouvelles classes de molécules naturelles que l'on peut extraire du règne végétal ou animal. Une source originale de molécules ayant des propriétés antalgiques provient des venins d'animaux et ciblent les canaux ioniques. Par exemple, la mambalgine du mamba noir, la crotalphine du crotale et certaines α-conotoxines de cônes marins (Vc1.1 et RegIA4) ciblent les ASICs, les canaux TRPs et les récepteurs nicotiniques de l'acétylcholine, et sont en cours de développement (Callaghan et al., 2008; King, 2011; Diochot et al., 2012; Bressan et al., 2016; Zambelli et al., 2016; Safavi-Hemami et al., 2018). Sans oublier de mentionner l'effet du venin d'abeille dilué qui atténuerait l'apparition d'allodynies, dans le cadre de douleurs neuropathiques, en diminuant l'expression des canaux TRPV1, TRPA1 et TRPM8 et de c-Fos au niveau des neurones de DRG (Koh et al., 2014).

Cependant, les canaux Na_V, K_V et Ca_V, qui régulent l'excitabilité membranaire, la genèse et la propagation des potentiels d'action axonaux, peuvent être la cible d'inhibiteurs ou d'activateurs qui ramèneront à la normale tous les paramètres d'excitabilité en cas de pathologie, et plus

particulièrement en cas de douleur (Figure 1-17). En effet, le ziconotide (ω-conotoxine MVIIA inhibant le sous-type $Ca_V2.2$ de canal calcium) est la seule toxine commercialisée par Neurex (une filiale d'Elan Pharmaceuticals) jusqu'à aujourd'hui, malgré une fenêtre d'utilisation thérapeutique très restreinte, *i.e.* uniquement pour des douleurs rebelles ne répondant plus à aucun traitement pharmacologique standard, et une voie d'administration intrathécale. Le ziconotide a une puissance remarquable dans les modèles animaux de douleur persistante et neuropathique. En particulier, chez un modèle de rat de douleur post-opératoire, ce composé a une puissance plus élevée et une activité plus longue que la morphine (Molinski et al., 2009). Cependant, chez l'homme, le ziconotide présente des effets secondaires (tels que des troubles de la mémoire, des épisodes confusionnels, des troubles de l'humeur ou des nausées) qui peuvent être limités par un titrage très progressif du composé administré par voie intrathécale (Raffaeli et al., 2011; Dupoiron et al., 2012). Le ziconotide reste malgré tout efficace pour traiter les douleurs chroniques cancéreuses et celles associées au SIDA, résistantes aux autres antalgiques (Staats et al., 2004).

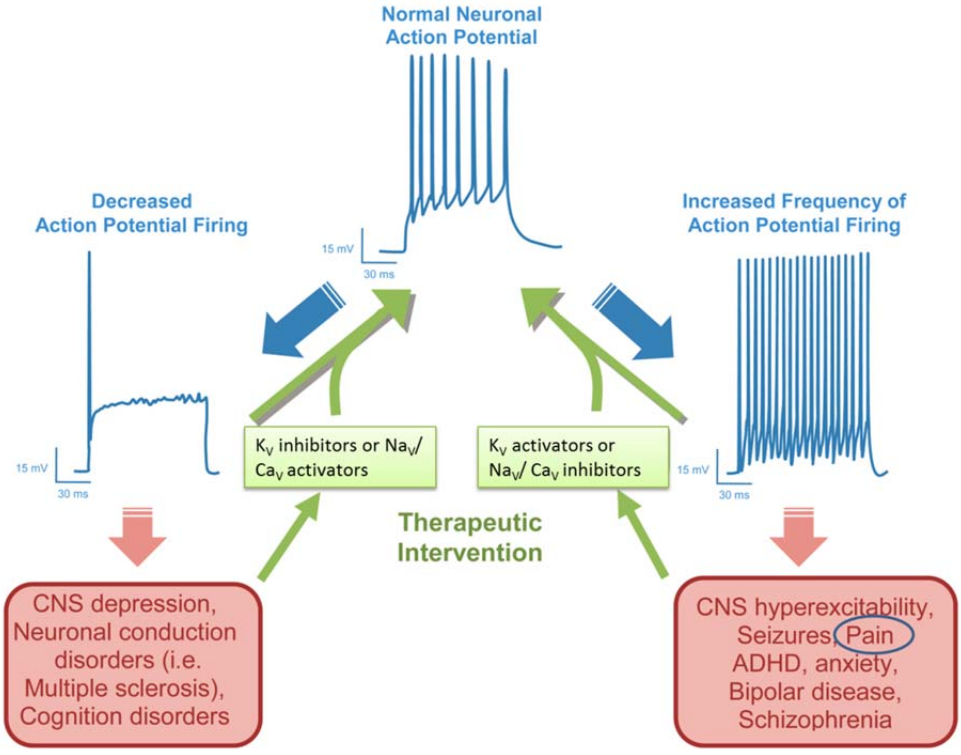

Figure 1-17. Effets théoriques des inhibiteurs/activateurs des canaux Na_V, Ca_V et K_V en cas d'activité neuronale altérée (adapté de Wulff et al., 2009). Les inhibiteurs de K_V ou activateurs de Na_V et Ca_V devraient restaurer le déclenchement normal des potentiels d'action, altéré dans certaines pathologies telles que la dépression ou le dysfonctionnement cognitif. En contrepartie, les activateurs de K_V ou inhibiteurs de Na_V et Ca_V devraient restaurer le déclenchement normal des potentiels d'action, altéré dans certaines pathologies telles que l'épilepsie et la douleur.

Le développement de l'ω-conotoxine CVID, ciblant le sous-type $Ca_V2.2$ de canal calcium, ainsi que celui de la toxine Ssm6a de centipède, inhibant le sous-type $Na_V1.7$ de canal sodium, n'ont pas

abouti car la première avait une activité trop proche de celle du ziconotide et la forme synthétique de la deuxième n'avait plus d'activité (Wang et al., 2016; Zambelli et al., 2016). D'autres toxines sont en court d'exploration dans l'axe thérapeutique douleur, comme la Phβ1α extraite du venin *Phoneutria nigriventer* inhibant le sous-type $Ca_V2.2$ (Rigo et al., 2017).

Dans cette optique, nous avons cherché de nouvelles molécules extraites de venins d'animaux, en criblant les fractions et sous-fractions de ces venins sur le sous-type $Na_V1.7$ de canal sodium, une cible antinociceptive de choix qui a été génétiquement validée (Tableaux 1-5 et 1-6).

Concernant les canalopathies liées à une absence de douleur, le mécanisme qui relie les mutants nuls murin et humain du sous-type $Na_V1.7$ et la voie des opioïdes endogènes a été largement étudié recemment. Chez le mutant nul murin ainsi que chez les patients présentant une insensibilité congénitale à la douleur, la naloxone, un antagoniste des opioïdes, peut réverser l'analgésie associée à la perte d'expression de $Na_V1.7$, démontrant ainsi une augmentation des effets dus aux opioïdes endogènes dans les deux cas. Le lien entre l'absence du sous-type $Na_V1.7$ et la balance "douleur en faveur de la voie antinociceptive (opioïdes)" serait une diminution du sodium intracellulaire qui agirait comme un messager secondaire pour activer la transcription des gènes des pré-pro-enképhalines (Figure 1-18; Minett et al., 2015; Insensee et al., 2017). L'utilisation d'antagonistes sélectifs du sous-type $Na_V1.7$ semble semble non applicable d'un point de vue pharmacologique car, pour obtenir un effet sur la voie antinociception (opioïdes) équivalent à celui chez les patients atteints d'insensibilité congénitale à la douleur (CIP), il faudrait une inhibition de 100% de la cible sur l'ensemble des neurones de DRG transmettant la douleur, sans produire d'effets secondaires, ce qui n'a pas encore été réalisé par de petites molécules, telles que la TTX, à des concentrations acceptables. Malgré cela, les recherches s'orientent vers un effet similaire avec des molécules qui ne passent pas la barrière hémato encéphalique (Emery et al., 2016). Une alternative invasive, et peu contrôlée, serait la thérapie génique neutralisant les ARN messagers du gène codant $Na_V1.7$. Il faudrait cependant trouver un système d'expression réversible, inductible par une molécule prise par le patient, qui ciblerait uniquement l'expression du sous-type $Na_V1.7$ au niveau des neurones de DRG impliqués dans la douleur, sans effet secondaire (Emery et al., 2016). La solution semble donc être la combinaison d'antagonistes sélectifs du sous-type $Na_V1.7$, en association avec des inhibiteurs des enképhalinases ou des opioïdes à faibles doses, qui peut entraîner une analgésie sans effet secondaire (Emery et al., 2016). L'action synergique entre certaines toxines peptidiques de venins d'animaux (telles que la PhlTx-1 et la Pn3a) et les opioïdes (ou les inhibiteurs des enképhalinases) a déjà été mise en évidence pour produire une analgésie (Brevet WO 2015036734 A1, 2015; Emery et al., 2016; Deuis et al., 2017).

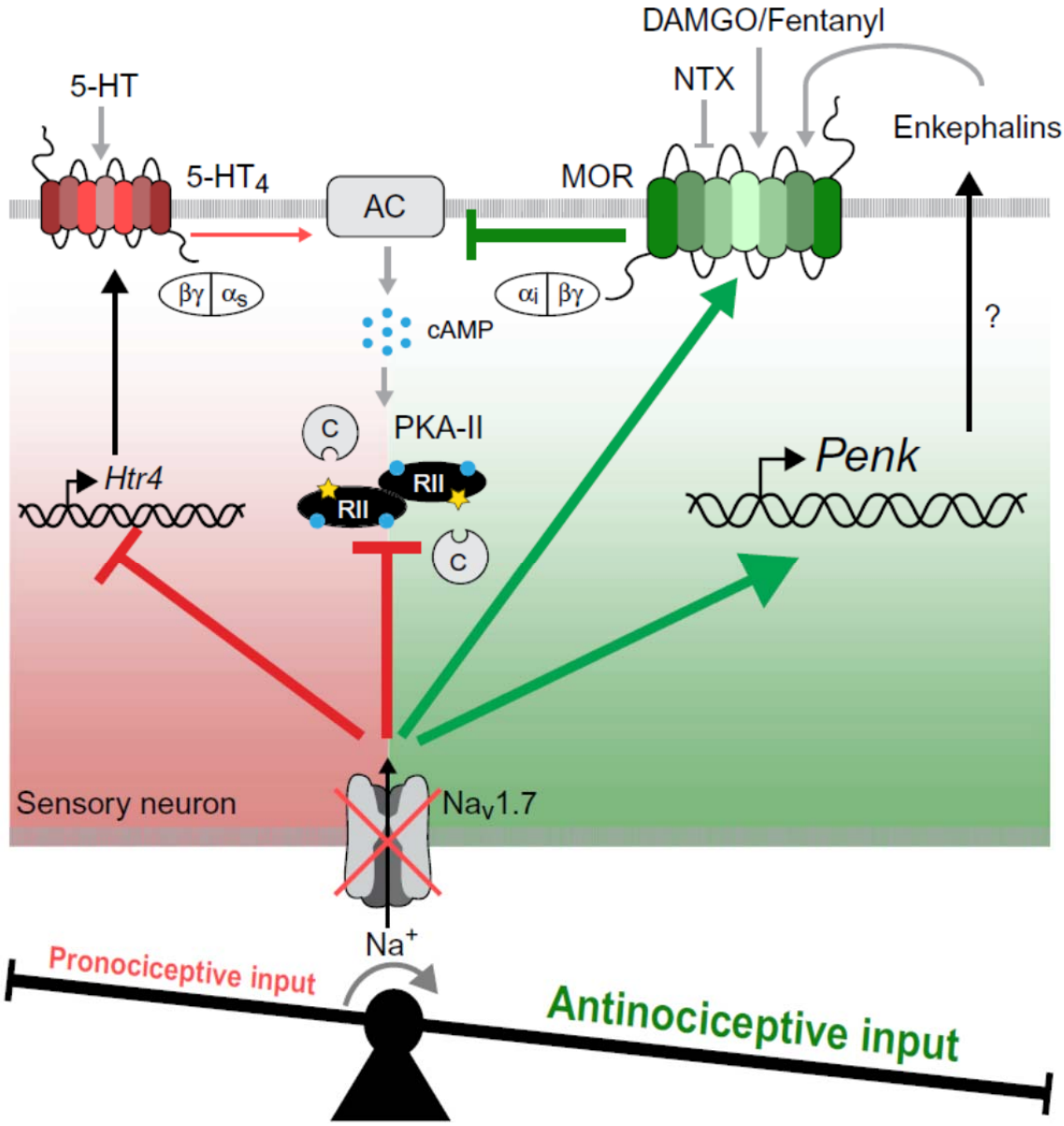

Figure 2-18. Régulation synergique de la signalisation pro- et antinociceptive chez des souris déficientes en $Na_V1.7$ (Isensee et al., 2017). Le déficit en Nav1.7 entraîne une réduction des récepteurs couplés aux protéines G (RCPG) sérotoninergiques (5-HT4), due à diminution de l'expression des gènes et de la sous-unité RIIb (et probablement aussi de la sous-unité catalytique) de la PKA-II. Ainsi, l'entrée pronociceptive dans les neurones sensoriels (en rouge) est fortement réduite. Simultanément, l'entrée antinociceptive (en vert) est augmentée en raison de l'activité accrue des RCPG des opioïdes et de l'expression accrue du gène codant le précurseur des peptides opioïdes endogènes (enképhalines). Cette régulation synergique déplace la balance vers la signalisation antinociceptive et contribue ainsi au phénotype indolore chez les souris déficientes en $Na_V1.7$. MOR, récepteurs mu des opioïdes; Penk, précurseur de la met-enkephaline; DAMGO, agoniste spécifique des MOR; NTX, naltrexone, antagoniste des MOR; AC, adénylate cyclase.

Actuellement, aucune toxine inhibant spécifiquement le sous-type $Na_V1.7$ n'est en essai clinique ou commercialisée (King, 2011; Zambelli et al., 2016). La Publication n°1 est une revue bibliographique qui vise à mettre en évidence comment des toxines d'araignée ciblant le sous-type $Na_V1.7$ dans les neurones de DRG peuvent être de puissants agents antidouleur.

1.3.3. Publication n°1

Frontiers in Pharmacology (2018) 9:1000. doi: 10.3389/fphar.2018.01000

"The $Na_V1.7$ channel subtype as an antinociceptive target for spider toxins in adult dorsal root ganglia neurons"

Tânia C. Gonçalves, Evelyne Benoit, Michel Partiseti & Denis Servent

frontiers in Pharmacology

REVIEW
published: 04 September 2018
doi: 10.3389/fphar.2018.01000

The $Na_V1.7$ Channel Subtype as an Antinociceptive Target for Spider Toxins in Adult Dorsal Root Ganglia Neurons

*Tânia C. Gonçalves[1,2], Evelyne Benoit[2,3], Michel Partiseti[1] and Denis Servent[2]**

[1] Sanofi R&D, Integrated Drug Discovery – High Content Biology, Paris, France, [2] Service d'Ingénierie Moléculaire des Protéines, CEA de Saclay, Université Paris-Saclay, Gif-sur-Yvette, France, [3] Institut des Neurosciences Paris-Saclay, UMR CNRS/Université Paris-Sud 9197, Gif-sur-Yvette, France

OPEN ACCESS

Edited by:
Yuri N. Utkin, Institute of Bioorganic Chemistry (RAS), Russia

Reviewed by:
Sandrine Cestèle, UMR7275 Institut de Pharmacologie Moléculaire et Cellulaire (IPMC), France
Maria Elena De Lima, Universidade Federal de Minas Gerais, Brazil

***Correspondence:**
Denis Servent
denis.servent@cea.fr

Specialty section:
This article was submitted to Pharmacology of Ion Channels and Channelopathies, a section of the journal Frontiers in Pharmacology

Received: *22 June 2018*
Accepted: *14 August 2018*
Published: *04 September 2018*

Citation:
Gonçalves TC, Benoit E, Partiseti M and Servent D (2018) The $Na_V1.7$ Channel Subtype as an Antinociceptive Target for Spider Toxins in Adult Dorsal Root Ganglia Neurons. Front. Pharmacol. 9:1000. doi: 10.3389/fphar.2018.01000

Although necessary for human survival, pain may sometimes become pathologic if long-lasting and associated with alterations in its signaling pathway. Opioid painkillers are officially used to treat moderate to severe, and even mild, pain. However, the consequent strong and not so rare complications that occur, including addiction and overdose, combined with pain management costs, remain an important societal and economic concern. In this context, animal venom toxins represent an original source of antinociceptive peptides that mainly target ion channels (such as ASICs as well as TRP, Ca_V, K_V and Na_V channels) involved in pain transmission. The present review aims to highlight the $Na_V1.7$ channel subtype as an antinociceptive target for spider toxins in adult dorsal root ganglia neurons. It will detail (i) the characteristics of these primary sensory neurons, the first ones in contact with pain stimulus and conveying the nociceptive message, (ii) the electrophysiological properties of the different Na_V channel subtypes expressed in these neurons, with a particular attention on the $Na_V1.7$ subtype, an antinociceptive target of choice that has been validated by human genetic evidence, and (iii) the features of spider venom toxins, shaped of inhibitory cysteine knot motif, that present high affinity for the $Na_V1.7$ subtype associated with evidenced analgesic efficacy in animal models.

Keywords: voltage-gated sodium channels, $Na_V1.7$ channel subtype, spider toxins, pain, dorsal root ganglia neurons, electrophysiology

Abbreviations: ASIC, acid-sensitive ionic channel; BGB, blood-ganglia-barrier; BNB, blood-nerve-barrier; Ca_V channel, voltage-gated calcium channel; CNS, central nervous system; DRG, dorsal root ganglia; EC_{50}, effective concentration necessary for increasing the response by 50%; GDNF, glial cell line-derivated neurotrophic factor; GMT, gating modifier toxin; GPCR, G-protein-coupled receptor; HnTx, hainantoxin; HwTx, huwentoxin; IC_{50}, effective concentration necessary for decreasing the response by 50%; iPSCs, induced pluripotent stem cells; JzTx, jingzhaotoxin; K_V channel, voltage-gated potassium channels; NaSpTx, spider Na_V channel toxins; NAT, natural antisense transcript; Na_V channel, voltage-gated sodium channel; NGF, nerve growth factor; PaurTx, Phrixotoxin; PcTx-1, psalmotoxin-1; PNS, peripheral nervous system; ProTx, protoxin; PSN, primary sensory neuron; PTM, post-translational modification; Ret, "rearranged during transfection" proto-oncogene; RUNX, Runt-related transcription factor; SSN, secondary sensory neuron; TRP channel, transient receptor potential channel; TSN, tertiary sensory neuron; TTX, tetrodotoxin.

INTRODUCTION

According to the International Association for the Study of Pain, at least 10% of the world's population suffer from pain since 1 over 10 adults has experienced or had (acute, chronic, intermittent or combined) pain with a median of suffering time around 7 years (Goldberg and McGee, 2011). The unpleasant sensation of pain is necessary to maintain the body integrity. However, it is often accompanied by long-term complications not only limited to comorbidities, as depression, but also including social and economic concerns as inability to work, social isolation and intrusive thoughts, leading to costs of more than 600 billion US dollars annually (Holmes, 2016). Pain care is thus a global public health priority whose management must be regulated in its totality by policies.

Nowadays, mild to moderate pain may be treated effectively with a combination of physical modalities (e.g., ice, rest and splints) and non-opioid analgesics (e.g., non-steroidal anti-inflammatory drugs, acetaminophen or other adjuvant medications). In contrast, the health system is pushed into its limits to treat debilitating chronic pain because the therapy is ineffective and/or associated with devastating effects. Indeed, management of chronic and severe pain, especially related to cancers or neuropathies, often requires opioids (Savage et al., 2008). Unfortunately, the opioid abuse and overdose often lead to death, which stimulates industries and academics to find an alternative with acceptable undesired effects (Negus, 2018).

In this context, the likely promising target for therapeutic treatment to fight pain and avoid central side-effects is the neuron located in the periphery dorsal root ganglia (DRG) which conveys pain from the skin and tendons to the central nervous system (CNS). The DRG neurons are well-known to express various families of transmembrane proteins, including ion channels, G-protein-coupled receptors (GPCRs) and gap junctions/pannexins (Pan et al., 2008; Spray and Hanani, 2017; Yekkirala et al., 2017). Among the ion channel family, the most extensively studied targets for pain treatment are voltage-gated calcium (Ca_V) and sodium (Na_V) channels. In particular, it is well established that small molecules that target Na_V channels attenuate chronic and debilitating pain in humans, as exemplified by tetrodotoxin (TTX). However, due to a lack of selectivity, pronounced side-effects have been described, such as nausea, dizziness, oral numbness and tingling, limiting thus the therapeutic development of this molecule (Hagen et al., 2017). During the last decade, the attraction of scientists for the $Na_V1.7$ channel subtype has greatly increased, due to its validation by human genetic diseases as a pain target. Many studies have been reported in the literature to describe gating modulators or pore blockers that affect the functional properties of this subtype (Vetter et al., 2017). Therefore, the present review will focus on the fascinating spider venom toxins which represent an original source of proteins possessing complex structures associated with specific electrophysiological effects and prone to be more selective for the $Na_V1.7$ channel subtype mainly expressed in DRG neurons.

PRIMARY SENSORY NEURONS AS FRONT DOOR FOR PAIN

The cellular elements involved in pain transmission from the peripheral to the CNS are detailed in **Figure 1**. The noxious information is first detected by the nociceptors of peripheral and visceral tissue, and then conveyed by the dendrites of primary sensory neurons (PSNs). The nociceptors are located at the level of free nerve endings of Aδ and C fibers of PSNs that respond to noxious stimuli and are widely found throughout skin and internal tissue. Three main types of pain receptors exist: the thermal, the mechanical and the polymodal receptors, activated by temperature, high pressure and mechanical, thermal or/and chemical stimuli, respectively (**Figure 1**, Box 1). The PSNs are pseudo-bipolar neurons which send their axons, components of dorsal roots, to the laminas I, II and V of the dorsal horn of spinal cord and establish synapses with the dendrites of secondary sensory neurons (SSNs) (**Figure 1**, Box 2). The SSNs, in turn, bring the noxious information to the hypothalamus and connect to tertiary sensory neurons (TSNs) whose cell bodies constitute, in part, the brain cortex (**Figure 1**, Box 3). At each CNS level, the information is integrated and modulated by different ascending/descending control systems such as the medullary control, named "gate control," and the diffuse inhibitory control including the noradrenergic and serotoninergic pathways induced by nociception from the higher centers to the dorsal horn, giving the affective, sensory and cognitive dimensions to the human experience of pain (Porreca and Navratilova, 2017).

The neuron bodies of PSNs constitute the 31 pairs of DRG, coming out all along the spinal marrow: 8 cervical (C1-C7, note that the first cervical spinal nerve is born above C1 and the eighth one below C7), 12 thoracic (T1–T12), 5 lumbar (L1–L5), 5 sacred (S1–S5), and 1 coccygeal (Co) which is vestigial. The cranial sensory (trigeminal or Gasser's) ganglion (nerve V) conveys facial skin sensitivity, the spiral (or cochlear) and vestibular (or Scarpa's) ganglia (nerve VIII) serve the hearing and balance senses, respectively, and the geniculate ganglion (nerve VII) transfers facial sensations, with the contribution of the superior and inferior (or petrous) ganglia of glossopharyngeal nerve (nerve IX) and the superior (or jugular) and inferior (or nodose) ganglia of vagus nerve (nerve X).

Dorsal root ganglia present a rich capillary bed in cell body area (**Figure 2**), with the particularity of high fenestrations between two endothelial cells being permeable to low and high molecular weight compounds (Petterson and Olsson, 1989; Parke and Whalen, 2002; Jimenez-Andrade et al., 2008; Berta et al., 2017). In contrast to the cell body area, the nerve fiber area wrapped by the epineural sheath, i.e., the dura mater continuum in peripheral nervous system (PNS), presents a blood-nerve barrier similar to the CNS blood-brain barrier (BNB), with a lot of tight junctions between cells that prevent the passage of unwanted drugs (Jimenez-Andrade et al., 2008; Liu et al., 2018).

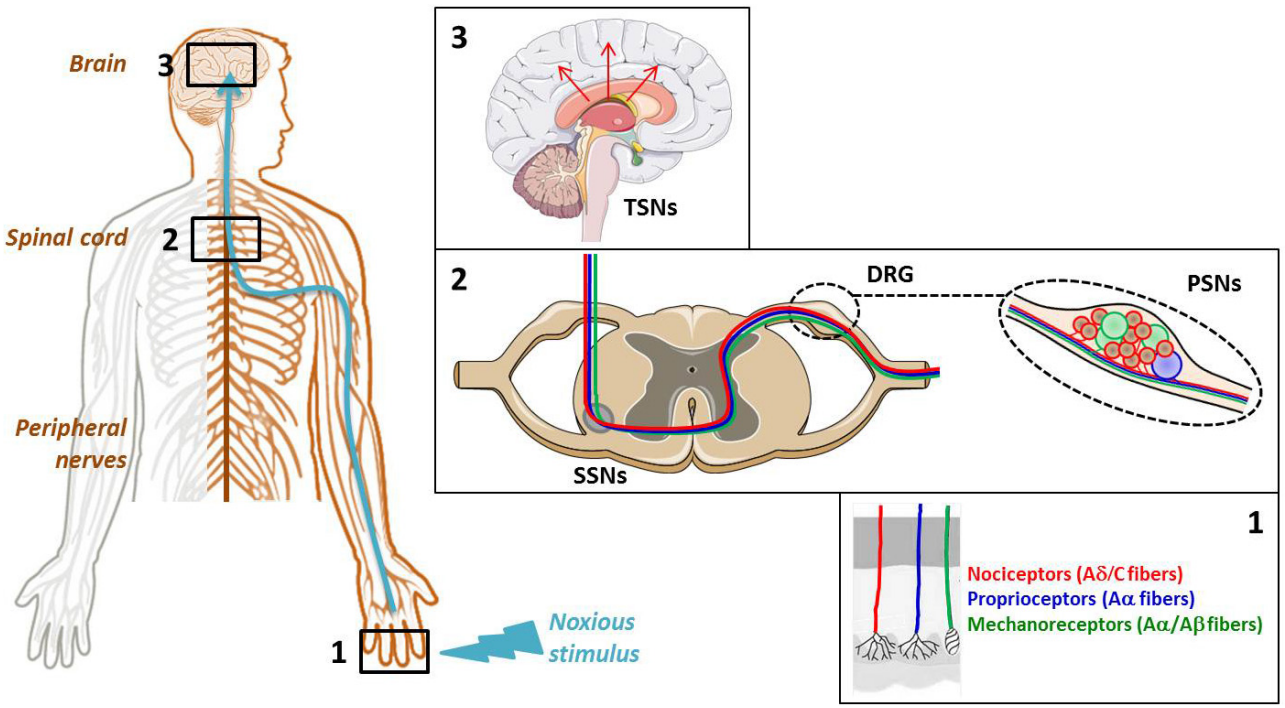

FIGURE 1 | Cellular elements involved in pain transmission from the peripheral to the central nervous system (CNS). **(Box 1)** The pain (thermal, high pressure, mechanical, chemical) information is first detected by the receptors located at the level of free nerve endings of primary sensory neuron (PSN) fibers. **(Box 2)** Then, it is conveyed by the dendrites of these neurons, components of dorsal root ganglia (DRG), to the dorsal horn of spinal cord where it is transmitted to the dendrites of secondary sensory neurons (SSNs). **(Box 3)** Finally, it is brought to the hypothalamus *via* the tertiary sensory neurons (TSNs) whose cell bodies constitute, in part, the brain cortex.

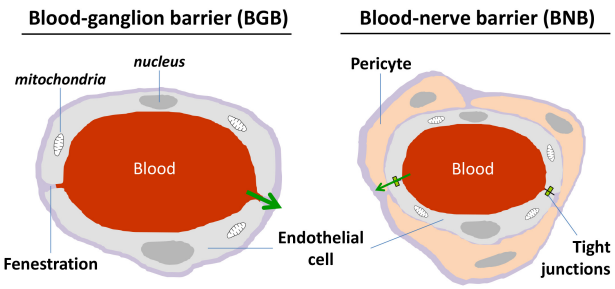

FIGURE 2 | Schematic representation of morphological characteristics of ganglion and nerve capillaries. Ganglion capillaries differ from nerve ones by the presence of fenestration and absence of narrow tight junctions. Nerve endothelial cells are surrounded by pericytes.

Soma of PSNs relaying the sensory information are part of the DRG which also contain other different cell types such as glial cells, endothelial cells and macrophages. Two groups of DRG neurons may be distinguished using light and electronic microscopy: the small dark neurons (cross-sectional area $\leq$ 800 μm^2 and diameter $\leq$ 30 μm) composed of high threshold, slowly-conducting unmyelinated (C) and/or thinly myelinated (Aδ) nerve fibers, and the large light neurons (cross-sectional area $>$ 800 μm^2 and diameter $>$ 30 μm) constituted of low threshold, fast-conducting thickly-myelinated (Aα and Aβ) nerve fibers (Elliott and Elliott, 1993; Taddese et al., 1995; Ho and O'Leary, 2011). The small DRG neurons that convey mainly pain message are subdivided into two groups: the non-peptidergic and the peptidergic neurons, depending on isolectin-IB4 labeling (**Table 1**). This subdivision of small neurons results from the expression level of runt-related transcription factor 1 (RUNX1), responsible for neuropeptide expression, regulated by the nerve growth factor (NGF) signaling during cell growth and differentiation (Luo et al., 2007). In adult DRG neurons, RUNX and neurogenin transcription factors regulate the expression of (i) glial cell line-derivated neurotrophic factor (GDNF) and tyrosine kinase c-Ret co-receptors (allowing the GDNF-ligand expression required for cell post-natal survival and indicative of non-peptidergic neurons), and (ii) the tropomyosin receptor-kinase receptors (TrkA, B and C which bind NGF or brain-derived neurotrophic factor, neurotrophin-4 and neurotrophin-3, respectively). The expression of growth factor receptors is therefore of great help to better characterizing adult DRG neurons (Ernsberger, 2009). Although only the small DRG neurons which are not labeled by isolectin-IB4 are peptidergic, the high dense-core vesicles of large neurons may also contain peptides, depending on both the vesicle size and the nerve condition, i.e., normal or injured (Wiesenfeld-Hallin and Xu, 2001). The peptidergic neurons deliver not only substance P and calcitonin gene-related peptide, but also somatostatin, vasoactive intestinal peptide and cholecystokinin. When released

TABLE 1 | Characteristics of DRG neurons.

	Small neurons (diameter ≤ 30 μm)		**Large neurons (diameter > 30 μm)**	
	Unmyelinated C fibers or thinly myelinated Aδ-fibers		**Thickly-myelinated Aα/Aβ fibers**	
Isolectin-IB4 labeling	YES (non-peptidergic)	NO (peptidergic)	NO	
Distribution	33%	33%	33%	
Transcription factors (during neurons development)		Neurogenin 1 (determines neuron formation)	Neurogenin 2 (regulates neuron formation)	
	RUNX1 (maintained by NGF signaling, inhibits neuropeptide expression)	Reduction of RUNX1 and Mrgpr (due to NGF signaling decrease)	RUNX3 (inhibits TrkB expression and contributes to specification of TrkC-positive neurons)	
Growth factor receptors (adult neurons)	GDNF and c-Ret co-receptors			
	GDNF family receptor α-2	GDNF family receptor α-3		
	P2X3 (absence of TrkA receptors)	TrkA receptors	TrkB receptors	TrkC receptors
Main Neuropeptides		– Substance P, NKA – CGRP, Somatostatin – VIP, PACAP-27 and 28 (upregulated after nerve injury) – Galanin – Cholescystokinin (upregulated after nerve injury)	– Substance P (upregulated after nerve injury) – CGRP – Neuropeptide Y (upregulated after nerve injury)	
Neuronal cytoskeleton	Peripherin		NF200	
Cell adhesion molecules	Necl-1	Necl-1	Necl-1	

The table illustrates the characteristics of DRG neurons regarding isolectin IB4-labeling, growth factor receptors, transcription factors, main neuropeptides, neuronal cytoskeleton composition, and cell adhesion molecules. GDNF, glial cell line-derived neurotrophic factor; Trk, Tropomyosin receptor-kinase; P2X3, P2X purinergic receptor subunit 3; RUNX, Runt-related transcription factor; NGF, Nerve Growth Factor; Mrgpr, Mas-related G- protein coupled receptor; NKA, neurokinin A; CGRP, Calcitonin Gene-Related Peptide; VIP, Vasoactive Intestine Peptide; PACAP, Pituitary Adenylate Cyclase-Activating Polypeptide; NF, Neurofilament; Necl, Nectin-like molecule. The increased gradient of Necl-1expression between small non-peptidergic, small peptidergic and large neurons are represented by an increasing size of letters.

in the CNS areas associated with pain transmission, these neuropeptides affect the expression pattern of SSNs, PSNs and peripheral organs (Moraes et al., 2014). The type of cytoskeleton neurofilaments present in DRG neurons is correlated with both the axonal diameter and the conduction velocity of action potential: intermediate neurofilament peripherin (57 kDa) is expressed in slowly-conducting unmyelinated (C) and/or thinly myelinated (Aδ) nerve fibers whereas the heavy neurofilament NF200 (200 kDa) is expressed in fast-conducting thickly-myelinated (Aα and Aβ) nerve fibers. The expression of the cell adhesion nectin-like molecule 1, interacting with the cytoskeleton, reflects the myelination level of nerve fibers (Ho and O'Leary, 2011).

Because of sequencing advances, a large scaled and more precise genetic characterization of DRG is now possible to better identifying the function and underlying mechanisms of each neuron. Therefore, an innovative approach to get rid of pain sensation, without affecting other physiological pain (or itch) pathways, would be to inhibit/remove only the population of DRG neurons that are responsible for the noxious disturbance (Liem et al., 2016; Li et al., 2018).

ELECTROPHYSIOLOGICAL STUDIES OF DRG NEURONS *IN VITRO*

Different types of tissues or individual cells can be used to perform electrophysiological studies of DRG neurons *in vitro*, each of them offering advantages and disadvantages. Hence, the primary cell cultures of rodent models (rats or mice) provide freshly isolated DRG neurons, however dissociated using enzymatic treatments which may disturb, in some extent, their functioning and thus their electrophysiological recordings. However, the two enzymatic procedures needed to replate the cells (i.e., detach and again deposit them on glass-slides) 24 h after their dissociation, in order to slow down extensive neurite growth that could limit adequate electrophysiological recordings, represent an aggressive cell treatment but were reported to have no marked effect on the neuronal action potential (Caviedes et al.,

1990). In any case, a delay of 4–7 days between cell dissociation and recordings is primordial to obtain adequate membrane conditions for experiments. A more physiological alternative to avoid cell dissociation and thus enzymatic procedures is to use DRG explants, i.e., slices of DRG previously inserted in 2% agar. Under these conditions, neurons are kept in their native environment and their plasma membrane is not altered (Scholz et al., 1998; Scholz and Vogel, 2000). However, the maximal life-time of DRG explants, as that of primary cell cultures, is of about 2 weeks.

Another possibility is thus the use of immortalized DRG neurons which offer the advantage of being maintained in cultures for long periods of time by changing freshly-made medium daily. The principle consists in immortalizing DRG neurons from human fetuses or rodents by using a tetracycline-responsive v-myc oncogene (Sah et al., 1997; Raymon et al., 1999), a medium previously conditioned with the rat thyroid cell line UCHT1 (Allen et al., 2002), or telomerase reverse transcriptase expression vectors added in the medium (Chen et al., 2007). Immortalized DRG neurons may also be directly obtained from transgenic rats harboring the temperature-sensitive large T-antigen gene (Nishiya et al., 2011). Immortalized human DRG neurons became an advance 30 years ago because of human tissue short supply. This type of more homogeneous cell lines is of great interest for high throughput screening of antinociceptive compounds.

Recently, the development of the induced pluripotent stem cell (iPSC) technology opens up new perspectives in personalized medicine, drug discovery or cell therapy. In the context of pain studies, iPSCs, derived for example from mesenchymal cells of a patient with inherited pain disease, are dedifferentiated to acquire the neuronal phenotype (bipolar cells) with the appropriate external medium containing neural growth factors. Then, the cell cultures will allow performing electrophysiological studies and pharmacological validation of a drug directly on targets presenting the mutation responsible for the patient pain phenotype (Cao et al., 2016; Sommer, 2016; Yang Y. et al., 2018).

VOLTAGE-GATED SODIUM CHANNELS EXPRESSED IN DRG NEURONS

Na_V channels are crucial transmembrane proteins for the communication of excitable cells in vertebrate and invertebrate organisms, due to their important role in action potential genesis and propagation. In terms of discovery, these channels are the founding members of a superfamily comprising more than 140 members grouped into eight families (voltage-gated Na, K and Ca channels, Ca-activated K channels, cyclic nucleotide-modulated ion channels, transient receptor potential (TRP) channel, inward-rectifying K channels and two-pore K channels) which, after the GPCRs, constitute the second largest group of signaling molecules encoded by the human genome (Yu and Catterall, 2004).

The fundamental functional features that allow Na_V channels to perform their role in cellular electrical signaling include a high selective permeation of Na ions and a gating system whose opening and closing are controlled by both the time and the membrane potential. Currently available data indicate that these channels consist of a pore-forming α-subunit (glycoprotein of 220–260 kDa) which is formed by four homologous domains (designated DI to DIV), each comprising six hydrophobic transmembrane α helices segments (designated S1–S6) connected by extra- and intra-cellular loops (**Figure 3**). The channel pore formation is attributed to the hairpin-like P loops connecting S5 and S6 segments (extracellular part of the pore) and to the S6 segments (intracellular part of the pore) of each domain. The channel activation (opening) is associated with the S4 segments of each domain, containing repeated motifs of positively charged amino acid residues (arginine) followed by two hydrophobic residues, which lead to the opening of the pore by moving outward under the influence of the membrane electric field to initiate protein conformational change. The channel inactivation (closing), meanwhile, is associated with the intracellular loop connecting DIII and DIV domains, including the isoleucine, phenylalanine and methionine (IFM) motif (Catterall, 2000; Goldin et al., 2000; Payandeh et al., 2011). Ten α-subunits of the mammalian Na_V channel, referred as $Na_V1.1$-1.10 (the first and second numbers indicating the gene subfamily and the specific channel isoform, respectively), have been identified so far. These subunits, which exhibit 40–70% sequence homology and closely related structures, can be distinguished according to their specific expression in tissues and their sensitivity to TTX, a well-known blocker of Na_V channels (**Table 2**). The structure, functional characteristics and phylogenetic relationships of the various Na_V channel subtypes have been largely detailed in the literature (Catterall, 2000; Goldin et al., 2000; Goldin, 2001, 2002; Catterall et al., 2005b, 2007).

The expression, pharmacology and functioning of Na_V channels can be altered by post-translational modifications (PTMs) of α-subunits, such as acetylation, phosphorylation, glycosylation and palmitoylation that occur after translation of mRNAs into peptidic chains or during secretory pathways. These PTMs greatly contribute to the development of chronic pain syndromes and may also modulate the toxin sensitivity of Na_V channels (Liu et al., 2012). In acquired, but not in inherited, pain syndromes, various signaling pathway activations may alter expression and functioning of Na_V channels (Laedermann et al., 2015). In mammals, the α-subunit is associated with an auxiliary β-subunit (glycoprotein of 30–40 kDa), consisting of a single transmembrane α helices segment, a long N-terminal extracellular immunoglobulin type V domain and a short C-terminal intracellular domain (**Figure 3**), which may in particular modulate the channel functioning, regulate its trafficking and expression at the membrane surface and/or link it to cytoskeleton proteins (Catterall, 2000; Xie et al., 2016). Therefore, it is likely that the β-subunit type and presence or absence in overexpression systems, or even in native tissues, will have big impact on Na_V channel readout during molecule screening experiments, in particular. Hence, the functional behavior of $Na_V1.8$ subtype has been reported to be highly dependent on the type of β-subunit expressed under normal and disease conditions (Vijayaragavan et al., 2004). Among the four auxiliary β-subunits (β1-β4) identified so far, only β2- and

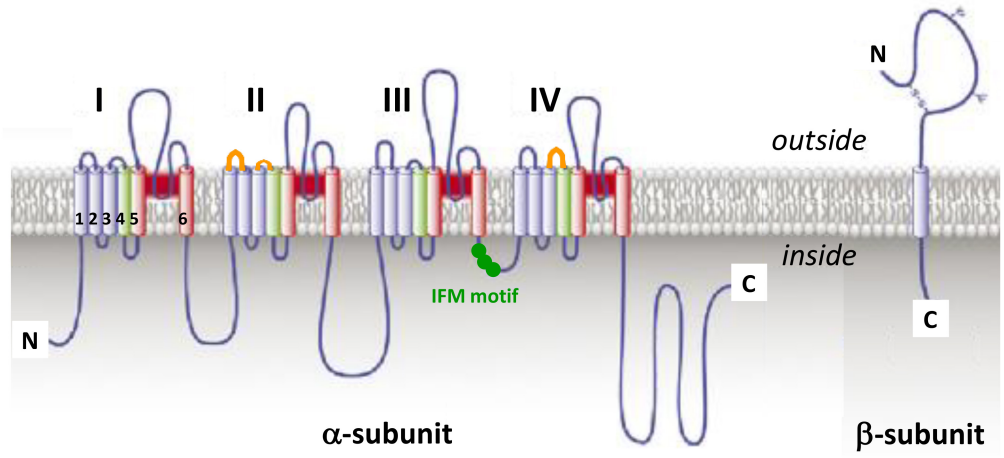

FIGURE 3 | The voltage-gated sodium channel. Schematic representations of α-subunit and auxiliary β-subunit of Na_V channels, in which cylinders are transmembrane α helices. In red: S5 and S6 pore-forming segments, in green: S4 voltage-sensor segment, and in blue: S1, S2, and S3 segments. IFM, isoleucine, phenylalanine and methionine residues. The orange loops in DII and DIV domains correspond to spider toxins binding sites (adapted from Catterall et al., 2007).

TABLE 2 | Expression in tissues and TTX sensitivity of Na_V channel subtypes.

Na_V subtype	Gene	Expression in tissues	TTX sensitivity
$Na_V1.1$	SCN1A	– PNS (**DRG**) – CNS (hippocampus, neocortex, cerebellum, retinal ganglion, microglia) – Keratinocytes	Yes
$Na_V1.2$	SCN2A	– PNS (**DRG**; unmyelinated or pre-myelinated axons and dendrites) – CNS (hippocampus, neocortex; cerebellum, astrocytes) – Fibroblast, islet β-cells, odontoblasts, osteoblasts	Yes
$Na_V1.3$ (fetal)	SCN3A	– PNS (early postnatal periods, adult **DRG** when nerve injury or inflammation, Schwann cells) – CNS (hippocampus, neocortex) – Fibroblasts, islet β-cells	Yes
$Na_V1.4$	SCN4A	– Skeletal muscle	Yes
$Na_V1.5$	SCN5A	– Heart – Skeletal muscle (denervated or fetal)	No
$Na_V1.6$	SCN8A	– PNS (**DRG**, nodes of Ranvier of motoneurons, Schwann cells) – CNS (Purkinje, pyramidal and granule neurons, nodes of Ranvier and axon initial segment of axons, astrocytes, microglia) – Cancer cells, endothelial cells, fibroblasts, keratinocytes, macrophages	Yes
$Na_V1.7$	SCN9A	– PNS (**DRG** and sympathetic ganglion neurons, neuroendocrine cells) – CNS (olfactory sensory neurons) – Smooth myocytes – Prostate and breast tumor cells, human erythroid progenitor cells, fibroblasts, immune cells	Yes
$Na_V1.8$	SCN10A	– PNS (**DRG**) – CNS (Purkinje neurons, astrocytes, Müller glia) – Endothelial cells, fibroblasts, keratinocytes, T lymphocytes	No
$Na_V1.9$	SCN11A	– PNS (**DRG**) – CNS (hypothalamus, astrocytes, Müller glia) – Cancer cells, endothelial cells, fibroblasts, T lymphocytes	No
$Na_V1.10$ ($Na_V1.x$, $Na_V2.1$-2.3)	SCN7A	– Lung, uterus, heart – PNS (**DRG**, Schwann cells) – CNS (thalamus, hippocampus, cerebellum, median preoptic nucleus)	No

The table illustrates the expression in tissues and sensitivity to TTX of Na_V channel α-subunits (adapted from Goldin, 2001; Trimmer and Rhodes, 2004; Black and Waxman, 2013). TTX, tetrodotoxin; PNS, peripheral nervous system; DRG, dorsal root ganglia; CNS, central nervous system.

β4-subunit have been reported to be covalently linked, by their N-terminal domain, to Na_V channel α-subunits (Namadurai et al., 2015). Recently, β4-subunit has been highlighted as a painkiller target because of its action of regulating fast resurgent Na currents in sensory neurons associated with pain disorders (Xie et al., 2013; Lewis and Raman, 2014; Barbosa et al., 2015).

Seven over the ten Na_V channel subtypes ($Na_V1.1$, 1.3, 1.6–1.10) which are expressed in DRG neurons are detailed in **Table 3**. All these subtypes are thus potentially involved in conveying noxious stimuli and may represent a target for pain treatment. Indeed, the $Na_V1.6$–1.9 subtypes, as main actors of pain anatomical and physiological integrities, have been genetically proved to be linked to human pain disorders. However, the high expression of $Na_v1.7$ subtype in DRG neurons (see **Figure 4**) and its multiple reported mutations inducing genetic-painful and painless disorders, largely documented in the literature, make this subtype one of the most promising target to alleviate pain. The contribution of $Na_V1.1$ and 1.10 subtypes to pain message was evidenced by pharmacological approaches, and the $Na_V1.3$ (fetal) subtype was reported to be overexpressed during injury-induced pain. It is worth noting that $Na_V1.2$ is the only subtype that does not transmit pain message in the PNS, although present in DRG neurons. In the CNS, mutations in the sequence coding for this subtype have been reported to induce epileptogenic and/or neurodevelopmental disorders (Liao et al., 2010; Hackenberg et al., 2014; Ben-Shalom et al., 2017; Wolff et al., 2017).

$Na_V1.1$, encoded by the SCN1A gene, is a TTX-sensitive, fast-activating and inactivating Na_V channel. Its expression is located in the CNS, PNS (more precisely in DRG neurons) and keratinocytes (Trimmer and Rhodes, 2004; Black and Waxman, 2013). This subtype was recently reported as a potential pain target involved in neuropathic pain (Irritable Bowel Syndrome, visceral hypersensitivity) and in acute pain and mechanical allodynia, due to the correlation between its activity and pain behaviors in rodent models using the activating spider toxin Hm1a and the selective inhibitory small molecule ICA-121431 (Osteen et al., 2016, 2017; Salvatierra et al., 2018). The important function of $Na_V1.1$ in the CNS is highlighted by more than 500 mutations in its coding sequence that cause epileptic syndromes (Febrile Seizure, Generalized Epilepsy with Febrile Seizures +, and Severe Myoclonic Epilepsy of Infancy also known as Dravet syndrome) (Catterall et al., 2010). Moreover, three of these mutations are also correlated to familial hemiplegic migraine, and several copy number variants have been linked to neurodevelopmental disorders such as intellectual disability, autism and psychiatric disease (Dichgans et al., 2005; Fry et al., 2016; Xiong et al., 2016).

$Na_V1.3$, encoded by the SCN3A gene, is also a TTX-sensitive, fast-activating and inactivating Na_V channel (Cummins et al., 2001). This fetal subtype is normally expressed in early postnatal periods. However, it is also expressed at very low levels in adult sensory primary afferents, and is rapidly upregulated in DRG after peripheral axotomy by sciatic nerve transection or chronic constriction (Waxman et al., 1994; Black et al., 1999; Dib-Hajj et al., 1999) or by tight ligation of the spinal nerve (Boucher et al., 2000; Kim et al., 2001), and in painful diabetic neuropathy (Tan et al., 2015; Yang et al., 2016). $Na_V1.3$ promotes the spontaneous ectopic discharge observed during nerve injury. In particular, its over-expression after spinal cord injury leads to rhythmic oscillatory burst firing, alternating with single spikes and silent periods, in second order dorsal horn sensory neurons, and to spindle wave firing mode in thalamus (ventral posterior lateral) neurons with identifiable peripheral receptive fields (Hains et al., 2003; Lai et al., 2003). The central neuropathic pain is also explained by $Na_V1.3$ upregulation which induces neuronal hyperexcitability and alters the process of somatosensory information (Hains et al., 2003; Hains et al., 2005, 2006). Recently, loss-of-function of the SCN3A gene, resulting in reduced expression or deficient trafficking to the plasma membrane of the protein, was reported to contribute to increased seizure susceptibility (Lamar et al., 2017).

$Na_V1.6$, encoded by the SCN8A gene, is a TTX-sensitive fast-activating and inactivating Na_V channel expressed in the PNS (DRG neurons, nodes of Ranvier of motoneurons, Schwann cells), in the CNS (Purkinje, pyramidal and granule neurons, nodes of Ranvier and initial segment of axons, astrocytes, microglia) and in non-neuronal tissues such as cancer cells, endothelial cells, fibroblasts, keratinocytes and macrophages (Trimmer and Rhodes, 2004; Black and Waxman, 2013; Israel et al., 2017). This subtype is upregulated in various peripheral pain pathways including oxaliplatin-induced cold allodynia (Deuis et al., 2013), type-2 diabetic neuropathic pain (Ren et al., 2012) and inflammatory pain (Xie et al., 2013). The $Na_V1.6$ α-subunit, covalently linked to the β4-subunit, can underlie excitatory, persistent and resurgent currents which induce repetitive firing and abnormal spontaneous activity of sensory neurons (Lewis and Raman, 2014; Barbosa et al., 2015; Xie et al., 2016). A $Na_V1.6$-gene mutation resulting in gain-of-function has been reported to potentiate transient and resurgent Na currents, leading to increased excitability in trigeminal neurons, exacerbating thus the pathophysiology of vascular compression and contributing to idiopathic trigeminal neuralgia (Grasso et al., 2016; Tanaka et al., 2016). In contrast to $Na_V1.1$ and 1.2, $Na_V1.6$ is involved in seizure resistance (Makinson et al., 2014). The knock-down of $Na_V1.6$ in the brain was shown to compensate the $Na_V1.1$-gene mutation-induced imbalance of excitation over inhibition involved in epileptogenic disorders, which motivates the necessity to find specific $Na_V1.6$ inhibitors to treat debilitating or fatal form of epilepsy such as the Dravet syndrome (Catterall, 2012; Anderson et al., 2017). Finally, more than ten human *de novo* mutations of $Na_V1.6$ gene have been identified in patients with two types of CNS disorders, epileptic encephalopathy and intellectual disability (O'Brien and Meisler, 2013).

$Na_V1.7$, encoded by the SCN9A gene, is a TTX-sensitive fast-activating and inactivating Na_V channel. It is expressed in the somatosensory system (mainly in C- and Aβ-type DRG neurons) and in the sympathetic ganglion neurons (myenteric and visceral sensory neurons) of PNS, but only in the olfactory sensory neurons of CNS. This subtype is also present in smooth myocytes (Jo et al., 2004; Israel et al., 2017; Vetter et al., 2017), and in non-excitable cells such as prostate and breast tumor cells, human erythroid progenitor cells, fibroblasts and immune cells (Black and Waxman, 2013; Israel et al., 2017). This subtype is

TABLE 3 | Electrophysiological properties and disorders associated with Na_V channel subtypes expressed in DRG neurons and involved in pain.

Na_V subtype	Activation (m) and inactivation (h) gating properties[1]		Pain signs	Genetic pain disorders	Pain-unrelated disorders
	Time-dependence	Voltage-dependence			
$Na_V1.1$	Fast (Tp = 1.23 ms)	$V_{m0.5} = -20$ mV $V_{h0.5} = -52$ mV	– Acute pain – Mechanical allodynia – Visceral hypersensitivity – Irritable Bowel syndrome		– Epileptic syndromes – Familial hemiplegic migraine – Neurodevelopmental disorders
$Na_V1.3$ (fetal)	Fast (Tp = 1.08 ms)	$V_{m0.5} = -20$ mV $V_{h0.5} = -58$ mV	– Painful nerve injury – Painful diabetic neuropathy – Central neuropathic pain		– Increased seizure susceptibility
$Na_V1.6$	Fast (Tp = 1.03 ms) ⇒ Resurgent/persistent currents	$V_{m0.5} = -19$ mV $V_{h0.5} = -56$ mV	– Oxaliplatin-induced cold allodynia – Painful diabetic neuropathy – Inflammatory pain	– Painful neuropathy (idiopathic trigeminal neuralgia)	– Seizure resistance – Epileptic encephalopathy – Intellectual disability – Cerebellar atrophy, behavioral deficits and ataxia
$Na_V1.7$	Fast (Tp = 1.09 ms) ⇒ Treshold current	$V_{m0.5} = -33$ mV $V_{h0.5} = -62$ mV	– Painful diabetic neuropathy – Inflammatory pain – Acute noxious mechanosensation	– Congenital insensivity to pain – Hereditary sensory and autonomic neuropathy – Genetic painful neuropathies	– Anosmia and hyposmia – Epileptic syndromes – Autism spectrum disorder – Irritating, itchy cough
$Na_V1.8$	Slow (Tp = 1.06 ms) ⇒ Persistent currents	$V_{m0.5} = -6$ mV $V_{h0.5} = -35$ mV	– Painful neuropathy (AIDS, diabetes, cancer) – Inflammatory pain – Maintenance of bone cancer pain	– Painful neuropathy (small fiber neuropathy, inherited erythromelalgia)	– Multiple sclerosis – Cardiac conduction abnormalities
$Na_V1.9$	Very slow (Tp > > 1 ms) ⇒ Treshold current	$V_{m0.5} = -48$ mV $V_{h0.5} = -31$ mV	– Inflammation-induced hyperalgesia and peripheral sensitization – Inflammatory, heat and mechanical pain hypersensitivity – Maintenance of bone cancer pain – Perception of cold pain – Visceral pain	– Congenital insensivity to pain – Hereditary sensory and autonomic neuropathy – Genetic painful neuropathies	– Hirschprung's disease (mega colon motility) – Bladder motility dysfunction – Essential tremor associated with familial episodic pain
$Na_V1.10$ ($Na_V1.x$, 2.1–2.3)	*Na-dependence (threshold value = 150 mM)*		– Bone cancer-related pain		– Chronic hypernatremia – Epileptogenic process

[1]*Adapted from Deuis et al. (2017a) and Inserra et al. (2017). Tp, time to peak current; $V_{m0.5}$, test-pulse voltage corresponding to 50% maximal activation; $V_{h0.5}$, pre-pulse voltage corresponding to 50% steady-state inactivation.*

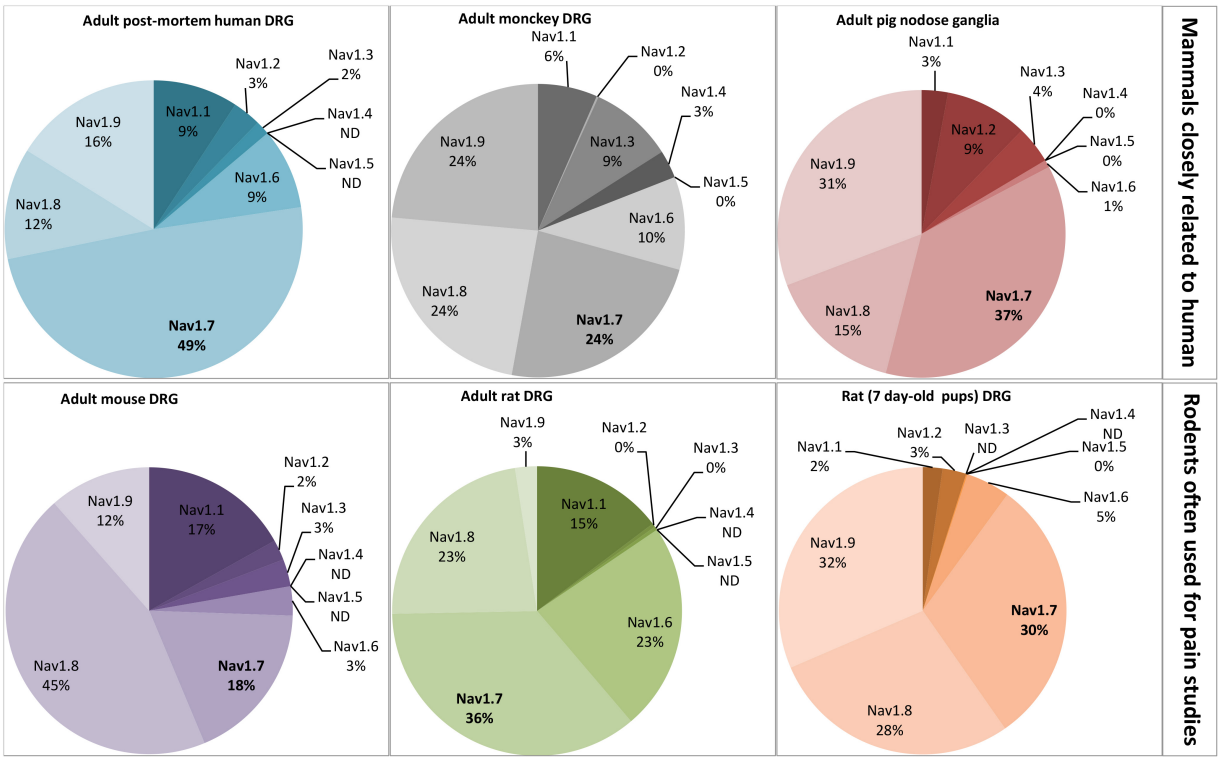

FIGURE 4 | Relative proportion of Na$_V$ channel α-subunits detected in mammalian dorsal root ganglia (DRG) neurons by RT-PCR. DRG neurons are from some representative mammals of different orders reported in the literature: primates, artyodactyla and rodents. The first order, including human and monkey, is closely related to the pig, belonging to the second order. The rodents, more distant from the human, represent the model often used for pain studies. The adult post-mortem human DRG neurons were obtained from healthy donors. All the data are from DRG neurons of adult mammals except those from 7 day-old rats. ND, non-determined. Adapted from Raymond et al. (2004), Berta et al. (2008), Ho and O'Leary (2011), Muroi and Undem (2014), and Chang et al. (2018).

a threshold channel since it is involved in the action potential (i.e., pain message) triggering by regulating the resting membrane potential of DRG. The implication of Na$_V$1.7 in neuropathic (diabetes) and inflammatory pain, as well as in acute noxious mechanosensation, has been explained by gene upregulation or variants (Dib-Hajj et al., 2013; Blesneac et al., 2018). In addition, multiple Na$_V$1.7 genetic mutations have been linked to painless or painful phenotypes. Hence, congenital SCN9A loss-of-function mutations, such as congenital insensivity to pain and type IID of hereditary sensory and autonomic neuropathy, can induce genetic diseases with a complete absence of pain. In contrast, the SCN9A gain-of-function mutations cause genetic painful neuropathies such as small fiber neuropathy, primary erythromelalgia and paroxysmal extreme pain disorder (de Lera Ruiz and Kraus, 2015; Vetter et al., 2017). The Na$_V$1.7 expression in the CNS is responsible for anosmia and hyposmia, always linked to painless phenotypes, and epilepsy (presence of different variants in patients showing seizures and Dravet syndrome, and of two SCN9A mutations related to epilepsy phenotype), as well as to autism spectrum disorder (Dib-Hajj et al., 2013; Mulley et al., 2013; Rubinstein et al., 2018; Yang C. et al., 2018). Na$_V$1.7 has also been reported to be the major Na$_V$ subtype in irritating, itchy cough conveyed by DRG neurons (Muroi and Undem, 2014; Sun et al., 2017).

Na$_V$1.8, encoded by the SCN10A gene, is a TTX-resistant Na$_V$ channel that exhibits slow activation and inactivation, as well as rapid repriming kinetics in C- and Aβ-type DRG neurons. With its slow kinetics and high activation threshold, this subtype corresponds to 80–90% of the inward current necessary to the rising phase of action potentials (Renganathan et al., 2001; Patrick Harty and Waxman, 2007). It is ectopically expressed in the CNS Purkinje neurons during multiple sclerosis disorder, and becomes thus a target of choice to develop a treatment for this disorder (Han et al., 2016). Na$_V$1.8 mRNAs were also detected and quantified in astrocytes, Müller glia, endothelial cells, fibroblasts, keratinocytes and T lymphocytes (Black and Waxman, 2013). This subtype has been reported to contribute to neuropathic pain, notably associated with acquired immunodeficiency syndrome, diabetes and cancer, as well as to inflammatory pain (Thakor et al., 2009; Qiu et al., 2012; Belkouch et al., 2014; Liu X. D. et al., 2014). Moreover, SCN10A gain-of-function mutations are associated, not only with the above mentioned neuropathic pain, but also with small fiber neuropathy and inherited erythromelalgia (Faber et al., 2012; Huang et al., 2016; Kist et al., 2016). Finally, genetic variations of SCN10A have been reported to correlate with cardiac conduction abnormalities in patients suffering from hypertrophic cardiomyopathy-like atrial fibrillation and Brugada

syndrome (Zimmer et al., 2014; Behr et al., 2015; Iio et al., 2015).

$Na_V1.9$, encoded by the SCN11A gene, is a TTX-resistant Na_V channel with very slow activation and inactivation kinetics. This subtype is also a threshold channel but exhibits different biophysical properties, compared with $Na_V1.7$ subtype. Roughly 80% of small-diameter sensory DRG neurons but only a few large-diameter ones and trigeminal ganglia (including C-type nociceptive cells) were reported to express $Na_V1.9$ mRNAs (Dib-Hajj et al., 1998). The expression pattern of this subtype is merely limited to the PNS, despite spots of expression in the CNS (hypothalamus, astrocytes, Müller glia), endothelial cells, fibroblasts, and T lymphocytes. It was also detected in some cancers such as lymphoma and small cell lung cancer (Black and Waxman, 2013; Israel et al., 2017). $Na_V1.9$ plays a major role (i) in inflammatory, heat and mechanical pain hypersensitivity, as revealed in both (sub) acute and chronic inflammatory pain models, (ii) in the maintenance of bone cancer pain (with the $Na_V1.8$ subtype), (iii) in the perception of cold pain under normal and pathological conditions, and (iv) in visceral pain (Lolignier et al., 2011; Qiu et al., 2012; Dib-Hajj et al., 2015; Lolignier et al., 2015; Hockley et al., 2016; Lolignier et al., 2016). More recently, multiple $Na_V1.9$ genetic mutations were linked to painless or painful phenotypes, making this subtype the second target of interest (after the $Na_V1.7$ subtype) to treat pain. Hence, on one hand, congenital SCN11A loss-of-function mutations, such as congenital insensitivity to pain and type VII of hereditary sensory and autonomic neuropathy, were reported to result in genetic diseases with a complete absence of pain (Leipold et al., 2013; Woods et al., 2015; Phatarakijnirund et al., 2016; Huang et al., 2017; King et al., 2017). On the other hand, the SCN11A gain-of-function mutations lead to genetic painful neuropathies such as small fiber neuropathy and rare inheritable pain disorders (Zhang et al., 2013; Huang et al., 2014; Han et al., 2015; Leipold et al., 2015; Kleggetveit et al., 2016; Okuda et al., 2016; Han et al., 2017). Finally, $Na_V1.9$ expression has also been linked to the Hirschprung's disease (affecting the mega colon motility), and implicated in the development of inflammation-based bladder motility dysfunction and in essential tremor associated with familial episodic pain (Ritter et al., 2009; O'Donnell et al., 2016; Leng et al., 2017).

$Na_V1.10$, encoded by the SCN7A gene and also named $Na_V1.x$ or $Na_V2.12.3$ (according to the species), is an atypical subtype associated with leak currents and considered as descendant of Na_V channel α1-subunits despite, notably, a less than 50% sequence homology and marked discrepancies in S4 segments and the intracellular loop connecting DIII and DIV domains (Goldin et al., 2000; Yu and Catterall, 2003; Nehme et al., 2012). In addition and in contrast to other Na_V channel subtypes, $Na_V1.10$ is not activated by the membrane potential but is sensitive to extracellular concentration of Na ions with a threshold value of 150 mM (Hiyama et al., 2002). It is expressed in the lung, uterus and heart, in the PNS neurons (e.g., medium to large-sized DRG neurons, non-myelinating Schwann cells) and in the CNS (e.g., thalamus, hippocampus, cerebellum, median preoptic nucleus) (Fukuoka et al., 2008; Garcia-Villegas et al., 2009) In particular, this subtype is clearly present in the primary regions implicated in hydromineral homeostasis, such as the subfornical organ, the vascular organ of the lamina terminalis and the median eminence which control the Na-intake behavior by changing neuronal excitability (Watanabe et al., 2006; Xing et al., 2015; Kinsman et al., 2017). It is involved in autoimmunity process causing chronic hypernatremia (Hiyama et al., 2010) and in epilectogenic process (Gorter et al., 2010). Recently, the inhibition or suppression of $Na_V1.10$ was reported to reduce pain behaviors in a bone cancer-induced model by decreasing the excitability of DRG neurons (Ke et al., 2012).

Using electrophysiological studies of DRG neurons *in vitro* for drug-discovery research may be limited by the relative proportions of targeted Na_V channel subtypes, as exemplified by the plant alkaloid paclitaxel whose effects differ between the models used (Chang et al., 2018). Indeed, the relative proportion of Na_V channel subtypes varies between small- and large-diameter DRG neurons, the first one expressing more TTX-resistant and less TTX-sensitive subtypes than the second one in both rodent and human neurons (Djouhri et al., 2003; Zhang et al., 2017). In addition, the relative proportion of Na_V subtypes varies according to the species studied. This is illustrated in **Figure 4** by the relative quantification of each Na_V channel subtype mRNA in small-diameter DRG neurons, the most documented in the literature because of their interest to treat pain, in various mammalian species. As expected from their importance in pain process, $Na_V1.6$–1.9 subtypes are relatively more expressed than $Na_V1.1$–1.3 subtypes, and the expression of the pain-unrelated $Na_V1.4$ and 1.5 subtypes, when detected, is extremely low and their function unknown (Ho et al., 2013).

The DRG neurons from rodent models are preferentially used for pain studies, compared with those from human, because they are rapidly available, easy to manipulate, cheap and exhibit well-conserved anatomical and physiological properties. However, adult mice and rat differ in their relative proportions of Na_V subtypes: more than 50% of mouse DRG Na_V subtypes are TTX-resistant (i.e., 45% of $Na_V1.8$ and 12% of $Na_V1.9$) whereas it is the opposite in rat DRG neurons (i.e., 15% of $Na_V1.1$, 23% of $Na_V1.6$ and 36% of $Na_V1.7$) (Berta et al., 2008; Chang et al., 2018). Interestingly, the level of expression of Na_V subtypes is greatly influenced by the age of mammal, i.e., the neuron maturation, as exemplified by the high expression of $Na_V1.9$ subtype in pup rat DRG neurons which is replaced by $Na_V1.1$ and 1.6 subtype expression in adult rat DRG neurons (Ho and O'Leary, 2011). PCR analysis of the seven Na_V subtypes expressed in DRG neurons reveals that post-mortem human DRG neurons from healthy donors show relatively high expression of $Na_V1.7$ (49%) and low expression of $Na_V1.8$ (12%), whereas the mouse DRG neurons present high expression of $Na_V1.8$ (45%) and low expression of $Na_V1.7$ (18%), the adult rat DRG neurons having an intermediate expression of $Na_V1.7$ (36%) and $Na_V1.8$ (23%) (Chang et al., 2018).

The mammals closely related to human (i.e., adult monkey and pig) roughly conserve the Na_V subtype expression pattern of post-mortem human DRG neurons, i.e., $Na_V1.7 \geq Na_V1.9 \geq Na_V1.8$ (Raymond et al., 2004; Muroi and Undem, 2014). Although the adult post-mortem human DRG neurons obtained from healthy donors are valuable in

terms of physiology to estimate the relative proportions of Na_V subtypes in living humans (Zhang et al., 2017; Chang et al., 2018), and even if some mammalian models seem closed to human, the message needs to be always shaded when extrapolated to human. Moreover, RT-PCR consists in averaging Na_V subtype mRNAs present in nucleus of cell population, and does not represent strictly the level of functional Na_V subtypes located in cell plasma membranes.

In several mammals DRG neurons, alternative splicing of Na_V α-subunit genes has been detected, resulting in the expression of multiple proteins. However, the functional significance of this process has not been completely elucidated (Dietrich et al., 1998; Schirmeyer et al., 2014). Some variants seem to lead to subunits showing redundant or no obvious pharmacological and/or functional differences, compared with the wild-type subunit (Schirmeyer et al., 2014). However, different pharmacological and functional properties between variant and wild-type subunits are evidenced in the literature, such as their sensitivity to drugs/toxins (Dietrich et al., 1998; Tan et al., 2002; Thompson et al., 2011; Boullot et al., 2017), their functional specificity regarding tissue/cell localization (Song et al., 2004), and their involvement in membrane excitability *via* the regulation of translational repression (Lin and Baines, 2015). Some alternative splice events are unique to DRG neurons. Hence, significant changes in the splicing patterns of Scn8a and Scn9a genes were observed in a rat model of neuropathic pain, leading to down-regulation of all transcripts (Raymond et al., 2004). Moreover, four alternative splice variants of SCN9A gene were reported to be expressed in human DRG neurons. The difference between two of them at the exon 5 level (exons 5A and 5N) results in two different amino acid residues, located in the S3 segment of DI domain acid. One of them, negatively charged, may be involved in modifications of Na_V channel activation and de-activation, impacting thus the paroxysmal extreme pain disorder disease phenotype (mutation I1461T). The two other alternative splice variants differ at the exon 11 level, leading to the presence (11L) or absence (11S) of an 11-amino acid sequence in the intracellular loop connecting DI and DII domains of Na_V channels, an important region for protein kinase A regulation which will thus influence neuronal excitability and pain sensation (Chatelier et al., 2008; Jarecki et al., 2009). Recently, a (NAT) was reported to be a potential candidate gene for patients with inherited (primary erythromelalgia, paroxysmal extreme pain disorder, and painful small fiber neuropathy) or acquired chronic pain disorders linked to the SCN9A locus, taking into account that the sense gene must not contain mutations which lead to sense gene-NAT pairing. This is the first example of a new therapy based on increased native antisense mRNAs to treat chronic pain in humans (Koenig et al., 2015).

ANALGESIC SPIDER TOXINS TARGETING THE $NA_V1.7$ CHANNEL SUBTYPE

Arachnids (araneae order) are the most diverse group of venomous animals with more than 46,000 extant species subdivided in araneomorph (crossing fangs) and mygalomorph (parallel fangs) suborders. Theraphosidae, the most studied and represented family in Arachnoserver 3.0 database, belongs to the latter suborder, with approximatively 470 species, a bit more than one quarter of all species (Pineda et al., 2018). Each spider venom contains from 100s to 1000s peptides (Escoubas, 2006), meaning that more than 10 million spider-venom peptides with an original sequence remain to be discovered since only approximatively 0.01% of these toxins have been explored until now (Klint et al., 2012, 2015b). The major components of most spider venoms are small disulfide-rich peptide toxins (Saez et al., 2010).

Because of their major role in action potential genesis and propagation in CNS, PNS, heart, smooth and skeletal muscles, Na_V channels are crucial for vital functions and are thus targeted by various groups of toxins that interact with at least six specific channel receptor-sites (Cestele and Catterall, 2000; Catterall et al., 2007; Gilchrist et al., 2014; Israel et al., 2017). Toxins that alter these channels may affect one or more of their three essential properties: activation, inactivation and ion selectivity. In that regard, toxins that have been isolated from different venomous animals (such as spiders, scorpions, cone snails, sea anemones and centipedes) may be classified as pore blockers and/or gating modifiers (Israel et al., 2017). The main source of the approximately 20 analgesic peptide toxins targeting the $Na_V1.7$ subtype is the venoms of tarantula constitutive of the theraphosidae family (**Figure 5**) (Klint et al., 2015b; Vetter et al., 2017). It is worth nothing that this family also contains many Na_V channel activators (Deuis et al., 2017b), such as Hm1a toxin which has been reported to induce a painful behavior when injected in rodents (Jami et al., 2017). A small amount of these toxins also target other ion channel types located at the level of DRG neurons and, thus, taking part into pain processing such as TRP channels A1 antagonized by Protoxin (ProTx)-I and Phα1β, acid-sensitive ionic channel (ASIC)1a inhibited with high affinity by psalmotoxin (PcTx)-1, and N-type Ca_V channels targeted by Phα1β, although with less potency than for TRPA1 (de Souza et al., 2013; Gui et al., 2014; Osmakov et al., 2014; Tonello et al., 2017).

Spider toxins targeting the $Na_V1.7$ subtype with an IC_{50} less than 500 nM are considered as analgesic toxin inhibitors (Klint et al., 2015a), and belong to the three first classes of spider Na_V channel toxins (NaSpTx), based on their primary structure and disulfide framework (**Figure 5**). It is worth noting that this classification also includes spider toxins which target not only the $Na_V1.7$ channel subtype but also other subtypes of ionic channels, as exemplified by the ω-TRTX-Gr2a toxin (GpTx-1) which was initially reported as a $Ca_V3.1$ subtype blocker after isolation from the Chilean tarantula, *Grammostola rosea*, venom (Ono et al., 2011). The NaSpTx peptides are gating modifier toxins (GMTs) because they alter channel gating by stabilizing voltage-sensors (mainly S3–S4 segments of DII domain) in a closed, or resting, configuration state (**Table 4**) (Klint et al., 2012). The $Na_V1.7$ analgesic spider toxin inhibitors are shaped by inhibitory cystine knot (ICK) scaffold due to 6 cysteines, arranged into a ring composed of two disulfide-bridges crossed by a third one (Saez et al., 2010). These peptides share a conserved amphipathic surface profile characterized by a high proportion

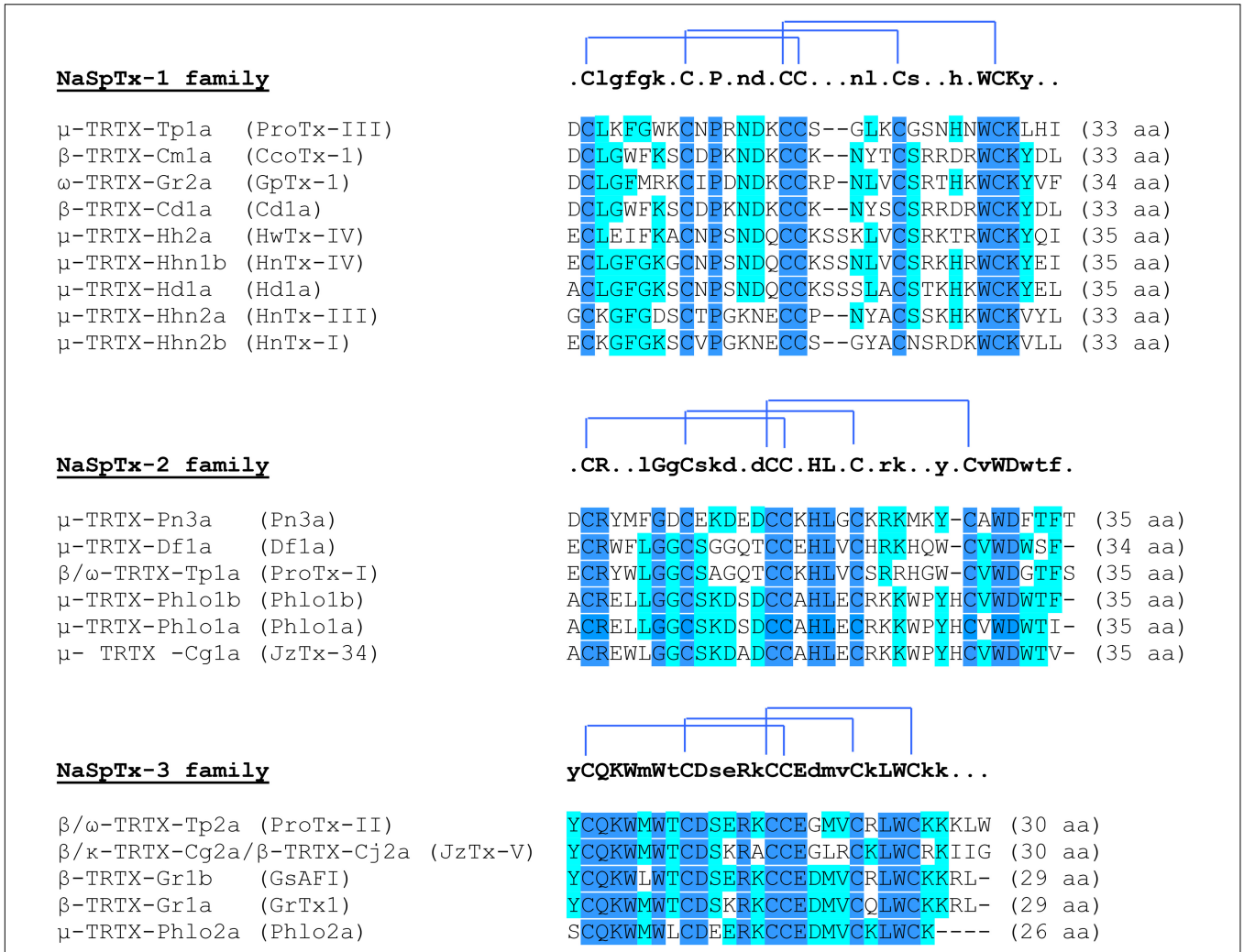

FIGURE 5 | Sequence alignment obtained by Multalin (version 5.4.1) of different potential analgesic toxins sorted by Na_V spider toxins families, using their UniProtKB identifiers. The consensus sequence is shown above each alignment, with the disulfide bond connectivity. In dark blue, highly conserved amino acid residues (100%), and in light blue, poorly conserved amino acid residues (>50%). The Greek letter(s) before the toxin name is associated to its type of action: μ for Na_V channel inhibition, β for shift in the voltage-dependence of Na_V channel activation, ω for Ca_V channel inhibition, and κ for K_V channel inhibition. ProTx, protoxin; HnTx, hainantoxin; CcoTx, ceratotoxin; HwTx, huwentoxin; JzTx, jingzhaotoxin; aa, amino acid residues; NaSpTx, spider Na_V channel toxin.

of hydrophobic/aromatic amino acid residues, such as Trp, Tyr and Phe, surrounded by charged amino acids which constitute a dipole potential with negative (Asp and Glu) and positive (Lys and Arg) zones (Jung et al., 2005; Cai et al., 2015). Finding more selective GMTs than pore-blockers of $Na_V1.7$ subtypes is likely because the voltage-sensors are more variable in terms of amino acid sequence than the pore region of Na_V channels (Catterall et al., 2005a; Payandeh et al., 2011).

ProTx-III, ceratotoxin-1, GpTx-1, Cd1a, huwentoxin (HwTx)-IV, hainantoxin (HnTx)-IV, Hd1a, HnTx-III and HnTx-I are $Na_V1.7$ potential analgesic peptide toxins, composed of 33–35 amino acid residues, that belong to NaSpTx-1 family, with nanomolar affinities (IC_{50} between 2.1 and 440 nM) for this Na_V subtype. According to their electrophysiological properties, these toxins act as pore blockers of the $Na_V1.7$ subtype and, except for ProTx-III and ceratotoxin-1, induce minor alterations (less than 5 mV) in the voltage-dependence of its activation and steady-state inactivation (**Figure 5** and **Table 4**). Various mutants of ProTx-III and ceratotoxin-1were produced, showing a 10–20-mV shift in the voltage-dependence of $Na_V1.7$ activation without any change in its fast and steady-state inactivation (Bosmans et al., 2006; Cardoso et al., 2015), in agreement with their interaction with the receptor-site 4 of Na_V channels (i.e., S3–S4 segments of DII domain). Models of docking toxins on Na_V channels have been reported, placing toxin peptides in the cleft between the channel S1–S2 and S3–S4 transmembrane α-helices (Minassian et al., 2013; Cai et al., 2015; Murray et al., 2016). Even the main channel amino acid residues involved in toxin-channel interactions were located in the extracellular loop connecting S3 and S4 segments of DII domain, some residues of the extracellular loop connecting S1 and S2 segments of DII

TABLE 4 | Selectivity profile, electrophysiological characteristics and channel binding site of $Na_V1.7$ potential analgesic peptide toxins representative of Na_V spider toxins (NaSpTx) families.

	GpTx-I (NaSpTx-1)	**HwTx-IV (NaSpTx-1)**		**Pn3a (NaSpTx-2)**	**ProTx-II (NaSpTx-3)**	
	ω-theraphotoxin-Gr2a	**μ-theraphotoxin-Hh2a**		**μ-theraphotoxin-Pn3a**	**β/ω-theraphotoxin-Tp2a**	
	Wild-type	**Wild-type**	**m3-HwTx-IV (E1G-E4G-Y33W)**	**Wild-type**	**Wild-type**	**GP-ProTX-II/JNJ63955918 (W7Q-W30L)**
Selectivity profile (IC_{50})[1]						
$hNa_V1.7$	4.4 nM	17–33 nM	0.4–3 nM	0.9 nM	0.3 nM	10 nM
$mNa_V1.7$				1.5 nM		
$rNa_V1.7$				4.4 nM		
$hNa_V1.1$		41 nM	8.1 nM	37 nM	16 nM	10 μM
$hNa_V1.2$		44 nM	11.9 nM	124 nM	41 nM	1.6 μM
$hNa_V1.3$	20 nM	190 nM	7.2 nM	210 nM	102 nM	
$hNa_V1.4$	301 nM	4–10 μM	369 nM	144 nM	39 nM	5 μM
$hNa_V1.5$	4.2 μM	>10 μM	>1 μM	800 nM	79–398 nM	>10 μM
$hNa_V1.6$		52–83.3 nM	6.8 nM	129 nM	26 nM	1 μM
$hNa_V1.8$	>10 μM	>10 μM	>1 μM	>10 μM	146 nM	
$hNa_V1.9$				2.4 μM		
$rK_V2.1$				>300 nM		
$hK_V11.1$ (Erg)	>10 μM	> 10 μM				
$hCa_V1.2$		>10 μM		>10 μM	*Inhibition*	
$hCa_V2.2$				>10 μM		
$hCa_V3.1$	9.8 nM				*Inhibition*	
hα7 nAChR				>10 μM		
hα3 nAChR				>10 μM		
TTX-S Na_V (DRG)	m: 6.3 nM	r-m: 30–130 nM		r: 300 nM		r: *78% inhibition by 300 nM*
TTX-R Na_V (DRG)		r-m: > 10 μM				r: *no effect of 300 nM*
Electrophysiology[2]						
Shift in m_V	−0.9 mV	−1.7 mV		+21.3 mV	+31.1 mV	+15.3 mV
Shift in h_V	−5.9 mV	−1.8 mV		−2.7 mV	*unchanged*	−6 mV
Fast inactivation	Unchanged	Unchanged		*Na_V dependent change*	Inhibited	Unchanged
Activation kinetics		Unchanged		Slowed		
Inactivation kinetics		Unchanged	Unchanged	Slowed		
τ_{ON}		25–34 s (1 μM)		167 s (30 nM)	2.5 s (1 μM)	<1 min (300 nM)
τ_{OFF}	*Reversible*	88 s			40 s	
Channel binding site (TTX-S Na_V subtypes)	Receptor-site 4 (S1–S2/S3–S4 of DII)	Receptor-site 4 (S1–S2/S3–S4 of DII)		Receptor-sites 3 and 4 (S3–S4 of DII/DIV)	Receptor-sites 3 and 4 (S3-S4 of DII/DIV)	

[1] IC_{50}, effective concentration necessary for decreasing the response by 50%; h, human; m, mouse, r, rat. [2] m_V, voltage-dependence of activation; h_V, voltage-dependence of inactivation; τ_{ON}, time constant of toxin effect, τ_{OFF}, time constant of toxin wash-out. TTX-S, tetrodotoxin-sensitive; TTX-R, tetrodotoxin-resistant.

domain helping to stabilize the toxin binding to the channel (**Figure 3**).

Pn3a, Df1a, ProTx-I, Phlo1b and jingzhaotoxin (JzTx)-34 are $Na_V1.7$ potential analgesic peptide toxins, composed of 34–35 amino acid residues, belonging to the NaSpTx-2 family and having also nanomolar affinities (IC_{50} between 0.9 and 610 nM) for this Na_V subtype (**Figure 5** and **Table 4**). This toxin family produces important alterations in the voltage-dependence of both activation (10–37-mV positive shifts) and steady-state inactivation (2.7–17.5-mV negative shifts). In addition, the fast inactivation of some TTX-sensitive Na_V channels is also affected by some of these toxins. This is in agreement with the known toxin receptor-sites 3 (i.e., S3-S4 segments of DIV domain) and 4 of Na_V channels (Deuis et al., 2017b).

ProTx-II, JzTx-V, GsAF1, GrTx-1 and Phlo2a are $Na_V1.7$ potential analgesic peptide toxins from the NaSpTx-3 family, composed of 26–30 amino acid residues, and showing nanomolar affinities (IC_{50} between 0.3 and 333 nM) for this Na_V subtype (**Figure 5** and **Table 4**). The toxin action consists in major alterations in the voltage-dependence of activation (10–31-mV positive shifts) with only minor modifications of the voltage-dependence of steady-state inactivation (up to 5-mV positive shifts). The channel binding sites of these toxins are the receptor-site 4 alone for JzTx-V or in addition with the receptor-site 3 for ProTx-II, those for the other toxins having not been reported (Smith et al., 2007; Moyer et al., 2018). As a consequence, the channel fast inactivation is altered by ProTx-II but not by JzTx-V.

Pn3a is the toxin that has been studied on the biggest panel of ionic channels and receptors reported so far (Deuis et al., 2017a), including all Na_V channel subunits, some cardiosafety targets (such as $K_V11.1$ and $Ca_V1.2$ channel subtypes) and other transmembrane proteins expressed at the membrane of DRG neurons ($K_V2.1$, α3-α7 nAChR, $Ca_V2.2$ subtypes). In particular, this toxin was tested on human and rodent (mouse and rat) $Na_V1.7$ subtypes, showing minor loss of potency (between 2 and 5 fold) for mouse and rat. These results are in agreement with the 93.0% (human *versus* mouse) and 92.8% (human *versus* rat) sequence identities between species [data obtained from high quality protein multiple sequence alignments using CLUSTAL Oméga version 1.2.3 (web version)]. The other toxins have not been screened exhaustively: mainly human Na_V subtypes and cardiovascular targets, such as $K_V11.1$, $Ca_V1.2$ and $Ca_V3.1$ subtypes. Big efforts were engaged to decrease toxin potency for $Na_V1.4$ and 1.5 subtypes to avoid neuromuscular and cardiac side-effects (Murray et al., 2016) or to directly find toxin possessing these characteristics (Xiao et al., 2008). Moreover, the interest to find analgesic toxins highly selective for $Na_V1.1$ and 1.6 subtypes, or to improve the toxin selectivity for these two subtypes, decreased during the past years because of the consequent inhibition of action potential transmission *via* axonal nodes of Ranvier which leads to central and peripheral (at the level of neuromuscular junctions) side-effects. Hence, the HwTx-IV mutant m3-HwTx-IV, presenting an additional hydrophobic patch (Gly1-Gly4-Trp33) has a reinforced inhibitory potency for the $Na_V1.7$ subtype while improving $Na_V1.1$, 1.2 and 1.6 subtype selectivity (Rahnama et al., 2017). Moreover, the ProTx-II mutant JNJ63955918/GP-ProTX-II (W7Q-W30L) presents a 14-fold decreased potency for the $Na_V1.7$ subtype but an improved selectivity against $Na_V1.1$, 1.2, 1.4, and 1.6 subtypes, thus avoiding side-effects such as seizures, arrhythmias and impaired motor functioning (Flinspach et al., 2017; Goncalves et al., 2018). A new strategy was recently proposed to increase the selectivity among the off-target panel, consisting in finding antagonist antibodies specific of $Na_V1.7$ subtype. The results obtained are controversial and need to be further confirmed (Lee et al., 2014; Liu et al., 2016). More recently, another approach was reported, using an antibody-drug conjugated: a potent $Na_V1.7$ toxin inhibitor (a GpTx-1 analog), connected by a PEG-linker to an antibody, showed greater stability in plasma and a biodistribution restricted to the regions expressing $Na_V1.7$ subtype, decreasing thus possible side-effect occurrence (Biswas et al., 2017).

Bilayer membranes that surrounded channel proteins seem to be important to stabilize the interactions between amphipathic GMTs and Na_V channels. Toxins and their mutants brought a better understanding of the so-called trimolecular complex relations. Hence, the affinity of GMTs for bilayer membrane lipids highlighted the type of amino acid residues implicated in these interactions that could also impact the toxin selectivity for Na_V channels (Deplazes et al., 2016; Henriques et al., 2016; Agwa et al., 2017, 2018; Zhang et al., 2018). Moreover, the pharmacological sensitivity of Na_V channels for toxins may be modulated by PTMs on the Na_V channel protein itself (Liu et al., 2012). Indeed, palmitoylation of rat $Na_V1.2$ subtype was reported to modify the subtype sensitivity to phrixotoxin (PaurTx)-3 and ProTx-II, producing a 10-fold increased affinity by binding to simultaneously the voltage-sensor domain and the surrounding membrane, without affecting ProTx-I binding (Bosmans et al., 2011; Henriques et al., 2016). PTMs could thus be of major interest and have to be also considered as potential therapeutic targets.

GpTx-1, HwTx-IV, HnTx-IV, HnTx-III, Pn3a, JzTx-34, ProTx-II and JzTx-V were tested on rodent DRG neurons, revealing high affinity for TTX-sensitive Na_V channels associated with high selectivity against TTX-resistant Na_V channels in mouse and rat DRG neurons (Liu et al., 2002, 2013; Peng et al., 2002; Deuis et al., 2016, 2017a; Flinspach et al., 2017; Goncalves et al., 2018; Moyer et al., 2018; Zeng et al., 2018). The action of HwTx-IV, meanwhile, is not equivalent on TTX-sensitive Na_V channels of rat and mouse DRG neurons, the IC_{50} being 4-fold lower in rat neurons likely due to the presence of high sensitive Na_V subtypes that are poorly or not expressed in mouse DRG neurons (Peng et al., 2002; Goncalves et al., 2018). Electrophysiological recordings under physiological conditions or quantification of altered expression of some proteins relevant in pain processing, in DRG neurons after toxin application, allowed characterizing the toxin potential analgesic effect at the cellular level. Hence, in DRG neurons, a JzTx-V mutant [CyA-JzTx-V (M6J-E17X-I28G), i.e., AM-0422] and ProTx-II were reported to inhibit or diminish action potential firing induced by chemical (capsaicin) and mechanical stimulation, or to alter spinal nociceptive processing induced by burn injury, respectively (Moyer et al., 2018; Torres-Perez et al., 2018).

Acute pain is a physiological function associated with injury that is essential for human survival. This kind of pain is normally short-lasting (<3 months). Beyond this period of time and without real injury, pathologic chronic pain is considered to result from damage in the transmission pain system itself. Several bioassays are available to appraise acute or chronic pain using standard or specific rodent models. Hence, mechanical and thermal stimulation assays or global gait analysis are classical to evaluate acute pain. The manual or electronic von Frey filament (or paw pressure) test is commonly used to assess to mechanical pain, while tail flick or water immersion and hot/cold plate tests are dedicated to assess to thermal pain. In these tests, the pain is provoked by pressure or extreme temperature on healthy rodent models. The inflammatory (caused by subcutaneously injected formalin, carrageenan or Freund's adjuvant compound, or intraperitoneally injected acid acetic) and neuropathic (caused by nerve constriction or ligation injury, chemotherapy-induced neuropathy) chronic pain are usually evaluated with the above mentioned mechanical and thermal stimulation assays, associated to a global evaluation of animal behavior. However, under these conditions, the pathological pain transmission system induced by inflammatory proteins or nerve injury is evaluated (Bridges et al., 2001; Mogil, 2009).

Various analgesic toxins have been proposed as candidates to replace opioids, because of their well-known side-effects. Hence, HwTx-IV, HnTx-IV, Pn3a and ProTx-II were shown to decrease pain at the level of morphine relief, in a dose-depending manner, in neuropathic (mainly spared nerve injury and diabetic neuropathy) and all inflammatory pain models, revealing a real evidence of their analgesic potential as drugs (Liu et al., 2014a,b, Tanaka et al., 2015; Deuis et al., 2017a; Flinspach et al., 2017). Pn3a and the ProTx-II mutant JNJ63955918 were also described as being effective on acute thermal pain tests (Deuis et al., 2017a; Flinspach et al., 2017). Despite the large number of pain tests, a new and original pharmacological one was recently proposed. It consists in specifically inhibiting fast inactivation and increasing peak current associated to $Na_V1.7$ subtype, by the local or systematical injection of OD1 scorpion toxin whose (EC_{50}) being in the nanomolar range (Deuis et al., 2016). This test has the advantages of being less invasive and more sensitive than neuropathic and inflammatory tests. Indeed, only a low amount of toxin candidate to be evaluated is necessary to relieve pain, as exemplified by GpTx-I, Cd1a, m3-HwTx-IV and Pn3a (Deuis et al., 2016; Cardoso et al., 2017; Rahnama et al., 2017; Sousa et al., 2017). However, the question of lack of physiological relevance of this test may be raised.

The best galenic form to make the patients compliant with their treatment is the pills for oral administration. However, in the pain tests, $Na_V1.7$ potential analgesic peptide toxins are often administrated by peripheral routes, such as subcutaneous (intraplantar), intraperitoneal or intramuscular injection) or intrathecal route. ProTx-II and its mutant, despite being the best candidate toxins with the highest affinity and selectivity, are unable to pass through the BNB (see **Figure 2**) and inhibit action potential transmission along nerves, except if a disruption of the perineurial barrier occurs (Schmalhofer et al., 2008; Hackel et al., 2012). After 24 h of intravenous infusion *in vivo*, ProTx-II can access DRG neurons but not sciatic nerves and CNS tissues (Liu et al., 2018). Thus, the fenestrations in Blood-Glangia-Barrier (BGB, see **Figure 2**) are the entry doors for large peptide toxins but their spreading to dorsal root of spinal cord and to distal nerve endings will depend on BNB. The intrathecal route is one possibility to bypass both the BBB and BNB, showing analgesic effects of ProTx-II in rodent pain tests with the risk of the post-lumbar puncture syndrome (headache down to the shoulders, nausea, vertigo and tinnitus) or the effects of the chemical compound itself if the injection is failed. The other possibility consists of toxin co-injection with hypertonic saline solution to disturb BNB (decrease claudin-1 mRNA, one protein responsible for tight-junction) and lead to toxin penetration (Hackel et al., 2012; Tanaka et al., 2015; Flinspach et al., 2017).

CONCLUSION

Venoms are usually associated with a lethal effect due to the presence in this complex mixture of toxins that have been selected during the evolution process to target crucial physiological systems of the preys. Nevertheless, due to their high affinity and selectivity profiles for specific receptors and ion channels involved in various pathophysiological processes, peptide toxins may be exploited as pharmacological tools and/or therapeutic drugs. Currently, six venom-derived drugs are used for the treatment of hypertension, acute coronary syndromes or diabetes, but the most promising therapeutic area is probably the pain and more precisely, the chronic pain. One peptide, isolated from cone snail venom, has been approved by FDA more than 14 years ago for the treatment of severe chronic pain (ziconotide), and several drug-leads, mainly issue from spider venoms, are actually in development. Among the various receptors and ion channels involved in pain transmission and which are targeted by venom peptides, the $Na_V1.7$ subtype is one of the most promising due to its peripheral location in DRG neurons which in addition present facilitated permeability to high molecular weight drugs. Furthermore, human genetic diseases, associated with $Na_V1.7$ mutations and leading to painless/painful phenotypes, validate this subtype as a pain target. Several spider toxins have been recently identified and characterized for their analgesic property due to their interactions with $Na_V1.7$. Furthermore, their engineering was associated with the optimization of their pharmacological (affinity for $Na_V1.7$ and selectivity profile) and biodistribution properties, reinforcing the potential of these venom-derived peptides as leads for therapeutic development. Finally, new paradigm used in the venom-peptide discovery, based on transcriptomic/proteomic technologies and on a toxin-driven approach, should increase the diversity of toxins identified and the rate of new drug lead discovery, more particularly for the treatment of chronic pain.

AUTHOR CONTRIBUTIONS

TG performed the major part of the bibliographic research and of the review writing. EB, MP, and DS critically read the review.

FUNDING

This research was funded by a collaborative grant (#153114) between Sanofi Research & Development (Chilly-Mazarin, France) and the French Alternative Energies and Atomic Energy Commission (CEA, Gif sur Yvette, France). TG was supported by a doctoral CIFRE fellowship from Sanofi.

REFERENCES

Agwa, A. J., Lawrence, N., Deplazes, E., Cheneval, O., Chen, R. M., Craik, D. J., et al. (2017). Spider peptide toxin HwTx-IV engineered to bind to lipid membranes has an increased inhibitory potency at human voltage-gated sodium channel hNaV1.7. *Biochim. Biophys. Acta* 1859, 835–844. doi: 10.1016/j.bbamem.2017.01.020

Agwa, A. J., Peigneur, S., Chow, C. Y., Lawrence, N., Craik, D. J., Tytgat, J., et al. (2018). Gating modifier toxins isolated from spider venom: modulation of voltage-gated sodium channels and the role of lipid membranes. *J. Biol. Chem.* 293, 9041–9052. doi: 10.1074/jbc.RA118.002553

Allen, D. D., Cardenas, A. M., Arriagada, C., Bennett, L. B., Garcia, C. J., Caviedes, R., et al. (2002). A dorsal root ganglia cell line derived from trisomy 16 fetal mice, a model for down syndrome. *Neuroreport* 13, 491–496. doi: 10.1097/00001756-200203250-00027

Anderson, L. L., Hawkins, N. A., Thompson, C. H., Kearney, J. A., and George, A. L. Jr. (2017). Unexpected efficacy of a novel sodium channel modulator in dravet syndrome. *Sci. Rep.* 7:1682. doi: 10.1038/s41598-017-01851-9

Barbosa, C., Tan, Z. Y., Wang, R., Xie, W., Strong, J. A., Patel, R. R., et al. (2015). Navbeta4 regulates fast resurgent sodium currents and excitability in sensory neurons. *Mol. Pain* 11:60. doi: 10.1186/s12990-015-0063-9

Behr, E. R., Savio-Galimberti, E., Barc, J., Holst, A. G., Petropoulou, E., Prins, B. P., et al. (2015). Role of common and rare variants in SCN10A: results from the Brugada syndrome QRS locus gene discovery collaborative study. *Cardiovasc. Res.* 106, 520–529. doi: 10.1093/cvr/cvv042

Belkouch, M., Dansereau, M. A., Tetreault, P., Biet, M., Beaudet, N., Dumaine, R., et al. (2014). Functional up-regulation of Nav1.8 sodium channel in Abeta afferent fibers subjected to chronic peripheral inflammation. *J. Neuroinflammation* 11:45. doi: 10.1186/1742-2094-11-45

Ben-Shalom, R., Keeshen, C. M., Berrios, K. N., An, J. Y., Sanders, S. J., and Bender, K. J. (2017). Opposing effects on NaV1.2 function underlie differences between SCN2A variants observed in individuals with autism spectrum disorder or infantile seizures. *Biol. Psychiatry* 82, 224–232. doi: 10.1016/j.biopsych.2017.01.009

Berta, T., Poirot, O., Pertin, M., Ji, R. R., Kellenberger, S., and Decosterd, I. (2008). Transcriptional and functional profiles of voltage-gated Na(+) channels in injured and non-injured DRG neurons in the SNI model of neuropathic pain. *Mol. Cell. Neurosci.* 37, 196–208. doi: 10.1016/j.mcn.2007.09.007

Berta, T., Qadri, Y., Tan, P. H., and Ji, R. R. (2017). Targeting dorsal root ganglia and primary sensory neurons for the treatment of chronic pain. *Expert Opin. Ther. Targets* 21, 695–703. doi: 10.1080/14728222.2017.1328057

Biswas, K., Nixey, T. E., Murray, J. K., Falsey, J. R., Yin, L., Liu, H., et al. (2017). Engineering antibody reactivity for efficient derivatization to generate NaV1.7 inhibitory GpTx-1 peptide-antibody conjugates. *ACS Chem. Biol.* 12, 2427–2435. doi: 10.1021/acschembio.7b00542

Black, J. A., Cummins, T. R., Plumpton, C., Chen, Y. H., Hormuzdiar, W., Clare, J. J., et al. (1999). Upregulation of a silent sodium channel after peripheral, but not central, nerve injury in DRG neurons. *J. Neurophysiol.* 82, 2776–2785. doi: 10.1152/jn.1999.82.5.2776

Black, J. A., and Waxman, S. G. (2013). Noncanonical roles of voltage-gated sodium channels. *Neuron* 80, 280–291. doi: 10.1016/j.neuron.2013.09.012

Blesneac, I., Themistocleous, A. C., Fratter, C., Conrad, L. J., Ramirez, J. D., Cox, J. J., et al. (2018). Rare NaV1.7 variants associated with painful diabetic peripheral neuropathy. *Pain* 159, 469–480. doi: 10.1097/j.pain.0000000000001116

Bosmans, F., Milescu, M., and Swartz, K. J. (2011). Palmitoylation influences the function and pharmacology of sodium channels. *Proc. Natl. Acad. Sci. U.S.A.* 108, 20213–20218. doi: 10.1073/pnas.1108497108

Bosmans, F., Rash, L., Zhu, S., Diochot, S., Lazdunski, M., Escoubas, P., et al. (2006). Four novel tarantula toxins as selective modulators of voltage-gated sodium channel subtypes. *Mol. Pharmacol.* 69, 419–429. doi: 10.1124/mol.105.015941

Boucher, T. J., Okuse, K., Bennett, D. L., Munson, J. B., Wood, J. N., and Mcmahon, S. B. (2000). Potent analgesic effects of GDNF in neuropathic pain states. *Science* 290, 124–127. doi: 10.1126/science.290.5489.124

Boullot, F., Castrec, J., Bidault, A., Dantas, N., Payton, L., Perrigault, M., et al. (2017). Molecular characterization of voltage-gated sodium channels and their relations with paralytic shellfish toxin bioaccumulation in the pacific oyster crassostrea gigas. *Mar. Drugs* 15:E21. doi: 10.3390/md15010021

Bridges, D., Thompson, S. W., and Rice, A. S. (2001). Mechanisms of neuropathic pain. *Br. J. Anaesth.* 87, 12–26. doi: 10.1093/bja/87.1.12

Cai, T., Luo, J., Meng, E., Ding, J., Liang, S., Wang, S., et al. (2015). Mapping the interaction site for the tarantula toxin hainantoxin-IV (beta-TRTX-Hn2a) in the voltage sensor module of domain II of voltage-gated sodium channels. *Peptides* 68, 148–156. doi: 10.1016/j.peptides.2014.09.005

Cao, L., Mcdonnell, A., Nitzsche, A., Alexandrou, A., Saintot, P. P., Loucif, A. J., et al. (2016). Pharmacological reversal of a pain phenotype in iPSC-derived sensory neurons and patients with inherited erythromelalgia. *Sci. Transl. Med.* 8:335ra356. doi: 10.1126/scitranslmed.aad7653

Cardoso, F. C., Dekan, Z., Rosengren, K. J., Erickson, A., Vetter, I., Deuis, J. R., et al. (2015). Identification and characterization of ProTx-III [mu-TRTX-Tp1a], a new voltage-gated sodium channel inhibitor from venom of the tarantula *Thrixopelma pruriens*. *Mol. Pharmacol.* 88, 291–303. doi: 10.1124/mol.115.098178

Cardoso, F. C., Dekan, Z., Smith, J. J., Deuis, J. R., Vetter, I., Herzig, V., et al. (2017). Modulatory features of the novel spider toxin mu-TRTX-Df1a isolated from the venom of the spider *Davus fasciatus*. *Br. J. Pharmacol.* 174, 2528–2544. doi: 10.1111/bph.13865

Catterall, W. A. (2000). From ionic currents to molecular mechanisms: the structure and function of voltage-gated sodium channels. *Neuron* 26, 13–25. doi: 10.1016/S0896-6273(00)81133-2

Catterall, W. A., Cestele, S., Yarov-Yarovoy, V., Yu, F. H., Konoki, K., and Scheuer, T. (2007). Voltage-gated ion channels and gating modifier toxins. *Toxicon* 49, 124–141. doi: 10.1016/j.toxicon.2006.09.022

Catterall, W. A., Goldin, A. L., and Waxman, S. G. (2005a). International union of pharmacology. XLVII. Nomenclature and structure-function relationships of voltage-gated sodium channels. *Pharmacol. Rev.* 57, 397–409.

Catterall, W. A., Perez-Reyes, E., Snutch, T. P., and Striessnig, J. (2005b). International union of pharmacology. XLVIII. Nomenclature and structure-function relationships of voltage-gated calcium channels. *Pharmacol. Rev.* 57, 411–425.

Catterall, W. A., Kalume, F., and Oakley, J. C. (2010). NaV1.1 channels and epilepsy. *J. Physiol.* 588, 1849–1859. doi: 10.1113/jphysiol.2010.187484

Catterall, W.A. (2012). "Sodium channel mutations and epilepsy," in *Jasper's Basic Mechanisms of the Epilepsies,* eds J. Noebels, M. Avoli, M. Rogawski, R. Olsen, and A. Delgado-Escueta (Rockville, MD: Bethesda). doi: 10.1093/med/9780199746545.003.0052

Caviedes, P., Ault, B., and Rapoport, S. I. (1990). Replating improves whole cell voltage clamp recording of human fetal dorsal root ganglion neurons. *J. Neurosci. Methods* 35, 57–61. doi: 10.1016/0165-0270(90)90094-V

Cestele, S., and Catterall, W. A. (2000). Molecular mechanisms of neurotoxin action on voltage-gated sodium channels. *Biochimie* 82, 883–892. doi: 10.1016/S0300-9084(00)01174-3

Chang, W., Berta, T., Kim, Y. H., Lee, S., Lee, S. Y., and Ji, R. R. (2018). Expression and role of voltage-gated sodium channels in human dorsal root ganglion neurons with special focus on Nav1.7, Species Differences, and Regulation by Paclitaxel. *Neurosci. Bull.* 34, 4–12. doi: 10.1007/s12264-017-0132-3

Chatelier, A., Dahllund, L., Eriksson, A., Krupp, J., and Chahine, M. (2008). Biophysical properties of human Na v1.7 splice variants and their regulation by protein kinase A. *J. Neurophysiol.* 99, 2241–2250. doi: 10.1152/jn.01350.2007

Chen, W., Mi, R., Haughey, N., Oz, M., and Hoke, A. (2007). Immortalization and characterization of a nociceptive dorsal root ganglion sensory neuronal line. *J. Peripher. Nerv. Syst.* 12, 121–130. doi: 10.1111/j.1529-8027.2007.00131.x

Cummins, T. R., Aglieco, F., Renganathan, M., Herzog, R. I., Dib-Hajj, S. D., and Waxman, S. G. (2001). Nav1.3 sodium channels: rapid repriming and slow closed-state inactivation display quantitative differences after expression in a mammalian cell line and in spinal sensory neurons. *J. Neurosci.* 21, 5952–5961. doi: 10.1523/JNEUROSCI.21-16-05952.2001

de Lera Ruiz, M., and Kraus, R. L. (2015). Voltage-gated sodium channels: structure, function, pharmacology, and clinical indications. *J. Med. Chem.* 58, 7093–7118. doi: 10.1021/jm501981g

de Souza, A. H., Castro, C. J. Jr., Rigo, F. K., De Oliveira, S. M., Gomez, R. S., et al. (2013). An evaluation of the antinociceptive effects of Phalpha1beta, a neurotoxin from the spider *Phoneutria nigriventer*, and omega-conotoxin MVIIA, a cone snail Conus magus toxin, in rat model of inflammatory and neuropathic pain. *Cell. Mol. Neurobiol.* 33, 59–67. doi: 10.1007/s10571-012-9871-x

Deplazes, E., Henriques, S. T., Smith, J. J., King, G. F., Craik, D. J., Mark, A. E., et al. (2016). Membrane-binding properties of gating modifier and pore-blocking toxins: membrane interaction is not a prerequisite for modification of channel gating. *Biochim. Biophys. Acta* 1858, 872–882. doi: 10.1016/j.bbamem.2016.02.002

Deuis, J. R., Dekan, Z., Wingerd, J. S., Smith, J. J., Munasinghe, N. R., Bhola, R. F., et al. (2017a). Pharmacological characterisation of the highly NaV1.7 selective spider venom peptide Pn3a. *Sci. Rep.* 7:40883. doi: 10.1038/srep40883

Deuis, J. R., Mueller, A., Israel, M. R., and Vetter, I. (2017b). The pharmacology of voltage-gated sodium channel activators. *Neuropharmacology* 127, 87–108. doi: 10.1016/j.neuropharm.2017.04.014

Deuis, J. R., Wingerd, J. S., Winter, Z., Durek, T., Dekan, Z., Sousa, S. R., et al. (2016). Analgesic effects of GpTx-1, PF-04856264 and CNV1014802 in a mouse model of NaV1.7-Mediated Pain. *Toxins* 8:E78. doi: 10.3390/toxins8030078

Deuis, J. R., Zimmermann, K., Romanovsky, A. A., Possani, L. D., Cabot, P. J., Lewis, R. J., et al. (2013). An animal model of oxaliplatin-induced cold allodynia reveals a crucial role for Nav1.6 in peripheral pain pathways. *Pain* 154, 1749–1757. doi: 10.1016/j.pain.2013.05.032

Dib-Hajj, S. D., Black, J. A., and Waxman, S. G. (2015). NaV1.9: a sodium channel linked to human pain. *Nat. Rev. Neurosci.* 16, 511–519. doi: 10.1038/nrn3977

Dib-Hajj, S. D., Fjell, J., Cummins, T. R., Zheng, Z., Fried, K., Lamotte, R., et al. (1999). Plasticity of sodium channel expression in DRG neurons in the chronic constriction injury model of neuropathic pain. *Pain* 83, 591–600. doi: 10.1016/S0304-3959(99)00169-4

Dib-Hajj, S. D., Tyrrell, L., Black, J. A., and Waxman, S. G. (1998). NaN, a novel voltage-gated Na channel, is expressed preferentially in peripheral sensory neurons and down-regulated after axotomy. *Proc. Natl. Acad. Sci. U.S.A.* 95, 8963–8968. doi: 10.1073/pnas.95.15.8963

Dib-Hajj, S. D., Yang, Y., Black, J. A., and Waxman, S. G. (2013). The Na(V)1.7 sodium channel: from molecule to man. *Nat. Rev. Neurosci.* 14, 49–62. doi: 10.1038/nrn3404

Dichgans, M., Freilinger, T., Eckstein, G., Babini, E., Lorenz-Depiereux, B., Biskup, S., et al. (2005). Mutation in the neuronal voltage-gated sodium channel SCN1A in familial hemiplegic migraine. *Lancet* 366, 371–377. doi: 10.1016/S0140-6736(05)66786-4

Dietrich, P. S., Mcgivern, J. G., Delgado, S. G., Koch, B. D., Eglen, R. M., Hunter, J. C., et al. (1998). Functional analysis of a voltage-gated sodium channel and its splice variant from rat dorsal root ganglia. *J. Neurochem.* 70, 2262–2272. doi: 10.1046/j.1471-4159.1998.70062262.x

Djouhri, L., Newton, R., Levinson, S. R., Berry, C. M., Carruthers, B., and Lawson, S. N. (2003). Sensory and electrophysiological properties of guinea-pig sensory neurones expressing Nav 1.7 (PN1) Na+ channel alpha subunit protein. *J. Physiol.* 546, 565–576. doi: 10.1113/jphysiol.2002.026559

Elliott, A. A., and Elliott, J. R. (1993). Characterization of TTX-sensitive and TTX-resistant sodium currents in small cells from adult rat dorsal root ganglia. *J. Physiol.* 463, 39–56. doi: 10.1113/jphysiol.1993.sp019583

Ernsberger, U. (2009). Role of neurotrophin signalling in the differentiation of neurons from dorsal root ganglia and sympathetic ganglia. *Cell Tissue Res.* 336, 349–384. doi: 10.1007/s00441-009-0784-z

Escoubas, P. (2006). Molecular diversification in spider venoms: a web of combinatorial peptide libraries. *Mol. Divers.* 10, 545–554. doi: 10.1007/s11030-006-9050-4

Faber, C. G., Lauria, G., Merkies, I. S., Cheng, X., Han, C., Ahn, H. S., et al. (2012). Gain-of-function Nav1.8 mutations in painful neuropathy. *Proc. Natl. Acad. Sci. U.S.A.* 109, 19444–19449. doi: 10.1073/pnas.1216080109

Flinspach, M., Xu, Q., Piekarz, A. D., Fellows, R., Hagan, R., Gibbs, A., et al. (2017). Insensitivity to pain induced by a potent selective closed-state Nav1.7 inhibitor. *Sci. Rep.* 7:39662. doi: 10.1038/srep39662

Fry, A. E., Rees, E., Thompson, R., Mantripragada, K., Blake, P., Jones, G., et al. (2016). Pathogenic copy number variants and SCN1A mutations in patients with intellectual disability and childhood-onset epilepsy. *BMC Med. Genet.* 17:34. doi: 10.1186/s12881-016-0294-2

Fukuoka, T., Kobayashi, K., Yamanaka, H., Obata, K., Dai, Y., and Noguchi, K. (2008). Comparative study of the distribution of the alpha-subunits of voltage-gated sodium channels in normal and axotomized rat dorsal root ganglion neurons. *J. Comp. Neurol.* 510, 188–206. doi: 10.1002/cne.21786

Garcia-Villegas, R., Lopez-Alvarez, L. E., Arni, S., Rosenbaum, T., and Morales, M. A. (2009). Identification and functional characterization of the promoter of the mouse sodium-activated sodium channel Na(x) gene (Scn7a). *J. Neurosci. Res.* 87, 2509–2519. doi: 10.1002/jnr.22069

Gilchrist, J., Olivera, B. M., and Bosmans, F. (2014). Animal toxins influence voltage-gated sodium channel function. *Handb. Exp. Pharmacol.* 221, 203–229. doi: 10.1007/978-3-642-41588-3_10

Goldberg, D. S., and McGee, S. J. (2011). Pain as a global public health priority. *BMC Public Health* 11:770. doi: 10.1186/1471-2458-11-770

Goldin, A. L. (2001). Resurgence of sodium channel research. *Annu. Rev. Physiol.* 63, 871–894. doi: 10.1146/annurev.physiol.63.1.871

Goldin, A. L. (2002). Evolution of voltage-gated Na(+) channels. *J. Exp. Biol.* 205, 575–584.

Goldin, A. L., Barchi, R. L., Caldwell, J. H., Hofmann, F., Howe, J. R., Hunter, J. C., et al. (2000). Nomenclature of voltage-gated sodium channels. *Neuron* 28, 365–368. doi: 10.1016/S0896-6273(00)00116-1

Goncalves, T. C., Boukaiba, R., Molgo, J., Amar, M., Partiseti, M., Servent, D., et al. (2018). Direct evidence for high affinity blockade of NaV1.6 channel subtype by huwentoxin-IV spider peptide, using multiscale functional approaches. *Neuropharmacology* 133, 404–414. doi: 10.1016/j.neuropharm.2018.02.016

Gorter, J. A., Zurolo, E., Iyer, A., Fluiter, K., Van Vliet, E. A., Baayen, J. C., et al. (2010). Induction of sodium channel Na(x) (SCN7A) expression in rat and human hippocampus in temporal lobe epilepsy. *Epilepsia* 51, 1791–1800. doi: 10.1111/j.1528-1167.2010.02678.x

Grasso, G., Landi, A., and Alafaci, C. (2016). A novel pathophysiological mechanism contributing to trigeminal neuralgia. *Mol. Med.* doi: 10.2119/molmed.2016.00172 [Epub ahead of print]. doi: 10.2119/molmed.2016.00172

Gui, J., Liu, B., Cao, G., Lipchik, A. M., Perez, M., Dekan, Z., et al. (2014). A tarantula-venom peptide antagonizes the TRPA1 nociceptor ion channel by binding to the S1-S4 gating domain. *Curr. Biol.* 24, 473–483. doi: 10.1016/j.cub.2014.01.013

Hackel, D., Krug, S. M., Sauer, R. S., Mousa, S. A., Bocker, A., Pflucke, D., et al. (2012). Transient opening of the perineurial barrier for analgesic drug delivery. *Proc. Natl. Acad. Sci. U.S.A.* 109, E2018-E2027. doi: 10.1073/pnas.1120800109

Hackenberg, A., Baumer, A., Sticht, H., Schmitt, B., Kroell-Seger, J., Wille, D., et al. (2014). Infantile epileptic encephalopathy, transient choreoathetotic movements, and hypersomnia due to a De Novo missense mutation in the SCN2A gene. *Neuropediatrics* 45, 261–264. doi: 10.1055/s-0034-1372302

Hagen, N. A., Cantin, L., Constant, J., Haller, T., Blaise, G., Ong-Lam, M., du Souich, P., et al. (2017). Tetrodotoxin for moderate to severe cancer-related pain: a multicentre, randomized, double-blind, placebo-controlled, parallel-design trial. *Pain Res. Manag.* 2017:7212713. doi: 10.1155/2017/7212713

Hains, B. C., Klein, J. P., Saab, C. Y., Craner, M. J., Black, J. A., and Waxman, S. G. (2003). Upregulation of sodium channel Nav1.3 and functional involvement in neuronal hyperexcitability associated with central neuropathic pain after spinal cord injury. *J. Neurosci.* 23, 8881–8892. doi: 10.1523/JNEUROSCI.23-26-08881.2003

Hains, B. C., Saab, C. Y., and Waxman, S. G. (2005). Changes in electrophysiological properties and sodium channel Nav1.3 expression in thalamic neurons after spinal cord injury. *Brain* 128, 2359–2371. doi: 10.1093/brain/awh623

Hains, B. C., Saab, C. Y., and Waxman, S. G. (2006). Alterations in burst firing of thalamic VPL neurons and reversal by Na(v)1.3 antisense after spinal cord injury. *J. Neurophysiol.* 95, 3343–3352. doi: 10.1152/jn.01009.2005

Han, C., Huang, J., and Waxman, S. G. (2016). Sodium channel Nav1.8: emerging links to human disease. *Neurology* 86, 473–483. doi: 10.1212/WNL.0000000000002333

Han, C., Yang, Y., De Greef, B. T., Hoeijmakers, J. G., Gerrits, M. M., Verhamme, C., et al. (2015). The domain II S4-S5 linker in Nav1.9: a missense mutation enhances activation, impairs fast inactivation, and produces human painful neuropathy. *Neuromolecular Med.* 17, 158–169. doi: 10.1007/s12017-015-8347-9

Han, C., Yang, Y., Te Morsche, R. H., Drenth, J. P., Politei, J. M., Waxman, S. G., et al. (2017). Familial gain-of-function Nav1.9 mutation in a painful channelopathy. *J. Neurol. Neurosurg. Psychiatry* 88, 233–240. doi: 10.1136/jnnp-2016-313804

Henriques, S. T., Deplazes, E., Lawrence, N., Cheneval, O., Chaousis, S., Inserra, M., et al. (2016). Interaction of tarantula venom peptide proTx-II with lipid membranes is a prerequisite for its inhibition of human voltage-gated sodium channel NaV1.7. *J. Biol. Chem.* 291, 17049–17065. doi: 10.1074/jbc.M116.729095

Hiyama, T. Y., Matsuda, S., Fujikawa, A., Matsumoto, M., Watanabe, E., Kajiwara, H., et al. (2010). Autoimmunity to the sodium-level sensor in the brain causes essential hypernatremia. *Neuron* 66, 508–522. doi: 10.1016/j.neuron.2010.04.017

Hiyama, T. Y., Watanabe, E., Ono, K., Inenaga, K., Tamkun, M. M., Yoshida, S., et al. (2002). Na(x) channel involved in CNS sodium-level sensing. *Nat. Neurosci.* 5, 511–512. doi: 10.1038/nn0602-856

Ho, C., and O'Leary, M. E. (2011). Single-cell analysis of sodium channel expression in dorsal root ganglion neurons. *Mol. Cell. Neurosci.* 46, 159–166. doi: 10.1016/j.mcn.2010.08.017

Ho, W. S., Davis, A. J., Chadha, P. S., and Greenwood, I. A. (2013). Effective contractile response to voltage-gated Na+ channels revealed by a channel activator. *Am. J. Physiol. Cell Physiol.* 304, C739–C747. doi: 10.1152/ajpcell.00164.2012

Hockley, J. R., Winchester, W. J., and Bulmer, D. C. (2016). The voltage-gated sodium channel NaV 1.9 in visceral pain. *Neurogastroenterol. Motil.* 28, 316–326. doi: 10.1111/nmo.12698

Holmes, D. (2016). The pain drain. *Nature* 535, S2–S3. doi: 10.1038/535S2a

Huang, J., Han, C., Estacion, M., Vasylyev, D., Hoeijmakers, J. G., Gerrits, M. M., et al. (2014). Gain-of-function mutations in sodium channel Na(v)1.9 in painful neuropathy. *Brain* 137, 1627–1642. doi: 10.1093/brain/awu079

Huang, J., Vanoye, C. G., Cutts, A., Goldberg, Y. P., Dib-Hajj, S. D., Cohen, C. J., et al. (2017). Sodium channel NaV1.9 mutations associated with insensitivity to pain dampen neuronal excitability. *J. Clin. Invest.* 127, 2805–2814. doi: 10.1172/JCI92373

Huang, Q., Chen, Y., Gong, N., and Wang, Y. X. (2016). Methylglyoxal mediates streptozotocin-induced diabetic neuropathic pain via activation of the peripheral TRPA1 and Nav1.8 channels. *Metabolism* 65, 463–474. doi: 10.1016/j.metabol.2015.12.002

Iio, C., Ogimoto, A., Nagai, T., Suzuki, J., Inoue, K., Nishimura, K., et al. (2015). Association between genetic variation in the SCN10A gene and cardiac conduction abnormalities in patients with hypertrophic cardiomyopathy. *Int. Heart* 56, 421–427. doi: 10.1536/ihj.14-411

Inserra, M. C., Israel, M. R., Caldwell, A., Castro, J., Deuis, J. R., Harrington, A. M., et al. (2017). Multiple sodium channel isoforms mediate the pathological effects of Pacific ciguatoxin-1. *Sci. Rep.* 7:42810. doi: 10.1038/srep42810

Israel, M. R., Tay, B., Deuis, J. R., and Vetter, I. (2017). Sodium channels and venom peptide pharmacology. *Adv. Pharmacol.* 79, 67–116. doi: 10.1016/bs.apha.2017.01.004

Jami, S., Erickson, A., Brierley, S. M., and Vetter, I. (2017). Pain-causing venom peptides: insights into sensory neuron pharmacology. *Toxins* 10:E15 doi: 10.3390/toxins10010015

Jarecki, B. W., Sheets, P. L., Xiao, Y., Jackson, J. O. II, and Cummins, T. R. (2009). Alternative splicing of Na(V)1.7 exon 5 increases the impact of the painful PEPD mutant channel I1461T. *Channels* 3, 259–267. doi: 10.4161/chan.3.4.9341

Jimenez-Andrade, J. M., Herrera, M. B., Ghilardi, J. R., Vardanyan, M., Melemedjian, O. K., and Mantyh, P. W. (2008). Vascularization of the dorsal root ganglia and peripheral nerve of the mouse: implications for chemical-induced peripheral sensory neuropathies. *Mol. Pain* 4:10. doi: 10.1186/1744-8069-4-10

Jo, T., Nagata, T., Iida, H., Imuta, H., Iwasawa, K., Ma, J., et al. (2004). Voltage-gated sodium channel expressed in cultured human smooth muscle cells: involvement of SCN9A. *FEBS Lett.* 567, 339–343. doi: 10.1016/j.febslet.2004.04.092

Jung, H. J., Lee, J. Y., Kim, S. H., Eu, Y. J., Shin, S. Y., Milescu, M., et al. (2005). Solution structure and lipid membrane partitioning of VSTx1, an inhibitor of the KvAP potassium channel. *Biochemistry* 44, 6015–6023. doi: 10.1021/bi0477034

Ke, C. B., He, W. S., Li, C. J., Shi, D., Gao, F., and Tian, Y. K. (2012). Enhanced SCN7A/Nax expression contributes to bone cancer pain by increasing excitability of neurons in dorsal root ganglion. *Neuroscience* 227, 80–89. doi: 10.1016/j.neuroscience.2012.09.046

Kim, C. H., Oh, Y., Chung, J. M., and Chung, K. (2001). The changes in expression of three subtypes of TTX sensitive sodium channels in sensory neurons after spinal nerve ligation. *Brain Res. Mol. Brain Res.* 95, 153–161. doi: 10.1016/S0169-328X(01)00226-1

King, M. K., Leipold, E., Goehringer, J. M., Kurth, I., and Challman, T. D. (2017). Pain insensitivity: distal S6-segment mutations in NaV1.9 emerge as critical hotspot. *Neurogenetics* 18, 179–181. doi: 10.1007/s10048-017-0513-9

Kinsman, B. J., Nation, H. N., and Stocker, S. D. (2017). Hypothalamic signaling in body fluid homeostasis and hypertension. *Curr. Hypertens. Rep.* 19:50. doi: 10.1007/s11906-017-0749-7

Kist, A. M., Sagafos, D., Rush, A. M., Neacsu, C., Eberhardt, E., Schmidt, R., et al. (2016). SCN10A mutation in a patient with erythromelalgia enhances c-fiber activity dependent slowing. *PLoS One* 11:e0161789. doi: 10.1371/journal.pone.0161789

Kleggetveit, I. P., Schmidt, R., Namer, B., Salter, H., Helas, T., Schmelz, M., et al. (2016). Pathological nociceptors in two patients with erythromelalgia-like symptoms and rare genetic Nav 1.9 variants. *Brain Behav.* 6:e00528. doi: 10.1002/brb3.528

Klint, J. K., Chin, Y. K., and Mobli, M. (2015a). Rational engineering defines a molecular switch that is essential for activity of spider-venom peptides against the analgesics target NaV1.7. *Mol. Pharmacol.* 88, 1002–1010. doi: 10.1124/mol.115.100784

Klint, J. K., Smith, J. J., Vetter, I., Rupasinghe, D. B., Er, S. Y., Senff, S., et al. (2015b). Seven novel modulators of the analgesic target NaV 1.7 uncovered using a high-throughput venom-based discovery approach. *Br. J. Pharmacol.* 172, 2445–2458. doi: 10.1111/bph.13081

Klint, J. K., Senff, S., Rupasinghe, D. B., Er, S. Y., Herzig, V., Nicholson, G. M., et al. (2012). Spider-venom peptides that target voltage-gated sodium channels: pharmacological tools and potential therapeutic leads. *Toxicon* 60, 478–491. doi: 10.1016/j.toxicon.2012.04.337

Koenig, J., Werdehausen, R., Linley, J. E., Habib, A. M., Vernon, J., Lolignier, S., et al. (2015). Regulation of Nav1.7: a conserved SCN9A natural antisense transcript expressed in dorsal root ganglia. *PLoS One* 10:e0128830. doi: 10.1371/journal.pone.0128830

Laedermann, C. J., Abriel, H., and Decosterd, I. (2015). Post-translational modifications of voltage-gated sodium channels in chronic pain syndromes. *Front. Pharmacol.* 6:263. doi: 10.3389/fphar.2015.00263

Lai, J., Hunter, J. C., and Porreca, F. (2003). The role of voltage-gated sodium channels in neuropathic pain. *Curr. Opin. Neurobiol.* 13, 291–297. doi: 10.1016/S0959-4388(03)00074-6

Lamar, T., Vanoye, C. G., Calhoun, J., Wong, J. C., Dutton, S. B. B., Jorge, B. S., et al. (2017). SCN3A deficiency associated with increased seizure susceptibility. *Neurobiol. Dis.* 102, 38–48. doi: 10.1016/j.nbd.2017.02.006

Lee, J. H., Park, C. K., Chen, G., Han, Q., Xie, R. G., Liu, T., et al. (2014). A monoclonal antibody that targets a NaV1.7 channel voltage sensor for pain and itch relief. *Cell* 157, 1393–1404. doi: 10.1016/j.cell.2014.03.064

Leipold, E., Hanson-Kahn, A., Frick, M., Gong, P., Bernstein, J. A., Voigt, M., et al. (2015). Cold-aggravated pain in humans caused by a hyperactive NaV1.9 channel mutant. *Nat. Commun.* 6:10049. doi: 10.1038/ncomms10049

Leipold, E., Liebmann, L., Korenke, G. C., Heinrich, T., Giesselmann, S., Baets, J., et al. (2013). A de novo gain-of-function mutation in SCN11A causes loss of pain perception. *Nat. Genet.* 45, 1399–1404. doi: 10.1038/ng.2767

Leng, X. R., Qi, X. H., Zhou, Y. T., and Wang, Y. P. (2017). Gain-of-function mutation p.Arg225Cys in SCN11A causes familial episodic pain and contributes to essential tremor. *J. Hum. Genet.* 62, 641–646. doi: 10.1038/jhg.2017.21

Lewis, A. H., and Raman, I. M. (2014). Resurgent current of voltage-gated Na(+) channels. *J. Physiol.* 592, 4825–4838. doi: 10.1113/jphysiol.2014.277582

Li, C., Wang, S., Chen, Y., and Zhang, X. (2018). Somatosensory neuron typing with high-coverage single-Cell RNA sequencing and functional analysis. *Neurosci. Bull.* 34, 200–207. doi: 10.1007/s12264-017-0147-9

Liao, Y., Anttonen, A. K., Liukkonen, E., Gaily, E., Maljevic, S., Schubert, S., et al. (2010). SCN2A mutation associated with neonatal epilepsy, late-onset episodic ataxia, myoclonus, and pain. *Neurology* 75, 1454–1458. doi: 10.1212/WNL.0b013e3181f8812e

Liem, L., Van Dongen, E., Huygen, F. J., Staats, P., and Kramer, J. (2016). The dorsal root ganglion as a therapeutic target for chronic pain. *Reg. Anesth. Pain Med.* 41, 511–519. doi: 10.1097/AAP.0000000000000408

Lin, W. H., and Baines, R. A. (2015). Regulation of membrane excitability: a convergence on voltage-gated sodium conductance. *Mol. Neurobiol.* 51, 57–67. doi: 10.1007/s12035-014-8674-0

Liu, D., Tseng, M., Epstein, L. F., Green, L., Chan, B., Soriano, B., Lim, D., et al. (2016). Evaluation of recombinant monoclonal antibody SVmab1 binding to Na V1.7 target sequences and block of human Na V1.7 currents. *F1000Res.* 5:2764.

Liu, H., Chen, Y., Huang, L., Sun, X., Fu, T., Wu, S., et al. (2018). Drug distribution into peripheral nerve. *J. Pharmacol. Exp. Ther.* 365, 336–345. doi: 10.1124/jpet.117.245613

Liu, X. D., Yang, J. J., Fang, D., Cai, J., Wan, Y., and Xing, G. G. (2014). Functional upregulation of nav1.8 sodium channels on the membrane of dorsal root Ganglia neurons contributes to the development of cancer-induced bone pain. *PLoS One* 9:e114623. doi: 10.1371/journal.pone.0114623

Liu, Y., Tang, J., Zhang, Y., Xun, X., Tang, D., Peng, D., et al. (2014a). Synthesis and analgesic effects of mu-TRTX-Hhn1b on models of inflammatory and neuropathic pain. *Toxins* 6, 2363–2378. doi: 10.3390/toxins6082363

Liu, Y., Wu, Z., Tang, D., Xun, X., Liu, L., Li, X., et al. (2014b). Analgesic effects of Huwentoxin-IV on animal models of inflammatory and neuropathic pain. *Protein Pept. Lett.* 21, 153–158. doi: 10.2174/09298665113206660119

Liu, Z., Cai, T., Zhu, Q., Deng, M., Li, J., Zhou, X., et al. (2013). Structure and function of hainantoxin-III, a selective antagonist of neuronal tetrodotoxin-sensitive voltage-gated sodium channels isolated from the Chinese bird spider *Ornithoctonus hainana*. *J. Biol. Chem.* 288, 20392–20403. doi: 10.1074/jbc.M112.426627

Liu, Z., Tao, J., Ye, P., and Ji, Y. (2012). Mining the virgin land of neurotoxicology: a novel paradigm of neurotoxic peptides action on glycosylated voltage-gated sodium channels. *J. Toxicol.* 2012:843787. doi: 10.1155/2012/843787

Liu, Z. H., Chen, P., and Liang, S. P. (2002). Synthesis and oxidative refolding of hainantoxin-IV. *Sheng Wu Hua Xue Yu Sheng Wu Wu Li Xue Bao* 34, 516–519.

Lolignier, S., Amsalem, M., Maingret, F., Padilla, F., Gabriac, M., Chapuy, E., et al. (2011). Nav1.9 channel contributes to mechanical and heat pain hypersensitivity induced by subacute and chronic inflammation. *PLoS One* 6:e23083. doi: 10.1371/journal.pone.0023083

Lolignier, S., Eijkelkamp, N., and Wood, J. N. (2015). Mechanical allodynia. *Pflugers Arch.* 467, 133–139. doi: 10.1007/s00424-014-1532-0

Lolignier, S., Gkika, D., Andersson, D., Leipold, E., Vetter, I., Viana, F., et al. (2016). New insight in cold pain: role of ion channels, modulation, and clinical perspectives. *J. Neurosci.* 36, 11435–11439. doi: 10.1523/JNEUROSCI.2327-16.2016

Luo, W., Wickramasinghe, S. R., Savitt, J. M., Griffin, J. W., Dawson, T. M., and Ginty, D. D. (2007). A hierarchical NGF signaling cascade controls Ret-dependent and Ret-independent events during development of nonpeptidergic DRG neurons. *Neuron* 54, 739–754. doi: 10.1016/j.neuron.2007.04.027

Makinson, C. D., Tanaka, B. S., Lamar, T., Goldin, A. L., and Escayg, A. (2014). Role of the hippocampus in Nav1.6 (Scn8a) mediated seizure resistance. *Neurobiol. Dis.* 68, 16–25. doi: 10.1016/j.nbd.2014.03.014

Minassian, N. A., Gibbs, A., Shih, A. Y., Liu, Y., Neff, R. A., Sutton, S. W., et al. (2013). Analysis of the structural and molecular basis of voltage-sensitive sodium channel inhibition by the spider toxin huwentoxin-IV (mu-TRTX-Hh2a). *J. Biol. Chem.* 288, 22707–22720. doi: 10.1074/jbc.M113.461392

Mogil, J. S. (2009). Animal models of pain: progress and challenges. *Nat. Rev. Neurosci.* 10, 283–294. doi: 10.1038/nrn2606

Moraes, E. R., Kushmerick, C., and Naves, L. A. (2014). Characteristics of dorsal root ganglia neurons sensitive to Substance P. *Mol. Pain* 10:73. doi: 10.1186/1744-8069-10-73

Moyer, B. D., Murray, J. K., Ligutti, J., Andrews, K., Favreau, P., Jordan, J. B., et al. (2018). Pharmacological characterization of potent and selective NaV1.7 inhibitors engineered from Chilobrachys jingzhao tarantula venom peptide JzTx-V. *PLoS One* 13:e0196791. doi: 10.1371/journal.pone.0196791

Mulley, J. C., Hodgson, B., Mcmahon, J. M., Iona, X., Bellows, S., Mullen, S. A., et al. (2013). Role of the sodium channel SCN9A in genetic epilepsy with febrile seizures plus and Dravet syndrome. *Epilepsia* 54, e122–e126. doi: 10.1111/epi.12323

Muroi, Y., and Undem, B. J. (2014). Targeting voltage gated sodium channels NaV1.7, Na V1.8, and Na V1.9 for treatment of pathological cough. *Lung* 192, 15–20. doi: 10.1007/s00408-013-9533-x

Murray, J. K., Long, J., Zou, A., Ligutti, J., Andrews, K. L., Poppe, L., et al. (2016). Single residue substitutions that confer voltage-gated sodium ion channel subtype selectivity in the NaV1.7 inhibitory peptide GpTx-1. *J. Med. Chem.* 59, 2704–2717. doi: 10.1021/acs.jmedchem.5b01947

Namadurai, S., Yereddi, N. R., Cusdin, F. S., Huang, C. L., Chirgadze, D. Y., and Jackson, A. P. (2015). A new look at sodium channel beta subunits. *Open Biol.* 5:140192. doi: 10.1098/rsob.140192

Negus, S. S. (2018). Addressing the opioid crisis: the importance of choosing translational endpoints in analgesic drug discovery. *Trends Pharmacol. Sci.* 39, 327–330. doi: 10.1016/j.tips.2018.02.002

Nehme, B., Henry, M., Mouginot, D., and Drolet, G. (2012). The expression pattern of the Na(+) Sensor, Na(X) in the hydromineral homeostatic network: a comparative study between the rat and mouse. *Front. Neuroanat.* 6:26. doi: 10.3389/fnana.2012.00026

Nishiya, Y., Yokokawa, S., Fukuda, A., Yamagata, T., Inayoshi, A., Obinata, M., et al. (2011). The generation of rat dorsal root ganglion cell lines to identify the target of KW-7158, a novel treatment for overactive bladder. *Neurosci. Res.* 71, 278–288. doi: 10.1016/j.neures.2011.07.1823

O'Brien, J. E., and Meisler, M. H. (2013). Sodium channel SCN8A (Nav1.6): properties and de novo mutations in epileptic encephalopathy and intellectual disability. *Front. Genet.* 4:213. doi: 10.3389/fgene.2013.00213

O'Donnell, A. M., Coyle, D., and Puri, P. (2016). Decreased Nav1.9 channel expression in Hirschsprung's disease. *J. Pediatr. Surg.* 51, 1458–1461. doi: 10.1016/j.jpedsurg.2016.05.007

Okuda, H., Noguchi, A., Kobayashi, H., Kondo, D., Harada, K. H., Youssefian, S., et al. (2016). Infantile pain episodes associated with novel Nav1.9 mutations in familial episodic pain syndrome in japanese families. *PLoS One* 11:e0154827. doi: 10.1371/journal.pone.0154827

Ono, S., Kimura, T., and Kubo, T. (2011). Characterization of voltage-dependent calcium channel blocking peptides from the venom of the tarantula *Grammostola rosea*. *Toxicon* 58, 265–276. doi: 10.1016/j.toxicon.2011.06.006

Osmakov, D. I., Andreev, Y. A., and Kozlov, S. A. (2014). Acid-sensing ion channels and their modulators. *Biochemistry* 79, 1528–1545. doi: 10.1134/S0006297914130069

Osteen, J. D., Herzig, V., Gilchrist, J., Emrick, J. J., Zhang, C., Wang, X., et al. (2016). Selective spider toxins reveal a role for the Nav1.1 channel in mechanical pain. *Nature* 534, 494–499. doi: 10.1038/nature17976

Osteen, J. D., Sampson, K., Iyer, V., Julius, D., and Bosmans, F. (2017). Pharmacology of the Nav1.1 domain IV voltage sensor reveals coupling between inactivation gating processes. *Proc. Natl. Acad. Sci. U.S.A.* 114, 6836–6841. doi: 10.1073/pnas.1621263114

Pan, H. L., Wu, Z. Z., Zhou, H. Y., Chen, S. R., Zhang, H. M., and Li, D. P. (2008). Modulation of pain transmission by G-protein-coupled receptors. *Pharmacol. Ther.* 117, 141–161. doi: 10.1016/j.pharmthera.2007.09.003

Parke, W. W., and Whalen, J. L. (2002). The vascular pattern of the human dorsal root ganglion and its probable bearing on a compartment syndrome. *Spine* 27, 347–352. doi: 10.1097/00007632-200202150-00004

Patrick Harty, T., and Waxman, S. G. (2007). Inactivation properties of sodium channel Nav1.8 maintain action potential amplitude in small DRG neurons in the context of depolarization. *Mol. Pain* 3:12.

Payandeh, J., Scheuer, T., Zheng, N., and Catterall, W. A. (2011). The crystal structure of a voltage-gated sodium channel. *Nature* 475, 353–358. doi: 10.1038/nature10238

Peng, K., Shu, Q., Liu, Z., and Liang, S. (2002). Function and solution structure of huwentoxin-IV, a potent neuronal tetrodotoxin (TTX)-sensitive sodium channel antagonist from Chinese bird spider *Selenocosmia huwena*. *J. Biol. Chem.* 277, 47564–47571. doi: 10.1074/jbc.M204063200

Petterson, C. A., and Olsson, Y. (1989). Blood supply of spinal nerve roots. An experimental study in the rat. *Acta Neuropathol.* 78, 455–461. doi: 10.1007/BF00687706

Phatarakijnirund, V., Mumm, S., Mcalister, W. H., Novack, D. V., Wenkert, D., Clements, K. L., et al. (2016). Congenital insensitivity to pain: fracturing without apparent skeletal pathobiology caused by an autosomal dominant, second mutation in SCN11A encoding voltage-gated sodium channel 1.9. *Bone* 84, 289–298. doi: 10.1016/j.bone.2015.11.022

Pineda, S. S., Chaumeil, P. A., Kunert, A., Kaas, Q., Thang, M. W. C., Le, L., et al. (2018). ArachnoServer 3.0: an online resource for automated discovery, analysis and annotation of spider toxins. *Bioinformatics* 34, 1074–1076. doi: 10.1093/bioinformatics/btx661

Porreca, F., and Navratilova, E. (2017). Reward, motivation, and emotion of pain and its relief. *Pain* 158(Suppl. 1), S43–S49. doi: 10.1097/j.pain.0000000000000798

Qiu, F., Jiang, Y., Zhang, H., Liu, Y., and Mi, W. (2012). Increased expression of tetrodotoxin-resistant sodium channels Nav1.8 and Nav1.9 within dorsal root ganglia in a rat model of bone cancer pain. *Neurosci. Lett.* 512, 61–66. doi: 10.1016/j.neulet.2012.01.069

Rahnama, S., Deuis, J. R., Cardoso, F. C., Ramanujam, V., Lewis, R. J., Rash, L. D., et al. (2017). The structure, dynamics and selectivity profile of a NaV1.7 potency-optimised huwentoxin-IV variant. *PLoS One* 12:e0173551. doi: 10.1371/journal.pone.0173551

Raymon, H. K., Thode, S., Zhou, J., Friedman, G. C., Pardinas, J. R., Barrere, C., et al. (1999). Immortalized human dorsal root ganglion cells differentiate into neurons with nociceptive properties. *J. Neurosci.* 19, 5420–5428. doi: 10.1523/JNEUROSCI.19-13-05420.1999

Raymond, C. K., Castle, J., Garrett-Engele, P., Armour, C. D., Kan, Z., Tsinoremas, N., et al. (2004). Expression of alternatively spliced sodium channel alpha-subunit genes. Unique splicing patterns are observed in dorsal root ganglia. *J. Biol. Chem.* 279, 46234–46241. doi: 10.1074/jbc.M406387200

Ren, Y. S., Qian, N. S., Tang, Y., Liao, Y. H., Yang, Y. L., Dou, K. F., et al. (2012). Sodium channel Nav1.6 is up-regulated in the dorsal root ganglia in a mouse model of type 2 diabetes. *Brain Res. Bull.* 87, 244–249. doi: 10.1016/j.brainresbull.2011.10.015

Renganathan, M., Cummins, T. R., and Waxman, S. G. (2001). Contribution of Na(v)1.8 sodium channels to action potential electrogenesis in DRG neurons. *J. Neurophysiol.* 86, 629–640. doi: 10.1152/jn.2001.86.2.629

Ritter, A. M., Martin, W. J., and Thorneloe, K. S. (2009). The voltage-gated sodium channel Nav1.9 is required for inflammation-based urinary bladder dysfunction. *Neurosci. Lett.* 452, 28–32. doi: 10.1016/j.neulet.2008.12.051

Rubinstein, M., Patowary, A., Stanaway, I. B., Mccord, E., Nesbitt, R. R., Archer, M., et al. (2018). Association of rare missense variants in the second intracellular loop of NaV1.7 sodium channels with familial autism. *Mol. Psychiatry* 23, 231–239. doi: 10.1038/mp.2016.222

Saez, N. J., Senff, S., Jensen, J. E., Er, S. Y., Herzig, V., Rash, L. D., et al. (2010). Spider-venom peptides as therapeutics. *Toxins* 2, 2851–2871. doi: 10.3390/toxins2122851

Sah, D. W., Ray, J., and Gage, F. H. (1997). Bipotent progenitor cell lines from the human CNS. *Nat. Biotechnol.* 15, 574–580. doi: 10.1038/nbt0697-574

Salvatierra, J., Castro, J., Erickson, A., Li, Q., Braz, J., Gilchrist, J., et al. (2018). NaV1.1 inhibition can reduce visceral hypersensitivity. *JCI Insight* 3:121000. doi: 10.1172/jci.insight.121000

Savage, S. R., Kirsh, K. L., and Passik, S. D. (2008). Challenges in using opioids to treat pain in persons with substance use disorders. *Addict. Sci. Clin. Pract.* 4, 4–25. doi: 10.1151/ascp08424

Schirmeyer, J., Szafranski, K., Leipold, E., Mawrin, C., Platzer, M., and Heinemann, S. H. (2014). Exon 11 skipping of SCN10A coding for voltage-gated sodium channels in dorsal root ganglia. *Channels* 8, 210–215. doi: 10.4161/chan.28146

Schmalhofer, W. A., Calhoun, J., Burrows, R., Bailey, T., Kohler, M. G., Weinglass, A. B., et al. (2008). ProTx-II, a selective inhibitor of NaV1.7 sodium channels, blocks action potential propagation in nociceptors. *Mol. Pharmacol.* 74, 1476–1484. doi: 10.1124/mol.108.047670

Scholz, A., Gruss, M., and Vogel, W. (1998). Properties and functions of calcium-activated K+ channels in small neurones of rat dorsal root ganglion studied in a thin slice preparation. *J. Physiol.* 513(Pt 1), 55–69. doi: 10.1111/j.1469-7793.1998.055by.x

Scholz, A., and Vogel, W. (2000). Tetrodotoxin-resistant action potentials in dorsal root ganglion neurons are blocked by local anesthetics. *Pain* 89, 47–52. doi: 10.1016/S0304-3959(00)00345-6

Smith, J. J., Cummins, T. R., Alphy, S., and Blumenthal, K. M. (2007). Molecular interactions of the gating modifier toxin ProTx-II with NaV 1.5: implied existence of a novel toxin binding site coupled to activation. *J. Biol. Chem.* 282, 12687–12697. doi: 10.1074/jbc.M610462200

Sommer, C. (2016). Exploring pain pathophysiology in patients. *Science* 354, 588–592. doi: 10.1126/science.aaf8935

Song, W., Liu, Z., Tan, J., Nomura, Y., and Dong, K. (2004). RNA editing generates tissue-specific sodium channels with distinct gating properties. *J. Biol. Chem.* 279, 32554–32561. doi: 10.1074/jbc.M402392200

Sousa, S. R., Wingerd, J. S., Brust, A., Bladen, C., Ragnarsson, L., Herzig, V., et al. (2017). Discovery and mode of action of a novel analgesic β-toxin from the African spider *Ceratogyrus darlingi*. *PLoS One* 12:e0182848. doi: 10.1371/journal.pone.0182848

Spray, D. C., and Hanani, M. (2017). Gap junctions, pannexins and pain. *Neurosci. Lett.* doi: 10.1016/j.neulet.2017.06.035 [Epub ahead of print].

Sun, H., Kollarik, M., and Undem, B. J. (2017). Blocking voltage-gated sodium channels as a strategy to suppress pathological cough. *Pulm. Pharmacol. Ther.* 47, 38–41. doi: 10.1016/j.pupt.2017.05.010

Taddese, A., Nah, S. Y., and Mccleskey, E. W. (1995). Selective opioid inhibition of small nociceptive neurons. *Science* 270, 1366–1369. doi: 10.1126/science.270.5240.1366

Tan, A. M., Samad, O. A., Dib-Hajj, S. D., and Waxman, S. G. (2015). Virus-mediated knockdown of Nav1.3 in dorsal root ganglia of STZ-induced diabetic rats alleviates tactile allodynia. *Mol. Med.* 21, 544–552. doi: 10.2119/molmed.2015.00063

Tan, J., Liu, Z., Nomura, Y., Goldin, A. L., and Dong, K. (2002). Alternative splicing of an insect sodium channel gene generates pharmacologically distinct sodium channels. *J. Neurosci.* 22, 5300–5309. doi: 10.1523/JNEUROSCI.22-13-05300.2002

Tanaka, B. S., Zhao, P., Dib-Hajj, F. B., Morisset, V., Tate, S., Waxman, S. G., and Dib-Hajj, S. D. (2016). A gain-of-function mutation in Nav1.6 in a case of trigeminal neuralgia. *Mol. Med.* 22, 338–348. doi: 10.2119/molmed.2016.00131

Tanaka, K., Sekino, S., Ikegami, M., Ikeda, H., and Kamei, J. (2015). Antihyperalgesic effects of ProTx-II, a Nav1.7 antagonist, and A803467, a Nav1.8 antagonist, in diabetic mice. *J. Exp. Pharmacol.* 7, 11–16. doi: 10.2147/JEP.S79973

Thakor, D. K., Lin, A., Matsuka, Y., Meyer, E. M., Ruangsri, S., Nishimura, I., and Spigelman, I. (2009). Increased peripheral nerve excitability and local NaV1.8 mRNA up-regulation in painful neuropathy. *Mol. Pain* 5:14. doi: 10.1186/1744-8069-5-14

Thompson, C. H., Kahlig, K. M., and George, A. L. Jr. (2011). SCN1A splice variants exhibit divergent sensitivity to commonly used antiepileptic drugs. *Epilepsia* 52, 1000–1009. doi: 10.1111/j.1528-1167.2011.03040.x

Tonello, R., Fusi, C., Materazzi, S., Marone, I. M., De Logu, F., Benemei, S., et al. (2017). The peptide phalpha1beta, from spider venom, acts as a TRPA1 channel antagonist with antinociceptive effects in mice. *Br. J. Pharmacol.* 174, 57–69. doi: 10.1111/bph.13652

Torres-Perez, J. V., Adamek, P., Palecek, J., Vizcaychipi, M., Nagy, I., and Varga, A. (2018). The NAv1.7 blocker protoxin II reduces burn injury-induced spinal nociceptive processing. *J. Mol. Med.* 96, 75–84. doi: 10.1007/s00109-017-1599-0

Trimmer, J. S., and Rhodes, K. J. (2004). Localization of voltage-gated ion channels in mammalian brain. *Annu. Rev. Physiol.* 66, 477–519. doi: 10.1146/annurev.physiol.66.032102.113328

Vetter, I., Deuis, J. R., Mueller, A., Israel, M. R., Starobova, H., Zhang, A., et al. (2017). NaV1.7 as a pain target - from gene to pharmacology. *Pharmacol. Ther.* 172, 73–100. doi: 10.1016/j.pharmthera.2016.11.015

Vijayaragavan, K., Powell, A. J., Kinghorn, I. J., and Chahine, M. (2004). Role of auxiliary beta1-, beta2-, and beta3-subunits and their interaction with Na(v)1.8 voltage-gated sodium channel. *Biochem. Biophys. Res. Commun.* 319, 531–540. doi: 10.1016/j.bbrc.2004.05.026

Watanabe, E., Hiyama, T. Y., Shimizu, H., Kodama, R., Hayashi, N., Miyata, S., et al. (2006). Sodium-level-sensitive sodium channel Na(x) is expressed in glial laminate processes in the sensory circumventricular organs. *Am. J. Physiol. Regul. Integr. Comp. Physiol.* 290, R568–R576. doi: 10.1152/ajpregu.00618.2005

Waxman, S. G., Kocsis, J. D., and Black, J. A. (1994). Type III sodium channel mRNA is expressed in embryonic but not adult spinal sensory neurons, and is reexpressed following axotomy. *J. Neurophysiol.* 72, 466–470. doi: 10.1152/jn.1994.72.1.466

Wiesenfeld-Hallin, Z., and Xu, X. J. (2001). Neuropeptides in neuropathic and inflammatory pain with special emphasis on cholecystokinin and galanin. *Eur. J. Pharmacol.* 429, 49–59. doi: 10.1016/S0014-2999(01)01305-X

Wolff, M., Johannesen, K. M., Hedrich, U. B. S., Masnada, S., Rubboli, G., Gardella, E., et al. (2017). Genetic and phenotypic heterogeneity suggest therapeutic implications in SCN2A-related disorders. *Brain* 140, 1316–1336. doi: 10.1093/brain/awx054

Woods, C. G., Babiker, M. O., Horrocks, I., Tolmie, J., and Kurth, I. (2015). The phenotype of congenital insensitivity to pain due to the NaV1.9 variant p.L811P. *Eur. J. Hum. Genet.* 23, 561–563. doi: 10.1038/ejhg.2014.166

Xiao, Y., Luo, X., Kuang, F., Deng, M., Wang, M., Zeng, X., and Liang, S. (2008). Synthesis and characterization of huwentoxin-IV, a neurotoxin inhibiting central neuronal sodium channels. *Toxicon* 51, 230–239. doi: 10.1016/j.toxicon.2007.09.008

Xie, W., Strong, J. A., Ye, L., Mao, J. X., and Zhang, J. M. (2013). Knockdown of sodium channel NaV1.6 blocks mechanical pain and abnormal bursting activity of afferent neurons in inflamed sensory ganglia. *Pain* 154, 1170–1180. doi: 10.1016/j.pain.2013.02.027

Xie, W., Tan, Z. Y., Barbosa, C., Strong, J. A., Cummins, T. R., and Zhang, J. M. (2016). Upregulation of the sodium channel NaVbeta4 subunit and its contributions to mechanical hypersensitivity and neuronal hyperexcitability in a rat model of radicular pain induced by local dorsal root ganglion inflammation. *Pain* 157, 879–891. doi: 10.1097/j.pain.0000000000000453

Xing, D., Wu, Y., Li, G., Song, S., Liu, Y., Liu, H., et al. (2015). Role of cerebrospinal fluid-contacting nucleus in sodium sensing and sodium appetite. *Physiol. Behav.* 147, 291–299. doi: 10.1016/j.physbeh.2015.04.034

Xiong, Z., Yi, L., Cao, D., He, W., Chen, J., Gao, S., and Sun, X. (2016). Dravet syndrome with autism inherited from a paternal mosaic heterozygous mutation on SCN1A. *J. Neurol. Sci.* 369, 53–56. doi: 10.1016/j.jns.2016.07.038

Yang, C., Hua, Y., Zhang, W., Xu, J., Xu, L., Gao, F., and Jiang, P. (2018). Variable epilepsy phenotypes associated with heterozygous mutation in the SCN9A gene: report of two cases. *Neurol. Sci.* 39, 1113–1115. doi: 10.1007/s10072-018-3300-y

Yang, Y., Mis, M. A., Estacion, M., Dib-Hajj, S. D., and Waxman, S. G. (2018). NaV1.7 as a pharmacogenomic target for pain: moving toward precision medicine. *Trends Pharmacol. Sci.* 39, 258–275. doi: 10.1016/j.tips.2017.11.010

Yang, L., Li, Q., Liu, X., and Liu, S. (2016). Roles of voltage-gated tetrodotoxin-sensitive sodium channels NaV1.3 and NaV1.7 in diabetes and painful diabetic neuropathy. *Int. J. Mol. Sci.* 17:E1479 doi: 10.3390/ijms17091479

Yekkirala, A. S., Roberson, D. P., Bean, B. P., and Woolf, C. J. (2017). Breaking barriers to novel analgesic drug development. *Nat. Rev. Drug Discov.* 16, 545–564. doi: 10.1038/nrd.2017.87

Yu, F. H., and Catterall, W. A. (2003). Overview of the voltage-gated sodium channel family. *Genome Biol.* 4:207.

Yu, F. H., and Catterall, W. A. (2004). The VGL-chanome: a protein superfamily specialized for electrical signaling and ionic homeostasis. *Sci. STKE* 2004:re15. doi: 10.1126/stke.2532004re15

Zeng, X., Li, P., Chen, B., Huang, J., Lai, R., Liu, J., and Rong, M. (2018). Selective closed-State Nav1.7 blocker JZTX-34 exhibits analgesic effects against pain. *Toxins* 10:E64. doi: 10.3390/toxins10020064

Zhang, A. H., Sharma, G., Undheim, E. A. B., Jia, X., and Mobli, M. (2018). A complicated complex: ion channels, voltage sensing, cell membranes and peptide inhibitors. *Neurosci. Lett.* 679, 35–47 doi: 10.1016/j.neulet.2018.04.030

Zhang, X., Priest, B. T., Belfer, I., and Gold, M. S. (2017). Voltage-gated Na(+) currents in human dorsal root ganglion neurons. *eLife* 6:e23235 doi: 10.7554/eLife.23235

Zhang, X. Y., Wen, J., Yang, W., Wang, C., Gao, L., Zheng, L. H., et al. (2013). Gain-of-function mutations in SCN11A cause familial episodic pain. *Am. J. Hum. Genet.* 93, 957–966. doi: 10.1016/j.ajhg.2013.09.016

Zimmer, T., Haufe, V., and Blechschmidt, S. (2014). Voltage-gated sodium channels in the mammalian heart. *Glob. Cardiol. Sci. Pract.* 2014, 449–463. doi: 10.5339/gcsp.2014.58

Conflict of Interest Statement: TG and MP are current or former employees of Sanofi.

The remaining authors declare that the research was conducted in the absence of any commercial or financial relationships that could be construed as a potential conflict of interest.

1.4. Objectifs de la thèse

Ces dernières décennies, un immense effort a été fourni par les chercheurs académiques et industriels afin de trouver des alternatives pharmacologiques par voie orale au fléau que constituent les opioïdes, traitement antalgique de palier III établi par l'Organisation mondiale de la Santé (OMS). En effet, leurs effets secondaires sont une véritable catastrophe sanitaire entrainant tolérance et dépendance sans oublier de mentionner la détresse respiratoire associée aux fortes doses qui augmente de façon catastrophique le nombre de décès par overdose aux opiacés, aux Etats Unis en particulier (Jones et al., 2013). Certaines équipes ont misé sur la découverte de petites molécules chimiques telles que les dérivés des sulfonamides qui inhibent les canaux Na_V impliqués dans la transmission du message douloureux. D'autres équipes ont misé sur la découverte d'opioïdes analgésiants avec des effets secondaires réduits tels que le PZM21 qui n'active que la voie intracellulaire de messagers secondaires liée au message douloureux. Finalement, certaines équipes ont misé sur une approche plus originale basée sur la découverte de peptides dérivés de venins d'animaux (McCormack et al., 2013; Sun et al., 2014; Ahuja et al., 2015; Manglik et al., 2016; Hamad et al., 2018).

Tous les récepteurs localisés au niveau des neurones sensoriels primaires et secondaires en périphérie, ou à l'entrée du système nerveux central, peuvent devenir la cible de ces peptides potentiellement antinociceptifs (Pan et al., 2008; Bennett & Woods, 2014; Waxman & Zamponi, 2014; Yekkirala et al., 2017). Cependant, le sous-type $Na_V1.7$ de canaux sodium dépendant du potentiel, hautement exprimé au niveau des DRG composés des corps cellulaires des neurones sensoriels primaires, joue un rôle primordial dans le processus de signalisation de la douleur (Vetter et al., 2017).

L'objectif de ma thèse était d'identifier, dans les venins d'animaux, des inhibiteurs efficaces pour bloquer avec une haute puissance et sélectivement le sous-type $Na_V1.7$ et de caractériser leur profil pharmacologique par des approches fonctionnelles multi-échelles. Pour ce faire, un criblage à haut débit de deux banques de venins a été réalisé sur ce sous-type de canal sodium et des peptides possédant des propriétés fonctionnelles originales ont été identifiés.

Partie 2

RESULTATS et DISCUSSION

Avant-propos

Les résultats sont présentés sous forme d'articles publiés ou en révision dans des journaux à comité de lecture, d'articles en préparation et de résultats non publiés. Cette partie est structurée en cinq sous-parties:

1. La première sous-partie présente l'identification et la caractérisation de la cyriotoxine-1a, isolée à partir du venin de l'araignée *Cyriopagopus schioedtei*, dont les propriétés fonctionnelles sont proches de celles des peptides appartenant à la famille 1 des toxines d'araignées inhibant les canaux Na_V (NaSpTx-1).
2. La deuxième sous-partie est consacrée à des études de "structure-activité" concernant la phlotoxine-1, une toxine découverte il y a une décennie dans le venin d'une araignée *Phlogiellus* au cours d'un criblage guidé par la toxicité produite chez les souris.
3. La troisième sous-partie décrit la mise en évidence de l'interaction entre l'huwentoxine-IV, toxine d'araignée déjà connue pour ses propriétés antinociceptives, et le sous-type $Na_V1.6$ de canaux sodium, principal responsable des effets moteurs indésirables observés lors de l'injection du peptide *in vivo*.
4. La quatrième sous-partie montre l'intérêt d'effectuer un profil de sélectivité sur un large éventail de sous-types de canaux ioniques qui peut révéler la véritable spécificité d'une toxine pour un sous-type différent de celui qui a permet de l'identifier initialement. C'est le cas de la poécitoxine-1a, mise en évidence par à un criblage sur le sous-type $Na_V1.7$ *versus* $Na_V1.5$ de canaux sodium, mais qui présente en fait une puissance accrue pour le sous-type $Ca_V1.2$ de canaux calcium.
5. La cinquième sous-partie est dédiée à la présentation des résultats du second criblage à haut débit, actuellement en cours, d'une banque de venins appartenant à SANOFI dont les sous-fractions les plus intéressantes proviennent de venins d'araignées et de scorpions non étudiés jusqu'à présent.

Les publications étant en anglais, nous présenterons en français, préalablement à chacune d'entre elles, le contexte dans lequel s'est faite l'étude puis, après la publication, un résumé des principaux résultats obtenus et éventuellement de ceux non publiés d'expériences complémentaires, suivi d'une brève conclusion.

2.1. De l'identification à la caractérisation fonctionnelle de la cyriotoxine-1a, une toxine issue du venin de l'araignée *Cyriopagopus schioedtei* ayant des propriétés antinociceptives

2.1.1. Contexte de l'étude

Un criblage à haut débit d'une banque de 117 venins appartenant à Smartox Biotechnology (Saint-Egrève, France) a été réalisé en utilisant des plateformes électrophysiologiques ("patch-clamp") automatisées. Dans un premier temps, la plateforme IonWorks Quattro® (Molecular Devices, Sunnyvale, CA, USA) a été employée pour un criblage rapide des fractions et sous-fractions de venins sur des lignées cellulaires recombinantes humaines (HEK-293 pour "human embryonic kidney") exprimant les sous-types $hNa_V1.7$ et 1.5, déposées dans des plaques de 384 puits et enregistrées en configuration "cellule entière" et en mode "cellule multiple" (le courant correspondant à la moyenne des courants obtenus à partir de 10 cellules). Dans un deuxième temps, la plateforme QPatch HTX (Sophion BioScience, Danemark) a été utilisée pour étudier les effets des peptides sélectionnés sur des lignées cellulaires recombinantes exprimant les sous-types de canaux ioniques étudiés, déposées dans des plaques de 48 puits et enregistrées *(1)* en configuration "cellule entière" et en mode "cellule multiple" (le courant enregistré correspondant à la sommation des courants obtenus à partir de 10 cellules), pour la caractérisation des propriétés pharmacologiques des sous-types de canaux ioniques étudiés et, en particulier, pour obtenir les courbes "concentration-réponse" en appliquant des concentrations cumulées de peptides, et *(2)* en configuration "cellule entière" et en mode "cellule unique" (le courant enregistré correspondant à celui obtenu à partir d'une seule cellule) pour la caractérisation des propriétés électrophysiologiques des sous-types de canaux ioniques étudiés et, en particulier, pour une détermination plus fine des effets des peptides sur certains de ces sous-types (Bertrand et al., 2016; Chambers et al., 2016).

Le criblage de la banque de 117 venins d'animaux (incluant les serpents, les araignées, les scorpions, les guêpes, les abeilles, les lézards et les poissons) a été mené sur des lignées cellulaires HEK-293 exprimant les sous-types $hNa_V1.7$ et 1.5 avec, pour objectif, de sélectionner des peptides ("hits") ayant une forte puissance vis-à-vis de $hNa_V1.7$ et n'étant pas ou que peu actifs sur $hNa_V1.5$. Ce criblage a permis de mettre en évidence de nombreux "hits" dont 80% sont des toxines issues de venins d'araignée. C'est dans ce contexte que la cyriotoxine-1a (CyrTx-1a) a été sélectionnée.

2.1.2. Publication n°2

British Journal of Pharmacology (publication en révision)

"Cyriotoxin-1a, the first toxin from *Cyriopagopus schioedtei* spider with antinociceptive properties: from identification to functional characterization"

Tânia C. Gonçalves, Evelyne Benoit, Michael Kurz, Laetitia Lucarain, Sophie Fouconnier, Stéphanie Combemale, Lucie Jaquillard, Brigitte Schombert, Jean-Marie Chambard, Rachid Boukaiba, Gerhard Hessler, Andrees Bohme, Laurent Bialy, Stéphane Hourcade, Rémy Béroud, Michel De Waard, Denis Servent & Michel Partiseti

RESEARCH PAPER

Title: Cyriotoxin-1a, the first toxin from *Cyriopagopus schioedtei* spider with antinociceptive properties: from identification to functional characterization

Full names of the authors: Tânia C. Gonçalves[†,#], Evelyne Benoit[#,‡], Michael Kurz[‖], Laetitia Lucarain[†], Sophie Fouconnier[†], Stéphanie Combemale[‡], Lucie Jaquillard[‡], Brigitte Schombert[†], Jean-Marie Chambard[†], Rachid Boukaiba[†], Gerhard Hessler[‖], Andrees Bohme[†], Laurent Bialy[‖], Stéphane Hourcade[!], Rémy Béroud[‡], Michel De Waard[‡,§], Denis Servent[#,]*, Michel Partiseti[†,]*

Authors' institutional affiliations: [†] Sanofi R & D, Integrated Drug Discovery – High Content Biology, F-94440 Vitry-sur-Seine, France. [#] Service d'Ingénierie Moléculaire des Protéines (SIMOPRO), CEA, Université Paris-Saclay, F-91191 Gif sur Yvette, France. [‡] Institut des Neurosciences Paris-Saclay (Neuro-PSI), UMR CNRS/Université Paris-Sud 9197, Université Paris-Saclay, F-91198 Gif sur Yvette, France/ [‖] Sanofi R & D, Integrated Drug Discovery – Synthetic Molecular Design, G-65929 Frankfurt, Germany. [‡] Smartox Biotechnology, 6 rue des Platanes, F-38120 Saint-Egrève, France. [!] Sanofi R & D, Neuroscience Therapeutic Area, Neurodegeneration Research, F-91385 Chilly-Mazarin, France. [§] Institut du Thorax, Inserm UMR 1087 / CNRS UMR 6291, LabEx "Ion Channels, Science & Therapeutics", F-44007 Nantes, France.

***Corresponding authors**: Denis Servent, PhD. Service d'Ingénierie Moléculaire des Protéines (SIMOPRO), CEA, Université Paris-Saclay, F-91191 Gif sur Yvette, France. Tel : 33 1 69 08 52 02. denis.servent@cea.fr ORCID 0000-0002-0774-1691. Michel Partiseti, PhD. Sanofi R & D, Integrated Drug Discovery – High Content Biology, F-94440 Vitry-sur-Seine, France. Tel: 33 1 58 93 29 96. Michel.Partiseti@sanofi.com

Word count (excluding abstract, methods, references and figure legends): **Intro: 609 + Results: 2519+ Discussion: 1510 : 4638**

Acknowledgements: This research was funded by a collaborative grant (#153114) between Sanofi Research & Development (Chilly-Mazarin, France) and the French Alternative Energies and Atomic Energy Commission (CEA, Gif sur Yvette, France). M.D.W. acknowledges financial support from the French Agence Nationale de la Recherche (grant ANR-11-LABX-0015). T.C.G. was supported by a doctoral CIFRE fellowship from Sanofi. The authors wish to thank Dr Muriel AMAR (CEA de Saclay, Gif sur Yvette, France) for her help in the calculation of kinetic parameters of sodium current activation and inactivation, and Dr Isabel LEFEVRE (Sanofi R & D, Chilly-Mazarin, France) for her critical reading of the manuscript.

Conflict of interest statement: The authors L. Bialy, A. Bohme, R. Boukaiba, J.M. Chambard, S. Fouconnier, T.C. Gonçalves, G. Hessler, S. Hourcade M. Kurz, L. Lucarain, B. Schombert, and M. Partiseti declare the following competing interest: current or former employees of Sanofi.

Author contributions: L.L. performed experiments and J.-M.C. analyzed the data for the venom fraction screenings. L.L. performed experiments and J.-M.C. analyzed the data for the venom fraction screenings. S.C. and L.J. performed experiments and M.D.W. and R.Bé. analyzed the data for the peptide purification, sequencing and synthesis experiments. T.C.G., S.F., R.Bo., B.S., A.B. and M.P. performed and analyzed experiments done on recombinant ion channel cell lines. T.C.G. and E.B. performed and analyzed experiments done on DRG neurons and mice. M.K. and G.H. determined 3D-structure. L.B. and S.H. aided in the preparation of the manuscript. T.C.G, E.B, M.P, M.D.W. and D.S wrote the manuscript and supervised the study. All authors approved the manuscript.

ABSTRACT

BACKGROUND AND PURPOSE : $Na_V1.7$ channel subtype is highly expressed in dorsal root ganglia of the sensory nervous system and plays a central role in the pain signalling process. We investigated venoms to identify selective inhibitors of this target.

EXPERIMENTAL APPROACH : We used high-throughput screening of a large venom collection using automated patch-clamp experiments on human voltage-gated sodium channel subtypes, and then *in vitro* and *in vivo* electrophysiological experiments to characterize the active peptides that have been purified, sequenced and chemically synthesized. Analgesic effects were evaluated *in vivo* in mice models.

KEY RESULTS : We identified the first peptide, cyriotoxin-1a (CyrTx-1a), isolated from the *Cyriopagopus schioedtei* spider venom. This 33 amino acids toxin belongs to the inhibitor cystine knot structural family and inhibits $hNa_V1.1$-1.3 and 1.6-1.7 in the low nanomolar range, compared to the micromolar range for $hNa_V1.4$-1.5 and 1.8. CyrTx-1a was 635 times more efficient at inhibiting tetrodotoxin (TTX)-sensitive than TTX-resistant sodium currents recorded from adult mouse dorsal root ganglia neurons and *in vivo* electrophysiological experiments showed that CyrTx-1a was approximately 170 times less efficient than huwentoxin-IV at altering mouse skeletal neuromuscular excitability properties. CyrTx-1a exhibited an analgesic effect in mice by increasing reaction time in the hot plate assay and decreasing tactile sensitivity in automated plantar von Frey experiments.

CONCLUSIONS AND IMPLICATIONS : The pharmacological profile of CyrTx-1a paves the way for further engineering studies aimed to optimize the potential antinociceptive properties of this peptide.

Key Words: *Cyriopagopus schioedtei* spider, cyriotoxin-1a, voltage-gated sodium channel subtypes, cell lines overexpressing ion channel subtypes, mouse dorsal root ganglia neurons, mouse tactile and cold pain sensitivity, mouse skeletal neuromuscular excitability *in vivo*.

Abbreviations: aPC, automated patch-clamp; Ca_V channel, voltage-gated calcium channel; CHO, Chinese hamster ovary; CMAP, compound muscle action potential; CyrTx-1a, cyriotoxin-1a;

DMEM, Dulbecco's modified Eagle's medium; DRG, dorsal root ganglia; ERG, *ether-a-go-go*-related gene; HEK, human embryonic kidney; HEPES, N-2-hydroxyethylpiperazine-N'-2-ethanesulfonic acid; HwTx-IV, huwentoxin-IV; i.m., intramuscular; IC_{50}, toxin concentration necessary to inhibit 50% of the response; ICK, inhibitor cystine knot; K_V channel, voltage-gated potassium channel; mPC, manual patch-clamp; NaSpTx, Na_V channel spider toxin; Na_V channel, voltage-gated sodium channel; PBS, phosphate buffered saline; PPC, population patch-clamp; TCEP, Tris (2-carboxyethyl) phosphine hydrochloride; TTX, tetrodotoxin; TTX-R, resistant to tetrodotoxin; TTX-S, sensitive to tetrodotoxin.

Introduction

Sensory neurons express many transmembrane proteins that are therapeutic target candidates for the treatment of pain. In particular, inhibitors of ion channels (such as voltage-gated sodium (Na_V) and calcium (Ca_V) channels, transient receptor potential channels, acid-sensing ion channels, piezo proteins, ionotropic P2X receptors), as well as potassium channel (K_V) enhancers, are being investigated as potential analgesics (Bennett *et al.*, 2014; Waxman *et al.*, 2014). Na_V channels include nine subtypes ($Na_V1.1$-1.9), each of them having non-redundant functions due to specific expression patterns and/or singular biophysical properties. During this last decade, attention has been given to several Na_V channel subtypes ($Na_V1.1$, 1.3 and 1.6-1.9) as potential analgesic targets (Cardoso *et al.*, 2017a).

Among these Na_V channel subtypes, the $Na_V1.7$ subtype seems to be the most interesting target to treat chronic debilitating pain. Indeed, this subtype is highly expressed in the sensory nervous system, principally in small and large dorsal root ganglia (DRG) neurons, the anatomic support of pain signalling from the skin and organs to the spinal cord (Dib-Hajj *et al.*, 2013). Furthermore, a multitude of genetic mutations of $Na_V1.7$ are linked to painless or painful phenotypes (de Lera Ruiz *et al.*, 2015; Vetter *et al.*, 2017). Moreover, it is well established that small molecules that target Na_V channels, like tetrodotoxin (TTX), attenuate chronic and debilitating pain in humans. However, pronounced side-effects have been described, such as nausea, dizziness, oral numbness and tingling, due to a lack of selectivity (Hagen *et al.*, 2017). The current challenge is thus to identify a new therapeutic class of analgesic molecules antagonizing the $Na_V1.7$ channel subtype with high selectivity compared to other Na_V subtypes, particularly the Nav1.5 subtype and the $Na_V1.6$ and 1.4 subtypes due to cardiac and neuromuscular safety issues, respectively.

Several peptide toxins from animal venoms (spiders, scorpions, cone snails, sea anemones, centipedes …) have been reported to block or modulate Na_V channel function (Israel *et al.*, 2017). Some of them, mainly isolated from spider venoms, showed promising selectivity for $Na_V1.7$ (Vetter *et al.*, 2017). Their sequence is mostly composed of 30-35 amino-acids, including three disulfide bridges with an inhibitor cystine knot (ICK) motif. These positively-charged toxins are gating-modifier peptides that bind to the receptor-sites 3 (on Domain IV) and/or 4 (on Domain II) of Na_V channels, inducing variable pharmacological effects in *in vitro* tests and *in vivo* pain models (Saez *et al.*, 2010). For instance, HwTx-IV and GpTx-1, two well-characterized $Na_V1.7$-blocking

spider toxins with high selectivity over $Na_V1.4$ and $Na_V1.5$ channel subtypes, have analgesic properties in animal models. However, they also produce strong side-effects such as inactivity, paralysis and death in standard pain tests in rodents, due to the lack of selectivity over the $Na_V1.6$ channel subtype (Deuis *et al.*, 2016; Goncalves *et al.*, 2018). Other spider toxins, such as protoxin-II, exhibit a 100-fold higher potency on Nav1.7 compared to all Na_V subtypes, except $Na_V1.6$. Interestingly, the *in vivo* safety margin of this toxin is increased for the mutant JNJ 63955918 due to an improved selectivity against $Na_V1.1$, 1.2 and 1.6 (Flinspach *et al.*, 2017). Very recently, the jingzhaotoxin-V analog AM-8145 was reported to display a more than 100-fold higher potency on $Na_V1.7$ compared to all Na_V subtypes (Moyer *et al.*, 2018).

The present work reports the identification, structural characterization and pharmacological profile of the first toxin isolated from the venom of *Cyriopagopus schioedtei* spider, using a high throughput electrophysiological screening assay on Na_V channel subtypes. This ICK toxin is shown to possess nanomolar range affinity for $Na_V1.1$-1.3, 1.6 and 1.7 subtypes, micromolar affinity for other channel subtypes and to exhibit analgesic effects in rodent pain models. It represents an interesting lead for future analogues designed to possess a better therapeutic window.

Methods

Isolation and purification of CyrTx-1a

A library was prepared from 117 different animal venoms by crude venom fractionation using an analytical RP-HPLC C18 column (XBridge™ BEH 130, 3.5 µm and 4.6 mm ID x 250 mm L column) attached to an Agilent 1260 HPLC (Agilent Technologies). Primary fractions were first evaluated in a functional screening assay on an engineered human embryonic kidney (HEK)-293 cell line overexpressing human (h) $Na_V1.7$ and $hNa_V1.5$ channel subtypes using the IonWorks Quattro platform (Molecular Devices, USA). For instance, the *Cyriopagopus schioedtei* spider venom, one of the venoms of interest, was separated into fractions that contained between 5 and 15 peptides each at an estimated concentration of 0.5 $\mu g.\mu L^{-1}$. Active fractions were finally subfractionated using cation exchange chromatography with a TOSOH Bioscience column (TSK gel SP-STAT, 7 µm, 4.6 mm ID x 10 cm L, TOSOH Bioscience, Germany) onto an Agilent 1260 HPLC (Agilent technologies) to individualize the compounds. The purified compounds were screened on HEK-293 cells overexpressing $hNa_V1.7$, $hNa_V1.2$, $hNa_V1.5$ and $hNa_V1.6$ channel subtypes, using the QPatch HTX automated electrophysiology platform (Sophion BioScience, Denmark), leading to the identification of CyrTx-1a as one of the peptides of interest.

Amino acid sequencing of CyrTx-1a

The peptide amino acid sequence was determined by *de novo* MS/MS sequencing and Edman degradation. The purified venom peptide obtained after successive RP-HPLC and cation exchange chromatography, from a starting material of 2 mg, was resuspended in 100 mM ammonium bicarbonate (pH 8), reduced with 17 mM Tris (2-carboxyethyl) phosphine hydrochloride (TCEP) (incubated at 55°C for 1 hr) and alkylated with 24 mM iodoacetamide (incubated at room

temperature in the dark for 1 hr) prior to enzyme digestion. The reduced/alkylated venom peptide was digested by using trypsin or V8 proteases. The enzyme was added at a 1:10 ratio (enzyme/peptide, w/w) and incubated overnight at 37°C before LC-MS(/MS) analyses.

A Waters Q-TOF Xevo G2S mass spectrometer equipped with an Acquity UHPLC system and Lockspray source was used for the acquisition of the LC-ESI-MS and LC-ESI-MS/MS data and the amino acid sequence determination based on Edman degradation was performed using an Applied Biosystems gas-phase sequencer model 492 (s/n: 9510287J). These protocols are detailed in the Supporting Information.

Chemical synthesis and folding of CyrTx-1a

CyrTx-1a was assembled stepwise using 2-chlorotrityl chloride resin (substitution rate of 1.6 $mmol.g^{-1}$) by solid-phase fmoc chemistry on a Symphony Synthesizer (Protein technologies Inc.). Amino acid coupling reaction was 15 min (repeated three times to increase the coupling yield). After resin cleavage and deprotection with 92.5% (vol) TFA, 2.5% H_2O and scavengers (1,3-dimethoxybenzene (2.5%) and triisopropylsilane (2.5%)), the peptide was purified to homogeneity by C18 RP-HPLC on a Jupiter Proteo column (Phenomenex, 4 µm, 21.2 mm ID x 250 mm L) using an Agilent Technologies preparative HPLC (1260 Infinity). Finally, CyrTx-1a was folded/oxidized in 50 mM Tris-HCl, pH 8.3 during 72 hrs. The resulting oxidized CyrTx-1a with its three disulfide bridges was purified to homogeneity (>99% purity according to the integration of the purified chromatogram peak at 214 nm) using RP-HPLC with the Jupiter Proteo column. The molecular mass of CyrTx-1a was determined by LC-ESI-QTOF MS. The absence of contaminant masses attested of the purity of synthetic CyrTx-1a.

3D-structure of CyrTx-1a

The structure of CyrTx-1a was determined by high-resolution NMR spectroscopy in an aqueous solution (10% D_2O) of 6 $mg.mL^{-1}$ peptide in a 50 mM phosphate buffer at pH 5.0 and a temperature of 305°K. Data were obtained on a Bruker Avance 700 MHz using standard 2D spectra. Resonances were assigned with 2D-spectra including DQF-COSY, TOCSY, NOESY, 1H- 13C-HSQC, and 1H-15N-HSQC. For conformational analysis, NOE based distance restraints were obtained from a NOESY spectrum with 200 ms mixing time. 431 distance restraints were used in a simulated annealing protocol starting from a linear, extended structure including 71 intra residual distances, 126 sequential distances, 69 medium distances (2-4 amino acids apart) and 165 long range distances (> 4 amino acids apart). Calculations were performed with the software package SYBYL version 2.1.1. All energy calculations were based on AMBER7 F99 force field. Distance restraints for non-separated methylene protons and methyl groups were used with pseudoatom correction: 0.9 Å were added to the upper bound for methylene groups, 1.0 Å was added for methyl groups. 20 structures were obtained which converged well. The rmsd over all backbone atoms was 0.465 ± 0.285 Å.

Toxins used for functional assays

Lyophilized synthetic CyrTx-1a (molecular mass of 3578.68, purity rate > 97%) was dissolved in phosphate buffered saline (PBS, 1X) solution to give a 6.8 mM stock solution. Lyophilized synthetic huwentoxin-IV (HwTx-IV; molecular mass of 4106.811, purity rate > 97%) was obtained

from Smartox Biotechnology (Saint-Egrève, France). This toxin was dissolved in PBS solution to give a 6.1 mM stock solution. TTX citrate (molecular mass of 319.27, purity rate > 98%) was purchased from Sigma-Aldrich (Saint-Quentin Fallavier, France). This toxin was dissolved in PBS solution to give a 2.85 mM stock solution. Just prior to experiments, successive dilutions were performed in the appropriate standard physiological medium to give the toxin final concentrations indicated in the text.

Cell lines, animals and primary culture of DRG neurons used for functional assays

Generation of inducible cell lines was achieved using the Flp-In® T-Rex® expression system (Invitrogen, USA). For this purpose, cDNAs encoding for $hNa_V1.5$ (NM_000335) and $hNa_V1.2$ (NM_021007.2) were cloned into the Flp-In® T-Rex® expression vector (Invitrogen) and subsequently transfected into HEK-293 cell lines. Recombinant HEK-293 cell lines stably expressing $hNa_V1.7$, $hNa_V1.1$ and $hNa_V1.8$ were purchased from Eurofins (St Charles, MO, USA), those for stably expressing $hNa_V1.6$ from ChanTest (Charles River, Cleveland, OH), and those stably expressing $hNa_V1.3$ and $hNa_V1.4$ from SB Drug Discovery (UK). Protocols for cell culture are detailed in the Supporting Information.

In vivo experiments (neuromuscular system, as well as heat and tactile pain sensitivity) and dissociation of DRG neurons were performed by using adult female Swiss mice (10-12 weeks of age and 28-32 g body weight) purchased from Janvier Elevage (Le Genest-Saint-Isle, France) and housed at the CEA animal facility. All animal experiments performed in this study were conducted in compliance with the guidelines established by the French Council on animal care "Guide for the Care and Use of Laboratory Animals" (EEC86/609 Council Directive – Decree 2001-131), and the experimental protocols were approved on November 27 2015 by the French General Directorate for Research and Innovation (project APAFIS#2671-2015110915123958v3 authorized to E.B.).

Mouse DRG were removed from the spinal cord and enzymatically dissociated, and neurons were maintained in culture, as detailed previously (Goncalves *et al.*, 2018). Experiments were carried out within 2 to 6 days after plating.

Electrophysiological recordings

Automated and manual patch-clamp recordings were performed on cell lines and DRG neurons as described in the Supporting Information. *In vivo* recordings from the neuromuscular system of anaesthetized mouse were obtained by means of a minimally-invasive electrophysiological method, using the Qtrac© software (Prof. H. Bostock, Institute of Neurology, London, United Kingdom), as previously detailed (Goncalves *et al.*, 2018). Briefly, the anaesthetized mice were placed on a heating pad to maintain body temperature throughout the experiments (35.99 ± 0.03°C, as determined in 29 mice using a rectal probe). Electrical stimulations were delivered to the caudal motor nerve (at the base of the tail) by surface electrodes, and the compound muscle action potential (CMAP) was recorded using needle-electrodes inserted into the tail muscle. To study the local action of CyrTx-1a and TTX, intramuscular (i.m.) injections (4-µL maximal volume) of PBS solution containing various concentrations of a given toxin were delivered with a 10-µL micro-syringe at the base of the tail, between stimulation and ground electrodes. Similar injections (4 µL)

were also done with PBS solution to test for any effect of the vehicle. On-line recordings were initiated approximately 5 min before a given injection to assess the toxin and/or vehicle effects on selected excitability parameters, such as the excitability threshold and CMAP amplitude continuously recorded over time. To better identify the underlying mechanism(s) of action and the duration of CyrTx-1a and TTX effects, five different excitability tests (stimulus-response, strength-duration and current-threshold relationships, as well as threshold electrotonus and recovery cycle (detailed in (Cerles *et al.*, 2017)) were performed together before and at various times (from 30 min to 12 hrs) after a given injection. As a whole, more than thirty parameters were determined from these five excitability tests and analyzed. Most of them provide specific and complementary information on the density and functional status of ion channels, receptors and pumps, as well as on the passive membrane properties of the neuromuscular system (Kiernan *et al.*, 2000; Krishnan *et al.*, 2008).

Heat and tactile pain sensitivity of mice in vivo

Prior to hot-plate testing, each mouse underwent a 30-min acclimation to the experimental laboratory environment (in its home cage). Then, mice were either not injected or received an intraplantar injection of 5-10 µL of PBS or toxin solution in each hind paw under low anaesthesia achieved by means of isoflurane (AErrane®, Baxter S.A., Lessines, Belgique) inhalation. After 60 min rest in its home cage, the mouse was put on the hot-plate set at the temperature of 55.0 ± 0.2°C. The measured parameter as the first pain-related manifestation was the latency (in sec) for the animal either to shake one of its two hind limbs or to jump. This latency, considered as a painful response to heat, was recorded simultaneously by two observers (one being blind to treatment group) with a timer integrated into the set-up. A maximal cut-off time of 30 sec was used to prevent tissue damage.

Tactile sensitivity was assessed using an automated plantar von Frey apparatus (Dynamic Plantar Aesthesiometer 37450, Ugo Basile, Comerio, Italy). Prior to testing, each mouse was placed on a mesh grid, surrounded by a clear Plexiglas barrier with a top cover, and left to calm down for 30 min without probing. After the settling phase, the mouse was motionless allowing for either of its hind limbs to be touched by a flexible plastic fibre of a fixed diameter. The fibre was pressed through the mesh grid against the plantar surface at a right angle, and the force of application increased slowly (at the determined rate of 1.67 $g.sec^{-1}$). The force intensity (in g) at which the animal removed its hind limb was recorded with a timer integrated into the set-up as the mean of at least four tests. A cut-off automatically occurred if the animal did not remove its hind limb when the point at which the greatest pre-set force was met, to prevent tissue damage. The force intensity was determined every 5 min during 30-45 min before and 15 min after intraplantar injection of 5 µL of PBS or toxin solution in each hind limb under low anaesthesia by means of isoflurane.

Data and statistical analyses

Concentration-response relationships were established by plotting the response, recorded in the presence of a given toxin (Rt) and expressed as percentage of the value obtained in absence of toxin (Rc), against the toxin concentration ([toxin]). The theoretical concentration-response curves were

calculated from typical sigmoid nonlinear regressions through data points (correlation coefficient = r^2) according to the Hill equation (GraphPad Prism 5 or QPatch assay software): Rt / Rc = 1 / [1 + ([toxin] / IC_{50}) n_H], where IC_{50} is the toxin concentration necessary to inhibit 50% of the response, and n_H is the Hill number. Conductance (g) was calculated according to the following equation: g = I / (V_T – V_{Na}), where I is the peak current amplitude, V_T is the test-pulse voltage, and V_{Na} is the equilibrium potential of Na ions. Conductance-voltage relationships were established by plotting the conductance, expressed as percentage of the maximal conductance (gmax) calculated at strongly positive test-pulses, as a function of test-pulse voltage. The theoretical curves correspond to data point fits according to the Boltzmann equation (GraphPad Prism 5 software): g / gmax = 1 – [1 / (1 + exp ((V_T – $V_{T50\%}$) / k_g))], where $V_{T50\%}$ is the test-pulse voltage corresponding to 50% maximal conductance, and k_g is the slope of the curve. Steady-state inactivation-voltage relationships were established by plotting the peak current amplitude, expressed as percentage of the maximal amplitude (Imax) recorded in response to strongly negative pre-pulses, as a function of pre-pulse voltage (V_P). The theoretical curves correspond to data point fits, according to the Boltzmann equation (GraphPad Prism 5 software): I / Imax = 1 / [1 + exp ((V_P – $V_{P50\%}$) / k_h)], where $V_{P50\%}$ is the pre-pulse voltage corresponding to 50% maximal peak amplitude of current, and k_h is the slope of the curve. Current kinetics were evaluated by calculating: (1) the time to peak (tp), defined as the time between test-pulse triggering and the peak current, and (2) the time constant (τh) of the current decay, for current inactivation that occurs as a mono-exponential decay as a function of time, *i.e.*, $I_{(t)} = I_{(0)}\, e^{(-t/\tau h)}$.

Data are expressed as means ± standard deviations (S.D.) of n different experiments. The statistical comparison of values was carried out using the parametric two-tailed Student's *t*-test (either paired samples for comparison within a single population or unpaired samples for comparison between two populations). Differences between values were considered to be statistically significant at $P \leq 0.05$.

Results

Isolation, purification and de novo *amino acid sequencing of CyrTx-1a*

A primary high-throughput screening of the Smartox venom collection was performed on automated patch-clamp (aPC) Ionworks Quattro platform using HEK-293 cells overexpressing $hNa_V1.7$ channel subtypes (Figure 1a). Following successful priming and sealing steps, a 10-pulse train protocol from -120 to -10 mV at 10 Hz was elicited, bringing $hNa_V1.7$ channel subtypes from closed to open configuration (Figure 1b). The so-called pre-scan performed in presence of extracellular buffer was used as a control signal. An average peak current from pulse 1 of 880 ± 280 pA (n = 29 plates) was elicited. A similar average amplitude was measured from pulse 10 on the same recording (no current rundown was observed under our conditions). In control experiments using the same protocol, no inhibitory effect of 0.1% bovine serum albumin was found. Conversely, addition of 1 µM TTX produced a full block of the elicited currents (n = 928 wells from 29 plates). This expected pharmacology was used as internal positive control (data not shown).

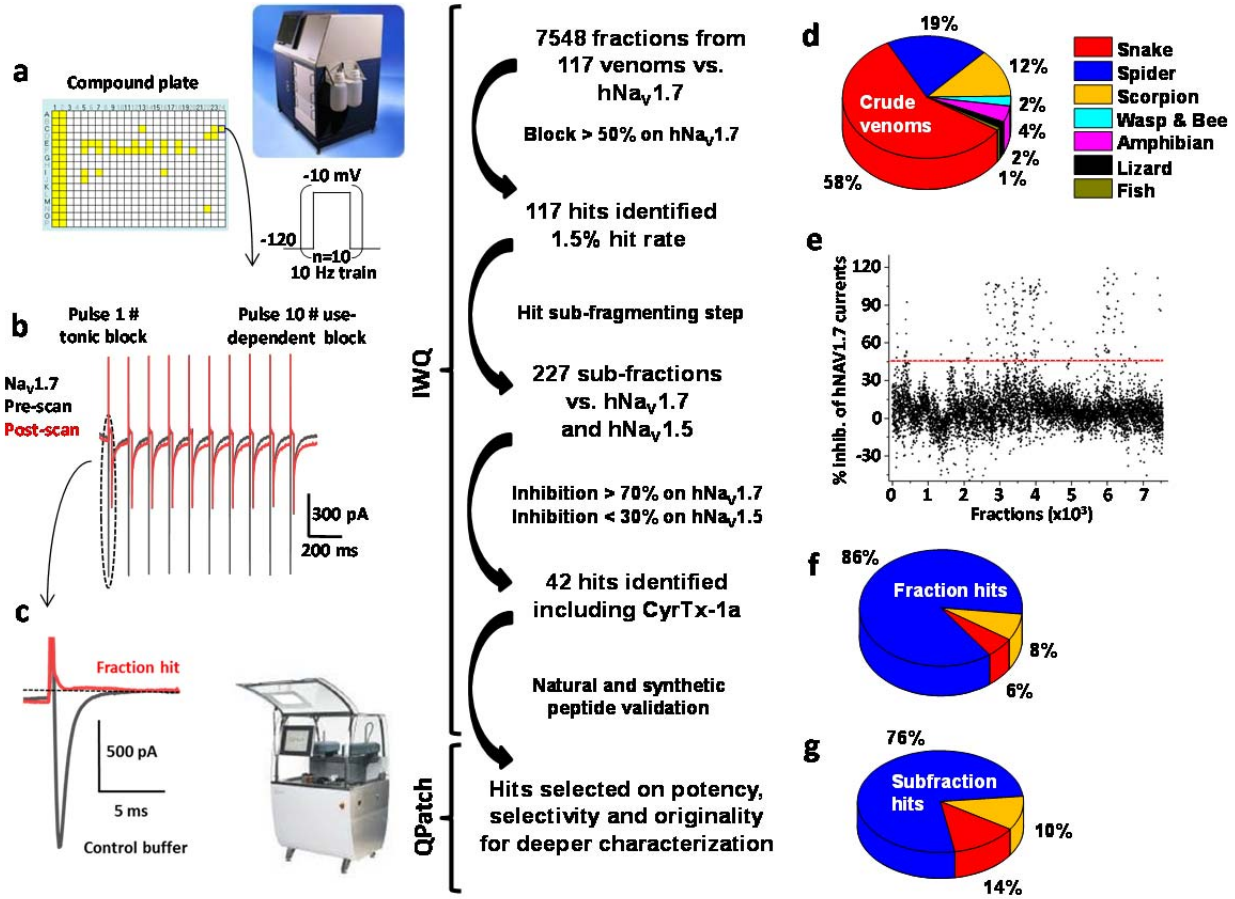

Figure 1: Screening flowchart from crude venom fraction to isolated peptide identification. (**a**) Collection of 117 venoms was prepared into 7548 fractions individually added to384-well plates (columns 1 and 2 are 1 µM TTX full block and columns 3 and 4 are maximal current obtained in extracellular buffer) for testing *versus* $hNa_V1.7$ on the Ionworks Quattro (IWQ, Molecular Devices). The train protocol described as an insert was applied before and after 10-min incubation of cells with the fraction containing the toxin of interest. Traces of pre-and post-scan are shown in full (**b**). Also, tonic block obtained on $hNa_V1.7$ has been enlarged (**c**). Source of the screened crude venom is shown in (**d**). Percentage of inhibition for all tested fractions was plotted. As shown in (**e**), a threshold was set at 50% block (red line). From the venom library tested, only 8% hits *versus* $hNa_V1.7$ came from scorpion venom, 6% from snake while the larger majority (86%) was spider fractions (**f**). (**g**) Hits were sub-fractioned and tested again *versus* $hNa_V1.7$ and $hNa_V1.5$ to identify most promising hits to be further characterized using whole-cell patch-clamp aPC (QPatch).

As mentioned in Figure 1, a total of 7548 fractions coming from 117 crude venoms were tested from a large variety of species including snake, spider, scorpion, wasp, bee, amphibians, lizard and fish (see Figure 1d). The 384-well screening plates were prepared in such a way that individual fractions were tested at an average concentration of 0.5 $\mu g.\mu L^{-1}$ (500 ng of dry ass suspended in water). An overview of the percentage of inhibition obtained for each fraction before and after application is given in Figure 1e. Note that 97 fractions were discarded because of a negative impact on the sealing process or because they disrupted seals over time. Also, 26 samples which elicited large sodium current increases were removed from the analysis. From the primary screening, 117 fractions were flagged based on their potency vs. recombinant $Na_V1.7$, then selected for sub-fractionation and compound isolation using cation exchange chromatography (Figure 1f). Following this process, 227 sub-fractions from 3 species (snake, spider and scorpion; Figure 1g) were prepared and used at a final estimated amount of 100 ng per well. These sub-fractions were tested in our functional automated patch-clamp $hNa_V1.7$ but also $hNa_V1.5$ assays (in conventional

closed to open configuration protocols), as a first line selectivity assay. From the 42 hits highlighted at this stage, 14 were discarded because of strong effects on $hNa_V1.5$.

Figure 2a,b illustrates the screening process for the spider venom *Cyriopagopus schioedtei* from primary fraction selection to individual purified compound selection by secondary screening. Following selection through the multi-step chromatographic approach, a new peptide was identified using combined orthogonal reversed-phase and ion exchange techniques (Figure 2c,d).

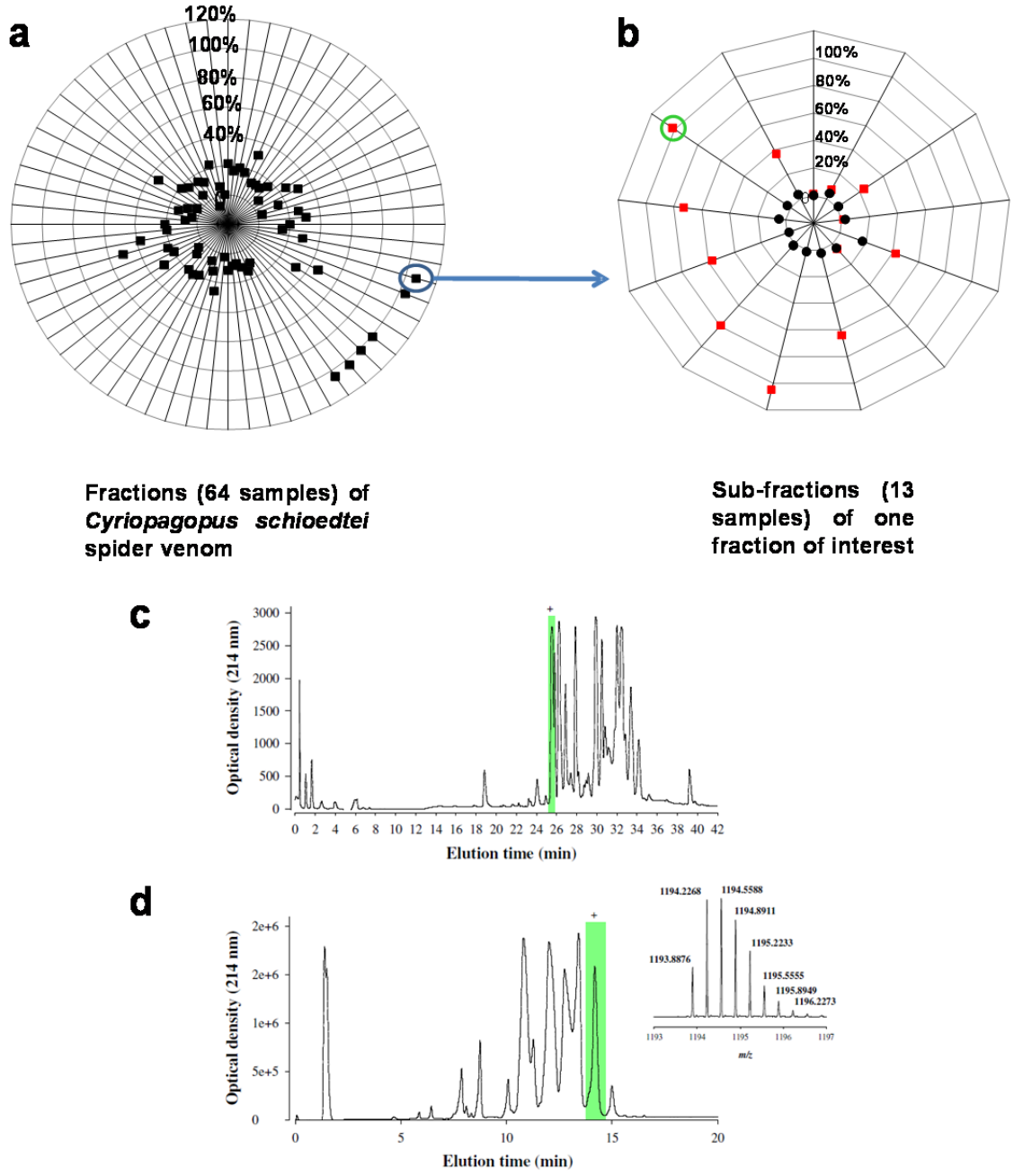

Figure 2: Flowchart for $hNa_V1.7$ hit peptide identification. (**a**) Percentage of inhibition of peak $hNa_V1.7$ elicited current by application of 0.05 µg of each of the 64 fractions obtained from *Cyriopagopus schioedtei* spider venom. (**b**) Each fraction of interest was then separated again to isolate one peptide per well. Sub-fractions were tested again in our automated patch-clamp Quattro assay. At this stage, $hNa_V1.7$ (red squares) and $hNa_V1.5$ (black circles) inhibition was investigated. (**c**) Fractionation of the crude venom from *Cyriopagopus schioedtei* by reversed-phase chromatography and detection by UV at 214 nm. The fraction containing the peptide of interest is highlighted in green. (**d**) Cation exchange sub-fractionation of the primary fraction highlighted in (**c**). The inset illustrates the MS of *m/z* 1193.8947 $[M+3H]^{3+}$.

Using the IonWorks Quattro automated patch-clamp system, the peptide (2.8 µM) displayed a potent blocking effect on $hNa_V1.7$ (98.9 ± 1.2% block, n = 3; Figure 2b) while fully sparing $hNa_V1.5$ (4.1 ± 1.2% inhibition, n = 3). The molecular mass value of 3578.68 Da for this peptide, as determined by LC-ESI QTOF MS, indicates that the peptide should be amenable to chemical synthesis (Inset in Figure 2d).

As this peptide belongs to a species that has not been genotyped, its sequence was determined by *de novo* sequencing using mass spectrometry analyses. Hence, the purified peptide was reduced using TCEP and alkylated with iodoacetamide. The alterations in molecular mass from 3578.7 to 3926.7 Da indicate that the peptide should contain six cysteine residues and hence three disulfide bridges if one takes into account the loss of 1 Da upon reduction of disulfide bridges and the addition of 57.02 Da upon alkylation on each cysteine residue. Samples of the reduced/alkylated toxin were then digested overnight with either trypsin or V8 proteases. The digests were next analysed by LC-ESI-MS(/MS) for *de novo* sequencing. Table S1 (Supporting Information) provides the list of fragments detected and sequenced after trypsin and Glu-C digestion. While full sequence coverage of the toxin was obtained by mass spectrometry, a complementary characterization was performed using Edman degradation, especially for the precise determination of the isobaric leucine and isoleucine residues. The final sequence is reported in Figure 3a with a single post-translational modification identified as C-terminal amidation of the peptide.

a

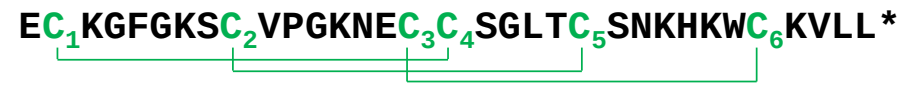

b

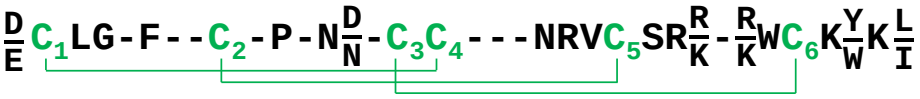

c

			Length	Identity (%)
Cyriotoxin-1a (CyrTx-1a)	*µ-theraphotoxin-Cs1a*	ECKGFGKSCVPGKNECCS--GLTCSNKHKWCKVLL	33	100
Hainantoxin-I (HnTx-I)	*µ-theraphotoxin-Hhn2b*	ECKGFGKSCVPGKNECCS--GYACNSRDKWCKVLL	33	82
Hainantoxin-III (HnTx-III)	*µ-theraphotoxin-Hhn2a*	GCKGFGDSCTPGKNECCP--NYACSSKHKWCKVYL	33	73
Haplopelma doriae 1a (Hd1a)	*µ-theraphotoxin-Hd1a*	ACLGFGKSCNPSNDQCCKSSSLACSTKHKWCKYEL	35	61
Hainantoxin-IV (HnTx-IV)	*µ-theraphotoxin-Hhn1b*	ECLGFGKGCNPSNDQCCKSSNLVCSRKHRWCKYEI	35	55
Protoxin-III (ProTx-III)	*µ-theraphotoxin-Tp1a*	DCLKFGWKCNPRNDKCCS--GLKCGSNHNWCKLHI	33	45
Ceratotoxin-I (CcoTx-1)	*β-theraphotoxin-Cm1a*	DCLGWFKSCDPKNDKCCK--NYTCSRRDRWCKYDL	33	45
Grammotola porteri Toxin-1 (GpTx-1a)	*ω-theraphotoxin-Gr2a*	DCLGFMRKCIPDNDKCCRP-NLVCSRTHKWCKYVF	34	45
Huwentoxin-IV (HwTx-IV)	*µ-theraphotoxin-Hs2a*	ECLEIFKACNPSNDQCCKSSKLVCSRKTRWCKYQI	35	42

Figure 3: Primary structure, disulfide bridge alignment and sequence homologies of CyrTx-1a. (**a**) Primary structure of CyrTx-1a. Asterik denotes amidation. Disulfide bridging, as defined by homology, occurs according to the C1-C4, C2-C5 and C3-C6 pattern. (**b**) Consensus sequence of the NaSpTx family 1, adapted from Klint et al. (2012). (**c**) Comparison of amino acid sequences between CyrTx-1a and the 9 most similar analgesic toxins from NaSpTx family 1. Sequence alignment performed with Clustal Omega (version 1.2.4 from Emboss programs, EBlosum62 matrix for two pair alignment). The green gradient was used to highlight the percentage of identity (Jalview program according to EBlosum62 matrix).

The peptide, composed of 33 amino acids (3578.68 Da), was identified as μ-theraphotoxin-Cs1a or cyriotoxin-1a (CyrTx-1a). It is the first toxin described so far from the crude venom of *Cyriopagopus schioedtei* spider, known as the Malaysian earth tiger tarantula, classified in the Ornithoctoninae subfamily. CyrTx-1a contains the ICK architectural motif previously reported in toxins from the same theraphosid spider family, the Na_V channel spider toxin (NaSpTx) family 1 (Figure 3b). Furthermore, comparison of amino acid sequences between CyrTx-1a and the 9 most similar toxins (of 33-35 amino acids) with analgesic properties from the NaSpTx family 1 revealed that the peptide shares 82% of identity with hainantoxin-I and μ-theraphotoxin-Hhn2b, and 73% of identity with hainantoxin-III and μ-theraphotoxin-Hhn2a (Figure 3c). In contrast, the well-known potent analgesic peptides ω-theraphotoxin-Gr2a (GpTx-1) and μ-theraphotoxin-Hh2a (HwTx-IV) share only 45% and 42% of identity, respectively, with CyrTx-1a.

Chemical synthesis and in vitro *folding of CyrTx-1a*

CyrTx-1a was chemically synthesized using solid-phase Fmoc chemistry. Figure S1a,b (Supporting Information) illustrates the HPLC profiles of the crude and purified synthesized peptide, respectively. Mass spectrometry data established that the purified reduced peptide had the expected mass with *m/z* value of 1195.9097 $[M+3H]^{3+}$. Finally, the reduced CyrTx-1a peptide was oxidized to produce oxidized/folded CyrTx-1a along with its three-disulfide bridges (Supporting Information Figure S1c). The yield of oxidation was 13%, indicating good formation of the secondary structures and easy disulfide bridge connectivity during oxidation. To confirm that the synthetic CyrTx-1a was indeed identical to its native counterpart, both peptides were mixed at equal concentrations and run simultaneously onto analytical RP-HPLC. As a single major peak was detected, we conclude that the two peptides co-elute, hence demonstrating identical retention times on the C18 column (Supporting Information Figure S1d). The experimental molecular mass of the synthetic peptide (Inset in Figure S1c, 1193.8956 $[M+3H]^{3+}$) was in close agreement with the theoretical mass (1193.8918).

3D-structure of CyrTx-1a

The three-dimensional solution structure of CyrTx-1a was determined by 2D homonuclear ^{1}H-NMR spectroscopy. Spectra were recorded at 305°K where the amid resonances show a good dispersion. One signal set of sharp and well-dispersed resonances is indicative of a single structure in solution (Figure 4b). NMR-derived interproton distances were used for structure calculations with a molecular dynamic-based protocol. An ensemble of 20 conformations was obtained, containing a well determined backbone conformation of an ICK motif (Figure 4a) (PDB: 6GFT). The 1H-chemical shifts of CyrTx-1a in H_2O/D_2O highlight the high precision and stereochemical quality of the ensemble of CyrTx-1a structures (Supporting Information Table S2). The entire structure has an electrical dipole moment with a larger positive pole, likely important for CyrTx-1a binding to Na_V channels (Figure 4c). Such a motif has also been found for other $Na_V1.7$ inhibitory peptides such as HnTx-IV, ProTx-III and HwTx-IV (Figure 4d).

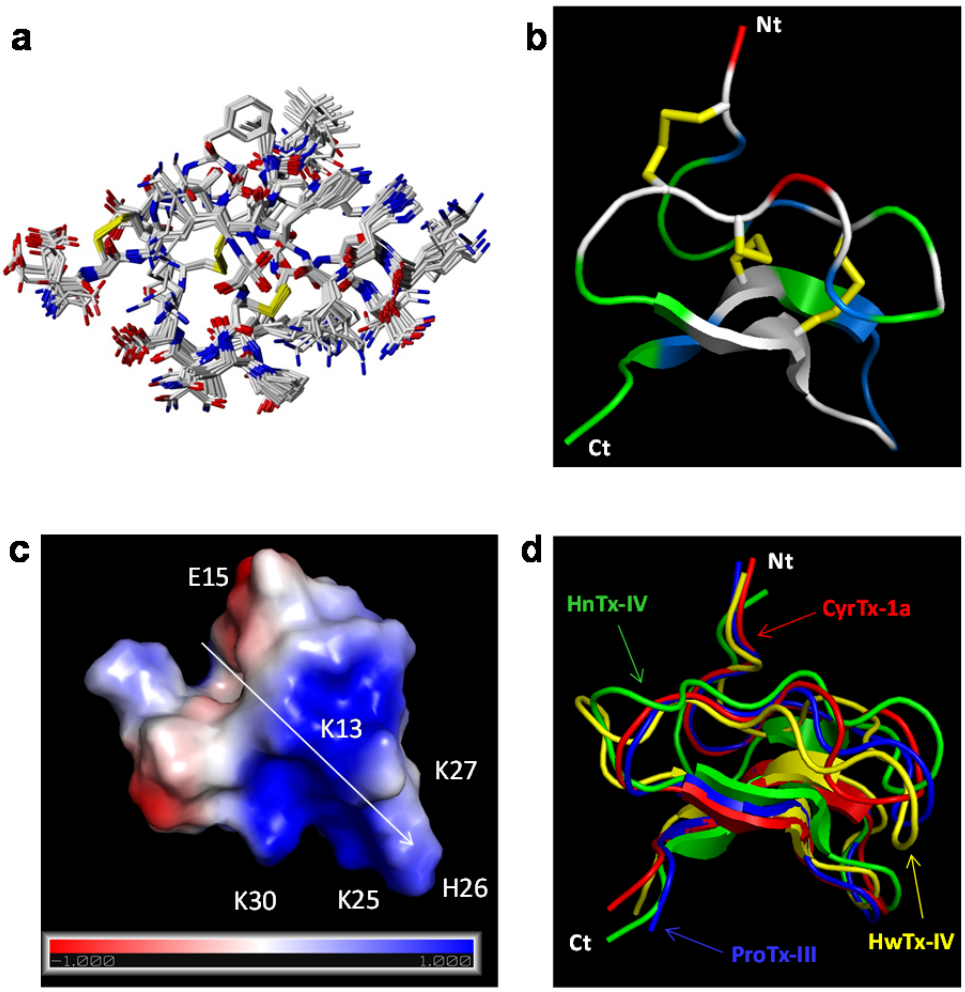

Figure 4: Representation of CyrTx-1a identified by PyMOL. (**a**) Superposition of 20 structures derived from a 6-ns restrained MD simulation (all heavy atoms are shown). All backbone atoms of residues 2-31 were used for fitting. Structures were sampled in 300 ps intervals and energy minimized. The rmsd over all backbone atoms (including residues 1-33) is 0.465 Å with a standard deviation of 0.157 Å. Considering all heavy atoms, the rmsd is 1.072 Å with a standard deviation of 0.285 Å (PDB: 6GFT). (**b**) Cartoon representation of the backbone peptide folding of CyrTx-1a determined by 1H 2D NMR method. The structure topology is composed of double stranded antiparallel β-sheet (arrows). The three disulfide bonds are C2–C17, C9–C22 and C16–C29 (in yellow). Hydrophobic residues are colored in green, and basic and acidic residues are colored in blue and red, respectively. The other polar residues are colored in white. (**c**) Electrostatic charged surface representation of CyrTx-1a. The molecule is rendered as a surface colored according to the electrostatic potential. As indicated in the colored legend, an excess of negative and positive charges near the surface are represented in red (-1000) and blue (1000), respectively, while fairly neutral potentials are represented in white. The entire structure has a clear dipole potential with E1 and E15 forming a negative zone while K3, K7, K13, K25, H26, K27 and K30 form a positive zone. (**d**) Superposition of backbone peptide folding of CyrTx-1a and three other toxins of the NaSpTx family 1 previously described to possess analgesic effects (PDB entries of HnTx-IV: 1NIY, ProTx-III: 2MXM and HwTx-IV: 1MB6).

384 *Effects of CyrTx-1a on hNa$_V$1.1-1.8-overexpressing HEK-293 cells and on CHO cells*
385 *overexpressing hCa$_V$1.2 and hK$_V$11.1 channel subtypes*

386 Whole-cell automated patch-clamp (QPatch HTX) experiments performed on HEK-293 cells
387 overexpressing hNa$_V$1.1-1.8 subtypes revealed that 1 µM of synthetic CyrTx-1a was effective to
388 block hNa$_V$1.1-1.2-1.3-1.6-1.7 currents while hNa$_V$1.4-1.5-1.8 currents were unaffected (Figure 5a).
389 The following increasing order for IC_{50} values was obtained from the concentration-response curves

of CyrTx-1a effects on currents flowing through the different subtypes (Figure 5b): $hNa_V1.2$ (75.5 ± 4.3 nM, n = 8) ≈ $hNa_V1.1$ (97.0 ± 6.4 nM, n = 3) ≈ $hNa_V1.6$ (115.0 ± 7.5 nM, n = 5) ≈ $hNa_V1.7$ (129.5 ± 2.1 nM, n = 7) > $hNa_V1.3$ (306.6 ± 15.2 nM, n = 8) >> $hNa_V1.4$ (7.7 ± 0.2 µM, n = 7) for TTX-sensitive (TTX-S) subtypes, and $hNa_V1.5$ = $hNa_V1.8$ (> 10 µM, n = 5-8) for TTX-resistant (TTX-R) subtypes. Additionally, the peptide had very low affinity for cardiac $hCa_V1.2$ and $hK_V11.1$ subtypes overexpressed in Chinese hamster ovary (CHO) cells, since 10 µM of toxin had no effect on currents flowing through these two channel subtypes (n = 2-5) (data not shown).

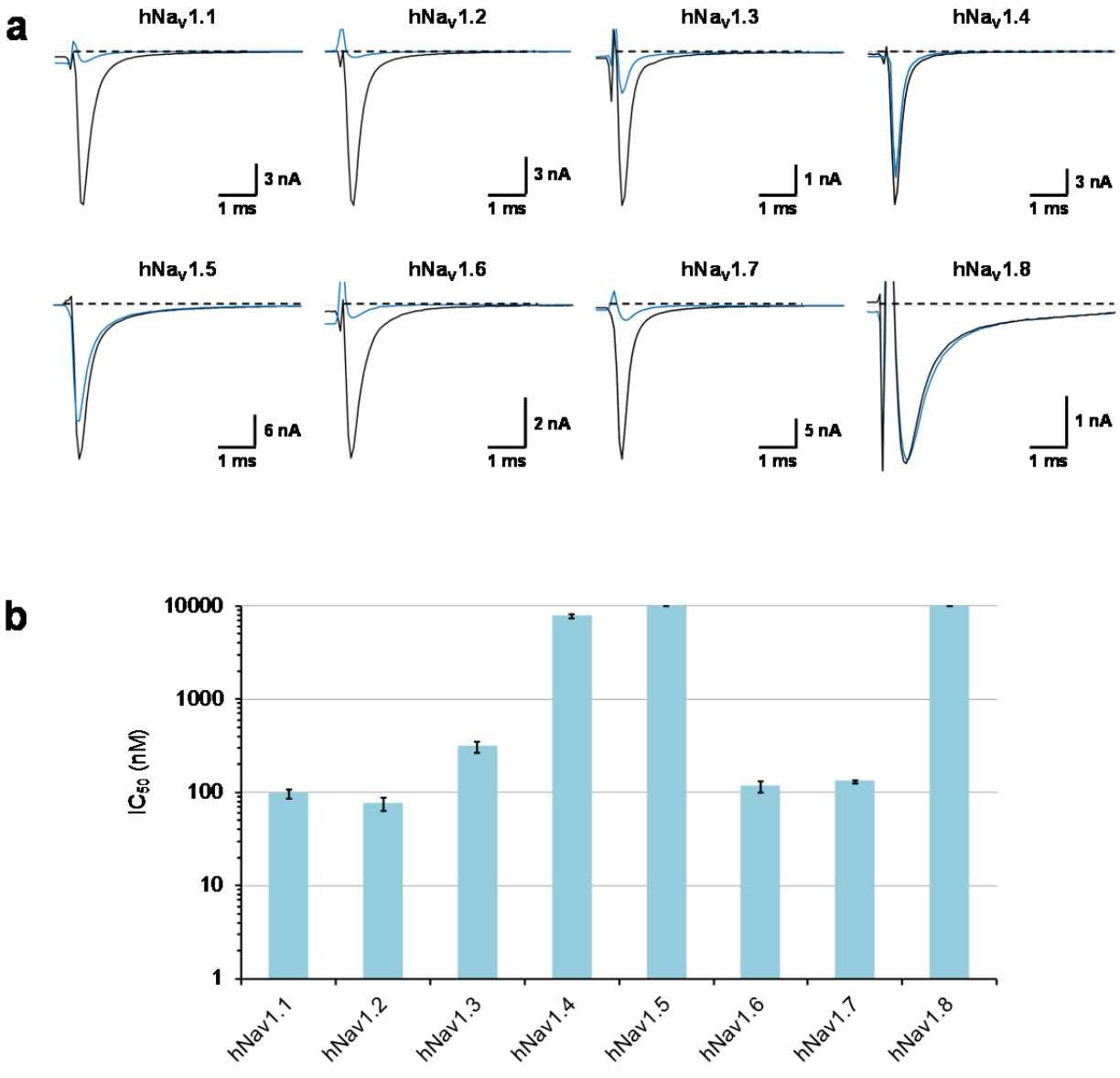

Figure 5: Effects of CyrTx-1a on HEK-293 cells overexpressing $hNa_V1.1$-1.8 channel subtypes, (**a**) Representative traces of sodium currents flowing through $hNa_V1.1$-1.8 channel subtypes, recorded before (in black) and after (in blue) exposure to 1 µM CyrTx-1a. (**b**) Histograms of IC_{50} values obtained from the concentration-response curves of CyrTx-1a effects on HEK-293 cells overexpressing $hNa_V1.1$-1.8 channel subtypes. Each value represents the mean ± S.D. of data obtained from 3-8 cells. Mean value ± S.D. of n_H was 1.1 ± 0.2.

Further investigation, using whole-cell manual patch-clamp, provided IC_{50} values of 59.6 nM from the concentration-response curves of CyrTx-1a effects on currents flowing through $hNa_V1.7$

channels overexpressed in HEK-293 cells (Figure 6b, left panel). This CyrTx-1a-induced blocking action occurred without any change in steady-state inactivation- and conductance-voltage relationships of $hNa_V1.7$ channel subtype (Figure 6c (left panel) and Supporting Information Table S3).

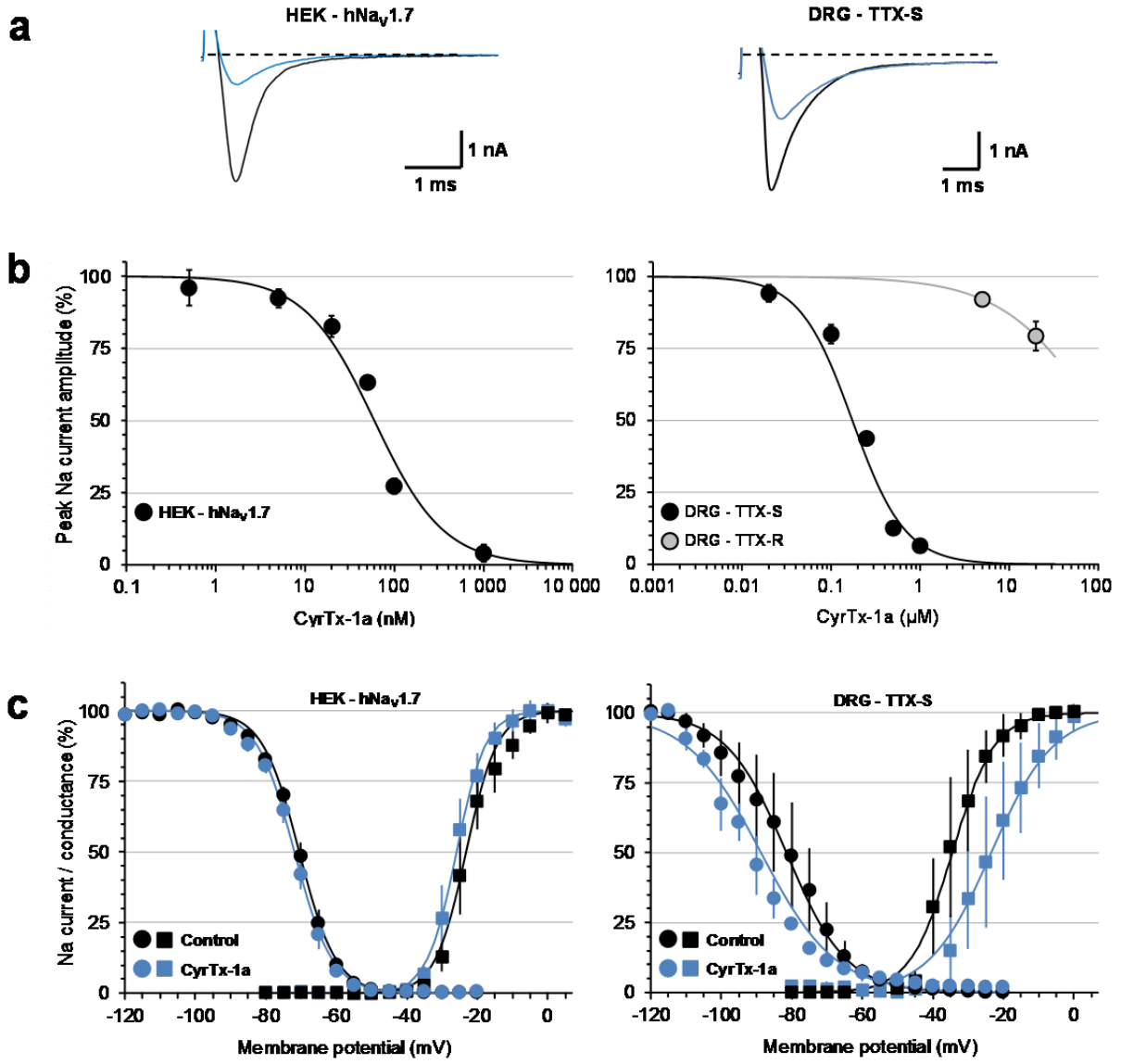

Figure 6: Effects of CyrTx-1a on HEK-293 cells overexpressing $hNa_V1.7$ channel subtype (left panels) and on TTX-S and TTX-R sodium currents of adult mouse DRG neurons (right panels). (**a**) Representative traces of sodium currents flowing through $hNa_V1.7$ channels and of TTX-S sodium currents of DRG neurons, recorded before (in black) and after (in blue) exposure to 100 and 250 nM CyrTx-1a, respectively. (**b**) Concentration-response curves of CyrTx-1a effects on $hNa_V1.7$ channel current and on TTX-S and TTX-R sodium currents of DRG neurons. Each value, expressed as percentage of that obtained before toxin application, represents the mean ± S.D. of data obtained from 2-5 HEK-293 cells and 2-4 DRG neurons. IC_{50} and n_H values were, respectively, 59.6 nM and 1.1 for $hNa_V1.7$ current ($r^2 = 0.976$), 0.17 µM and 1.4 for TTX-S current ($r^2 = 0.965$), and 108 µM and 0.8 for TTX-R current ($r^2 = 1.000$). (**c**) Steady-state inactivation- (circles) and conductance- (squares) voltage relationships for HEK-293 cells overexpressing $hNa_V1.7$ channels and for neurons having TTX-S current, before (black symbols) and after (blue symbols) exposure to50 nM and 0.25-0.5 µM CyrTx-1a, respectively. Each value represents the mean ± S.D. of data obtained from 3-4 HEK-293 cells and 4 DRG neurons, and is expressed as percentage of either maximal peak amplitude of current at strongly negative pre-pulse voltages or maximal conductance calculated at strongly positive test-pulse voltages. The theoretical curves correspond to data point fits with the mean $V_{P50\%}$, k_h, $V_{T50\%}$ and k_g values indicated in Table S3.

Effects of CyrTx-1a and TTX on adult mouse DRG neurons

Before evaluating the effects of CyrTx-1a on the sodium currents of DRG neurons, the sensitivity of these currents to 100 nM TTX was first determined. Under this condition, two types of neurons were recorded. The first type (82%, *i.e.*, 9/11 neurons) had only TTX-S current, which was blocked by the toxin to 3 ± 2% of initial peak amplitude values within 1 min. The effects of CyrTx-1a (from 0.02 to 1 µM) on these neurons were evaluated by expressing the current peak amplitude recorded in the presence of the peptide relatively to its initial value determined after washing-out TTX with a toxin-free solution for 8-10 min. The second type of neurons (18%, *i.e.*, 2/11 neurons) had a mixed TTX-S and TTX-R current, which was decreased by the toxin to around 60% of initial peak amplitude values. The effects of CyrTx-1a (from 5 to 20 µM) on these neurons were evaluated by expressing the current peak amplitude recorded in the presence of the peptide relatively to its initial value determined in the presence of 100 nM TTX.

Exposing neurons to standard physiological solutions containing various CyrTx-1a concentrations, using a fast solution application system, produced a decrease of sodium current amplitude which was dependent on peptide concentration and duration of exposure and on the current sensitivity to TTX. In particular, the concentration-response curves of CyrTx-1a effects on the peak amplitude of TTX-S and TTX-R currents revealed IC_{50} values of 0.17 and 108 µM, respectively (Figure 6b, right panel). The peptide was thus approximately 635 times more efficient to inhibit TTX-S than TTX-R sodium currents of adult mouse DRG neurons. The blocking effects of CyrTx-1a on the peak amplitude of TTX-S current were stationary 5 and 1.5 min after the application of 0.02 and 1 µM of peptide, respectively. Those on the peak amplitude of the TTX-R current were stationary 4 min after the application of 20 µM of peptide. The CyrTx-1a effects on the TTX-R current, not very noticeable, were not further studied, in contrast to those on the TTX-S current.

The peak amplitude of TTX-S current, which was 6 ± 2% of initial values after exposure to 1 µM CyrTx-1a returned to 29 ± 7% of initial values (n = 4) by exposing neurons to a peptide-free solution for 12-14 min, indicating that the effect of CyrTx-1a was at least partially reversible. The analyses of activation and inactivation kinetics of TTX-S sodium current in the absence and in the presence of 0.25 and 0.5 µM CyrTx-1a revealed that the peptide did not affect these kinetics since the time to peak (tp) and the time constant of the current decay (τh) were not significantly modified (Supporting Information Table S4). Similarly, CyrTx-1a (0.25-0.5 µM) did not produce any alteration of steady-state inactivation- and conductance-voltage relationships for neurons exhibiting TTX-S current (Figure 6c, right panel, and Supporting Information Table S3).

Effects of CyrTx-1a on heat and tactile sensitivity of mice in vivo *- Comparison with HwTx-IV*

Hot-plate testing in mice was performed by intraplantar injection of 102 $nmol.kg^{-1}$ of CyrTx-1a or 49 $nmol.kg^{-1}$ of HwTx-IV. Under these conditions, a marked increase in the treated-mouse reaction time to heat, *i.e.*, the latency either to shake one of the two hind limbs or to jump, was observed compared to animals injected with PBS (Figure 7a). In particular, the reaction time was increased by 1.83 times for mice injected with CyrTx-1a (17.2 ± 1.7 s, n = 13) and by 1.64 times for animals

injected with HwTx-IV (15.4 ± 1.9 s, n = 13), *versus* animals injected with PBS (9.4 ± 0.6 s, n = 12), the difference between the two peptide effects being not significant. Similarly, tactile sensitivity testing showed an increase in the force intensity at which the mice, injected with 102 nmol.kg^{-1} of CyrTx-1a or 49 nmol.kg^{-1} of HwTx-IV, removed their hind limb submitted to an increasing fiber pressure, *i.e.*, 8.6 ± 1.1 g (n = 8) and 8.5 ± 1.4 g (n = 8), respectively, compared to animals injected with PBS, *i.e.*, 7.0 ± 1.7 g (n = 19) (Figure 7b). The injection itself was innocuous since no difference in the reaction time or force intensity occurred between mice injected with PBS and non-injected animals (Figure 7).

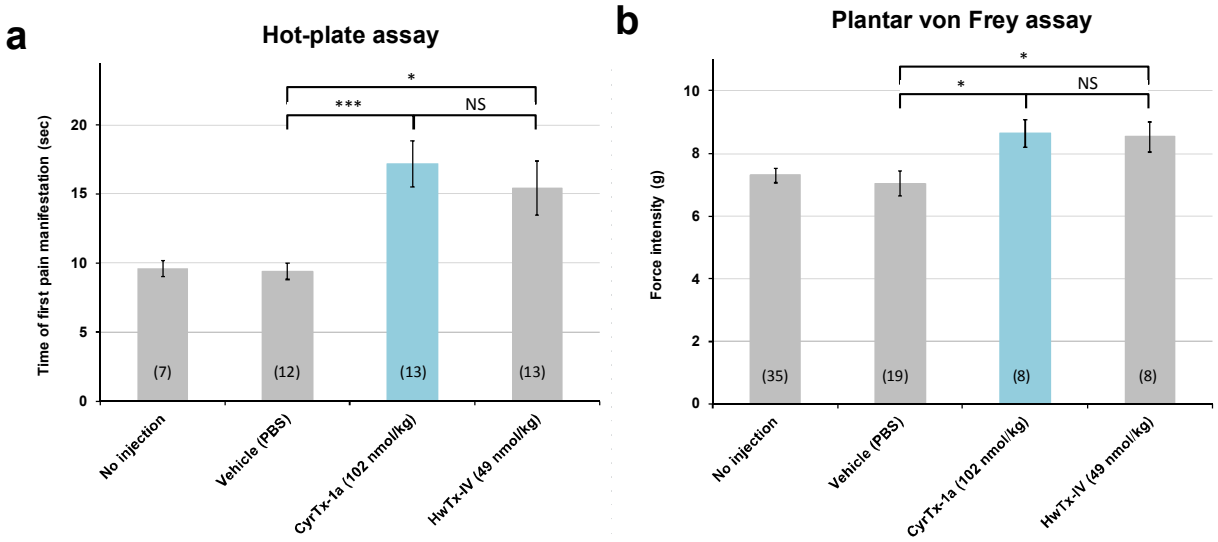

Figure 7: Effects of CyrTx-1a on heat and tactile sensitivity of mice *in vivo*. (**a**) The heat sensitivity of mice was assessed using a hot-plate set at 55.0 ± 0.2°C, by determining the latency for the animals either to shake one of their two hind limbs or to jump. Three groups of mice were tested after intraplantar injection in each hind limb of 5 µL of PBS, CyrTx-1a (*i.e.*, 102 nmol.kg^{-1}) or HwTx-IV (*i.e.*, 49 nmol.kg^{-1}), while another group of animals was tested without any injection. (**b**) The tactile sensitivity of mice was assessed using an automated plantar von Frey apparatus, by determining the force intensity at which the animals removed their hind limb submitted to an increasing fiber pressure. The same mice were tested before (no injection) and 15 min after intraplantar injection in each hind limb of 5 µL of PBS, CyrTx-1a (*i.e.*, 102 nmol.kg^{-1}) or HwTx-IV (*i.e.*, 49 nmol.kg^{-1}). (**a**) and (**b**) Means ± S.D. of data obtained from 7-19 mice under each condition, *i.e.*, before and/or 60 min after injection. *: $0.0113 \leq P \leq 0.0425$ and ***: $P = 0.0005$ *versus* PBS. NS: non-significant between CyrTx-1a and HwTx-IV.

Effects of CyrTx-1a, compared to HwTx-IV, on the mouse neuromuscular system in vivo

Online recordings revealed that the major effect of i.m. injections of PBS solutions containing various concentrations of either CyrTx-1a (from 0.3 to 448.7 nmol.kg^{-1} mouse) or HwTx-IV (from 4.1 pmol.kg^{-1} to 41.4 nmol.kg^{-1} mouse) to anaesthetized mice was a marked decrease of CMAP amplitude. This is exemplified in Figure 8a for CMAP recordings performed before and between 10 and 15 min after injections of 29.4 nmol CyrTx-1a and 41.4 nmol HwTx-IV per kg of mouse. The maximal CMAP amplitude measured 30 min after injections of PBS solution alone, and compared to values before injections, was not significantly affected, *i.e.*, 97.8 ± 2.3% (n = 8 mice), indicating that injections of the toxin vehicle had no effect on the maximal CMAP amplitude and that no marked run-down of the response occurred.

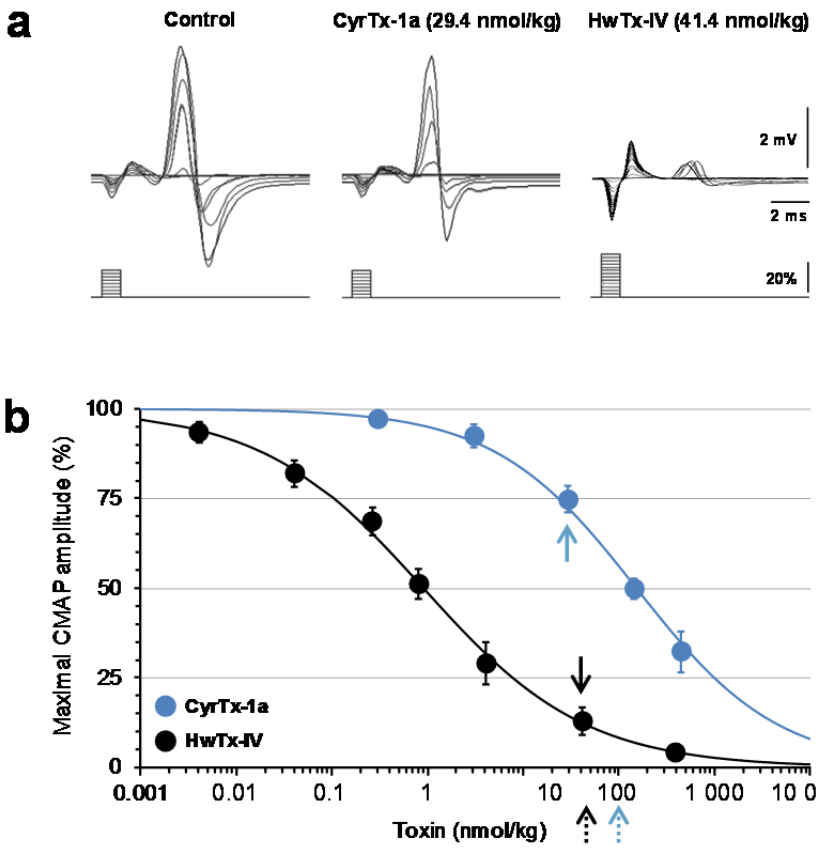

Figure 8: Effects of CyrTx-1a and HwTx-IV on the CMAP recorded *in vivo* from mouse tail muscle in response to caudal motor nerve stimulation. (**a**) Superimposed traces of CMAP following increasing intensities of stimulation (scheme), before (control) and after CyrTx-1a (29.4 nmol.kg^{-1} mouse, full blue arrow in (**b**)) or HwTx-IV (41.4 nmol.kg^{-1} mouse, full black arrow in (**b**)) injection. (**b**) Concentration-response curves of the effects of CyrTx-1a (blue circles) and HwTx-IV (black circles) on the maximal CMAP amplitude. Each value, expressed as percentage of that obtained before injection, represents the mean ± S.D. of data obtained from 4-5 mice. IC_{50} and n_H values were, respectively, 152.3 nmol.kg^{-1} mouse and 0.6 for CyrTx-1a (r^2 = 0.992) and 0.9 nmol.kg^{-1} mouse and 0.5 for HwTx-IV (r^2 = 0.998). The dashed arrows indicate the toxin concentrations used for hot-plate and von Frey assays.

The toxin blocking effect was quantified by establishing the concentration-response curves and determining the IC_{50} values. As shown in Figure 8b, the concentration-response curves for CyrTx-1a and HwTx-IV revealed IC_{50} values of 152.3 and 0.9 nmol.kg^{-1} mouse, respectively. The five different excitability tests (stimulus-response, strength-duration and current-threshold relationships, as well as threshold electrotonus and recovery cycle) were performed together before and 30 min after i.m. injections of PBS solution containing CyrTx-1a (448.7 nmol.kg^{-1} mouse) and the derived neuromuscular excitability parameters were determined (Supporting Information Figure S2 and Table S5). With the exception of decreased maximal CMAP amplitude and increased stimulus intensity required to generate a 50% maximal amplitude CMAP (stimulus-response relationship), analysis of strength-duration relationship, threshold electrotonus, current-threshold relationship, and recovery cycle did not reveal other CyrTx-1a effects. The CyrTx-1a-induced effects were completely reversed within 12 hrs after peptide injections.

In vivo *toxicity of CyrTx-1a, compared to HwTx-IV, in mice*

No death of animals occurred following intraplantar injection of 102 nmol CyrTx-1a and 49 nmol

HwTx-IV per kg of mouse. In contrast, i.m. injection of 144.4 nmol CyrTx-1a per kg of mouse (a concentration which produced an inhibition of ~50% of maximal CMAP amplitude), at the tail base, caused death of 50% (2/4) of animals within one hour. By comparison, a similar *in vivo* toxicity was observed following injection of an approximatively 3.5 times lower HwTx-IV concentration, *i.e.*, 41.4 $nmol.kg^{-1}$. These results strongly suggest a lower *in vivo* toxicity of CyrTx-1a, compared to HwTx-IV, following i.m. injections of toxins at the base of mouse tail, suggesting that CyrTx-1a may possess an interesting therapeutic potential for pain treatment at non-toxic doses.

Discussion and Conclusion

This study was undertaken to identify a peptide with antinociceptive properties, among the Smartox venom collection. The strategy consisted of (1) a high throughput screening of 117 different venoms using automated patch-clamp platforms on cells overexpressing the antinociceptive target $hNa_V1.7$ and the cardiac $hNa_v1.5$ subtypes, (2) the isolation and identification of a new peptide, CyrTx-1a, from the *Cyriopagopus schioedtei* venom, (3) its structure characterization and chemical synthesis, and (4) the evaluation of the synthetic peptide functional properties using multiscale (from individual cell to *in vivo*) approaches.

With the identification of a large number of hits from our primary screening campaigns, a triage was performed based on potency, in both tonic and use-dependent current inhibition protocols. The use of venoms from different species (snakes, spiders, scorpions, wasps, bees, amphibians, lizards and fishes) provided interesting information with regard to the target on which these libraries were screened on. The most striking observation was that spider venoms contain by far the greatest number of compounds active on $hNa_V1.7$ with a hit rate (for the primary screening) that was 7-times higher than scorpion venoms and up to 40-fold higher than snake venoms. These data point to the impressive specialization of spider venoms for targeting Na_V channels. Based on this screening procedure, we focused our attention on CyrTx-1a which was identified in the screening and highlighted for progression in our flowchart for deeper *in vitro* and *in vivo* investigation.

The isolation of CyrTx-1a followed a two-step purification procedure using a double *in vitro*-guided assay (block of $hNa_v1.7$ and inactivity on the cardiac safety-compromising $hNa_v1.5$). Once the activity of the purified compound was confirmed by patch-clamp, the toxin entered the phase of sequence deconvolution. Any doubts on Leu or Ile residues were solved by Edman sequencing. The peptide was then synthesized and properly folded according to mass determination and coelution properties, a *sine qua non* condition for *in vitro* characterization and *in vivo* evaluation.

Despite a high sequence identity with HnTx-I (82%), CyrTx-1a shares more pharmacological properties with less similar toxins, such as HwTx-IV (42% identity) and GpTx-1 (45% identity). This is likely mainly due to the presence of Asn^{23} instead of Ser^{23} in the HnTx-I sequence that excludes any $Na_V1.7$ activity (Klint *et al.*, 2015), while a high potency for $Na_V1.7$ associated with a good selectivity against $Na_V1.5$ and $Na_V1.4$ is due to the conservation of highly functional residues (Xiao *et al.*, 2008; Murray *et al.*, 2015). Indeed, CyrTx-1a possesses several highly conserved and

crucial amino-acids, known to govern the Nav activity, such as the Phe^{5}, Pro^{11}, Leu^{20}, Ser^{23}, His^{26}, and more importantly the Trp^{28} and Lys^{30} residues (Minassian *et al.*, 2013; Murray *et al.*, 2016; Shcherbatko *et al.*, 2016). In addition, its sequence includes a hydrophobic patch (Gly^{4}, Gly^{6}, Val^{31}) that has been described to reinforce the inhibitory potency of ICK toxins at $Na_V1.7$ channels (Agwa *et al.*, 2017). Due to these similarities, CyrTx-1a may share the same binding site on TTX-sensitive Na_V channels as the one determined by mutational analysis and *in silico* docking for HnTx-IV, HwTx-IV and GpTx-1a (Cai *et al.*, 2015; Minassian *et al.*, 2013; Murray *et al.*, 2016). Indeed, positively-charged amino acids Lys^{25}, His^{26}, Lys^{27}, Lys^{30}, surrounded by hydrophobic Phe^{5} and Trp^{28} clustered on one toxin face may be involved in interactions with negatively charged Glu^{753}, Glu^{811}, Asp^{816} and Glu^{818} or aliphatic residues (Met^{750}) located in S1-S2 and S3-S4 loops of DII domain of TTX-sensitive Na_V channels (Klint *et al.*, 2014; Li *et al.*, 2004; Liu *et al.*, 2012; Xiao *et al.*, 2008; Xiao *et al.*, 2010).

The first step to evaluate CyrTx-1a functional properties was to study the effects of the synthetic peptide on cells overexpressing $hNa_V1.1$-1.8 subtypes, using patch-clamp techniques. This study allowed (1) to test whether the potent blocking effect of the synthetic peptide, compared to the native molecule, was conserved on $hNa_V1.7$, (2) to reinforce the evaluation of its selectivity profile on the various Na_V channel subtypes.

Synthetic (1 µM) and native (0.57 µM) CyrTx-1a produced 89.1 ± 4.1% (n = 7) and 98.8 ± 0.7% (n = 3) inhibition of $hNa_V1.7$, respectively, indicating that the two peptides were similarly and highly potent to interact with this subtype. The mean IC_{50} values of CyrTx-1a interaction with $hNa_V1.7$, obtained from automated and manual patch-clamp experiments, were 129.5 and 59.6 nM, respectively. From this point of view and compared to toxins belonging to the NaSpTx family 1 such as HnTx-I, HnTx-III, Hd1a, HnTx-IV, ProTx-III, Cm1a, GpTx-1 and HwTx-IV previously reported to interact with this subtype, CyrTx-1a is thus among the most efficient peptides (Cardoso *et al.*, 2015; Klint *et al.*, 2014; Klint *et al.*, 2015; Liu *et al.*, 2012; Liu *et al.*, 2013; Murray *et al.*, 2015; Murray *et al.*, 2016; Shcherbatko *et al.*, 2016; Xiao *et al.*, 2008). In addition to $hNa_V1.7$, CyrTx-1a was also shown to be highly potent to block the TTX-S $hNa_V1.1$, 1.2, 1.3 and 1.6 subtypes with the following increasing order for mean IC_{50} values (between approximately 75 and 300 nM): $hNa_V1.2 \approx hNa_V1.1 \approx hNa_V1.6 \approx hNa_V1.7 > hNa_V1.3$. The recent discovery that $Na_V1.1$ and 1.3 subtypes are involved in pain pathways (Cardoso *et al.*, 2017b; Chen *et al.*, 2014; Osteen *et al.*, 2016) and that the $Na_V1.2$ subtype is only located in the central nervous system (de Lera Ruiz *et al.*, 2015) does not impair further development of CyrTx-1a as a potential antinociceptive agent to access only peripheral Na_V channel subtypes. Moreover, the native and synthetic peptides have at best micromolar affinities for $hNa_V1.5$, $hCa_V1.2$ and $hK_V11.1$ subtypes, well-known targets in cardiac safety (Crumb *et al.*, 2016). However, although fully sparing the skeletal muscle $hNa_V1.4$ subtype, the fact that CyrTx-1a also targets the peripheral nerve $hNa_V1.6$ subtype may represent a limitation for its *in vivo* efficacy and will require the development of analogues with improved selectivity.

The second step to evaluate CyrTx-1a's functional properties was to study the peptide effects on TTX-S and TTX-R sodium currents of adult mouse DRG neurons, including mainly the TTX-S

$Na_V1.1$, 1.6 and 1.7 subtypes and the TTX-R $Na_V1.8$ and 1.9 subtypes (Rush *et al.*, 2007). This study was motivated by the well-known physiological importance of DRG neurons in pain signalling. As expected, the preferential blocking effect of TTX-S Na_V channel subtypes by CyrTx-1a was confirmed on mouse DRG neurons since the peptide was 635 times more efficient to inhibit the peak amplitude of TTX-S than TTX-R sodium currents recorded from these neurons. These results are consistent with previous observations on adult rodent DRG neurons showing that other potential antinociceptive toxins, such as HnTx-IV, GpTx-1 and HwTx-IV, inhibit TTX-S current without markedly affecting TTX-R current (Liu *et al.*, 2003; Murray *et al.*, 2015; Peng *et al.*, 2002). Most of these peptides, including CyrTx-1a, inhibit $hNa_V1.7$ and/or TTX-S currents without any significant modification of activation and inactivation kinetics and/or voltage-dependence.

The third step to evaluate CyrTx-1a functional properties, and to go deeper in the antinociceptive appraisal of the peptide, was to study its effects on heat and tactile sensitivity of mice *in vivo*. Following intraplantar injections, the peptide (102 $nmol.kg^{-1}$) was as efficient as HwTx-IV (49 $nmol.kg^{-1}$) to increase both the time to first pain manifestation of animals to nociceptive heat and the force intensity at which the animals removed their hind limb. The fact that CyrTx-1a also targets the $Na_V1.6$ subtype with high affinity, a subtype located in motor axons innervating skeletal muscles (Caldwell *et al.*, 2000), could limit the safe use of this peptide as an antinociceptive agent. Experiments were thus also conducted to test CyrTx-1a effects on the mouse neuromuscular system *in vivo*. These effects mainly consisted in a CMAP inhibition, as shown in the present work and previously reported for HwTx-IV (Goncalves *et al.*, 2018). These results strongly suggest that the two peptides produce a marked decrease of the density of functional "transient" Na_V channels. Besides these effects, CyrTx-1a, as HwTx-IV (Goncalves *et al.*, 2018), did not modify other excitability parameters, indicating that the peptide does not affect the density of other functional ion channels, receptors and pumps, nor the passive membrane properties of the neuromuscular system (Kiernan *et al.*, 2000; Krishnan *et al.*, 2008). CyrTx-1a was approximately 170 times less efficient than HwTx-IV to inhibit CMAP. Assuming that both toxins have also similar affinity on the mouse $Na_V1.6$ subtype, we infer that the accessibility to this subtype, located mainly at the nodes of Ranvier of motor myelinated axons (Caldwell *et al.*, 2000), is somehow more limited for CyrTx-1a than for HwTx-IV. The pharmacokinetic properties of CyrTx-1a should therefore be favorable for its further development as an antinociceptive compound.

In conclusion, the present results highlight that CyrTx-1a, the first toxin purified from *Cyriopagopus schioedtei* spider venom, is an attractive compound for the development of an antinociceptive agent. Further pharmacokinetics and Structure-Activity Relationships (SAR) studies will be necessary to improve the Na_V profile selectivity of CyrTx-1a. In particular, it is likely that synthetic modified homologues, associated with Molecular Dynamics simulation using CyrTx-1a and Na_V channels, will reinforce the potential use of the peptide as a lead molecule for the development of novel pain therapeutics.

ASSOCIATED CONTENT

Supporting information: Tables and additional figures illustrating the fragments sequenced by LC-MS/MS analyses of CyrTx-1a digests, chemical synthesis, refolding and 1H-chemical shifts of CyrTx-1a, detailed *in vitro* and *in vivo* electrophysiological parameters, and a supplementary Experimental Section. This material is available free of charge via the Internet at http://pubs.acs.org.

Accession Codes: PDB code for CyrTx-1a is 6GFT. Authors will release the atomic coordinates and experimental data upon article publication.

References

Agwa AJ, Huang YH, Craik DJ, Henriques ST, Schroeder CI (2017). Lengths of the C-Terminus and Interconnecting Loops Impact Stability of Spider-Derived Gating Modifier Toxins. Toxins 9**:** 248-263.

Bennett DL, Woods CG (2014). Painful and painless channelopathies. Lancet Neurol. 13**:** 587-599.

Cai T, Luo J, Meng E, Ding J, Liang S, Wang S, *et al.* (2015). Mapping the interaction site for the tarantula toxin hainantoxin-IV (beta-TRTX-Hn2a) in the voltage sensor module of domain II of voltage-gated sodium channels. Peptides 68**:** 148-156.

Caldwell JH, Schaller KL, Lasher RS, Peles E, Levinson SR (2000). Sodium channel Na(v)1.6 is localized at nodes of ranvier, dendrites, and synapses. Proc. Natl. Acad. Sci. U S A 97**:** 5616-5620.

Cardoso FC, Dekan Z, Rosengren KJ, Erickson A, Vetter I, Deuis JR, *et al.* (2015). Identification and Characterization of ProTx-III [mu-TRTX-Tp1a], a New Voltage-Gated Sodium Channel Inhibitor from Venom of the Tarantula Thrixopelma pruriens. Mol. Pharmacol. 88**:** 291-303.

Cardoso FC, Dekan Z, Smith JJ, Deuis JR, Vetter I, Herzig V, *et al.* (2017a). Modulatory features of the novel spider toxin mu-TRTX-Df1a isolated from the venom of the spider Davus fasciatus. Br. J. Pharmacol. 174**:** 2528-2544.

Cardoso FC, Lewis RJ (2017b). Sodium channels and pain: from toxins to therapies. Br. J. Pharmacol.

Cerles O, Benoit E, Chereau C, Chouzenoux S, Morin F, Guillaumot MA, *et al.* (2017). Niclosamide Inhibits Oxaliplatin Neurotoxicity while Improving Colorectal Cancer Therapeutic Response. Mol. Cancer Ther. 16**:** 300-311.

Chen HP, Zhou W, Kang LM, Yan H, Zhang L, Xu BH, *et al.* (2014). Intrathecal miR-96 inhibits Nav1.3 expression and alleviates neuropathic pain in rat following chronic construction injury. Neurochem. Res. 39**:** 76-83.

Crumb WJ, Jr., Vicente J, Johannesen L, Strauss DG (2016). An evaluation of 30 clinical drugs against the comprehensive in vitro proarrhythmia assay (CiPA) proposed ion channel panel. J. Pharmacol. Toxicol. Methods 81**:** 251-262.

de Lera Ruiz M, Kraus RL (2015). Voltage-Gated Sodium Channels: Structure, Function, Pharmacology, and Clinical Indications. J. Med. Chem. 58**:** 7093-7118.

Deuis JR, Wingerd JS, Winter Z, Durek T, Dekan Z, Sousa SR, *et al.* (2016). Analgesic Effects of GpTx-1, PF-04856264 and CNV1014802 in a Mouse Model of NaV1.7-Mediated Pain. Toxins 8**:** 78-87.

Dib-Hajj SD, Yang Y, Black JA, Waxman SG (2013). The Na(V)1.7 sodium channel: from molecule to man. Nat. Rev. Neurosci. 14**:** 49-62.

Flinspach M, Xu Q, Piekarz AD, Fellows R, Hagan R, Gibbs A, *et al.* (2017). Insensitivity to pain induced by a potent selective closed-state Nav1.7 inhibitor. Sci. Rep. 7**:** 39662.

Goncalves TC, Boukaiba R, Molgo J, Amar M, Partiseti M, Servent D, *et al.* (2018). Direct evidence for high affinity blockade of NaV1.6 channel subtype by huwentoxin-IV spider peptide, using multiscale functional approaches. Neuropharmacology 133**:** 404-414.

Hagen NA, Cantin L, Constant J, Haller T, Blaise G, Ong-Lam M, *et al.* (2017). Tetrodotoxin for Moderate to Severe Cancer-Related Pain: A Multicentre, Randomized, Double-Blind, Placebo-Controlled, Parallel-Design Trial. Pain Res. Manag. 2017**:** 7212713.

Israel MR, Tay B, Deuis JR, Vetter I (2017). Sodium Channels and Venom Peptide Pharmacology. Adv.

Pharmacol. 79**:** 67-116.

Kiernan MC, Bostock H (2000). Effects of membrane polarization and ischaemia on the excitability properties of human motor axons. Brain 123**:** 2542-2551.

Klint JK, Berecki G, Durek T, Mobli M, Knapp O, King GF*, et al.* (2014). Isolation, synthesis and characterization of omega-TRTX-Cc1a, a novel tarantula venom peptide that selectively targets L-type Cav channels. Biochem. Pharmacol. 89**:** 276-286.

Klint JK, Chin YKY, Mobli M (2015). Rational Engineering Defines a Molecular Switch That Is Essential for Activity of Spider-Venom Peptides against the Analgesics Target Na(V)1.7. Mol. Pharmacol. 88**:** 1002-1010.

Krishnan AV, Lin CSY, Park SB, Kiernan MC (2008). Assessment of nerve excitability in toxic and metabolic neuropathies. J. Periph. Nerv. Syst. 13**:** 7-26.

Li D, Xiao Y, Xu X, Xiong X, Lu S, Liu Z*, et al.* (2004). Structure--activity relationships of hainantoxin-IV and structure determination of active and inactive sodium channel blockers. J. Biol. Chem. 279**:** 37734-37740.

Liu Y, Li D, Wu Z, Li J, Nie D, Xiang Y*, et al.* (2012). A positively charged surface patch is important for hainantoxin-IV binding to voltage-gated sodium channels. Journal of peptide science : an official publication of the European Peptide Society 18**:** 643-649.

Liu Z, Cai T, Zhu Q, Deng M, Li J, Zhou X*, et al.* (2013). Structure and function of hainantoxin-III, a selective antagonist of neuronal tetrodotoxin-sensitive voltage-gated sodium channels isolated from the Chinese bird spider Ornithoctonus hainana. J. Biol. Chem. 288**:** 20392-20403.

Liu Z, Dai J, Chen Z, Hu W, Xiao Y, Liang S (2003). Isolation and characterization of hainantoxin-IV, a novel antagonist of tetrodotoxin-sensitive sodium channels from the Chinese bird spider Selenocosmia hainana. Cell Mol. Life Sci. 60**:** 972-978.

Minassian NA, Gibbs A, Shih AY, Liu Y, Neff RA, Sutton SW*, et al.* (2013). Analysis of the structural and molecular basis of voltage-sensitive sodium channel inhibition by the spider toxin huwentoxin-IV (mu-TRTX-Hh2a). J. Biol. Chem. 288**:** 22707-22720.

Moyer BD, Murray JK, Ligutti J, Andrews K, Favreau P, Jordan JB*, et al.* (2018). Pharmacological characterization of potent and selective NaV1.7 inhibitors engineered from Chilobrachys jingzhao tarantula venom peptide JzTx-V. PloS one 13**:** e0196791.

Murray JK, Ligutti J, Liu D, Zou A, Poppe L, Li H*, et al.* (2015). Engineering potent and selective analogues of GpTx-1, a tarantula venom peptide antagonist of the Na(V)1.7 sodium channel. J. Med. Chem. 58**:** 2299-2314.

Murray JK, Long J, Zou A, Ligutti J, Andrews KL, Poppe L*, et al.* (2016). Single Residue Substitutions That Confer Voltage-Gated Sodium Ion Channel Subtype Selectivity in the NaV1.7 Inhibitory Peptide GpTx-1. J. Med. Chem. 59**:** 2704-2717.

Osteen JD, Herzig V, Gilchrist J, Emrick JJ, Zhang C, Wang X*, et al.* (2016). Selective spider toxins reveal a role for the Nav1.1 channel in mechanical pain. Nature 534**:** 494-499.

Peng K, Shu Q, Liu Z, Liang S (2002). Function and solution structure of huwentoxin-IV, a potent neuronal tetrodotoxin (TTX)-sensitive sodium channel antagonist from Chinese bird spider Selenocosmia huwena. J. Biol. Chem. 277**:** 47564-47571.

Rush AM, Cummins TR, Waxman SG (2007). Multiple sodium channels and their roles in electrogenesis within dorsal root ganglion neurons. J. Physiol. 579**:** 1-14.

Saez NJ, Senff S, Jensen JE, Er SY, Herzig V, Rash LD*, et al.* (2010). Spider-venom peptides as therapeutics. Toxins 2**:** 2851-2871.

Shcherbatko A, Rossi A, Foletti D, Zhu G, Bogin O, Galindo Casas M*, et al.* (2016). Engineering Highly Potent and Selective Microproteins against Nav1.7 Sodium Channel for Treatment of Pain. J. Biol. Chem. 291**:** 13974-13986.

Vetter I, Deuis JR, Mueller A, Israel MR, Starobova H, Zhang A*, et al.* (2017). NaV1.7 as a pain target - From gene to pharmacology. Pharmacol. Ther. 172**:** 73-100.

Waxman SG, Zamponi GW (2014). Regulating excitability of peripheral afferents: emerging ion channel targets. Nat. Neurosci. 17**:** 153-163.

Xiao Y, Bingham JP, Zhu W, Moczydlowski E, Liang S, Cummins TR (2008). Tarantula huwentoxin-IV inhibits neuronal sodium channels by binding to receptor site 4 and trapping the domain ii voltage sensor in the closed configuration. J. Biol. Chem. 283**:** 27300-27313.

Xiao Y, Blumenthal K, Jackson JO, 2nd, Liang S, Cummins TR (2010). The tarantula toxins ProTx-II and huwentoxin-IV differentially interact with human Nav1.7 voltage sensors to inhibit channel activation and inactivation. Mol. Pharmacol. 78**:** 1124-1134.

Supporting information for:

Cyriotoxin-1a, the first toxin from *Cyriopagopus schioedtei* spider with antinociceptive properties: from identification to functional characterization

Tânia C. Gonçalves[†,#], Evelyne Benoit[#,‡], Michael Kurz[‖], Laetitia Lucarain[†], Sophie Fontaine[†], Stéphanie Combemale[‡], Lucie Jaquillard[‡], Brigitte Schombert[†], Jean-Marie Chambard[†], Rachid Boukaiba[†], Gerhard Hessler[‖], Andrees Bohme[†], Laurent Bialy[‖], Stéphane Hourcade[!], Rémy Béroud[‡], Michel De Waard[‡,§], Denis Servent[#,]*, Michel Partiseti[†,]*

[†] *Sanofi R & D, Integrated Drug Discovery – High Content Biology, F-94440 Vitry-sur-Seine, France.*
[#] *Service d'Ingénierie Moléculaire des Protéines (SIMOPRO), CEA, Université Paris-Saclay, F-91191 Gif sur Yvette, France.*
[‡] *Institut des Neurosciences Paris-Saclay (Neuro-PSI), UMR CNRS/Université Paris-Sud 9197, Université Paris-Saclay, F-91198 Gif sur Yvette, France.*
[‖] *Sanofi R & D, Integrated Drug Discovery – Synthetic Molecular Design, Frankfurt, Germany.*
[‡] *Smartox Biotechnology, 6 rue des Platanes, 38120 Saint-Egrève, France.*
[!] *Sanofi R & D, Neuroscience Therapeutic Area, Neurodegeneration Research, F-91385 Chilly-Mazarin, France.*
[§] *Institut du Thorax, Inserm UMR 1087 / CNRS UMR 6291, LabEx "Ion Channels, Science & Therapeutics", F-44007 Nantes, France.*

Table S1. Fragments sequenced by LC-MS/MS analyses of the CyrTx-1a digests. Symbol * indicates C-terminal amidation, and all cysteine residues were detected as carbamidomethyl derivates with the addition of 57 Da.

	Sequence	Mass	*m/z*	Relative error
Trypsin digestion	SCVPGK	646.3109	324.1636	2.9 ppm
	HKWCK	757.3694	379.6914	-1.6 ppm
	ECKGFGK	824.3851	413.1994	-1.0 ppm
	SGLTCSNK	865.3964	433.7061	1.5 ppm
	CSGLTCSNK	1025.4270	513.7209	0.3 ppm
	SCVPGKNEC	1049.4270	525.7209	0.3 ppm
	SCVPGKNECC	1209.4576	605.7358	-0.4 ppm
	NECCSGLTCSNK	1428.5432	715.2799	1.4 ppm
	PGK NECCSGLTCSNK	1710.7124	856.3679	5.1 ppm
	SCVPGKNECCSGLTCSNK	2056.8435	1029.4368	7.5 ppm
	SCVPGKNECCSGLTCSNKHK	2321.9973	775.0079	2.0 ppm
Glu-C	ECKGFGKSCVPGKNE	1695.7709	566.2644	0.3 ppm
	CCSGLTCSNKHKWCKVLL*	2249.0691	1125.5420	0.2 ppm

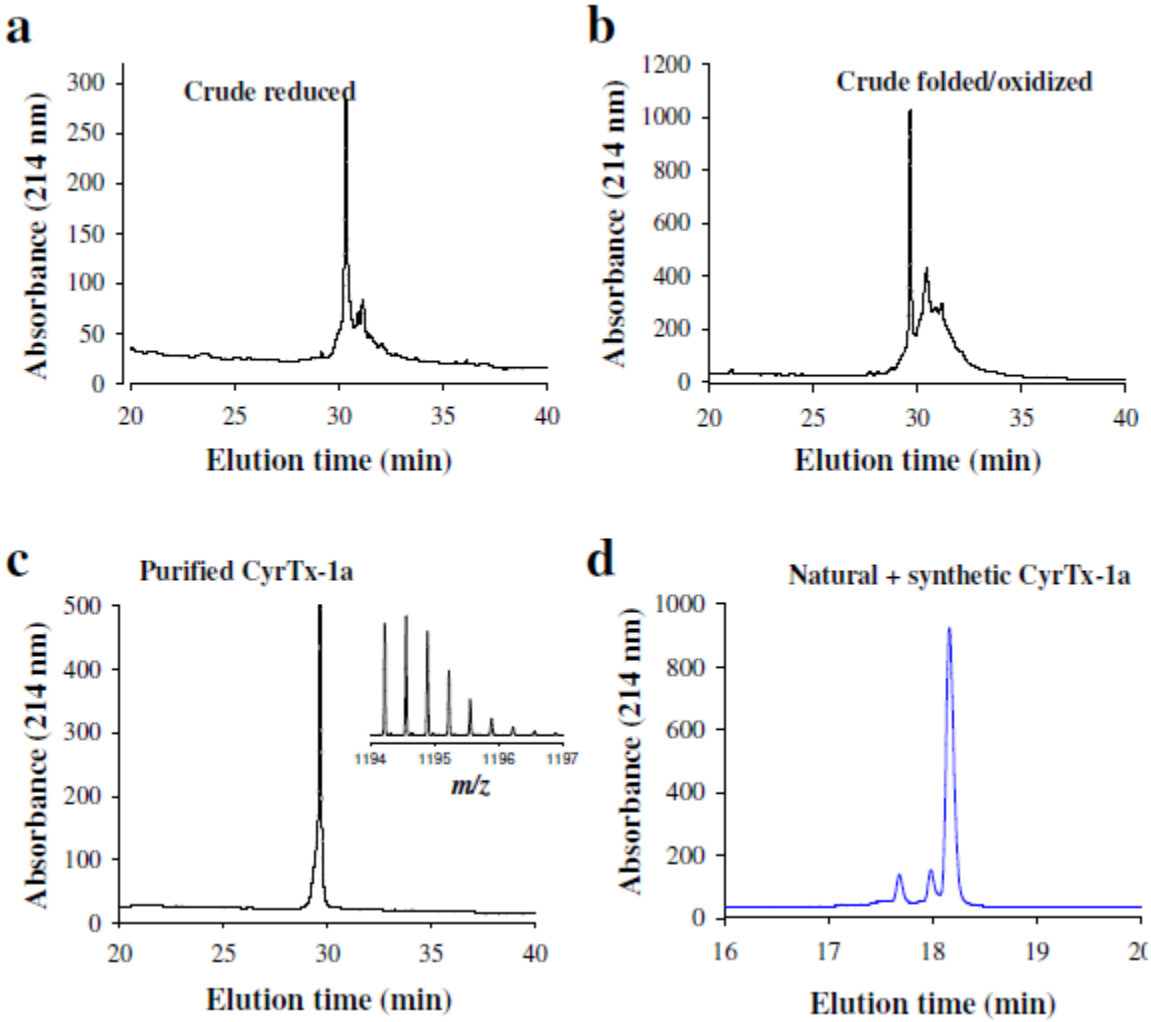

Figure S1. Chemical synthesis and refolding of CyrTx-1a. (**a**) Crude CyrTx-1a synthesis as revealed by a C18 reversed-phase chromatography. (**b**) Crude folded/oxidized CyrTx-1a. (**c**) Purified folded/oxidized CyrTx-1a illustrating the purity of the synthetic compound. Inset: illustrates the MS of synthetic CyrTx-1a of *m/z* 1193.8556 $[M+3H]^{3+}$. (**d**) C18 coelution profile of natural CyrTx-1a (4 µg) mixed with synthetic CyrTx-1a (4 µg). The presence of a single uniform peak demonstrates the identity of both compounds. The two contaminating peaks preceding the major peak represent contaminants from the natural peptide.

Table S2. ^{1}H-chemical shifts of CyrTx-1a in H_2O/D_2O, 50 mM phosphate buffer, pH 5.0 at 305°K (concentration: 6 mg/mL)*.

No.	Residue	NH	Hα	Hβ	Others
1	Glu	-	4.17	2.17	γ: 2.53
2	Cys	8.74	4.89	3.26/2.95	
3	Lys	8.86	4.39	1.82/1.71	γ: 1.60/1.41, δ: 1.78/ 1.50, ε: 2.99
4	Gly	8.05	4.08/3.68		
5	Phe	8.45	3.79	3.07/2.82	δ: 7.10, ε: 7.44, ζ: 7.34
6	Gly	8.78	3.55/2.73		
7	Lys	7.66	4.44	2.05/1.83	γ: 1.48/1.19, δ: 1.62, ε: 3.02/2.96
8	Ser	8.48	4.93	4.01/3.96	
9	Cys	8.17	4.97	3.17/2.95	
10	Val	8.42	4.38	1.79	γ: 0.96, γ': 0.90
11	Pro	-	4.01	2.30/1.93	γ: 2.16/1.74, δ: 4.07/3.77
12	Gly	9.19	4.33/3.78		
13	Lys	7.54	4.50	2.03/1.80	γ: 1.42/1.28, δ: 1.60, ε: 2.98/2.94
14	Asn	8.81	4.72	3.08/2.72	NH_2: 7.60/6.89
15	Glu	9.03	4.28	2.11/2.02	γ: 2.27
16	Cys	8.55	5.18	3.06/2.87	
17	Cys	9.14	4.54	3.46/2.59	
18	Ser	8.26	4.255	3.89/3.86	
19	Gly	8.95	4.40/3.72		
20	Leu	8.19	5.38	2.30/1.31	γ: 1.47, δ: 0.91, δ': 0.87
21	Thr	9.29	4.62	3.98	γ: 1.02
22	Cys	8.83	4.68	3.19/2.98	
23	Ser	8.35	4.49	4.05/3.75	
24	Asn	9.09	4.27	2.79/2.70	NH_2: 7.62/6.98
25	Lys	7.89	4.01	1.51/1.21	γ: 1.07/0.84, δ: 1.51, ε: 2.86
26	His	7.68	4.26	1.52/1.41	δ: 7.16, ε: 8.60
27	Lys	8.19	3.99	2.34/2.02	γ: 1.22, δ: 1.70/1.60, ε: 2.97
28	Trp	6.93	5.59	3.10/2.53	H1: 10.26, H2: 6.89, H4: 7.35, H5: 7.02, H6: 7.01, H7: 7.01
29	Cys	8.58	5.00	3.28/2.69	
30	Lys	9.67	5.02	2.14/1.83	γ: 1.55/1.31, δ: 1.78/1.71, ε: 2.92
31	Val	8.45	4.10	2.09	γ: 1.05, γ': 1.00
32	Leu	8.17	4.32	1.60/1.21	γ: 1.43, δ: 0.91, δ': 0.88
33	Leu	8.28	4.39	1.68/1.58	γ: 1.64, δ: 0.95, δ': 0.89, NH_2: 7.56/7.03

*: Proton chemical shifts are referenced to sodium-3-(Trimethylsilyl)propionate-2,2,3,3-d_4.

Table S3. Parameters of steady-state inactivation- ($V_{P50\%}$ and k_h) and conductance- ($V_{T50\%}$ and k_g) voltage relationships for HEK-293 cells overexpressing the $hNa_V1.7$ channel subtype (means ± S.D. of 3-4 cells) and mouse DRG neurons displaying endogenous TTX-S sodium current (means ± S.D. of 4 neurons).

	$V_{P50\%}$ (mV)	k_h (mV^{-1})	$V_{T50\%}$ (mV)	k_g (mV^{-1})
$hNa_V1.7$ current before CyrTx-1a	-70 ± 1	5.2 ± 0.4	-23 ± 2	4.5 ± 0.7
$hNa_V1.7$ current after CyrTx-1a	-71 ± 1	5.4 ± 0.1	-26 ± 2	4.0 ± 0.6
TTX-S current before CyrTx-1a	-82 ± 7	8.5 ± 0.3	-34 ± 6	3.2 ± 1.0
TTX-S current after CyrTx-1a perfusion[3]	-89 ± 9	10.5 ± 1.3	-24 ± 9	4.6 ± 1.9

[1] 50 nM, [2] 300 nM, and [3] 0.25-0.5 µM.

Table S4. Kinetic parameters of activation (tp) and inactivation (τh) of endogenous TTX-S sodium current recorded from DRG neurons under the indicated conditions (means ± S.D. of 4 cells).

	tp (ms)	**τh** (ms)
TTX-S current after TTX[1] wash-out	1.27 ± 0.21	0.81 ± 0.26
TTX-S current after CyrTx-1a	1.78 ± 0.12[3]	1.49 ± 0.18[4]

[1] 100 nM, [2] 0.25-0.5 µM. [3] $P = 0.056$ and [4] $P = 0.055$ (*versus* current after TTX wash-out).

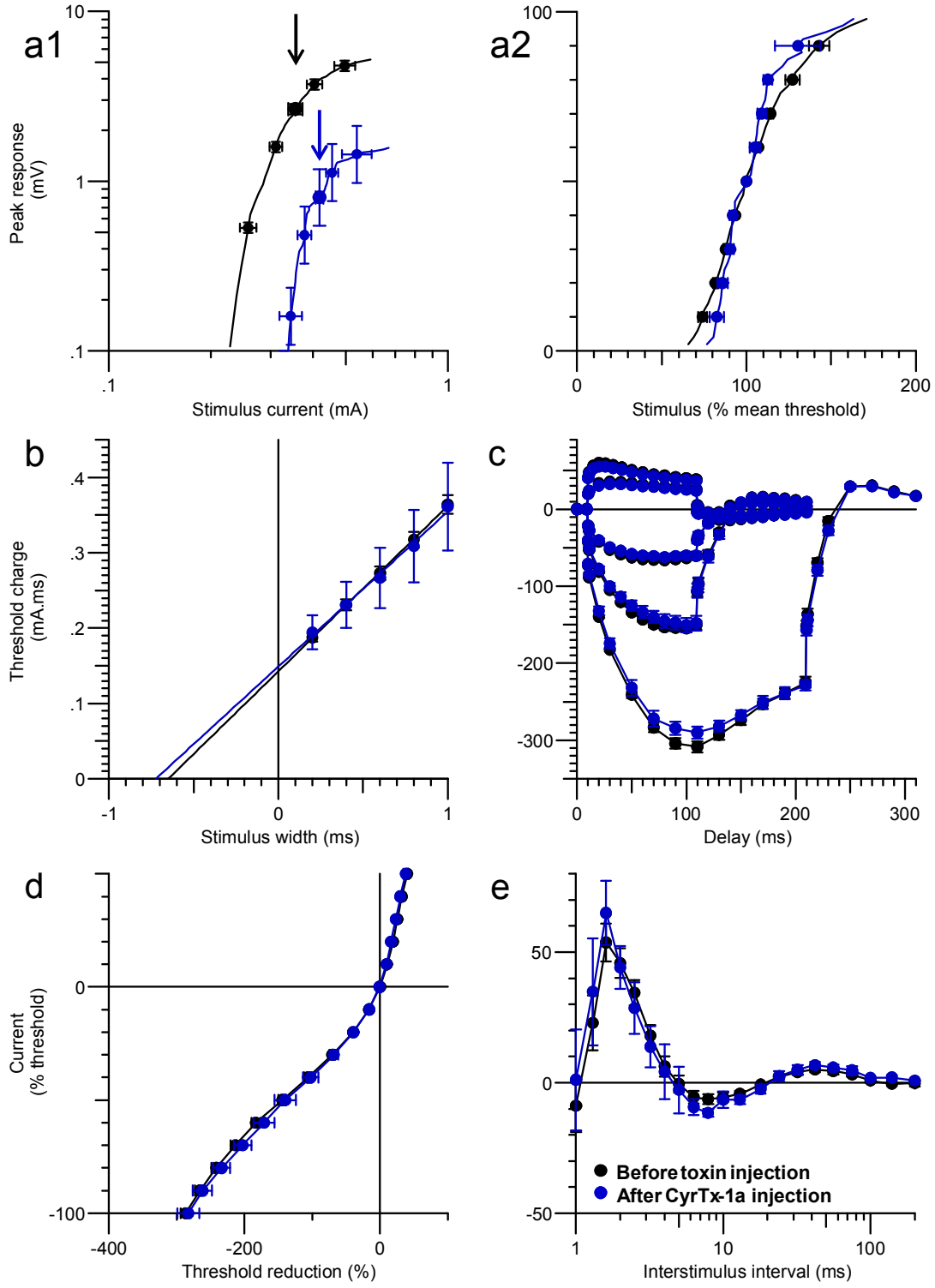

Figure S2. Superimposed excitability curves obtained *in vivo* by stimulating the mouse caudal motor nerve and recording the CMAP from tail muscle before (black circles, n = 29 mice) and ~30 min after injections of CyrTx-1a (448.7 nmol/kg mouse, blue circles, n = 4 mice). Data are represented as means ± S.D. (**a**) stimulus-response relationships [absolute (**a1**) and relative (**a2**) CMAP amplitudes], (**b**) strength-duration relationship, (**c**) threshold electrotonus, (**d**) current-threshold relationship, and (**e**) recovery cycle. In **a1**, arrows indicate stimulus currents for 50% maximal response.

Table S5. Comparison of neuromuscular excitability parameters (means ± S.D.) from mouse tail muscle recordings before toxin injections (control, n = 29 mice) and ~30 min after injections of CyrTx-1a (448.7 nmol/kg mouse, n = 4 mice).

	Excitability parameter[2]	Before toxin Injection	After CyrTx-1a injection
a[1]	Peak response (mV)	5.31 ± 0.57	1.60 ± 0.47**
a	Latency (ms)	3.89 ± 0.06	4.05 ± 0.15
a	Stimulus (mA) for 50% max response	0.35 ± 0.05	0.42 ± 0.03*
a	Stimulus-response slope	3.11 ± 0.18	3.42 ± 0.15
b[1]	Strength-duration time constant (ms)	0.69 ± 0.12	0.88 ± 0.12
b	Rheobase (mA)	0.21 ± 0.04	0.18 ± 0.09
c[1]	TEd (10-20 ms, 40%)	59.53 ± 1.27	54.93 ± 2.57
c	TEd (peak, 40%)	59.00 ± 1.17	54.95 ± 2.33
c	TEd (peak, 20%)	35.81 ± 0.75	32.99 ± 1.61
c	TEd (40-60 ms, 40%)	47.92 ± 1.14	45.25 ± 2.01
c	TEd (90-100 ms, 40%)	39.52 ± 1.27	37.49 ± 1.55
c	Accommodation half-time (ms, 40%)	46.02 ± 0.93	45.66 ± 2.28
c	TEd (undershoot, 40%)	-15.34 ± 1.01	-13.64 ± 1.57
c	TEh (10-20 ms, -40%)	-93.31 ± 1.12	-88.95 ± 4.09
c	TEh (20-40 ms, -40%)	-120.1 ± 1.9	-113.3 ± 5.7
c	TEh (90-100 ms, -40%)	-152.7 ± 5.2	-149.3 ± 9.2
c	TEh (slope 101-140 ms, -40%)	2.62 ± 0.17	2.75 ± 0.25
c	TEh (peak, -70%)	-312.4 ± 6.7	-291.3 ± 16.2
c	TEh (overshoot, -40%)	17.33 ± 1.05	15.89 ± 1.77
d[1]	Resting slope	0.89 ± 0.09	0.88 ± 0.12
d	Minimum slope	0.23 ± 0.01	0.23 ± 0.02
d	Hyperpolarization slope	0.49 ± 0.03	0.44 ± 0.06
e[1]	Refractoriness at 2 ms (%)	45.82 ± 5.60	44.08 ± 8.16
e	Refractoriness at 2.5 ms (%)	34.48 ± 4.78	28.58 ± 9.97
e	Relative refractory period (ms)	4.38 ± 1.09	4.09 ± 1.17
e	Superexcitability (%)	-19.00 ± 3.91	-13.93 ± 4.05
e	Superexcitability at 5 ms (%)	-0.49 ± 3.26	-2.75 ± 8.92
e	Superexcitability at 7 ms (%)	-5.94 ± 2.06	-10.46 ± 2.16
e	Subexcitability (%)	5.60 ± 1.09	6.43 ± 1.15

[1] a: stimulus-response relationship, b: strength-duration relationship, c: threshold electrotonus, d: current-threshold relationship, and e: recovery cycle. [2] TEd: threshold electrotonus from depolarizing currents and TEh: threshold electrotonus from hyperpolarizing currents. Differences (*versus* control), considered to be significant at $P \leq 0.05$ (*: $P = 0.038$, **: $P = 4.3 \times 10^{-5}$), are highlighted in blue.

SUPPLEMENTARY EXPERIMENTAL SECTION

Protocols for amino acid sequencing of CyrTx-1a. A Waters Q-TOF Xevo G2S mass spectrometer equipped with an Acquity UHPLC system and Lockspray source was used for the acquisition of the LC-ESI-MS and LC-ESI-MS/MS data. Five µL of each digested peptide sample was injected into an Acquity UPLC BEH300 C18 column (1.7 µm, 2.1 mm ID × 150 mm L, Waters). Peptide elutions were performed at a flow rate of 0.4 mL/min with a 10-70% gradient of buffers B/A over 10 min (solvent A composition: H_2O/formic acid, 99.9/0.1 (v/v) and solvent B composition: ACN/formic acid, 99.9/0.1 (v/v)). The eluted solution was directly injected into the coupled MS system. Acquisition and analysis of the peptide samples were carried out in the positive mode, within a mass range of *m/z* 100-2,000 using the Agilent MassLynx software version 4.1 (Waters). The mass spectrometer settings for the MS analyses were: capillary voltage, 0.5 kV; cone voltage, 40 V; source temperature, 150°C; desolvation temperature, 600°C; gas flow, 80 L/hr; and gas desolvation, 1000 L/hr. MS data were acquired using a data-dependent acquisition method (DDA) for which MS/MS data were acquired using CID activation mode based on mass and charge state of the candidate ions. For calibration, an external lock mass was used with a separate reference spray (LockSpray) using a solution of leucine enkephalin eluted at a flow rate of 5 µL/min. The calibration was based on the MS detection of m/z 278.1141 and 556.2771 ions at collision energy of 23 eV. The resulting MS/MS spectra data were analysed by *De Novo* sequencing using PEAKS® studio version 5.2 software (Bioinformatics Solutions Inc.) with the following settings: trypsin or V8 protease; carbamidomethyl (C) as a fixed modification and amidation as variable modification; mass accuracy for MS/MS data at 0.05 Da; and mass accuracy for the precursor mass at 20 ppm. Amino acid sequence scores between 50 and 100 were recorded.

Amino acid sequence determination based on Edman degradation was performed using an Applied Biosystems gas-phase sequencer model 492 (s/n: 9510287J). Phenylthiohydantoin amino acid derivatives generated at each sequence cycle were identified and quantitated on-line with an Applied Biosystems Model 140C HPLC system using the data analysis system for protein sequencing from Applied Biosystems (software Procise PC v2.1). The PTH-amino acid standard kit (Perkin-Elmer P/N 4340968) was used and reconstituted according to the manufacturer's instructions. The procedures and reagents used were those recommended by the manufacturer. Chromatography was used to identify and quantify the derivatized amino acid removed at each sequence cycle. Retention times and integration values of peaks were compared to the chromatographic profile obtained for a standard mixture of derivatized amino acids.

Protocols for cell line culture. HEK-293 cells heterologously overexpressing the $hNa_V1.7$ channel subtype were cultured in suspension in FreestyleTM293 (Gibco). Those overexpressing $hNa_V1.6$ and $hNa_V1.8$ subtypes were cultured in Dulbecco's modified Eagle's medium (DMEM)/F12 Glutamax (Gibco), while those overexpressing $hNa_V1.3$ and $hNa_V1.4$ subtypes were cultured in MEM (Sigma, M5650). The complete media contain 10% FBS (Gibco) and selected antibiotics and

additives as recommended by the manufacturer. In-house HEK-Flip-In-T-REx cells were kept in culture under standard conditions (37°C, air supplemented with 5% CO_2) in DMEM (Invitrogen) supplemented with 10% fetal calf serum (Invitrogen), 50 µg/mL hygromycin (Invitrogen), and 15 µg/mL blasticidin (Invivogen). Cells were sub-cultured every 3 to 4 days using accutase® (Sigma) or TrypLE Select (Gibco) as enzymatic dissociation to detach the cells. At least 12 to 24 h prior to assays, doxycycline (BD Biosciences) was added to induce target expression when needed.

CHO cells heterologously overexpressing $hCa_V1.2/\beta2/\alpha2\delta1$ channel subtype (ChanTest, Cleveland, OH, USA) were cultured in Ham's F12 nutrient mix with GlutaMAX™ medium (Gibco). Those overexpressing the $hK_V11.1$ channel subtype (B'SYS GmbH, Switzerland), encoded by the human *ether-a-go-go*-related gene (hERG), were cultured in DMEM/F12 nutrient mixture Ham's medium (Sigma). All culture media contained fetal bovine serum (10% v/v) and selected antibiotics and additives, as recommended by the manufacturer. Cells were grown in flasks, in a humidified 5% CO_2 incubator at 37°C, and subcultured/passaged every 3-4 days using TrypLE Select enzyme (Gibco).

Automated patch-clamp recordings. For primary screening, planar assay electrophysiology recordings were made on an IonWorks Quattro® system (Molecular Devices, Sunnyvale, CA, USA) enabling population patch-clamp (PPC) measurement. HEK-293 cell suspensions were prepared as described in a previous article using similar technology.{Chambard, 2014 #240} For electrophysiological recordings, cells were resuspended in 5 mL pre-filtered external buffer containing (in mM): 137 NaCl, 4 KCl, 1 $MgCl_2$, 1.8 $CaCl_2$, 10 HEPES, 5 glucose (osmolarity set at 306 mOsm/L and pH 7.3 adjusted with NaOH). All recordings were made using an internal solution containing (in mM): 100 K-gluconate, 40 KCl, 1 $MgCl_2$, 1 EGTA, 5 glucose and 10 HEPES (osmolarity set at 300 mOsm/L and pH 7.4 adjusted with KOH). Sealing process and access of the perforated patch-clamp configuration were obtained as already described in the literature.{Trivedi, 2008 #237} Cells/wells were clamped using the electronics (E-) head held at -120 mV (with reference to a common "intracellular" ground electrode). Pre-compound currents were recorded, followed by addition of test peptide venoms prepared in external solution complemented with 0.2% bovine serum albumin (BSA; Sigma). Fractions were incubated for 10 min before the post-compound response was recorded. The pre- and post-compound responses were evoked by a voltage train as follows: after a 10-sec period holding at -120 mV, ten pulses, each consisting of a 50 ms step to the voltage of the peak current of the current-voltage relationship for each channel followed by a 300 ms step back to -120 mV, were applied at 10 Hz. The current signal was sampled at 10 kHz. Currents were leak-subtracted based on the estimate of current evoked during the -10 mV step at the start of the voltage pulse protocol. Pre- and post-compound sodium current amplitudes were measured automatically from the leak-subtracted traces by the IonWorks software through averaging a 10 ms current during the initial holding period at -90 mV (baseline current) and subtracting this from the peak of the current response for each of the eight voltage steps. Data shown are calculated for pulse 1 (tonic block) or pulse 10 (use-dependent block). Filters were set to a pre-scan seal resistance of 40 MΩ, pre-scan $hNa_V1.7$ current amplitude of 200 pA, and post-scan

seal resistance of 40 MΩ. Cells that did not meet these criteria were discarded from the measurements. Dividing the post-scan current amplitude by the respective pre-scan current amplitude for each well assessed the degree of inhibition of the $hNa_V1.7$ current.

Secondary screening for hit confirmation, as well as rapid selectivity check, were also performed on an automated patch-clamp system, the QPatch HTX (Sophion Bioscience, Denmark) recording currents in whole-cell configuration, allowing both signal acquisition and data analyses.[3] The day of their use, HEK-293 and CHO cells were transferred into Eppendorf tubes containing a FreeStyle 293 expression medium (Gibco) which were then placed in the automated electrophysiology platform. The extracellular medium composition for hNa_V-overexpressing HEK-293 cells was (in mM): NaCl 154, KCl 4, $CaCl_2$ 2, $MgCl_2$ 1, and HEPES 10 (pH 7.4, adjusted with NaOH), and that of intracellular (*i.e.*, path-clamp pipette) medium: CsF 150, EGTA/CsOH 1/50, HEPES 10, NaCl 10, $MgCl_2$ 1, and $CaCl_2$ 1 (pH 7.4, adjusted with CsOH). The extracellular medium composition for $hCa_V1.2$-overexpressing CHO cells was (in mM): NaCl 145, KCl 4, $CaCl_2$ 10, and HEPES 10 (pH 7.4, adjusted with NaOH), and that of intracellular medium: CsF 27, CsCl 112, EGTA 8.2, HEPES 10, NaCl 2, and MgATP 4 (pH 7.4, adjusted with CsOH). The extracellular medium composition for $hK_V11.1$-overexpressing CHO cells was (in mM): NaCl 145, KCl 4, $CaCl_2$ 2, $MgCl_2$ 1, HEPES 10, and D-glucose 10 (pH 7.4, adjusted with NaOH), and that of intracellular medium: KCl 120, $CaCl_2$ 5.4, EGTA 10, HEPES 10, Mg-ATP 4, and $MgCl_2$ 1.75 (pH 7.4, adjusted with KOH). Venom fractions and sub-fractions, as well as CyrTx-1a, were diluted in the extracellular medium supplemented with bovine serum albumin (0.1%), to give the final concentrations indicated in the text. The times of incubation varied between ~2 and ~7 min to achieve steady-state effects. The experiments were carried out at room temperature (20-22°C). The hNa_V-overexpressing HEK-293 cells were maintained at a holding potential of either -90 mV ($hNa_V1.5$) or -100 mV (other hNa_V channel subtypes). Currents were elicited at a frequency of 0.2 Hz by 20-ms test-pulses to -20 mV ($hNa_V1.1$, 1.2, 1.4, and 1.7), -10 mV ($hNa_V1.3$), -40 mV ($hNa_V1.5$), -15 mV ($hNa_V1.6$) or +10 mV ($hNa_V1.8$), preceded by 200-ms ($hNa_V1.5$) or 40-ms ($hNa_V1.7$) pulses to -120 mV, or not ($hNa_V1.1$, 1.2, 1.3, 1.4 and 1.6). The $hCa_V1.2$-overexpressing CHO cells were maintained at a holding potential of -50 mV, and currents were elicited at a frequency of 0.05 Hz by 200-ms test-pulses to +0 mV. The $hK_V11.1$-overexpressing CHO cells were maintained at a holding potential of -80 mV, and tail currents were elicited at a frequency of 0.07 Hz by 5-sec test-pulses to -50 mV, preceded by 4.8-sec pulses to +20 mV following 20-ms pulses to -50 mV. The leakage current was not compensated for. The concentration-response relationships were established by expressing the peak amplitude of the sum of ten cell currents recorded after 2-7 min in the presence of a given toxin concentration relatively to that of the sum of these currents recorded before toxin incubation.

Manual patch-clamp recordings. A few days before experiments, HEK-293 cells were transferred to 12-mm glass coverslips placed in 35-mm Petri dishes. The day of their use, the culture medium was changed to a standard physiological medium of the following composition (in mM): NaCl 134, KCl 3, $CaCl_2$ 1, $MgCl_2$ 1, D-glucose 10, tetraethylammonium chloride 10, $CdCl_2$ 0.1, and N-2-

hydroxyethylpiperazine-N'-2-ethanesulfonic acid (HEPES) 10 (pH 7.35, adjusted with NaOH), for a minimum of 15 min at 37°C prior to recordings. The day of their use, the DRG neurons plated on coverslips were transferred, for a minimum of 30 min at 37°C prior to recordings, in 35-mm Petri dishes filled with a standard physiological medium similar to that used for HEK-293 cells. The HEK-293 cells or DRG neurons, plated on coverslips, were then transferred in the recording bath filled with the standard physiological medium.

Whole-cell manual patch-clamp experiments were performed by using a MultiClamp 700B integrating patch-clamp amplifier and the pClamp10.6 software (Molecular Devices), as previously described.[4] The patch-clamp pipettes were filled with a medium composed of (in mM): CsCl 90, $CsMeSO_3$ 40, NaCl 10, $MgCl_2$ 2, EGTA 2, Na_2ATP 4, and HEPES 10 (pH 7.32, adjusted with CsOH), and had ~3-MΩ resistance in the standard physiological medium. A fast solution application system allowed changing the solution (standard physiological medium supplemented or not with a given toxin concentration) around the recorded cell or neuron within a few seconds. The experiments were carried out at constant room temperature (22°C).

The cells and neurons were maintained at a holding potential of -60 mV, and currents were elicited at a frequency of 0.5 Hz by 50-ms test-pulses to -20 mV preceded by 1-sec pulses to -120 mV. The concentration-response relationships were established by expressing the peak current amplitude measured in the presence of a given toxin concentration relatively to that before toxin application. Current-voltage relationships were obtained by varying test-pulses from -80 to +10 mV in 5-mV increments, and steady-state inactivation-voltage relationships by changing pre-pulses from -120 to -20 mV in 5-mV increments.

References

[1] Chambard JM, Tagat E, Boudeau P, Partiseti M (2014). Transforming TRP channel drug discovery using medium-throughput electrophysiological assays. J. Biomol. Screen 19: 468-477.

[2] Trivedi S, Dekermendjian K, Julien R, Huang J, Lund PE, Krupp J, Kronqvist R, Larsson O, Bostwick R (2008). Cellular HTS assays for pharmacological characterization of Na(V)1.7 modulators. Assay Drug Dev. Technol. 6: 167-179.

[3] Bell DC, Dallas ML (2017). Using automated patch clamp electrophysiology platforms in pain-related ion channel research: insights from industry and academia. Br. J. Pharmacol. doi: 10.1111/bph.13916.

[4] Goncalves TC, Boukaiba R, Molgo J, Amar M, Partiseti M, Servent D*, et al.* (2018). Direct evidence for high affinity blockade of NaV1.6 channel subtype by huwentoxin-IV spider peptide, using multiscale functional approaches. Neuropharmacology 133**:** 404-414.

2.1.3. Résumé des résultats obtenus

La CyrTx-1a, aussi nommée μ-théraphotoxine-Cs1a, est la première toxine isolée et purifiée à partir du venin de l'araignée *Cyriopagopus schioedtei*, une mygale connue sous le nom de "tigre terrestre malaisienne" qui appartient à la sous-famille des Ornithoctoninae. Ce peptide de 3578,68 Da fait partie de la famille NaSpTx-1, possède 33 acides aminés et se structure autour du motif architectural ICK (pour "inhibitor cystine knot"), très conservé parmi les peptides de cette famille.

D'un point de vue fonctionnel, la CyrTx-1a inhibe les sous-types $hNa_V1.1$-1.3 et 1.6-1.7 à une concentration de l'ordre de la centaine de nanomolaires et les sous-types $hNa_V1.4$ et 1.8 ainsi que les principales cibles moléculaires cardiaques $hNa_V1.5$, $hCa_V1.2$ et $hK_V11.1$ à une concentration supérieure à 10 μM. Il est à souligner qu'à une concentration de 3,3 μM, cette toxine n'affecte pas notablement certains autres sous-types de canaux ioniques également impliqués plus particulièrement dans le potentiel d'action cardiaque ($hCa_V2.2$, 3.1 et 3.2, $hK_V7.1$ et hKir2.1). La CyrTx-1a présente une puissance pour les canaux sodium des neurones de DRG sensibles à la tétrodotoxine (TTX-S) de souris adultes qui est 635 fois plus élevée que celle pour les canaux sodium des neurones de DRG résistants à la tétrodotoxine (TTX-R). Bien que la CyrTx-1a ne possède qu'un faible pourcentage d'identité de séquence (42%) avec la μ-théraphotoxine-Hh2a ou huwentoxine-IV (HwTx-IV), autre toxine de la famille NaSpTx-1, les deux peptides possèdent des profils similaires de sélectivité. Nous avons donc utilisé l'HwTx-IV comme contrôle positif lors des expériences *in vivo*. À des doses équivalentes aux concentrations de peptides inhibant de 50% le courant $hNa_V1.7$ (IC_{50}), les injections locales intramusculaires (i.m.) de CyrTx-1a sont 170 fois moins efficaces que celles d'HwTx-IV pour altérer, *in vivo*, les propriétés d'excitabilité du système neuromusculaire de souris anesthésiées. Les injections de peptides, à des doses relativement élevées, produisent occasionnellement le décès d'animaux et là encore, la CyrTx-1a est environ 3,5 fois moins efficace que l'HwTx-IV. Finalement, les sensibilités à la température et à une stimulation mécanique chez des souris ayant subi des injections intraplantaires de CyrTx-1a (102 nmol par kg de souris) et d'HwTx-IV (49 nmol par kg de souris) ont été évaluées en utilisant, respectivement, les tests de plaque chauffante (55°C) et de von Frey automatisé. Les résultats obtenus montrent que les deux peptides, de façon similaire, diminuent les sensibilités à la température et mécanique des animaux.

Des expériences complémentaires, dont les résultats ne sont pas inclus dans la publication, ont été réalisées récemment afin d'étoffer le profil de sélectivité de la CyrTx-1a en étudiant les effets de 10 μM de ce peptide sur des lignées cellulaires recombinantes exprimant certains sous-typesde canaux calcium et potassium: hCa_V, hK_V et hKir. A cette concentration, la CyrTx-1a n'affecte pas certains sous-types de canaux ioniques impliqués plus particulièrement dans le potentiel d'action

cardiaque (hCa$_V$ 3.1 et 3.2 et hKir2.1), à l'exception du sous-type hK$_V$4.3 qui est inhibé de 95,5 ± 0,7% [IC_{50} = 707 ± 136 nM; coefficient de Hill (n_H) = 1,2 ± 0,2; moyenne ± ES de 4 expériences) et des sous-types hCa$_V$2.2 et hK$_V$7.1 dont les courants sont notablement augmentés en présence du peptide (Figure 2-1).

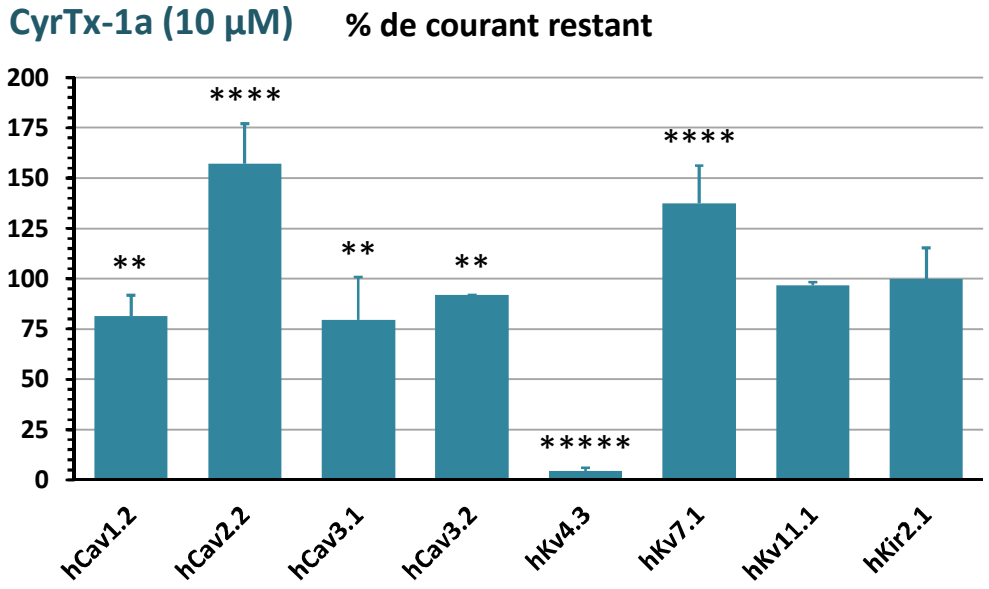

Figure 2-1. Effets de la CyrTx-1a sur les courants hCa$_V$, hK$_V$ et hKir. Pourcentage de courant restant en présence de 10 µM de peptide (moyenne ± ES, n = 4-13) en fonction du sous-type de canal indiqué. **: 0.002 < p < 0.006, ****: 0.00001 < p < 0.00003 et *****: p < 0.000001, *versus* contrôle.

L'effet de la CyrTx-1a sur le sous-type hCa$_V$2.2 exprimé dans les cellules CHO (pour "Chinese hamster ovary") est original puisqu'une augmentation progressive de 19,3 ± 6,2% à 57,1 ± 20,0% du courant se produit en présence de 0,12 µM et 10 µM de peptide, respectivement (moyenne ± ES de 5 à 6 expériences; Figure 2-2A, B et C). Il est à souligner que hCa$_V$2.2 est un sous-type neuronal de Ca$_V$ impliqué dans la douleur et qui est la cible principale du Prialt® (ω-conotoxine-MVIIA provenant du venin du cône *Conus magus*) qui a obtenu l'autorisation de mise sur le marché (AMM) en 2004 pour traiter les douleurs chroniques récalcitrantes par voie intrathécale (Molinski et al., 2009). L'augmentation du courant hCa$_V$2.2 produite par 10 µM de CyrTx-1a est réversible en environ 10 min (Figure 2-2B et C) et est spécifique puisqu'en présence de 10 µM de peptide et de 100 µM de chlorure de cadmium, le courant ne représente plus que 12,4 ± 8,2% du courant contrôle (moyenne ± ES de 5 expériences). En présence de 10 µM de CyrTx-1a, aucune modification notable des cinétiques et des dépendances vis-à-vis du potentiel de membrane de l'activation et de l'inactivation du courant hCa$_V$2.2 n'a été observée (Figure 2-2C et D). Il est donc fortement probable que l'augmentation du courant hCa$_V$2.2 produite par le peptide résulte d'un accroissement du nombre de sous-types exprimés à la membrane et/ou de leur conductance unitaire.

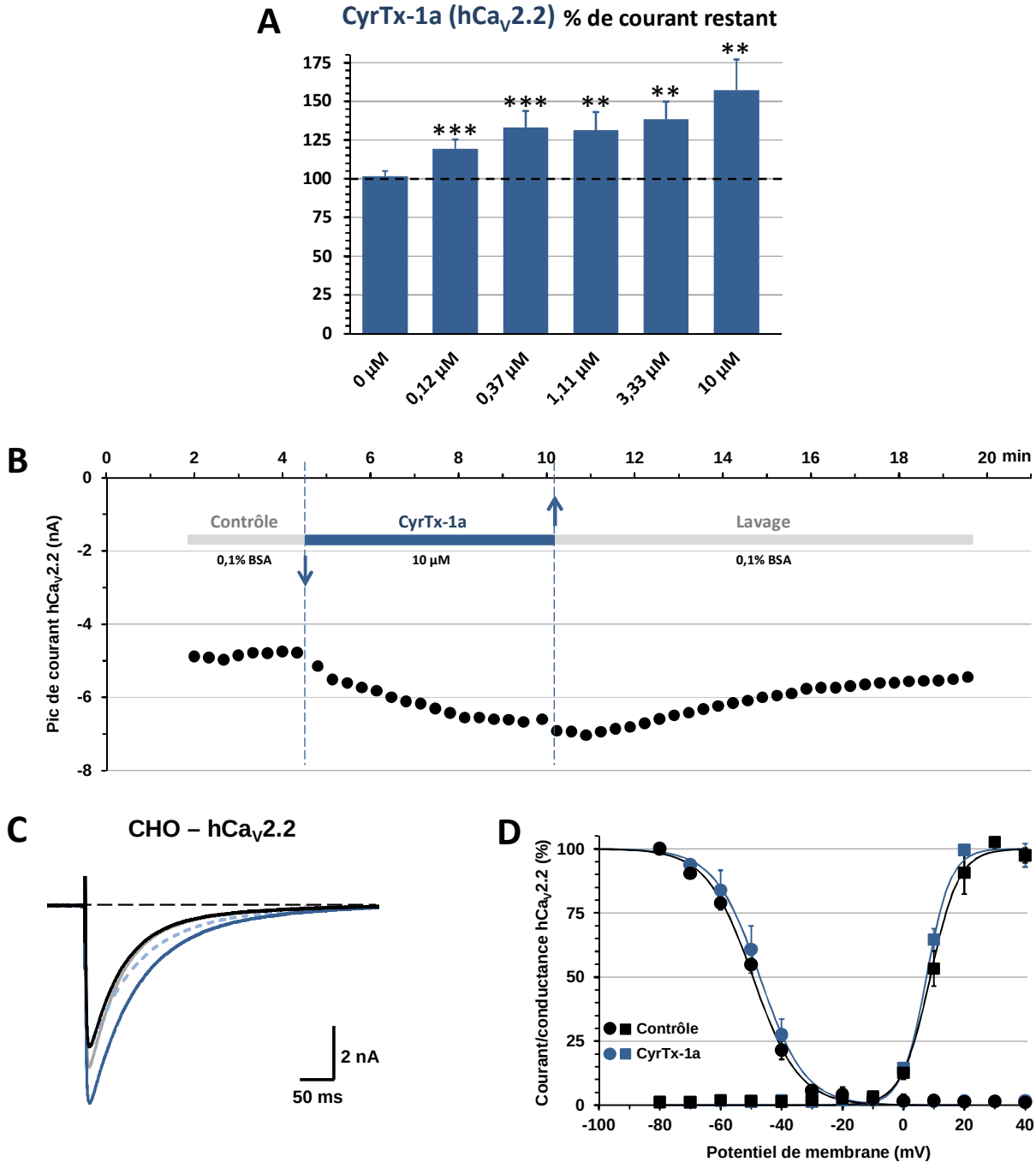

<u>Figure 2-2.</u> Effets de la CyrTx-1a sur le courant hCa$_V$2.2. (**A**) Pourcentage de courant restant (moyenne ± ES, n = 5-6) en fonction de la concentration de peptide. **: 0.001 < p < 0.004 et ***: 0.0006 < p < 0.0007, *versus* contrôle. (**B**) Cinétiques de l'effet de 10 µM de CyrTx-1a et du lavage du peptide sur le pic de courant. (**C**) Traces représentatives du courant avant (en noir) et après soit 10 µM de CyrTx-1a (en bleu) soit le lavage du peptide (en gris). La trace bleue en pointillés représente le courant enregistré en présence du peptide et normalisé par rapport au pic de courant contrôle. (**D**) Courbes d'inactivation stationnaire (cercles) et de conductance (carrés) en fonction du potentiel de membrane, avant (symboles noirs) et après (symboles bleus) exposition des cellules CHO à 10 µM de CyrTx-1a. Chaque valeur représente la moyenne ± ES des données de 3 cellules, exprimée en pourcentage de l'amplitude maximale du courant à des valeurs fortement négatives de pré-potentiel ou de la conductance maximale calculée à des valeurs fortement positives de potentiel-test. Les courbes théoriques correspondent aux ajustements des points de données avec les valeurs moyennes $V_{P50\%}$ = -49,4 ± 0,7 mV, k_h = -7,6 ± 0,6 mV^{-1}, $V_{T50\%}$ = 8,8 ± 2,0 mV et k_g = 4,7 ± 0,3 mV^{-1} (contrôle) et $V_{P50\%}$ = -47,1 ± 0,2 mV, k_h = -7,4 ± 0,5 mV^{-1}, $V_{T50\%}$ = 7,6 ± 0,4 mV et k_g = 4,0 ± 0,3 mV^{-1} (CyrTx-1a).

L'effet de la CyrTx-1a sur le sous-type $hK_V7.1$ exprimé dans les cellules U2OS (pour "human bone osteosarcoma epithelium") consiste également en une augmentation progressive de 6,4 ± 7,8% à 37,4 ± 18,8% du courant en présence de 0,12 µM et 10 µM de peptide, respectivement (moyenne ± ES de 3 à 13 expériences; Figure 2-3A, B et C).

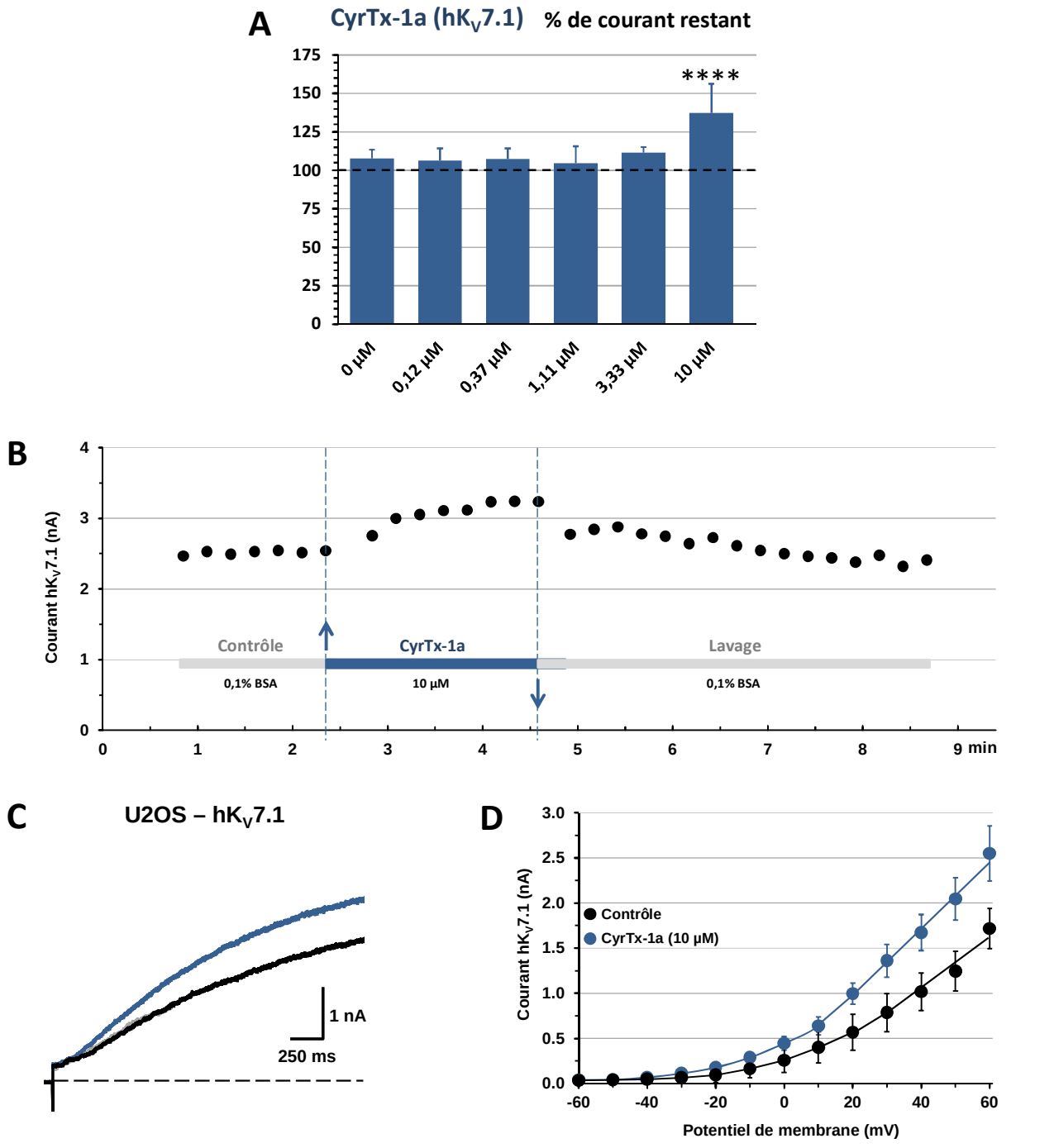

Figure 2-3. Effets de la CyrTx-1a sur le courant $hK_V7.1$. (**A**) Pourcentage de courant restant (moyenne ± ES, n = 3-13) en fonction de la concentration de peptide. ****: p = 0.00001 *versus* contrôle. (**B**) Cinétiques de l'effet de 10 µM de CyrTx-1a et du lavage du peptide sur le courant. (**C**) Traces représentatives du courant avant (en noir) et après soit 10 µM de CyrTx-1a (en bleu) soit le lavage du peptide (en gris). (**D**) Courbes "courant-potentiel" avant (cercles noirs) et après (cercles bleus) exposition des cellules U2OS à 10 µM de CyrTx-1a. Chaque valeur représente la moyenne ± ES des données obtenues à partir de 6 cellules. Les courbes ont été tracées manuellement.

L'augmentation du courant $hK_V7.1$ produite par 10 µM de CyrTx-1a est réversible en environ 3 min (Figure 2-3B et C) et est spécifique puisqu'en présence de 10 µM de peptide et de 10 µM d'HMR 1556, le courant ne représente plus que 11,3 ± 7,5% du courant contrôle (moyenne ± ES de 4 expériences). En présence de 10 µM de CyrTx-1a, aucune modification notable de la cinétique et de la dépendance vis-à-vis du potentiel de membrane de l'activation du courant $hK_V7.1$ n'a été observée (Figure 2-3C et D). Il est donc fortement probable que, là encore, l'augmentation du courant $hK_V7.1$ produite par le peptide résulte d'un accroissement du nombre de sous-types exprimés à la membrane et/ou de leur conductance unitaire.

Des expériences de "patch-clamp" en configuration "cellule attachée", qui permettent d'enregistrer le courant unitaire ne traversant que quelques sous-types de canaux, seraient nécessaires pour pouvoir conclure définitivement sur l'origine de l'augmentation des courants $hCa_V2.2$ et $hK_V7.1$ produite par la CyrTx-1a.

2.1.4. Conclusion

Les résultats présentés dans cette sous-partie mettent en évidence la purification, la synthèse, la détermination de la structure et la caractérisation fonctionnelle de la première toxine qui, à notre connaissance, ait été extraite du venin de l'araignée *Cyriopagopus schioedtei*. Cette toxine possède des propriétés antinociceptives indéniables et représente une molécule intéressante pour servir de base au développement d'analogues peptidiques synthétiques ayant une puissance accrue pour le sous-type $hNa_V1.7$ et ainsi une fenêtre thérapeutique plus importante. En particulier, le profil de sélectivité de la CyrTx-1a vis-à-vis des sous-types Na_V TTX-S, $Ca_V2.2$ et $K_V4.3$ pourrait être amélioré par des études de mutagénèse du peptide.

2.2. Relations “structure-activité” d’une toxine d’araignée *Phlogiellus* ciblant le sous-type $Na_V1.7$ de canaux sodium

2.2.1. Contexte de l’étude

La phlotoxine-1 (PhlTx-1), aussi nommée µ-théraphotoxine-Pspp1, est une toxine isolée et purifiée à partir du venin d’une araignée du genre *Phlogiellus* vivant en Papouasie-Nouvelle-Guinée. Comme la CyrTx-1a, ce peptide de 4055,77 Da et constitué de 34 acides aminés fait partie de la famille NaSpTx-1 et se structure autour du motif architectural ICK (Bosmans et al., 2005; Escoubas et al., 2006; www.uniprot.org/uniprot/P0DM14). Il présente un fort pourcentage d’identité de séquence (76% d’après la recherche Blast sur le compte NCBI des protéines) avec le peptide insecticide actif par voie orale OAIP-2 (pour "orally active insecticidal peptide") issue de la mygale *Selenotypus Plumipes* (Hardy et al., 2013; Wong et al., 2013).

L’étude de cette toxine a été entreprise en 2000 par Escoubas et collaborateurs à l’Institut Suntory pour la Recherche Bioorganique, au Japon. Les résultats obtenus ont été présentés pour la première fois en 2005, lors des Rencontres en Toxinologie organisées par la SFET (Société Française pour l’Etude des Toxines) à Paris, puis en 2006 lors du congrès international de l’IST (pour "International Society on Toxinology") à Glasgow en Ecosse (voir page suivante). En particulier, les effets de la PhlTx-1 avaient été étudiés sur différents sous-types de canaux Na_V exprimés avec la sous-unité β1 dans les ovocytes de xénope. A une concentration de 1 µM, la toxine inhibe de plus de 90% le courant $Na_V1.7$ (IC_{50} = 260 nM), de 35-39% les courants $Na_V1.4$ et 1.6 et de moins de 10% les courants $Na_V1.1$, 1.2, 1.3, 1.5 et $Na_V1.8$, ainsi que le courant Para/TipE de la drosophile. Les premiers essais évaluant la douleur neuropathique et les deux phases (aigüe et inflammatoire) de la douleur mettent en évidence des effets anti-allodynies et analgésiques de la PhlTx-1 qui sont toutefois moins importants que ceux de la morphine. Ces résultats ont été confirmés par la suite par l’équipe de John Wood (Collège de Londres, Angleterre) qui, de plus, a montré l’action synergique entre le peptide et des opioïdes pour obtenir une analgésie pendant la phase inflammatoire dite "II" de la douleur (Brevet WO 2015036734 A1, 2015; Emery et al., 2016; Deuis et al., 2017).

Dans le but de compléter l’étude de PhlTx-1, nous avons entrepris des expériences de "structure-activité" visant à évaluer les profils de sélectivité de la toxine et de certains de ses analogues peptidiques synthétiques sur un large éventail de sous-types de canaux ioniques.

Société Française pour l'Etude des Toxines

13èmes Rencontres en toxinologie
"Toxines et Douleur"
Paris, 1 et 2 décembre 2005

Isolation and characterization of Phlotoxin 1 (PhlTx1), a novel peptide active on voltage-gated sodium channels

F. BOSMANS[1], P. ESCOUBAS[2], S. DIOCHOT[2], D. MEBS[3], D. CRAIK[5], J. HILL[5], T. NAKAJIMA[4], M. LAZDUNSKI[2], J. TYTGAT[1]

(1) Laboratory of Toxicology, University of Leuven, E. Van Evenstraat 4, 3000 Leuven, Belgium; (2) Institut de Pharmacologie Moléculaire et Cellulaire, 660 Route des Lucioles, Valbonne, France ; (3) Zentrum der Rechtsmedizin, University of Frankfurt, Kennedyallee 104, Frankfurt, Germany; (4) Suntory Institute for Bioorganic Research, Mishima-Gun, Shimamoto-Cho, , Osaka, Japan; (5) University of Queensland, Centre for Drug Research and Development, Brisbane, Australia

Phlotoxin 1 (PhlTx1), a novel toxin from tarantula venom (*Phlogiellus* sp., Theraphosidae Selenocosmiinae endemic to Papua New Guinea) was isolated as the major toxic component of this venom. Its sequence was determined and confirmed by chemical synthesis:

ACLGQWDSCDPKASKCCPNYACEWKYPWCRYKLF

MALDI-TOF analysis of PhlTx1 revealed a molecular mass of 4058.83 and indicated that the C-terminus of this peptide has a carboxylic form. PhlTx1 is homologous to the other tarantula venom toxins TlTx1 (73 %, a Kv4.2 inhibitor) and HnTxIII (65%, a voltage-gated sodium channel inhibitor). Mouse intracerebroventricular injections of the crude venom showed unusual toxicity symptoms: the mice died rapidly, from gradual cardiac and respiratory failure, without the symptoms of neurotoxicity (excitotoxicity, convulsion, paralysis) usually associated with spider venoms. In order to determine its molecular target, PhlTx1 was tested on an array of ion channels expressed in either *X. laevis* oocytes or COS cells. The principal effects were seen on voltage-gated sodium channels (Nav1.1/β1 – Nav1.8/β1, para/tipE). The activation of both Nav1.2/β1 and Nav1.3/β1 was shifted towards more hyperpolarized voltages and Nav1.7/β1 was almost completely blocked (90%) at a concentration of 1.2 µM (IC50 = 260 ± 46 nM).

Poster 45: Phlotoxin 1, a toxin from tarantula venom, is a potent modulator of Nav1.7 sodium channels and a potential analgesic

Escoubas P.[1*], Bosmans F.[2], Cuypers E.[2], Diochot S.[1], Mebs D.[3], Craik D.[4], Hill J.[4], Maertens C.[2], Nakajima T.[5], Lazdunski M.[1], Tytgat J.[2]

*[1] Institut de Pharmacologie Moléculaire et Cellulaire – CNRS, Valbonne, France, *escoubas@ipmc.cnrs.fr; [2] Laboratory of Toxicology, University of Leuven, Leuven, Belgium; [3] Zentrum der Rechtsmedizin, University of Frankfurt, Frankfurt, Germany; [4] Institute for Molecular Bioscience, University of Queensland, Brisbane, Australia; [5] Suntory Institute for Bioorganic Research, Mishima-Gun, Shimamoto-Cho, Osaka, Japan*

Voltage-gated sodium (Nav) channels play an essential role in the biophysical properties of nociceptive neurons. Several Nav subtypes are key components of nociceptive neurotransmission and are potential targets for the development of novel analgesic strategies. Importantly, the Nav1.7 channel is found in peripheral primary sensory, and sympathetic, neurons and is involved in acute and inflammatory pain. We report here the discovery, structural characterization and pharmacological properties of phlotoxin 1 (PhlTx1), a novel 34-residue peptide toxin from the venom of a tarantula of the genus *Phlogiellus*, which selectively inhibits Nav1.7. PhlTx1 was isolated as the major component of the venom and its sequence was determined and confirmed by solid-phase peptide synthesis. Homology modelling revealed that it belongs to the inhibitory cystine knot (ICK) family of spider toxins and mass spectrometry indicates three disulfide bridges. PhlTx1 shows limited homology with other Nav toxins from Chinese tarantulas (Hainantoxins, Huwentoxins). PhlTx1 almost completely blocked (~90%) Nav1.7 channel currents at a concentration of 1.2 µM and the dose-response relationship on heterologously expressed channels revealed an IC50 value of 260 nM. The voltage-dependence of steady-state Nav1.7 channel activation and inactivation were not affected, suggesting that Phltx1 does not act as a gating-modifier toxin but rather blocks or impedes ion flux through the channel pore. PhlTx1 was almost exclusively selective for the Nav1.7 channel subtype, failing to modulate other Nav channels at concentrations up to 2 µM. In a model of inflammatory pain (mouse paw injection of formalin), intrathecal injection of PhlTtx1 resulted in a significantly reduced response to the pain stimulus in both the acute and inflammatory phases, strongly suggesting that PhlTx1 produces an analgesic effect through inhibition of the Nav1.7 channel in dorsal root ganglion neurones. Phlotoxin 1 may therefore represent a lead for the development of novel analgesic agents.

2.2.2. Publication n°3

Publication en préparation

"Structure-activity relationships of phlotoxin-1, a $Na_V1.7$-targetting toxin from a *Phlogiellus* spider"

Tania C. Gonçalves, Pierre Lesport, Sarah Kuylle, Justyna Ciolek, Gilles Mourier, Denis Servent, Emmanuel Bourinet, Evelyne Benoit & Nicolas Gilles

Structure-activity relationships of phlotoxin-1, a $Na_V1.7$-targetting toxin from a *Phlogiellus* genus spider with antinociceptive properties

Tânia C. Gonçalves[1,2], Pierre Lesport[3], Sarah Kuylle[1], Justyna Ciolek[1], Gilles Mourier[1], Denis Servent[1], Emmanuel Bourinet[3], Evelyne Benoit[1,4,*], Nicolas Gilles[1]

[1]Service d'Ingénierie Moléculaire des Protéines (SIMOPRO), CEA, Université Paris-Saclay, F-91191 Gif sur Yvette, France; [2]Sanofi R&D, Integrated Drug Discovery – High Content Biology, F-94440 Vitry-sur-Seine, France; [3]Institut de Génomique Fonctionnelle (IGF), CNRS-UMR 5203, Inserm-U661, Université de Montpellier UM1-UM2, F-34094 Montpellier, France; [4]Institut des Neurosciences Paris-Saclay (Neuro-PSI), UMR CNRS/Université Paris-Sud 9197, Université Paris-Saclay, F-91198 Gif sur Yvette, France

**Corresponding author: evelyne.benoit@cea.fr*

ABBREVIATIONS – Ala, alanine; Arg, arginine; Asn, asparagine; Asp, aspartic acid; BLAST, basic local alignment search tool; BSA, bovine serum albumin; Ca_V channel, voltage-gated calcium channel; CD, circular dichroism; CHO, Chinese hamster ovary; Cm, ceratotoxin; Cys, cysteine; Delta-C-ter mutant, C-terminal-deleted mutant; DMEM, Dulbecco's modified Eagle's medium; DMSO, dimethylsulfoxyde; ERG, *ether-a-go-go*-related gene; Gln, glutamine; Glu, glutamic acid; GPCR, G-protein-coupled receptor; GSH, reduced glutathione; GSSG, oxidized glutathione; h, human; HEK, human embryonic kidney; HEPES, N-2-hydroxyethylpiperazine-N'-2-ethanesulfonic acid; His, histidine; HnTx, hainantoxin; HOAT, 1-hydroxy-7-azabenzotriazole; HwTx, huwentoxin; IC_{50}, molecule concentration necessary to inhibit 50% of the response; ICK, inhibitor cystine knot; K_V channel, voltage-gated potassium channel; MEM, minimum essential medium; MS, mass spectrometry; NaSpTx, Na_V channel spider toxin; Na_V channel, voltage-gated sodium channel; n_H, Hill number; OD1, toxin 1 from the *Odonthobuthus doriae* scorpion; PBS, phosphate buffered saline; PDB, protein data bank; PhlTx-1, phlotoxin-1; RP-HPLC, analytical reversed-phase high pressure liquid chromatography; SAR, structure-activity relationship; Ser, serine; Thr, threonine; Trp, tryptophan; TTX-R, resistant to tetrodotoxin; TTX-S, sensitive to tetrodotoxin; Tyr, tyrosine.

ABSTRACT

Over the two last decades, venom toxins have been explored as alternatives to opioids widely overconsumed in developed countries to treat chronic debilitating pain. Actually, approximatively 20 potential analgesic toxins, mainly from spider venoms, are known to inhibit with high affinity the $Na_V1.7$ subtype of voltage-gated sodium (Na_V) channels, the most promising genetically validated antinociceptive target identified so far. The present study aimed to consolidate the clinical development of phlotoxin-1 (PhlTx-1), a 34-amino acid and 3-disulfide bridge peptide of a *Phlogiellus* genus spider, as an antinociceptive agent by improving its affinity and selectivity for the $Na_V1.7$ subtype. As a first step, PhlTx-1 was synthetized, as well as some of its mutants using

an alanine scanning mutagenesis approach. The synthetic peptide and each of its 8 successfully synthetized mutants equilibrated between two active forms whose relative amounts were dependent on the temperature. As a second step, the effects of PhlTx-1 wild-type and mutant forms were studied on cell lines stably overexpressing human (h) Na_V subtypes, as well as two cardiac targets, the $hCa_V1.2$ and $hK_V11.1$ subtypes of voltage-gated calcium (Ca_V) and potassium (K_V) channels, respectively, using automated whole-cell patch-clamp electrophysiology. PhlTx-1 and D7A-PhlTx-1 were shown to inhibit $hNa_V1.1$-1.3 and 1.5-1.7 at hundred nanomolar concentrations, while their affinities for $hNa_V1.4$ and 1.8, $hCa_V1.2$ and $hK_V11.1$ were over micromolar concentrations. Despite similar selectivity profiles, the affinity of the peptide mutant form was at least 4 times higher than that of the wild-type form for the $Na_V1.7$ subtype. Finally, the wild-type form of PhlTx-1 exhibited potent analgesic effects in a mouse model of inflammatory pain, those of D7A-PhlTx-1 being still under investigation. In conclusion, the present SAR study of PhlTx-1 results in an improved affinity of the molecule for the $Na_V1.7$ subtype but without any marked change in the molecule selectivity against the other studied ion channel subtypes. Further experiments are therefore necessary before considering the clinical development of PhlTx-1.

Keywords – *Phlogiellus* spider, phlotoxin-1, human voltage-gated ion channel subtypes, $Na_V1.7$ channel subtype, cell lines overexpressing ion channel subtypes, human induced pluripotent stem cell-derived cardiomyocytes, mouse model of $Na_V1.7$-mediated pain.

1. INTRODUCTION

More than 10% of the worldwide population is complaining about pain (Goldberg and McGee, 2011). The first anatomic supports of pain transmission from the periphery to the central nervous system are the dorsal root ganglia (DRG) neurons. These neurons express a multitude of transmembrane proteins, such as G-protein-coupled receptors (GPCRs) and ion channels, which can be considered as targets for therapeutic treatment of pain. Hence, some molecules interacting with GPCRs or ion channels have been reported to be involved in pain relief (Pan et al., 2008; Bennett and Woods, 2014; Waxman and Zamponi, 2014; Spray et al., 2017; Yekkirala et al., 2017). However, in developed countries, and mainly in the United States, an overconsumption of opioids is observed due to unjustified medical prescriptions, as well as the tolerance acquisition and non-evitable dependence of patients to these GPCR-targetting painkillers. Finding pharmacological, chirurgical and/or behavioral alternatives has thus become an emergency (Savage et al., 2008; Negus et al., 2018).

In this context, venom toxins have been explored over the two last decades as an original source of innovative antinociceptive drugs targetting different ion channel subtypes. Only one of these toxins, the ω-conotoxin-MVIIA isolated from a cone snail and which inhibits the N-type, $Ca_V2.2$ subtype of voltage-gated calcium (Ca_V) channels, was commercialized as Prialt® after the FDA approval in 2004. However, the narrow spectrum of use of this molecule and its intrathecal route of administration, associated to side-effects, represent major drawbacks for the treatment of chronic debilitating pain (Molinski et al., 2009). Among voltage-gated sodium (Na_V) channels,

the $Na_V1.7$ subtype was widely reported to be the most incriminated in channelopathies related to pain, although mutations in the genes encoding some of the eight other Na_V subtypes, identified so far, result in painful or painless diseases with strong phenotypes (de Lera Ruiz and Kraus, 2015; Vetter et al., 2017; Gonçalves et al., 2018b). Hence, numerous high-throughput screenings of venom banks from various animals (spiders, scorpions, snakes, lizards, cone snails …) have been performed on the $Na_V1.7$ subtype, leading to the discovery of potential analgesic candidates mainly from spider venoms. Actually, approximatively 20 spider toxins, comprising between 26 and 35 amino acids and sharing the same inhibitor cystine knot (ICK) architectural motif, are known to inhibit with high affinity the $Na_V1.7$ subtype (reviewed by Gonçalves et al., 2018b). However, the lack of target selectivity of most of these peptides greatly impairs the neuromuscular and/or cardiac safety issues and thus compromises their clinical development as potential antinociceptive agents (Liu et al., 2014; Deuis et al., 2016; Flinspach et al., 2017; Rahnama et al., 2017; Gonçalves et al., 2018c).

More than 10 years ago, a toxin, identified as μ-theraphotoxin-Pspp1 and also named phlotoxin-1 (PhlTx-1), was purified from the venom of a *Phlogiellus* genus spider endemic to Papua New Guinea. PhlTx-1 (4058.83 Da), characterized by a 34 amino acid sequence with three disulfide bridges and structured around the ICK architectural motif, was shown to belong to the Na_V channel spider toxin (NaSpTx) family 1. This peptide was reported to inhibit the $Na_V1.7$ subtype expressed in *Xenopus* oocytes with high affinity and selectivity against the other studied Na_V subtypes and to produce, although with lower efficiency than morphine, analgesic effects in a mouse model of inflammatory pain (www.uniprot.org/uniprot/P0DM14; Bosmans et al., 2005, Escoubas et al., 2006). More recently, a synergistic action between PhlTx-1 and opioids (at low, non-therapeutic doses) was revealed to induce analgesia during the phase II of inflammatory pain (Patent # WO 2015036734 A1, 2015; Emery et al., 2016; Deuis et al., 2017).

The aim of the present study was to consolidate the clinical development of PhlTx-1 as an antinociceptive agent by studying the peptide interactions with a large panel of ion channels, to ensure its neuromuscular and cardiac safety properties, and by evaluating the structure-activity relationships (SARs) of the molecule to improve its affinity and selectivity for the target of interest (*i.e.* the $Na_V1.7$ subtype). The effects of synthetic PhlTx-1 and some of its mutants, obtained by the alanine (Ala) scanning mutagenesis approach, were thus investigated on cell lines stably overexpressing human (h) Na_V subtypes, as well as two cardiac targets, $hCa_V1.2$ and the $hK_V11.1$ subtype of voltage-gated potassium (K_V) channels encoded by the human *ether-a-go-go*-related gene (hERG), using automated whole-cell patch-clamp electrophysiology. Some preliminary experiments were also carried-out to evaluate the analgesic properties of the peptide and of its most promising mutant.

2. EXPERIMENTAL SECTION

2.1. Chemical synthesis and *in vitro* folding of PhlTx-1 and its mutants

The assembly of different peptides was carried out using the stepwise solid-phase method

with dicyclohexylcarbodiimide/1-hydroxy-7-azabenzotriazole (HOAT) as coupling reagents and N-methylpyrrolidone as solvent. Fmoc-protected amino acids were used with the following side chain protections: tert-butyl ester (Glu, Asp), tert-butyl ether (Ser, Thr, Tyr), trityl group (Cys, His, Asn, Gln), 2,2,5,7,8-pentamethyl-chromane-6-sulfonyl group (Arg), and tert-butyloxycarbonyl group (Trp). The peptides were assembled on a Fmoc-Phe(OtBu)-Wang resin (0.5 mmol/g loading), with the exception of the C-terminal-deleted (Delta-C-ter) mutant which was assembled on a Fmoc-Cys(Boc)-Wang resin (0.55 mmol/g loading). Automated chain assembly was performed on a standard Applied Biosystems 433 peptide synthesizer (Applied Biosystems, Foster City, CA, USA). The different syntheses were run on a modified version of the Applied Biosystems standard 0.1-mmol small-scale program using 0.05 mmol of each resin. The linear peptide forms were purified from the crude synthetic products by analytical reversed-phase high pressure liquid chromatography (RP-HPLC). The maturation of peptides was performed in 100 mM tris-HCl buffer (pH 8) added with 2 mM of reduced (GSH) and oxidized glutathione (GSSG), during 48 hr at 4°C. Mass spectrometry (MS) analysis was performed on a 4800 MALDI TOF/TOF™ Analyzer (Applied Biosystems). Temperature dependent circular dichroism (CD) spectra were obtained using a Jasco J-815 spectropolarimeter equipped with a Peltier cell holder Jasco CDF-426S.

Protected amino acid derivatives, resins and dicyclohexylcarbodiimide were from Novabiochem (Meudon, France), HOAT from Applied Biosystems (Courtaboeuf, France), N-methylpyrrolidone from Carlo Erba Reactifs - Sds (Peypin, France), and GSH, GSSG and L-cysteine from Sigma-Aldrich (Saint-Quentin-Fallavier, France).

2.2. Predicted 3D-structure of PhlTx-1

Computational modelling was performed, using the PyMOL software, to deduce the 3D-structure of PhlTx-1 from those of closely-related toxins archived in the protein data bank (PDB): ceratotoxin-1 (Cm1a, PDB: 6BRO), ceratotoxin-2 (Cm1b, PDB: 6BTV), F8A mutant of Pre-1a (PDB: 5I1X), peptide Hs1a (PDB: 2MT7), hainantoxin-III (HnTx-III, PDB: 2JTB) and huwentoxin-I (HwTx-I, PDB: 1QK6).

2.3. Toxins, chemicals and cell lines used for functional assays

Lyophilized synthetic PhlTx-1 wild-type and mutant forms (purity rate > 97%) were dissolved in appropriate solutions to give adequate stock solutions. All compounds used as reference molecules to pharmacologically validate the current flowing through each channel subtype, as indicated in Table 1, were purchased from Sigma-Aldrich and Smartox Biotechnology (Saint-Egrève, France). The toxins were dissolved in distilled water to give a 100-µM stock solution, and the chemicals were dissolved in 100% dimethylsulfoxyde (DMSO, Sigma-Aldrich) to give a 10-mM stock solution. Just prior to experiments, successive dilutions were performed in the appropriate standard physiological medium [supplemented with 0.1% bovine serum albumin (BSA, Sigma-Aldrich) for toxins to avoid plastic adherence, and with 0.3% DMSO for chemicals to maintain solubility], to give the compound final concentrations indicated in the text.

Generation of inducible cell lines was achieved by cloning cDNAs encoding for $hNa_V1.2$ (NM_021007.2) and $hNa_V1.5$ (NM_000335) subtypes into the Flp-In® T-Rex® expression vector

(Invitrogen, USA) and subsequently transfected them into human embryonic kidney (HEK)-293 cell lines. These cell lines were cultured under standard conditions (37°C, 5% CO_2) in Dulbecco's modified Eagle's medium (DMEM, Invitrogen) supplemented with 10% fetal calf serum (Invitrogen), 50 µg/mL hygromycin (Invitrogen) and 15 µg/mL blasticidin (Invivogen). They were sub-cultured every 3-4 days using accutase® (Sigma-Aldrich) or TrypLE Select (Gibco, Thermo Fisher Scientific, France) enzyme. Doxycycline (BD Biosciences, France) was added to induce target expression, at least between 12 and 24 hr prior to experiments.

Table 1. Compounds used as reference molecules to pharmacologically validate the current flowing through each hNa_V, hCa_V and hK_V channel subtype.

Channel subtype	Drug reference			Provider	$IC_{90\text{-}95}$ [2]
	Name	MM	Purity rate		
$hNa_V1.1$-1.8	Tetrodotoxin (citrate)	319.27	> 98%	Sigma-Aldrich	1 µM
$hCa_V1.2$	Nifedipine	346.33	> 98%	Sigma-Aldrich	10 µM
	Cadmium (Cl)[1]	183.32	> 99.99%	Sigma-Aldrich	200 µM
$hK_V11.1$	BeKm-1	4091.70	> 97%	Smartox Biotechnology	1 µM

[1]Cl: chloride, [2]$IC_{90\text{-}95}$, compound concentration necessary to inhibit 90-95% of current.

Recombinant HEK-293 cell lines, stably overexpressing the other hNa_V subtypes, were purchased from SB Drug Discovery (UK; $hNa_V1.3$ and 1.4), ChanTest (Cleveland, OH, USA; $hNa_V1.6$) and Eurofins (St Charles, MO, USA; $hNa_V1.1$, 1.7 and 1.8/β1). These cell lines were cultured in Eagle's minimum essential medium (MEM, Sigma-Aldrich; $hNa_V1.3$ and 1.4), in DMEM/F-12 nutrient mixture with GlutaMAX™ (Gibco; $hNa_V1.1$, 1.6 and 1.8/β1) or in suspension in FreestyleTM293 (Gibco, $hNa_V1.7$). The Chinese hamster ovary (CHO) cells heterologously overexpressing $hCa_V1.2$/β2/α2δ1 (purchased from ChanTest) were cultured in Ham's F12 nutrient mix with GlutaMAX™ medium (Gibco), and those overexpressing $hK_V11.1$ (purchased from B'SYS GmbH, Switzerland) in DMEM/F-12 nutrient mixture Ham's medium (Sigma-Aldrich). All culture media contained 10% fetal bovine serum (Gibco) and selected antibiotics and additives, as recommended by the manufacturers. The cells were grown in flasks (37°C, 5% CO_2), and sub-cultured every 3-4 days using TrypLE Select enzyme.

2.4. Automated whole-cell patch-clamp electrophysiology

The effects of synthetic PhlTx-1 and some of its mutants were investigated on the cell lines overexpressing $hNa_V1.1$-1.8, $hCa_V1.2$ and $hK_V11.1$ subtypes, using an automated patch-clamp system, the QPatch HTX (Sophion Bioscience, Denmark), allowing current recordings in whole-cell configuration and both signal acquisition and data analyses, as previously reported (Gonçalves et al., 2018a). The day of their use, HEK-293 and CHO cells were transferred into Eppendorf tubes containing a FreeStyle 293 expression medium (Gibco) which were then placed in the automated electrophysiology platform. The extracellular medium composition for hNa_V-overexpressing HEK-293 cells was (in mM): NaCl 154, KCl 4, $CaCl_2$ 2, $MgCl_2$ 1, and HEPES 10 (pH 7.4 adjusted with NaOH), and that of intracellular (*i.e.* path-clamp pipette) medium: CsF 150, EGTA/CsOH 1/50, HEPES 10, NaCl 10, $MgCl_2$ 1, and $CaCl_2$ 1 (pH 7.4 adjusted with CsOH). The extracellular medium

composition for $hCa_V1.2$-overexpressing CHO cells was (in mM): NaCl 145, KCl 4, $CaCl_2$ 10, and HEPES 10 (pH 7.4 adjusted with NaOH), and that of intracellular medium: CsF 27, CsCl 112, EGTA 8.2, HEPES 10, NaCl 2, and Mg-ATP 4 (pH 7.4 adjusted with CsOH). The extracellular medium composition for $hK_V11.1$-overexpressing CHO cells was (in mM): NaCl 145, KCl 4, $CaCl_2$ 2, $MgCl_2$ 1, HEPES 10, and D-glucose 10 (pH 7.4 adjusted with NaOH), and that of intracellular medium: KCl 120, $CaCl_2$ 5.4, EGTA 10, HEPES 10, Mg-ATP 4, and $MgCl_2$ 1.75 (pH 7.4 adjusted with KOH). The time of cell incubation with PhlTx-1 wild-type and mutant forms, as well as reference molecules, was adjusted to achieve steady-state effects, *i.e.* between approximately 2 and 7 minutes. The experiments were carried out at room temperature (20-22°C).

In addition to the classical "closed-open" protocol, a "fully-inactivated" protocol was also used to test an eventual inactivated-state-dependent effect of peptides on hNa_V subtypes. During the **"closed-open" protocol**, the hNa_V-overexpressing HEK-293 cells were maintained at a holding potential of either -90 mV ($hNa_V1.5$) or -100 mV (other hNa_V subtypes), and currents were elicited at a frequency of 0.2 Hz by 20-ms test-pulses to -20 mV ($hNa_V1.2$ and 1.7), -40 mV ($hNa_V1.5$) or 10 mV ($hNa_V1.8$), preceded by 40-ms ($hNa_V1.7$) or 200-ms ($hNa_V1.5$) pulses to -120 mV, or not ($hNa_V1.2$ and 1.8). The $hCa_V1.2$-overexpressing CHO cells were maintained at a holding potential of -50 mV, and currents were elicited at a frequency of 0.05 Hz by 200-ms test-pulses to 0 mV. The $hK_V11.1$-overexpressing CHO cells were maintained at a holding potential of -80 mV, and tail currents were elicited at a frequency of 0.07 Hz by 5-sec test-pulses to -50 mV, preceded by 4.8-sec pulses to 20 mV following 20-ms pulses to -50 mV. During the **"fully-inactivated" protocol**, the hNa_V-overexpressing HEK-293 cells were maintained at a holding potential of either -40 mV ($hNa_V1.1$, 1.2 and 1.6) or -50 mV (other hNa_V subtypes), and currents were elicited at a frequency of 0.2 Hz by 20-ms test-pulses to -40 mV ($hNa_V1.5$) or -20 mV (other hNa_V subtypes), preceded by 40-ms ($hNa_V1.3$ and 1.4) or 20-ms (other hNa_V subtypes) pulses to -120 mV.

The concentration-response relationships were established by plotting the peak amplitude of the sum of ten cell currents recorded in the presence of a given molecule (Pm), expressed relatively to that of the sum of these currents recorded before molecule application (Pc), against the molecule concentration ([m]). The theoretical concentration-response curves were calculated from typical sigmoid nonlinear regressions through data points according to the Hill equation (QPatch assay software): $Pm / Pc = 1 / [1 + ([m] / IC_{50}) n_H]$, where IC_{50} is the molecule concentration necessary to inhibit 50% of the response, and n_H is the Hill number.

2.5. Mouse model of inflammatory pain

The experiments were performed on 8-week adult male and female C57BL/6 mice purchased from Janvier Elevage (Le Genest-Saint-Isle, France) and housed at the IGF animal facility 3-4 per cage, under 12 hr light/dark cycles, with standard rodent chow and free access to food and water *ad-libitum*. They were conducted in compliance with the guidelines established by the French Council on animal care "Guide for the Care and Use of Laboratory Animals" (EEC86/609 Council Directive – Decree 2001-131), and the experimental protocols were approved on November 27 2015 by the French General Directorate for Research and Innovation (project APAFIS#2671-2015110915123958v4 authorized to E.B.).

The peptide analgesic effects were studied at room temperature on mouse model of $Na_V1.7$-mediated pain, based on intraplantar injection of toxin 1 from the *Odonthobuthus doriae* scorpion (OD1, Smartox Biotechnology) that potently enhances the activity of $Na_V1.7$ by inhibiting channel fast inactivation and increasing peak current, as previously described (Deuis et al., 2016). The pain behavior of mice was quantified by the number of spontaneous licking, flinching, shaking and biting of the paw, injected with 40-µL phosphate buffered saline (PBS) solution containing either 300 nM OD1 alone or OD1 and 3, 30 or 300 nM PhlTx-1, during 5-min periods following the injection. The experiments were video recorded and blind analysis of mouse pain behavior was done, off-line, by an observer unaware of which treatment each animal has received.

2.6. Statistical analyses

Data are expressed as means ± standard deviations (S.D.) or ± standard error of the mean (S.E.M.) of n different experiments. The statistical comparison of values was carried out *(i)* using the parametric two-tailed Student's *t*-test (either paired samples for comparison within a single population or unpaired samples for comparison between two independent populations) for *in vitro* data, or *(ii)* using the one-way analysis of variance (ANOVA, for comparison between three or more independent populations) for *in vivo* data. Differences between values were considered to be statistically significant at $P \leq 0.05$.

3. RESULTS

3.1. Chemical synthesis and *in vitro* folding of PhlTx-1

PhlTx-1, a 34-amino acid toxin containing 6 cysteines (Figure 1A), was synthesized using the Fmoc strategy (Figure 1Ba). The linear peptide was purified and different folding protocols were tested according to the nature and pH of the buffer and to the redox couple used which are crucial parameters. The Tris-HCl buffer at pH 8.5 was associated with the reduced and oxidized glutathione (GSH/GSSG, 1/1) while the HEPES buffer at pH 7.5 was associated with L-cysteine/L-cystine (Cys/C–C, 1/0.1). For solubilization purposes, the chosen additives were 20% acetonitrile and glycerol. The reaction was left for 48 hr at 4°C to slow down the oxidation kinetics, which resulted in a more stable toxin. The best folding condition was found to be the Tris-HCl buffer and redox glutathione couple (Figure 1Bb). Folding of the linear peptide generated a complicated profile with two main peaks, A and B, B being surrounded by two side-peaks, C and D. Mass analysis of these four peaks revealed a similar mass corresponding to the full oxidation of the three disulfide bridges. The pharmacological activity of 1 µM of these four peaks was tested on HEK-293 cell lines stably overexpressing the $hNa_V1.7$ subtype. Only the peak A was observed to strongly inhibit the $hNa_V1.7$ current, the peak B and peaks C and D showing moderate and no activity, respectively (data not shown). Therefore, the peak A was further analyzed in detail by analytical RP-HPLC chromatography. The results revealed the existence of two peaks, A' and A'', of similar areas and separated by retention times of almost 4 minutes (Figure 1Bc). The peaks A' and A'', injected separately, generated again two peaks (data not shown). This demonstrates that the product equilibrated between two structural organizations having different interaction properties

463 with the column phase.

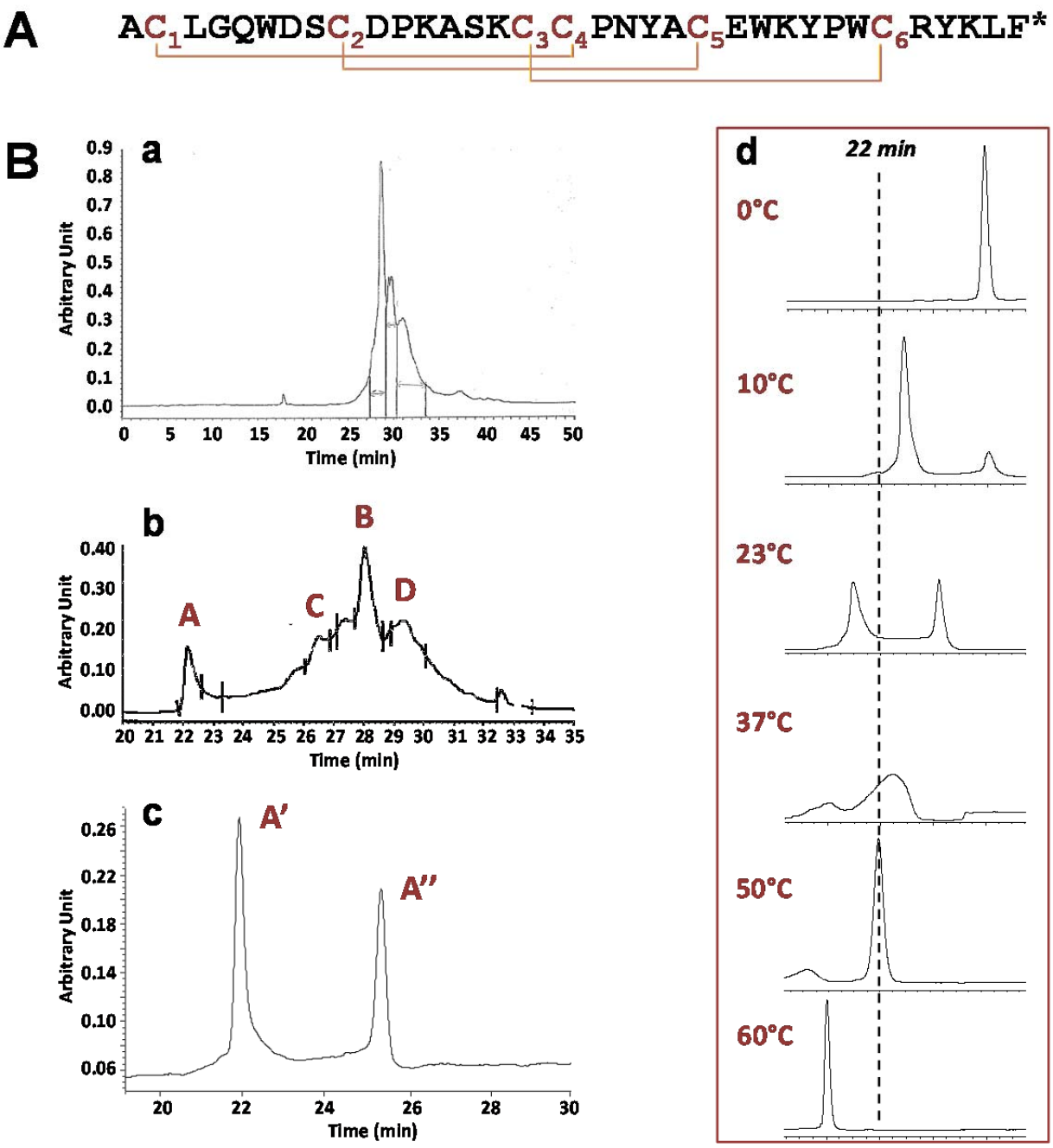

Figure 1. Primary structure, chemical synthesis and *in vitro* folding of PhlTx-1. (**A**) Primary structure of PhlTx-1, a 34-amino acid and amidated (*) peptide including 3 disulfide bridges, as defined by homology with toxins from the NaSpTx family 1, *i.e.* occurring according to the C1-C4, C2-C5 and C3-C6 pattern. (**B**) Chemical synthesis of PhlTx-1. Analytical RP-HPLC profiles, detected at 214 nm, of crude peptide synthesis (**a**), crude peptide folding using the Tris-HCl buffer, the redox glutathione couple and acetonitrile (**b**), and peak A (**c**) detected in (b). Note that the presence of two peaks in (c) limits a non-well defined peak. (**d**) Effect of temperature on the equilibrium between the two peaks A' and A'', revealed by analytical RP-HPLC analysis of peak A at the indicated temperatures.

464 The influence of temperature (between 0 and 60°C) was studied on the equilibrium between
465 the two forms, A' and A'', of peak A (Figure 1Bd). Decreasing the temperature from 23 to 0°C
466 produced a decrease of the area of peak A'', which finally disappeared at 0°C, while that of peak A'
467 increased. On the opposite, increasing the temperature from 23 to 60°C was favorable to peak A''.
468 It is worth noting that the elution times of the different forms of PhlTx-1 were inversely

proportional to the temperature.

All these characterizations demonstrated that the folding of PhlTx-1 generated many forms visible onto analytical RP-HPLC analysis. The pharmacological activity of these forms clearly indicated that peak A was associated to the purest and the most active peptide, whatever the analytical RP-HPLC conditions were, with a CD spectrum coherent with its ICK architectural motif (data not shown).

3.2. Comparison of amino acid sequences and 3D-structures of PhlTx-1 with closely-related toxins

The 3D-structure of PhlTx-1, containing the ICK motif in its backbone conformation expected by the amino acid sequence, was modelled by structural homology with the closest toxins from NCBI basic local alignment search tool (BLAST) (Figure 2A and Table 2). Six of the 14 toxins extracted from NCBI BLAST had their 3D-structure defined by 2D-homonuclear ^{1}H-NMR spectroscopy, which helped the computational determination of PhlTx-1 3D-structure (Figure 2B). All the 3D-structures were similar except those of F8A-Pre-1a and Hs1a, which displayed the 3D-structure of peptide precursors with a long N-terminal (Figure 2B), and those of CcoTx2 and HwTx-I pointing out three β leaflets instead of two for the other peptides.

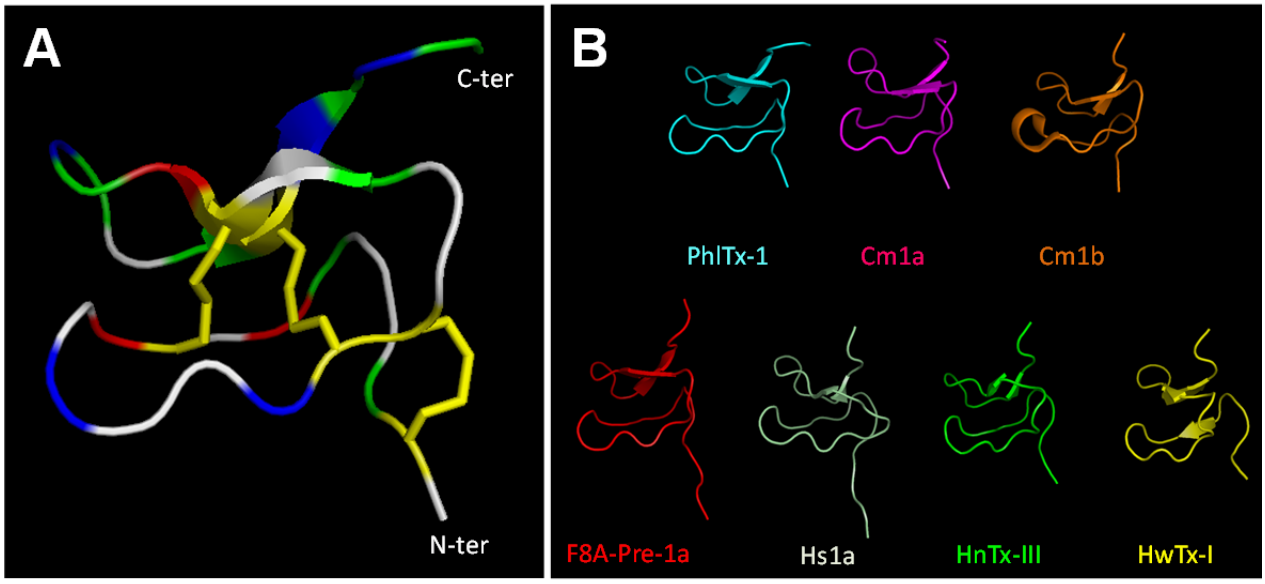

Figure 2. 3D-Structure modelling of PhlTx-1. (**A**) Ribbon representation indicating elements of secondary structure. The structure topology is composed of double stranded antiparallel β-sheet (arrows). The three disulfide bonds are C2-C17, C9-C22 and C16-C29 (in yellow). Hydrophobic residues are colored in green, and basic and acidic residues in blue and red, respectively. The other polar residues are colored in white. (**B**) Backbone peptide folding of PhlTx-1 and toxins with PDB entries and showing the highest percentage of amino acid sequence identity with PhlTx-1 (PDB entries of Cm1a: 6BRO, Cm1b: 6BTV, F8A-Pre-1a: 5I1X, Hs1a: 2MT7, HnTx-III: 2JTB, and HwTx-I: 1QK6).

All the toxins with percentage of sequence identity close to PhlTx-1 (between 45 and 76%) were Na_V, K_V and/or Ca_V channel ligands (Table 2). These toxins have homologous amino acid sequences including three amino acids highly conserved (G4, P11 and W28), in addition to the four charged patches necessary for toxin-ion channel binding (Table 2; Minassian et al., 2013; Murray

et al., 2016; Shcherbatko et al., 2016). Some of these toxins, such as Cd1a, CcoTx1 and HnTx-III, were described to target the $Na_V1.7$ subtype with nanomolar affinities (IC_{50} between 2 and 232 nM, Table 2) and, thus, with potential implications in the pain therapeutic field (Liu et al., 2013; Shcherbatko et al., 2016; Sousa et al., 2017).

Table 2. Comparison of amino acid sequences between PhlTx-1 and the 14 most similar and/or well-documented toxins described in the literature. The sequence alignment was performed with ClustalIW (version 12.1 from Emboss programs, EBlosum62 matrix for two pair alignment). The cysteine scaffold and conserved residues are indicated in red, and important residues for toxin interaction with ion channels are surrounded in blue. The percentage of sequence identity with PhlTx-1, the known targets and the activity (IC_{50} in nM reported for $hNa_V1.7$ subtype) are described in the right columns, according to data sourced from Pubmed and ArachnoServer (Herzig et al., 2011).

Name*		Amino acid sequence	Identity	Target	Activity
PhlTx-1	(μ-TRTX-Pspp-1)	--A--CLGQWDSCDPKASKCCPNYACEWKYPWCRYKLF-	100%	Na_V	254
OAIP2		--D--CLGQWASCEPKNSKCCPNYACTWKYPWCRYRAGK	76%	?	-
TlTx1	(κ-TRTX-Tb1a)	-AA--CLGMFESCDPNNDKCCPNRECNRKHKWCKYKLW-	59%	K_V	-
Osp1b	(μ-TRTX-Osp1b)	--E--CLGWMKGCEPKNNKCCSSYVCTYKYPWCRYDL--	58%	Na_V	-[1]
TlTx2	(κ-TRTX-Tb1b)	-DD--CLGMFSSCDPKNDKCCPNRVCRSRDQWCKYKLW-	56%	K_V	-
Cd1a	(β-TRTX-Cd1a)	--D--CLGWFKSCDPKNDKCCKNYSCSRRDRWCKYDL--	55%	Na_V	16[2]
CcoTx1	(β-TRTX-Cm1a)	--D--CLGWFKSCDPKNDKCCKNYTCSRRDRWCKYDL--	55%	Na_V	2-130[3,4]
CcoTx2	(β-TRTX-Cm1b)	--D--CLGWFKSCDPKNDKCCKNYTCSRRDRWCKYYL--	55%	Na_V	95[4]
TlTx3	(κ-TRTX-Tb1c)	-DD--CLGMFSSCDPNNDKCCPNRVCRVRDQWCKYKLW-	53%	K_V	-
Pre1a	(β/δ-TRTX-Pre1a)	-ED--CLGWFSRCSPKNDKCCPNYKCSSKDLWCKYKIW-	53%	Na_V	114[5]
Hs1a		GND--CLGFWSACNPKNDKCCANLVCSSKHKWCKGKL-	52%	Na_V	-[6]
HnTxIII	(μ-TRTX-Hhn2a)	----GCKGFGDSCTPGKNECCPNYACSSKHKWCKVYLGK	50%	Na_V	232[7]
Ccy1b	(μ-TRTX-Ccy1b)	-DD--CLGFFKSCNPDNDKCCENYKCNRRDKWCKYVL--	48%	Na_V	-[1]
Pmr1a	(μ-TRTX-Pmr1a)	-DD--CLGMFSSCDPDNDKCCEGRKCNRKDKWCKYVL--	48%	Na_V	-[8]
HwTxI	(μ/ω-TRTX-Hs1a)	----ACKGVFDACTPGKNECCPNRVCSDKHKWCKWKL--	45%	Na_V/Ca_V	<200[9]

**The Greek letter(s) before the toxin name is associated to its type of action: μ for Na_V channel inhibition, β for shift in the voltage-dependence of Na_V channel activation, δ for delay inactivation of Na_V channels, ω for Ca_V channel inhibition, and κ for K_V channel inhibition. TRTX, theraphotoxin. [1]Klint et al. (2015b), [2]Sousa et al. (2017), [3]Shcherbatko et al. (2016), [4]Agwa et al. (2018), [5]Wingerd et al. (2017), [6]Klint et al. (2015a, unpublished data), [7]Liu et al. (2013), [8]Meir et al. (2012, unpublished data), [9]Wang et al. (2012).*

3.3. Effects of PhlTx-1 on $hNa_V1.1$-1.8, $hCa_V1.2$ and $K_V11.1$ channel subtypes

Whole-cell automated patch-clamp (QPatch HTX) experiments performed on HEK-293 cells overexpressing $hNa_V1.1$-1.8 channel subtypes revealed, whatever the electrophysiological protocol was, that 1 μM PhlTx-1 was effective to inhibit $hNa_V1.1$-1.7 currents, without any marked subtype selectivity, while the $hNa_V1.8$ current was unaffected (Figure 3A and B). Hence, the following increasing order for IC_{50} values was obtained from the concentration-response curves of PhlTx-1 effects on currents flowing through the different channel subtypes: $hNa_V1.2$ (73.7 ± 46.3 nM, n = 12) ≈ $hNa_V1.3$ (201.5 ± 109.8 nM, n = 6) ≈ $hNa_V1.7$ (254.3 ± 147.6 nM, n = 5) ≈ $hNa_V1.1$ (280.3 ± 117.7 nM, n = 11) > $hNa_V1.6$ (491.2 ± 109.0 nM, n = 6) >> $hNa_V1.4$ (> 2.1 ± 1.3 μM, n = 9) for tetrodotoxin-sensitive (TTX-S) channel subtypes, and $hNa_V1.5$ (710.6 ± 32.7 nM, n = 10) < $hNa_V1.8$ (> 10 μM, n = 4) for tetrodotoxin-resistant (TTX-R) channel subtypes. Thus, all the TTX-S hNa_V channel subtypes studied, with the exception of $hNa_V1.4$, were sensitive to PhlTx-1, as well as the TTX-R cardiac sodium channel subtype $hNa_V1.5$ (although at hundred nanomolar concentrations), while the TTX-R $hNa_V1.8$ subtype was resistant to the peptide (at ten micromolar concentrations). Additionally, PhlTx-1 had very low affinity for cardiac $hCa_V1.2$ and $hK_V11.1$ channel subtypes overexpressed in CHO cells, since 10 μM of peptide had no effect on the $hK_V11.1$

current (n = 4) and had only low effect on the $hCa_V1.2$ current (IC_{50} = 5.9 ± 2.1 µM, n = 6; Figure 3B).

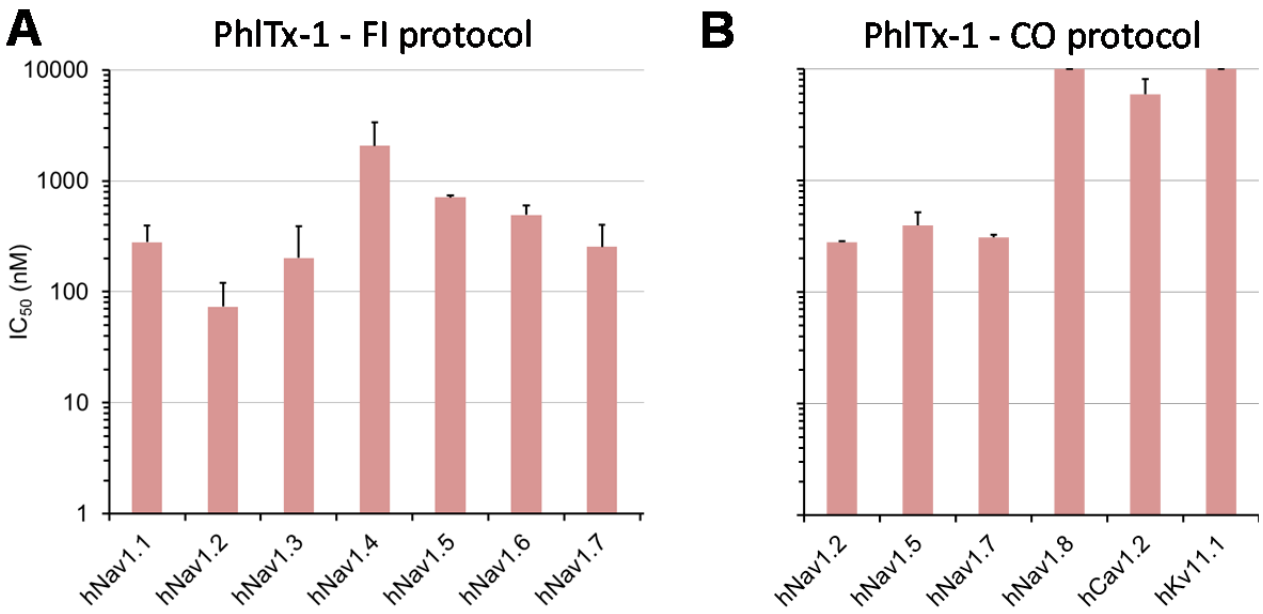

Figure 3. Effects of PhlTx-1 on HEK-293 cells overexpressing hNa_V subtypes and on CHO cells overexpressing $hCa_V1.2$ and $hK_V11.1$ subtypes. (**A**) Histogram of IC_{50} values (in nM) obtained from the concentration-response curves of PhlTx-1 effects on $hNa_V1.1$-1.8 currents recorded during a "fully inactivated" (FI) protocol. Each value represents the mean ± S.D. of data obtained from 4-12 cells. Mean value ± S.D. of n_H was 1.15 ± 0.42. (**B**) Histogram of IC_{50} values (in nM) obtained from the concentration-response curves of PhlTx-1 effects on $hNa_V1.2$, 1.5 and 1.7-1.8, $hCa_V1.2$ and $hK_V11.1$ currents recorded during a "closed-open" (CO) protocol. Each value represents the mean ± S.D. of data obtained from 2-3 cells. Mean value ± S.D. of n_H was 1.05 ± 0.15. The recording protocols are detailed in the Experimental section.

3.4. Structure-activity relationships of PhlTx-1 using an alanine scanning mutagenesis approach

The SAR study was carried out on PhlTx-1 by replacing each amino acid of its sequence with an alanine residue which possesses a non-bulky and chemically inert methyl group, with two exceptions: the first amino acid which was a pyroglutamic acid-modified alanine, and the five C-terminal amino acids that were removed. This alanine scanning mutagenesis approach has thus the advantage to highlight the importance of amino acids in the peptide secondary structure.

Linear forms of all peptide mutants were synthesized and purified, and between 5.5 and 12.3 mg were obtained for each peptide (Table 3). The experimental conditions of their folding were similar to those used to perform the folding of PhlTx-1 (see section 3.1). However, only 8 over 21 mutants were obtained with the adequate biophysical characteristics. As observed for PhlTx-1, all of them equilibrated between two forms, depending on the temperature (only one peak was detected at the extreme temperatures of 0 and 60°C), and had CD spectra close to that of PhlTx-1 (data not shown). The 13 other mutants resulted in misfolded toxins (Table 3). This may be due to the fact that the substitution of amino acids produced changes in the peptide sequences that were in contact with the solvent or that the substituted amino acids were buried inside the peptide structure, which may affect dramatically the peptide folding properties.

Table 3. Production and biochemical and pharmacological characterizations of wild-type (WT) PhlTx1 and its mutants obtained by an alanine scanning mutagenesis approach.

PhlTx1	Production			Biochemical characterization			Pharmacological characterization	
	Linear (mg)	Oxidized (mg)	Folding yield	CD	Theo. mass	Exp. mass	$hNa_V1.7$ IC_{50} (nM)	Ratio (*vs* WT)
WT	150	17.3	12	OK	4055.72	4055.73	254	1.00
A1Z*	9.8	1.1	11	OK	4095.71	4095.71	171	0.67
L3A	5.3	0	0					
Q5A	12.5	0	0					
W6A	11.3	0	0					
D7A	12.1	2.5	21	OK	4011.73	4011.72	47	0.18
S8A	9.9	0.55	6	OK	4039.72	4039.70	180	0.71
D10A	8.5	0	0					
P11A	7.3	0	0					
K12A	9.5	0.75	8	OK	3998.66	3998.67	253	1.00
S14A	9.4	0	0					
K15A	8.6	1.1	13	OK	3998.66	3998.66	706	2.78
P18A	11	0	0					
N19A	12.3	0	0					
Y20A	14.2	0	0					
E23A	7.8	0	0					
W24A	9	1.1	12	OK	3940.68	3940.68	> 10000	> 39.37
K25A	9.2	2	22	OK	3998.66	3998.67	> 10000	> 39.37
Y26A	11.1	2.5	23	OK	3963.69	3963.68	> 10000	> 39.37
P27A	11.5	0	0					
W28A	5.5	0	0					
Delta-C-ter**	9.7	0	0					

**Z pyroglutamic acid; **PhlTx-1 without its five last C-terminal residues; Theo. Mass: theoretical mass; Exp. Mass: experimental mass.*

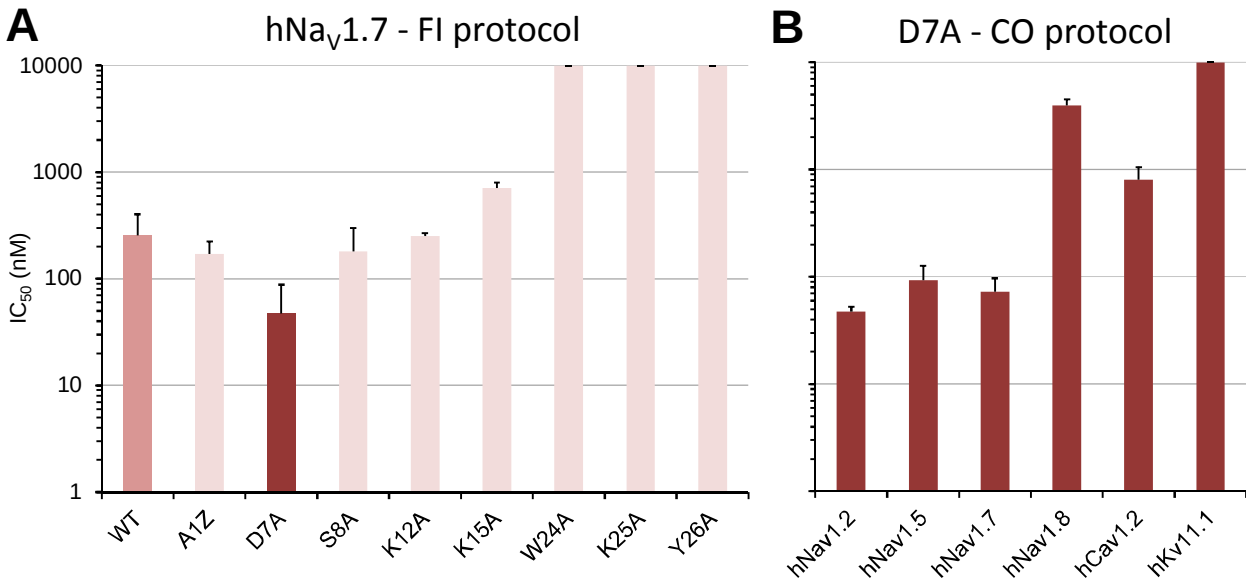

Figure 4. Structure-activity relationships of PhlTx-1 using an alanine scanning mutagenesis approach. (**A**) Effects of PhlTx-1 wild-type (WT) and mutants on HEK-293 cells overexpressing the $hNa_V1.7$ subtype. Histogram of IC_{50} values (in nM) obtained from the concentration-response curves of peptide effects on the current recorded during a "fully inactivated" (FI) protocol. Each value represents the mean ± S.D. of data obtained from 3-5 cells. Mean value ± S.D. of n_H was 0.99 ± 0.42. (**B**) Effects of D7A-PhlTx-1 on HEK-293 cells overexpressing $hNa_V1.2$, 1.5 and 1.7-1.8 subtypes and on CHO cells overexpressing $hCa_V1.2$ and $hK_V11.1$ subtypes. Histogram of IC_{50} values (in nM) obtained from the concentration-response curves of peptide effects on the currents recorded during a "closed-open" (CO) protocol. Each value represents the mean ± S.D. of data obtained from 3 cells. Mean value ± S.D. of n_H was 1.06 ± 0.13.

The substitution of amino acids close to the peptide C-terminus with alanine produced a loss of affinity for the $hNa_V1.7$ subtype, whereas the mutations more close to the peptide N-terminus had either little effect on this affinity or even induced a gain of affinity, as observed for D7A-PhlTx-1 which had a ratio of 0.18 *versus* PhlTx-1 (Figure 4A and Table 3). Indeed, this mutant, compared to PhlTx-1, had a 4.2-fold higher affinity for the $hNa_V1.7$ and 1.5 subtypes [73.0 ± 23.7 nM *versus* 308.9 ± 17.0 nM (n = 3), and 93.3 ± 32.9 nM *versus* 395.6 ± 121.6 nM (n = 2-3), respectively], a 5.9-fold higher affinity for the $hNa_V1.2$ subtype [47.3 ± 5.2 nM *versus* 279.4 ± 6.1 (n = 3)], and at least 2.5- and 7.4-fold higher affinities for the $hNa_V1.8$ and $hCa_V1.2$ subtypes, respectively [4.0 ± 0.5 µM *versus* > 10 µM (n = 3-4), and 799.6 ± 253.3 nM *versus* 5.9 ± 2.2 µM (n = 3-6), respectively], while an absence of affinity still remained for the $K_V11.1$ subtype (Figures 3B and 4B).

3.5. Effects of PhlTx-1 on OD1-induced painful behavior of mice

The *in vivo* analgesic effects of PhlTx-1 were studied on mouse model of $Na_V1.7$-mediated pain, based on intraplantar injection of OD1. When PBS containing only OD1 (300 nM) was injected to mice, the animal pain behavior, quantified the number of spontaneous licking, flinching, shaking and biting of the paw, reached a maximal value between 5 and 10 minutes following the injection and then disappeared progressively over 40 minutes. Under these conditions, the pain behavior occurring during the first 10 minutes following PBS and OD1 injection was 117.2 ± 15.8 (n = 6). This pain behavior was not significantly modified by the co-injection of PBS, OD1 (300 nM) and 3 or 30 nM PhlTx-1, *i.e.* 124.5 ± 17.0 (n = 6) and 117.5 ± 18.3 (n = 6), respectively (Figure 5). In contrast, the co-injection with 300 nM PhlTx-1 produced a 2-fold decrease of mouse pain behavior (*i.e.* 56.7 ± 17.2, n = 6), indicating that this peptide concentration reversed, to some extent, the OD1-induced pain (Figure 5).

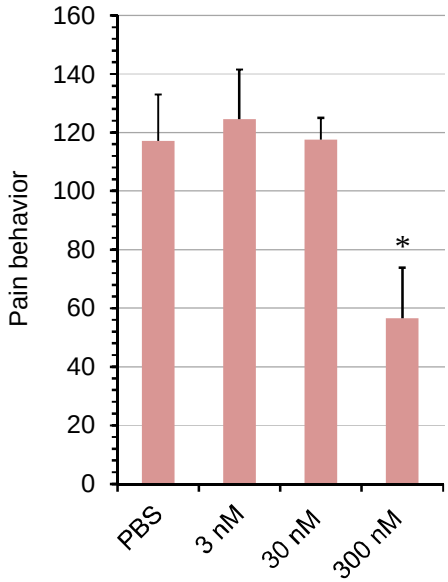

Figure 5. Effects of PhlTx-1 on OD1-induced painful behavior of mice. Pain behavior was quantified by the number of spontaneous licking, flinching, shaking and biting of the paw occurring during the first 10 minutes following intraplantar injection of PBS + 300 nM OD1, added or not with 3, 30 or 300 nM PhlTx-1. Mean ± S.E.M. of 6 mice under each condition. **P* = 0.014 *versus* PBS.

4. DISCUSSION

The present study was undertaken to better characterize PhlTx-1, previously described as a potential antinociceptive agent, in order to consolidate the clinical development of this peptide. The research strategy consisted of *(1)* a home-made chemical synthesis and a computational

modelling of 3D-structure to better understand the peptide effects already studied for closely-related toxins, *(2)* a deep pharmacological evaluation (from individual cells to *in vivo*) of synthetic PhlTx-1, and *(3)* a SAR study carried out on PhlTx-1, using an alanine scanning mutagenesis approach, to improve the peptide affinity and selectivity.

The effects of synthetic PhlTx-1 were studied on HEK-293 cells overexpressing $hNa_V1.1$-1.8 subtypes and on CHO cells overexpressing $hCa_V1.2$ and $hK_V11.1$ subtypes, using whole-cell automated patch-clamp technique. This studied was undertaken *(i)* to reinforce, on human Na_V subtypes, the previous evaluation of the peptide selectivity profile performed on undetailed species of Na_V subtypes, and *(ii)* to ensure its cardiac safety properties. More than ten years ago, the effects of PhlTx-1 were studied on different Na_V subtypes expressed with the β1 subunit in *Xenopus* oocytes (Bosmans et al., 2005, Escoubas et al., 2006). At a concentration of 1 µM, the peptide produced a more than 90% inhibition of $Na_V1.7$ current, a 35-39% inhibition of $Na_V1.4$ and 1.6 currents, and a less than 10% inhibition of $Na_V1.1$-1.3, 1.5 and 1.8 currents, as well as of *Drosophila* Para/TipE current. The comparison of these results obtained from undetailed or *Drosophila* species of Na_V subtypes expressed in *Xenopus* oocytes with those we got from human Na_V subtypes stably overexpressed in mammalian cell lines is not accurate, although similar mean IC_{50} values were determined for PhlTx-1 interaction with the $Na_V1.7$ subtype (*i.e.* 260 and 254-309 nM, respectively). Therefore, this study allows confirming both the peptide efficacy on the human $Na_V1.7$ subtype and some of its cardiac safety properties since the two cardiac $hCa_V1.2$ and $hK_V11.1$ targets were relatively saved (*i.e.* $IC_{50} \geq 5.9$ µM).

Compared to toxins belonging to the NaSpTx family 1, such as HnTx-I, HnTx-III, Hd1a, HnTx-IV, ProTx-III, Cm1a, GpTx-1 and HwTx-IV, previously reported in the literature to interact with the $hNa_V1.7$ subtype, PhlTx-1 is among the lowest potent peptides (Xiao et al., 2008; Liu et al., 2012; Liu et al., 2013; Cardoso et al., 2015; Klint et al., 2015a; Klint et al., 2015b; Murray et al., 2015; Murray et al., 2016; Shcherbatko et al., 2016). In addition, the peptide displayed a less than 10-fold selectivity towards the TTX-R (with the exception of $hNa_V1.8$) and other TTX-S (with the exception of $hNa_V1.4$) hNa_V subtypes (mean IC_{50} values between 74 and 711 nM). It is worth noting that relatively similar IC_{50} values were obtained from the "fully-inactivated" and classical "closed-open" protocols, suggesting that no inactivated-state-dependent effect of PhlTx-1 occurred on the studied hNa_V subtypes. The poor peptide selectivity towards the $hNa_V1.1$ and 1.3 subtypes may be an advantage since these two subtypes have been reported to be also involved in in pain pathways (see Gonçalves et al., 2018b). That towards the $hNa_V1.2$ subtype, located at the level of the central nervous system, will have no important consequence taking into account the peripheral administration of PhlTx-1. Therefore, the only problem of the peptide is its poor selectivity towards the $hNa_V1.5$ and 1.6 subtypes since its potential use as an analgesic molecule may be associated with *in vivo* cardiac and neuromuscular side-effects, respectively.

The antinociceptive properties as well as the cardiac and neuromuscular side-effects of PhlTx-1 were evaluated *in vivo* on OD1-induced painful behavior of mice. The results revealed that the intraplantar co-injection of OD1 and PhlTx-1 (300 nM) was efficient to produce a 2-fold decrease of animal pain behavior induced by the injection of only OD1. These results indicate that PhlTx-1

exhibited antinociceptive properties since this peptide concentration reversed, to some extent, the OD1-induced pain. Further experiments are needed to test whether higher PhlTx-1 concentrations will be able to completely reverse the OD1-induced pain. Interestingly, no sign of cardiac and neuromuscular side-effects was detected during these experiments. This strongly suggests that, under our experimental conditions, the poor peptide selectivity towards the $hNa_V1.5$ and 1.6 subtypes has no consequence *in vivo*. PhlTx-1 was previously reported to produce, although with lower efficiency than morphine, anti-allodynies and analgesic effects in rodent models of acute and inflammatory neuropathic pain (Escoubas et al., 2006). The effects of 9 toxins, showing higher affinity than PhlTx-1 for the $hNa_V1.7$ subtype [with the following increasing order for mean IC_{50} values (between 0.9 and 130 nM): Pn3a, Df1a-NH_2, m3-HwTx-IV, GpTx-1, ProTx-III, Cd1a, Df1a-OH, CcoTx2 and CcoTx1], were also tested *in vivo* on OD1-induced painful behavior of mice (Cardoso et al., 2015; Murray et al., 2015; Shcherbatko et al., 2016; Cardoso et al., 2017; Deuis et al., 2016, 2017; Rahmana et al., 2017; Sousa et al., 2017; Agwa et al., 2018). Although Pn3a has the highest affinity for the $hNa_V1.7$ subtype, close doses of intraperitoneal injection of this toxin and intraplantar injection of PhlTx-1 have similar effects on OD1-induced painful behavior of mice. This questions the existence of a correlation between a peptide $hNa_V1.7$ affinity and its *in vivo* effects on OD1-induced pain rodent models. The evaluation of m3-HwTx-IV, GpTx-1 and ProTx-III, performed under similar experimental conditions as that of PhlTx-1, revealed that these toxins produced a 10-, 5- and 2-fold decrease of animal pain behavior induced by OD1, respectively. However, marked neuromuscular side-effects were reported for m3-HwTx-IV and GpTx-1. The other 5 toxins were also efficient to diminish or completely reverse the OD1-induced manifestations of pain but at relatively high concentrations (1 µM for Cd1a, CcoTx1 and CcoTx2 and 10 µM for Df1a-NH_2 and Df1a-OH). Recently, a synergistic action between PhlTx-1 or Pn3a and low, non-therapeutic doses of opioids (such as oxycodone or buprenorphine) or enkephalinase inhibitors (such as thiorphan) was revealed to induce analgesia during the phase II of inflammatory pain. From this point of view, PhlTx-1 was reported to be more efficient than Pn3a (Patent # WO 2015036734 A1, 2015; Emery et al., 2016; Deuis et al., 2017).

The relatively low affinity of PhlTx-1 for the $hNa_V1.7$ subtype motivated a SAR study using an alanine scanning mutagenesis approach. Among the 8 peptide mutant forms tested on HEK-293 cells overexpressing the $hNa_V1.7$ subtype, D7A-PhlTx-1 was the only one showing an approximately 5-fold improved affinity for this subtype (mean IC_{50} values of 47-73 nM for D7A-PhlTx-1 *versus* 254-309 nM for PhlTx-1). However, a gain of affinity (between 2.5- and 7.4-fold) was also observed not only for the $hNa_V1.2$ and 1.8 subtypes, but also for the $hNa_V1.5$ and $hCa_V1.2$ subtypes.

5. CONCLUSION

The results obtained from the exhaustive characterization of physicochemical and functional properties of PhlTx-1 and some of its mutants, on a wide range of ion channel subtypes, highlight a relatively interesting molecule, D7A-PhlTx-1, with improved affinity for the $hNa_V1.7$ subtype. Further experiments are needed to improve the mutant selectivity and to study its effects on the

633 OD1-induced painful behavior of mice and/or its synergistic action with non-therapeutic doses of
634 opioids or enkephalinase inhibitors.

635

636 **ACKNOWLEDGMENTS –**T.C.G. was supported by a doctoral CIFRE fellowship from Sanofi. The
637 authors wish to thank Enrico A. Stura (SIMOPRO, CEA of Saclay, France) for PhlTx-1 3D-structure
638 modelling, and Andrees Bohme and Brigitte Schombert (Sanofi R&D, Vitry-sur-Seine, France) for
639 their help in experiments regarding cardiosafety issue.

640

641 **CONFLICT OF INTEREST –** The author, T.C. Gonçalves, declares the following competing interest:
642 current or former employees of Sanofi.

643

644 **REFERENCES**

645 Agwa, A.J., Peigneur, S., Chow, C.Y., Lawrence, N., Craik, D.J., Tytgat, J., King, G.F., Henriques, S.T., and
646 Schroeder, C.I. (2018). Gating modifier toxins isolated from spider venom: Modulation of voltage-gated
647 sodium channels and the role of lipid membranes. J Biol Chem 293, 9041-9052.

648 Bell, D.C., and Dallas, M.L. (2017). Using automated patch clamp electrophysiology platforms in pain-
649 related ion channel research: insights from industry and academia. Br J Pharmacol.

650 Bennett, D.L., and Woods, C.G. (2014). Painful and painless channelopathies. Lancet Neurol 13, 587-599.

651 Bosmans, F., Escoubas, P., Diochot, S., Mebs, D., Craik, D., Hill, J., Nakajima, T., Lazdunski M., and Tytgat, J.
652 (2005). Isolation and characterization of Phlotoxin 1 (PhlTx1), a novel peptide active on voltage-gated
653 sodium channels. Dans: 13èmes Rencontres en Toxinologie "Toxines et douleur" organisées par la
654 Société Française pour l'Etude des Toxines, Paris, 1 et 2 décembre 2005. Recueil des abstracts, p. 12.

655 Cardoso, F.C., Dekan, Z., Rosengren, K.J., Erickson, A., Vetter, I., Deuis, J.R., Herzig, V., Alewood, P.F., King,
656 G.F., and Lewis, R.J. (2015). Identification and Characterization of ProTx-III [mu-TRTX-Tp1a], a New
657 Voltage-Gated Sodium Channel Inhibitor from Venom of the Tarantula Thrixopelma pruriens. Mol
658 Pharmacol 88, 291-303.

659 Cardoso, F.C., Dekan, Z., Smith, J.J., Deuis, J.R., Vetter, I., Herzig, V., Alewood, P.F., King, G.F., and Lewis, R.J.
660 (2017). Modulatory features of the novel spider toxin mu-TRTX-Df1a isolated from the venom of the
661 spider Davus fasciatus. Br J Pharmacol 174, 2528-2544.

662 De Lera Ruiz, M., and Kraus, R.L. (2015). Voltage-Gated Sodium Channels: Structure, Function,
663 Pharmacology, and Clinical Indications. J Med Chem 58, 7093-7118.

664 Deuis, J.R., Dekan, Z., Wingerd, J.S., Smith, J.J., Munasinghe, N.R., Bhola, R.F., Imlach, W.L., Herzig, V.,
665 Armstrong, D.A., Rosengren, K.J., Bosmans, F., Waxman, S.G., Dib-Hajj, S.D., Escoubas, P., Minett, M.S.,
666 Christie, M.J., King, G.F., Alewood, P.F., Lewis, R.J., Wood, J.N., and Vetter, I. (2017). Pharmacological
667 characterisation of the highly NaV1.7 selective spider venom peptide Pn3a. Sci Rep 7, 40883.

668 Deuis, J.R., Wingerd, J.S., Winter, Z., Durek, T., Dekan, Z., Sousa, S.R., Zimmermann, K., Hoffmann, T.,
669 Weidner, C., Nassar, M.A., Alewood, P.F., Lewis, R.J., and Vetter, I. (2016). Analgesic Effects of GpTx-1,
670 PF-04856264 and CNV1014802 in a Mouse Model of NaV1.7-Mediated Pain. Toxins (Basel) 8.

671 Emery, E.C., Luiz, A.P., and Wood, J.N. (2016). Nav1.7 and other voltage-gated sodium channels as drug
672 targets for pain relief. Expert Opin Ther Targets 20, 975-983.

673 Escoubas, P., Bosmans, F., Cuypers, E., Diochot, S., Mebs, D., Craik, D., Hill, J., Nakajima, T., Lazdunski M.,
674 and Tytgat, J. (2006). Phlotoxin-1, a toxin from tarantula venom, is a potent modulator of $Na_V1.7$ sodium
675 channels and a potential analgesic. In: 15th World congress on Animal, plant & microbial toxins
676 organized by the International Society on Toxinology, Glasgow, Scotland, 23-28 July 2006. *Abstract book*,
677 p. 220.

678 Flinspach, M., Xu, Q., Piekarz, A.D., Fellows, R., Hagan, R., Gibbs, A., Liu, Y., Neff, R.A., Freedman, J., Eckert,
679 W.A., Zhou, M., Bonesteel, R., Pennington, M.W., Eddinger, K.A., Yaksh, T.L., Hunter, M., Swanson, R.V.,
680 and Wickenden, A.D. (2017). Insensitivity to pain induced by a potent selective closed-state Nav1.7
681 inhibitor. Sci Rep 7, 39662.

682 Goldberg, D.S., and Mcgee, S.J. (2011). Pain as a global public health priority. BMC Public Health 11, 770.

683 Gonçalves, T.C., Benoit, E., Kurz, M., Lucarain, L., Fouconnier, S., Combemale, S., Jaquillard, L., Schombert,
684 B., Chambard, J.-M., Boukaiba, R., Hessler, G., Bohme, A., Bialy, L., Hourcade, S., Béroud, R., De Waard,
685 M., Servent, S., and Partiseti, M. (2018a). Cyriotoxin-1a, the first toxin from Cyriopagopus schioedtei
686 spider with antinociceptive properties: from identification to functional characterization. Br J Pharmacol
687 (in revision).

688 Gonçalves, T.C., Benoit, E., Partiseti, M., and Servent, D. (2018b). The NaV1.7 Channel Subtype as an
689 Antinociceptive Target for Spider Toxins in Adult Dorsal Root Ganglia Neurons. Front Pharmacol 9, 1000.

690 Gonçalves, T.C., Boukaiba, R., Molgo, J., Amar, M., Partiseti, M., Servent, D., and Benoit, E. (2018c). Direct
691 evidence for high affinity blockade of NaV1.6 channel subtype by huwentoxin-IV spider peptide, using
692 multiscale functional approaches. Neuropharmacology 133, 404-414.

693 Herzig, V., Wood, D.L., Newell, F., Chaumeil, P.A., Kaas, Q., Binford, G.J., Nicholson, G.M., Gorse, D., and
694 King, G.F. (2011). ArachnoServer 2.0, an updated online resource for spider toxin sequences and
695 structures. Nucleic Acids Res 39, D653-657.

696 Klint, J.K., Castro, J., Vetter, I., Er, S.Y., Cardoso, F., Liu, Y., Hagan, R., Neff, R., Minassian, N., Huang, J.X.,
697 Cooper, M.A., Wickenden, A., Mobli, M., Jin, L., Nicolazzo, J.A., Lewis, R.J., Bosmans, F., Brierley, S.M.,
698 and King, G.F. (2015a). Nav1.7 inhibitors normalise mechanical responses in chronic visceral
699 hypersensitivity. Submitted to Protein Data Bank.

700 Klint, J.K., Smith, J.J., Vetter, I., Rupasinghe, D.B., Er, S.Y., Senff, S., Herzig, V., Mobli, M., Lewis, R.J.,
701 Bosmans, F., and King, G.F. (2015b). Seven novel modulators of the analgesic target NaV 1.7 uncovered
702 using a high-throughput venom-based discovery approach. Br J Pharmacol 172, 2445-2458.

703 Liu, Y., Li, D., Wu, Z., Li, J., Nie, D., Xiang, Y., and Liu, Z. (2012). A positively charged surface patch is
704 important for hainantoxin-IV binding to voltage-gated sodium channels. J Pept Sci 18, 643-649.

705 Liu, Y., Tang, J., Zhang, Y., Xun, X., Tang, D., Peng, D., Yi, J., Liu, Z., and Shi, X. (2014). Synthesis and analgesic
706 effects of mu-TRTX-Hhn1b on models of inflammatory and neuropathic pain. Toxins (Basel) 6, 2363-
707 2378.

708 Liu, Z., Cai, T., Zhu, Q., Deng, M., Li, J., Zhou, X., Zhang, F., Li, D., Li, J., Liu, Y., Hu, W., and Liang, S. (2013).
709 Structure and function of hainantoxin-III, a selective antagonist of neuronal tetrodotoxin-sensitive
710 voltage-gated sodium channels isolated from the Chinese bird spider Ornithoctonus hainana. J Biol
711 Chem 288, 20392-20403.

712 Meir, A., Cherki, R.S., Kolb, E., Langut, Y., and Bajayo, N. (2012). Novel peptides isolated from spider
713 venom, and uses thereof. Submitted to UniProtKB.

714 Minassian, N.A., Gibbs, A., Shih, A.Y., Liu, Y., Neff, R.A., Sutton, S.W., Mirzadegan, T., Connor, J., Fellows, R.,
715 Husovsky, M., Nelson, S., Hunter, M.J., Flinspach, M., and Wickenden, A.D. (2013). Analysis of the
716 structural and molecular basis of voltage-sensitive sodium channel inhibition by the spider toxin
717 huwentoxin-IV (mu-TRTX-Hh2a). J Biol Chem 288, 22707-22720.

718 Molinski, T.F., Dalisay, D.S., Lievens, S.L., and Saludes, J.P. (2009). Drug development from marine natural
719 products. Nat Rev Drug Discov 8, 69-85.

720 Murray, J.K., Ligutti, J., Liu, D., Zou, A., Poppe, L., Li, H., Andrews, K.L., Moyer, B.D., Mcdonough, S.I.,
721 Favreau, P., Stocklin, R., and Miranda, L.P. (2015). Engineering potent and selective analogues of GpTx-1,
722 a tarantula venom peptide antagonist of the Na(V)1.7 sodium channel. J Med Chem 58, 2299-2314.

723 Murray, J.K., Long, J., Zou, A., Ligutti, J., Andrews, K.L., Poppe, L., Biswas, K., Moyer, B.D., Mcdonough, S.I.,
724 and Miranda, L.P. (2016). Single Residue Substitutions That Confer Voltage-Gated Sodium Ion Channel
725 Subtype Selectivity in the NaV1.7 Inhibitory Peptide GpTx-1. J Med Chem 59, 2704-2717.

726 Negus, S.S. (2018). Addressing the Opioid Crisis: The Importance of Choosing Translational Endpoints in
727 Analgesic Drug Discovery. Trends Pharmacol Sci 39, 327-330.

728 Pan, H.L., Wu, Z.Z., Zhou, H.Y., Chen, S.R., Zhang, H.M., and Li, D.P. (2008). Modulation of pain transmission
729 by G-protein-coupled receptors. Pharmacol Ther 117, 141-161.

730 Rahnama, S., Deuis, J.R., Cardoso, F.C., Ramanujam, V., Lewis, R.J., Rash, L.D., King, G.F., Vetter, I., and
731 Mobli, M. (2017). The structure, dynamics and selectivity profile of a NaV1.7 potency-optimised
732 huwentoxin-IV variant. PLoS One 12, e0173551.

733 Savage, S.R., Kirsh, K.L., and Passik, S.D. (2008). Challenges in using opioids to treat pain in persons with
734 substance use disorders. Addict Sci Clin Pract 4, 4-25.

735 Shcherbatko, A., Rossi, A., Foletti, D., Zhu, G., Bogin, O., Galindo Casas, M., Rickert, M., Hasa-Moreno, A.,
736 Bartsevich, V., Crameri, A., Steiner, A.R., Henningsen, R., Gill, A., Pons, J., Shelton, D.L., Rajpal, A., and
737 Strop, P. (2016). Engineering Highly Potent and Selective Microproteins against Nav1.7 Sodium Channel
738 for Treatment of Pain. J Biol Chem 291, 13974-13986.

739 Sousa, S.R., Wingerd, J.S., Brust, A., Bladen, C., Ragnarsson, L., Herzig, V., Deuis, J.R., Dutertre, S., Vetter, I.,
740 Zamponi, G.W., King, G.F., Alewood, P.F., and Lewis, R.J. (2017). Discovery and mode of action of a novel
741 analgesic beta-toxin from the African spider Ceratogyrus darlingi. PLoS One 12, e0182848.

742 Spray, D.C., and Hanani, M. (2017). Gap junctions, pannexins and pain. Neurosci Lett.

743 Vetter, I., Deuis, J.R., Mueller, A., Israel, M.R., Starobova, H., Zhang, A., Rash, L.D., and Mobli, M. (2017).
744 NaV1.7 as a pain target - From gene to pharmacology. Pharmacol Ther 172, 73-100.

745 Wang, M., Rong, M., Xiao, Y., and Liang, S. (2012). The effects of huwentoxin-I on the voltage-gated sodium
746 channels of rat hippocampal and cockroach dorsal unpaired median neurons. Peptides 34, 19-25.

747 Waxman, S.G., and Zamponi, G.W. (2014). Regulating excitability of peripheral afferents: emerging ion
748 channel targets. Nat Neurosci 17, 153-163.

749 Wingerd, J.S., Mozar, C.A., Ussing, C.A., Murali, S.S., Chin, Y.K., Cristofori-Armstrong, B., Durek, T., Gilchrist,
750 J., Vaughan, C.W., Bosmans, F., Adams, D.J., Lewis, R.J., Alewood, P.F., Mobli, M., Christie, M.J., and
751 Rash, L.D. (2017). The tarantula toxin beta/delta-TRTX-Pre1a highlights the importance of the S1-S2
752 voltage-sensor region for sodium channel subtype selectivity. Sci Rep 7, 974.

753 Xiao, Y., Bingham, J.P., Zhu, W., Moczydlowski, E., Liang, S., and Cummins, T.R. (2008). Tarantula
754 huwentoxin-IV inhibits neuronal sodium channels by binding to receptor site 4 and trapping the domain
755 ii voltage sensor in the closed configuration. J Biol Chem 283, 27300-27313.

756 Yekkirala, A.S., Roberson, D.P., Bean, B.P., and Woolf, C.J. (2017). Breaking barriers to novel analgesic drug
757 development. Nat Rev Drug Discov 16, 545-564.

2.2.3. Résumé des résultats obtenus

D'un point de vue physico-chimique, la PhlTx-1 s'équilibre entre deux formes actives sur les canaux Na_V dont l'une des deux peut être favorisée par des variations de température. D'un point de vue fonctionnel, la PhlTx-1 inhibe les sous-types $hNa_V1.1$-1.3 et 1.5-1.7 à une concentration de l'ordre de la centaine de nanomolaires, les sous-types $hNa_V1.4$ et 1.8 à une concentration supérieure à 2,1 et 10 µM respectivement, et deux des trois principales cibles moléculaires cardiaques, $hCa_V1.2$ et $hK_V11.1$, à une concentration supérieure à 5,9 et 10 µM respectivement, quel que soit le protocole d'enregistrement utilisé, *i.e.* que le potentiel de maintien produise préalablement ou ne produise pas l'inactivation des canaux.

Une étude de "structure-activité" a été réalisée sur la PhlTx-1 en remplaçant chacun de ses acides aminés par une alanine qui possède une chaîne latérale méthyle non encombrante et chimiquement non chargée à pH neutre mais apolaire, ce qui a permis de mettre en évidence l'importance des autres acides aminés dans la fonction du peptide et définir ainsi son pharmacophore. Cette approche "alanine scanning" a été faite à deux exceptions près: le premier acide aminé, qui était une alanine modifiée par un acide pyroglutamique, et 5 acides aminés en C-terminal qui ont été enlevés. Des 21 analogues peptidiques synthétiques ainsi créés, seuls 8 ont pu être oxydés et repliés. Le remplacement des acides aminés en C-terminal par une alanine a produit une perte de puissance de la toxine pour le sous-type $hNa_V1.7$ alors que les mutations en N-terminal ont eu peu d'effet sur cette puissance, à l'exception de l'analogue D7A. En effet, pour cet analogue, nous avons observé un gain de puissance d'un facteur 4,2 pour les sous-types $hNa_V1.7$ et 1.5, d'un facteur 5,9 pour le sous-type $hNa_V1.2$ et d'un facteur 2,5 pour le sous-type $hNa_V1.8$, ainsi qu'une valeur d'IC_{50} proche de 1 µM pour le sous-type cardiaque $hCa_V1.2$.

Finalement, chez un modèle murin de douleur produite par l'OD1, une toxine du scorpion *Odonthobuthus doriae* qui inhibe plus spécifiquement l'inactivation du sous-type $hNa_V1.7$ (Deuis et al., 2016b), nous avons observé une diminution d'un facteur 2 des comportements douloureux des souris produits par cette toxine (nombre de léchages, de tremblements, de morsures…), pendant les 10 premières minutes suivant la co-injection d'OD1 (300 nM) et de PhlTx-1 (300 nM).

2.2.4. Conclusion

Les résultats obtenus de la caractérisation exhaustive des propriétés physico-chimiques et fonctionnelles de la PhlTx-1 et de certains de ses analogues peptidiques synthétiques, sur un large éventail de sous-types de canaux ioniques, mettent en évidence une molécule intéressante, l'analogue D7A, dont les effets sur les comportements douloureux des souris, produits par l'OD1, restent à être étudiés.

2.3. Mise en évidence d'un blocage de haute puissance du sous-type $Na_V1.6$ de canaux sodium par le peptide d'araignée huwentoxine-IV, en utilisant des approches fonctionnelles multi-échelles

2.3.1. Contexte de l'étude

Actuellement, une vingtaine de toxines sont décrites dans la littérature pour exercer un pouvoir antinociceptif en agissant de façon puissante et sélective sur le sous-type $Na_V1.7$ de canaux sodium (Vetter et al., 2017; Cardoso et al., 2018; Gonçalves et al., 2018a). Cependant, le manque de sélectivité des molécules vis-à-vis des autres sous-types de canaux sodium TTX-S est un problème pour leur développement thérapeutique. La sélectivité de ces molécules vis-à-vis du sous-type fœtal $Na_V1.3$ n'est pas requise car ce sous-type n'est exprimé chez l'adulte que lors de lésions nerveuses de type mécanique, inflammatoire ou neuropathique (Waxman et al., 1994; Black et al., 1999; Dib-Hajj et al., 1999; Boucher et al., 2000; Kim et al., 2001; Tan et al., 2015; Yang et al., 2016). La faible sélectivité des toxines vis-à-vis des sous-types TTX-S est à l'origine de troubles indésirables au niveau du système nerveux central (*via* l'inhibition de $Na_V1.1$, 1.2 et/ou 1.6) et du système neuromusculaire (*via* l'inhibition de $Na_V1.4$ et/ou 1.6). Les troubles indésirables au niveau du système neuromusculaire sont les plus souvent mentionnés dans la littérature car ils peuvent entrainer le décès des animaux par arrêt respiratoire lors des expérimentations. En effet, la voie d'administration des peptides se faisant majoritairement par voie i.m., intrapéritonéale (i.p.) ou intrapleurale (i.pl.), les sous-types de canaux ioniques exprimés dans le système nerveux central sont épargnés (Liu et al., 2014b; Liu et al., 2014c; Deuis et al., 2016b; Flinspach et al., 2017; Rahnama et al., 2017).

Parmi ces toxines, l'HwTx-IV est une des premières à avoir été bien caractérisée comme molécule potentiellement analgésique sur des modèles animaux (rongeurs) de douleur inflammatoire et neuropathique (Liu et al., 2014c). L'HwTx-IV est issue du venin de l'araignée-oiseau chinoise *Cyriopagopus schmidti*, plus connue sous le nom de *Haplopelma schmidti* (Schmidt, 2010), qui appartient à la sous-famille des Ornithoctoninae. Cette toxine peptidique 4113,9 Da est composée de 35 acides aminés, est structurée autour du motif architectural ICK et appartient à la famille NaSpTx-1 (Klint et al., 2012). L'HwTx-IV a été initialement identifiée comme étant un puissant inhibiteur du sous-type $Na_V1.7$ avec une forte sélectivité vis-à-vis du sous-type cardiaque $Na_V1.5$ et du sous-type du muscle squelettique $Na_V1.4$ de canaux sodium qui sont relativement insensibles au peptide (Xiao et al., 2008). Sa forte puissance est conservée pour les sous-types de canaux sodium TTX-S des

neurones de DRG de rat (IC_{50} = 30 nM; Peng et al., 2002). L'HwTx-IV, validée comme molécule analgésique par des tests sur des modèles rongeurs de douleur inflammatoire et neuropathique (Liu et al., 2014c), semblait donc prometteuse comme agent thérapeutique. Cependant, peu d'informations existaient dans la littérature concernant l'interaction du peptide avec le sous-type neuronal $Na_V1.6$ de canaux sodium présent, plus particulièrement, au niveau des neurones de DRG et des nœuds de Ranvier des motoneurones α, et concernant donc les effets secondaires indésirables résultant de cette interaction *in vivo* (Rahnama et al., 2017).

Lors de notre étude des effets fonctionnels de la CyrTx-1a (voir sous-partie 2.1), notre attention a été attirée par les altérations relativement importantes provoquées par l'HwTx-IV au niveau des propriétés d'excitabilité du système neuromusculaire de souris *in vivo*. Nous avons donc entrepris une étude afin de déterminer la puissance de cette toxine vis-à-vis du sous-type $Na_V1.6$ de canaux sodium, en utilisant des approches fonctionnelles multi-échelles (de l'organisme *in vivo* à la cellule unique).

2.3.2. Publication n°4

Neuropharmacology (2018) 133 : 404-414

"Direct evidence for high affinity blockade of $Na_V1.6$ channel subtype by huwentoxin-IV spider peptide, using multiscale functional approaches"

Tânia C. Gonçalves, Rachid Boukaiba, Jordi Molgó, Muriel Amar, Michel Partiseti, Denis Servent & Evelyne Benoit

Neuropharmacology 133 (2018) 404–414

Contents lists available at ScienceDirect

Neuropharmacology

journal homepage: www.elsevier.com/locate/neuropharm

Direct evidence for high affinity blockade of $Na_V1.6$ channel subtype by huwentoxin-IV spider peptide, using multiscale functional approaches

Tânia C. Gonçalves [a, b], Rachid Boukaiba [a], Jordi Molgó [b, c], Muriel Amar [b], Michel Partiseti [a], Denis Servent [b], Evelyne Benoit [b, c, *]

[a] Sanofi R & D, Integrated Drug Discovery, In Vitro Biology & Pharmacology, F-94440, Vitry-sur-Seine, France
[b] Service d'Ingénierie Moléculaire des Protéines (SIMOPRO), CEA, Université Paris-Saclay, F-91191, Gif sur Yvette, France
[c] Institut des Neurosciences Paris-Saclay (Neuro-PSI), UMR CNRS/Université Paris-Sud 9197, Université Paris-Saclay, F-91198, Gif sur Yvette, France

ARTICLE INFO

Article history:
Received 27 October 2017
Received in revised form
16 January 2018
Accepted 19 February 2018
Available online 21 February 2018

Keywords:
Huwentoxin-IV
Voltage-gated sodium channels
Na_V channel subtypes
Electrophysiology
Mouse neuromuscular excitability
Mouse dorsal root ganglia neurons
Cell lines overexpressing Na_V channel subtypes

ABSTRACT

The Chinese bird spider huwentoxin-IV (HwTx-IV) is well-known to be a highly potent blocker of $Na_V1.7$ subtype of voltage-gated sodium (Na_V) channels, a genetically validated analgesic target, and thus promising as a potential lead molecule for the development of novel pain therapeutics. In the present study, the interaction between HwTx-IV and $Na_V1.6$ channel subtype was investigated using multiscale (from *in vivo* to individual cell) functional approaches. HwTx-IV was approximatively 2 times more efficient than tetrodotoxin (TTX) to inhibit the compound muscle action potential recorded from the mouse skeletal neuromuscular system *in vivo*, and 30 times more effective to inhibit nerve-evoked than directly-elicited muscle contractile force of isolated mouse hemidiaphragms. These results strongly suggest that the inhibition of nerve-evoked skeletal muscle functioning, produced by HwTx-IV, resulted from a toxin-induced preferential blockade of $Na_V1.6$, compared to $Na_V1.4$, channel subtype. This was confirmed by whole-cell automated patch-clamp experiments performed on human embryonic kidney (HEK)-293 cells overexpressing $hNa_V1.1-1.8$ channel subtypes. HwTx-IV was also approximatively 850 times more efficient to inhibit TTX-sensitive than TTX-resistant sodium currents recorded from mouse dorsal root ganglia neurons. Finally, based on our data, we predict that blockade of the $Na_V1.6$ channel subtype was involved in the *in vivo* toxicity of HwTx-IV, although this toxicity was more than 2 times lower than that of TTX. In conclusion, our results provide detailed information regarding the effects of HwTx-IV and allow a better understanding of the side-effect mechanisms involved *in vivo* and of channel subtype interactions resulting from the toxin activity.

1. Introduction

Pain treatment diversification remains a big health and economic concern, and animal venom peptides seem to be an original source of new antinociceptive drugs targeting ion channels implicated in pain signalling pathways. Their modest size, compact structure due to disulfide bridges, physicochemical resistance to enzyme degradation and tissue clearance make them good candidates (Saez et al., 2010). A FDA-approved painkiller is already commercialized as Prialt® since a decade. This peptide derived from a conus venom toxin, blocks the $Ca_V2.2$ subtype (N-type) of voltage-gated calcium (Ca_V) channels to relieve chronic pain of spinal cord injury non treatable by opioid therapy (Molinski et al., 2009). Unfortunately, the peptide administered *via* intrathecal injection induces severe side-effects which restrain its wider application (Wang et al., 2016). Even if Prialt® is still the only venom-derived drug approved for pain treatment, many other toxins entered in pre-clinical or clinical development due to their capacity to interact with major molecular targets of pain pathways, such as sodium, calcium, and acid-sensing ion channels, as well as nicotinic receptors (Netirojjanakul and Miranda, 2017).

Due to their major role in initiating and propagating action potentials, voltage-gated sodium (Na_V) channels are implicated in

* Corresponding author. Current address: CEA de Saclay, SIMOPRO, Bât. 152, 91191, Gif-sur-Yvette, France.
E-mail address: evelyne.benoit@cea.fr (E. Benoit).

https://doi.org/10.1016/j.neuropharm.2018.02.016
0028-3908/

Abbreviations

Ca_V	voltage-gated calcium channel
CHO	Chinese hamster ovary
CMAP	compound muscle action potential
DMEM	Dulbecco's modified Eagle's medium
DRG	dorsal root ganglia
ERG	*ether-a-go-go*-related gene
h	human
HEK	human embryonic kidney
HEPES	N-2-hydroxyethylpiperazine-N′-2-ethanesulfonic acid
HwTx-IV	huwentoxin-IV
i.m.	intramuscular
IC_{50}	toxin concentration necessary to inhibit 50% of the response
ICK	inhibitory cystine knot
K_V	voltage-gated potassium channel
NaSpTx	voltage-gated sodium channel spider toxin
Na_V	voltage-gated sodium channel
PBS	phosphate buffered saline
ProTx-II	protoxin-II
r	rat
TTX	tetrodotoxin
TTX-R	resistant to tetrodotoxin
TTX-S	sensitive to tetrodotoxin

numerous pain diseases. Some of these diseases can be directly linked to mutations of genes encoding the $Na_V1.7$ channel subtype, leading to either exacerbation of pain, such as inherited erythromelalgia, paroxysmal extreme pain disorder and small fiber neuropathy, or no pain sensation at all, such as congenital insensitivity to pain or type-IID hereditary sensory and autonomic neuropathy (de Lera Ruiz and Kraus, 2015; Vetter et al., 2016). Na_V channels are transmembrane proteins composed of a pore-forming α subunit constituted by four domains, each containing 6 transmembrane segments, the S1-S4 forming the voltage-sensing domain and the S5 connected to the S6 with an extracellular re-entrant P-loop constituting the ion-conducting pore (Goldin et al., 2000; Catterall, 2000; de Lera Ruiz and Kraus, 2015). The gating properties and turnover of Na_V channels may be modified by some members of the cell adhesion molecule superfamily, the β subunits, linked to the α subunit (Namadurai et al., 2015).

More than ten toxins have been reported so far to act selectively and potently on $Na_V1.7$ channel subtype (Vetter et al., 2016). Among these toxins, protoxin-II (β/ω-theraphotoxin-Tp2a or ProTx-II) and huwentoxin-IV (μ-theraphotoxin-Hs2a or HwTx-IV) have been well characterized (Xiao et al., 2014). HwTx-IV, extracted from the venom of the Chinese bird spider *Cyriopagopus schmidti*, formerly known as *Haplopelma schmidti* (Schmidt, 2010), is a 35 amino acid peptide, with an inhibitory cystine knot (ICK) architectural motif, belonging to Na_V channel spider toxin (NaSpTx) family 1 (Klint et al., 2012). HwTx-IV was first identified as a highly potent blocker of the genetically validated analgesic target $Na_V1.7$ channel subtype, showing in addition a marked selectivity for this channel subtype compared, in particular, to the heart channel subtype $Na_V1.5$ and the skeletal muscle channel subtype $Na_V1.4$ which were relatively resistant to the peptide (Xiao et al., 2008). Great efforts were then provided to link the promising toxin to an anti-nociceptive effect *via* Na_V channels. The first report introduced the toxin as having a high efficacy on tetrodotoxin (TTX)-sensitive Na_V channels located in rat dorsal root ganglia (DRG) neurons [toxin concentration necessary to inhibit 50% of the response (IC_{50}) of 30 nM] which are involved in pain pathway (Peng et al., 2002). More recently, HwTx-IV was reported to have analgesic effects in rodent inflammatory and neuropathic pain models (Liu et al., 2014a). The peptide was thus promising as a potential lead molecule for the development of novel pain therapeutics. However, until now, very few information was reported about the efficiency of HwTx-IV to interact with the $Na_V1.6$ channel subtype, a TTX-sensitive (TTX-S) Na_V channel subtype present in the brain, in DRG neurons and in Ranvier nodes of α–motoneurons, as well as the resulting *in vivo* side-effects resulting from this interaction (Rahnama et al., 2017). This point is very important since such interaction would, in particular, impair the neuromuscular system functioning, leading to the death of experimental animals, as previously suggested (Liu et al., 2014b; Flinspach et al., 2017; Rahnama et al., 2017; Deuis et al., 2016).

The present study was therefore undertaken to determine the interaction between HwTx-IV and $Na_V1.6$ channel subtype, using multiscale (from *in vivo* to individual cell) functional approaches. Our results provide detailed information regarding the effects of the peptide on the mouse neuromuscular system *in vivo*, on isolated mouse neuromuscular preparations, on mouse DRG neurons and on human embryonic kidney (HEK)-293 cells heterologously overexpressing the human (h) $Na_V1.6$ channel subtype, therefore providing a clue to understand the mechanisms of *in vivo* motor side-effects resulting from HwTx-IV and $Na_V1.6$ channel subtype interaction.

2. Material and methods

2.1. Toxins

Lyophilized synthetic HwTx-IV (molecular weight of 4106.811, purity rate > 97%) was obtained from Smartox Biotechnology (Saint Martin d'Hères, France). This toxin was dissolved in phosphate buffered saline (PBS 1×) solution to give a 2.5×10^{-2} g/mL (*i.e.* 6.1 mM) stock solution. TTX citrate (molecular weight of 319.27, purity rate > 98%) was purchased from Sigma-Aldrich (Saint-Quentin Fallavier, France). This toxin was dissolved in PBS 1× solution to give a 9×10^{-4} g/mL (*i.e.* 2.85 mM) stock solution. Just prior to experiments, successive dilutions were performed in the adequate standard physiological medium to give the HwTx-IV and TTX final concentrations indicated in the text.

2.2. Experimental animals

Adult female Swiss mice (10–12 weeks of age and 28–32 g body weight) were purchased from Janvier Elevage (Le Genest-Saint-Isle, France) and housed at the CEA animal facility. The experiments were performed in accordance with the guidelines established by the French Council on animal care "Guide for the Care and Use of Laboratory Animals" (EEC86/609 Council Directive – Decree, 2001–131), on mice under anaesthesia by means of isoflurane (AErrane®, Baxter S.A., Lessines, Belgique) inhalation. The experimental protocols were approved on November 27, 2015 by the French General Directorate for Research and Innovation (project APAFIS#2671-2015110915123958v3 authorized to E.B.).

2.3. Isolated mouse neuromuscular preparations

Mouse hemidiaphragms with their respective associated

phrenic nerve were rapidly and carefully dissected after anaesthesia (by isoflurane inhalation) and euthanasia (by cervical vertebrae dislocation) of mice. After removal, the isolated neuromuscular preparation was mounted on a silicone-lined organ bath (4 mL volume) filled with a standard physiological medium of the following composition (in mM): NaCl 145, KCl 5, $CaCl_2$ 2, $MgCl_2$ 1, D-glucose 11, and N-2-hydroxyethylpiperazine-N′-2-ethanesulfonic acid (HEPES) 5 (pH 7.4, adjusted with NaOH), continuously gassed with pure O_2 throughout the experiment.

2.4. Primary cultures of mouse DRG neurons

Mouse DRG were removed from the animal spinal cord, placed in iced-Ham's F-12 medium (Sigma-Aldrich) and enzymatically dissociated with collagenase type IA (2 mg/mL; Sigma-Aldrich) and dispase (5 mg/mL; Gibco, Thermo Fisher Scientific, Villebon-sur-Yvette, France). Neurons were then plated on 12-mm glass coverslips placed in a 24-wells plate coated with 10 μg/mL of poly-D-lysine and 100 μg/mL of murin laminin (Sigma-Aldrich). The cells were maintained in culture at 37 °C (in 95% air and 5% CO_2) in Neurobasal A medium (Gibco) containing horse serum (5%; Gibco), penicillin/streptomycin (47.64 U/mL; Gibco), nerve growth factor (83.33 ng/mL; Sigma-Aldrich), N2 supplement (3.18×; Gibco), Dulbecco's phosphate-buffered saline (1×) w/o $CaCl_2$ and $MgCl_2$ (1.68%; Gibco), bovine serum albumin (16.83 μg/mL; Sigma-Aldrich), corticosteron (214.85 nM; Sigma-Aldrich), T3 hormone (56.06 nM; Sigma-Aldrich) and L-glutamine (1.90 mM; Sigma-Aldrich). Cytosine β-D-arabinofuranoside (2 μM; Sigma-Aldrich) was added to the culture medium, 24 h later, to stop astrocyte proliferation.

Experiments were carried out within 2–6 days after cell plating. The day of their use, the neurons plated on coverslips were transferred, for a minimum of 30 min at 37 °C prior to manual patch-clamp recordings, in 35-mm Petri dishes filled with a standard physiological medium of the following composition (in mM): NaCl 134, KCl 3, $CaCl_2$ 1, $MgCl_2$ 1, D-glucose 10, tetraethylammonium chloride (TEA) 10, $CdCl_2$ 0.1, and HEPES 10 (pH 7.35, adjusted with NaOH), and then in the recording bath filled with the standard physiological medium.

2.5. HEK-293 and Chinese hamster ovary (CHO) cell line cultures

HEK-293 cells heterologously overexpressing $hNa_V1.7$ (Eurofins, Discovery Services, St Charles, MO, USA) were cultured in suspension in FreestyleTM293 (Gibco; #12338–018). Those overexpressing $hNa_V1.1$ (Eurofins), $hNa_V1.6$ (ChanTest, Cleveland, OH, USA) or $hNa_V1.8$ (Eurofins) were cultured in Dulbecco's modified Eagle's medium (DMEM)/F-12 nutrient mixture with GlutaMAX™ supplement (Gibco; #31331), those overexpressing $hNa_V1.2$ (SB Drug Discovery, Glasgow, United Kingdom) and $hNa_V1.5$ (Sanofi, Frankfurt, Germany) in DMEM with GlutaMAX™ supplement (Gibco; #31966), and those overexpressing $hNa_V1.3$ and 1.4 (SB Drug Discovery) in minimum essential medium (Sigma-Aldrich; #M5650). CHO cells heterologously overexpressing $hCa_V1.2/\beta2/\alpha2\delta1$ (ChanTest, Cleveland, OH, USA) were cultured in Ham's F12 nutrient mix with GlutaMAX™ medium (Gibco; #31765). Those overexpressing the voltage-gated potassium (K_V) channel subtype $hK_V11.1$ (B'SYS GmbH, Switzerland), encoded by the human *ether-a-go-go*-related gene (hERG), were cultured in DMEM/F-12 nutrient mixture Ham's medium (Sigma; #D6434). All culture media contained fetal bovine serum (10% v/v) and selected antibiotics and additives, as recommended by the manufacturer. Cells were grown in flasks, in a humidified 5% CO_2 incubator at 37 °C, and subcultured/passaged every 3–4 days using TrypLE Select enzyme (Gibco).

For manual patch-clamp recordings, a few days before experiments, the cells were transferred on 12-mm glass coverslips placed in 35-mm Petri dishes. The day of their use, the culture medium was changed to a standard physiological medium, similar to that used for DRG neurons (see paragraph 2.4), for a minimum of 15 min at 37 °C prior to experiments. The cells plated on coverslips were then transferred in the recording bath filled with the standard physiological medium. For automated patch-clamp recordings, the day of their use, the cells were transferred in Eppendorf tubes containing a FreeStyle 293 expression medium (Gibco; #12338) which were then placed in the automated electrophysiology platform.

2.6. Electrophysiological recordings from the mouse neuromuscular system in vivo

Recordings from the neuromuscular system of anaesthetized mouse were obtained by means of a minimally-invasive electrophysiological method, using the Qtrac© software (Prof. H. Bostock, Institute of Neurology, London, United Kingdom), as previously detailed (Marrouchi et al., 2013). Briefly, the anaesthetized mice were placed on a heating pad to maintain body temperature throughout the experiments (between 35.94 ± 0.05 and 35.99 ± 0.03 °C, as determined in 29 mice using a rectal probe). Electrical stimulations were delivered to the caudal motor nerve (at the base of the tail) by surface electrodes, and the compound muscle action potential (CMAP) was recorded using needle-electrodes inserted into the tail muscle. To study the local action of HwTx-IV and TTX, intramuscular (i.m.) injections (4-μL maximal volume) of PBS 1× solution containing various concentrations of a given toxin were delivered with a 10-μL micro-syringe at the base of mouse tail, between stimulation and ground electrodes. Similar injections (4 μL) were also done with PBS 1× solution to test an eventual effect of the vehicle.

On-line recordings were initiated approximatively 5 min before a given injection to determine the toxin and/or vehicle effects on selected excitability parameters, such as the excitability threshold and CMAP amplitude continuously registered as a function of time. To better identify the underlying mechanism(s) of action and the duration of HwTx-IV and TTX effects, five different excitability tests (stimulus-response, strength-duration and current-threshold relationships, as well as threshold electrotonus and recovery cycle; detailed in Cerles et al., 2017) were performed together before and at various times (from ~30 min to ~12 h) after a given injection. As a whole, more than thirty parameters were determined from these five excitability tests, and analyzed. Most of them provide specific and complementary information on the density and functional status of ion channels, receptors and pumps, as well as on the passive membrane properties of the neuromuscular system (Kiernan and Bostock, 2000; Krishnan et al., 2008).

2.7. Mechanical recordings from isolated mouse neuromuscular preparations

Measurements of isometric contractile force (*i.e.* single twitch), elicited by stimulating the muscle either indirectly *via* the phrenic nerve or directly, were performed as previously described (Schlumberger et al., 2010). Briefly, the central tendon of the hemidiaphragm was attached to an isometric force displacement transducer (FT03 model; Grass Instruments, West Warwick, RI, USA) *via* an adjustable stainless-steel hook, and the other tendon (at the rib side) was securely anchored onto the silicone-coated bath. A mobile micrometer stage allowed adjusting the muscle length to obtain maximal contractile responses. The resting tension was monitored and kept constant throughout the experiment.

Electrical square pulses of 200 μs duration and supramaximal voltage (15–20 V for nerve stimulation and 80–100 V for direct stimulation) were delivered by a stimulator (S-48 model; Grass Instruments) at a frequency of 0.1 Hz. Signals from the force transducer were amplified, collected, and digitized with the aid of a computer equipped with an analog-to-digital converter (Digidata-1322A model; Molecular Devices, Sunnyvale, CA, USA) managed by the Axoscope 9.2 software (Molecular Devices). The collected signals were analyzed off-line using the Clampfit 9.2 program (Molecular Devices). The experiments were carried out at constant room temperature (22 °C).

2.8. Automated patch-clamp recordings from HEK-293 and CHO cells

Whole-cell automated patch-clamp experiments were performed on a QPatch HTX automated electrophysiology platform (Sophion Bioscience, Ballerup, Denmark), allowing both signal acquisition and data analyses (Bell and Dallas, 2017). The extracellular medium composition of hNa_V-overexpressing HEK293 cells was (in mM): NaCl 154, KCl 4, $CaCl_2$ 2, $MgCl_2$ 1, and HEPES 10 (pH 7.4, adjusted with NaOH), and that of intracellular (*i.e.* path-clamp pipette) medium: CsF 150, EGTA/CsOH 1/50, HEPES 10, NaCl 10, $MgCl_2$ 1, and $CaCl_2$ 1 (pH 7.4, adjusted with CsOH). The extracellular medium composition of $hCa_V1.2$-overexpressing CHO cells was (in mM): NaCl 145, KCl 4, $CaCl_2$ 10, and HEPES 10 (pH 7.4, adjusted with NaOH), and that of intracellular medium: CsF 27, CsCl 112, EGTA 8.2, HEPES 10, NaCl 2, and Mg-ATP 4 (pH 7.4, adjusted with CsOH). The extracellular medium composition of $hK_V11.1$-overexpressing CHO cells was (in mM): NaCl 145, KCl 4, $CaCl_2$ 2, $MgCl_2$ 1, HEPES 10, and D-glucose 10 (pH 7.4, adjusted with NaOH), and that of intracellular medium: KCl 120, $CaCl_2$ 5.4, EGTA 10, HEPES 10, Mg-ATP 4, and $MgCl_2$ 1.75 (pH 7.4, adjusted with KOH). HwTx-IV was diluted in the extracellular medium added with bovine serum albumin (0.1%), to give the final concentrations indicated in the text. The times of incubation varied between ~2 and ~7 min to achieve steady-state effects. The experiments were carried out at room temperature (20–22 °C).

The hNa_V-overexpressing HEK-293 cells were maintained at a holding potential of either −90 mV ($hNa_V1.5$) or −100 mV (other hNa_V channel subtypes). Currents were elicited at a frequency of 0.2 Hz by 20-ms test-pulses to −20 mV ($hNa_V1.1$, 1.2, 1.4, and 1.7), −10 mV ($hNa_V1.3$), −40 mV ($hNa_V1.5$), −15 mV ($hNa_V1.6$) or +10 mV ($hNa_V1.8$), preceded by 200-ms ($hNa_V1.5$) or 40-ms ($hNa_V1.7$) pulses to −120 mV, or not ($hNa_V1.1$, 1.2, 1.3, 1.4 and 1.6). The $hCa_V1.2$-overexpressing CHO cells were maintained at a holding potential of −50 mV, and currents were elicited at a frequency of 0.05 Hz by 200-ms test-pulses to +0 mV. The $hK_V11.1$-overexpressing CHO cells were maintained at a holding potential of −80 mV, and tail currents were elicited at a frequency of 0.07 Hz by 5-s test-pulses to −50 mV, preceded by 4.8-s pulses to +20 mV following 20-ms pulses to −50 mV. The concentration-response relationships were established by expressing the peak amplitude of the sum of ten cell currents recorded in the presence of a given HwTx-IV concentration relatively to that of the sum of these currents recorded before toxin incubation.

2.9. Manual patch-clamp recordings from HEK-293 cells and mouse DRG neurons

Whole-cell manual patch-clamp experiments were performed by using a MultiClamp 700B integrating patch-clamp amplifier and the pClamp10.6 software (Molecular Devices, Sunnyvale, CA, USA), as previously described (Schlumberger et al., 2014). The signals, acquired at a 4-kHz sample rate, were filtered at 2 kHz with a low-pass Bessel filter and digitized with the aid of a computer equipped with an analog-to-digital converter (Digidata-1440A model; Molecular Devices). The patch-clamp pipettes were filled with a medium composed of (in mM): CsCl 90, $CsMeSO_3$ 40, NaCl 10, $MgCl_2$ 2, EGTA 2, ATP-Na_2 4, and HEPES 10 (pH 7.32, adjusted with CsOH), and had ~3-MΩ resistance in the standard physiological medium. A fast perfusion system allowed changing the solution (standard physiological medium added or not with a given toxin concentration) around the recorded cell within a few seconds. The experiments were carried out at constant room temperature (22 °C).

The cells were maintained at a holding potential of −60 mV, and currents were elicited at a frequency of 0.5 Hz by 50-ms test-pulses to −20 mV (+10 mV for $hNa_V1.6$-overexpressing HEK-293 cells) preceded by 1-s pulses to −120 mV. The concentration-response relationships were established by expressing the peak current amplitude measured in the presence of a given toxin concentration relatively to that before toxin application. Current-voltage relationships were obtained by varying test-pulses from −80 to +10 mV in 5-mV increments, and steady-state inactivation-voltage relationships by changing pre-pulses from −120 to −20 mV in 5-mV increments.

2.10. Data and statistical analyses

Concentration-response relationships were established by plotting the response, recorded in the presence of a given toxin (Rt) and expressed as percentage of the value obtained in absence of toxin (Rc), against the toxin concentration ([toxin]). The theoretical concentration-response curves were calculated from typical sigmoid nonlinear regressions through data points (correlation coefficient $= r^2$) according to the Hill equation (GraphPad Prism 5 or QPatch assay software): $Rt/Rc = 1/[1 + ([toxin]/IC_{50})\ n_H]$, where n_H is the Hill number.

Conductance (g) was calculated according to the following equation: $g = I/(V_T - V_{Na})$, where I is the peak current amplitude, V_T is the test-pulse voltage, and V_{Na} is the equilibrium potential of Na ions. Conductance-voltage relationships were established by plotting the conductance, expressed as percentage of the maximal conductance (gmax) calculated at large positive test-pulses, as a function of test-pulse voltage. The theoretical curves correspond to data point fits, according to the Boltzmann equation (GraphPad Prism 5 software): $g/gmax = 1 - [1/(1 + \exp((V_T - V_{T50\%})/k_g))]$, where $V_{T50\%}$ is the test-pulse voltage corresponding to 50% maximal conductance, and k_g is the slope of the curve.

Steady-state inactivation-voltage relationships were established by plotting the peak current amplitude, expressed as percentage of the maximal amplitude (Imax) recorded in response to large negative pre-pulses, as a function of pre-pulse voltage (V_P). The theoretical curves correspond to data point fits, according to the Boltzmann equation (GraphPad Prism 5 software): $I/Imax = 1/[1 + \exp((V_P - V_{P50\%})/k_h)]$, where $V_{P50\%}$ is the pre-pulse voltage corresponding to 50% maximal peak amplitude of current, and k_h is the slope of the curve.

Current kinetics were evaluated by calculating the two following activation and inactivation parameters: (1) the time to peak (tp), defined as the time between test-pulse triggering and the peak current, and (2) the time constant (τh) of the current decay, assuming that the current inactivation is a mono-exponential decay as a function of time, *i.e.* $I_{(t)} = I_{(0)}\ e^{(-t/\tau h)}$.

Data are expressed as means ± standard deviations (S.D.) of n different experiments. The statistical comparison of values was carried out using the parametric two-tailed Student's *t*-test (either paired samples for comparison within a single population or unpaired samples for comparison between two populations), the 2-factor ANOVA test or the nonparametric Mann-Whitney *U* test,

according to the equality of sample variances estimated with the Lilliefors test. Differences between values were considered to be statistically significant at $P \leq 0.05$.

3. Results

3.1. Effects of HwTx-IV and TTX on the mouse neuromuscular system in vivo

On-line recordings revealed that the major effect of i.m. injections of PBS 1× solutions containing various concentrations of either HwTx-IV (from 4.1 pmol/kg to 41.4 nmol/kg mouse) or TTX (from 3.4 pmol/kg to 166.5 nmol/kg mouse) to anaesthetized mice was a marked concentration-dependent decrease of CMAP amplitude. This is exemplified in Fig. 1A (insets) for CMAP recordings performed before and ~10 min after injections of 41.4 nmol HwTx-IV and 166.5 nmol TTX per kg of mouse. This effect occurred within various times, depending on the concentration of toxin injected, ranging from ~10 to ~20 min (Fig. 1A). It is worth noting that the maximal CMAP amplitude remained stable before toxin injections and during ~25 min after injection of 3.4 pmol/kg mouse of TTX. Moreover, the maximal CMAP amplitude measured ~30 min after injections of PBS 1× solution alone, and compared to values before injections, was not significantly affected, *i.e.* 97.8 ± 2.3% (n = 8 mice), indicating (i) that injections of the toxin vehicle had no effect on the maximal CMAP amplitude and (ii) that no marked run-down of the response occurred.

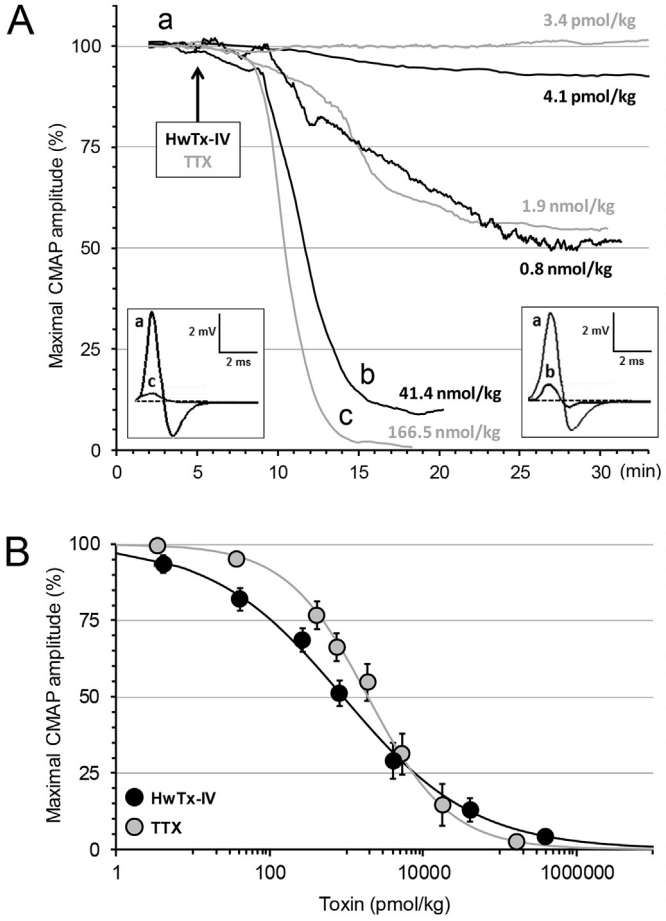

Fig. 1. Effects of HwTx-IV and TTX on the maximal CMAP amplitude recorded *in vivo* from mouse tail muscle in response to caudal motor nerve stimulation. **A**: Representative time-course of the effects of HwTx-IV (from 4.1 pmol/kg to 41.4 nmol/kg mouse, in black) and TTX (from 3.4 pmol/kg to 166.5 nmol/kg mouse, in grey) on the maximal CMAP amplitude recorded continuously as a function of time. Values are expressed as percentage of those before injections (indicated by the arrow). **Insets**: Superimposed traces of maximal CMAP, before (**a**) and ~10 min after HwTx-IV (41.4 nmol/kg mouse, **b**) or TTX (166.5 nmol/kg mouse, **c**) injection. **B**: Concentration-response curves of the effects of HwTx-IV (black circles) and TTX (grey circles) on the maximal CMAP amplitude. Each value, expressed as percentage of that obtained before injection, represents the mean ± S.D. of data obtained from 4 to 8 mice. IC_{50} and n_H values were, respectively, 0.9 nmol/kg mouse and 0.5 for HwTx-IV ($r^2 = 0.998$) and 1.9 nmol/kg mouse and 0.8 for TTX ($r^2 = 0.997$).

The toxin blocking effect was quantified by establishing the concentration-response curves, *i.e.* the maximal CMAP amplitude as a function of the concentration of toxin injected, and determining the IC_{50} values (see for more details the Material and methods section). As shown in Fig. 1B, the concentration-response curves for HwTx-IV and TTX revealed IC_{50} values of 0.9 and 1.9 nmol/kg mouse, respectively. It thus appears that HwTx-IV was approximatively 2 times more efficient than TTX, on equimolar basis, to inhibit the CMAP.

The five different excitability tests (stimulus-response, strength-duration and current-threshold relationships, as well as threshold electrotonus and recovery cycle) were performed together before and ~30 min after i.m. injections of PBS 1× solution containing HwTx-IV (4.1–41.4 nmol/kg mouse) or TTX (5.3–17.8 nmol/kg mouse), and the derived neuromuscular excitability parameters were determined (Supplementary data, Fig. S1, Fig. S2 and Table S1). With the exception of decreased maximal CMAP amplitude and increased stimulus intensity required to generate a 50% maximal amplitude CMAP (stimulus-response relationship; Fig.S1Aa, Fig. S2Aa and Table S1), analysis of strength-duration relationship, threshold electrotonus, current-threshold relationship, and recovery cycle did not reveal other HwTx-IV and TTX effects since no significant modification of excitability waveforms and derived parameters was detected (Fig. S1B-E, Fig. S2B-E and Table S1). The toxin-induced effects were completely reversed within ~12 h after HwTx-IV (4.1–41.4 nmol/kg mouse) or TTX (5.3–17.8 nmol/kg mouse) injections (Fig. S3 and Table S1).

It should be emphasized that injections of 41.4 and 394.3 nmol HwTx-IV per kg of mouse (concentrations corresponding to 46 and 438 times the IC_{50} value, respectively) caused death of 40% (2/5) and 80% (4/5) of the mice, respectively, within 1 h. Similarly, injections of 17.8 and 166.5 nmol TTX per kg of mouse (*i.e.* 9 and 88 times the IC_{50} value, respectively) produced death of 43% (3/7) and 75% (6/8) of the animals, respectively, within 1 h. These results indicate a more than 2-time lower *in vivo* toxicity of HwTx-IV compared to TTX.

3.2. Effects of HwTx-IV on isolated mouse neuromuscular preparations

The evaluation of HwTx-IV effects on isolated mouse phrenic nerve-hemidiaphragm preparations revealed that various toxin concentrations (from 152 nM to 14 μM) produced an inhibition of both nerve-evoked and directly-elicited muscle contractile force of single twitches. This is illustrated in Fig. 2A (insets) for twitch recordings performed in the absence and in the presence of 14 μM HwTx-IV. The toxin-induced blockade of nerve-evoked muscle twitch was concentration- and time-dependent (Fig. 2). In particular, a complete inhibition of nerve-evoked contractile response occurred within ~8 min after addition of 14 μM HwTx-IV to the standard physiological medium, as exemplified by the representative time-course of toxin effect shown in Fig. 2A.

Similarly, the toxin (14 μM) produced a marked decrease of directly-elicited muscle twitch within ~8 min (Fig. 2A). However, the maximal amplitude of directly-elicited muscle twitch was much less affected by HwTx-IV concentrations from 152 nM to

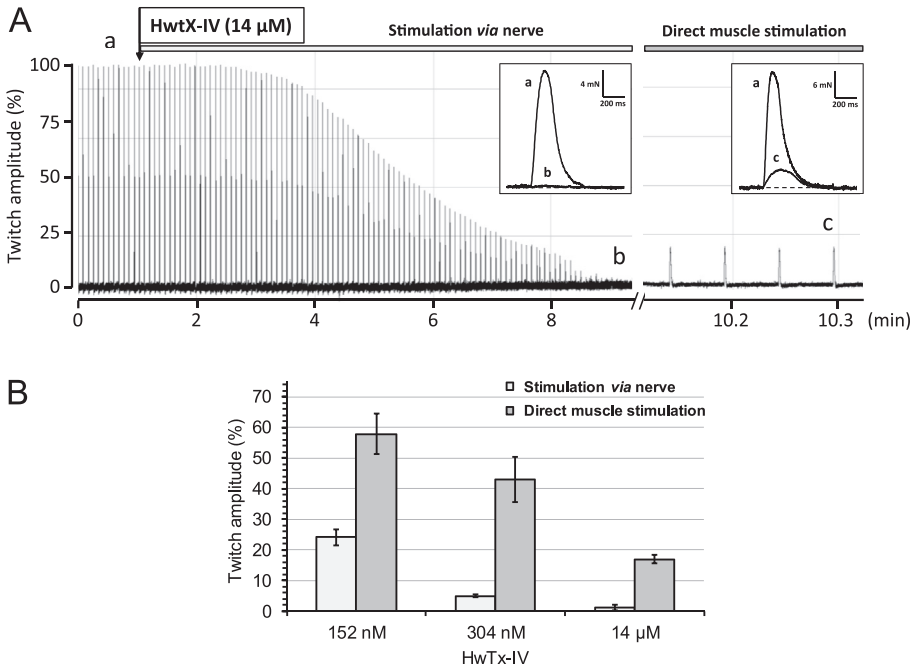

Fig. 2. Effects of HwTx-IV on nerve-evoked and directly-elicited muscle contractile force (single twitch) of isolated mouse phrenic nerve-hemidiaphragm preparation. **A**: Representative time-course of HwTx-IV (14 µM) effects on the maximal twitch amplitude recorded continuously as a function of time, and expressed as percentage of that before toxin addition to the standard physiological medium (indicated by the arrow), in response to stimulation applied either indirectly *via* the motor nerve (light grey) or directly to muscle (dark grey). **Insets**: Superimposed traces of maximal twitch recorded before (**a**) and ~10 min after HwTx-IV (14 µM) addition to the standard physiological medium (**b** and **c**), and elicited *via* nerve stimulation (**b**) or by direct muscle stimulation (**c**). **B**: Histogram representing nerve-evoked (light grey) and directly-elicited muscle (dark grey) maximal twitch amplitude determined in the presence of indicated HwTx-IV concentrations. Each value, expressed as percentage of that obtained before toxin addition to the standard physiological medium, represents the mean ± S.D. of data obtained from 4 to 10 muscles.

14 µM than the nerve-evoked twitch. In particular, when muscle twitch evoked by nerve stimulation was completely blocked by 14 µM HwTx-IV (*i.e.* maximal amplitude reduced to 1.2 ± 0.9% of initial values measured in the absence of toxin, n = 5 muscles), a contractile response, although of low maximal amplitude (*i.e.* 16.9 ± 1.3% of initial values measured in the absence of toxin, n = 5 muscles), could be still obtained by direct stimulation of hemidiaphragms. For comparison, an only slightly higher maximal amplitude (*i.e.* 24.2 ± 2.6% of initial values measured in the absence of toxin, n = 10 muscles) was obtained when muscle twitch was evoked by nerve stimulation in the presence of 152 nM HwTx-IV (Fig. 2B). It is worth noting that no decrease of twitch amplitude occurred when neuromuscular preparations were only bathed with standard physiological medium for 20 min (data not shown). This indicates, in particular, that there was no important run-down of twitch amplitude under these experimental conditions.

Assuming that n_H was equal to 1, IC_{50} values of 30 and 900 nM were calculated according to the Hill equation (see Material and methods section for more details), for the toxin-induced decrease of maximal amplitude of nerve-evoked and directly-elicited muscle twitches, respectively. HwTx-IV was therefore 30 times more efficient to inhibit nerve-evoked than directly-elicited muscle contractile force of isolated mouse hemidiaphragms.

3.3. Effects of HwTx-IV and TTX on $hNa_V1.1$-1.8-overexpressing HEK-293 cells and on CHO cells overexpressing hCav1.2 and hKv11.1 channel subtypes

Whole-cell automated patch-clamp experiments performed on HEK-293 cells overexpressing $hNa_V1.1$–1.8 channel subtypes revealed the following increasing order for IC_{50} values obtained from the concentration-response curves of HwTx-IV effects on

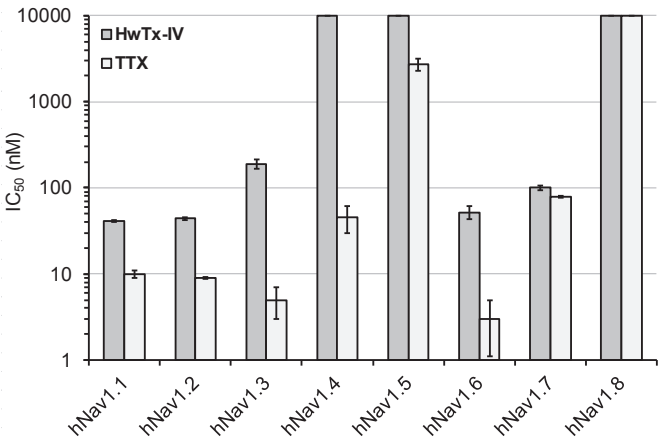

Fig. 3. Effects of HwTx-IV and TTX on HEK-293 cells overexpressing $hNa_V1.1$–1.8 channel subtypes. Histogram of IC_{50} values obtained from the concentration-response curves of HwTx-IV (dark grey) and TTX (light grey) effects on $hNa_V1.1$–1.8 currents. Each value represents the mean ± S.D. of data obtained from 2 to 10 cells. Mean values ± S.D. of n_H were 1.3 ± 0.2 and 1.0 ± 0.1 for HwTx-IV and TTX effects, respectively.

currents flowing through the different channel subtypes (Fig. 3): $hNa_V1.1$ (41 ± 1 nM, n = 4) > $hNa_V1.2$ (44 ± 2 nM, n = 10) > $hNa_V1.6$ (52 ± 9 nM, n = 3) > $hNa_V1.7$ (100 ± 6 nM, n = 4) > $hNa_V1.3$ (190 ± 24 nM, n = 7) > $hNa_V1.4$ (>10 µM, n = 8) for TTX-S (IC_{50} values between 3 ± 2 and 78 ± 2 nM, n = 2–5) channel subtypes, and $hNa_V1.5$ = $hNa_V1.8$ (>10 µM, n = 7–9) for TTX-resistant (TTX-R; IC_{50} values of 3 ± 1 and >10 µM, respectively, n = 5) channel subtypes. Therefore, all the TTX-R channel subtypes studied were also relatively resistant to HwTx-IV while all the TTX-S channel

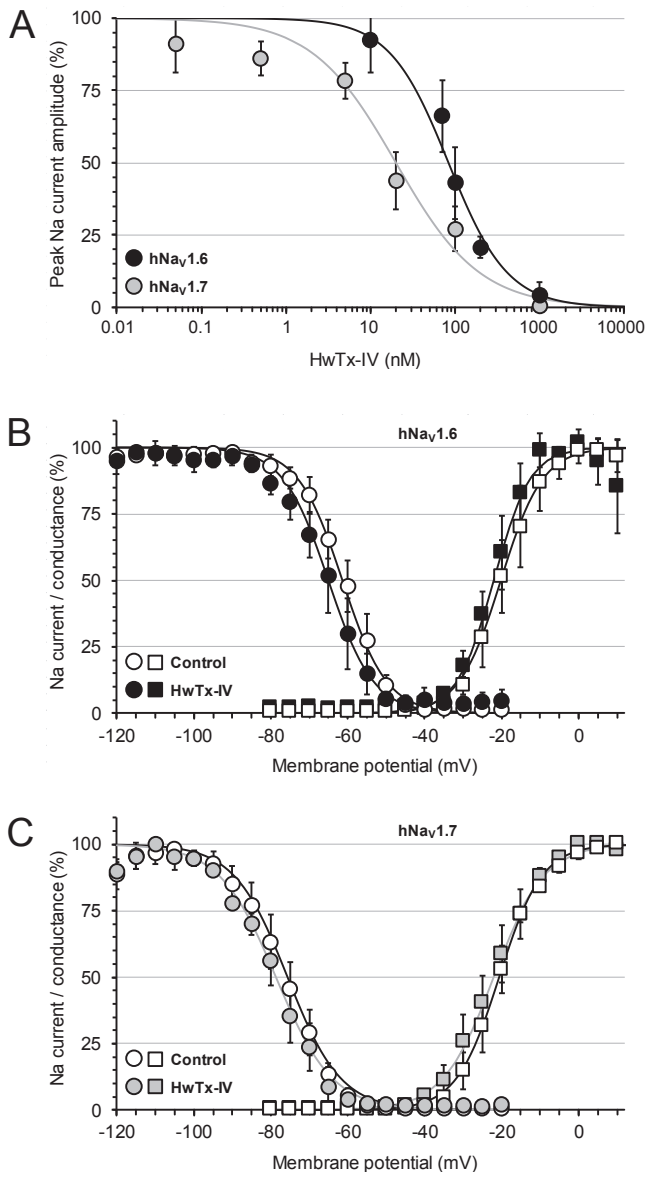

Fig. 4. Effects of HwTx-IV on HEK-293 cells overexpressing $hNa_V1.6$ and $hNa_V1.7$ channel subtypes. **A**: Concentration-response curves of HwTx-IV effects on $hNa_V1.6$ (black circles) and $hNa_V1.7$ (grey circles) currents. Each value, expressed as percentage of that obtained before toxin perfusion, represents the mean ± S.D. of data obtained from 4 to 9 cells. IC_{50} and n_H values were, respectively, 83.3 nM and 1.2 for $hNa_V1.6$ current ($r^2 = 0.983$), and 32.6 nM and 0.8 for $hNa_V1.7$ current ($r^2 = 0.901$). **B** and **C**: Steady-state inactivation- (circles) and conductance- (squares) voltage relationships for HEK-293 cells overexpressing $hNa_V1.6$ (**B**) and $hNa_V1.7$ (**C**) channel subtypes, before (open symbols) and after (close symbols) perfusion of 70–100 nM (**B**) or 20 nM (**C**) HwTx-IV. Each value represents the mean ± S.D. of data obtained from 4 to 5 cells, and is expressed as percentage of either maximal peak amplitude of current at large negative pre-pulse voltages or maximal conductance calculated at large positive test-pulse voltages. The theoretical curves correspond to data point fits with the mean $V_{P50\%}$, k_h, $V_{T50\%}$ and k_g values indicated in Table 1.

subtypes studied, with the exception of $hNa_V1.4$ channel subtype, were also relatively sensitive to HwTx-IV. Additionally, HwTx-IV was ~2 times more potent to block $hNa_V1.6$ than $hNa_V1.7$ channel subtypes. It is worth noting that the toxin had very low affinity for $hCa_V1.2$ and $hK_V11.1$ channel subtypes overexpressed in CHO cells since the IC_{50} values obtained from the concentration-response curves of HwTx-IV effects on currents flowing through these two ion channels were higher than 10 μM (n = 2–4, data not shown).

Detailed experiments, using whole-cell manual patch-clamp, displayed IC_{50} values of 83.3 and 32.6 nM from the concentration-response curves of HwTx-IV effects on currents flowing through $hNa_V1.6$ and $hNa_V1.7$ channel subtypes overexpressed in HEK-293 cells, respectively (Fig. 4A). Under these conditions, the toxin was thus approximatively 2.5 times less efficient to block $hNa_V1.6$ than $hNa_V1.7$ channel subtypes. This HwTx-IV-induced blocking action occurred without any change in steady-state inactivation- and conductance-voltage relationships of $hNa_V1.6$ and $hNa_V1.7$ channel subtypes, as shown in Fig. 4B–C and Table 1 for toxin concentrations of 70–100 and 20 nM, respectively, *i.e.* close to the IC_{50} values.

3.4. Effects of HwTx-IV and TTX on mouse DRG neurons

Before evaluating the effects of HwTx-IV on the sodium currents of DRG neurons, the TTX sensitivity of these currents was first determined by perfusion of cells with a standard physiological medium containing 100 nM TTX. Under this condition, two types of neurons were recorded (Fig. 5A): those (67%, *i.e.* 12/18 cells) having TTX-S current, *i.e.* which was blocked by the toxin to 5 ± 5% of initial peak amplitude values within 1 min, and those (33%, *i.e.* 6/18 cells) having TTX-R current, *i.e.* which was blocked by the toxin, perfused for ~6 min, to 83 ± 6% of initial peak amplitude values but was completely inhibited by 100 μM TTX. It should be noted that the activation and inactivation kinetics of TTX-R current were significantly slower than those of TTX-S current (Fig. 5A and Table 2).

After washing-out TTX by perfusion of neurons with a toxin-free solution for 8–10 min, the cell perfusion with standard physiological solutions containing various HwTx-IV concentrations (from 5 nM to 20 μM) produced then a decrease of sodium current amplitude which was dependent on the time following the perfusion, the toxin concentration and the current sensitivity to TTX. In particular, the concentration-response curves of HwTx-IV effects on the peak amplitude of TTX-S and TTX-R currents revealed IC_{50} values of 0.13 and 110 μM, respectively (Fig. 5B). It thus appears that the toxin was approximatively 850 times more efficient to inhibit TTX-S than TTX-R sodium currents of mouse DRG neurons. The blocking effects of HwTx-IV on the peak amplitude of TTX-S current were stationary approximatively 7 and 2 min after perfusion of 0.005 and 1 μM of toxin, respectively. Those on the peak amplitude of TTX-R current were stationary approximatively 6 min after perfusion of 10–20 μM of toxin. The HwTx-IV effects on TTX-R current, not very noticeable, were not further studied, in contrast to those on TTX-S current.

The peak amplitude of TTX-S current, which was 9 and 3% of initial values after perfusion of 1 and 10 μM HwTx-IV, respectively, returned to 43 ± 17% of initial values (n = 9) by perfusion of neurons with a toxin-free solution for 15–20 min. The analyses of activation and inactivation kinetics of TTX-S sodium current in the absence and in the presence of HwTx-IV concentrations close to the IC_{50} value (*i.e.* 0.1 μM) revealed that the toxin did not affect these kinetics since tp and τh were not significantly modified (Table 2). Similarly, HwTx-IV (0.1 μM) did not produce any alteration of steady-state inactivation- and conductance-voltage relationships for neurons exhibiting TTX-S current (Fig. 5C and Table 1).

4. Discussion

The present study was undertaken to determine the interaction between HwTx-IV and $Na_V1.6$ channel subtype, using multiscale (from *in vivo* to individual cell) functional approaches. The results obtained can be summarized as follow: (i) HwTx-IV was approximatively 2 times more efficient than TTX to inhibit the CMAP recorded from the mouse skeletal neuromuscular system *in vivo*, (ii) HwTx-IV was approximatively 30 times more effective to inhibit

Table 1
Parameters of steady-state inactivation- ($V_{P50\%}$ and k_h) and conductance- ($V_{T50\%}$ and k_g) voltage relationships for HEK-293 cells overexpressing $hNa_V1.6$ and $hNa_V1.7$ channel subtypes (means ± S.D. of 4–5 cells) and mouse DRG neurons having TTX-S sodium current (means ± S.D. of 4 neurons).

	$V_{P50\%}$ (mV)	k_h (mV^{-1})	$V_{T50\%}$ (mV)	k_g (mV^{-1})
$hNa_V1.6$ current before HwTx-IV perfusion	−61 ± 3	5.7 ± 0.3	−20 ± 2	5.4 ± 0.4
$hNa_V1.6$ current after HwTx-IV perfusion[a]	−65 ± 2	5.9 ± 0.4	−22 ± 3	4.8 ± 0.4
$hNa_V1.7$ current before HwTx-IV perfusion	−76 ± 3	6.9 ± 0.3	−21 ± 2	5.6 ± 0.5
$hNa_V1.7$ current after HwTx-IV perfusion[b]	−79 ± 3	7.4 ± 0.6	−22 ± 2	6.6 ± 0.5
TTX-S current before HwTx-IV perfusion	−80 ± 2	7.0 ± 0.6	−38 ± 4	3.7 ± 1.4
TTX-S current after HwTx-IV perfusion[c]	−86 ± 7	6.3 ± 0.5	−38 ± 3	4.4 ± 1.7

[a] 70–100 nM.
[b] 20 nM, and.
[c] 0.1 μM.

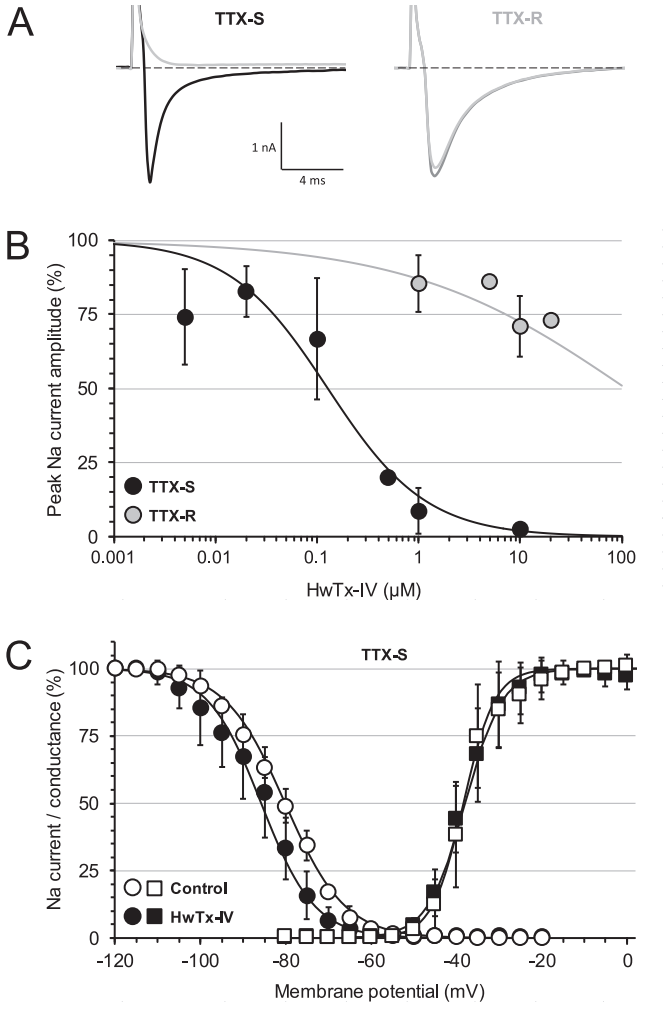

Fig. 5. Effects of HwTx-IV on TTX-S and TTX-R sodium currents of mouse DRG neurons. **A**: Representative traces of sodium currents recorded from two different neurons having either TTX-S (left) or TTX-R (right) current. In each case, the current was recorded before (black or dark grey) and 1–5 min after (light grey) perfusion of 100 nM TTX. **B**: Concentration-response curves of HwTx-IV effects on the peak amplitude of TTX-S (black circles) and TTX-R (grey circles) sodium currents. Each value, expressed as percentage of that obtained before toxin perfusion, represents the mean ± S.D. of data obtained from 2 to 9 neurons. IC_{50} and n_H values were, respectively, 0.13 μM and 0.9 for TTX-S current ($r^2 = 0.967$), and 110 μM and 0.4 for TTX-R current ($r^2 = 0.612$). **C**: Steady-state inactivation- (circles) and conductance- (squares) voltage relationships for neurons having TTX-S current, before (open symbols) and after (close symbols) perfusion of 0.1 μM HwTx-IV. Each value represents the mean ± S.D. of data obtained from 4 neurons, and is expressed as percentage of either maximal peak amplitude of current at large negative pre-pulse voltages or maximal conductance calculated at large positive test-pulse voltages. The theoretical curves correspond to data point fits with the mean $V_{P50\%}$, k_h, $V_{T50\%}$ and k_g values indicated in Table 1.

Table 2
Kinetics parameters of current activation (tp) and inactivation (τh) calculated from TTX-S and TTX-R sodium currents recorded from DRG neurons under the indicated conditions (means ± S.D. of 4–12 cells).

	tp (ms)	τh (ms)
TTX-S current before TTX perfusion[1]	1.22 ± 0.29	0.78 ± 0.40
TTX-S current after TTX wash-out	0.81 ± 0.04	0.63 ± 0.18
TTX-S current after HwTx-IV perfusion[2]	0.75 ± 0.06	0.60 ± 0.12
TTX-R current before TTX perfusion	2.31 ± 0.62*	1.11 ± 0.24*

[1] 100 nM, [2] 0.1 μM *: $P \leq 0.032$ (*versus* TTX-S current before TTX perfusion).

nerve-evoked than directly-elicited muscle contractile force in isolated mouse hemidiaphragms, (iii) HwTx-IV was more potent to block TTX-S ($hNa_V1.1$, 1.2, 1.3, 1.6 and 1.7, with the exception of $hNa_V1.4$) than TTX-R ($hNa_V1.5$ and 1.8) Na_V channel subtypes overexpressed in HEK-293 cells, (iv) HwTx-IV was approximatively 850 times more efficient to inhibit TTX-S than TTX-R sodium currents of mouse DRG neurons, and (v) the *in vivo* toxicity of HwTx-IV was more than 2 times lower than that of TTX.

The effects of i.m. injections of HwTx-IV and TTX on the mouse neuromuscular system *in vivo* consisted in an inhibition of CMAP and an increase in the stimulus intensity required to generate a 50% maximal amplitude CMAP. The duration of the observed effects was less than 12 h. These results strongly suggest that HwTx-IV and TTX produce a marked and reversible decrease of sodium currents, *i.e.* of the density and/or functional status of "transient" Na_V channels, as might be expected with toxins known to block these types of channels (Cestèle and Catterall, 2000). Besides these effects, HwTx-IV and TTX did not modify other excitability parameters, indicating that the two toxins do not affect the density and functional status of other types and subtypes of ion channels, receptors and pumps, nor the passive membrane properties of the neuromuscular system (Kiernan and Bostock, 2000; Krishnan et al., 2008).

The HwTx-IV-induced inhibition of CMAP could be explained by an *in vivo* action of this toxin on the Na_V channel subtypes identified so far in adult nerves and skeletal muscles, *i.e.* the $Na_V1.6$ and $Na_V1.4$ channel subtypes, respectively (Caldwell et al., 2000; de Lera Ruiz and Kraus, 2015). HwTx-IV would be approximatively 2 times more efficient than TTX to interact with and to block $Na_V1.6$ and/or $Na_V1.4$ channel subtypes. Available *in vitro* evidence indicated however that the $Na_V1.4$ channel subtype is not preferentially sensitive to HwTx-IV since the toxin affinity for this channel subtype ($IC_{50} > 10$ μM; Xiao et al., 2008) was more than 1000 times less than that of TTX ($IC_{50} \approx 8$ nM; Tsukamoto et al., 2017), without giving information on the interaction between HwTx-IV and $Na_V1.6$ channel subtype. It was therefore probable that the relative high efficiency of HwTx-IV to inhibit *in vivo* the CMAP, compared to TTX, results from toxin-induced preferential blockade of the $Na_V1.6$ and not $Na_V1.4$ channel subtype. This hypothesis was tested directly by studying the HwTx-IV effects on isolated mouse neuromuscular

preparations and recording the isometric contractile force elicited by stimulating either directly the muscle or indirectly *via* its associated motor nerve.

The study of HwTx-IV effects on isolated mouse phrenic nerve-hemidiaphragm preparations reveals that the toxin produced an inhibition of the nerve-evoked contractile force with a calculated IC_{50} value of 30 nM. These results confirm those obtained *in vivo* on the CMAP recorded from tail muscle in response to caudal motor nerve stimulation, *i.e.* the relative high affinity of HwTx-IV for $Na_V1.6$ and/or $Na_V1.4$ channel subtypes. It is worth noting that HwTx-IV was previously reported to completely block the conduction of isolated mouse phrenic nerve-hemidiaphragm preparations, by acting on multiple ion channel proteins, especially the Ca_V channels (Yu et al., 2014). However, this is not supported by the present results showing a very low affinity of the peptide for hCaV1.2 channel subtype overexpressed in CHO cells.

Additionally, HwTx-IV also inhibited the directly-elicited muscle twitch of isolated mouse hemidiaphragms with a calculated IC_{50} value of 300 nM. The conditions of direct muscle stimulation are very interesting because it makes possible to decrease the implication of $Na_V1.6$ channel subtype (located in nerves and not in muscles; Caldwell et al., 2000) in the contractile response, and thus to get direct information on the affinity of interaction between HwTx-IV and $Na_V1.4$ channel subtype (located in skeletal muscles and not in nerves; de Lera Ruiz and Kraus, 2015). The results obtained under these conditions therefore strongly suggest that the toxin was 30 times less potent to block the $Na_V1.4$ than the $Na_V1.6$ channel subtype. These results confirm the hypothesis that the HwTx-IV-induced inhibition of nerve-evoked hemidiaphragm twitch and of the CMAP recorded *in vivo* from tail muscle in response to caudal motor nerve stimulation resulted from a preferential blockade of $Na_V1.6$ channel subtype by the toxin.

The following step was thus to undertake the study of HwTx-IV effects on HEK-293 cells overexpressing $hNa_V1.1$–1.8 channel subtypes to get complementary information on the relative selectivity of interaction between the toxin and $Na_V1.6$ channel subtype, as well as on the relative IC_{50} value of HwTx-IV on this channel subtype, since poor evidence was available in the literature (Rahnama et al., 2017).

The results obtained from whole-cell automated patch-clamp experiments performed on HEK-293 cells overexpressing $hNa_V1.1$–1.8 channel subtypes highlighted two groups of channel subtypes: (i) a relatively HwTx-IV-sensitive group (IC_{50} = 41–190 nM) including, by increasing order of IC_{50} values, $hNa_V1.1 > hNa_V1.2 > hNa_V1.6 > hNa_V1.7 > hNa_V1.3$, and (ii) a relatively HwTx-IV-resistant group ($IC_{50} > 10\ \mu M$) composed of $hNa_V1.4 \approx hNa_V1.5 \approx hNa_V1.8$. These results are similar to the following sequence of peptide affinities reported so far in the literature, with respect to the Na_V channel subtype overexpressed in HEK-293 cells: $hNa_V1.7$ (IC_{50} = 26 nM) > $rNa_V1.2$ (IC_{50} = 150 nM) > $rNa_V1.3$ (IC_{50} = 338 nM) >> $rNa_V1.4 \approx hNa_V1.5$ ($IC_{50} > 10\ \mu M$) (Xiao et al., 2008). The slight IC_{50} differences between the two studies may reflect those between the species, human or rat (r), of the Na_V channel subtypes studied. It seems therefore that the selectivity of HwTx-IV towards $hNa_V1.7$ is not as important as previously reported since the toxin is also highly potent to block $hNa_V1.1$, $h(r)Na_V1.2$, $h(r)Na_V1.3$ and $hNa_V1.6$ channel subtypes. However, the discovery that $Na_V1.1$ and 1.3 channel subtypes are involved in pain pathways (Chen et al., 2014; Osteen et al., 2016; Cardoso and Lewis, 2017) and that $Na_V1.2$ channel subtype is only located in the central nervous system (see de Lera Ruiz and Kraus, 2015) does not impair further development of HwTx-IV as a potential antinociceptive agent to access only peripheral Na_V channel subtypes. In contrast, the fact that this toxin also targets $Na_V1.6$ channel subtype is more problematic because of the resulting side-effects which limit its *in vivo* efficacy in preclinical pain models.

The poor selectivity of HwTx-IV for $hNa_V1.7$ over $hNa_V1.6$ channel subtypes is further supported by the recent characterization of the effects of a triple-mutant of HwTx-IV (E1G, E4G and Y33W; m3-HwTx-IV) on either HEK-293 cells overexpressing $hNa_V1.1$–1.5 channel subtypes, and the β1 auxiliary subunit, or CHO cells overexpressing $hNa_V1.6$–1.7 and $hNa_V1.8$/β3 channel subtypes (Rahnama et al., 2017). Despite the fact that mutations may influence the peptide selectivity over Na_V channel subtypes, this study revealed quite similar Na_V channel subtype selectivity, but higher blockade potency of the recombinant peptide, compared to HwTx-IV (present results): $hNa_V1.7 > hNa_V1.6 > hNa_V1.3 > hNa_V1.1 > hNa_V1.2$ (IC_{50} = 3.3–11.9 nM) >> $hNa_V1.4$ (IC_{50} = 369 nM) >> $hNa_V1.5 \approx hNa_V1.8$ ($IC_{50} > 1\ \mu M$). Taken altogether, these data indicate that all the TTX-R channel subtypes studied (TTX IC_{50} = 3–10 μM) were also resistant to HwTx-IV and m3-HwTx-IV blockade, while all the TTX-S channel subtypes studied (TTX IC_{50} = 3–78 nM), with the exception of $hNa_V1.4$ channel subtype, were also sensitive to HwTx-IV and m3-HwTx-IV inhibition.

The effects of HwTx-IV were further investigated on TTX-S and TTX-R Na_V channel subtypes of adult mouse DRG neurons, *i.e.* mainly the TTX-S $Na_V1.1$, 1.6 and 1.7 channel subtypes and the TTX-R $Na_V1.8$ and 1.9 channel subtypes (Rush et al., 2007). This study was motivated, on one hand, by the well-known important role of DRG neurons as the primary sensitive pathway of chronic pain and, on the other hand, by the absence of report of such study in mouse, until now. The effects consisted in a marked and reversible decrease of the peak amplitude of TTX-S sodium current (IC_{50} = 0.13 μM), without any significant modification of activation and inactivation kinetics and voltage-dependencies. As expected from the results obtained from whole-cell automated patch-clamp experiments, the peptide was approximatively 850 times less efficient in inhibiting the peak amplitude of TTX-R sodium current (IC_{50} = 110 μM). From this point of view, HwTx-IV is very interesting compared to TTX which was only approximately 90 times more potent to block TTX-S than TTX-R Na_V channel subtypes (IC_{50} values of 5.5 and 500 nM, respectively).

These results are consistent with previous observations on adult rat DRG neurons showing that 0.1 μM HwTx-IV inhibited TTX-S sodium current, without any alteration of activation and inactivation kinetics, but had no effect on TTX-R currents (Peng et al., 2002). Interestingly, the activation and inactivation kinetics of TTX-R sodium current were slower than those of TTX-S sodium current. This is due to the prevalence of TTX-R $Na_V1.8$ and to a less extent of $Na_V1.9$ channel subtypes which are exceptionally characterized by slow ($Na_V1.8$) and even very slow ($Na_V1.9$) activation and inactivation kinetics (Rush et al., 2007).

During experiments aimed to study the effects of i.m. injections of HwTx-IV and TTX on the mouse neuromuscular system *in vivo*, 17.8 and 166.5 nmol TTX per kg of mouse (corresponding to 9 and 88 times the *in vivo* IC_{50} value, respectively) produced death of 43% and 75% of the animals, respectively, within 1 h. These values are close to those reported in the literature, *i.e.* i.m. injections of 5.3 μg (16.6 nmol) TTX per kg rodent caused the death of 50% of the animals (Xu et al., 2003). By comparison, i.m. injections of HwTx-IV concentrations corresponding to 46 and 438 times the *in vivo* IC_{50} value produced death of 40% and 80% of the mice, respectively, within 1 h. Although these results indicate a more than 2-time lower *in vivo* toxicity of HwTx-IV compared to TTX, the resulting side-effects of the peptide may limit its use as a potential lead molecule for the development of novel pain therapeutics. In particular, the therapeutic window of HwTx-IV as an analgesic

appears to be markedly reduced taking into account that the peptide was previously reported to have analgesic activity at 100 μg/kg mouse (*i.e.* 24 nmol/kg mouse) when i.m. injected to animals (Liu et al., 2014a).

Since HwTx-IV had very low affinity for $hNa_V1.5$ channel subtype, as well as for $hCa_V1.2$ and $hK_V11.1$ channel ($IC_{50} > 10$ μM), it is unlikely that the death of mice resulted from heart dysfunctioning. In contrast, given the poor selectivity of the peptide over $Na_V1.6$ channel subtype, it is likely that impaired motor functioning is involved since peptides interacting with this subtype of Na_V channels are well-known to typically lead to such severe side-effects.

5. Conclusion

To the best of our knowledge, this is the first report showing directly that high affinity interaction occurs between HwTx-IV and $Na_V1.6$ channel subtype. Indeed, the toxin has been reported so far in the literature as being highly specific for the $Na_V1.7$ channel subtype, without effects on the $Na_V1.6$ channel subtype being evidenced. The present study showing quite similar affinities of HwTx-IV for $Na_V1.6$ and $Na_V1.7$ channel subtypes allows better understanding the mechanisms of motor *in vivo* side-effects produced by this peptide, and makes this molecule significantly less attractive for an eventual therapeutic use as antinociceptive agent.

Conflicts of interest

The authors declare that they have no actual or potential conflict of interest including any financial, personal or other relationships with other people or organizations within three years of beginning this work.

Acknowledgments

This research was funded by a collaborative grant (#153114) between Sanofi Research & Development (Chilly-Mazarin, France) and the French Alternative Energies and Atomic Energy Commission (CEA, Gif-sur-Yvette, France). T.C.G. was supported by a doctoral CIFRE fellowship from Sanofi. The authors are grateful to thank Dr Andrees Bohme and Brigitte Schombert for their help in the establishment of $hCa_V1.2$ and $hK_V11.1$ electrophysiological protocols, and Sophie Fontaine for her technical assistance for the Na_V cell lines management.

Appendix A. Supplementary data

Supplementary data related to this article can be found at https://doi.org/10.1016/j.neuropharm.2018.02.016.

References

Bell, D.C., Dallas, M.L., 2017. Using automated patch clamp electrophysiology platforms in pain-related ion channel research: insights from industry and academia. Br. J. Pharmacol. https://doi.org/10.1111/bph.13916 (in press).

Caldwell, J.H., Schaller, K.L., Lasher, R.S., Peles, E., Levinson, S.R., 2000. Sodium channel Na(v)1.6 is localized at nodes of Ranvier, dendrites, and synapses. Proc. Natl. Acad. Sci. U.S.A. 97, 5616–5620.

Cardoso, F.C., Lewis, R.J., 2017. Sodium channels and pain: from toxins to therapies. Br. J. Pharmacol. https://doi.org/10.1111/bph.13962 (in press).

Catterall, W.A., 2000. From ionic currents to molecular mechanisms: the structure and function of voltage-gated sodium channels. Neuron 26, 13–25.

Cerles, O., Benoit, E., Chéreau, C., Chouzenoux, S., Morin, F., Guillaumot, M.A., Coriat, R., Kavian, N., Loussier, T., Santulli, P., Marcellin, L., Saidu, N.E., Weill, B., Batteux, F., Nicco, C., 2017. Niclosamide inhibits oxaliplatin neurotoxicity while improving colorectal cancer therapeutic response. Mol. Canc. Therapeut. 16, 300–311.

Cestèle, S., Catterall, W.A., 2000. Molecular mechanisms of neurotoxin action on voltage-gated sodium channels. Biochimie 82, 883–892.

Chen, H.P., Zhou, W., Kang, L.M., Yan, H., Zhang, L., Xu, B.H., Cai, W.H., 2014. Intrathecal miR-96 inhibits NaV1.3 expression and alleviates neuropathic pain in rat following chronic construction injury. Neurochem. Res. 39, 76–83.

de Lera Ruiz, M., Kraus, R.L., 2015. Voltage-gated sodium channels: structure, function, pharmacology, and clinical indications. J. Med. Chem. 58, 7093–7118.

Deuis, J.R., Wingerd, J.S., Winter, Z., Durek, T., Dekan, Z., Sousa, S.R., Zimmermann, K., Hoffmann, T., Weidner, C., Nassar, M.A., Alewood, P.F., Lewis, R.J., Vetter, I., 2016. Analgesic Effects of GpTx-1, PF-04856264 and CNV1014802 in a Mouse Model of NaV1.7-mediated Pain, vol. 8. Toxins, Basel pii: E78.

Flinspach, M., Xu, Q., Piekarz, A.D., Fellows, R., Hagan, R., Gibbs, A., Liu, Y., Neff, R.A., Freedman, J., Eckert, W.A., Zhou, M., Bonesteel, R., Pennington, M.W., Eddinger, K.A., Yaksh, T.L., Hunter, M., Swanson, R.V., Wickenden, A.D., 2017. Insensitivity to pain induced by a potent selective closed-state Nav1.7 inhibitor. Sci. Rep. 7, 39662.

Goldin, A.L., Barchi, R.L., Caldwell, J.H., Hofmann, F., Howe, J.R., Hunter, J.C., Kallen, R.G., Mandel, G., Meisler, M.H., Netter, Y.B., Noda, M., Tamkun, M.M., Waxman, S.G., Wood, J.N., Catterall, W.A., 2000. Nomenclature of voltage-gated sodium channels. Neuron 28, 365–368.

Kiernan, M.C., Bostock, H., 2000. Effects of membrane polarization and ischaemia on the excitability properties of human motor axons. Brain 123, 2542–2551.

Klint, J.K., Senff, S., Rupasinghe, D.B., Er, S.Y., Herzig, V., Nicholson, G.M., King, G.F., 2012. Spider-venom peptides that target voltage-gated sodium channels: pharmacological tools and potential therapeutic leads. Toxicon 60, 478–491.

Krishnan, A., Park, S., Lin, C.S., Kiernan, M.C., 2008. Assessment of nerve excitability in toxic and metabolic neuropathies. J. Peripher. Nerv. Syst. 13, 7–26.

Liu, Y., Wu, Z., Tang, D., Xun, X., Liu, L., Li, X., Nie, D., Xiang, Y., Yi, J., Yi, J., 2014a. Analgesic effects of huwentoxin-IV on animal models of inflammatory and neuropathic pain. Protein Pept. Lett. 21, 153–158.

Liu, Y., Tang, J., Zhang, Y., Xun, X., Tang, D., Peng, D., Yi, J., Liu, Z., Shi, X., 2014b. Synthesis and analgesic effects of μ-TRTX-Hhn1b on models of inflammatory and neuropathic pain. Toxins 6, 2363–2378.

Marrouchi, R., Rome, G., Kharrat, R., Molgó, J., Benoit, E., 2013. Analysis of the action of gymnodimine-A and 13-desmethyl spirolide C on the mouse neuromuscular system *in vivo*. Toxicon 75, 27–34.

Molinski, T.F., Dalisay, D.S., Lievens, S.L., Saludes, J.P., 2009. Drug development from marine natural products. Nat. Rev. Drug Discov. 8, 69–86.

Namadurai, S., Yereddi, N.R., Cusdin, F.S., Huang, C.L., Chirgadze, D.Y., Jackson, A.P., 2015. A new look at sodium channel β subunits. Open Biol. 5, 140192.

Netirojjanakul, C., Miranda, L.P., 2017. Progress and challenges in the optimization of toxin peptides for development as pain therapeutics. Curr. Opin. Chem. Biol. 38, 70–79.

Osteen, J.D., Herzig, V., Gilchrist, J., Emrick, J.J., Zhang, C., Wang, X., Castro, J., Garcia-Caraballo, S., Grundy, L., Rychkov, G.Y., Weyer, A.D., Dekan, Z., Undheim, E.A., Alewood, P., Stucky, C.L., Brierley, S.M., Basbaum, A.I., Bosmans, F., King, G.F., Julius, D., 2016. Selective spider toxins reveal a role for the NaV1.1 channel in mechanical pain. Nature 534, 494–499.

Peng, K., Shu, Q., Liu, Z., Liang, S., 2002. Function and solution structure of huwentoxin-IV, a potent neuronal tetrodotoxin (TTX)-sensitive sodium channel antagonist from Chinese bird spider *Selenocosmia huwena*. J. Biol. Chem. 277, 47564–47571.

Rahnama, S., Deuis, J.R., Cardoso, F.C., Ramanujam, V., Lewis, R.J., Rash, L.D., King, G.F., Vetter, I., Mobli, M., 2017. The structure, dynamics and selectivity profile of a NaV1.7 potency-optimised huwentoxin-IV variant. PLoS One 12 e0173551.

Rush, A.M., Cummins, T.R., Waxman, S.G., 2007. Multiple sodium channels and their roles in electrogenesis within dorsal root ganglion neurons. J. Physiol. Lond 579, 1–14.

Saez, N.J., Senff, S., Jensen, J.E., Er, S.Y., Herzig, V., Rash, L.D., King, G.F., 2010. Spider-venom peptides as therapeutics. Toxins 2, 2851–2871.

Schlumberger, S., Kristan, K.C., Ota, K., Frangež, R., Molgó, J., Sepčić, K., Benoit, E., Maček, P., 2014. Permeability characteristics of cell-membrane pores induced by ostreolysin A/pleurotolysin B, binary pore-forming proteins from the oyster mushroom. FEBS Lett. 588, 35–40.

Schlumberger, S., Ouanounou, G., Girard, E., Sasaki, M., Fuwa, H., Louzao, M.C., Botana, L.M., Benoit, E., Molgó, J., 2010. The marine polyether gambierol enhances muscle contraction and blocks a transient K(+) current in skeletal muscle cells. Toxicon 56, 785–791.

Schmidt, G., 2010. Wie lautet der korrekte Name von Selenocosmia huwena Wang, Peng & Xie, 1993? Tarantulas World 142, 23–27.

Tsukamoto, T., Chiba, Y., Wakamori, M., Yamada, T., Tsunogae, S., Cho, Y., Sakakibara, R., Imazu, T., Tokoro, S., Satake, Y., Adachi, M., Nishikawa, T., Yotsu-Yamashita, M., Konoki, K., 2017. Differential binding of tetrodotoxin and its derivatives to voltage-sensitive sodium channel subtypes (Nav1.1 to Nav1.7). Br. J. Pharmacol. https://doi.org/10.1111/bph.13985 (in press).

Vetter, I., Deuis, J.R., Mueller, A., Israel, M.R., Starobova, H., Zhang, A., Rash, L., Mobli, M., 2016. NaV 1.7 as a pain target – from gene to pharmacology. Pharmacol. Ther. 172, 73–100.

Wang, F., Yan, Z., Liu, Z., Wang, S., Wu, Q., Yu, S., Ding, J., Dai, Q., 2016. Molecular basis of toxicity of N-type calcium channel inhibitor MVIIA. Neuropharmacology 101, 137–145.

Xiao, Y., Bingham, J.P., Zhu, W., Moczydlowski, E., Liang, S., Cummins, T.R., 2008. Tarantula huwentoxin-IV inhibits neuronal sodium channels by binding to receptor site 4 and trapping the domain II voltage sensor in the closed configuration. J. Biol. Chem. 283, 27300–27313.

Xiao, Y., Blumenthal, K., Cummins, T.R., 2014. Gating-pore currents demonstrate selective and specific modulation of individual sodium channel voltage-sensors by biological toxins. Mol. Pharmacol. 86, 159–167.
Xu, Q., Huang, K., Gao, L., Zhang, H., Rong, K., 2003. Toxicity of tetrodotoxin towards mice and rabbits. Wei Sheng Yan Jiu (Chinese) 32, 371–374.
Yu, H., Liu, H., Yan, Y., Duan, Z., Wang, X., 2014. Detection and identification of huwentoxin-IV interacting proteins by biotin-avidin chemistry combined with mass spectrometry. J. Venom. Anim. Toxins Incl. Trop. Dis. 20, 18.

Direct evidence for high affinity blockade of NaV1.6 channel subtype by huwentoxin-IV spider peptide, using multiscale functional approaches

T.C. Gonçalves, R. Boukaiba, J. Molgó, M. Amar, M. Partiseti, D. Servent, and E. Benoit

SUPPLEMENTARY FIGURE 1

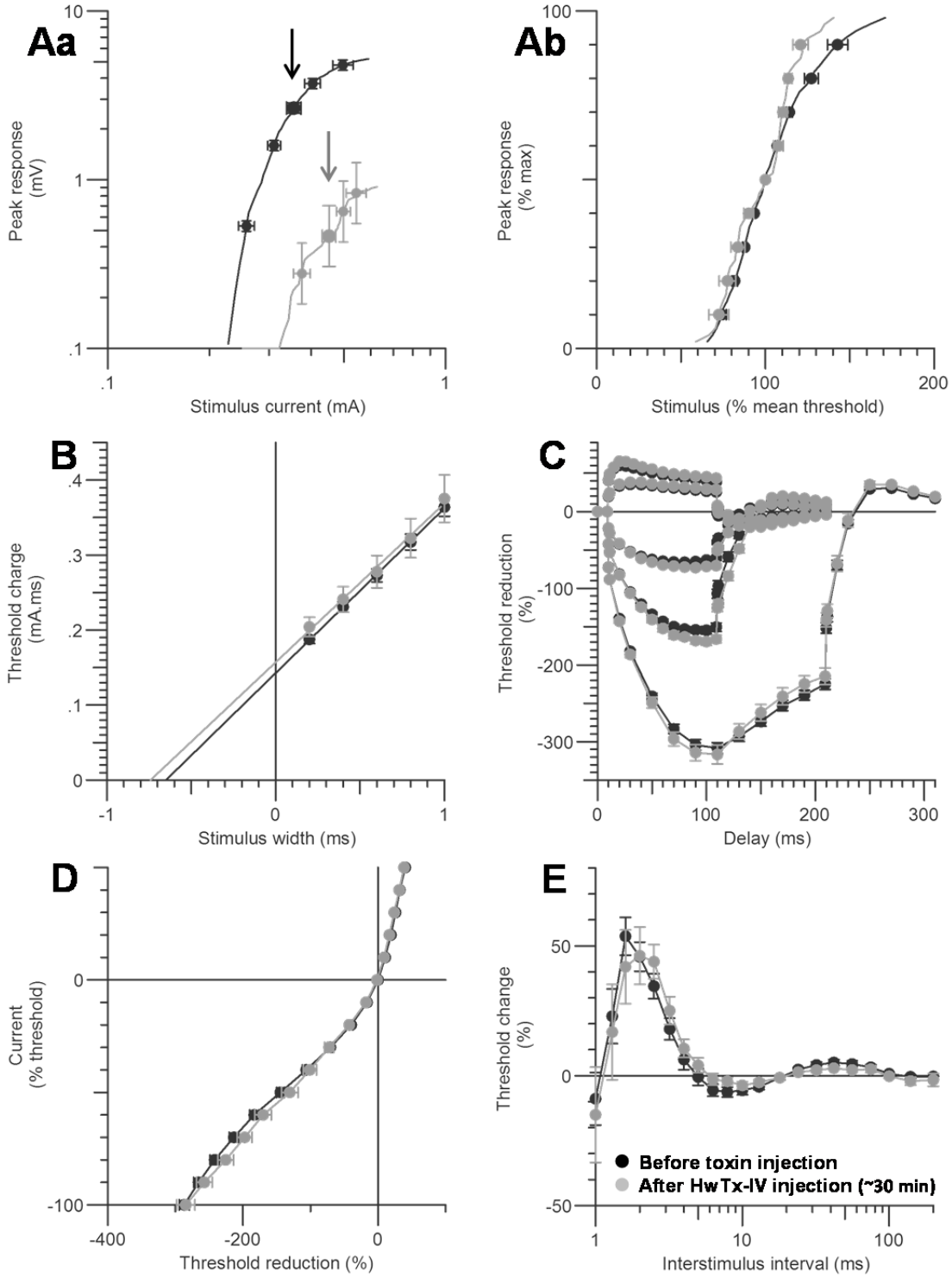

Figure S1. Superimposed excitability curves obtained *in vivo* by stimulating the mouse caudal motor nerve and recording the CMAP from tail muscle before (black circles, n = 29 mice) and ~30 min after injections of HwTx-IV (4.1-41.4 nmol/kg mouse, grey circles, n = 6 mice). Data are represented as means ± S.D. **A**: stimulus-response relationships [absolute (**a**) and relative (**b**) CMAP amplitudes], **B**: strength-duration relationship, **C**: threshold electrotonus, **D**: current-threshold relationship, and **E**: recovery cycle. In Aa, arrows indicate stimulus currents for 50% maximal response.

Direct evidence for high affinity blockade of NaV1.6 channel subtype by huwentoxin-IV spider peptide, using multiscale functional approaches

T.C. Gonçalves, R. Boukaiba, J. Molgó, M. Amar, M. Partiseti, D. Servent, and E. Benoit

SUPPLEMENTARY FIGURE 2

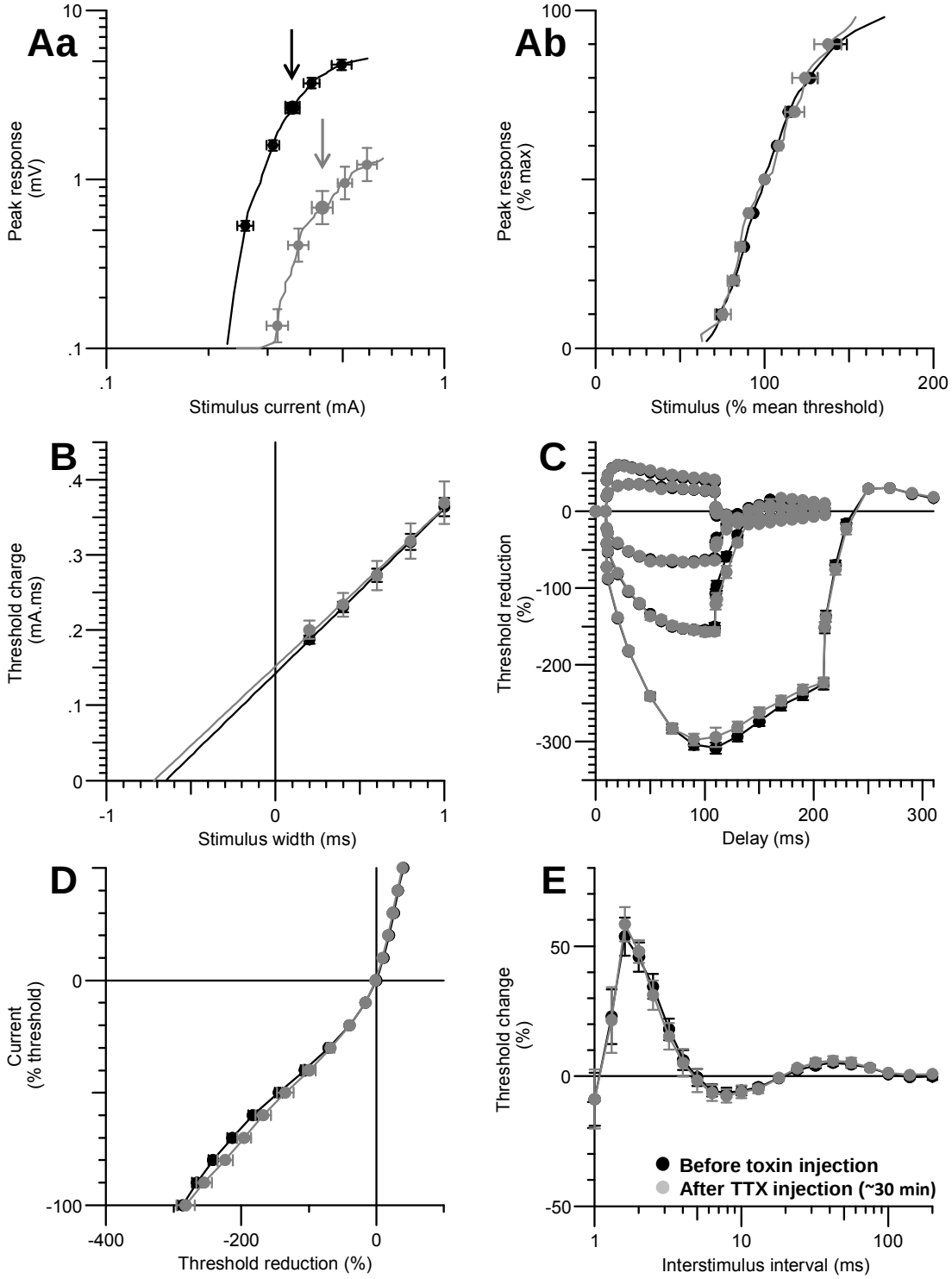

Figure S2. Superimposed excitability curves obtained *in vivo* by stimulating the mouse caudal motor nerve and recording the CMAP from tail muscle before (black circles, n = 29 mice) and ~30 min after injections of TTX (5.3-17.8 nmol/kg mouse, grey circles, n = 9 mice). Data are represented as means ± S.D. **A**: stimulus-response relationships [absolute (**a**) and relative (**b**) CMAP amplitudes], **B**: strength-duration relationship, **C**: threshold electrotonus, **D**: current-threshold relationship, and **E**: recovery cycle. In Aa, arrows indicate stimulus currents for 50% maximal response.

Direct evidence for high affinity blockade of NaV1.6 channel subtype by huwentoxin-IV spider peptide, using multiscale functional approaches
T.C. Gonçalves, R. Boukaiba, J. Molgó, M. Amar, M. Partiseti, D. Servent, and E. Benoit

SUPPLEMENTARY FIGURE 3

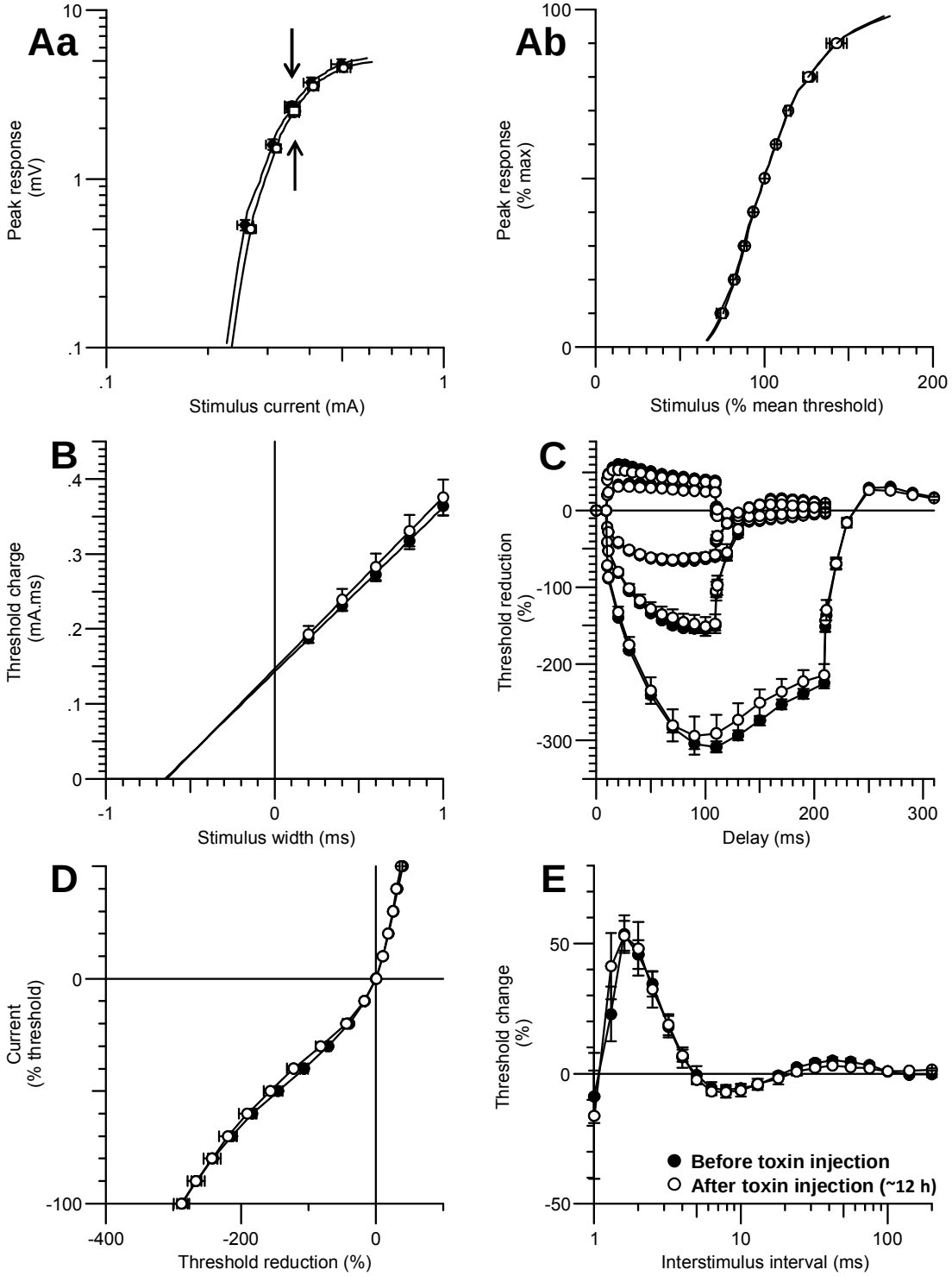

Figure S3. Superimposed excitability curves obtained *in vivo* by stimulating the mouse caudal motor nerve and recording the CMAP from tail muscle before (black circles, n = 29 mice) and ~12 h after injections (white circles, n = 12 mice) of HwTx-IV (4.1-41.4 nmol/kg mouse) or TTX (5.3-17.8 nmol/kg mouse). Data are represented as means ± S.D. **A**: stimulus-response relationships [absolute (**a**) and relative (**b**) CMAP amplitudes], **B**: strength-duration relationship, **C**: threshold electrotonus, **D**: current-threshold relationship, and **E**: recovery cycle. In Aa, arrows indicate stimulus currents for 50% maximal response.

Direct evidence for high affinity blockade of NaV1.6 channel subtype by huwentoxin-IV spider peptide, using multiscale functional approaches

T.C. Gonçalves, R. Boukaiba, J. Molgó, M. Amar, M. Partiseti, D. Servent, and E. Benoit

SUPPLEMENTARY TABLE 1

Table S1. Comparison of neuromuscular excitability parameters (means ± S.D.) from mouse tail muscle recordings before toxin injections (control, n = 29 mice), ~30 min after injections of HwTx-IV (4.1-41.4 nmol/kg mouse, n = 6 mice) or TTX (5.3-17.8 nmol/kg mouse, n = 9 mice), and ~12 h after toxin injections (n = 12 mice).

	Excitability parameter[2]	**Before toxin injection**	**~30 min after injection**		**~12 h after toxin injection**
			HwTx-IV	**TTX**	
A[1]	Peak response (mV)	5.31 ± 0.57	0.92 ± 0.31**	1.36 ± 0.25**	5.04 ± 0.56
A	Latency (ms)	3.89 ± 0.06	4.09 ± 0.26	4.09 ± 0.12	3.91 ± 0.04
A	Stimulus (mA) for 50% max response	0.35 ± 0.05	0.46 ± 0.05*	0.44 ± 0.08*	0.36 ± 0.06
A	Stimulus-response slope	3.11 ± 0.18	3.42 ± 0.17	2.96 ± 0.17	3.21 ± 0.16
B[1]	Strength-duration time constant (ms)	0.69 ± 0.12	0.86 ± 0.14	0.87 ± 0.11	0.66 ± 0.03
B	Rheobase (mA)	0.21 ± 0.04	0.19 ± 1.16	0.19 ± 0.03	0.22 ± 0.08
C[1]	TEd (10-20 ms, 40%)	59.53 ± 1.27	54.84 ± 1.58	59.19 ± 1.84	56.07 ± 2.07
C	TEd (peak, 40%)	59.00 ± 1.17	63.62 ± 1.43	60.52 ± 1.96	56.28 ± 1.92
C	TEd (peak, 20%)	35.81 ± 0.75	38.65 ± 1.69	36.14 ± 1.03	33.57 ± 1.53
C	TEd (40-60 ms, 40%)	47.92 ± 1.14	51.90 ± 1.09	50.17 ± 2.03	43.29 ± 2.29
C	TEd (90-100 ms, 40%)	39.52 ± 1.27	41.49 ± 1.25	42.20 ± 1.67	36.56 ± 2.41
C	Accommodation half-time (ms, 40%)	46.02 ± 0.93	44.09 ± 1.15	46.05 ± 1.70	45.16 ± 2.69
C	S2 accommodation	19.48 ± 0.77	19.13 ± 1.32	18.32 ± 0.89	18.72 ± 1.45
C	TEd (undershoot, 40%)	-15.34 ± 1.01	-12.26 ± 1.27	-17.67 ± 1.35	-13.43 ± 1.29
C	TEh (10-20 ms, -40%)	-93.31 ± 1.12	-94.49 ± 1.56	-91.87 ± 2.14	-90.88 ± 4.93
C	TEh (20-40 ms, -40%)	-120.1 ± 1.9	-124.0 ± 3.0	-119.8 ± 3.4	-116.2 ± 7.5
C	TEh (90-100 ms, -40%)	-152.7 ± 5.2	-167.9 ± 4.9	-156.7 ± 5.6	-149.4 ± 12.1
C	TEh (slope 101-140 ms, -40%)	2.62 ± 0.17	2.74 ± 0.11	2.93 ± 0.20	2.60 ± 0.30
C	TEh (peak, -70%)	-312.4 ± 6.7	-321.8 ± 11.0	-300.3 ± 10.1	-297.8 ± 22.8
C	S3 (-70%)	80.28 ± 6.98	102.1 ± 11.4	80.48 ± 7.91	78.85 ± 11.20
C	TEh (overshoot, -40%)	17.33 ± 1.05	20.23 ± 1.41	17.70 ± 1.20	15.62 ± 1.71
D[1]	Resting slope	0.89 ± 0.09	0.86 ± 0.12	0.89 ± 0.11	0.96 ± 0.26
D	Minimum slope	0.23 ± 0.01	0.23 ± 0.02	0.23 ± 0.02	0.24 ± 0.02
D	Hyperpolarization slope	0.49 ± 0.03	0.39 ± 0.05	0.40 ± 0.06	0.48 ± 0.05
E[1]	Refractoriness at 2 ms (%)	45.82 ± 5.60	46.20 ± 11.00	47.91 ± 4.41	48.05 ± 10.20
E	Refractoriness at 2.5 ms (%)	34.48 ± 4.78	43.90 ± 6.62	31.13 ± 5.72	32.36 ± 7.01
E	Relative refractory period (ms)	4.38 ± 1.09	5.05 ± 1.22	4.36 ± 1.11	4.70 ± 1.07
E	Superexcitability (%)	-19.00 ± 3.91	-23.53 ± 8.01	-17.94 ± 3.74	-9.00 ± 3.17
E	Superexcitability at 5 ms (%)	-0.49 ± 3.26	3.98 ± 2.84	-1.63 ± 4.46	-2.40 ± 1.75
E	Superexcitability at 7 ms (%)	-5.94 ± 2.06	-1.78 ± 1.69	-7.06 ± 2.83	-7.01 ± 1.76
E	Subexcitability (%)	5.60 ± 1.09	3.29 ± 0.85	6.61 ± 1.46	2.93 ± 0.64

[1] A: stimulus-response relationship, B: strength-duration relationship, C: threshold electrotonus, D: current-threshold relationship, and E: recovery cycle. [2] TEd: threshold electrotonus from depolarizing currents and TEh: threshold electrotonus from hyperpolarizing currents. Differences (*versus* control), considered to be significant at $P \leq 0.05$ (*: $P \leq 0.032$, **: $P \leq 9.4 \times 10^{-8}$), are highlighted in grey.

2.3.3. Résumé des résultats obtenus

Les résultats obtenus fournissent des informations détaillées concernant les effets du peptide *(i)* sur les sous-types $Na_V1.6$ et 1.4 de canaux sodium impliqués dans les propriétés d'excitabilité du système neuromusculaire de souris *in vivo*, *(ii)* sur ces mêmes sous-types impliqués dans la contraction musculaire enregistrée au niveau de préparations neuromusculaires isolées de souris, *(iii)* sur les sous-types Na_V TTX-S et TTX-R des neurones de DRG de souris adultes et *(iv)* sur le sous-type $hNa_V1.6$ exprimé dans des cellules recombinantes HEK-293. En particulier, les injections locales i.m. d'HwTx-IV sont aussi efficaces que celles de la TTX pour altérer, *in vivo*, les propriétés d'excitabilité du système neuromusculaire de souris anesthésiées. Au niveau de préparations neuromusculaires isolées de souris, le peptide est 30 fois plus efficace pour inhiber la contraction musculaire obtenue suite à la stimulation du nerf que celle obtenue suite à la stimulation directe du muscle. De même, l'HwTx-IV présente une puissance pour les sous-types Na_V TTX-S des neurones de DRG de souris qui est 850 fois plus élevée que celle pour les sous-types TTX-R. Finalement, des puissances similaires du peptide ont été déterminées pour les sous-types $hNa_V1.6$ et 1.7 (IC_{50} de 83.3 et32.6 nM, respectivement) exprimés dans des cellules HEK-293. L'ensemble de ces résultats montre une interaction directe et de haute puissance entre l'HwTx-IV et le sous-type $Na_V1.6$ de canaux sodium. Comme l'HwTx-IV a une très faible puissance pour les sous-types cardiaques $hNa_V1.5$, $hCa_V1.2$ et $hK_V11.1$ (IC_{50} > 10 µM), il est peu probable que le décès des animaux injectés avec ce peptide soit dû à un arrêt cardiaque lors des expérimentations. En revanche, il est fort probable qu'il résulte d'un arrêt respiratoire, *i.e.* un des troubles indésirables produits par l'HwTx-IV au niveau du système neuromusculaire, suite à l'interaction de haute puissance entre le peptide et le sous-type $Na_V1.6$ puisque le sous-type $Na_V1.4$ est peu sensible à ce peptide. Cette interaction entre l'HwTx-IV et le sous-type $Na_V1.6$ permet également de mieux comprendre les mécanismes des effets secondaires indésirables produits par ce peptide au niveau du système neuromusculaire.

Des expériences complémentaires, dont les résultats ne sont pas inclus dans la publication, ont été réalisées récemment afin d'étoffer le profil de sélectivité de l'HwTx-IV en étudiant ses effets sur des lignées cellulaires recombinantes exprimant certains sous-types hCa_V, hK_V et hKir non étudiés jusqu'à ce jour. A une concentration de 10 µM, l'HwTx-IV n'affecte pas notablement certains sous-types de canaux ioniques impliqués plus particulièrement dans le potentiel d'action cardiaque ($hCa_V1.2$, 2.2, 3.1 et 3.2, $hK_V7.1$ et 11.1, hKir2.1). En revanche, comme observé précédemment avec la CyrTx-1a (voir sous-partie 2.1), le sous-type $hK_V4.3$ est inhibé de 82,8 ± 1,7% en présence de 10 µM d'HwTx-IV (IC_{50} = 2,3 ± 0,3 µM; n_H = 1,2 ± 0,1; moyenne ± ES de 6 expériences; Figure 2-4).

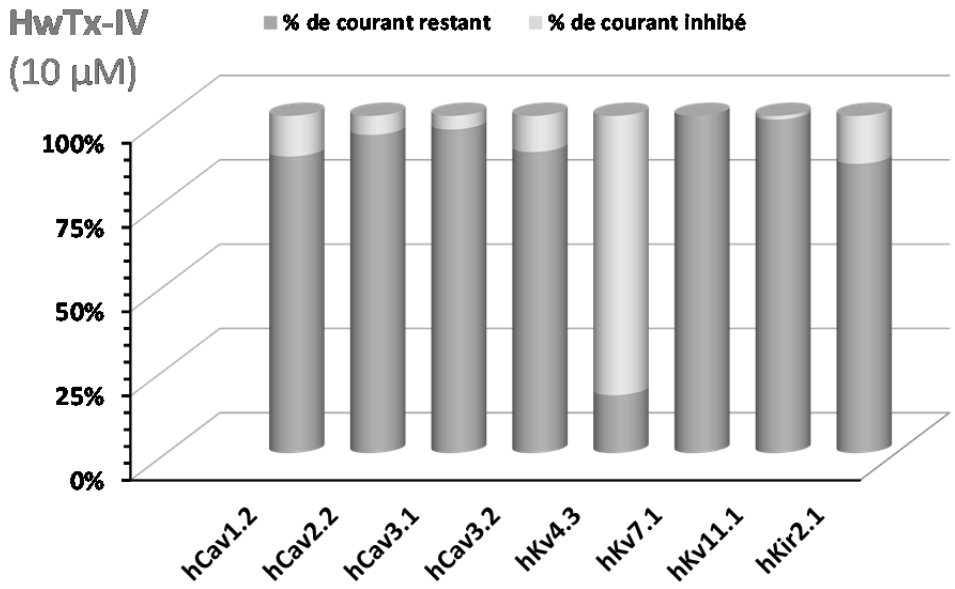

Figure 2-4. Effets de l'HwTx-IV sur les courants hCa_V, hK_V et hKir. Histogramme exprimant les pourcentages de courant restant (en gris foncé) et inhibé (en gris clair) en fonction du sous-type de canal indiqué, en présence de 10 µM de peptide (moyenne ± ES, n = 2-17).

2.3.4. Conclusion

Cette étude est la première montrant une interaction directe et de haute puissance entre l'HwTx-IV et le sous-type $Na_V1.6$ de canaux sodium. En effet, cette toxine avait été décrite dans la littérature pour être hautement spécifique du sous-type $Na_V1.7$ sans aucune mention de ses effets éventuels sur le sous-type $Na_V1.6$. Or, nos résultats mettent en évidence des puissances similaires de l'HwTx-IV pour ces deux sous-types de canaux sodium, permettant de mieux comprendre les mécanismes des effets secondaires indésirables produits par ce peptide au niveau du système neuromusculaire. De plus, les résultats obtenus des expériences complémentaires montre que l'HwTx-IV, à de plus fortes concentrations, exerce également un effet inhibiteur sur le sous-type $K_V4.3$ de canaux potassium responsable de la première phase de repolarisation (rapide) du potentiel d'action cardiaque (Huo et al., 2014), ce qui peut éventuellement entrainer des arythmies. En conséquence, cette molécule, potentiellement antinociceptive, est nettement moins attractive pour son développement en tant qu'agent thérapeutique.

2.4. Profil de sélectivité original de la poécitoxine-1a de l'araignée *Poecilotheria subfusca* pour les sous-types humains de canaux ioniques dépendants du potentiel

2.4.1. Contexte de l'étude

Parmi les sous-types de canaux Na_V, le sous-type $Na_V1.7$ semble être la cible la plus intéressante pour traiter notamment la douleur chronique débilitante (de Lera Ruiz & Kraus, 2015; Vetter et al., 2017; Gonçalves et al., 2018a). Cependant, la découverte de nouveaux peptides qui ciblent ce sous-type de canaux Na_V reste un défi dans le traitement pharmacologique de la douleur car ces peptides analgésiques potentiels peuvent également produire des effets secondaires non négligeables en raison de leur manque de sélectivité vis-à-vis des autres types et sous-types de canaux ioniques (Gonçalves et al., 2018b). Pour répondre correctement à la question de la sélectivité, il est donc nécessaire d'étudier les effets d'un peptide d'intérêt non seulement sur d'autres sous-types de canaux Na_V, tels que $Na_V1.4$, 1.5 et 1.6, mais aussi sur certains sous-types de canaux K_V, Kir et Ca_V pour s'assurer d'une action limitée du peptide sur les systèmes cardiaque et neuromusculaire.

Trois grandes familles de canaux Ca_V ont été identifiées à ce jour (Catterall, 2011): les canaux à haut seuil d'activation $Ca_V1.x$ de type L, les canaux $Ca_V2.x$ neuronaux de types N, P/Q et R, et les canaux à bas seuil d'activation $Ca_V3.x$ de type T (voir partie 1). Aux Etats-Unis, le sous-type $Ca_V1.2$, comme les sous-types de canaux $Na_V1.5$, $K_V4.3$, $K_V7.1$, $K_V11.1$ et Kir2.1, est inclus dans la liste des canaux ioniques cardiaques mentionnés par la FDA (pour "Food and Drug Administration") dans son initiative CiPA (pour "Comprehensive *in vitro* Proarrhythmia Assay"). Il a été signalé que le blocage de ce sous-type, responsable notamment du "plateau" des potentiels d'action cardiaques, contrebalançait le syndrome du QT long, qu'il soit congénital (*i.e.* d'origine génétique) ou produit par certains médicaments inhibiteurs du sous-type $K_V11.1$, et la tachycardie ventriculaire associée dite "torsade de pointes" (Crumb et al. 2016).

Le criblage de la banque de 117 venins, menée sur des lignées cellulaires HEK-293 exprimant les sous-types $hNa_V1.7$ et 1.5 de canaux sodium et réalisée pour mettre en évidence la CyrTx-1a (voir sous-partie 2.1), nous a également permis d'identifier une autre toxine, la poécitoxine-1a (PecTx-1a) dans le venin de l'araignée *Poecilotheria subfusca*. Cette toxine a été purifiée, séquencée, synthétisée chimiquement, et son profil pharmacologique a été établi sur une large gamme de sous-types de canaux hNa_V, hK_V, hKir et hCa_V exprimés dans différentes lignées cellulaires recombinantes.

2.4.2. Publication n°5

Publication en préparation

"Original selectivity profile of *Poecilotheria subfusca* spider poecitoxin-1a for human voltage-gated ion channel subtypes"

Tânia C. Gonçalves, Evelyne Benoit, Michel De Waard, Michael Kurz, Camille Sanson, Brigitte Schombert, Andrees Bohme, Jean-Marie Chambard, Rémy Béroud, Jean-Michel Itier, Denis Servent & Michel Partiseti

Original selectivity profile of *Poecilotheria subfusca* spider poecitoxin-1a for human voltage-gated ion channel subtypes

Tânia C. Gonçalves[1,2], Evelyne Benoit[2,3], Michel De Waard[4,5], Michael Kurz[6], Camille Sanson[1], Brigitte Schombert[1], Andrees Bohme[1], Jean-Marie Chambard[1], Rémy Béroud[4], Jean-Michel Itier[7], Denis Servent[2], Michel Partiseti[1,*]

[1]Sanofi R&D, Integrated Drug Discovery – High Content Biology, F-94440 Vitry-sur-Seine, France; [2]Service d'Ingénierie Moléculaire des Protéines (SIMOPRO), CEA, Université Paris-Saclay, F-91191 Gif sur Yvette, France; [3]Institut des Neurosciences Paris-Saclay (Neuro-PSI), UMR CNRS/Université Paris-Sud 9197, Université Paris-Saclay, F-91198 Gif sur Yvette, France; [4]Smartox Biotechnology, 6 rue des Platanes, F-38120 Saint-Egrève, France; [5]Institut du Thorax, Inserm UMR 1087 / CNRS UMR 6291, LabEx "Ion Channels, Science & Therapeutics", F-44007 Nantes, France; [6]Sanofi R&D, Integrated Drug Discovery – Synthetic Molecular Design, G-65929 Frankfurt, Germany; [7]Sanofi R&D, Translational sciences – Cell-omics, F-94440 Vitry-sur-Seine, France

**Corresponding author: Michel.Partiseti@sanofi.com*

ABBREVIATIONS – BMP, bone morphogenetic protein; BSA, bovine serum albumin; Ca_V channel, voltage-gated calcium channel; CHO, Chinese hamster ovary; DMEM, Dulbecco's modified Eagle's medium; DMSO, dimethylsulfoxyde; ECG, electrocardiogram; ERG, *ether-a-go-go*-related gene; FBS, fetal bovine serum; GPCR, G-protein-coupled receptor; h, human; HEK, human embryonic kidney; HEPES, N-2-hydroxyethylpiperazine-N'-2-ethanesulfonic acid; hiPSC-CM, human induced pluripotent stem cell-derived cardiomyocyte; IC_{50}, toxin concentration necessary to inhibit 50% of the response; $IC_{90\text{-}95}$, compound concentration necessary to inhibit 90-95% of current; ICK, inhibitor cystine knot; IWR-1, inhibitor type 1 of Wnt response; JzTx, jingzhaotoxin; Kir channel, inward-rectifier potassium channel; K_V channel, voltage-gated potassium channel; NaSpTx, Na_V channel spider toxin; Na_V channel, voltage-gated sodium channel; PBS, phosphate buffered saline; PecTx-1a, poecitoxin-1a; PTM, post-translational modification; RPMI, Roswell Park Memorial Institute; TEA, tetraethylammonium; TTX, tetrodotoxin; TTX-R, resistant to tetrodotoxin; TTX-S, sensitive to tetrodotoxin; U2OS cell, human bone osteosarcoma epithelial cell.

ABSTRACT

Over the last two decades, animal venom toxins have been explored as an original source of new antinociceptive drugs targeting different ion channel subtypes. Although the gold standard remains the time-consuming manual patch-clamp, automated patch-clamp platforms were developed to increase the number of positive hits. The experimental approach of the present study was to perform high-throughput screening of a large collection of venom toxins through automated whole-cell patch-clamp experiments on human embryonic kidney (HEK)-293 cells overexpressing the genetically validated antinociceptive target $Na_V1.7$ and the cardiac $Na_V1.5$

human (h) subtypes of voltage-gated sodium (Na_V) channels. This first step aimed to identify bioactive peptides that were then purified, sequenced and chemically synthesized. The second step consisted in characterizing the synthetic peptide of interest on hNa_V, voltage-gated potassium (hK_V) and calcium (hCa_V), as well as on inward-rectifier potassium (hKir), channel subtypes overexpressed in cells and on calcium currents of human induced pluripotent stem cell-derived cardiomyocytes. The key results are the identification of a new bioactive peptide, poecitoxin-1a (PecTx-1a), the first one isolated from the *Poecilotheria subfusca* spider venom, as a 35 amino acid toxin belonging to the inhibitor cystine knot (ICK) structural family. This peptide inhibited the $hCa_V1.2$ channel subtype with very high affinity (5 nM producing 50% current inhibition) and selectivity against the studied hNa_V, hK_V, hKir and other hCa_V subtypes, including those implicated in cardiac action potential. In conclusion, PecTx-1a is the first ICK spider toxin specifically targeting the L-type, $hCa_V1.2$ channel subtype with an original selectivity profile. This peptide represents thus, at least, a valuable tool to study the $Ca_V1.2$ subtype function and location and, at best, a valuable drug to treat some cardiomyopathies such as the long QT syndrome.

Keywords – *Poecilotheria subfusca* spider, poecitoxin-1a, human voltage-gated ion channel subtypes, $Ca_V1.2$ channel subtype, cell lines overexpressing ion channel subtypes, human induced pluripotent stem cell-derived cardiomyocytes.

1. INTRODUCTION

Pain transmission is conveyed by neurons from the periphery (*i.e.* skin and tendons) to the brain. These neurons express many proteins at the plasmatic membrane surface that may be considered as targets for therapeutic treatment of pain, as well as some enzymes such as cyclooxygenase already attained by nonsteroidal anti-inflammatory drugs. The transmembrane proteins, often human (h) genetically validated, are part of big families including ion channels and G-protein-coupled receptors (GPCRs). The agonists of GPCRs (such as opioid, cannabinoid, angiotensin type II, α2-adrenergic, muscarinic acetylcholine, γ-aminobutyric acid B, groups II and III metabotropic glutamate, chemokine and somatostatin receptors) have been reported to exhibit antinociceptive effects (Pan et al., 2008; Yekkirala et al., 2017). In addition, the blockers of ion channels [such as voltage-gated sodium (Na_V) and calcium (Ca_V) channels, transient receptor potential channels, acid sensing ion channels, piezo proteins, ionitropic P2X receptors], as well as potassium channel enhancers, have been shown to be involved in pain relief (Bennett and Woods, 2014; Waxman and Zamponi, 2014).

In many cases, peptides derived from animal venoms are the most potent modulators of the above channels and receptors. In particular, animal venom toxins have been explored over the last two decades as an original source of new antinociceptive drugs targeting different types of ion [Na_V, Ca_V and voltage-gated potassium (K_V)] channels, giving more recently an attention to Na_V channel subtypes (Cardoso and Lewis, 2017). Nine Na_V channel subtypes ($Na_V1.1$-1.9), composed of a voltage-sensing pore forming α-subunit surrounded by small regulatory β subunits, are known to be distributed in the mammal organism where they are responsible for action potential generation and

propagation (Catterall, 2000; Goldin et al., 2000; de Lera Ruiz and Kraus, 2015; Namadurai et al., 2015). These subtypes have specific expression pattern and/or biophysical properties: $Na_V1.1$-1.3 and 1.6 are expressed in the central nervous system, $Na_V1.5$ is mainly present in the heart, $Na_V1.4$ is located in the skeletal muscle innervated by motoneurons α where $Na_V1.6$ is expressed, and $Na_V1.7$-1.9 convey mainly pain message through dorsal root ganglia neurons from the periphery to the central nervous system (Cardoso and Lewis, 2017; Israel et al., 2017).

Among Na_V channel subtypes, the $Na_V1.7$ subtype seems to be the most interesting target to treat chronic debilitating pain (de Lera Ruiz and Kraus, 2015; Vetter et al., 2017; Gonçalves et al., 2018a). However, finding out new peptides that target the $Na_V1.7$ subtype remains a challenge in the pharmacological treatment of pain because these potential analgesic peptides may also produce strong side-effects due to their lack of target selectivity (Gonçalves et al., 2018b). To properly address the question of selectivity, additional experiments are therefore necessary to study the effects of the peptide of interest not only on other Na_V subtypes, such as $Na_V1.4$, 1.5 and 1.6, but also on some Ca_V, K_V and Kir channel subtypes to ensure neuromuscular and cardiac safety issues. In particular, three superfamilies of Ca_V channels have been identified nowadays (Catterall, 2011): Ca_V1 (high voltage-activated, L-type channels), Ca_V2 (intermediate voltage-activated, P/Q-, N- and R-type channels) and Ca_V3 (low voltage-activated, T-type channels). The $Ca_V1.2$ subtype is expressed in neurons, adrenal chromaffin cells, pancreatic islets cells, the heart (sinoatrial and atrioventricular nodes, cardiomyocytes), the vascular system and intestinal/bladder smooth muscles. This subtype is required for normal brain and endocrine functioning, and exerts different roles in the heart (Zamponi et al., 2015). The $Ca_V1.2$ channel subtype, like the $Na_V1.5$, $K_V4.3$, $K_V7.1$, $K_V11.1$ and Kir2.1 channel subtypes, belongs to the panel of cardiac ion channels mentioned in the FDA's Comprehensive *in-vitro* Proarrhythmia Assay initiative. It is notably responsible for the "plateau" of cardiac action potentials. Blocking this subtype has been reported to counteract drug-induced (by $K_V11.1$ blockers, for example) or mutation-induced long QT syndromes and eventual associated "torsade de pointes" ventricular arrhythmia (Crumb et al., 2016).

In the present study, we identified a new bioactive peptide, poecitoxin-1a (PecTx-1a), from the *Poecilotheria subfusca* spider venom, following high-throughput screening of a large venom collection using automated patch-clamp electrophysiology on cells overexpressing the $hNa_V1.7$ channel subtype. This peptide was purified, sequenced, chemically synthesized, and its pharmacological profile was established on various subtypes of hNa_V, hK_V, hKir and hCa_V channels overexpressed in cell lines. PecTx-1a, a 35 amino acid toxin belonging to the inhibitor cystine knot (ICK) structural family, was shown to inhibit the $hCa_V1.2$ channel subtype at nanomolar concentrations, *i.e.* with high affinity *versus* hNav1.7 and high selectivity against the other studied channel subtypes, including those involved in the cardiac action potential.

2. EXPERIMENTAL SECTION

2.1. Isolation, purification and amino acid sequencing of PecTx-1a

The *Poecilotheria subfusca* spider venom was fractionated using an analytical RP-HPLC C18

column (XBridge™ BEH 130, 3.5 µm and 4.6 mm ID x 250 mm L column) attached to an Agilent 1260 HPLC (Agilent Technologies). Fractions that contained between 5 and 15 peptides each, at an estimated average concentration of 0.5 µg/µL (500 ng of dry mass suspended in water), were first evaluated in a functional screening assay on engineered human embryonic kidney (HEK)-293 cell lines overexpressing the human (h)$Na_V1.7$ channel subtype, using the IonWorks Quattro platform (Molecular Devices, USA), as previously reported (Gonçalves et al., 2018c). To individualize the compounds, active fractions were finally sub-fractionated using cation exchange chromatography with a TOSOH Bioscience column (TSK gel SP-STAT, 7 µm, 4.6 mm ID x 10 cm L, TOSOH Bioscience, Germany) onto an Agilent 1260 HPLC. The purified compounds were screened on HEK-293 cells overexpressing h$Na_V1.7$ and h$Na_V1.5$ channel subtypes, using the QPatch HTX automated electrophysiology platform (Sophion BioScience, Denmark), leading to the identification of PecTx-1a as one of the peptides of interest.

The peptide amino acid sequence was determined by *de novo* MS/MS sequencing and EDMAN degradation. The purified venom peptide obtained after successive RP-HPLC and cation exchange chromatography was resuspended in 100 mM ammonium bicarbonate (pH 8), reduced with 17 mM TCEP (incubated at 55°C for 1 hr) and alkylated with 24 mM iodoacetamide (incubated at room temperature in the dark for 1 hr) prior to enzyme digestion. The reduced/alkylated venom peptide was digested by using trypsin or V8 proteases. The enzyme was added at a 1:10 ratio (enzyme/peptide, w/w) and incubated overnight at 37°C before LC-MS(/MS) analyses. A Waters Q-TOF Xevo G2S mass spectrometer equipped with an Acquity UHPLC system and Lockspray source was used for the acquisition of the LC-ESI-MS and LC-ESI-MS/MS data, and the amino acid sequence determination, based on Edman degradation, was performed using an Applied Biosystems gas-phase sequencer model 492 (s/n: 9510287J), as previously detailed (Gonçalves et al., 2018c).

2.2. Chemical synthesis, folding and 3D-structure of PecTx-1a

PecTx-1a was assembled stepwise using a 2-chlorotrityl chloride resin (substitution rate of 1.6 mmol/g) by solid-phase fmoc chemistry on a Symphony Synthesizer (Protein technologies Inc.). The coupling reaction of each amino acid took 15 min and the reaction was repeated 3 times to increase the amino acid coupling yield. After resin cleavage and deprotection with 92.5% (vol) trifluoroacetic acid (TFA), 2.5% H_2O and scavengers [1,3-dimethoxybenzene (2.5%) and triisopropylsilane (2.5%)], the peptide was purified to homogeneity by C18 RP-HPLC on a Jupiter Proteo column (Phenomenex, 4 µm, 21.2 mm ID x 250 mm L), using an Agilent Technologies preparative HPLC (1260 Infinity). Finally, PecTx-1a was folded/oxidized in 50 mM Tris-HCl (pH 8.3) for 72 hr. The resulting oxidized PecTx-1a with its three disulfide bridges was purified to homogeneity (> 99% purity according to the integration of the purified chromatogram peak at 214 nm) using RP-HPLC, again with the Jupiter Proteo column. The molecular mass of PecTx-1a was determined by LC-ESI-QTOF MS. The absence of contaminant masses attested of the purity of synthetic PecTx-1a.

The 3D-structure of PecTx-1a was determined by high-resolution NMR spectroscopy in an aqueous solution (10% D_2O) of 3 mg peptide in 600 µL of 100 mM acetate buffer (pH 5), at 307°K.

Data were obtained on a Bruker Avance 700 MHz using standard 2D spectra. Resonances were assigned with 2D-spectra including DQF-COSY, TOCSY, NOESY, ^{1}H-^{13}C-HSQC and ^{1}H-^{15}N-HSQC. For conformational analysis, NOE based distance restraints were obtained from a NOESY spectrum with 100 ms mixing time. 648 distance restraints were used in a simulated annealing protocol starting from a linear, extended structure including 97 intra residual distances, 174 sequential distances, 132 medium distances (2-4 amino acids apart) and 245 long range distances (> 4 amino acids apart). Calculations were performed with the software package SYBYL (version 2.1.1). All energy calculations were based on AMBER7 F99 force field. Distance restraints for non-separated methylene protons and methyl groups were used with pseudoatom correction: 0.9 Å were added to the upper bound for methylene groups, and 1.0 Å was added for methyl groups. Ten well-converged structures were obtained. The rmsd over all backbone atoms was 0.353 ± 0.141 Å, and that over all heavy atoms was 0.659 ± 0.271 Å.

2.3. Toxins, chemicals and cell lines used for functional assays

Lyophilized synthetic PecTx-1a (molecular mass of 3996.6, purity rate > 99%) was dissolved in appropriate solutions to give adequate stock solutions. A reduced (S-carboxymethylated) inactive form of the peptide (molecular mass of 4347.1, purity rate > 95%) was used in some experiments. This reduced form was obtained by shaking 1 mg of oxidized peptide in 1 mL of solution containing 100 mM Tris-HCl and 10 mM dithiotreitol (pH 8), for 90 min at 37°C. Then, the molecule was S-carboxymethylated by adding 20 µL of a solution containing 1.25 M iodoacetic acid and 6 M gadolinium, and by shaking for 2 hr in the dark before being acidified (20% TFA, pH 1) and purified using an analytical RP-HPLC C18 column. All compounds used as reference molecules to pharmacologically validate the current flowing through each channel subtype, as indicated in Table 1, were purchased from Sigma-Aldrich (Saint-Quentin Fallavier, France) or obtained from Smartox Biotechnology (Saint-Egrève, France) and Sanofi-Aventis (Vitry-sur-Seine, France). The toxins were dissolved in distilled water to give a 100-µM stock solution, and the chemicals were dissolved in 100% dimethylsulfoxyde (DMSO, Sigma-Aldrich) to give a 10-mM stock solution. Just prior to experiments, successive dilutions were performed in the appropriate standard physiological medium [supplemented with 0.1% bovine serum albumin (BSA, Sigma-Aldrich) for toxins to avoid plastic adherence, and with 0.3% DMSO for chemicals to maintain solubility], to give the compound final concentrations indicated in the text.

Generation of inducible cell lines was achieved by cloning cDNAs encoding for $hNa_V1.2$ (NM_021007.2), $hNa_V1.5$ (NM_000335), $hCa_V3.2$ (NM_021098.2), $hCa_V3.1$ (NM_018896.4) and $hK_V1.5$ (NM_002234.3) channel subtypes into the Flp-In® T-Rex® expression vector (Invitrogen, USA) and subsequently transfected them into HEK-293 or Chinese hamster ovary (CHO) cell lines. The cDNA encoding for the $hK_V7.1$ subtype (NM_000218.2) was cloned into the Jump-In® T-Rex® expression vector (Invitrogen) and subsequently transfected into human bone osteosarcoma epithelial (U2OS) cell line. Recombinant HEK-293 cell lines, stably overexpressing the other hNa_V subtypes, were purchased from SB Drug Discovery (UK; $hNa_V1.4$), ChanTest (Cleveland, OH, USA; $hNa_V1.6$) and Eurofins (St Charles, MO, USA; $hNa_V1.7$ and $hNa_V1.8/\beta1$). CHO cells, heterologously overexpressing hKir2.1 and the other hCa_V and hK_V subtypes, were purchased from ChanTest

197 (hCa$_V$1.2/β2/α2δ1, hCa$_V$2.2/β3/α2δ1, hKir2.1 and hK$_V$4.3/KCHIP2.2) and B'SYS GmbH [Switzerland;
198 hK$_V$11.1 encoded by the human *ether-a-go-go*-related gene (hERG)].

Table 1. Compounds used as reference molecules to pharmacologically validate the current flowing through each hNa$_V$, hCa$_V$ and hK$_V$ channel subtype.

Channel subtype	Drug reference			Provider	IC$_{90-95}$ [3]
	Name	MM	Purity rate		
hNa$_V$1.1-1.8	Tetrodotoxin (citrate)	319.27	> 98%	Sigma-Aldrich	1 µM
hCa$_V$1.2	Nifedipine	346.33	> 98%	Sigma-Aldrich	10 µM
	Cadmium (Cl)[1]	183.32	> 99.99%	Sigma-Aldrich	200 µM
hCa$_V$2.2	ω-Conotoxin GVIA[A]	3036.05	> 95%	Smartox Biotechnology	1 µM
hCa$_V$3.1-3.2	Mibefradil (H_2Cl)[2]	568.55	> 98%	Sigma-Aldrich	30 µM
	Nickel (Cl)[1]	237.69	> 99.99%	Sigma-Aldrich	2 mM
hK$_V$1.5	Quinidine	324.42	> 98%	Sigma-Aldrich	100 µM
hK$_V$4.3	SNX-482	4495.00	> 98%	Sigma-Aldrich	1 µM
hK$_V$7.1	HMR 1556	411.44	> 99.99%	Sanofi-Aventis	1 µM
hK$_V$11.1	BeKm-1	4091.70	> 97%	Smartox Biotechnology	1 µM
hKir2.1	Barium (Cl)[1]	208.23	> 99.99%	Sigma-Aldrich	30 µM

[1]Cl: chloride, [2]H_2Cl, dihydrochloride, [3]IC$_{90-95}$, compound concentration necessary to inhibit 90-95% of current.

A. Concentration-response curve of ω-conotoxin GVIA effects on hCa$_V$2.2 peak current (not documented in the literature). Each value, expressed as percentage of that obtained before toxin application, represents the mean ± S.D. of data obtained from 3-4 cells. The theoretical curve corresponds to data point fit with IC$_{50}$ and n_H values of 229.4 nM and 2.2, respectively (r^2 = 0.993).

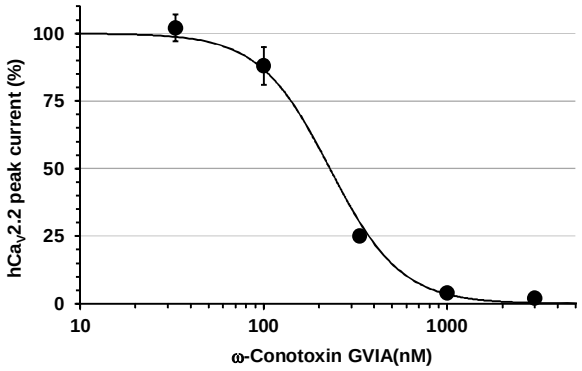

199 Transfected or stably overexpressing hNa$_V$1.1-8, hCa$_V$1.2 and hK$_V$11.1 cells were cultured as
200 previously reported (Gonçalves et al., 2018c). CHO cells heterologously overexpressing hCa$_V$2.2
201 and hK$_V$4.3 channel subtypes were cultured in Ham's F-12 Nutrient Mix with GlutaMAX™ medium
202 (Gibco, Thermo Fisher Scientific, France). Those overexpressing hKir2.1 subtype were cultured in
203 Dulbecco's modified Eagle's medium (DMEM)/F-12 Glutamax (Gibco). The complete media contain
204 10% fetal bovine serum (FBS, Gibco) and selected antibiotics and additives as recommended by
205 the manufacturer. In-house CHO-Flip-In-T-REx cells were kept in culture under standard conditions
206 (37°C, 5% CO_2) in Ham's F-12 Nutrient Mix with GlutaMAX™ medium supplemented with 10%
207 fetal calf serum (Invitrogen), 300 µg/mL hygromycin (Invitrogen) and 30 µg/mL blasticidin
208 (Invivogen). In-house U2OS-Jump-In-T-REx cells were kept in culture under standard conditions
209 (37°C, 5% CO_2) in McCoy's 5A (modified) with GlutaMAX™ medium (Gibco) supplement with 10%

fetal calf serum (Invitrogen), 0.1 mM of non-essential amino acids (Gibco), 25 mM N-2-hydroxyethylpiperazine-N'-2-ethanesulfonic acid (HEPES), 1 µg/mL puromycin (Invitrogen) and 5 µg/mL blasticidin (Invivogen). Cells were sub-cultured/passaged every 3-4 days using accutase® (Sigma-Aldrich) or TrypLE Select (Gibco) enzyme. Doxycycline (BD Biosciences, France) was added to induce target expression when needed, at least between 12 and 24 hr prior to experiments.

The human induced pluripotent stem cell-derived cardiomyocyte (hiPSC-CM) UB47 cell line was purchased from Univercell Biosolutions (Toulouse, France). The cells, derived from skin fibroblasts were cultured in m-TeSR^{TM}1 medium (StemCell Techonologies, Vancouver, Canada) on matrigel-coated (BD Biosciences) dishes. They were sub-cultured/passaged once per week using accutase® at a cell density of $5x10^3$ cells/cm. Four days before induction of cardiac differentiation, $2x10^6$ cells were platted on 60-mm diameter Petri dishes. The basal medium used for cardiac induction was the Roswell Park Memorial Institute (RPMI) medium 1640 (Gibco) supplemented with 500 µg/mL of human serum albumin (Sigma-Aldrich) and 213 µg/mL of ascorbic acid (StemCell Techonologies). The first day of induction, the basal medium was supplemented with 4 µM CHIR99021 (Miltenyi Biotech, Bergisch Gladbach, Allemagne) and 10 ng/mL bone morphogenetic protein (BMP) 4 (Miltenyi Biotech). On Day 2, the medium was replaced with the basal medium supplemented with 2 µM Wnt-C59 antagonist (Selleckchem, Texas, USA) and then, on Day 3, with the basal medium supplemented with 2.5 µM inhibitor type 1 of Wnt response (IWR-1, Sigma-Aldrich). On Day 4 and later, the cells were maintained in DMEM/F-12 medium added with 5% FBS, 1% of non-essential amino acids, 1% of GlutaMax^{TM}, 1% of Penicillin-Steptomycin (Gibco) and 0.2% of β-mercaptoethanol (Gibco). From Day 25 to Day 27, Multi Tissue Dissociation Kits and the human PSC-Derived Cardiomyocyte Isolation Kit (Miltenyi Biotech) were used to dissociate the beating cell layer and purify the cardiomyocytes which were then platted on glass coverslips coated with 10 µg/mL of human fibronectin (Corning, New York, USA) for subsequent experiments.

2.4. Electrophysiological recordings

Automated patch-clamp recordings. For screening of venom fractions, planar assay current recordings from HEK-293 cells, in perforated patch-clamp configuration, were made on an IonWorks Quattro® system (Molecular Devices, Sunnyvale, CA, USA) enabling population patch-clamp measurement, as previously detailed (Trivedi et al., 2008; Chambard et al., 2014; Gonçalves et al., 2018c). Cells were resuspended in 5 mL pre-filtered external buffer containing: 137 mM NaCl, 4 mM KCl, 1 mM $MgCl_2$, 1.8 mM $CaCl_2$, 10 mM HEPES, and 5 mM D-glucose (osmolarity set at 306 mOsm/L and pH 7.3 adjusted with NaOH). The internal solution had the following composition: 100 mM K-gluconate, 40 mM KCl, 1 mM $MgCl_2$, 1 mM EGTA, 10 mM HEPES, and 5 mM D-glucose (osmolarity set at 300 mOsm/L and pH 7.4 adjusted with KOH). The experiments were carried out at room temperature (20-22°C). After a 10-sec period holding at -100 mV, currents were evoked by ten pulses, each consisting of a 50-ms step to the voltage of the peak current of the current-voltage relationship for each channel subtype, followed by a 300-ms step back to -120 mV, applied at 10 Hz. Currents were recorded before and 10 min after incubation of cells in external solution added with venom fractions and supplemented with 0.1% BSA. The

degree of current inhibition was assessed by expressing the ratio of peak currents, calculated for pulse 1 (tonic block) or pulse 10 (use-dependent block), recorded after and before fraction application.

Screening of venom sub-fractions, as well as for hit confirmation and channel subtype selectivity of PecTx-1a, was also performed on an automated patch-clamp system, the QPatch HTX (Sophion Bioscience, Denmark), recording currents in whole-cell configuration and allowing both signal acquisition and data analyses, as previously reported (Bell and Dallas, 2017; Gonçalves et al., 2018c). The day of their use, HEK-293, CHO and U2OS cells were transferred into Eppendorf tubes containing a FreeStyle 293 expression medium (Gibco) which were then placed in the automated electrophysiology platform. The extracellular medium composition for hNa_V-overexpressing HEK-293 cells was: 154 mM NaCl, 4 mM KCl, 2 mM $CaCl_2$, 1 mM $MgCl_2$, and 10 mM HEPES (pH 7.4 adjusted with NaOH), and that of intracellular (*i.e.* path-clamp pipette) medium: 150 mM CsF, 1/50 mM EGTA/CsOH, 10 mM HEPES, 10 mM NaCl, 1 mM $MgCl_2$, and 1 mM $CaCl_2$ (pH 7.4 adjusted with CsOH). The extracellular medium composition for hCa_V-overexpressing CHO cells was: 145 mM NaCl, 4 mM KCl, 10 mM $CaCl_2$, and 10 mM HEPES (pH 7.4 adjusted with NaOH), and that of intracellular medium: 27 mM CsF, 112 mM CsCl, 8.2 mM EGTA, 10 mM HEPES, 2 mM NaCl, and 4 mM Mg-ATP (pH 7.4 adjusted with CsOH). The extracellular medium composition for hK_V-overexpressing CHO and U2OS cells was: 145 mM NaCl, 4 mM KCl, 2 mM $CaCl_2$, 1 mM $MgCl_2$, 10 mM HEPES, and 10 mM D-glucose (pH 7.4 adjusted with NaOH). That of intracellular medium was : 120 mM KCl, 5.4 mM $CaCl_2$, 10 mM EGTA, 10 mM HEPES, 4 mM Mg-ATP, and 1.75 mM $MgCl_2$ (pH 7.4 adjusted with KOH) for hK_V11.1-overexpressing CHO cells; 130 mM potassium aspartate, 5 mM EGTA, 10 mM HEPES, and 5 mM $MgCl_2$ (pH 7.4 adjusted with KOH) for hK_V1.5- and hKv4.3-overexpressing CHO cells; 120 mM potassium fluoride, 20 mM KCl, 10/31.25 mM EGTA/KOH, 10 mM EDTA, and 10 mM HEPES (pH 7.2 adjusted with KOH) for hK_V7.1-overexpressing U2OS cells; and 120 mM KCl, 10 mM EGTA, 5mM $CaCl_2$, 10 mM HEPES, and 1.75 mM $MgCl_2$ (pH 7.4 adjusted with KOH) for hKir2.1-overexpressing CHO cells. Venom sub-fractions and PecTx-1a were diluted in the extracellular medium supplemented with BSA (0.1%), to give the final concentrations indicated in the text. The times of incubation were adjusted to achieve steady-state effects. The concentration-response relationships were established by expressing the maximal amplitude of the sum of ten cell currents recorded in the presence of a given sub-fraction or toxin concentration relatively to that of the sum of these currents recorded before sub-fraction or toxin application.

The experiments were carried out at room temperature (20-22°C). The hNa_V-overexpressing HEK-293 cells were maintained at a holding potential of either -90 mV (hNa_V1.5) or -100 mV (other hNa_V channel subtypes). Currents were elicited at a frequency of 0.2 Hz by 20-ms test-pulses to -20 mV (hNa_V1.2, 1.4, and 1.7), -40 mV (hNa_V1.5), -15 mV (hNa_V1.6) or 10 mV (hNa_V1.8), preceded by 40-ms (hNa_V1.7) or 200-ms (hNa_V1.5) pulses to -120 mV, or not (hNa_V1.2, 1.4, 1.6, and 1.8). The hCa_V-overexpressing CHO cells were maintained at a holding potential of -50 mV (hCa_V1.2), -90 mV (hCa_V2.2) or -100 mV (hCa_V3.1 and 3.2), and currents were elicited at a frequency of 0.05 Hz by 200-ms test-pulses to 0 mV (hCa_V1.2), by 500-ms test-pulses to 20 mV (hCa_V2.2) or by 500-ms test-

pulses to -20 mV ($hCa_V3.1$ and 3.2). The $hK_V11.1$-overexpressing CHO cells were maintained at a holding potential of -80 mV, and tail currents were elicited at a frequency of 0.07 Hz by 5-sec test-pulses to -50 mV, preceded by 4.8-sec pulses to 20 mV following 20-ms pulses to -50 mV. The hKir2.1-overexpressing CHO cells were maintained at a holding potential of -20 mV, and currents were elicited at a frequency of 0.03 Hz by 500-ms test-pulses to -120 mV followed by 1-sec potential ramps from -120 to 0 mV. The $hK_V1.5$-overexpressing CHO cells were maintained at a holding potential of -90 mV, and currents were elicited at a frequency of 0.05 Hz by 500-ms test-pulses to 20 mV. The $hK_V4.3$-overexpressing CHO cells were maintained at a holding potential of -90 mV, and currents were elicited at a frequency of 0.1 Hz by 300-ms test-pulses to 20 mV. The $hK_V7.1$-overexpressing U2OS cells were maintained at a holding potential of -60 mV, and currents were elicited at a frequency of 0.07 Hz by 1-sec test-pulses to 40 mV preceded by 200-ms pulses to -80 mV.

Manual patch-clamp recordings. Whole-cell manual patch-clamp experiments were performed on hiPSC-CMs by using an Axopatch 200B integrating patch-clamp amplifier and the pClamp10.2 software (Molecular Devices, Sunnyvale, CA, USA). The signals, acquired at a 4-kHz sample rate, were filtered at 2 kHz with a low-pass Bessel filter and digitized with the aid of a computer equipped with an analog-to-digital converter (Digidata-1440A model; Molecular Devices). The patch-clamp pipettes were filled with a medium composed of: 110 mM CsCl, 20 mM tetraethylammonium (TEA) chloride, 10 mM EGTA, 5 mM Mg-ATP, 2 mM $MgCl_2$, and 10 mM HEPES (pH 7.2, adjusted with CsOH), and had about 2-MΩ resistance in the standard physiological medium. A fast perfusion system allowed changing the extracellular medium (added or not with a given toxin concentration) around the recorded hiPSC-CM within a few seconds. The composition of the extracellular physiological medium was: 120 mM N-methyl-d-glucamine chloride, 20 mM TEA chloride, 10 mM $CaCl_2$, 2 mM $MgCl_2$, 10 mM HEPES, and 10 mM D-glucose (pH 7.4 adjusted with TEA hydroxide). The experiments were carried out at constant room temperature (22°C). The cells were maintained at a holding potential of -80 mV, and currents were elicited at a frequency of 1 Hz by 300-ms test-pulses varying from -70 to 50 mV in 5-mV increments.

2.5. Data and statistical analyses

Concentration-response relationships were established by plotting the response, recorded in the presence of a given toxin (Rt) and expressed as percentage of the value obtained in absence of toxin (Rc), against the toxin concentration ([toxin]). The theoretical concentration-response curves were calculated from typical sigmoid nonlinear regressions through data points (correlation coefficient = r^2) according to the Hill equation (GraphPad Prism 5 or QPatch assay software): $Rt / Rc = 1 / [1 + ([toxin] / IC_{50}) n_H]$, where IC_{50} is the toxin concentration necessary to inhibit 50% of the response, and n_H is the Hill number. Conductance (g) was calculated according to the following equation: $g = I / (V_T - V_X)$, where I is the peak current amplitude, V_T is the test-pulse voltage, and V_X is the equilibrium potential of ions. Conductance-voltage relationships were established by plotting the conductance, expressed as percentage of the maximal conductance (gmax) calculated at strongly positive test-pulses, as a function of test-pulse voltage. The theoretical curves correspond to data point fits, according to the Boltzmann equation (GraphPad

Prism 5 software): g / gmax = 1 – [1 / (1 + exp ((V_T – $V_{T50\%}$) / k_g))], where $V_{T50\%}$ is the test-pulse voltage corresponding to 50% maximal conductance, and k_g is the slope of the curve. Steady-state inactivation-voltage relationships were established by plotting the peak current amplitude, expressed as percentage of the maximal amplitude (Imax) recorded in response to strongly negative pre-pulses, as a function of pre-pulse voltage (V_P). The theoretical curves correspond to data point fits, according to the Boltzmann equation (GraphPad Prism 5 software): I / Imax = 1 / [1 + exp ((V_P – $V_{P50\%}$) / k_h)], where $V_{P50\%}$ is the pre-pulse voltage corresponding to 50% maximal peak amplitude of current, and k_h is the slope of the curve. Current kinetics were evaluated by calculating: (1) the time to peak (tp), defined as the time between test-pulse triggering and the peak current, and (2) the time constant (τh) of the current decay, for current inactivation that occurs as a mono-exponential decay as a function of time, *i.e.* $I_{(t)} = I_{(0)} e^{(-t/\tau h)}$ (Equation 1) where $I_{(0)}$ is the current at time zero of depolarization.

Data are expressed as means ± standard deviations (S.D.) of n different experiments. The statistical comparison of values was carried out using the parametric two-tailed Student's *t*-test (either paired samples for comparison within a single population or unpaired samples for comparison between two populations). Differences between values were considered to be statistically significant at $P \leq 0.05$.

3. RESULTS

3.1. Isolation, purification and *de novo* amino acid sequencing of PecTx-1a

The screening process for the spider venom *Poecilotheria subfusca*, from primary fraction selection to individual purified compound selection by secondary screening, is presented in Figure 1A-B. The primary screening of venom fractions was performed on automated patch-clamp Ionworks Quattro platform using HEK-293 cells overexpressing the $hNa_V1.7$ channel subtype. It is worth noting that, under our experimental conditions, no control current rundown was observed, since the average peak current from pulse 1 was similar to that from pulse 10. In addition, no inhibitory effect of 0.1% BSA was detected on the elicited current while it was fully blocked by 1 µM TTX (used as internal positive control during the screening process). The percentage of inhibition of peak $hNa_V1.7$ current obtained for each of the 64 fractions (tested at an average concentration of 0.5 µg/µL for a 10-min incubation period) is shown in Figure 1A (left panel). Based on their relatively high potency for the $hNa_V1.7$ channel subtype, one fraction was selected from this primary screening for sub-fractionation and compound isolation using cation exchange chromatography. Hence, 5 sub-fractions were prepared and tested, at a final estimated amount of 100 ng per well, on HEK-293 cells overexpressing $hNa_V1.7$ and $hNa_V1.5$ channel subtypes, using the QPatch HTX automated electrophysiology platform (Figure 1A, right panel). Two of them, SF03 and SF05, were shown to display a potent blocking effect on $hNa_V1.7$ (94.7-96.9% block) while being less efficient on $hNa_V1.5$ (35.0-75.4% block) channel subtypes. However, the SF05 sub-fraction also produced a marked slow-down of $hNa_V1.7$ inactivation and was thus discarded.

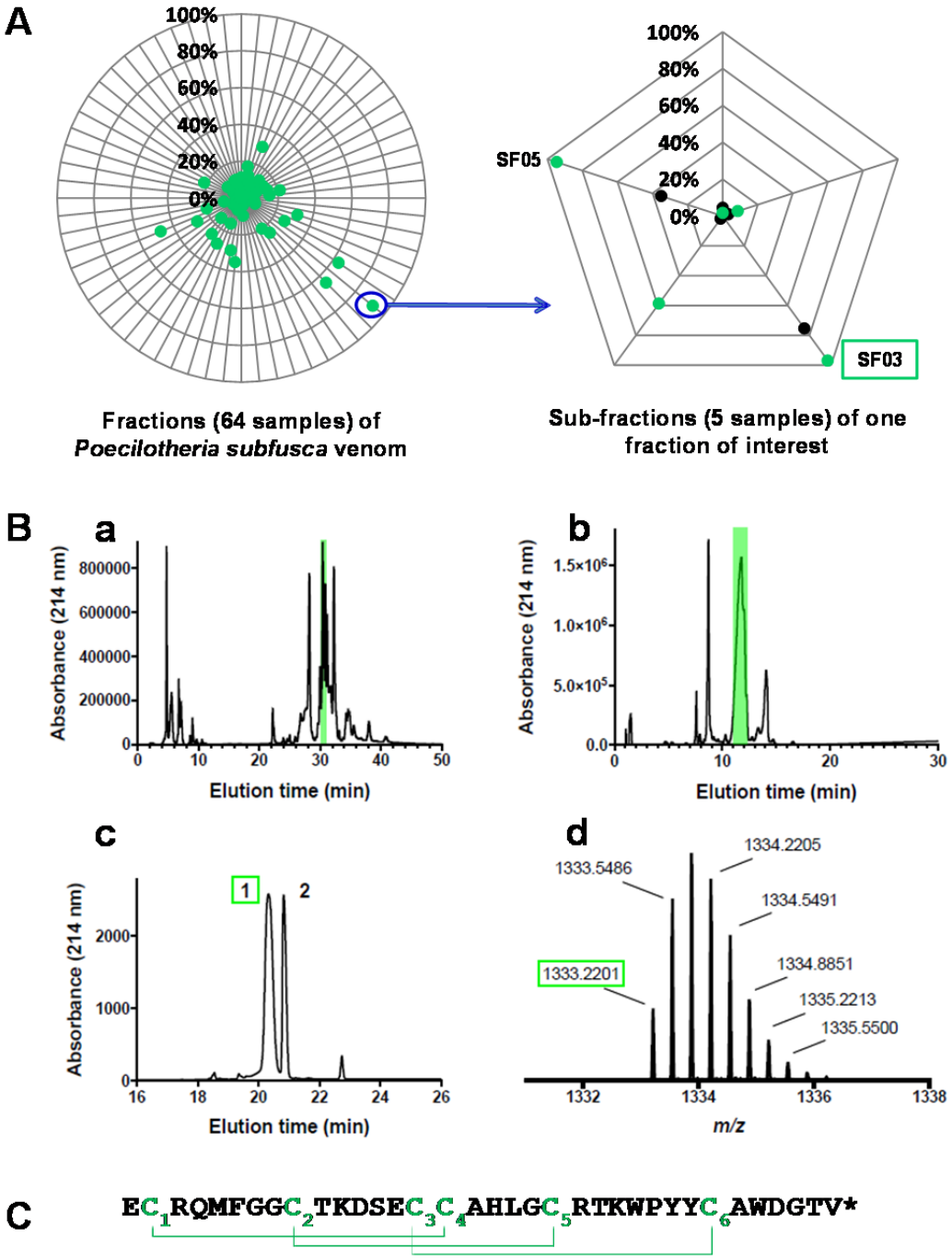

Figure 1. Isolation, purification and *de novo* amino acid sequencing of PecTx-1a. (**A**) Percentage of inhibition of peak $hNa_V1.7$ current by 0.5 µg/µL of each of the 64 fractions obtained from *Poecilotheria subfusca* spider venom (left panel) and 100 ng per well of each of the 5 sub-fractions (SF) obtained from the fraction of interest (right panel), tested on HEK-293 cells overexpressing $hNa_V1.7$ (green circles) and $hNa_V1.5$ (black circles) channel subtypes. (**Ba** and **b**) Fractionation of the *Poecilotheria subfusca* crude venom by reversed-phase chromatography (RP-HPLC) and detection by UV at 214 nm. The fraction containing the peptide of interest is highlighted in green. (**Bc**) MALDI-TOF mass spectrometry of the primary fraction highlighted in (Bb), showing two predominant peaks corresponding to PecTx-1a (**1**, 3996.6 Da) and a non-characterized toxin (**2**, 3835.5 Da). (**Bd**) ESI-MS spectrum of PecTx-1a $[M+3H]^{3+}$ detected at *m/z* 1333.2201. (**C**) Primary structure and disulfide bridge alignment of PecTx-1a. Disulfide bridging of the amidated (*) peptide of 35 amino acid residues including 6 cysteines, as defined by homology with toxins from the NaSpTx family 2, occurs according to the C1-C4, C2-C5 and C3-C6 pattern.

Finally, through the multi-step chromatographic approach, two new peptides, 1 and 2, were identified from SF03 sub-fraction using combined orthogonal reversed-phase and ion exchange techniques (Figure 1Ba-c). The molecular mass values of 3996.6 and 3835.5 Da for peptides 1 and

2, respectively, determined by LC-ESI QTOF MS (as exemplified for peptide 1 in Figure 1Bd), indicated that these peptides should be amenable to chemical synthesis. However, natural peptide 2 was observed to be 66 times less potent than natural peptide 1 on HEK-293 cells overexpressing $hNa_V1.7$ channel subtype and was thus discarded.

As peptide 1 belongs to a species that has not been genotyped, its primary sequence was determined by *de novo* sequencing using a combination of analytical techniques including top-down and bottom-up approaches with high resolution mass spectrometry. Hence, the purified peptide was reduced using Tris (2-carboxyethyl) phosphine hydrochloride (TCEP) and alkylated with iodoacetamide. The alterations in molecular mass from 3996.6 to 4344.6 Da indicate that the peptide should contain six cysteine residues and hence three disulfide bridges if one takes into account the loss of 1 Da upon reduction of disulfide bridges and the addition of 57.02 Da upon alkylation on each cysteine residue. Samples of the reduced/alkylated toxin were then digested overnight with either trypsin or V8 proteases. The digests were next analysed by LC-ESI-MS(/MS) for *de novo* sequencing. While full sequence coverage of the toxin was obtained by mass spectrometry, a complementary characterization was performed using Edman degradation, especially for the precise determination of the isobaric residues leucine and isoleucine. The final sequence, with cysteine bonds assigned by blast homology with structurally related toxins, is reported in Figure 1C. A C-terminal amidation of the peptide was identified as a post-translational modification (PTM).

Peptide 1, composed of 35 amino acids (3996.6 Da), was identified as μ/ω-theraphotoxin-Ps1a, also named poecitoxin-1a or PecTx-1a. It is the first toxin described so far from the venom of *Poecilotheria subfusca* spider, known as the ivory-billed ornamental or montane tiger spider, an arboreal tarantula endemic to Sri Lanka and classified in the Selenocosmiinae-Poecilotheriini subfamily. PecTx-1a contains the ICK architectural motif previously reported in toxins from the same Theraphosidae spider family. Moreover, the primary sequence of the peptide was submitted to the SwissProt database using the protein Blast of NCBI. Although appearing as undescribed and innovative compound, PecTx-1a shows high sequence identity (66-74%) and similarity (74-80%) with peptides issued from the Chinese tarantula *Chilobrachys jingzhao* (previously named *Chilobrachys guangxiensis*) for most of them, characterized by a 33-35 amino acid sequence with three disulfide bridges, and belonging to the Na_V channel spider toxin (NaSpTx) family 2.

3.2. Chemical synthesis, *in vitro* folding and 3D-structure of PecTx-1a

PecTx-1a was chemically synthesized using solid-phase Fmoc chemistry, and the reduced PecTx-1a peptide was oxidized to produce oxidized/folded PecTx-1a along with its three-disulfide bridges. The yield of oxidation indicated good formation of the secondary structures and easy disulfide bridge connectivity during oxidation. To confirm that the synthetic PecTx-1a was identical to its natural counterpart, the retention time of the natural peptide extracted from the crude venom of *Poecilotheria subfusca* spider was compared to that of the synthetic folded analog by analytical RP-HPLC-UV. Single uniform peak signals were detected for natural and synthetic PecTx-1a (Figure 2Aa-b). In addition, both peptides were mixed at equal concentrations and run simultaneously onto analytical RP-HPLC. As a single major peak was detected (Figure 2Ac), we

411 conclude that the two peptides co-elute, hence demonstrating identical retention times on the
412 C18 column.

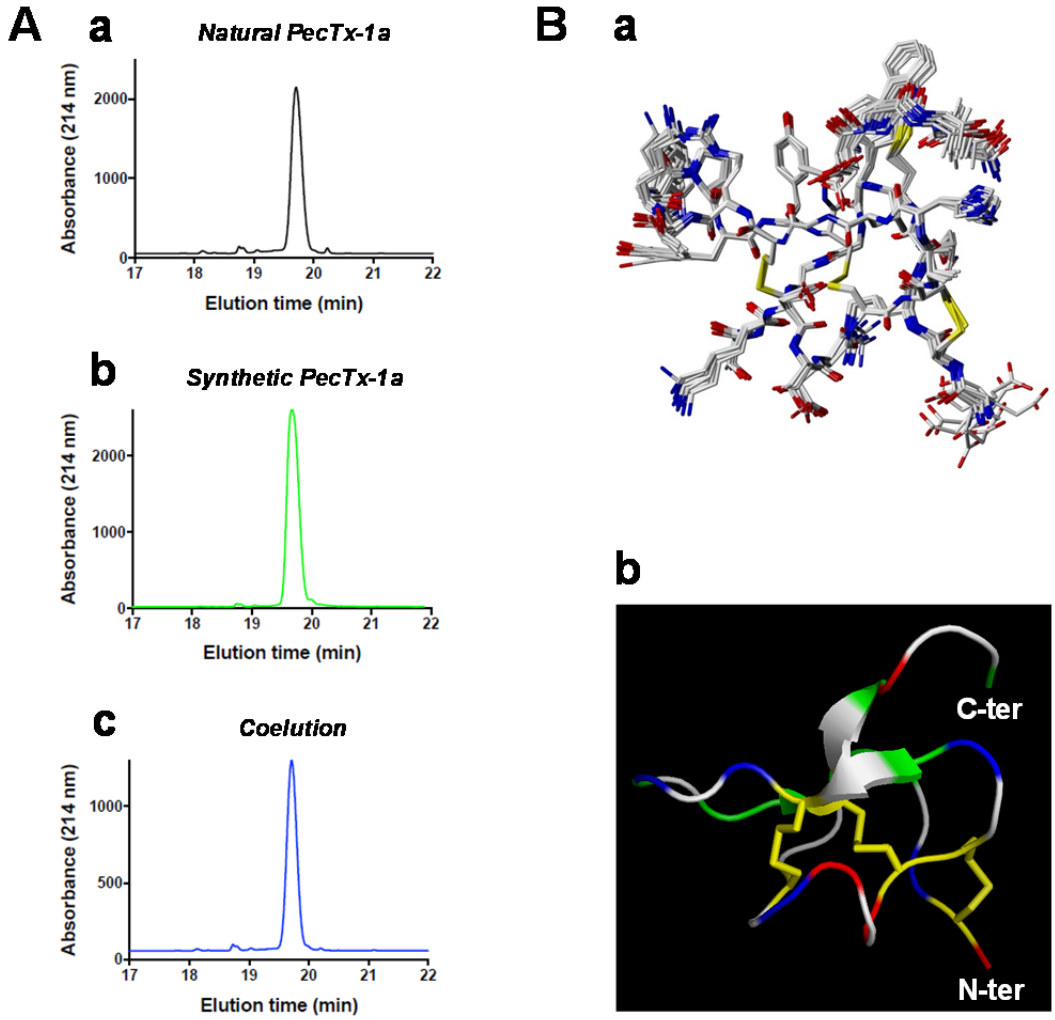

Figure 2. Chemical synthesis, *in vitro* folding and 3D-structure of PecTx-1a. (**A**) RP-HPLC-UV profiles observed at 214 nm for natural (**a**) and synthetic folded (**b**) PecTx-1a, as well as for both (**c**). The presence of single uniform peaks demonstrates the suchness of the two compounds. (**B**) 3D-Structure of PecTx-1a. (**a**) Superposition of 10 structures derived from a 2-ns restrained MD simulation "in water" (all heavy atoms are shown). All backbone atoms of residues 2-32 were used for fitting. Structures were sampled in 50 ps intervals and energy minimized. The rmsd over all backbone atoms is 0.353 ± 0.141 Å. Considering all heavy atoms, the rmsd is 0.659 ± 0.271 Å (PDB: XXXX). (**b**) Ribbon representation indicating elements of secondary structure. The structure topology is composed of double stranded antiparallel β-sheet (arrows). The three disulfide bonds are C2-C17, C9-C22 and C16-C29 (in yellow). Hydrophobic residues are colored in green, and basic and acidic residues in blue and red, respectively. The other polar residues are colored in white.

413 The experimental molecular mass of the non-reduced form (with its disulfide bridges) of the
414 synthetic peptide (Figure 1Bd, *m/z* 1333.2201 for $[M+3H]^{3+}$) was in close agreement with the
415 theoretical mass of the postulated sequence (*m/z* 1333.2260 for $[M+3H]^{+}$). Moreover, synthetic
416 and natural peptides had similar potencies to interact with the $hNa_V1.7$ channel subtype
417 overexpressed in HEK-293 cells.

418 The 3D-structure of PecTx-1a was determined by 2D homonuclear ^{1}H-NMR spectroscopy
419 (Figure 2B). Spectra were recorded at 307°K where the amid resonances show a good dispersion.
420 One signal set of sharp and well-dispersed resonances is indicative of a single structure in solution.

NMR-derived interproton distances were used for structure calculations with a molecular dynamic-based protocol. An ensemble of 10 conformations was obtained, containing a well determined backbone conformation of an ICK motif (PDB: XXXX). The ^{1}H-chemical shifts of PecTx-1a in H_2O/D_2O highlight the high precision and stereochemical quality of the ensemble of PecTx-1a structures (Table 2).

Table 2. ^{1}H-chemical shifts of PecTx-1a in H_2O/D_2O, 100 mM acetate buffer, pH 5 at 307°K (3 mg in 600 µL)*.

No.	Residue	NH	Hα	Hβ	Others
1	Glu	-	4.16	2.19/2.15	γ: 2.46
2	Cys	8.765	4.73	3.17/2.86	
3	Arg	9.14	4.51	2.08	γ: 1.96/1.79, δ: 3.34/3.26, ε: 7.27
4	Gln	8.23	4.05	2.32/1.87	γ: 2.57/2.46, ε: 7.63/6.83
5	Met	8.19	3.656	1.74/1.59	γ: 1.935/1.27, ε: 1.86
6	Phe	8.925	3.565	3.42/3.00	δ: 6.60, ε: 7.245, ζ: 7.245
7	Gly	9.01	4.23/3.515		
8	Gly	8.71	4.38/3.85		
9	Cys	7.77	5.09	3.22/3.18	
10	Thr	9.81	4.46	4.21	γ: 1.20
11	Lys	7.82	4.71	2.01/1.78	γ: 1.37, δ: 1.61, ε: 2.90
12	Asp	8.89	4.15	2.89/2.69	
13	Ser	8.18	4.245	4.06/3.885	
14	Glu	7.44	4.26	2.37/2.15	γ: 2.37/2.21
15	Cys	8.03	5.16	3.17/2.88	
16	Cys	8.97	4.60	3.48/2.50	
17	Ala	7.85	3.98	1.14	
18	His	8.48	4.10	3.63/3.39	δ: 7.17, ε: 8.52
19	Leu	7.74	5.05	2.17/1.10	γ: 1.49, δ: 0.74, δ': 0.63
20	Gly	8.96	4.35/3.67		
21	Cys	9.59	4.71	2.70/2.55	
22	Arg	8.07	4.11	2.14/1.79	γ: 1.71, δ: 2.94/2.22, ε: 7.05
23	Thr	8.03	4.285	4.54	γ: 1.245
24	Lys	7.22	4.61	1.76/1.57	γ: 1.43, δ: 1.71, ε: 3.03
25	Trp	8.30	3.09	2.99	H1: 10.21, H2: 7.18, H4: 7.22, H5: 7.13, H6: 7.25, H7: 7.51
26	Pro	-	2.75	1.31/0.82	γ: 1.43/0.99, δ: 3.18/3.00
27	Tyr	7.53	4.305	3.305/3.11	δ: 7.19, ε: 6.85
28	Tyr	6.785	5.555	2.76/2.675	δ: 6.86, ε: 6.68
29	Cys	8.89	5.02	3.00/2.66	
30	Ala	9.72	4.88	1.51	
31	Trp	8.585	4.84	3.35/3.18	H1: 10.46, H2: 7.61, H4: 7.61, H5: 7.13, H6: 7.13, H7: 7.24
32	Asp	8.216	4.45	2.75/2.32	
33	Gly	~6.46	3.65/~2.61		
34	Thr	8.075	4.44	4.30	γ: 1.135
35	Val	8.13	4.09	2.00	γ: 0.90, γ': 0.90, NH_2: 7.49/6.99

*Proton chemical shifts are referenced to sodium-3-(Trimethylsilyl)propionate-2,2,3,3-d_4.

3.3. Effects of PecTx-1a on hNa$_V$ channel subtypes

Automated patch-clamp experiments performed on HEK-293 cells overexpressing hNa$_V$1.2 and 1.4-1.8 channel subtypes revealed that 1 µM of synthetic PecTx-1a was effective to block hNa$_V$1.5 and 1.7 currents while fully sparing hNa$_V$1.2, 1.4, 1.6 and 1.8 currents (Figure 3A). The following increasing order for IC$_{50}$ values was obtained from the concentration-response curves of PecTx-1a effects on currents flowing through the different hNa$_V$ channel subtypes (Figure 3B): hNa$_V$1.7 (118.4 ± 23.7 nM, n ≥ 3) > hNa$_V$1.5 (260.9 ± 8.9 nM, n = 3) > hNa$_V$1.6 (> 3200 nM, n = 9) ≥ hNa$_V$1.2 (> 4200 nM, n = 3) ≥ hNa$_V$1.4 (> 10000 nM, n = 4) ≥ hNa$_V$1.8 (> 10000 nM, n = 3). This indicates that the main hNa$_V$ channel subtypes affected by low concentrations of peptide (below 1 µM) were restricted to hNa$_V$1.7 and 1.5 (Table 3A). It is worth noting that some preliminary experiments revealed that PecTx-1a seems to be at least between 15 and 26 times more potent to interact with hNa$_V$1.7 than hNa$_V$1.3 (IC$_{50}$ > 1800 nM, n = 3) and hNa$_V$1.1 (IC$_{50}$ > 3100 nM, n = 3) channel subtypes.

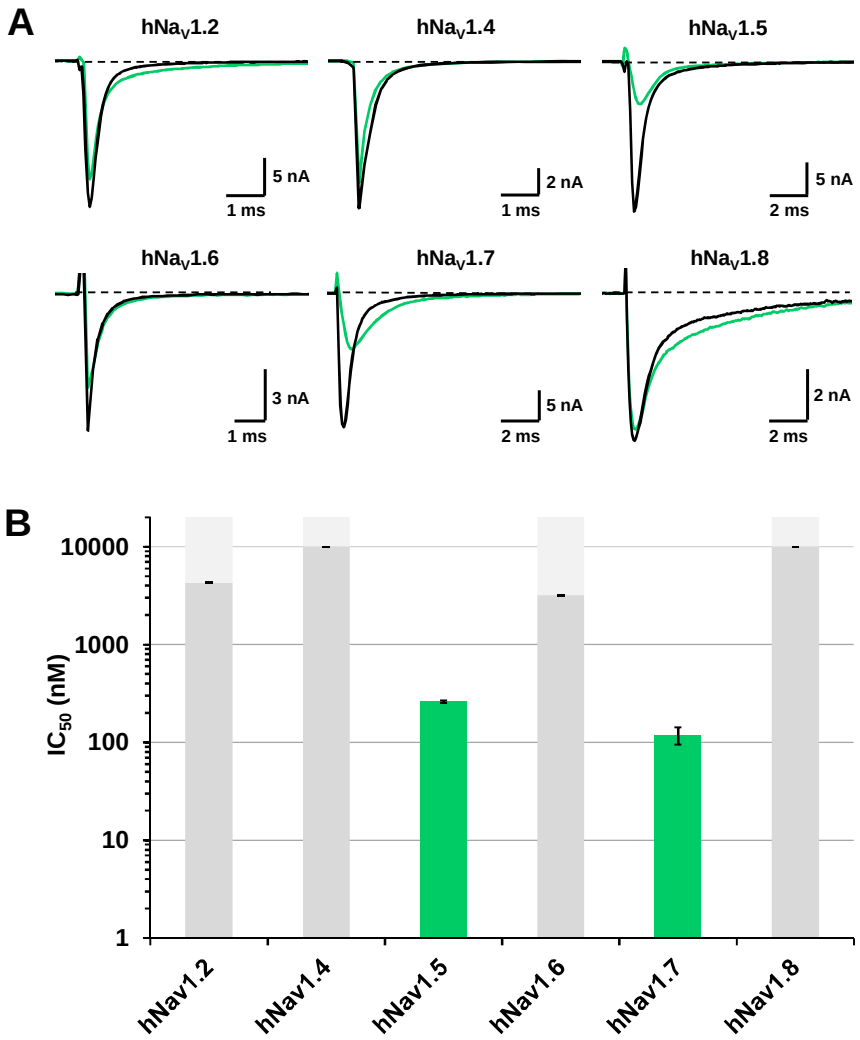

Figure 3. Effects of PecTx-1a on HEK-293 cells overexpressing hNa$_V$ channel subtypes. (**A**) Representative traces of sodium currents flowing through hNa$_V$1.2, and 1.4-1.8 channel subtypes, recorded before (in black) and after (in green) exposure to 1 µM PecTx-1a. The recording protocols are detailed in the Experimental section. (**B**) Histograms of IC$_{50}$ values (in nM) obtained from the concentration-response curves of PecTx-1a effects on HEK-293 cells overexpressing hNa$_V$1.2, and 1.4-1.8 channel subtypes. Each value represents the mean ± S.D. of data obtained from 3-10 cells. Mean value ± S.D. of n_H was 0.7 ± 0.1. The dark grey bars indicate the minimum values determined under our experimental conditions.

Table 3. Changes in current amplitude (I) and activation (tp) and inactivation (τh) kinetic parameters induced by 1 and 10 µM concentrations of PecTx-1a ([PecTx-1a]) on HEK-293 cells overexpressing hNa_V channel subtypes (**A**), changes in current amplitude, activation and inactivation kinetic parameters and voltage curves (shift) induced by 0.1-10 µM of peptide on CHO and U2OS cells overexpressing hKir and hK_V channel subtypes (**B**), and on CHO cells overexpressing hCa_V channel subtypes (**C**).

A	**[PecTx-1a]**	**I change**	**τh change**	**tp change**	***Conclusion***
$hNa_V1.2$	1 µM	22% ↘	1.5x ↗	0.9x ↘	*No marked effect at low [PecTx-1a]*
	10 µM	*nd*	*nd*	*nd*	
$hNa_V1.4$	1-10 µM	→	→	→	*No effect, even at high [PecTx-1a]*
$hNa_V1.5$	1 µM	75% ↘	1.8x ↗	1.4x ↗	***At low [PecTx-1a]**, decreased peak current and moderated effects on activation and inactivation kinetics*
	10 µM	97% ↘	*nd*	*nd*	
$hNa_V1.6$	1 µM	→	→	→	*No effect at low [PecTx-1a]*
	10 µM	*nd*	*nd*	*nd*	
$hNa_V1.7$	1 µM	57% ↘	4.8x ↗	1.7x ↗	***At low [PecTx-1a]**, decreased peak current and marked slow-down of activation and inactivation*
	10 µM	86% ↘	5.7x ↗	2.0x ↗	
$hNa_V1.8$	1 µM	→	1.6x ↗	→	***At high [PecTx-1a]**, increased peak current due to marked slow-down of inactivation*
	10 µM	37% ↗	6.6x ↗	1.1x ↗	
B	**[PecTx-1a]**	**I change**	**Kinetic change**	**Voltage shift**	***Conclusion***
$hKir2.1$	0.1 µM	→	→	*nd*	*No effect, even at high [PecTx-1a]*
	10 µM	→	→	*nd*	
$hK_V1.5$	0.1 µM	9% ↗	*nd*	*nd*	***At high [PecTx-1a]**, increased current not associated with current-voltage shift*
	10 µM	70-90% ↗	*nd*	→	
$hK_V4.3$	0.1 µM	43% ↘	1.3-1.7x ↗	Positive shift	***At low [PecTx-1a]**, decreased peak current due to marked current-voltage positive shift*
	10 µM	46% ↘	1.4-1.8x ↗	Positive shift	
$hK_V7.1$	0.1 µM	*nd*	*nd*	*nd*	*No marked effect, even at high [PecTx-1a]*
	10 µM	19% ↗	*nd*	→	
$hK_V11.1$	0.1 µM	16% ↘	*nd*	*nd*	***At high [PecTx-1a]**, decreased current*
	10 µM	75% ↘	*nd*	*nd*	
C	**[PecTx-1a]**	**I change**	**Kinetic change**	**Voltage shift**	***Conclusion***
$hCa_V1.2$	0.1 µM	94% ↘	*nd*	*nd*	***At low [PecTx-1a]**, decreased current*
$hCa_V2.2$	0.1-10 µM	→	→	*nd*	*No effect, even at high [PecTx-1a]*
$hCa_V3.1$	0.1 µM	→	→	*nd*	*No marked effect, even at high [PecTx-1a]*
	10 µM	19% ↘	→	*nd*	
$hCa_V3.2$	0.1-10 µM	→	→	*nd*	*No effect, even at high [PecTx-1a]*

nd: not determined, ↘: decreased, ↗: increased, →: unchanged.

Further investigation was performed to detail the effects of PecTx-1a on the biophysical properties of $hNa_V1.7$ and 1.5 channel subtypes (Figure 4). In addition to a decreased peak current, the peptide also produced a marked and significant slow-down of the activation and

inactivation of $hNa_V1.7$ channel subtype, while the effects on those of $hNa_V1.5$ channel subtype were moderated and non-significant (Figure 4A, Tables 3A and 4). To overcome the potential increase that might arise from the effects of PecTx-1a on activation and inactivation kinetics, the current was calculated at time zero of depolarization (time-0 current or $I_{(0)}$), according to Equation 1 (see Experimental section). Under these conditions, IC_{50} values of 61.7 and 260.9 nM were determined from the concentration-response curves of PecTx-1a effects on $hNa_V1.7$ and 1.5 time-0 currents, respectively (Figure 4B). It is worth noting that similar IC_{50} values were obtained for $hNa_V1.5$ time-0 and peak currents (Figure 4B, right panel). On the contrary, the IC_{50} value for the $hNa_V1.7$ peak current was higher than that of the $hNa_V1.7$ time-0 current (Figure 4B, left panel). In particular, for peptide concentrations between 1 and 10 µM, the $hNa_V1.7$ peak current re-increased as the variations of activation and inactivation kinetic parameters (tp and τh, respectively) became higher (Figure 4B, left panel, dashed grey rectangle). In addition, PecTx-1a induced marked negative and positive shifts of steady-state inactivation- and conductance-voltage relationships of $hNa_V1.7$ channel subtype, respectively, while the peptide-induced blocking action occurred without any significant change in these relationships for $hNa_V1.5$ channel subtype (Figure 4C and Table 4). The $hNa_V1.5$ peak current, which was decreased to 4.1 ± 1.6% (n = 3) by 10 µM PecTx-1a, recovered to 30.8 ± 6.3% (n = 2) after peptide wash-out for periods up to 3 min, compared to control values determined before cell exposure to PecTx-1a. In addition, the $hNa_V1.5$ peak current decrease measured in the presence of 250 nM of folded and reduced inactive forms of PecTx-1a was of 48.2 ± 2.1% (n=7) and 2.5 ± 1.0% (n = 8), respectively, compared to control values determined before cell exposure to any peptide form, further supporting the specificity of PecTx-1a action.

Table 4. Kinetic parameters of activation (tp) and inactivation (τh), and parameters of steady-state inactivation- ($V_{P50\%}$ and k_h) and conductance- ($V_{T50\%}$ and k_g) voltage relationships for HEK-293 cells overexpressing $hNa_V1.7$ and $hNa_V1.5$ channel subtypes, and CHO cells overexpressing $hCa_V1.2$ and $hK_V4.3$ channel subtypes (means ± S.D. of 3-10 cells).

		tp (ms)	**τh** (ms)	**$V_{P50\%}$** (mV)	**k_h** (mV^{-1})	**$V_{T50\%}$** (mV)	**k_g** (mV^{-1})
$hNa_V1.7$	Control	0.71 ± 0.03	0.49 ± 0.03	-65 ± 1	4.4 ± 0.2	-26 ± 2	3.4 ± 0.5
	PecTx-1a[1]	1.00 ± 0.06[5]	1.02 ± 0.09[5]	-75 ± 2[5]	7.5 ± 0.5[5]	-16 ± 2[5]	7.0 ± 1.0[5]
$hNa_V1.5$	Control	0.83 ± 0.05	0.63 ± 0.08	-71 ± 2	4.8 ± 0.2	-51 ± 2	4.6 ± 0.7
	PecTx-1a[2]	0.97 ± 0.05	0.84 ± 0.11	-74 ± 2	4.9 ± 0.1	-43 ± 4	8.3 ± 3.5
$hK_V4.3$	Control	8.79 ± 0.31	69.21 ± 3.32	-33 ± 2	5.0 ± 0.7	*nd*	*nd*
	PecTx-1a[3]	15.04 ± 0.58[5]	89.32 ± 1.98[5]	-23 ± 3[5]	6.8 ± 0.4[5]	*nd*	*nd*
$hCa_V1.2$	Control	3.82 ± 0.14	16.47 ± 3.13	-28 ± 2	3.2 ± 0.7	-10 ± 3	4.6 ± 0.6
	PecTx-1a[4]	4.05 ± 0.31	17.82 ± 3.88	-33 ± 3[5]	3.9 ± 0.7	-9 ± 3	5.6 ± 1.6

[1]351.5 nM, [2]250 nM, [3]37 nM, and [4]3.3 nM. [5]$P < 0.05$ (*versus* control). *nd*: not determined.

The effects of high concentrations (*i.e.* > 1 µM) of PecTx-1a were also studied on some other hNa_V channel subtypes (see Table 3A). While no significant alteration of $hNa_V1.4$ current was detected, the $hNa_V1.8$ peak current was markedly increased and its inactivation markedly slowed down by the peptide (Figure 4bisA and B). The increase in peak current was dependent on PecTx-

468 1a concentration and was completely reversed by peptide wash-out for periods up to 4 min
469 (Figure 4bisA). Hence, the current, which was enhanced to 137 ± 4% (n = 3) by 10 µM PecTx-1a,
470 recovered to 101 ± 6% (n = 3) after wash-out, compared to values determined before cell
471 exposure to the peptide. Interestingly, similar IC_{50} values were obtained from the concentration-
472 response curves of PecTx-1a effects on $hNa_V1.8$ peak current and τh variations, *i.e.* 2.5 and 2.8
473 µM, respectively (Figure 4bisC).

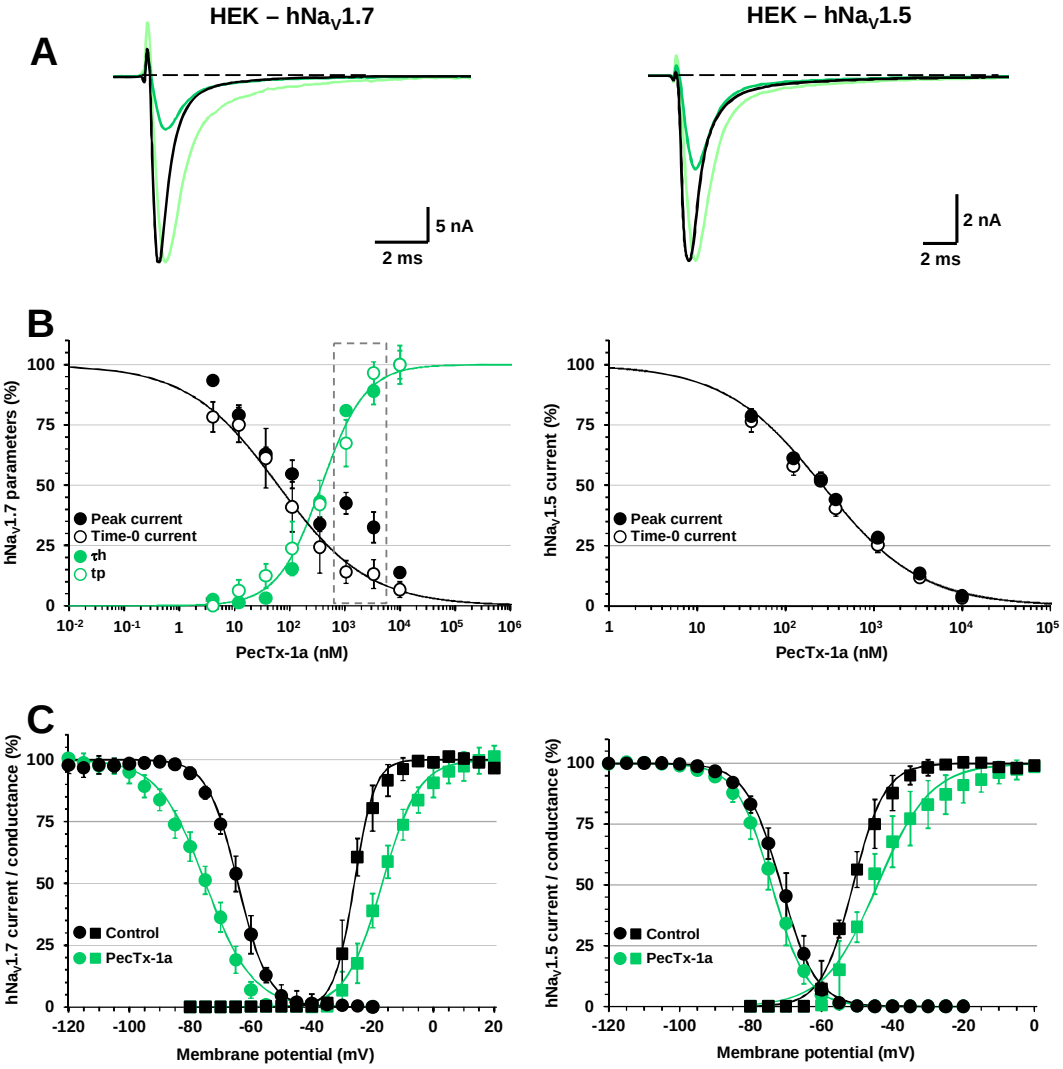

Figure 4. Effects of PecTx-1a on HEK-293 cells overexpressing $hNa_V1.7$ (left panels) and 1.5 (right panels) channel subtypes. (**A**) Representative traces of currents flowing through $hNa_V1.7$ and 1.5 subtypes, recorded before (in black) and after (in green) exposure to 351.5 and 250 nM PecTx-1a, respectively. In light green, current recorded in the presence of PecTx-1a and expressed relatively to the peak control current. (**B**) Concentration-response curves of PecTx-1a effects on peak (black closed circles) and time-0 (black open circles) currents, and on the variations of activation (tp, green open circles) and inactivation (τh, green closed circles) kinetic parameters. Each value, expressed as percentage of that obtained before toxin application, represents the mean ± S.D. of data obtained from 3-9 cells. The theoretical curves correspond to data point fits with IC_{50} and n_H values of, respectively, 61.7 nM and 0.6 (r^2 = 0.976, black curve in left panel), 378.0 nM and 1.1 (r^2 = 0.956, green curve in left panel), and 260.9 nM and 0.8 (r^2 = 0.986, black curve in right panel). (**C**) Steady-state inactivation- (circles) and conductance- (squares) voltage relationships for HEK-293 cells overexpressing $hNa_V1.7$ and 1.5 subtypes, before (black symbols) and after (green symbols) exposure to 351.5 and 250 nM PecTx-1a, respectively. Each value represents the mean ± S.D. of data obtained from 3-6 cells, and is expressed as percentage of either maximal peak amplitude of current at strongly negative pre-pulse voltages or maximal conductance calculated at strongly positive test-pulse voltages. The theoretical curves correspond to data point fits with the mean $V_{P50\%}$, k_h, $V_{T50\%}$ and k_g values indicated in Table 4.

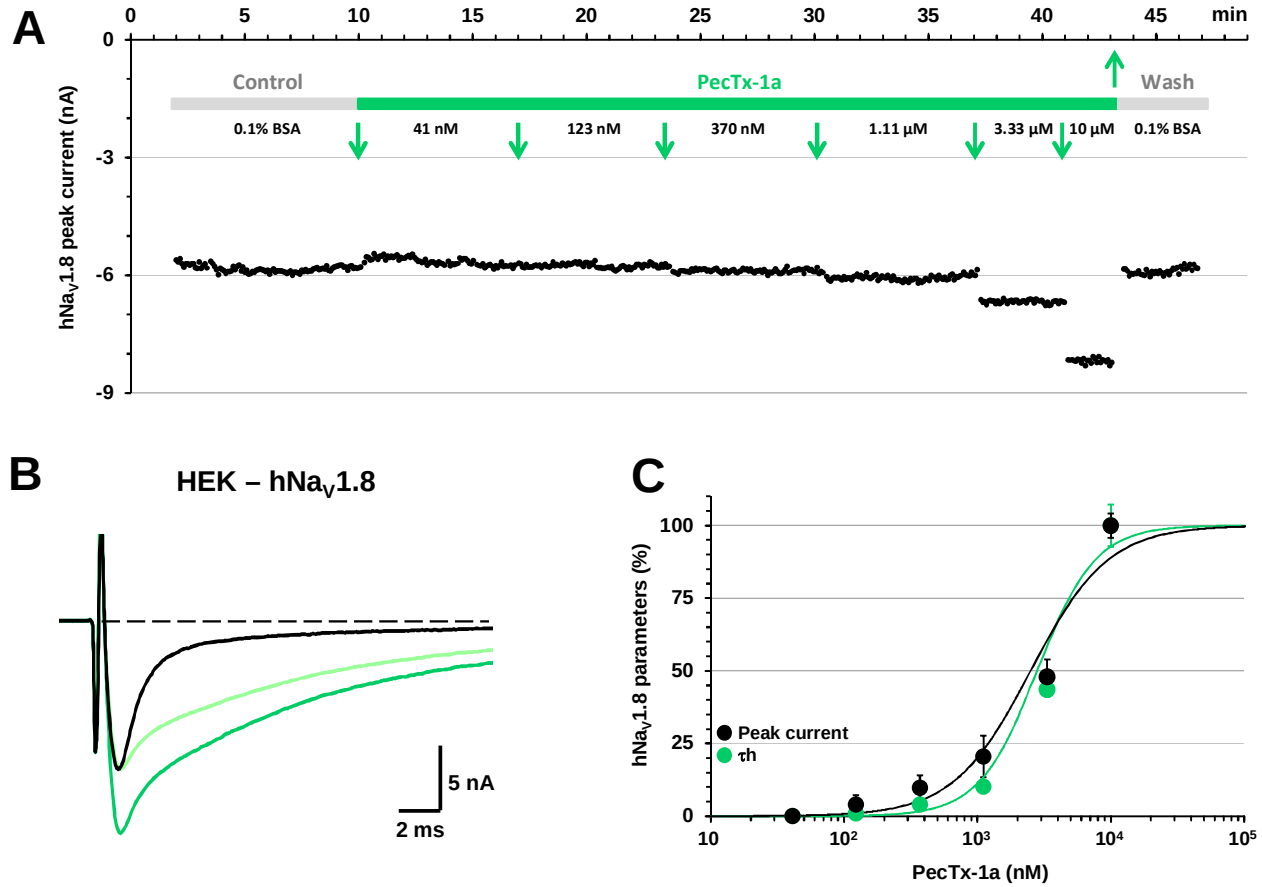

Figure 4bis. Effects of PecTx-1a on HEK-293 cells overexpressing the $hNa_V1.8$ channel subtype. (**A**) Representative time course of the effects of successive applications of various PecTx-1a concentrations (from 41 nM to 10 µM), and peptide wash-out, on the amplitude of peak current flowing through $hNa_V1.8$ subtype. (**B**) Representative traces of current flowing through $hNa_V1.8$ subtype, recorded before (in black) and after (in green) exposure to 10 µM PecTx-1a. In light green, current recorded in the presence of PecTx-1a and expressed relatively to the peak control current. (**C**) Concentration-response curves of PecTx-1a effects on the peak current (black circles) and inactivation kinetic parameter (τh, green circles) variations. Each value, expressed as percentage of that obtained before toxin application, represents the mean ± S.D. of data obtained from 3 cells. The theoretical curves correspond to data point fits with IC_{50} and n_H values of, respectively, 2.5 µM and 1.5 (r^2 = 0.982, black curve), and 2.8 µM and 2.0 (r^2 = 0.985, green curve).

3.4. Effects of PecTx-1a on hKir and hK_V channel subtypes

Automated patch-clamp experiments performed on CHO and U2OS cells overexpressing hKir2.1 and hK_V1.5, 4.3, 7.1 and 11.1 channel subtypes revealed that 100 nM PecTx-1a was efficient to block the hK_V4.3 current without any marked alteration of hKir2.1 and hK_V1.5, 7.1 and 11.1 currents (Figure 5A). The following increasing order for IC_{50} values was obtained from the concentration-response curves of PecTx-1a effects on currents flowing through the different hKir and hK_V channel subtypes (Figure 5B): hK_V4.3 (7.2-37 nM, n ≥ 4) > hK_V11.1 (2931 ± 1587 nM, n = 4) > hK_V1.5 (> 10000 nM, n = 10) ≥ hK_V7.1 (> 10000 nM, n = 4) ≥ hKir2.1 (> 10000, n = 8). This indicates that, among the studied hK_V channel subtypes, hK_V4.3 was the only one affected by low concentrations of peptide (below 100 nM, Table 3B).

Further investigation was performed to detail the effects of PecTx-1a on the biophysical properties of hK_V4.3 channel subtype (Figure 6). In addition to a decreased peak current, the peptide also produced moderated but significant slow-down of hK_V4.3 activation and inactivation

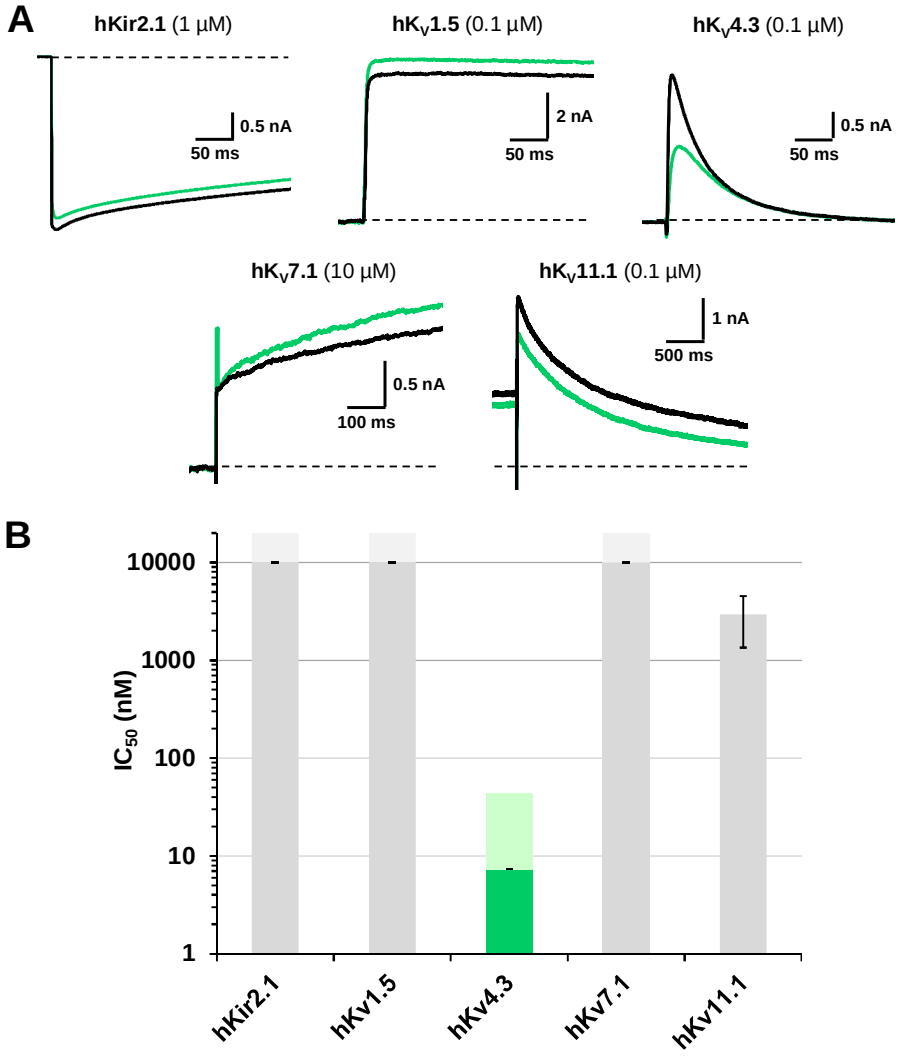

Figure 5. Effects of PecTx-1a on CHO and U2OS cells overexpressing hKir and hK_V channel subtypes. (**A**) Representative traces of potassium currents flowing through hKir2.1, and hK_V1.5, 4.3, 7.1 and 11.1 channel subtypes, recorded before (in black) and after (in green) exposure to 0.1-10 µM PecTx-1a. The recording protocols are detailed in the Experimental section. (**B**) Histograms of IC_{50} values (in nM) obtained from the concentration-response curves of PecTx-1a effects on CHO and U2OS cells overexpressing hKir2.1, and hK_V1.5, 4.3, 7.1 and 11.1 channel subtypes. Each value represents the mean ± S.D. of data obtained from 4-8 cells. Mean value ± S.D. of n_H was 0.9 ± 0.1. The dark grey and green bars indicate the minimum values determined under our experimental conditions.

kinetics (Figure 6A, Tables 3 and 4). The concentration-response curve of PecTx-1a effect on hK_V4.3 current revealed that the peak current was not completely inhibited by the peptide (Figure 6B). Hence, in the presence of PecTx-1a concentrations varying from 37 nM to 10 µM, the peak amplitude was 56.87 ± 2.13% (n = 6-26) of its control value. Taking into account only the blocked peak current, an IC_{50} value of 7.2 nM was determined from the concentration-response curve. PecTx-1a also induced a marked positive shift of the hK_V4.3 peak current-voltage relationship without modifying the maximal conductance, *i.e.* the slope of curves (Figure 6C). The shift magnitude was dependent on the peptide concentration: it increased between 3.3 and 37 nM and then remained at a constant value of about 35 mV between 37 nM and 10 µM. Interestingly, the decrease of hK_V4.3 peak current only due to positive shifts of current-voltage relationship perfectly fits with the concentration-response curve established for the blocked peak current (Figure 6B). Finally, PecTx-1a produced a moderated but significant positive shift of the hK_V4.3

steady-state inactivation-voltage relationship (Figure 6D and Table 4). The effects of PecTx-1a on $hK_V4.3$ current were not easily reversed upon wash-out of cells with peptide-free standard physiological solution for periods up to 3 min. Hence, the peak current, which was decreased to 54 ± 6% (n = 11) by 10 µM PecTx-1a, recovered to only 58 ± 6% (n = 6) after wash-out, compared to values determined before cell exposure to the peptide (data not shown).

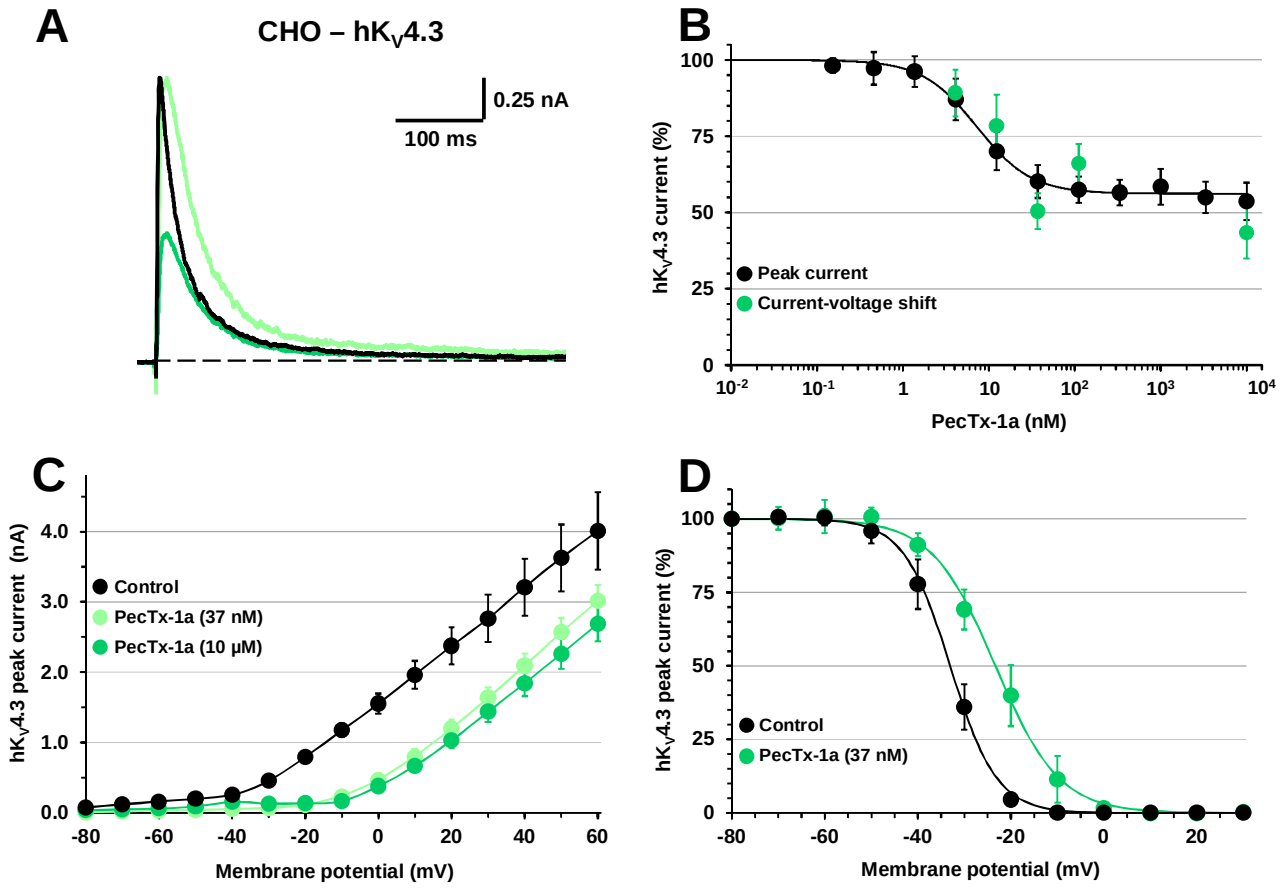

Figure 6. Effects of PecTx-1a on CHO cells overexpressing the $hK_V4.3$ channel subtype. (**A**) Representative traces of current flowing through the $hK_V4.3$ subtype, recorded before (in black) and after (in green) exposure to 37 nM PecTx-1a. In light green, the current recorded in the presence of PecTx-1a and expressed relatively to the peak control current. (**B**) Concentration-response curves of PecTx-1a effect on $hK_V4.3$ peak current (black circles), recorded during a 20-mV test-pulse voltage, and that on the decrease of $hK_V4.3$ peak current only due to positive shifts of the current-voltage relationship (green circles). Each value, expressed as percentage of that obtained before toxin application, represents the mean ± S.D. of data obtained from 4-26 cells. The theoretical curve corresponds to data point fit with IC_{50} and n_H values of, respectively, 7.2 nM and 1.4 (r^2 = 0.992). (**C**) Current-voltage relationships for $hK_V4.3$ peak current, before (black circles) and after exposure to 37 nM (light green circles) and 10 µM (dark green circles) PecTx-1a. Each value represents the mean ± S.D. of data obtained from 5-6 cells. The curves were drawn by eye. (**D**) Steady-state inactivation-voltage relationships for $hK_V4.3$ peak current, before (black circles) and after (green circles) exposure to 37 nM PecTx-1a. Each value represents the mean ± S.D. of data obtained from 6-7 cells, and is expressed as percentage of maximal peak amplitude of current at strongly negative pre-pulse voltages. The theoretical curves correspond to data point fits with the mean $V_{P50\%}$ and k_h indicated in Table 4.

The effects of high concentrations (*i.e.* 10 µM) of PecTx-1a were also studied on hKir2.1 and some other hK_V channel subtypes (see Table 3B). While no significant alteration of hKir2.1 and $hK_V7.1$ currents was detected, the $hK_V11.1$ current was decreased to 25% of its control value, as expected from the corresponding IC_{50} value close to 3 µM (see Figure 5). In contrast, the $hK_V1.5$

current was between 70 and 90 times increased by 10 µM PecTx-1a (Figure 6bisA and B). This effect was associated with an increased maximal conductance, *i.e.* the slope of the current-voltage curve, without any significant shift of the current-voltage relationship (Figure 6bisC). The increase in $hK_V1.5$ current was completely reversed by peptide wash-out for periods up to 5 min (Figure 6bisA and B). Hence, the current, which was enhanced to 168 ± 25% (n = 3) by 10 µM PecTx-1a, recovered to 107 ± 4% (n = 3) after wash-out, compared to values determined before cell exposure to the peptide.

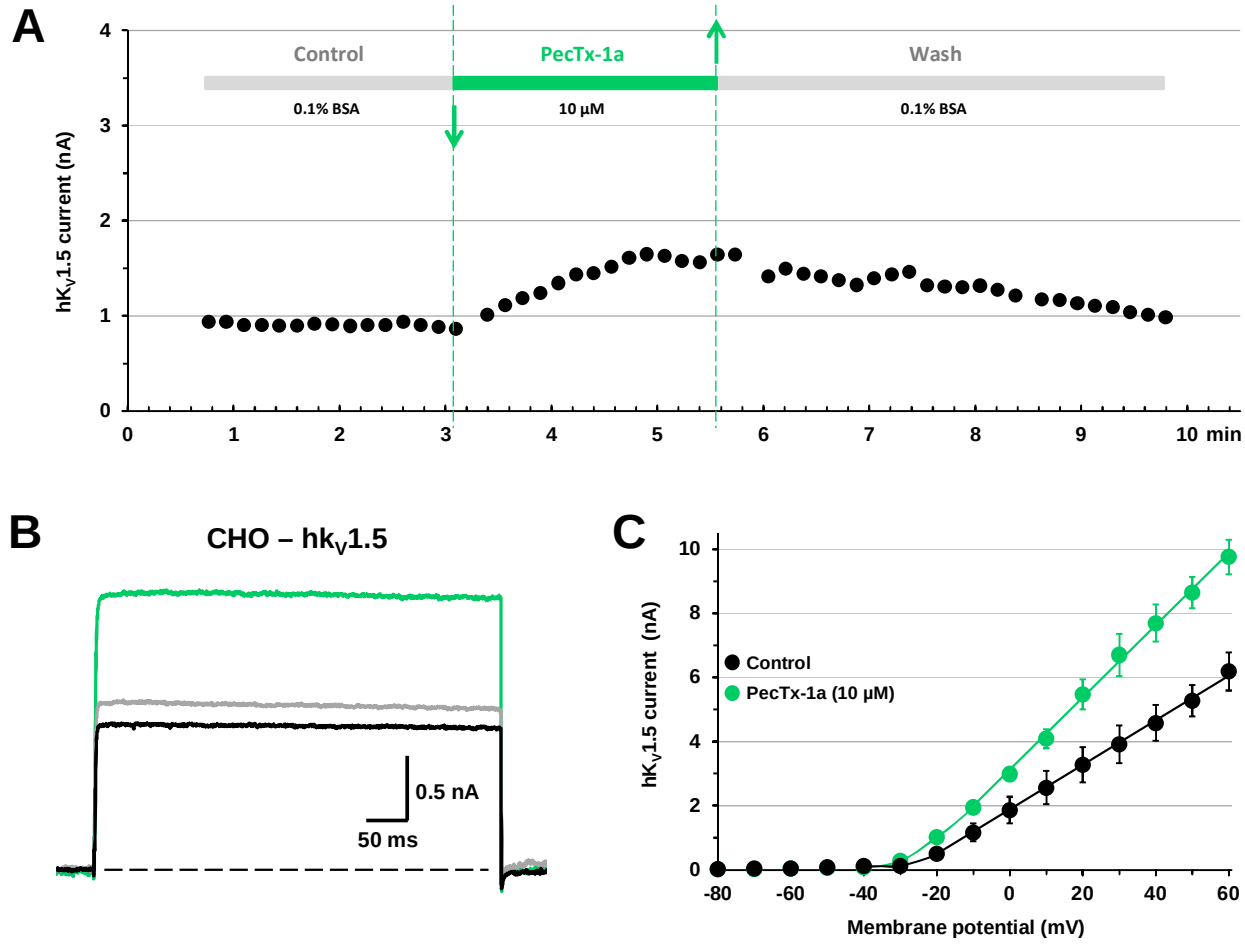

Figure 6bis. Effects of PecTx-1a (10 µM) on CHO cells overexpressing the $hK_V1.5$ channel subtype. (**A**) Representative time course of the effect of PecTx-1a application and peptide wash-out on the amplitude of current flowing through $hK_V1.5$ subtype. (**B**) Representative traces of current flowing through $hK_V1.5$ subtype, recorded before (in black) and after (in green) exposure to PecTx-1a, and after peptide wash-out (in grey). (**C**) Current-voltage relationships for $hK_V1.5$ current, before (black circles) and after (green circles) exposure to PecTx-1a. Each value represents the mean ± S.D. of data obtained from 4 cells. Curves drawn by eye.

3.5. Effects of PecTx-1a on hCa_V channel subtypes

Automated patch-clamp experiments performed on CHO cells overexpressing $hCa_V1.2$, 2.2, 3.1 and 3.2 channel subtypes revealed that less than 100 nM PecTx-1a was efficient to almost completely block the $hCa_V1.2$ current without any marked alteration of $hCa_V2.2$, 3.1 and 3.2 currents (Figure 7A). From the concentration-response curves of PecTx-1a effects on currents flowing through the different hCa_V channel subtypes, an IC_{50} value of 4.96 ± 0.09 nM (n = 4-6) was

obtained for the $hCa_V1.2$ channel subtype, while those for $hCa_V2.2$, 3.1 and 3.2 channel subtypes were over 10 µM (n = 4-6) (Figure 7B). This indicates that, among the studied hCa_V channel subtypes, $hCa_V1.2$ was the only one affected by PecTx-1a, even at high concentrations of peptide (*i.e.* 10 µM, Table 3C).

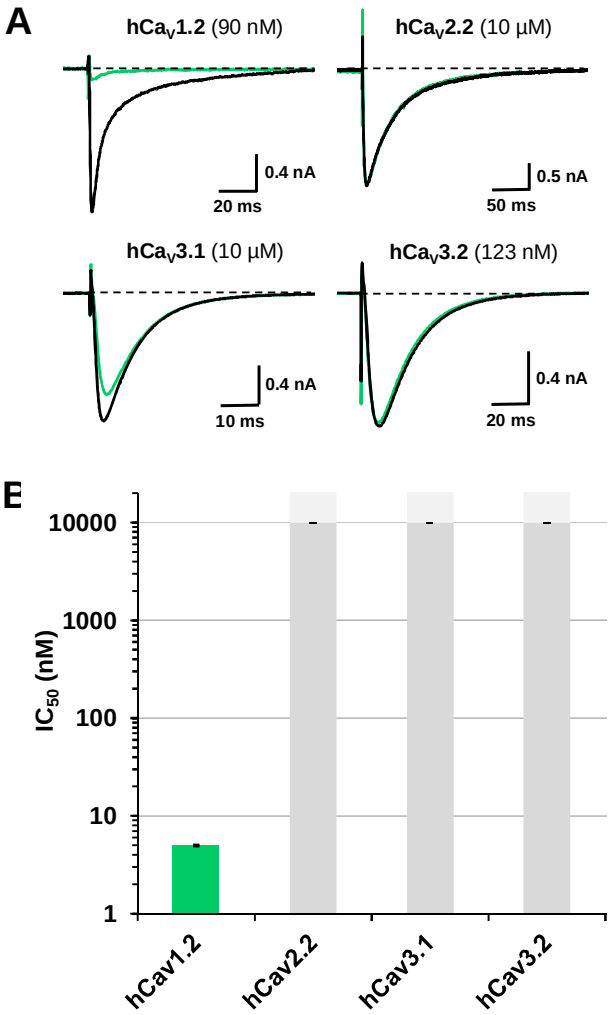

Figure 7. Effects of PecTx-1a on CHO cells overexpressing hCa_V channel subtypes. (**A**) Representative traces of calcium currents flowing through $hCa_V1.2$, 2.2, 3.1 and 3.2 channel subtypes, recorded before (in black) and after (in green) exposure to 0.09-10 µM PecTx-1a. The recording protocols are detailed in the Experimental section. (**B**) Histograms of IC_{50} values (in nM) obtained from the concentration-response curves of PecTx-1a effects on CHO cells overexpressing hCa_V channel subtypes. Each value represents the mean ± S.D. of data obtained from 4-6 cells. Mean value ± S.D. of n_H was 0.8 ± 0.1. The dark grey bars indicate the minimum values determined under our experimental conditions.

Further investigation was performed to detail the effects of PecTx-1a on the biophysical properties of $hCa_V1.2$ channel subtype (Figure 8). The decrease of $hCa_V1.2$ peak current was dependent on PecTx-1a concentration and was partly reversed by peptide wash-out for periods up to 4 min (Figure 8A). Hence, the current, which was decreased to 6.3 ± 3.9% (n = 4) by 90 nM PecTx-1a, recovered to 51 ± 2% (n = 2) after wash-out, compared to values determined before cell exposure to the peptide. The blocking effect of PecTx-1a on the $hCa_V1.2$ channel subtype was not associated with alteration of current activation and inactivation kinetics (Figure 8B, Table 4).

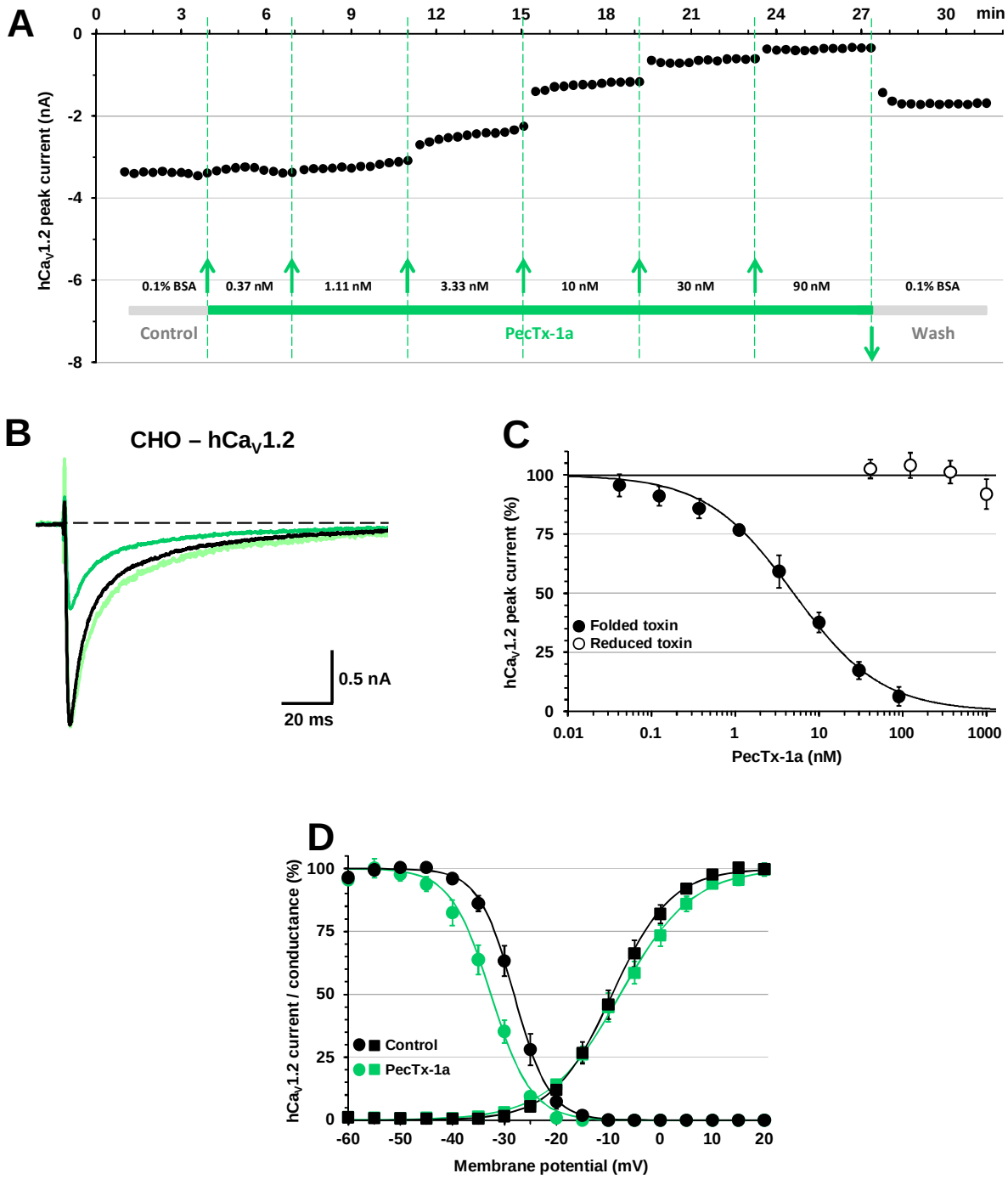

Figure 8. Effects of PecTx-1a on CHO cells overexpressing the hCa$_V$1.2 channel subtype. (**A**) Representative time course of the effects of successive applications of various PecTx-1a concentrations (from 0.37 to 90 nM), and peptide wash-out, on the amplitude of peak current flowing through hCa$_V$1.2 subtype. (**B**) Representative traces of current flowing through hCa$_V$1.2 subtype, recorded before (in black) and after (in green) exposure to 3.3 nM PecTx-1a. In light green, current recorded in the presence of PecTx-1a and expressed relatively to the peak control current. (**C**) Concentration-response curves of folded (black closed circles) and reduced (black open circles) PecTx-1a effects on hCa$_V$1.2 peak current. Each value, expressed as percentage of that obtained before toxin application, represents the mean ± S.D. of data obtained from 3-7 cells. The theoretical curve for the folded toxin corresponds to data point fit with IC_{50} and n_H values of 4.96 nM and 0.8, respectively (r^2 = 0.997). That for the reduced toxin corresponds to a straight line through the mean of data points, *i.e.* 99.91% (r^2 = 0.947). (**D**) Steady-state inactivation- (circles) and conductance- (squares) voltage relationships for CHO cells overexpressing the hCa$_V$1.2 subtype, before (black symbols) and after (green symbols) exposure to 3.3 nM PecTx-1a. Each value represents the mean ± S.D. of data obtained from 6-7 cells, and is expressed as percentage of either maximal peak amplitude of current at strongly negative pre-pulse voltages or maximal conductance calculated at strongly positive test-pulse voltages. The theoretical curves correspond to data point fits with the mean $V_{P50\%}$, k_h, $V_{T50\%}$ and k_g values indicated in Table 4.

To further support the specificity of peptide action, the concentration-response curves of the effects of both the folded and reduced inactive forms of PecTx-1a on $hCa_V1.2$ peak current were established (Figure 8C). Under these conditions, an IC_{50} value of 4.96 nM was calculated for the folded toxin while the reduced one was without any significant effect at concentrations up to 10 µM, *i.e.* the current decrease measured in the presence of 10 µM of reduced form was of 4 ± 8% (n = 3) compared to control value determined before cell exposure to this peptide form. Finally, PecTx-1a produced a moderated but significant negative shift of the $hCa_V1.2$ steady-state inactivation-voltage relationship without any significant change in the conductance-voltage relationship (Figure 8D and Table 4).

Manual patch-clamp experiments were performed on hCa_V channels of hiPSC-CMs. These channels included $hCa_V1.1$, 1.2 and 1.3 subtypes, responsible for the L-type calcium current having maximal peak amplitude at 0-mV test-pulse, and $hCa_V3.1$ and 3.2 subtypes, responsible for the T-type calcium current having maximal peak amplitude at -40-mV test-pulse (Ivashchenko et al., 2013). Among the 22 studied hiPSC-CMs, 27% (*i.e.* 6 cells over 22) had a 118 ± 41 pF membrane capacity and exhibited only L-type current, 5% (*i.e.* 1 cell over 22) had a 15 pF membrane capacity and exhibited only T-type current, and 68% (*i.e.* 15 cells over 22) had a 51 ± 8 pF membrane capacity and exhibited both L-and T-type currents. The effects of PecTx-1a were studied at 100 nM, a peptide concentration that fully inhibited the L-type, $hCa_V1.2$ channel subtype while sparing the T-type, $hCa_V3.1$ and 3.2 subtypes. The cell perfusion with standard physiological solution containing 100 nM PecTx-1a had no significant effect on the T-type calcium current but produced a marked decrease of the L-type current (Figure 9A). The ratio of L-type to T-type peak calcium currents, recorded during test-pulses to 0 and -40 mV, respectively, was calculated before and after cell exposure to 100 nM PecTx-1a. As shown in Figure 9B, this ratio was decreased by 58% by the peptide, *i.e.* from 5.70 ± 1.25 (n = 13) to 2.41 ± 0.67 (n = 13), and further reduced to 1.26 ± 0.43 (n = 4) by 10 µM nifedipine. Taking into account that this nifedipine concentration fully inhibited the L-type calcium current (Ivashchenko et al., 2013), these results indicate that the percentages of L- and T-type calcium currents in hiPSC-CMs were 78% and 22%, respectively.

4. DISCUSSION

The present study was undertaken to identify a new peptide with antinociceptive properties, among the Smartox venom collection by a high-throughput screening of 117 different animal venoms using automated patch-clamp platforms on HEK-293 cells overexpressing the genetically validated antinociceptive target $hNa_V1.7$ and the cardiac $hNa_V1.5$ channel subtypes. This approach led to the purification and identification of PecTx-1a from the *Poecilotheria subfusca* spider venom and, then, to the peptide chemical synthesis and 3D-structure characterization.

PecTx-1a, identified as a 35 amino acid peptide including three disulfide bridges and the ICK architectural motif, belongs to the NaSpTx family 2. Among the toxins belonging to this family, the peptide shows more particularly relative high sequence identity (66-74%) and similarity (74-80%) with three jingzhaotoxins (JzTxs) issued from the Chinese tarantula *Chilobrachys jingzhao* (also known as Chinese fawn tarantula), one of the most venomous spiders inhabiting the hilly areas of

573 Hainan province in China (Table 5).

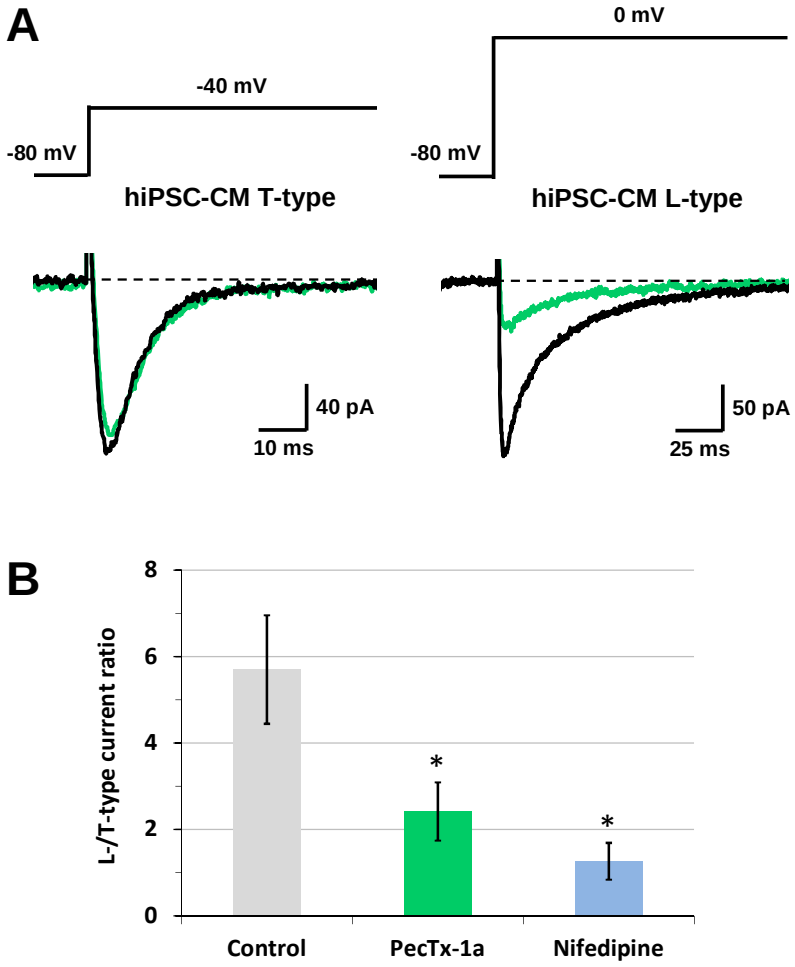

Figure 9. Effects of PecTx-1a (100 nM) on L- and T-type Ca_V channels of hiPSC-CMs. (**A**) Representative traces of T-type calcium current, recorded during test-pulses to -40 mV from a holding potential of -80 mV (left panel) and L-type calcium current, recorded during test-pulses to 0 mV from a holding potential of -80 mV (right panel), before (in black) and after (in green) cell exposure to PecTx-1a. (**B**) Ratio of L-type to T-type peak calcium currents, recorded during test-pulses to 0 and -40 mV, respectively, calculated before (in grey) and after cell exposure to PecTx-1a (in green) and then to 10 µM nifedipine (in blue). Each bar represents the mean ± S.D. of data obtained from 4-13 cells. *: $P < 0.01$ (*versus* control).

574 **4.1. 3D-structure of PecTx-1a**

575 The ensemble of the 10 structures derived from the calculations "in water" showed a well-
576 determined backbone conformation which is typical of an ICK motif. The pattern of hydrogen
577 bonds is very similar to that observed for the antinociceptive cyriotoxin-1a, the first toxin found
578 out previously from *Cyriopagopus schioedtei* spider venom using a similar approach (Gonçalves et
579 al., 2018c). Interestingly, the amide bond between Trp25 and Pro26 obtained a cis conformation.
580 This is indicated by a very intensive NOE between Trp25-Hα and Pro26-Hα (corresponding to a
581 distance of 2.53 Å), as well as by the large difference of ^{13}C-chemical shifts between Pro26-Cβ and
582 Pro-Cγ ($\Delta^{13}C_{\beta,\gamma}$ = 8.7 ppm, whereas the difference is in the order of 4-5 ppm in case of a trans
583 conformation). The cis conformation seemed to be stabilized by hydrogen bonds between the
584 polar protons of the Arg22 side chain (Hε and Hη) and the carbonyl groups of Trp25 and Pro26.

The well-defined orientation of the Arg22 side chain was confirmed by numerous NOEs and the large differences of chemical shifts obtained for the Arg22 δ-protons (2.94 and 2.22 ppm, respectively). The conformation of the three N-terminal amino acids (Gly33, Thr34 and Val35) seemed to be less well-defined (not reflected by the ensemble of the 10 conformers shown in Figure 2Ba). This is indicated by several constraint violations in this region and NOEs, which cannot be explained by a single conformation (some of these NOEs have not been used for the final calculations). Another indication of flexibility might be the extreme line broadening observed for the signals of Gly33.

4.2. Evaluation of synthetic PecTx-1a functional properties

The evaluation of PecTx-1a functional properties on HEK-293 cells overexpressing $hNa_V1.1$-1.8 channel subtypes reveals that the potent blocking effect of the synthetic peptide, compared to the native molecule, was conserved on $hNa_V1.7$ channel subtype. Hence, the mean IC_{50} value of PecTx-1a effect on the $hNa_V1.7$ peak current was 118.4 nM, a value in the range of those previously reported for the interaction between this channel subtype and potential analgesic peptide toxins belonging to the NaSpTx family 2, such as Pn3a, Df1a, ProTx-I, Phlo1b, Phlo1a and JzTx-34 (IC_{50} between 0.9 and 610 nM, respectively) showing relatively low percentages (between 44 and 66%) of amino acid sequence identity with PecTx-1a (Table 5; Gonçalves et al., 2018a). Some of these toxins, in addition to a decreased peak current and as observed for PecTx-1a, were shown to markedly slow-down the inactivation of certain tetrodotoxin-sensitive (TTX-S) Na_V channel subtypes, including the $hNa_V1.7$ subtype, leading to an overestimation of IC_{50} values corresponding to peak current blockage. Hence, the mean IC_{50} value of PecTx-1a effect on the $hNa_V1.7$ current calculated at time zero of depolarization (time-0 current), to overcome the peak current increase arising from the peptide effects on currents kinetics, was only 61.7 nM, *i.e.* about 2-times lower than that for the peak current. These results strongly suggest that the peptide acts not only as a pore-blocker molecule but also as a channel functioning modulator by binding to the well-known toxin receptor-sites 3 (*i.e.* S3-S4 segments of DIV domain) and 4 of Na_V channels (Deuis et al., 2017). Interestingly, and although at high peptide concentrations (*i.e.* > 1 µM), the effects of PecTx-1a on the TTX-S $hNa_V1.8$ channel subtype consisted in slowing-down the current inactivation, leading to a marked peak current increase, while no inhibitory action of the peptide was detected on this type of channel subtype (*i.e.* IC_{50} > 10 µM). Furthermore, PecTx-1a induced 10-mV positive and negative shifts of conductance- and steady-state inactivation-voltage relationships of hNaV1.7 channel subtype, respectively, in agreement with the alterations in the voltage-dependence of both activation (10-37-mV positive shifts) and steady-state inactivation (2.7-17.5-mV negative shifts) produced by some toxins belonging to the NaSpTx family 2 (Gonçalves et al., 2018a).

PecTx-1a was at least 15 times more potent to interact with $hNa_V1.7$ than $hNa_V1.1$-1.4, 1.6 and 1.8 channel subtypes. The fact that the peptide had over micomolar range affinities for the $hNa_V1.4$ and 1.6 channel subtypes is of great interest in the optic to further develop the molecule as a potential antinociceptive agent since the neuromuscular safety issue is likely to be ensured, which will not limit the peptide *in vivo* efficacy (Gonçalves et al., 2018b). However, PecTx-1a was

also shown to be highly potent to decrease the $hNa_V1.5$ peak current within nanomolar range affinities (*i.e.* IC_{50} = 260.9 nM). As expected for this TTX-resistant (TTX-R) cardiac subtype, the peptide-induced blocking effect occurred without any significant change in the current activation and inactivation kinetics (similar IC_{50} values were obtained for $hNa_V1.5$ time-0 and peak currents) and in conductance- and steady-state inactivation-voltage relationships. The main hNa_V channel subtypes affected by low concentrations of PecTx-1a (below 1 µM) were therefore restricted to $hNa_V1.7$ and 1.5, the interaction between the latter channel subtype and the peptide greatly impairing its cardiac safety properties and thus its development as potential antinociceptive agent.

Table 5. Comparison of amino acid sequences between PecTx-1a and the 8 most similar and well documented toxins in literature from NaSpTx family 2. Sequence alignment performed with Clustal Omega (version 1.2.4 from Emboss programs, EBlosum62 matrix for two pair alignment). Cysteine scaffold is indicated in red, and important residues for toxin interaction with the $hK_V2.1$ subtype are surrounded in green. The percentage of sequence identity with PecTx-1a is shown in parentheses, and the activity (IC_{50}) reported for each peptide toxin is described in the far right columns according to data sourced from Pubmed and ArachnoServer database (Herzig et al., 2011). All these toxins are amidated at their C-terminal amino acid sequence ending.

		$hNa_V1.7$	**$hNa_V1.5$**	**$hK_V2.1$**
PecTx-1a	ECRQMFGGCTKDSECCAHLGCRTKWPYYCAWDGTV	118 nM	261 nM	*nd*
JzTx-IX (74%)	ECTKLLGGCTKDSECCPHLGCRKKWPYHCGWDGTF-	*nd*	450 nM	3.3 µM
JzTx-XI (69%)	ECRKMFGGCSVDSDCCAHLGCKPT_K-YCAWDGTF-	*nd*	437 nM	96 nM
JzTx-34 (66%)	ACREWLGGCSKDADCCAHLECRKKWPYHCVWDWTV-	610 nM	> 10 µM	> 10 µM
Phlo1a (66%)	ACRELLGGCSKDSDCCAHLECRKKWPYHCVWDWTI-	459 nM	> 1 µM	*nd*
Phlo1b (66%)	ACRELLGGCSKDSDCCAHLECRKKWPYHCVWDWTF-	360 nM	> 1 µM	*nd*
Pn3a (62%)	DCRYMFGDCEKDEDCCKHLGCKRKMKY-CAWDFTFT	0.9 nM	800 nM	> 300 nM
ProTx-I (47%)	ECRYWLGGCSAGQTCCKHLVCSRRHGW-CVWDGTFS	51 nM	*nd*	411 nM
Df1a (44%)	ECRWFLGGCSGGQTCCEHLVCHRKHQW-CVWDWSF-	1.9 nM	45 nM	> 1 µM

nd: not determined.

The $hNa_V1.5$ channel subtype was previously reported to be blocked with IC_{50} values of 437-450 nM, *i.e.* in the range of that determined for PecTx-1a, by two toxins from the NaSpTx family 2, JzTx-IX and JzTx-XI, showing relatively high percentages (between 66 and 74%) of amino acid sequence identity with our peptide of interest (Table 5; Gonçalves et al., 2018a). In contrast, JzTx-34, which shows also 66% of amino acid sequence identity with PecTx-1a, was not efficient to affect this channel subtype (IC_{50} > 10 µM), probably due to the presence of negatively-charged

amino acid residues between Cys2 and Cys21 which impede the peptide binding to $hNa_V1.5$, as previously described for JzTx-XIII (Yuan et al., 2012). The amino acid residues K23, Y27 and H28, located between Cys21 and Cys29 in the JzTx-IX sequence, could be involved in modifying the Na_V channel gating properties, as proposed for some ceratotoxins isolated from the tarantula *Ceratogyrus cornuatus* venom (Bosmans et al., 2006). However, this is unlikely because these three residues are among the seven that are not identical or not conservatively substituted between JzTx-IX, JzTx-XI and PecTx-1a, some of them being even highly conserved in other toxins from the NaSpTx family 2 that cannot target the $hNa_V1.5$ channel subtype (Deng et al., 2009). Further experiments are thus necessary to study the PecTx-1a structure-activity relationship before definitively establishing the key amino acid residues that are involved in the peptide binding to $hNa_V1.7$ and 1.5 channel subtypes.

The evaluation of PecTx-1a functional properties on CHO and U2OS cells overexpressing hKir and hK_V channel subtypes reveals that the peptide was at least 80 and 280 times more potent to decrease the $hK_V4.3$ current than the $hK_V11.1$ and hKir2.1, $hK_V1.5$ or $hK_V7.1$ current, respectively. Among the studied hKir and hK_V channel subtypes, the $hK_V4.3$ subtype was thus the only one affected by low concentrations of PecTx-1a (below 100 nM). The peptide effects on the $hK_V4.3$ channel subtype consisted in a marked concentration-dependent (IC_{50} = 7.2 nM) positive shift of the peak current-voltage relationship without any modification of the maximal conductance and with only moderated, but significant, positive shift of the steady-state inactivation-voltage relationship and slow-down of activation and inactivation kinetics. As a consequence of this channel functioning modulator and not pore-blocker action produced by PecTx-1a, a 43% maximal decrease of $hK_V4.3$ peak current was observed in the presence of 36 nM to 10 µM of peptide. Similarly, no PecTx-1a inhibitory action was detected on the $hK_V1.5$ channel subtype since the peptide, although at a high concentration (*i.e.* 10 µM), produced an increased current due to an increased maximal conductance. Therefore, PecTx-1a was highly potent to act on the $hNa_V1.7$ channel subtype as a pore-blocker and on the $hK_V4.3$ channel subtype as a channel functioning modulator.

Among the toxins from the NaSpTx family 2 showing at least 44% of amino acid sequence identity with PecTx-1a, and to the best of our knowledge, JzTx-XI is the only one reported to interact with hK_V channel subtypes at concentrations below 100 nM. In particular, the key amino acid residues that are involved in the peptide binding to $hK_V2.1$ have been identified (Table 5). Hence, the 34 times lower affinity of JzTx-IX for this channel subtype has been attributed to the presence of a threonine (T3) instead an arginine (R3) in the peptide sequence (Chi et al., 2011). Similarly, the loss of affinity of JzTx-34 for $hK_V2.1$ channel subtype was explained by the presence of a glutamic acid (E20), a negatively-charged amino acid, instead of a glycine (G20) in the peptide sequence (Chen et al., 2009). The hydrophobic patch surrounded by positively-charged amino acids was thus proposed to be necessary for peptide binding to the $hK_V2.1$ channel subtype, in particular the one located at position 24 in the peptide sequence which interacts with the negatively-charged amino acid located at position 277 in the channel subtype (Wang et al., 2004; Deng et al., 2009). Taking into account the relatively conserved key amino acids for the peptide

binding to $hK_V2.1$ between PecTx-1a and JzTx-XI, it would be interesting to study the effects of the former on this channel subtype.

The evaluation of PecTx-1a functional properties on CHO cells overexpressing $hCa_V1.2$, 2.2, 3.1 and 3.2 channel subtypes reveals that the peptide produced a $hCa_V1.2$ current decrease with very high affinity (IC_{50} = 4.96 nM) and selectivity against the other studied hCa_V currents (IC_{50} > 10 µM). This decrease occurred without any significant alteration of current activation and inactivation kinetics, as well as conductance-voltage relationship, and with only moderated, but significant, negative shift (5 mV) of the steady-state inactivation-voltage relationship, indicating that the peptide acted mainly as a pore-blocker on this L-type, channel subtype. In agreement, PecTx-1a (100 nM) produced an about 60% decrease of L-type ($hCa_V1.1$, 1.2 and 1.3) current while sparing the T-type ($hCa_V3.1$ and 3.2) current in hiPSC-CMs. Taking into account that 100 nM of peptide fully inhibited the L-type, $hCa_V1.2$ channel subtype overexpressed in CHO cells, these results strongly suggest that PecTx-1a was less potent to interact with the L-type, $hCa_V1.1$ and/or 1.3 channel subtype(s). Further experiments on cells overexpressing these two channel subtypes are necessary to definitively conclude.

To the best of our knowledge, PecTx-1a is the first molecule showing such high affinity for the L-type, $Ca_V1.2$ channel subtype and selectivity against the various studied Na_V, K_V, Kir and other Ca_V channel subtypes. Hence, drugs exhibiting hundred nanomolar affinities for the $Ca_V1.2$ channel subtype, such as verapamil, diltiazem and dihydropyridines, have been widely described in the literature (Crumb et al., 2016). However, three snake toxins of roughly 60 amino acids and 3-4 disulfide bridges, the *Dendroaspis polylepis* calciseptine, as well as a natural variant (FS2 with 3 different amino acids), and the *Dendroaspis angusticeps* calcicludine, were reported to have higher affinities than the above drugs for L-type channels without any mention of their selectivity between the four L-type, channel subtypes (Yasuda et al., 1994; Pringos et al., 2011). One snake venom metalloproteinase was also described to inhibit the vascular L-type Ca_V channel with high affinity (Zhang et al., 2009). The neuronal L-type Ca_V channel was preferentially targeted by two scorpion toxins (Dutra et al., 2008; Liu et al., 2014), as well as by three spider toxins of 55-70 amino acids, with some relative selectivity among the Ca_V channel types (Sutton et al., 1998; Kubista et al., 2007; Villegas et al., 2008). Although the spider κ-theraphotoxin-Gr2c (GsAFII) is well-known to produce analgesic effects *via* the stretch-activated ion channels, the peptide was also reported to exhibit relatively high affinity for the rat $Ca_V1.2$ channel subtype overexpressed in *Xenopus* oocytes (IC_{50} close to 17 nM; (Ono et al., 2011). The ω-theraphotoxin-Cc1a, the only spider toxin more documented nowadays to interact with the rabbit $Ca_V1.2$ channel subtype, shows relatively low affinity (IC_{50} = 825 nM) and selectivity between rabbit/rat $Ca_V2.x$, $hNa_V1.5$ and $hNa_V1.7$ channel subtypes (Klint et al., 2014). Finally, the two spider toxins ProTx-I and ProTx-II were described to potently inhibit the $Ca_V1.2$ channel subtype but, once again, with relatively low selectivity against Na_V, K_V and other Ca_V channel subtypes (Middleton et al., 2002; Priest et al., 2007).

5. CONCLUSION

To the best of our knowledge, PecTx-1a is the first ICK spider toxin specifically targeting the L-

type, $Ca_V1.2$ channel subtype with high affinity and selectivity against the studied Na_V, K_V, Kir and other Ca_V channel subtypes. This peptide represents thus a valuable tool to study the $Ca_V1.2$ subtype function and location at the cell level by *ex vivo* adding a tag to track the target of interest. In addition, as responsible for the "plateau" of cardiac action potential, it may be a valuable drug to treat some cardiomyopathies such as the long QT syndrome.

ACKNOWLEDGMENTS – This research was funded by a collaborative grant (#153114) between Sanofi Research & Development (Chilly-Mazarin, France) and the French Alternative Energies and Atomic Energy Commission (CEA, Gif sur Yvette, France). M.D.W. acknowledges financial support from the French Agence Nationale de la Recherche (grant ANR-11-LABX-0015). T.C.G. was supported by a doctoral CIFRE fellowship from Sanofi. The authors wish to thank Sandra VIALE (Sanofi R&D, Vitry-sur-Seine, France) for providing hiPSC-CMs cells, Dr Gilles MOURIER and Margot VANDEN DRIESSCHE (CEA de Saclay, Gif sur Yvette, France) for their help in peptide linearization, Laetitia LUCARAIN (Sanofi R&D, Vitry-sur-Seine, France) for her help in screening experiments and Lucille JAQUILLARD (Smartox Biotechnology, Saint-Egrève, France) for her help in peptide purification, sequencing and synthesis experiments.

CONFLICT OF INTEREST – The authors, T.C. Gonçalves, M. Kurz, C. Sanson, B. Schombert, A. Bohme, J.-M. Chambard, J.-M. Itier and M. Partiseti declare the following competing interest: current or former employees of Sanofi.

Accession Codes – PDB code for PecTx-1a is XXXX. Authors will release the atomic coordinates and experimental data upon article publication.

REFERENCES

Bell, D.C., and Dallas, M.L. (2017). Using automated patch clamp electrophysiology platforms in pain-related ion channel research: insights from industry and academia. *Br J Pharmacol*.

Bennett, D.L., and Woods, C.G. (2014). Painful and painless channelopathies. *Lancet Neurol.* 13**,** 587-599.

Bosmans, F., Rash, L., Zhu, S., Diochot, S., Lazdunski, M., Escoubas, P., and Tytgat, J. (2006). Four novel tarantula toxins as selective modulators of voltage-gated sodium channel subtypes. *Mol Pharmacol* 69**,** 419-429.

Cardoso, F.C., and Lewis, R.J. (2017). Sodium channels and pain: from toxins to therapies. *Br. J. Pharmacol.*

Catterall, W.A. (2000). From ionic currents to molecular mechanisms: the structure and function of voltage-gated sodium channels. *Neuron* 26**,** 13-25.

Catterall, W.A. (2011). Voltage-gated calcium channels. *Cold Spring Harb Perspect Biol* 3**,** a003947.

Chambard, J.M., Tagat, E., Boudeau, P., and Partiseti, M. (2014). Transforming TRP channel drug discovery using medium-throughput electrophysiological assays. *J. Biomol. Screen* 19**,** 468-477.

Chen, J., Zhang, Y., Rong, M., Zhao, L., Jiang, L., Zhang, D., Wang, M., Xiao, Y., and Liang, S. (2009). Expression and characterization of jingzhaotoxin-34, a novel neurotoxin from the venom of the tarantula Chilobrachys jingzhao. *Peptides* 30**,** 1042-1048.

Chi, Y., Deng, M., Wu, Y., Luo, J., Rong, M., Zhang, Y., Zhang, D., Zeng, X., and Liang, S. (2011). [Synthesis, refolding and identification of pharmacological activities of neurotoxin JZTX-XI and R3A-JZTX-XI]. *Sheng Wu Gong Cheng Xue Bao* 27**,** 900-908.

Crumb, W.J., Jr., Vicente, J., Johannesen, L., and Strauss, D.G. (2016). An evaluation of 30 clinical drugs against the comprehensive in vitro proarrhythmia assay (CiPA) proposed ion channel panel. *J Pharmacol Toxicol Methods* 81**,** 251-262.

De Lera Ruiz, M., and Kraus, R.L. (2015). Voltage-Gated Sodium Channels: Structure, Function, Pharmacology, and Clinical Indications. *J. Med. Chem.* 58**,** 7093-7118.

Deng, M., Kuang, F., Sun, Z., Tao, H., Cai, T., Zhong, L., Chen, Z., Xiao, Y., and Liang, S. (2009). Jingzhaotoxin-IX, a novel gating modifier of both sodium and potassium channels from Chinese tarantula Chilobrachys jingzhao. *Neuropharmacology* 57**,** 77-87.

Deuis, J.R., Dekan, Z., Wingerd, J.S., Smith, J.J., Munasinghe, N.R., Bhola, R.F., Imlach, W.L., Herzig, V., Armstrong, D.A., Rosengren, K.J., Bosmans, F., Waxman, S.G., Dib-Hajj, S.D., Escoubas, P., Minett, M.S., Christie, M.J., King, G.F., Alewood, P.F., Lewis, R.J., Wood, J.N., and Vetter, I. (2017). Pharmacological characterisation of the highly NaV1.7 selective spider venom peptide Pn3a. *Sci Rep* 7**,** 40883.

Dutra, A.A., Sousa, L.O., Resende, R.R., Brandao, R.L., Kalapothakis, E., and Castro, I.M. (2008). Expression and characterization of LTx2, a neurotoxin from Lasiodora sp. effecting on calcium channels. *Peptides* 29**,** 1505-1513.

Goldin, A.L., Barchi, R.L., Caldwell, J.H., Hofmann, F., Howe, J.R., Hunter, J.C., Kallen, R.G., Mandel, G., Meisler, M.H., Netter, Y.B., Noda, M., Tamkun, M.M., Waxman, S.G., Wood, J.N., and Catterall, W.A. (2000). Nomenclature of voltage-gated sodium channels. *Neuron* 28**,** 365-368.

Gonçalves, T.C., Benoit, E., Partiseti, M., and Servent, D. (2018a). The $Na_V1.7$ channel subtype as an antinociceptive target for spider toxins in adult dorsal root ganglia neurons. *Front Pharmacol* 9:1000. doi: 10.3389/fphar.2018.01000.

Gonçalves, T.C., Boukaiba, R., Molgo, J., Amar, M., Partiseti, M., Servent, D., and Benoit, E. (2018b). Direct evidence for high affinity blockade of NaV1.6 channel subtype by huwentoxin-IV spider peptide, using multiscale functional approaches. *Neuropharmacology* 133**,** 404-414.

Gonçalves, T.C., Benoit, E., Kurz, M., Lucarain, L., Fouconnier, S., Combemale, S., Jaquillard, L., Schombert, B., Chambard, J.-M., Boukaiba, R., Hessler, G., Bohme, A., Bialy, L., Hourcade, S., Béroud, R., De Waard, M., Servent, S., and Partiseti, M. (2018c). Cyriotoxin-1a, the first toxin from Cyriopagopus schioedtei spider with antinociceptive properties: from identification to functional characterization. *Br J Pharmacol* (in revision).

Herzig, V., Wood, D.L., Newell, F., Chaumeil, P.A., Kaas, Q., Binford, G.J., Nicholson, G.M., Gorse, D., and King, G.F. (2011). ArachnoServer 2.0, an updated online resource for spider toxin sequences and structures. *Nucleic Acids Res* 39**,** D653-657.

Israel, M.R., Tay, B., Deuis, J.R., and Vetter, I. (2017). Sodium Channels and Venom Peptide Pharmacology. *Adv. Pharmacol.* 79**,** 67-116.

Ivashchenko, C.Y., Pipes, G.C., Lozinskaya, I.M., Lin, Z., Xiaoping, X., Needle, S., Grygielko, E.T., Hu, E., Toomey, J.R., Lepore, J.J., and Willette, R.N. (2013). Human-induced pluripotent stem cell-derived cardiomyocytes exhibit temporal changes in phenotype. *Am J Physiol Heart Circ Physiol* 305**,** H913-922.

Klint, J.K., Berecki, G., Durek, T., Mobli, M., Knapp, O., King, G.F., Adams, D.J., Alewood, P.F., and Rash, L.D. (2014). Isolation, synthesis and characterization of omega-TRTX-Cc1a, a novel tarantula venom peptide that selectively targets L-type Cav channels. *Biochem. Pharmacol.* 89**,** 276-286.

Kubista, H., Mafra, R.A., Chong, Y., Nicholson, G.M., Beirao, P.S., Cruz, J.S., Boehm, S., Nentwig, W., and Kuhn-Nentwig, L. (2007). CSTX-1, a toxin from the venom of the hunting spider Cupiennius salei, is a selective blocker of L-type calcium channels in mammalian neurons. *Neuropharmacology* 52**,** 1650-1662.

Liu, X., Li, C., Chen, J., Du, J., Zhang, J., Li, G., Jin, X., and Wu, C. (2014). AGAP, a new recombinant neurotoxic polypeptide, targets the voltage-gated calcium channels in rat small diameter DRG neurons. *Biochem Biophys Res Commun* 452**,** 60-65.

Middleton, R.E., Warren, V.A., Kraus, R.L., Hwang, J.C., Liu, C.J., Dai, G., Brochu, R.M., Kohler, M.G., Gao, Y.D., Garsky, V.M., Bogusky, M.J., Mehl, J.T., Cohen, C.J., and Smith, M.M. (2002). Two tarantula peptides inhibit activation of multiple sodium channels. *Biochemistry* 41**,** 14734-14747.

Namadurai, S., Yereddi, N.R., Cusdin, F.S., Huang, C.L., Chirgadze, D.Y., and Jackson, A.P. (2015). A new look at sodium channel beta subunits. *Open Biol.* 5**,** 140192.

Ono, S., Kimura, T., and Kubo, T. (2011). Characterization of voltage-dependent calcium channel blocking peptides from the venom of the tarantula Grammostola rosea. *Toxicon* 58**,** 265-276.

Pan, H.L., Wu, Z.Z., Zhou, H.Y., Chen, S.R., Zhang, H.M., and Li, D.P. (2008). Modulation of pain transmission by G-protein-coupled receptors. *Pharmacol. Ther.* 117**,** 141-161.

Priest, B.T., Blumenthal, K.M., Smith, J.J., Warren, V.A., and Smith, M.M. (2007). ProTx-I and ProTx-II: gating modifiers of voltage-gated sodium channels. *Toxicon* 49**,** 194-201.

Pringos, E., Vignes, M., Martinez, J., and Rolland, V. (2011). Peptide neurotoxins that affect voltage-gated calcium channels: a close-up on omega-agatoxins. *Toxins (Basel)* 3**,** 17-42.

Sutton, K.G., Siok, C., Stea, A., Zamponi, G.W., Heck, S.D., Volkmann, R.A., Ahlijanian, M.K., and Snutch, T.P. (1998). Inhibition of neuronal calcium channels by a novel peptide spider toxin, DW13.3. *Mol Pharmacol* 54**,** 407-418.

Trivedi, S., Dekermendjian, K., Julien, R., Huang, J., Lund, P.E., Krupp, J., Kronqvist, R., Larsson, O., and Bostwick, R. (2008). Cellular HTS assays for pharmacological characterization of Na(V)1.7 modulators. *Assay Drug Dev. Technol.* 6**,** 167-179.

Vetter, I., Deuis, J.R., Mueller, A., Israel, M.R., Starobova, H., Zhang, A., Rash, L.D., and Mobli, M. (2017). NaV1.7 as a pain target - From gene to pharmacology. *Pharmacol Ther* 172**,** 73-100.

Villegas, E., Adachi-Akahane, S., Bosmans, F., Tytgat, J., Nakajima, T., and Corzo, G. (2008). Biochemical characterization of cysteine-rich peptides from Oxyopes sp. venom that block calcium ion channels. *Toxicon* 52**,** 228-236.

Wang, J.M., Roh, S.H., Kim, S., Lee, C.W., Kim, J.I., and Swartz, K.J. (2004). Molecular surface of tarantula toxins interacting with voltage sensors in K(v) channels. *J Gen Physiol* 123**,** 455-467.

Waxman, S.G., and Zamponi, G.W. (2014). Regulating excitability of peripheral afferents: emerging ion channel targets. *Nat Neurosci* 17**,** 153-163.

Yasuda, O., Morimoto, S., Jiang, B., Kuroda, H., Kimura, T., Sakakibara, S., Fukuo, K., Chen, S., Tamatani, M., and Ogihara, T. (1994). FS2. a mamba venom toxin, is a specific blocker of the L-type calcium channels. *Artery* 21**,** 287-302.

Yekkirala, A.S., Roberson, D.P., Bean, B.P., and Woolf, C.J. (2017). Breaking barriers to novel analgesic drug development. *Nat. Rev. Drug Discov.* 16**,** 545-564.

Yuan, C., Liu, Z., Hu, W., Gao, T., and Liang, S. (2012). JZTX-XIII, a Kv channel gating modifier toxin from Chinese tarantula Chilobrachys jingzhao. *Toxicon* 59**,** 265-271.

Zamponi, G.W., Striessnig, J., Koschak, A., and Dolphin, A.C. (2015). The Physiology, Pathology, and Pharmacology of Voltage-Gated Calcium Channels and Their Future Therapeutic Potential. *Pharmacol Rev* 67**,** 821-870.

Zhang, P., Shi, J., Shen, B., Li, X., Gao, Y., Zhu, Z., Zhu, Z., Ji, Y., Teng, M., and Niu, L. (2009). Stejnihagin, a novel snake metalloproteinase from Trimeresurus stejnegeri venom, inhibited L-type Ca2+ channels. *Toxicon* 53**,** 309-315.

2.4.3. Résumé des résultats obtenus

La PecTx-1a, aussi nommée μ/ω-théraphotoxine-Ps1a, a été extraite du venin de l'araignée *Poecilotheria subfusca*, une mygale arboricole endémique au Sri Lanka aussi connue sous le nom "d'araignée de tigre ornementale" ou de "montane à bec d'ivoire". Ce peptide de 3999,66 Da fait partie de la famille 2 des toxines d'araignées inhibant les canaux Na_V (NaSpTx-2), possède 35 acides aminés et se structure autour du motif architectural ICK. Son profil de sélectivité a été établi sur différentes lignées cellulaires recombinantes exprimant les sous-types hNa_V, hK_V, hKir et hCa_V de canaux ioniques.

L'évaluation des propriétés fonctionnelles de la PecTx-1a sur des cellules HEK-293 exprimant les sous-types $hNa_V1.1$-1.8 révèle que le peptide est au moins 15 fois plus puissant pour interagir avec le sous-type $hNa_V1.7$ (IC_{50} = 118,4 nM) qu'avec les sous-types $hNa_V1.1$-1.4, 1.6 et 1.8 (IC_{50} > 1800 nM). Le fait que le peptide agisse à des concentrations de l'ordre du micromolaire sur les sous-types $hNa_V1.4$ et 1.6 est intéressant car son action sur le système neuromusculaire sera limitée. Cependant, la PecTx-1a s'est avérée également être très puissante pour interagir avec le sous-type cardiaque $hNa_V1.5$ (IC_{50} = 260,9 nM), ce qui compromet fortement le développement de la molécule en tant qu'agent antinociceptif potentiel. Outre une diminution du pic de courant, le peptide produit une modification des cinétiques d'activation et d'inactivation, et leur dépendance vis-à-vis du potentiel, non seulement du sous-type $hNa_V1.7$ mais aussi d'autres sous-types de canaux Na_V TTX-S. En particulier, et bien qu'à des concentrations élevées (*i.e.* > 1 μM), l'inactivation du sous-type $hNa_V1.8$ est fortement ralentie, ce qui conduit à une augmentation du pic de courant. L'évaluation des propriétés fonctionnelles de la PecTx-1a sur des cellules CHO et U2OS exprimant les sous-types hK_V et hKir révèle que le peptide est au moins 80 fois plus puissant pour interagir avec le sous-type $hK_V4.3$ (IC_{50} = 37 nM) qu'avec les sous-types $hK_V1.5$, 7.1 ou 11.1 et hKir2.1 (IC_{50} > 2900 nM). Les effets de la PecTx-1a sur le sous-type $hK_V4.3$ consistent en une diminution maximale de 43% du pic de courant, indépendante de la concentration de peptide entre 36 nM et 10 μM et principalement due à un déplacement positif de la courbe "conductance-potentiel" [concentration effective produisant 50% de l'effet (EC_{50}) de 7,2 nM], sans modification notable de la conductance maximale. Finalement, l'évaluation des propriétés fonctionnelles de la PecTx-1a sur des cellules CHO exprimant les sous-types $hCa_V1.2$, 2.2, 3.1 et 3.2 révèle que le peptide est au moins 2000 fois plus puissant pour interagir avec le sous-type $hCa_V1.2$ (IC_{50} = 4,96 nM) qu'avec les autres sous-types de canaux Ca_V étudiés (IC_{50} > 10 μM). Les effets de la PecTx-1a sur le sous-type $hCa_V1.2$ consistent en une diminution du pic de courant sans modification notable des cinétiques d'activation et d'inactivation, et leur dépendance vis-à-vis du potentiel. La PecTx-1a (100 nM) produit également une diminution d'environ 60% du

courant de type L ($hCa_V1.1$, 1.2 et 1.3) sans modifier le courant de type T ($hCa_V3.1$ et 3.2) de cardiomyocytes dérivés de cellules souches pluripotentes humaines (hiPSC-CM pour "human induced pluripotent stem cell derived cardiomyocytes"). Compte tenu du fait que 100 nM de peptide bloque complètement le sous-type $hCa_V1.2$ exprimé dans les cellules CHO, ces résultats suggèrent fortement que la PecTx-1a est moins efficace pour interagir avec les sous-types $hCa_V1.1$ et/ou 1.3, l'expression du sous-type $hCa_V1.1$ au niveau des hiPSC-CM restant à démontrer.

Des expériences similaires, dont les résultats ne sont pas inclus dans la publication, ont été réalisées récemment en utilisant la protoxine-II (ProTx-II) décrite également pour inhiber le sous-type $Ca_V1.2$ avec une forte puissance. Ce peptide de 3823 Da, extrait du venin de la mygale péruvienne de velours vert connue sous le nom de *Thrixopelma pruriens*, fait partie de la famille 3 des toxines d'araignées inhibant les canaux Na_V (NaSpTx-3), possède 30 acides aminés et se structure autour du motif architectural ICK. La ProTx-II a été décrite pour la première fois au début des années 2000 comme étant une toxine inhibitrice de tous les sous-types Na_V (IC_{50} < 150 nM) mais aussi de certains sous-types $Ca_V1.x$, $Ca_V3.x$ et K_V (Middleton et al., 2002). Cependant, peu de résultats quantitatifs de la puissance du peptide pour ces cibles sont rapportés dans la littérature (Kraus et al., 2000; Kraus et al., 2002; Priest et al., 2007; Bladen et al., 2014). Afin de quantifier le profil de sélectivité de la ProTx-II, nous avons étudié ses effets sur des lignées cellulaires recombinantes exprimant certains sous-types hNa_V, hCa_V, hK_V et hKir de canaux ioniques (Figure 2-5).

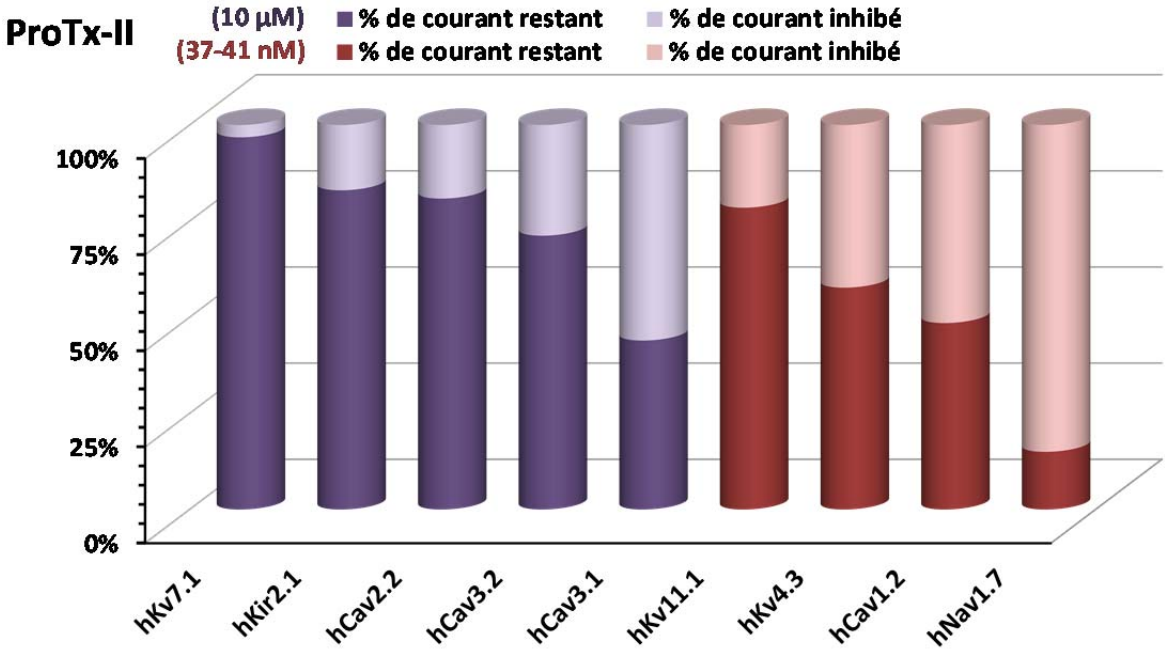

Figure 2-5. Effets de la ProTx-II sur les courants hNa_V, hCa_V, hK_V et hKir. Histogramme exprimant les pourcentages de courant restant (en foncé) et inhibé (en clair) en fonction du sous-type de canal indiqué, en présence de 10 µM (en violet) et de 37-41 nM (en bordeaux) de peptide (moyenne ± ES, n = 3-15).

La puissance de la ProTx-II pour les différents sous-types de canaux ioniques est estimée par l'action inhibitrice de 10 µM et de 37-41 nM de peptide sur les courants transitant par ces sous-types (moyenne ± ES de 3-15 expériences). Ainsi, à une concentration de 10 µM, la ProTx-II affecte de façon croissante les courants $hK_V7.1$ (inhibition de 3,2 ± 0,1%) < hKir2.1 (inhibition de 17,0 ± 4,6%) < $hCa_V2.2$ (inhibition de 19,1 ± 2,3%) < $hCa_V3.2$ (inhibition de 28,8 ± 0,1%) < $hCa_V3.1$ (inhibition de 56,0 ± 0,1%) (Figure 2-5, colonnes violettes), les courants $hNa_V1.7$, $hCa_V1.2$, $hK_V4.3$ et $hK_V11.1$ étant bloqué entre 90 et 100%. Le peptide a donc une puissance relativement forte pour les sous-types $hNa_V1.7$, $hCa_V1.2$, $hK_V4.3$ et $hK_V11.1$ de canaux ioniques. Ainsi, à une concentration de 37-41 nM, la ProTx-II affecte de façon croissante les courants $hK_V11.1$ (inhibition de 21,5 ± 5,4 %) < $hK_V4.3$ (inhibition de 42,3 ± 1.4 %) < $hCa_V1.2$ (inhibition de 51,5 ± 4,5%) < $hNa_V1.7$ (inhibition de 85,0 ± 0,1%) (Figure 2-5, colonnes bordeaux). Bien que la très haute puissance de la ProTx-II pour le sous-type $Na_V1.7$ soit maintenue, une forte puissance est également détectable pour les sous-types $hCa_V1.2$, $hK_V4.3$ et $hK_V11.1$ impliqués dans le potentiel d'action cardiaque.

2.4.4. Conclusion

Bien que mise en évidence par sa puissance relativement haute vis-à-vis du sous-type $hNa_V1.7$ de canaux sodium, la PecTx-1a se révèle être 24 fois plus efficace pour bloquer le sous-type $hCa_V1.2$ de canaux calcium. De plus, ce peptide présente une grande sélectivité vis-à-vis des autres sous-types de canaux ioniques, en particulier ceux impliqués dans le potentiel d'action cardiaque, contrairement à la ProTx-II qui possède une puissance similaire pour les sous-types $Ca_V1.2$, $Na_V1.7$, $K_V4.3$ et, de façon moindre, pour le sous-type $K_V11.1$. Outre la ProTx-II, de nombreuses toxines de venins de serpents, de scorpions et d'araignées sont décrites dans la littérature comme ciblant les canaux Ca_V de type L, incluant le sous-type $Ca_V1.2$. Cependant, certains critères les concernant en font de mauvais candidats pour un développement thérapeutique comme *(1)* leur grande taille (55-70 acides aminés, 4 ponts disulfures) rendant difficile leur synthèse chimique et leur repliement structural, *(2)* leur manque de sélectivité vis-à-vis des autres sous-types de canaux Ca_V de type L (*i.e.* $Ca_V1.1$, 1.3 et 1.4), ou de types T, P/Q, N et R, de canaux Na_V et de canaux K_V, *(3)* les fonctions multiples que peuvent avoir certaines d'entre elles, comme par exemple les métalloprotéinases, *(4)* leur puissance validée sur le sous-type $Ca_V1.2$ d'une espèce non humaine (rongeurs ou lagomorphe), et *(5)* leur faible puissance (d'une dizaine à plusieurs centaines de nanomolaires) pour le sous-type $Ca_V1.2$ (Yasuda et al., 1994; Sutton et al., 1998; Kubista et al., 2007; Dutra et al., 2008; Villegas et al., 2008; Ono et al., 2011; Pringos et al., 2011; Klint et al., 2014; Liu et al., 2014a).

La PecTx-1a représente donc un outil précieux pour étudier l'expression, la localisation et la fonction du sous-type $Ca_V1.2$ au niveau cellulaire. De plus, en tant que responsable du "plateau" du potentiel d'action cardiaque, elle peut être envisagée comme agent thérapeutique potentiel pour traiter le syndrome du QT long afin d'avoir une alternative aux molécules non peptidiques (telles que le vérapamil, le diltiazem et les dihydropyridines) déjà présentes sur le marché et n'étant pas ou que peu très peu sélectives d'un sous-type donné de canaux Ca_V de type L (Crumb et al., 2016).

2.5. Criblage à haut débit d'une banque de venins appartenant à SANOFI

2.5.1. Contexte de l'étude

Parallèlement à l'étude des propriétés pharmacologiques et fonctionnelles des 4 toxines présentée précédemment (voir sous-parties 2.1 à 2.4), nous avons effectué le criblage à haut débit de 9 venins d'une banque rachetée par SANOFI à l'entreprise de biotechnologie "VenomeTech" (Valbonne) et contenant 450 venins de diverses espèces animales (araignées, cônes, scorpions, serpents et insectes). Le but de ce second criblage est de révéler des toxines originales par leur provenance et/ou leur spécificité vis-à-vis non seulement du sous-type $hNa_V1.7$ mais également des sous-types $hNa_V1.2$ et 1.6 de canaux sodium, tout en épargnant le sous-type cardiaque $hNa_V1.5$.

Le choix de ces 3 sous-types de canaux a été guidé par l'optique de mettre en évidence *(1)* des toxines analgésiques, *i.e.* ayant une forte spécificité pour le sous-type $hNa_V1.7$, *(2)* des toxines inhibant spécifiquement le sous-type neuronal $hNa_V1.2$, pour une meilleure connaissance de l'expression, de la localisation et du rôle de ce sous-type dans les différentes régions du cerveau, et *(3)* des toxines inhibant spécifiquement le sous-type $hNa_V1.6$, afin de concevoir des agents thérapeutiques pour traiter l'épilepsie et certains cancers impliquant ce sous-type de canal (Catterall, 2012; Hernandez-Plata et al., 2012). Dans cette dernière optique, nous cherchons plus particulièrement des toxines ayant un effet anti-invasif au niveau de cellules cancéreuses exprimant le sous-type $hNa_V1.6$ ou pouvant être utilisées comme outils moléculaires de marquage afin de caractériser le stade de développement du cancer.

2.5.2. Résultats obtenus

2.5.2.1. Criblage primaire de la banque de venins

Un premier criblage des fractions de venins avait été préalablement mené en utilisant une plateforme automatisée de "patch-clamp", le système à haut débit IonWorks Quattro® (voir sous-partie 2.1). Ce criblage avait été réalisé sur des lignées cellulaires recombinantes humaines HEK-293 exprimant les sous-types $hNa_V1.7$ et 1.5 et enregistrées en configuration "membrane perforée" et en mode "cellule multiple" (Figure 2-6).

Dans un premier temps, toutes les fractions de venins produisant une perte de scellement (*i.e.*

collage hermétique entre la pipette de "patch" et la membrane cellulaire) ont été éliminées de notre étude. En effet, une perte de scellement avait été rapportée antérieurement lors de l'étude de venins cytotoxiques contenant de la phospholipase A2 et/ou des peptides formant des pores membranaires (Jami et al., 2017), comme cela était le cas pour les fractions des deux venins de cobras (*Naja* sp.) appartenant à la sous-famille Elapidae stricto sensu que nous avions étudiées (A3-x pour *Naja naja Philippinensis* et B3-x pour *Naja oxiana*). Outre les fractions de venins produisant une perte de scellement, et par précaution, l'ensemble des fractions de ces deux venins ont été éliminées de notre étude, incluant même celles pour lesquelles le scellement était préservé. Dans un deuxième temps, toutes les factions de venins considérées comme ayant une faible activité sur le sous-type $hNa_V1.7$ (*i.e.* celles produisant une inhibition inférieure à 40% à une concentration de 0,5 µg/µL) ont été également éliminées de notre étude, à savoir les fractions des venins des deux espèces de cônes (C3-x pour *Conus radiatus* et D3-x pour *Conus geographus*) et d'insecte (A4-x pour *Pachycondila strigulosa*).

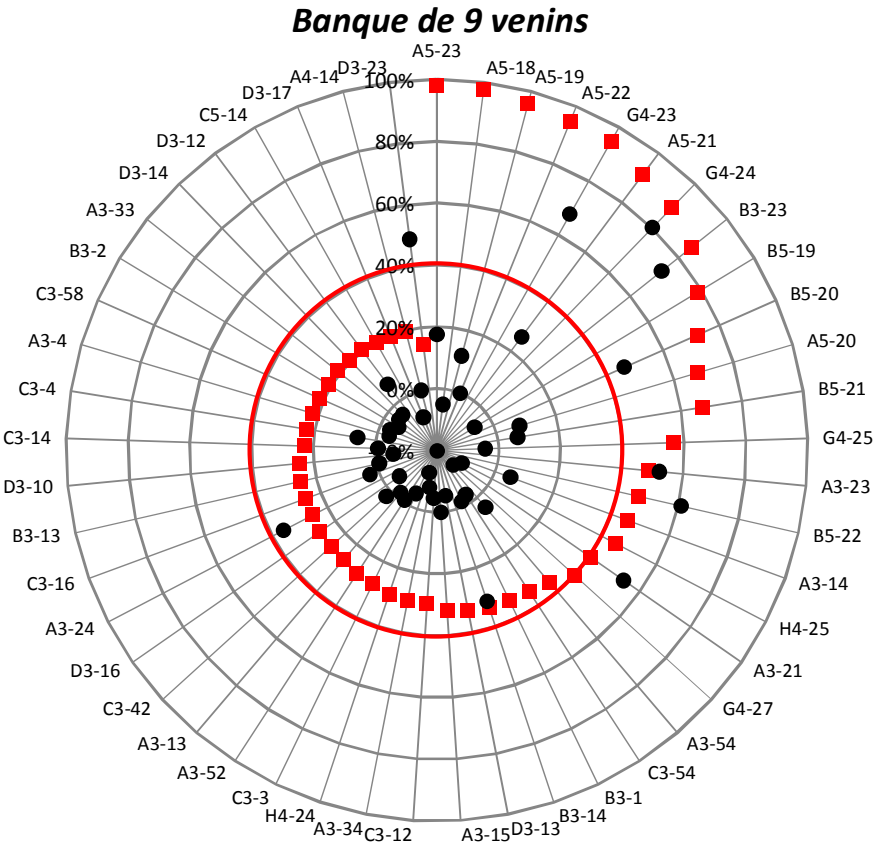

<u>Figure 2-6.</u> Criblage primaire de la banque de venins appartenant à SANOFI. Pourcentage d'inhibition des pics de courants $hNa_V1.7$ (carrés rouges) et $hNa_V1.5$ (ronds noirs) suite à l'application de 0,5 µg/µL de chacune des 49 fractions obtenues à partir des venins d'araignées (A5-x pour *Selenotypus plumipes* et B5-x pour *Phoneyusa celerieri*), de scorpions (G4-x pour *Hottentota gentili* et H4-x pour *Hottentota jayakari*), de serpents (A3-x pour *Naja naja Philippinensis* et B3-x pour *Naja oxiana*), de cônes (C3-x pour *Conus radiatus* et D3-x pour *Conus geographus*) et d'insecte (A4-x pour *Pachycondila strigulosa*). Le cercle rouge à hauteur de 40% d'inhibition marque la limite au-delà de laquelle les fractions ont été analysées en détail.

Suite à ce criblage primaire, les fractions les plus intéressantes qui ont été analysées en détail proviennent des venins de deux espèces d'araignées (A5-x pour *Selenotypus plumipes* et B5-x pour *Phoneyusa celerieri*) et de deux espèces de scorpions (G4-x pour *Hottentota gentili* et H4-x pour *Hottentota jayakari*), venins qui n'avaient jamais, voire que très peu, été étudiés jusqu'à présent.

2.5.2.2. Etude du venin de l'araignée *Selenotypus plumipes* (A5-x)

Bien que *Selenotypus plumipes* soit une araignée endémique du Queensland, en Australie, son venin n'a été étudié que par l'équipe de Glenn F. King (Brisbane, Australie) pour son activité létale sur les termites, les coléoptères ainsi que les larves de lépidoptères (Hardy et al., 2013; Wong et al., 2013). Deux toxines, actives par voie orale, ont été ainsi décrites suite à un criblage bioguidé pour leur activité insecticide: l'OAIP-1 constituée de 34 acides aminés et l'OAIP-4 constituée de 29 acides aminés réticulés par 3 ponts disulfures (Tableau 2-1).

Tableau 2-1. Caractéristiques des deux toxines (OAIP-1 et OAIP-4) extraites du venin de *Selenotypus plumipes* et déjà décrites dans la littérature.

Nom scientifique	Nom d'usage	Masse (Da)	Séquence en acides aminés
U_1-théraphotoxine-Spl1a	OAIP-1	3813,72	DCGHLHDPCPNDRPGHRTCCIGLQCRYGKCLVRV*
U_4-théraphotoxine-Spl1a	OAIP-4	3651,53	YCQKWMWTCDAERKCCEDMACELWCKKRL*

*U: cible moléculaire inconnue. *: amidation en C-terminal. La masse correspond à la masse mono-isotopique de la toxine oxydée. En rouge, les 6 résidus cystéine qui structurent la toxine.*

En utilisant la plateforme automatisée QPatch HTX de "patch-clamp" (voir sous-partie 2.1), nous avons réalisé un criblage plus sensible de 42 sous-fractions du venin de *Selenotypus plumipes* sur des lignées cellulaires recombinantes humaines HEK-293 exprimant les sous-types $hNa_V1.7$, 1.2, 1.6 et 1.5 et enregistrées en configuration "cellule entière" et en mode "cellule multiple" (Figure 2-7).

Sur ces 42 sous-fractions de venin, 6 produisaient une forte inhibition du sous-type $hNa_V1.7$ sans affecter le sous-type $hNa_V1.5$. Malheureusement, elles ont dû être éliminées de notre étude à cause de leur manque de sélectivité vis-à-vis des sous-types $hNa_V1.2$ et 1.6 (sous-fractions A5-18-7, A5-19-4-4, A5-19-6, A5-21-1, A5-21-4 et A5-23-4 soulignées en rouge dans la Figure 2-7).

En revanche, 7 sous-fractions de venin produisaient une forte inhibition des sous-types $hNa_V1.2$ et/ou 1.6 et présentaient une forte sélectivité vis-à-vis des sous-types $hNa_V1.5$ et 1.7. Leur analyse a donc été poursuivie (sous-fractions A5-19-2, A5-19-3, A5-19-4-5, A5-20-3, A5-20-4, A5-20-6 et A5-22-5 soulignées en vert dans la Figure 2-7).

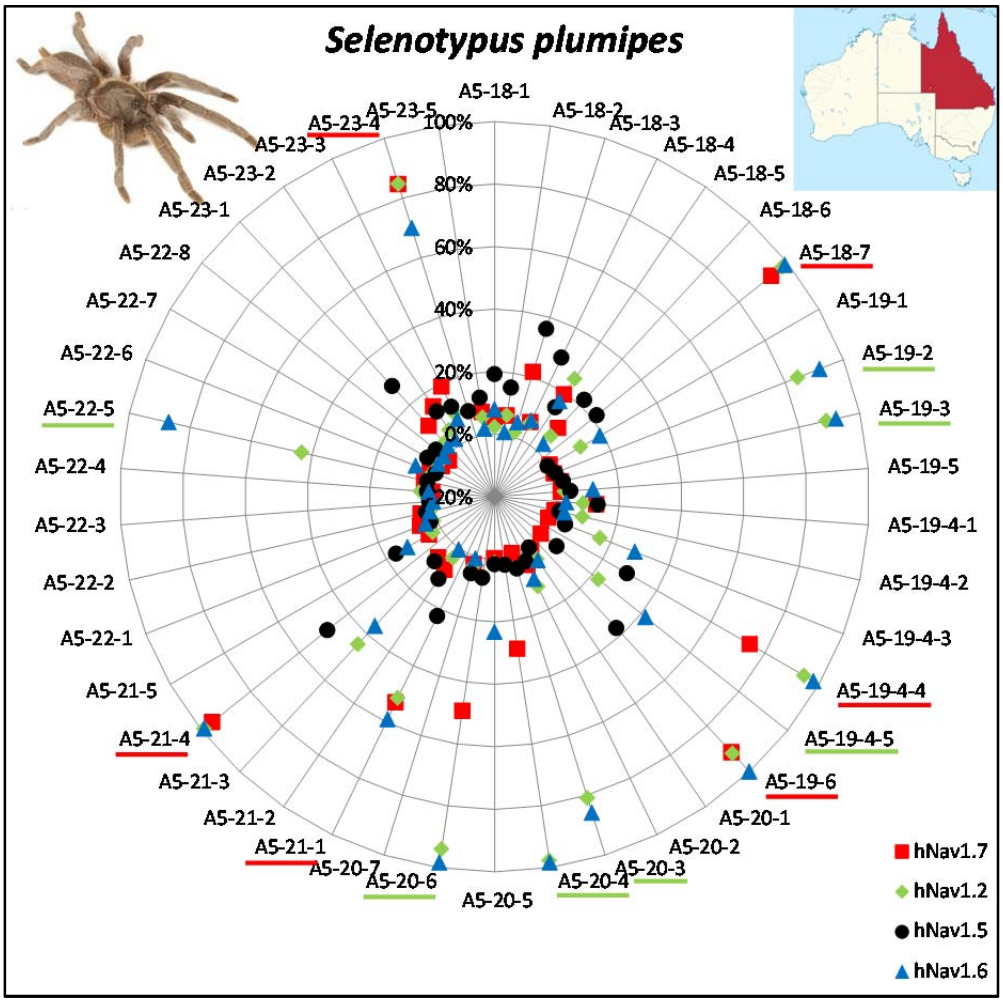

Figure 2-7. Criblage des sous-fractions du venin de *Selenotypus plumipes*. Pourcentage d'inhibition du pic de courant $hNa_V1.7$ (carrés rouges), suite à l'application de 5 ng/µL de chacune des 42 sous-fractions secondaires et tertiaires, et des pics de courants $hNa_V1.5$ (ronds noirs), $hNa_V1.2$ (losanges verts) et $hNa_V1.6$ (triangles bleus), suite à l'application de 23 ng/µL de ces mêmes sous-fractions. Les sous-fractions manquant de sélectivité sont soulignées en rouge et ont été éliminées de notre étude. Celles présentant une sélectivité originale ($hNa_V1.2$ et/ou 1.6 *versus* $hNa_V1.7$) sont soulignées en vert et leur analyse a été poursuivie. Les cercles rouges indiquent le pourcentage d'inhibition non négligeable du courant $hNa_V1.7$ produit par deux d'entre elles.

Ces 7 sous-fractions, en quantité limitée, ne contenaient chacune qu'une à deux toxines qui ont été identifiées par leur masse. Le regroupement de certaines sous-fractions contenant des masses similaires a permis d'avoir la quantité nécessaire pour réaliser directement le séquençage des toxines correspondantes. En particulier, deux toxines étaient présentes dans différentes sous-fractions: la toxine de 3791,5-3791,9 Da présente dans 5 sous-fractions et celle de 4362,1-4362,6 Da présente dans 3 sous-fractions, la faible variation de masse (de 0,4-0,5 Da) étant probablement due à une imprécision dans la mesure (Tableau 2-2). En tenant compte de ces similitudes de masse, nous avons donc identifié 6 toxines dans les 7 sous-fractions d'intérêt.

Avant d'effectuer le séquençage de ces 6 toxines, nous avons recherché les toxines déjà décrites dans la littérature et ayant des masses proches, voire identiques, à celles de nos toxines d'intérêt,

dans la base de données "ArachnoServer" (Pineda et al., 2018) qui est une source d'informations sur les toxines de venins d'araignées (Tableau 2-3). Il est à souligner qu'une étude précédente de prédiction informatique des séquences en acides aminés des toxines matures, à partir du transcriptome du venin de *Selenotypus plumipes*, révèle que de nombreuses séquences sont retrouvées dans le venin d'autres araignées de type mygalomorphe telles que *Chilobrachys guangxiensis* avec laquelle *Selenotypus plumipes* a un peu plus de 90% des séquences en commun (Figure 2-8; Wong et al., 2013).

Tableau 2-2. Masse mono-isotopique des toxines oxydées identifiées dans les 7 sous-fractions d'intérêt du venin de *Selenotypus plumipes*.

Sous-fraction	Masse (Da)
A5-19-2	3791,9 et 4324,9
A5-19-3	3791,9 et 4362,1
A5-19-4-5	3791,5 et 4362,1
A5-20-3	3791,9 et 4362,6
A5-20-4	3791,9 et 4376,2
A5-20-6	3923,1
A5-22-5	4124,1

Tableau 2-3. Toxines trouvées dans ArachnoServer (AS) dont les masses avoisinent celles des 6 toxines présentes dans les 7 sous-fractions d'intérêt du venin de *Selenotypus plumipes* (*Sp*).

Masse *Sp* (Da)	Masse AS (Da)	Nom scientifique	Nom d'usage	Araignée
3791,5 3791,9	3792,73	U_2-Agatoxine-Ao1d	Agel_03	*Agelena orientalis*
	3793,14	M-Ctenitoxine-Cs1d	Cupiennine 1d	*Cupiennius salei*
	3793,51	ω-Hexatoxine-Ar1b	ω-Atracotoxine-Ar1b	*Atrax robustus*
3923,1	3923,43	δ-Amaurobitoxine-Pl1c	δ-Palutoxine IT3	*Pireneitega luctuosa*
4124,1	4124,37	M-Oxotoxine-Ot2a	Oxyopinine-2a	*Oxyopes takobius*
4324,9	4325,00	U_3-Théraphotoxine-Cg1a	Jingzhaotoxine-8.2	*Chilobrachys guangxiensis*
4362,1 4362,6	4362,03	ω-Hexatoxine-Hv2i	-	*Hadronyche versuta*
	4362,23	ω-Théraphotoxine-Bs1b	Brachypelma smithi toxine 5	*Brachypelma smithi*
4376,2	4375,83	U_{21}-Théraphotoxine-Hs1a	Huwentoxine-XIXa1	*Haplopelma schmidti*
	4376,24	ω-Théraphotoxine-Ba1c	Peptide Ba3 de venin	*Brachypelma albiceps*

U: cible moléculaire inconnue. M: toxines inhibitrices des canaux mécano-sensoriels. ω: toxines inhibitrices des canaux Ca_V. δ: toxines ralentissant l'inactivation des canaux Na_V. La masse correspond à la masse mono-isotopique de la toxine oxydée.

Les séquences primaires (en acides aminés) de 5 sur 6 de nos peptides naturels d'intérêt ont été déterminées par séquençage *de novo* en utilisant la spectrométrie de masse en tandem (MS/MS) et la dégradation d'Edman, soit une combinaison de techniques analytiques incluant une approche ascendante ("bottom-up") et une spectrométrie de masse à haute résolution (Tableau 2-4).

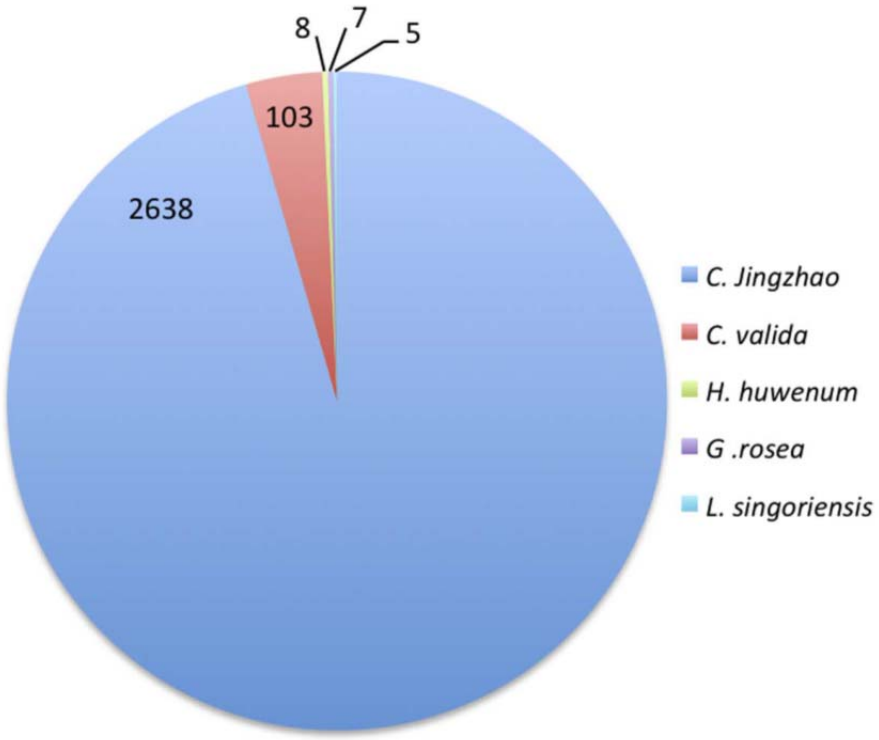

Figure 2-8. Nombres de séquences de *Selenotypus plumipes* qui ont une homologie avec celles des toxines de différentes espèces d'araignées d'après la base de données "ArachnoServer". Ne sont mentionnées que les paires issues de chaque Blast avec un fort pourcentage d'identité. Les nombres sont ceux des séquences de *Selenotypus plumipes* qui correspondent aux toxines connues des espèces suivantes: *Chilobrachys jing zhao* (tarentule-tigre chinoise), *Coremiocnemis valida* (tarentule brune de Singapour), *Haplopelma huwenum* (araignée-oiseau chinoise), *Grammostola rosea* (mygale rose du Chili) et *Lycosa singoriensis* (araignée-loup). À l'exception de *Lycosa singoriensis*, toutes ces araignées sont des mygalomorphes primitives apparentées à *Selenotypus plumipes*. D'après Wong et al., 2013.

Tableau 2-4. Séquences en acides aminés des toxines contenues dans les 7 sous-fractions d'intérêt du venin de *Selenotypus plumipes*.

Peptide	Sous-fraction d'origine	Masse (Da)	Séquence en acides aminés
A5-19-2-1	A5-19-3/A5-19-4-5/A5-20-3	4325,0	LFECSFSCDIKKNGKPCKGSGEKKCSGGWRCKMNFCVKV
A5-20-3-2	A5-19-2	4362,1	FECVLKCDIQYNGKNCKGKGENKCSGGWRCRFKLCLKI
A5-20-4-1	A5-19-2/A5-19-3/A5-20-3/ A5-20-4	3791,5	DCLGQWSGCDPKNSKCCPSYACTSKYPWCRYHI*
A5-20-5-1	A5-20-4	4376,2	FECVLKCDIQYNGKNCKGKGEKKCSGGWRCRFKLCLKI
A5-20-6-1	A5-20-6	3921,3	*Non déterminée*
A5-22-5-2	A5-22-5	4123,7	ECLGQWSGCDPNDNKCCPNYACTWKYPWCRKYLW

**: amidation en C-terminal. La masse correspond à la masse mono-isotopique de la toxine oxydée. En rouge, les 6 résidus cystéine qui structurent la toxine. En vert, le seul acide aminé (en position 22) qui diffère l'A5-20-5-1 de l'A5-20-3-2.*

Deux des séquences primaires déterminées, celles de l'**A5-19-2-1** et de l'**A5-20-3-2**, sont repliées par 3 ponts disulfures caractérisés par un appariement spécial des cystéines (C_I–C_{III}, C_{II}–C_V, C_{IV}–C_{VI}) et

sont déjà connues. La séquence primaire de l'A5-19-2-1, de 39 résidus d'acides aminés, correspond à 100% à celle de la jinghaotoxine (JzTx)-8.2, aussi nommée U_3-théraphotoxine-Cg1a, dont la cible était inconnue jusque-là (Chen et al., 2008). La séquence primaire de l'A5-20-3-2, de 38 résidus d'acides aminés, correspond à 100% à celle de l'OAIP-5 dont la cible était, là encore, inconnue jusque-là (Wong et al., 2013). La séquence primaire de l'**A5-20-5-1** montre que cette toxine est un variant qui ne diffère que par un seul acide aminé de l'A5-20-3-2 [une lysine (K) à la place d'une asparagine (N) en position 22, ce qui explique la différence de 14,1 Da entre les deux masses; Tableau 2-4]. Ces trois séquences ont la particularité d'être très riches en acides aminés basiques: 8 à 9 lysines (K) et 1 à 2 arginines (R). Les séquences primaires de l'**A5-20-4-1**, de 33 résidus d'acides aminés, et celle de l'**A5-22-5-2**, de 34 résidus d'acides aminés, partagent 79% et 53% d'identité, respectivement, avec celle de l'OAIP-2 qui, comme les OAIP-1 et 4, se structure autour du motif architectural ICK et est caractérisée par un appariement des cystéines (C_I–C_{IV}, C_{II}–C_V, C_{III}–C_{VI}) fréquemment retrouvé dans les toxines décrites comme antinociceptives (voir partie 1). Il est à souligner que la séquence primaire de l'A5-22-5-2 partage 73% d'identité avec celle de la β-théraphotoxine-Pmr1a connue pour son action inhibitrice de certains sous-types de canaux Na_V, *i.e.* $Na_V1.3$ et 1.8 (Meir et al., 2012).

Les synthèses des 3 toxines JzTx-8.2/A5-19-2-1, OAIP-5/A5-20-3-2 et son variant K22N-OAIP-5/A5-20-5-1, incluant une structure en épingle à cheveux β, ont été très difficiles à réaliser de par une étape d'oxydation compliquée. Les synthèses des 2 toxines originales se structurant autour du motif ICK ont conduit à une qualité correcte des séquences brutes, malgré un repliement difficile pour l'A5-20-4-1. Après l'utilisation de méthodes de chromatographie en phase liquide à haute performance (HPLC pour "high performance liquid chromatography"), sur phase inverse, et de chromatographie échangeuse de cations, la purification des produits de synthèse s'est traduite par l'obtention de larges pics, chacun contenant des peptides de même masse, mais ayant probablement des appariements de ponts disulfure variables, ce qui nous a souvent amené à étudier 2 à 3 produits de synthèse pour un peptide naturel donné (Tableau 2-5).

Les effets de chaque produit de synthèse ont été évalués sur les lignées cellulaires recombinantes humaines HEK-293 exprimant les sous-types $hNa_V1.2$, 1.6 et 1.7, en utilisant la même plateforme automatisée de "patch-clamp" que celle utilisée pour le criblage primaire de la banque de venins, à savoir le système à haut débit IonWorks Quattro®. Les résultats obtenus montrent que seuls les produits de synthèse 1690 F1X1F1 (une fraction de l'A5-20-4-1) et 1853 F1, 1853 F5 et 1853 F6 (les trois fractions de l'A5-22-5-2) produisaient une inhibition des courants $hNa_V1.2$, 1.6 et 1.7 avec une valeur moyenne d'IC_{50} proche de 1 µM, les valeurs moyennes d'IC_{50} pour les autres produits de synthèse étant supérieures à 10 µM (Tableau 2-5).

Tableau 2-5. Produits de synthèse obtenus après le séquençage des peptides naturels contenus dans les 7 sous-fractions d'intérêt du venin de *Selenotypus plumipes*.

Peptide naturel	Produit de synthèse	Pureté	IC_{50} moyen ($hNa_V1.2$, 1.6 et 1.7)
A5-19-2-1 (JzTx-8.2)	1687 F2	Plusieurs motifs de repliement	> 10 µM
A5-20-3-2 (OAIP-5)	1688 F1 1688 F2 1688 F3	Plusieurs motifs de repliement	> 10 µM
A5-20-4-1	1690 F1 1690 F1X1F1	94% 83%	> 10 µM ≈ 1 µM
A5-20-5-1 (K22N-OAIP-5)	1781 F1 1781 F2 1781 F3	Plusieurs motifs de repliement	> 10 µM
A5-22-5-2	1853 F1 1853 F5 1853 F6	99% 82% 91%	≈ 1 µM

Suite à ces résultats, il nous a semblé intéressant de mieux caractériser la puissance des produits de synthèse contenus dans les trois fractions de l'A5-22-5-2 pour les cibles d'intérêt, à savoir les sous-types $hNa_V1.2$, 1.5, 1.6 et 1.7 de canaux Na_V, en utilisant la plateforme automatisée QPatch HTX de "patch-clamp". Les produits de synthèse agissaient préférentiellement sur les sous-types TTX-S ($hNa_V1.2$, 1.6 et 1.7), avec une sélectivité moyenne vis-à-vis du sous-type TTX-R cardiaque $hNa_V1.5$ (facteur de sélectivité supérieur à 11, Tableau 2-6). Leurs effets consistent en une diminution des pics de courant sans modification notable des cinétiques d'activation et d'inactivation, et de leur dépendance vis-à-vis du potentiel. Ces propriétés suggèrent fortement un mode d'action du type " bloqueurs de pore". Le produit 1853 F1 possède une forte puissance (IC_{50} de plusieurs dizaines de nanomolaires) pour les 3 sous-types TTX-S. La puissance des produits 1853 F5 et 1853 F6 est moins importante pour ces 3 sous-types (IC_{50} de plusieurs centaines de nanomolaires) mais le produit 1853 F5 semble être plus efficace pour interagir avec le sous-type $hNa_V1.2$ (Tableau 2-6). Cependant, avec un facteur de sélectivité inférieur à 6 vis-à-vis des sous-types $hNa_V1.6$ et 1.7, ce produit est peu intéressant comme outil potentiel visant le sous-type $hNa_V1.2$.

Tableau 2-6. Puissance des produits de synthèse des trois fractions de l'A5-22-5-2 (IC_{50} moyen ± ES en nM, n = 2-6) pour les sous-types $hNa_V1.2$, 1.5, 1.6 et 1.7.

Produit de synthèse	$hNa_V1.7$	$hNa_V1.2$	$hNa_V1.5$	$hNa_V1.6$
1853 F1	79 ± 20	126 ± 18	1605 ± 279	50 ± 15
1853 F5	3761 ± 1064	659 ± 226	> 10000	1197 ± 103
1853 F6	2602 ± 607	903 ± 294	> 10000	1187 ± 34

2.5.2.3. Etude du venin de l'araignée *Phoneyusa celerieri* (B5-x)

Phoneyusa celerieri (aussi nommée *Hysterocrates celerieri*) est une araignée babouin endémique de l'Afrique subsaharienne et du Moyen-Orient. En utilisant la plateforme automatisée QPatch HTX de "patch-clamp", nous avons réalisé un criblage secondaire de 11 sous-fractions du venin de cette araignée sur des lignées cellulaires recombinantes humaines HEK-293 exprimant les sous-types hNa$_V$1.7, 1.2, 1.6 et 1.5 et enregistrées en configuration "cellule entière" et en mode "cellule multiple" (Figure 2-9).

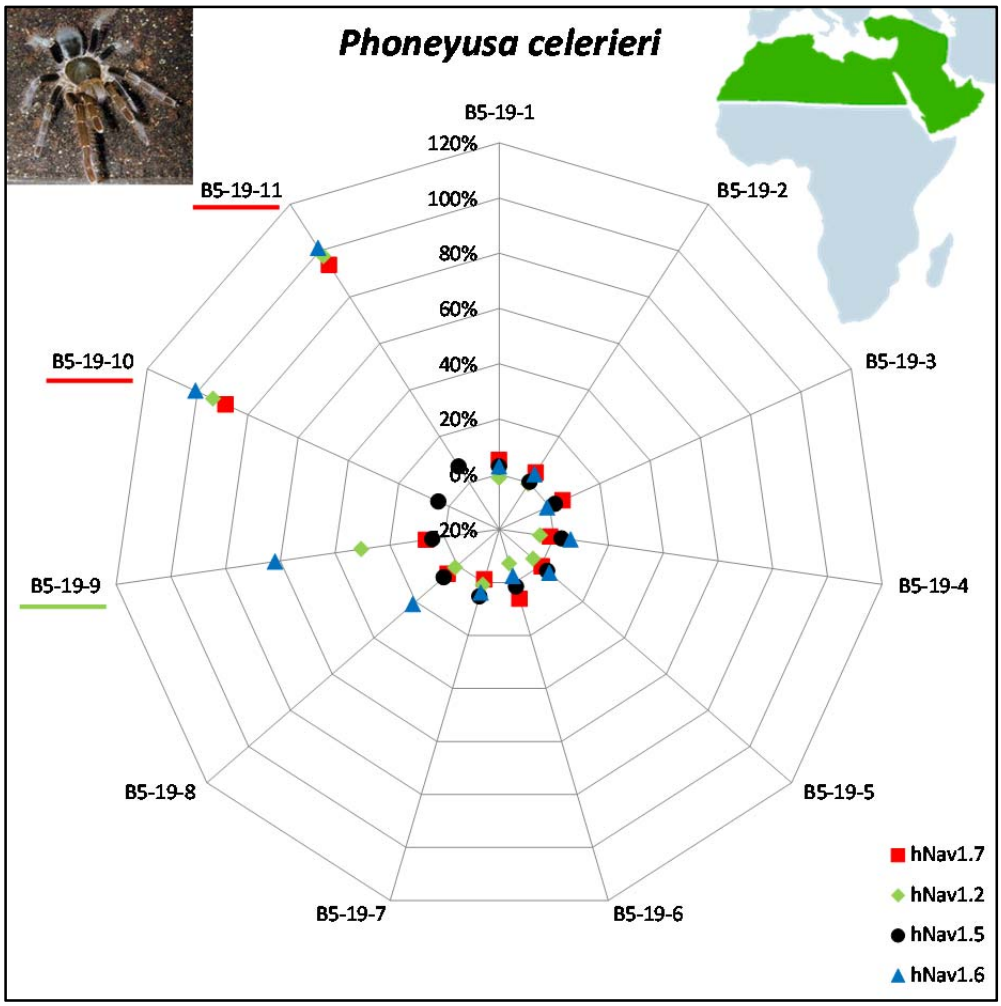

Figure 2-9. Criblage des sous-fractions du venin de *Phoneyusa celerieri*. Pourcentage d'inhibition du pic de courant hNa$_V$1.7 (carrés rouges), suite à l'application de 5 ng/µL de chacune des 11 sous-fractions secondaires, et des pics de courants hNa$_V$1.5 (ronds noirs), hNa$_V$1.2 (losanges verts) et hNa$_V$1.6 (triangles bleus), suite à l'application de 23 ng/µL de ces mêmes sous-fractions. Les sous-fractions manquant de sélectivité sont soulignées en rouge. Celle présentant une sélectivité originale (hNa$_V$1.6 et 1.2 *versus* hNa$_V$1.7) est soulignée en vert.

Sur ces 11 sous-fractions, 2 produisaient une inhibition de plus de 90% du sous-type hNa$_V$1.7 sans affecter le sous-type hNa$_V$1.5, mais manquaient de sélectivité vis-à-vis des sous-types hNa$_V$1.2 et

1.6 (sous-fractions B5-19-10 et B5-19-11 soulignées en rouge dans la Figure 2-9). En revanche, comparée à ces deux sous-fractions, une troisième sous-fraction de venin produisait une inhibition relativement moins forte des sous-types $hNa_V1.6$ et 1.2 mais présentait une sélectivité relativement plus forte vis-à-vis du sous-type $hNa_V1.7$ (sous-fraction B5-19-9 soulignée en vert dans la Figure 2-9). L'analyse de 2 de ces 3 sous-fractions, B5-19-9 et B5-19-11, a été poursuivie.

Ces 2 sous-fractions ne contenaient chacune qu'une à deux toxines identifiées par leur masse (Tableau 2-7). En tenant compte de la similitude de masse, nous avons identifié 2 toxines dans les 2 sous-fractions d'intérêt: une de 3792,7-3793,7 Da et l'autre de 5299,6 Da. Cette dernière a été éliminée de notre étude compte-tenu de sa masse relativement élevée et du fait que la sous-fraction d'origine manquait de sélectivité vis-à-vis des sous-types $hNa_V1.2$, 1.6 et 1.7 (voir Figure 2-9). Nous avons recherché les toxines déjà décrites dans la littérature et ayant des masses proches, voire identiques, à notre toxine d'intérêt dans la base de données "ArachnoServer" (Tableau 2-8). Il est à souligner que la masse de cette toxine d'intérêt du venin de *Phoneyusa celerieri* (3792,7-3793,7) est proche de celle d'une des toxines identifiées dans certaines sous-fractions du venin de *Selenotypus plumipes* (3791,5-3791,9). En conséquence, il n'est pas étonnant que les toxines ayant une masse apparentée et trouvées dans ArachnoServer soient les mêmes (voir Tableaux 2.3 et 2.8).

Tableau 2-7. Masse mono-isotopique des toxines oxydées identifiées dans 2 sous-fractions d'intérêt du venin de *Phoneyusa celerieri*.

Sous-fraction	Masse (Da)
B5-19-9	3793,7 et 5299,6
B5-19-11	3792,7

Tableau 2-8. Toxines trouvées dans ArachnoServer (AS) dont les masses avoisinent celles de la toxine présente dans 2 sous-fractions d'intérêt du venin de *Phoneyusa celerieri* (*Pc*).

Masse *Pc* (Da)	Masse AS (Da)	Nom scientifique	Nom d'usage	Araignée
3792,7 3793,7	3792,73	U_2-Agatoxine-Ao1d	Agel_03	*Agelena orientalis*
	3793,14	M-Ctenitoxine-Cs1d	Cupiennine 1d	*Cupiennius salei*
	3793,51	ω-Hexatoxine-Ar1b	ω-Atracotoxine-Ar1b	*Atrax robustus*

U: cible moléculaire inconnue. M: toxines inhibitrices des canaux mécano-sensoriels. ω: toxines inhibitrices des canaux Ca_V. La masse correspond à la masse mono-isotopique de la toxine oxydée.

La séquence primaire de notre peptide naturel d'intérêt a été déterminée par séquençage *de novo* en utilisant la spectrométrie de MS/MS et la dégradation d'Edman, malgré un doute sur l'originalité de séquence entre la toxine de 3792,7-3793,7 Da du venin de *Phoneyusa celerieri* et celle de 3791,5-3791,9 Da du venin de *Selenotypus plumipes*. La séquence primaire déterminée (toxine B5-

19-10-1 de 3793,7 Da) inclut 34 résidus d'acides aminés dont 6 cystéines qui structurent la toxine autour du motif architectural ICK (Tableau 2-9). Elle ne partage que 53% d'identité avec celle de l'A5-20-4-1 de *Selenotypus plumipes*, bien que les deux peptides aient des masses similaires. En revanche, avec un résidu glycine (G) en plus en N-terminal et un résidu asparagine (N) au lieu d'un résidu aspartate (D) pour l'acide aminé suivant, la séquence de la B5-19-10-1 correspond à 100% à celle du peptide Hs1a d'une araignée du genre *Hysterocrates* qui comprend 35 résidus d'acides aminés et dont la structure (2MT7) a été déposée dans la base de données des protéines (PDB pour "protein data bank") par Klint et collaborateurs en août 2014 (DOI: 10.2210/pdb2MT7/pdb). Comme rapporté par ces auteurs, le peptide Hs1a produit une diminution de l'hypersensibilité chronique viscérale en interagissant avec le sous-type $Na_V1.7$.

Tableau 2-9. Séquence en acides aminés de la toxine contenue dans 2 sous-fractions d'intérêt du venin de *Phoneyusa celerieri*.

Peptide	Sous-fraction d'origine	Masse (Da)	Séquence en acides aminés
B5-19-10-1	B5-19-11	3793,7	DDCLGFWSACNPKNDKCCANLVCSSKHKWCKGKL*

**: amidation en C-terminal. La masse correspond à la masse mono-isotopique de la toxine oxydée. En rouge, les 6 résidus cystéine qui structurent la toxine autour du motif architectural ICK.*

La synthèse de la toxine B5-19-10-1 (probablement associée à un motif structural de type ICK) a été de nouveau suivie d'une étape de repliement complexe conduisant en fin de purification à l'obtention de larges pics isomassiques. Nous avons évalué les effets de 6 fractions de ces pics, soit 6 produits de synthèse pour ce peptide naturel, sur les lignées cellulaires HEK-293 exprimant les sous-types $hNa_V1.2$, 1.6 et 1.7, en utilisant le système à haut débit IonWorks Quattro® (Tableau 2-10). Les résultats obtenus montrent que seuls les produits de synthèse 1722 F1, 1722 F5 et 1722 F6 produisaient une inhibition des courants $hNa_V1.2$, 1.6 et 1.7 avec une valeur moyenne d'IC_{50} proche de 1 µM, les valeurs moyennes d'IC_{50} pour les 3 autres produits de synthèse étant supérieures à 10 µM.

Tableau 2-10. Produits de synthèse obtenus après le séquençage du peptide naturel contenu dans 2 sous-fractions d'intérêt du venin de *Phoneyusa celerieri*.

Peptide naturel	Produit de synthèse	Pureté	IC_{50} moyen ($hNa_V1.2$, 1.6 et 1.7)
B5-19-10-1	1722 F1	97%	≈ 1 µM
	1722 F5	72%	
	1722 F6	83%	
	1722 F7	62% et 37% (2 pics)	> 10 µM
	1722 F8	70% et 28% (2 pics)	
	1722 F11	90%	

La caractérisation de la puissance des produits de synthèse 1722 F1, 1722 F5 et 1722 F6 pour les sous-types $hNa_V1.2$, 1.5, 1.6 et 1.7 de canaux Na_V a été poursuivie en utilisant la plateforme automatisée QPatch HTX de "patch-clamp". Comme nous l'avions déjà observé pour les produits de synthèse décrits lors de l'étude du venin de l'araignée *Selenotypus plumipes*, les produits 1722 F1, 1722 F5 et 1722 F6 agissaient préférentiellement sur les sous-types TTX-S ($hNa_V1.2$, 1.6 et 1.7), avec une sélectivité vis-à-vis du sous-type TTX-R cardiaque $hNa_V1.5$ qui était très forte pour le produit 1722 F1 (facteur de sélectivité supérieur à 150) mais plus faible pour les produits 1722 F5 et 1722 F6 (facteur de sélectivité supérieur à 7) (Tableau 2-11). Leurs effets consistent en une diminution des pics de courant sans modification notable des cinétiques d'activation et d'inactivation, et de leur dépendance vis-à-vis du potentiel. Le produit 1722 F1 possède une forte puissance (IC_{50} de quelques dizaines de nanomolaires) pour les 3 sous-types TTX-S alors que celle de 1722 F5 et 1722 F6 est moins importante (IC_{50} de plusieurs centaines de nanomolaires). Cependant, aucun de ces peptides n'est sélectif de l'un des 3 sous-types étudiés, excluant leur utilisation comme outil pharmacologique visant les sous-types $Na_V1.2$, 1.6 ou 1.7.

Tableau 2-11. Puissance de 3 produits de synthèse du peptide naturel B5-19-10-1 (IC_{50} moyen ± ES en nM, n = 2-6) pour les sous-types $hNa_V1.2$, 1.5, 1.6 et 1.7.

Produit de synthèse	$hNa_V1.7$	$hNa_V1.2$	$hNa_V1.5$	$hNa_V1.6$
1722 F1	43 ± 5	65 ± 12	> 10000	23 ± 6
1722 F5	736 ± 79	344 ± 75	> 10000	392 ± 58
1722 F6	1475 ± 532	706 ± 249	> 10000	625 ± 112

2.5.2.4. Etude du venin du scorpion *Hottentotta gentili* (G4-x)

Hottentotta gentili est un scorpion endémique du Maroc et de l'Algérie. En utilisant la plateforme automatisée QPatch HTX de "patch-clamp", nous avons réalisé un criblage secondaire de 7 sous-fractions du venin de ce scorpion sur des lignées cellulaires HEK-293 exprimant les sous-types $hNa_V1.7$, 1.2, 1.6 et 1.5 et enregistrées en configuration "cellule entière" et en mode "cellule multiple" (Figure 2-10).

Sur ces 7 sous-fractions, une seule produisait une inhibition de plus de 70% du sous-type $hNa_V1.7$ mais manquait de sélectivité vis-à-vis des sous-types $hNa_V1.2$, 1.6 et même 1.5 puisqu'elle bloquait également les sous-types $hNa_V1.2$ et 1.6 d'environ 60% et le sous-type $hNa_V1.5$ d'environ 30%, (sous-fraction G4-24-3 soulignée en rouge dans la Figure 2-10). Des résultats similaires, bien que les inhibitions soient moins marquées, ont été obtenus avec la sous-fraction G4-24-4. Finalement, une troisième sous-fraction de venin produisait une inhibition de 50 à 60% des sous-types $hNa_V1.2$ et 1.6 et présentait une certaine sélectivité vis-à-vis du sous-type $hNa_V1.7$ mais pas vis-à-vis du sous-type

hNa$_V$1.5 qui étaient bloqués d'environ 10 et 35%, respectivement (sous-fraction G4-24-5 soulignée en vert dans la Figure 2-10). L'analyse de ces 3 sous-fractions a été malgré tout poursuivie.

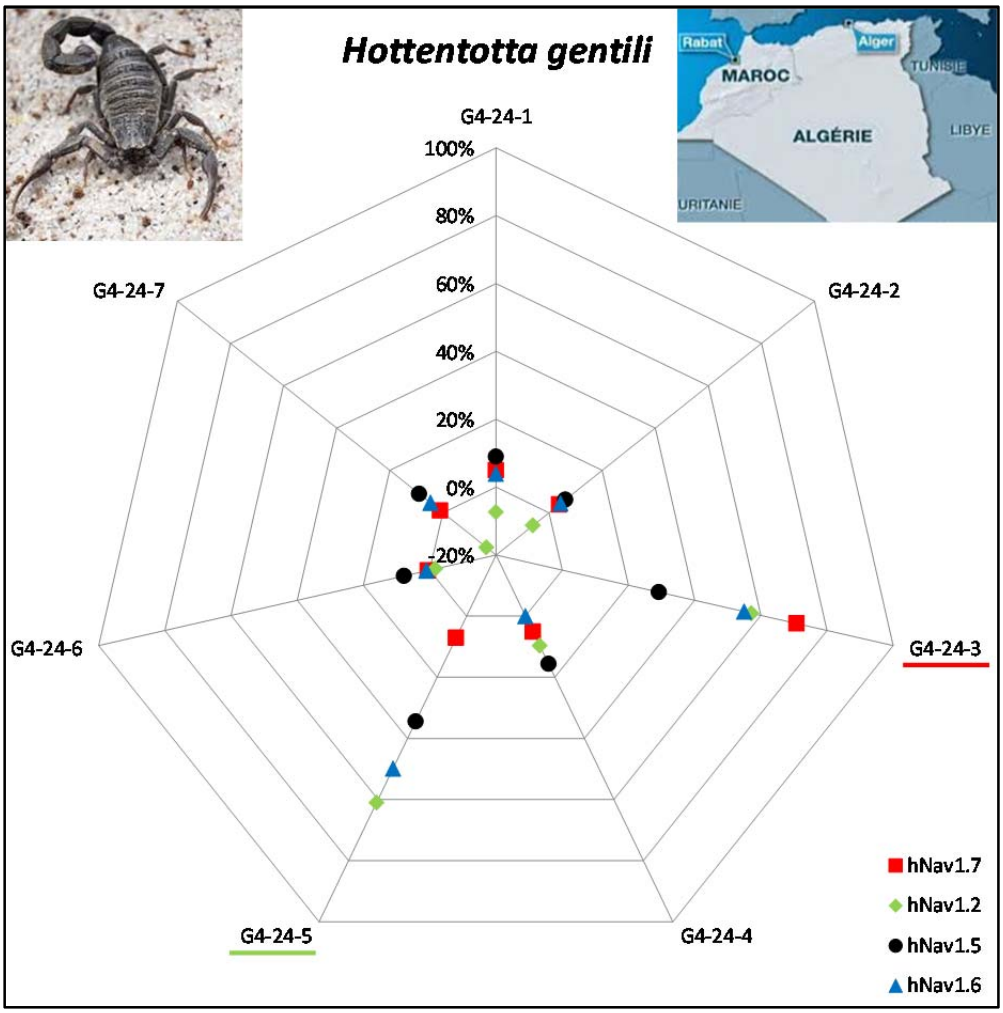

Figure 2-10. Criblage des sous-fractions du venin de *Hottentotta gentili*. Pourcentage d'inhibition du pic de courant hNa$_V$1.7 (carrés rouges), suite à l'application de 5 ng/µL de chacune des 7 sous-fractions secondaires, et des pics de courants hNa$_V$1.5 (ronds noirs), hNa$_V$1.2 (losanges verts) et hNa$_V$1.6 (triangles bleus), suite à l'application de 23 ng/µL de ces mêmes sous-fractions. La sous-fraction manquant de sélectivité est soulignée en rouge. Celle présentant une sélectivité originale (hNa$_V$1.6 et 1.2 *versus* hNa$_V$1.7) est soulignée en vert.

Ces 3 sous-fractions contenaient chacune une (sous-fraction G4-24-3) à cinq (sous-fraction G4-24-4) toxines identifiées par leur masse (Tableau 2-12). En tenant compte de la similitude de masse, nous n'avons identifié qu'une seule toxine présente dans 2 sous-fractions d'intérêt: celle de 7046,1 Da présente dans les sous-fractions G4-24-4 et G4-24-5 et dont la masse est identique à celle de la toxine LqhIII, une toxine de type α issue du scorpion *Leiurus quinquestriatus hebraeus* (Benoit & Gordon, 2001). La variabilité des masses était particulièrement marquée dans ces sous-fractions. Ainsi, nous avons pu mettre en évidence une protéine de 14741 Da, identifiée comme étant probablement une phospholipase A2, dans la sous-fraction G4-24-5.

Tableau 2-12. Masse mono-isotopique des toxines oxydées identifiées dans 3 sous-fractions d'intérêt du venin de *Hottentotta gentili*.

Sous-fraction	Masse (Da)
G4-24-3	6938,99
G4-24-4	3788,7/6938,9/7046,1/7229,8/8138,7
G4-24-5	7046,1/7815,4/14741

La détermination des séquences primaires des toxines identifiées dans les 3 sous-fractions et leur synthèse, incluant leur repliement, n'ont pas été envisagées dans le cadre de ma thèse de par le manque de temps et les difficultés prévisibles au vu de leur grande taille et de leur nombre de ponts disulfures probablement supérieur à 3. La seule tentative de séquençage que nous ayons effectuée est celle de la toxine de 7815,4 Da, originale par sa masse, de la sous-fraction G4-24-5. Malheureusement, elle s'est soldée par un échec car la toxine était en quantité insuffisante et a été perdue au cours de la procédure. La caractérisation des toxines a donc été poursuivie en étudiant les effets des 3 sous-fractions sur les lignées cellulaires HEK-293 exprimant les sous-types hNa_V1.7, 1.2, et 1.6 et enregistrées en configuration "cellule entière" et en mode "cellule multiple" en utilisant la plateforme automatisée QPatch HTX de "patch-clamp".

Avant de rentrer dans le détail de l'analyse des résultats obtenus, il est à rappeler que les **toxines α de scorpion**, en général de faible masse et qui se fixent sur le site 3 des canaux Na_V, altèrent leur inactivation ce qui implique, au niveau du courant, *(1)* une inhibition d'une partie de son inactivation et un ralentissement de sa cinétique d'inactivation, sans modification notable de l'amplitude du pic de courant, et *(2)* une altération de la dépendance vis-à-vis du potentiel de l'inactivation sans que celle de l'activation ne soit notablement modifiée. Ces effets se traduisent par une forte augmentation de la durée des potentiels d'action, comme cela est le cas, par exemple, de ceux de la toxine LqhIII sur le sous-type Na_V1.6 (Benoit & Gordon, 2001). Les **toxines β de scorpion**, en général de masse plus élevée et qui se fixent sur le site 4 des canaux Na_V, bloquent ces canaux et altèrent leur activation ce qui implique, au niveau du courant, *(1)* une diminution de l'amplitude du pic de courant, sans modification de ses cinétiques d'activation et d'inactivation, et *(2)* une altération de la dépendance vis-à-vis du potentiel de l'activation sans que celle de l'inactivation ne soit notablement modifiée. Ces effets se traduisent par l'apparition, à une fréquence plus élevée, de potentiels d'action de plus faible amplitude (Cestele et al., 1998).

Les résultats obtenus des effets des sous-fractions G4-24-3, G4-24-4 et G4-24-5 sur les sous-types Na_V1.7, 1.2 et 1.6 sont présentés dans les Figures 2-11 et 2-12 et dans le Tableau 2-13.

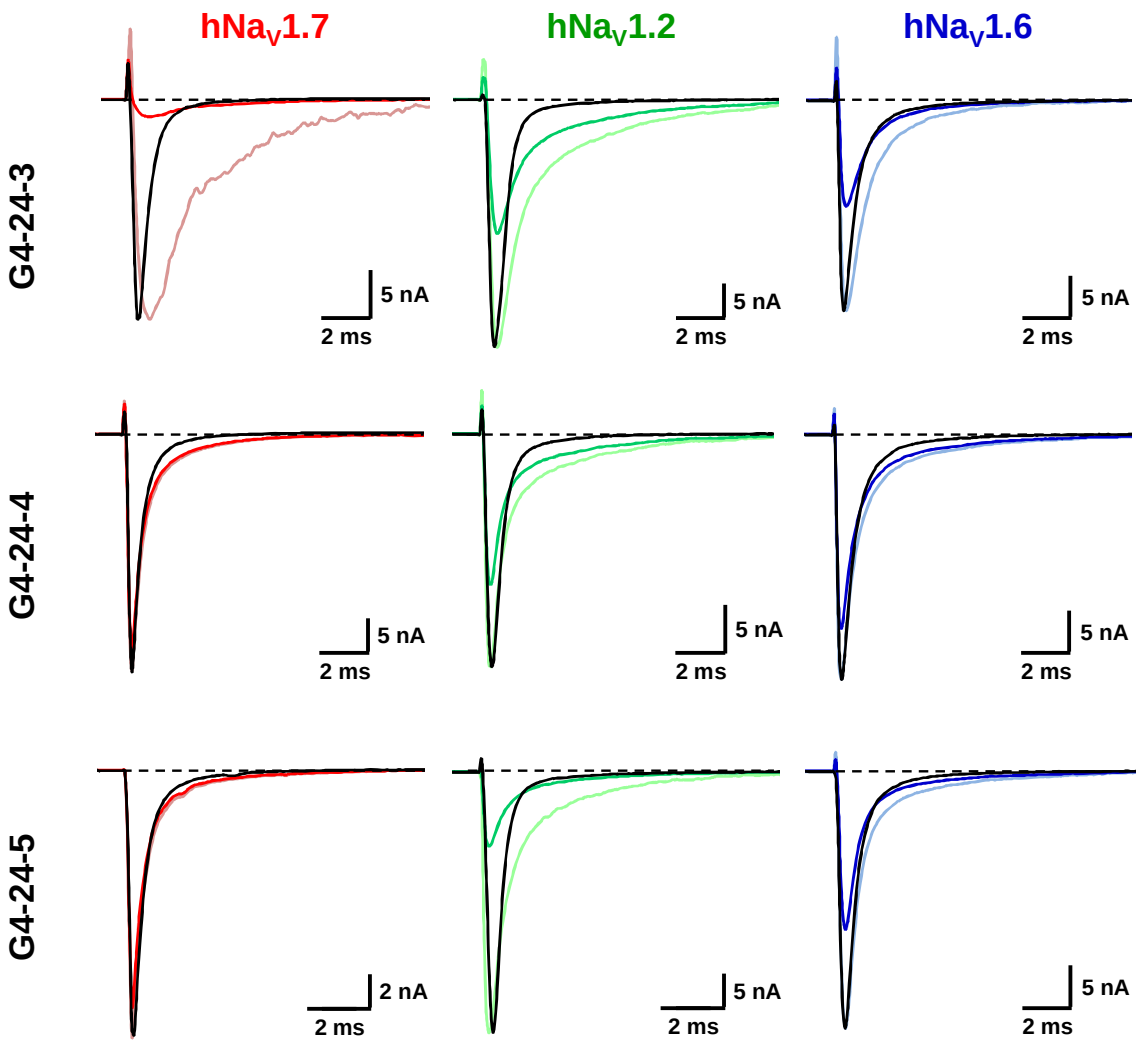

<u>Figure 2-11.</u> Effets des sous-fractions secondaires du venin de *Hottentotta gentili* sur les courants hNa$_V$1.7 (en rouge), hNa$_V$1.2 (en vert) et hNa$_V$1.6 (en bleu). Traces représentatives des courants avant (en noir) et après soit 5 ng/µL (en rouge) soit 23 ng/µL (en vert et en bleu) de chacune des 3 sous-fractions (G4-24-3, G4-24-4 et G4-24-5). Les traces de couleur claire représentent le courant enregistré en présence d'une sous-fraction donnée et normalisé par rapport au pic de courant contrôle.

Les effets de la sous-fraction **G4-24-3**, qui ne contient qu'une seule masse à priori, sur le sous-type hNa$_V$1.7 consistent en une forte diminution du pic de courant, principalement due à un déplacement positif de la courbe "conductance-potentiel", sans que les cinétiques d'activation et d'inactivation du courant ne soient altérées, le ralentissement apparent de l'inactivation résultant de l'imprécision des mesures due à la forte diminution du courant. Cette sous-fraction est un peu moins efficace pour inhiber les sous-types hNa$_V$1.2 et 1.6 dont la diminution du pic de courant peut être due, en partie, au léger déplacement négatif de leur courbe "inactivation stationnaire-potentiel", sans que la dépendance de leur activation vis-à-vis du potentiel ne soit notablement modifiée. Aucun de ces effets ne peut être relié à la présence d'une toxine α ou β de scorpion dans la sous-fraction G4-24-3.

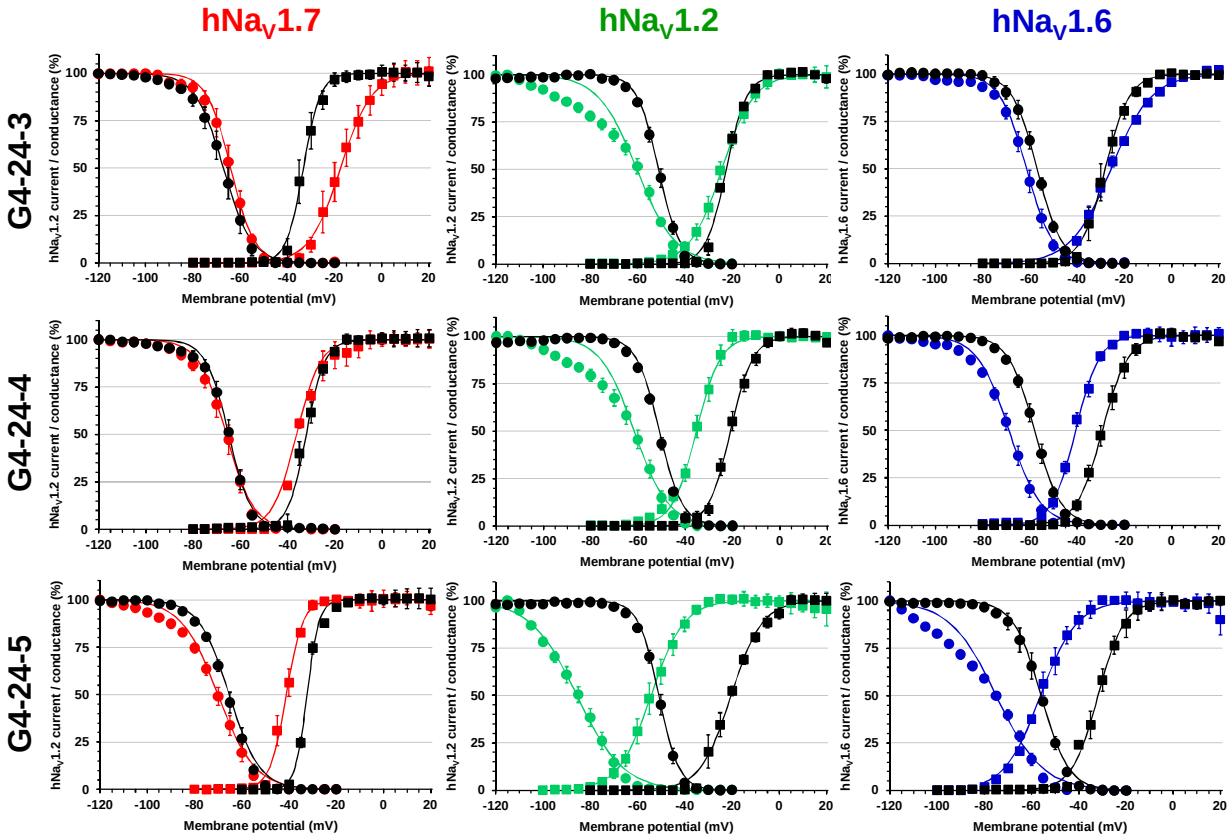

Figure 2-12. Effets des sous-fractions secondaires du venin de *Hottentotta gentili* sur la dépendance vis-à-vis du potentiel de membrane de l'inactivation stationnaire et de la conductance des sous-types hNa$_V$1.7 (en rouge), hNa$_V$1.2 (en vert) et hNa$_V$1.6 (en bleu). Courbes d'inactivation stationnaire (cercles) et de conductance (carrés) en fonction du potentiel de membrane, avant (symboles noirs) et après (symboles rouges, verts et bleus) exposition des cellules HEK à soit 5 ng/µL (en rouge) soit 23 ng/µL (en vert et en bleu) de chacune des 3 sous-fractions (G4-24-3, G4-24-4 et G4-24-5). Chaque valeur représente la moyenne ± ESM des données de 4 à 6 cellules, exprimée en pourcentage de l'amplitude maximale du courant à des valeurs fortement négatives de pré-potentiel ou de la conductance maximale calculée à des valeurs fortement positives de potentiel-test. Les courbes théoriques correspondent aux ajustements des points de données avec les valeurs moyennes indiquées dans le Tableau 2-13.

Tableau 2-13. Effets des sous-fractions secondaires du venin de *Hottentotta gentili* sur les paramètres (moyenne ± ESM de 4-6 cellules) associés à la dépendance vis-à-vis du potentiel de l'inactivation stationnaire ($V_{P50\%}$[1] et k_h[2]) et de la conductance ($V_{T50\%}$[1] et k_g[2]) des sous-types hNa$_V$1.7, 1.2 et 1.6.

	$V_{P50\%}$ (mV)	k_h (mV^{-1})	$V_{T50\%}$ (mV)	k_g (mV^{-1})	$V_{P50\%}$ (mV)	k_h (mV^{-1})	$V_{T50\%}$ (mV)	k_g (mV^{-1})
	Contrôle				**G4-24-3**			
hNa$_V$1.7[3]	-67.1 ± 0.3	5.9 ± 0.2	-33.3 ± 0.3	3.6 ± 0.3	-64.0 ± 0.2	5.0 ± 0.2	-17.5 ± 0.3	6.6 ± 0.3
hNa$_V$1.2[4]	-51.1 ± 0.2	4.5 ± 0.1	-22.4 ± 0.3	4.3 ± 0.2	-60.2 ± 1.2	6.7 ± 1.1	-24.3 ± 0.2	6.7 ± 0.1
hNa$_V$1.6[4]	-65.4 ± 0.2	6.4 ± 0.2	-32.4 ± 0.3	2.5 ± 0.3	-70.1 ± 0.4	7.8 ± 0.4	-41.1 ± 0.4	3.5 ± 0.3
	Contrôle				**G4-24-4**			
hNa$_V$1.7[3]	-64.9 ± 0.3	4.8 ± 0.2	-32.1 ± 0.4	3.9 ± 0.3	-66.0 ± 0.3	5.8 ± 0.3	-36.2 ± 0.7	5.0 ± 0.6
hNa$_V$1.2[4]	-51.0 ± 0.2	4.8 ± 0.2	-20.9 ± 0.3	4.7 ± 0.2	-61.6 ± 1.6	7.2 ± 1.2	-35.3 ± 0.2	5.1 ± 0.2
hNa$_V$1.6[4]	-50.9 ± 0.2	4.3 ± 0.1	-20.4 ± 0.5	6.5 ± 0.4	-85.6 ± 0.7	9.8 ± 0.6	-54.2 ± 0.3	6.9 ± 0.3
	Contrôle				**G4-24-5**			
hNa$_V$1.7[3]	-57.0 ± 0.2	5.2 ± 0.1	-28.1 ± 0.3	5.1 ± 0.2	-61.4 ± 0.2	5.7 ± 0.2	-25.6 ± 0.5	8.5 ± 0.5
hNa$_V$1.2[4]	-58.0 ± 0.2	5.6 ± 0.1	-29.9 ± 0.2	5.4 ± 0.2	-68.8 ± 0.4	6.7 ± 0.3	-40.6 ± 0.2	5.0 ± 0.2
hNa$_V$1.6[4]	-56.0 ± 0.2	5.8 ± 0.2	-31.9 ± 0.4	5.5 ± 0.3	-75.0 ± 1.1	9.8 ± 1.1	-56.2 ± 0.5	7.7 ± 0.4

[1]$V_{P50\%}$ et $V_{T50\%}$: potentiel de membrane correspondant à une diminution de 50% de l'inactivation stationnaire et de la conductance, respectivement. [2]k_h et k_g: pentes des courbes de l'inactivation stationnaire et de la conductance en fonction du potentiel de membrane, respectivement. [3]5 ng/µL. [4]23 ng/µL.

La sous-fraction **G4-24-4** ne montre aucun effet détectable sur le sous-type hNa$_V$1.7 ce qui, à priori, la rend peu attractive pour poursuivre l'étude des 5 toxines qu'elle contient dans le cadre de la thématique de ma thèse. En revanche, les effets de cette sous-fraction, similaires sur les sous-types hNa$_V$1.2 et 1.6, consistent en une faible diminution des pics de courant associée à des déplacements négatifs des courbes "inactivation stationnaire-potentiel" et "conductance-potentiel", sans que les cinétiques d'activation et d'inactivation des courants ne soient altérées. Là encore, aucun de ces effets ne peut être relié à la présence d'une toxine α (en particulier la toxine LqhIII) ou β de scorpion dans la sous-fraction G4-24-3. Une possibilité est que les effets observés résultent d'une modification des charges de surface au niveau de l'environnement membranaire des sous-types de canaux, ce qui impliquerait que ces charges soient différentes entre, d'une part, le sous-type hNa$_V$1.7 et, d'autre part, les sous-types hNa$_V$1.2 et 1.6.

Les effets de la sous-fraction **G4-24-5** sur les sous-types hNa$_V$1.7, 1.2 et 1.6 sont qualitativement similaires à ceux de la sous-fraction G4-24-4 mais, quantitativement, environ 4 fois plus importants. Il est peu probable que ces effets soient ceux de la seule toxine présente dans ces deux sous-fractions et dont la masse est identique à celle de la toxine LqhIII (voir Benoit & Gordon, 2001).

2.5.2.5. Etude du venin du scorpion *Hottentotta jayakari* (H4-x)

Hottentotta jayakari est un scorpion endémique de la péninsule Arabique. En utilisant la plateforme automatisée QPatch HTX de "patch-clamp", nous avons réalisé un criblage secondaire de 3 sous-fractions du venin de ce scorpion sur des lignées cellulaires HEK-293 exprimant les sous-types hNa$_V$1.7, 1.2, 1.6 et 1.5 et enregistrées en configuration "cellule entière" et en mode "cellule multiple".

Bien que nous ayons observé une inhibition du sous-type hNa$_V$1.7 d'environ 45% par la fraction primaire H4-25 lors du criblage des fractions des 9 venins (voir Figure 2-6), les 3 sous-fractions dérivant de cette fraction ne montrent aucun effet notable sur les sous-types hNa$_V$1.2, 1.5, 1.6 et 1.7 étudiés (Figure 2-13). Le fait que l'activité d'origine n'ait pas été retrouvée lors du criblage secondaire est probablement dû à une quantité insuffisante de produit(s) bioactif(s) dans les sous-fractions, ce qui implique soit une perte de ce(s) produit(s) lors du sous-fractionnement, soit une dispersion entre plusieurs sous-fractions. L'identification des toxines présentes dans les 3 sous-fractions, par leur masse, pourrait confirmer ou infirmer cette hypothèse.

2.5.3. Conclusion

Le criblage primaire à haut débit de la banque de 9 venins originaux appartenant à SANOFI a

permis de mettre en évidence des fractions intéressantes provenant des venins de deux espèces d'araignées (*Selenotypus plumipes* et *Phoneyusa celerieri*) et de deux espèces de scorpions (*Hottentota gentili* et *Hottentota jayakari*), venins qui n'avaient jamais, ou très peu, été étudiés jusqu'à présent. Le criblage secondaire des sous-fractions de ces venins a conduit à l'identification d'un certain nombre de toxines d'intérêt dans des sous-fractions de *Selenotypus plumipes*, *Phoneyusa celerieri* et *Hottentota gentili* mais, malheureusement, pas dans celles d'*Hottentota jayakari*.

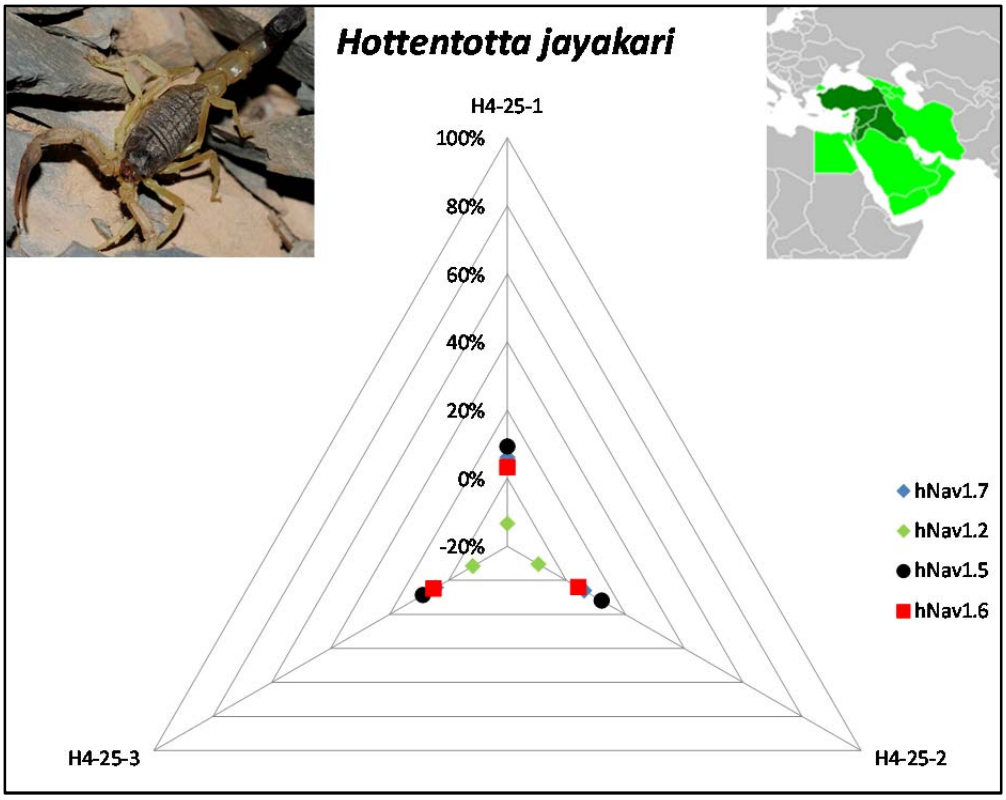

Figure 2-13. Criblage des sous-fractions du venin de *Hottentotta jayakari*. Pourcentage d'inhibition du pic de courant hNa$_V$1.7 (carrés rouges), suite à l'application de 5 ng/µL de chacune des 3 sous-fractions secondaires, et des pics de courants hNa$_V$1.5 (ronds noirs), hNa$_V$1.2 (losanges verts) et hNa$_V$1.6 (triangles bleus), suite à l'application de 23 ng/µL de ces mêmes sous-fractions.

Sur les 5 toxines séquencées de l'araignée *Selenotypus plumipes*, 3 étaient déjà décrites dans la littérature [**A5-19-2-1** = JzTx-8.2 (Chen et al., 2008), **A5-20-3-2** = OAIP-5 (Wong et al., 2013) et **A5-20-5-1** = K22N-OAIP-5]. Bien que leurs cibles moléculaires ne soient toujours pas identifiées à ce jour, nos résultats montrent qu'il est peu probable que les sous-types de canaux Na$_V$ étudiés soient impliqués. Les 2 autres toxines séquencées, l'**A5-20-4-1** et l'**A5-22-5-2**, non rapportées dans la littérature, présentent cependant 79% d'identité de séquence avec l'OAIP-2 (Hardy et al., 2013; Wong et al., 2013) et 73% d'identité de séquence avec la β-théraphotoxine-Pmr1a décrite pour bloquer les sous-types Na$_V$1.3 et 1.8 à des concentrations micromolaires (Meir et al., 2012),

respectivement. Les résultats obtenus avec l'A5-20-4-1 sont difficilement interprétables de par la grande différence de puissance entre les deux produits de synthèse, obtenus à partir de ce peptide naturel, pour les sous-types de canaux Na_V TTX-S étudiés. En revanche, ceux des effets de l'A5-22-5-2 suggèrent fortement que les 3 produits de synthèse issus de ce peptide naturel interagissent préférentiellement avec les sous-types de canaux Na_V TTX-S étudiés, à des concentrations de plusieurs dizaines/centaines de nanomolaires mais avec des sélectivités assez limitées.

La seule toxine séquencée de l'araignée *Phoneyusa celerieri* (la **B5-19-10-1**) correspond, avec un résidu glycine (G) en plus en N-terminal et un résidu asparagine (N) au lieu d'un résidu aspartate (D) pour l'acide aminé suivant, au peptide Hs1a d'une araignée du genre *Hysterocrates* déposé dans la PDB comme inhibiteur du sous-type $Na_V1.7$ (DOI: 10.2210/pdb2MT7/pdb). Nos résultats non seulement confirment cette interaction mais suggèrent également et fortement l'implication des sous-types $Na_V1.2$ et 1.6 TTX-S mais pas celle du sous-type $Na_V1.5$ TTX-R.

L'interprétation des résultats des effets des sous-fractions secondaires du venin de *Hottentotta gentili* est être d'autant plus complexe et les conclusions d'autant moins fiables qu'aucune des toxines n'apparaissait comme étant majoritaire dans ces sous-fractions, à l'exception de la sous-fraction **G4-24-3** qui ne contenait qu'une seule toxine de 6938,99 Da. Il ne semble cependant pas très intéressant de poursuivre l'étude de cette toxine, tout comme celle des 5 toxines présentes dans la sous-fraction **G4-24-4**, au vu des effets non originaux et peu sélectifs de ces sous-fractions sur les 3 sous-types de canaux Na_V étudiés. En revanche, les déplacements négatifs importants (d'environ 30 mV) des courbes "inactivation stationnaire-potentiel" et "conductance-potentiel" produits par la sous-fraction **G4-24-5** sur les sous-types $hNa_V1.2$ et 1.6 sont des effets peu courants qui justifieraient de poursuivre l'étude des 3 toxines contenues dans cette sous-fraction. Ils pourraient résulter de l'action combinée d'une ou plusieurs toxines α et β ou montrant des caractéristiques fonctionnelles mixtes α/β, comme cela l'a déjà été rapporté pour certaines toxines de scorpion telles que la toxine CssII du scorpion *Centruroides suffusus suffusus* (Saucedo et al., 2012).

En conclusion, il apparait que notre objectif initial de mettre en évidence des toxines interagissant spécifiquement avec le sous-type $hNa_V1.7$, 1.2 ou 1.6, en criblant la banque de 9 venins originaux appartenant à SANOFI, n'ait pas été atteint. Cependant, nous avons obtenu des informations intéressantes sur les cibles de certaines des toxines étudiées (en particulier celles des venins des deux araignées) et/ou sur leur mécanisme d'action (en particulier celui des toxines du venin de *Hottentotta gentili*) qui mériteraient d'être consolidées par des études approfondies.

Partie 3

CONCLUSION et PERSPECTIVES

Les objectifs de cette thèse étaient, au début, *(i)* de mettre en évidence et de caractériser, par une approche pharmacologique multi-échelle (de la cellule individuelle à l'organisme *in vivo*) de nouvelles toxines à potentiel analgésique agissant principalement sur le sous-type $Na_V1.7$ de canal sodium, et aussi *(ii)* d'étudier les limites éventuelles d'utilisation de celles-ci dues à l'apparition d'effets secondaires principalement au niveau du système neuromusculaire. Parallèlement à ces études, la puissance et le profil de sélectivité d'une toxine déjà connue pour son action intéressante en synergie avec de faibles doses d'opioïdes ont été caractérisés. D'autre part, de façon inattendue, nous avons mis en évidence une toxine ayant un profil de sélectivité différent de celui des toxines analgésiques et qui pourrait être utilisée comme outil moléculaire pour étudier les canaux Ca_V de type L au niveau cardiovasculaire. Finalement, un criblage de la banque de venins appartenant à SANOFI a été initié dans l'espoir de trouver des toxines ayant un profil de sélectivité original.

3.1. Profils de sélectivité et applications potentielles des 4 toxines étudiées

Les effets des 4 toxines synthétiques étudiées vis-à-vis des lignées cellulaires exprimant la sous-unité α humaine de $Na_V1.7$ ont été déterminés par des méthodes électrophysiologiques de "patch-clamp" automatique et manuel. Les résultats obtenus mettent en évidence les puissances suivantes (par ordre décroissant): HwTx-IV > CyrTx-1a > PecTx-1a > PhlTx-1a. L'évaluation des effets de ces 4 toxines sur des lignées cellulaires exprimant des sous-types de canaux Na_V, autres que $hNa_V1.7$, révèlent que l'HwTx-IV et la CyrTx-1a inhibent également la sous-unité α humaine de $Na_V1.6$ (qui a 69% d'identité de séquence avec celle de $hNa_V1.7$) avec une puissance environ 5 à 10 fois moindre mais qui est cependant suffisante pour être à l'origine d'effets secondaires indésirables en cas de développement thérapeutique de ces 2 toxines (paralysie musculaire pouvant provoquer la mort par détresse respiratoire). L'évaluation des effets des toxines synthétiques au niveau de systèmes natifs a porté *(i)* sur des cultures primaires de neurones de DRG de souris adultes, premier relais du message douloureux (étude préalable à l'évaluation du niveau de douleur chez la souris par des tests comportementaux), et *(ii)* sur le système neuromusculaire de souris adultes, *ex vivo* et *in vivo*, ce qui a permis, en particulier, d'étudier leurs effets indésirables éventuels sur les sous-types Nav1.6 et 1.4 de canaux sodium.

Les résultats obtenus avec l'HwTx-IV et la CyrTx-1a montrent que ces 2 toxines inhibent, avec une forte puissance, le courant sodium TTX-S des neurones de DRG ($Na_V1.1$, 1.2, 1.3, 1.6 et 1.7) et, avec une moindre puissance, celui TTX-R ($Na_V1.8$ et 1.9). Ces deux toxines inhibent aussi, avec une

forte puissance, la contraction et le potentiel d'action composé enregistrés, respectivement *ex vivo* et *in vivo*, au niveau du muscle suite à la stimulation du nerf (le sous-type $Na_V1.6$ étant principalement exprimé au niveau du nerf), la CyrTx-1a offrant une plus grande marge de sécurité. Par conséquent, les potentialités d'exploitation en tant qu'antalgique/analgésique de l'HwTx-IV et de la CyrTx-1a ne semblent pas optimales mais, en revanche, ces toxines peuvent être envisagées comme outils pour disséquer pharmacologiquement les sous-types $Na_V1.4$ et $Na_V1.6$ *versus* $Na_V1.7$ de canaux sodium. Des études de "structure-activité", utilisant des techniques d'ingénierie, seraient nécessaires pour obtenir des analogues synthétiques de ces toxines ayant un meilleur profil de sélectivité vis-à-vis des différents sous-types de canaux Na_V.

Il est à noter que de grandes campagnes de mutagénèse des toxines les plus intéressantes ont été menées par quelques sociétés pharmaceutiques dans le monde. Par exemple, la société Astra Zeneca, suite à des stratégies "alanine scanning" et de mutations ponctuelles, a obtenu une toxine triplement mutée, la m3-HwTx-IV, qui présente la même sélectivité sur les Na_V que l'HwTx-IV mais avec une puissance accrue pour le sous-type $Na_V1.7$ (Revell et al., 2013; Rahnama et al., 2017). La société Amgen, quant à elle, a créé une centaine d'analogues peptidiques synthétiques à partir de la GpTx-1, en utilisant l'analogie par balayage positionnel multi-attributs (MAPS pour "Multi Attribute Positional Scan analoging") qui ont été analysés sur 3 sous-types de canaux sodium (Murray et al., 2015b, Murray et al., 2016). Cette approche consiste à remplacer chaque acide aminé non-cystéine par un des acides aminés suivants: A, W, 1-Nal (l'encombrement et l'hydrophobicité étant croissants), E (acide aminé acide), R et K (acides aminés basiques). Elle permet de cibler rapidement les acides aminés importants pour la liaison de la molécule au canal sodium ou encore d'identifier les analogues qui présentent une puissance augmentée. La combinaison de plusieurs d'entre eux a permis l'obtention d'un quadruple mutant agissant à une concentration de l'ordre du nanomolaire et avec une sélectivité *versus* les sous-types cardiaque et du muscle squelettique supérieure d'un facteur 1000. De plus, ces toxines mutées possèdent des propriétés antinociceptives non associées à des effets secondaires sur la locomotion mais qui sont dépendantes de l'activation des voies de signalisation des opioïdes (Murray et al., 2016; Chen et al. 2018).

La société Janssen a remplacé chacun des 24 acides aminés de la ProTx-II par tous les acides aminés excepté la cystéine et la méthionine, leur combinaison ayant finalement conduit à la JNJ-63955918 ayant une puissance et une sélectivité améliorées par rapport à la toxine naturelle. Bien que les analogues améliorés de l'HwTx-IV et de la GpTx-1 présentent une faible sélectivité envers les sous-types Na_V TTX-S, celle de la JNJ-63955918 est importante même comparée à la ProTx-II naturelle, ce qui laisse présager une plus large fenêtre thérapeutique évitant les effets locomoteurs.

Parallèlement à l'optimisation par la création d'analogues peptidiques synthétiques, des dimères de GpTx-1, des conjugués peptide-anticorps ainsi que des anticorps monoclonaux, dont le Svmab1, ont été créés mais leur apport au développement de la thématique reste mitigé, voire controversé (Lee et al., 2014; Murray et al., 2015a; Liu et al., 2016; Biswas et al., 2017).

Les profils de sélectivité de la PecTx-1a et de la PhlTx-1 sont différents des deux premières toxines puisqu'ils ne mettent pas en évidence de sélectivité particulière vis-à-vis d'un sous-type donné de canal Na_V. La PhlTx-1, montrant une faible sélectivité et une puissance moyenne (active à une concentration de l'ordre de la centaine de nanomolaires) pour les canaux Na_V à l'exception du sous-type $Na_V1.8$, est une toxine déjà connue pour ses effets analgésiques indéniables. En particulier, elle agit en synergie avec les opioïdes avec des quantités de toxine et d'opioïdes diminuées par rapport à celles nécessaires lors de l'utilisation de l'une de ces molécules seule. Nous avons observé *in vivo*, chez un modèle murin de douleur, que la PhlTx-1 (300 nM) diminue d'un facteur 2 les comportements douloureux des souris produits par l'OD1. Il serait intéressant d'étudier de plus fortes doses de PhlTx-1 afin de vérifier si ces effets antalgiques dépendent de la dose injectée et s'ils sont éventuellement associés à des effets secondaires non désirés. L'analogue D7A de cette même toxine, obtenu par une approche "alanine scanning", possède une puissance améliorée d'un facteur 4 pour la cible d'intérêt. Il reste à déterminer s'il faudrait une quantité moindre de cet analogue pour produire les mêmes effets analgésiques que la molécule d'origine. Cependant, et bien que les souris ne présentaient pas de signes évoquant l'apparition d'effets secondaires neuromusculaires sur les images vidéo enregistrées lors de cette étude, il serait nécessaire d'évaluer en détail certains paramètres, tels que la force musculaire et ceux liés à la locomotion des souris injectées avec la PhlTx-1 ou son analogue D7A, en mettant en place un test rotarod pour les quantifier.

Quant à la PecTx-1a, elle a un profil de sélectivité particulier et intéressant qui nécessiterait une exploration approfondie des effets de cette toxine sur la fonction cardiaque par des expériences *in vitro* et *in vivo*. En effet, la PecTx-1a a pour cible principale le sous-type $Ca_V1.2$ de canal calcium avec lequel elle interagit avec une grande puissance et une sélectivité importante vis-à-vis des sous-types Na_V, K_V, Kir et des autres sous-types de canaux Ca_V. Nous avons aussi évalué les effets de cette toxine (100 nM) sur des cardiomyocytes dérivés de cellules souches pluripotentes humaines et avons observé qu'elle inhibait 40% du courant calcium de type L ($hCa_V1.1$, 1.2 et 1.3), contrairement à la nifédipine (10 µM) qui inhibait 100% de ce type de courant. Compte tenu du fait que 100 nM de PecTx-1a bloque complètement le sous-type $hCa_V1.2$ exprimé dans les cellules CHO, ces résultats suggèrent fortement que la PecTx-1a est moins efficace pour interagir avec les sous-types $hCa_V1.1$ et/ou 1.3. Afin de confirmer ce dernier point, des expériences seraient nécessaires pour étudier les

effets du peptide *(i)* sur des tissus musculaires squelettiques qui n'expriment que le sous-type $Ca_V1.1$, pour une première approche de la sélectivité $Ca_V1.2$ *versus* $Ca_V1.1$, et *(ii)* sur des lignées recombinantes surexprimant les sous-types $Ca_V1.1$, 1.3 ou 1.4 (ces lignées n'étant pas accessibles commercialement, leur fabrication devra être envisagée). La PecTx-1a constitue par conséquent un outil précieux qui, modifié par un tag, permettrait le suivi du sous-type $Ca_V1.2$ et ainsi l'étude de sa fonction et de sa localisation au niveau cellulaire. De plus, le sous-type $Ca_V1.2$ étant responsable du "plateau" du potentiel d'action cardiaque, la PecTx-1a pourrait être également utilisée comme traitement de certaines cardiomyopathies comme le syndrome du QT long. Cependant, et au préalable, des expériences seraient nécessaires au niveau de systèmes natifs tels que *(i)* les fibres de Purkinje cardiaques de lapin, dont le potentiel d'action est particulièrement sensible pour déceler des effets transposables à l'homme, *(ii)* les cœurs isolés de lapin afin d'évaluer les effets du peptide sur un organe dont les fonctions mécaniques sont préservées, et *(iii)* des cardiomyocytes humains prélevés sur des cadavres.

3.2. Limites et avantages d'un criblage à haut débit d'une banque contenant une quantité importante de venins

Les deux collections de venins de chez Smartox et de SANOFI ont permis de mettre en évidence un nombre de hits très importants *versus* $hNa_V1.7$ et d'espèces variées (scorpions, araignée, serpents…). Ceci étant, les principaux hits étaient extraits de venins d'araignées. Ceci est loin d'être surprenant puisque les 20 toxines décrites dans la littérature pour cibler $hNa_V1.7$ avec un potentiel thérapeutique antalgique sont des petites toxines d'une trentaine d'acides aminés structurés autour d'un motif ICK de 3 ponts disulfures, très compactes et ayant une résistance physico-chimique élevée. Cependant, les profils de sélectivité de nombreuses toxines synthétiques obtenus après le criblage des banques de venins appartenant à Smartox et à SANOFI, comme par exemple l'A5-22-5-2 et la B5-19-10-1, ne sont pas assez discriminants pour envisager de continuer la caractérisation pharmacologique de ces toxines.

Il serait peut-être plus judicieux de réaliser le criblage primaire des banques sur une autre cible antinociceptive telle que $Na_V1.8$ ou $Na_V1.9$ dont les sites de liaison potentiels sont très différents de ceux des sous-types Na_V TTX-S. En effet, ces deux sous-types, comme le sous-type $Na_V1.7$, sont préférentiellement exprimés au niveau des petits neurones sensoriels de DRG non myélinisés de rat et jouent un rôle majeur dans la genèse et/ou la propagation du potentiel d'action, ainsi que dans sa rythmicité (Rush et al., 2007; Ho & O'Leary, 2011; Deuis et al., 2016a; Dick et al., 2016).

L'optimisation des "hits" par ingénierie protéique ainsi que leur caractérisation pharmacologique sur un plus large éventail de sous-types de canaux ioniques (Na_V, K_V et Ca_V) pourraient être beaucoup plus prometteur que la réduction de l'étude à une seule famille de canaux ioniques. L'idée, derrière ces quelques lignes, est qu'il faudrait d'abord étudier les toxines par une approche pharmacologique, pour mieux les appréhender, puis, si un profil pharmacologique original en ressort, leur trouver par la suite une application thérapeutique voire même, dans le meilleur des cas, théranostique.

La sélection de "hits" parmi une banque importante de venins, guidée par des tests biologiques, peut être un frein à la découverte de toxines ayant des propriétés et des profils de sélectivité qui nous intéressent. En effet, leur quantité dans le venin criblé est souvent insuffisante pour générer une inhibition importante de la fonction de la cible d'intérêt lors du criblage primaire réalisé, dans la plupart des cas, à une dose unique. Pour les venins n'ayant pas conduit à l'identification de fractions actives, une analyse des données pharmacologiques brutes autres que le simple pourcentage d'inhibition devrait être systématique, comme, par exemple, celui du scorpion *Hottentota jakayari*. En effet, dans ce cas-là, on peut supposer que les quantités de peptides bioactifs soient faibles, ce qui conduit à une inhibition limitée de la cible. Ainsi, le pourcentage d'inhibition en présence de 0,5 µg/µL de fractions et/ou sous-fractions ne devrait pas toujours être conservé comme seul critère pour la sélection des venins dans le cadre d'une recherche plus approfondie, on devrait aussi s'intéresser aux altérations biophysiques sur les cibles étudiées que peuvent provoquer certaines de ces fractions et/ou sous-fractions sans induire un pourcentage d'inhibition très élevé.

La biodiversité des venins d'animaux étant importante, l'exploration exhaustive de celle-ci est donc un élément majeur pour la découverte de différentes familles pouvant moduler la cible d'intérêt avec une activité similaire (soit, dans notre cas, l'inhibition du sous-type $hNa_V1.7$). Les toxines trouvées peuvent donc être originales par leur provenance (venins de scorpions, d'araignées, de cônes, de centipèdes…), leur séquence (diversité parmi les toxines d'araignée) et leur activité (inhibiteurs de pore et/ou modulateurs des propriétés fonctionnelles du pore).

Par conséquent, une fois qu'un "hit" a été identifié, il est souvent utile d'explorer davantage les espèces animales de la même lignée phylogénétique. En effet, des peptides ayant des séquences similaires peuvent avoir des profils pharmacologiques différents et donc des puissances différentes pour une cible d'intérêt. En tirant parti de la sélection naturelle, il est bien établi que la diversification génétique a conduit à une grande diversité de toxines de venins, à partir de quelques échafaudages moléculaires judicieusement choisis. En effet, des isoformes d'une toxine donnée sont présentes non seulement dans le même venin, mais également dans les venins d'espèces apparentées. Il faut se rappeler que l'évolution a choisi ces peptides pour leur activité biologique et que la mutagenèse qui

s'est naturellement produite a donné lieu à la conservation d'un ensemble limité de formes peptidiques actives (Fry et al., 2009).

L'analyse des propriétés pharmacologiques des isoformes de toxines, combinée à la création d'une banque de variants grâce une approche de type "MAPS" par synthèse chimique ou par "phage display", peut aider à orienter l'ingénierie future des peptides. Par ailleurs, une alternative au criblage bioguidé peut être envisagée en faisant appel à des études transcriptomiques et protéomiques des venins, permettant ainsi de constituer une banque de séquences de toxines qu'il faudra alors produire par voie chimique ou recombinante (Figure 3-1). Cette stratégie a été mise en œuvre dans le cadre du projet européen "Venomics" et a conduit à l'obtention d'une banque synthétique de plusieurs milliers de toxines (Gilles & Servent, 2014).

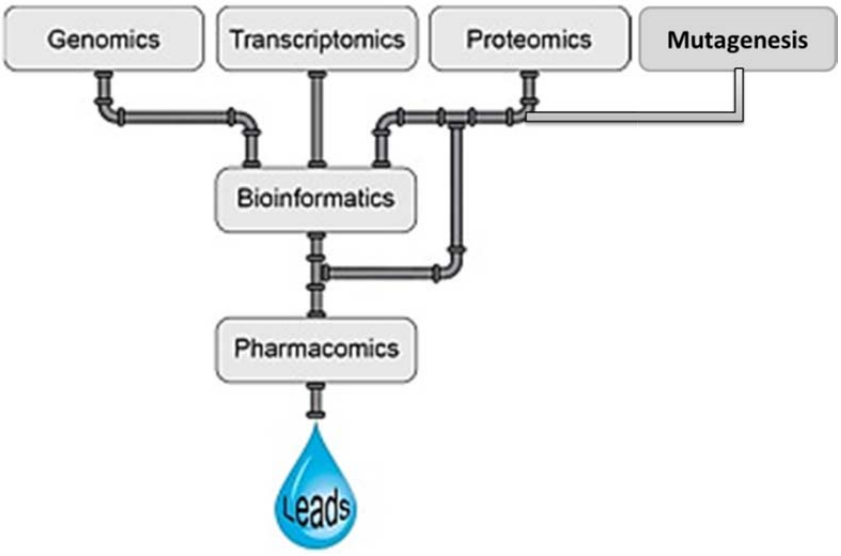

Figure 3-1. Représentation schématique du projet "Venomics" dans la découverte de pistes thérapeutiques à base de venin. Adapté de Wilson et Daly (2018).

La synthèse par voie chimique ou recombinante de ces "hits" présente aussi un frein au choix d'un criblage bioguidé de ces venins. En effet, les toxines synthétiques ont parfois une perte de puissance si on les compare aux toxines naturelles ou encore certaines ne sont pas synthétisables (Yang et al., 2013; Wang et al., 2017a). Cela peut éventuellement s'expliquer par un repliement différent de la structure 3D des molécules ou par des modifications post-traductionnelles non présentes sur les toxines synthétiques (Wright et al., 2017).

Finalement, au vue du nombre important de "hits" obtenus, le criblage bioguidé permet l'identification de nombreuses toxines ayant un profil de sélectivité pharmacologique intéressant, telles que la CyrTx-1a et la PecTx-1a.

Liste des illustrations

Partie 1 – Introduction

Partie 2 – Résultats et Discussion

Partie 3 – Conclusion et Perspectives

Références bibliographiques

Ahern, C.A., Payandeh, J., Bosmans, F., & Chanda, B. (2016). The hitchhiker's guide to the voltage-gated sodium channel galaxy. *J Gen Physiol* 147, 1-24.

Ahuja, S., Mukund, S., Deng, L., Khakh, K., Chang, E., Ho, H., Shriver, S., Young, C., Lin, S., Johnson, J.P., Jr., Wu, P., Li, J., Coons, M., Tam, C., Brillantes, B., Sampang, H., Mortara, K., Bowman, K.K., Clark, K.R., Estevez, A., Xie, Z., Verschoof, H., Grimwood, M., Dehnhardt, C., Andrez, J.C., Focken, T., Sutherlin, D.P., Safina, B.S., Starovasnik, M.A., Ortwine, D.F., Franke, Y., Cohen, C.J., Hackos, D.H., Koth, C.M., & Payandeh, J. (2015). Structural basis of Nav1.7 inhibition by an isoform-selective small-molecule antagonist. *Science* 350, aac5464.

Alexander, S.P., Striessnig, J., Kelly, E., Marrion, N.V., Peters, J.A., Faccenda, E., Harding, S.D., Pawson, A.J., Sharman, J.L., Southan, C., Davies, J.A., & Collaborators, C. (2017). THE CONCISE GUIDE TO PHARMACOLOGY 2017/18: Voltage-gated ion channels. *Br J Pharmacol* 174 Suppl 1, S160-S194.

Bahring, R., Dannenberg, J., Peters, H.C., Leicher, T., Pongs, O., & Isbrandt, D. (2001). Conserved Kv4 N-terminal domain critical for effects of Kv channel-interacting protein 2.2 on channel expression & gating. *J Biol Chem* 276, 23888-23894.

Barbosa, C., Tan, Z.Y., Wang, R., Xie, W., Strong, J.A., Patel, R.R., Vasko, M.R., Zhang, J.M., & Cummins, T.R. (2015). Navbeta4 regulates fast resurgent sodium currents and excitability in sensory neurons. *Mol Pain* 11, 60.

Bennett, D.L., & Woods, C.G. (2014). Painful and painless channelopathies. *Lancet Neurol* 13, 587-599.

Benoit, E., & Gordon, D. (2001). The scorpion alpha-like toxin Lqh III specifically alters sodium channel inactivation in frog myelinated axons. *Neuroscience* 104, 551-559.

Bertrand, D., Biton, B., Licher, T., Chambard, J.M., Lanneau, C., Partiseti, M., & Lefevre, I.A. (2016). Functional Studies of Sodium Channels: From Target to Compound Identification. *Curr Protoc Pharmacol* 75, 9 21 21-29 21 35.

Biswas, K., Nixey, T.E., Murray, J.K., Falsey, J.R., Yin, L., Liu, H., Gingras, J., Hall, B.E., Herberich, B., Holder, J.R., Li, H., Ligutti, J., Lin, M.J., Liu, D., Soriano, B.D., Soto, M., Tran, L., Tegley, C.M., Zou, A., Gunasekaran, K., Moyer, B.D., Doherty, L., & Miranda, L.P. (2017). Engineering Antibody Reactivity for Efficient Derivatization to Generate NaV1.7 Inhibitory GpTx-1 Peptide-Antibody Conjugates. *ACS Chem Biol* 12, 2427-2435.

Black, J.A., Cummins, T.R., Plumpton, C., Chen, Y.H., Hormuzdiar, W., Clare, J.J., & Waxman, S.G. (1999). Upregulation of a silent sodium channel after peripheral, but not central, nerve injury in DRG neurons. *J Neurophysiol* 82, 2776-2785.

Black, J.A., & Waxman, S.G. (2013). Noncanonical roles of voltage-gated sodium channels. *Neuron* 80, 280-291.

Bladen, C., Hamid, J., Souza, I.A., & Zamponi, G.W. (2014). Block of T-type calcium channels by protoxins I and II. *Mol Brain* 7, 36.

Bosmans, F., Escoubas, P., Diochot, S., Mebs, D., Craik, D., Hill, J., Nakajima, T., Lazdunski M., & Tytgat, J. (2005). Isolation and characterization of Phlotoxin 1 (PhlTx1), a novel peptide active on voltage-gated sodium channels. Dans: 13èmes Rencontres en Toxinologie "Toxines et douleur" organisées par la Société Française pour l'Etude des Toxines, Paris, 1 et 2 décembre 2005. *Recueil des abstracts*, p. 12.

Boucher, T.J., Okuse, K., Bennett, D.L., Munson, J.B., Wood, J.N., & Mcmahon, S.B. (2000). Potent analgesic effects of GDNF in neuropathic pain states. *Science* 290, 124-127.

Bouhassira, D., Lanteri-Minet, M., Attal, N., Laurent, B., & Touboul, C. (2008). Prevalence of chronic pain with neuropathic characteristics in the general population. *Pain* 136, 380-387.

Bourdin, B., Shakeri, B., Tetreault, M.P., Sauve, R., Lesage, S., & Parent, L. (2015). Functional characterization of CaValpha2delta mutations associated with sudden cardiac death. *J Biol Chem* 290, 2854-2869.

Bourdain, F., & Fontaine, B. (2005). [Voltage-gating ionic channels and neuromuscular disorders]. *EMC-Neurologie* 2, 403-429.

Brackenbury, W.J. & Isom L.L. (2011). Na Channel β Subunits: Overachievers of the Ion Channel Family. *Front Pharmacol.* 28;2:53.

Brackenbury, W.J. (2012). Voltage-gated sodium channels and metastatic disease. *Channels (Austin)* 6, 352-361.

Bressan, E., Touska, F., Vetter, I., Kistner, K., Kichko, T.I., Teixeira, N.B., Picolo, G., Cury, Y., Lewis, R.J., Fischer, M.J., Zimmermann, K., & Reeh, P.W. (2016). Crotalphine desensitizes TRPA1 ion channels to alleviate inflammatory hyperalgesia. *Pain* 157, 2504-2516.

Bridges, D., Thompson, S.W., & Rice, A.S. (2001). Mechanisms of neuropathic pain. *Br J Anaesth* 87, 12-26.

Callaghan, B., Haythornthwaite, A., Berecki, G., Clark, R.J., Craik, D.J., & Adams, D.J. (2008). Analgesic alpha-conotoxins Vc1.1 and Rg1A inhibit N-type calcium channels in rat sensory neurons via GABAB receptor activation. *J Neurosci* 28, 10943-10951.

Cardoso, F.C., Dekan, Z., Smith, J.J., Deuis, J.R., Vetter, I., Herzig, V., Alewood, P.F., King, G.F., & Lewis, R.J. (2017). Modulatory features of the novel spider toxin mu-TRTX-Df1a isolated from the venom of the spider Davus fasciatus. *Br. J. Pharmacol.* 174, 2528-2544.

Cardoso, F.C., & Lewis, R.J. (2018). Sodium channels and pain: from toxins to therapies. *Br J Pharmacol* 175, 2138-2157.

Catterall, W.A. (2011). Voltage-gated calcium channels. *Cold Spring Harb Perspect Biol* 3, a003947.

Catterall, W.A. (2012). "Sodium Channel Mutations and Epilepsy," in *Jasper's Basic Mechanisms of the Epilepsies,* eds. Th, J.L. Noebels, M. Avoli, M.A. Rogawski, R.W. Olsen & A.V. Delgado-Escueta. (Bethesda (MD)).

Catterall, W.A., Cestele, S., Yarov-Yarovoy, V., Yu, F.H., Konoki, K., & Scheuer, T. (2007). Voltage-gated ion channels and gating modifier toxins. *Toxicon* 49, 124-141.

Catterall, W.A., Goldin, A.L., & Waxman, S.G. (2005a). International Union of Pharmacology. XLVII. Nomenclature and structure-function relationships of voltage-gated sodium channels. *Pharmacol Rev* 57, 397-409.

Catterall, W.A., Perez-Reyes, E., Snutch, T.P., & Striessnig, J. (2005b). International Union of Pharmacology. XLVIII. Nomenclature and structure-function relationships of voltage-gated calcium channels. *Pharmacol Rev* 57, 411-425.

Catterall, W.A., & Swanson, T.M. (2015). Structural Basis for Pharmacology of Voltage-Gated Sodium and Calcium Channels. *Mol Pharmacol* 88, 141-150.

Catterall, W.A., Wisedchaisri, G., & Zheng, N. (2017). The chemical basis for electrical signaling. *Nat Chem Biol* 13, 455-463.

Cerles, O., Benoit, E., Chéreau, C., Chouzenoux, S., Morin, F., Guillaumot, M.A., Coriat, R., Kavian, N., Loussier, T., Santulli, P., Marcellin, L., Saidu, N.E., Weill, B., Batteux, F., & Nicco, C. (2017) Niclosamide Inhibits Oxaliplatin Neurotoxicity while Improving Colorectal Cancer Therapeutic Response. *Mol Cancer Ther* 16, 300-311.

Cestele, S., Qu, Y., Rogers, J.C., Rochat, H., Scheuer, T., & Catterall, W.A. (1998). Voltage sensor-trapping: enhanced activation of sodium channels by beta-scorpion toxin bound to the S3-S4 loop in domain II. *Neuron* 21, 919-931.

Chai, Z., Wang, C., Huang, R., Wang, Y., Zhang, X., Wu, Q., Wang, Y., Wu, X., Zheng, L., Zhang, C., Guo, W., Xiong, W., Ding, J., Zhu, F., & Zhou, Z. (2017). CaV2.2 Gates Calcium-Independent but Voltage-Dependent Secretion in Mammalian Sensory Neurons. *Neuron* 96, 1317-1326 e1314.

Chambers, C., Witton, I., Adams, C., Marrington, L., & Kammonen, J. (2016). High-Throughput Screening of Na(V)1.7 Modulators Using a Giga-Seal Automated Patch Clamp Instrument. *Assay Drug Dev Technol* 14, 93-108.

Chen, C., Xu, B., Shi, X., Zhang, M., Zhang, Q., Zhang, T., Zhao, W., Zhang, R., Wang, Z., Li, N., & Fang, Q. (2018). GpTx-1 and [Ala(5) , Phe(6) , Leu(26) , Arg(28)]GpTx-1, two peptide NaV 1.7 inhibitors: analgesic and tolerance properties at the spinal level. *Br J Pharmacol* 175, 3911-3927.

Chen, J., Deng, M., He, Q., Meng, E., Jiang, L., Liao, Z., Rong, M., & Liang, S. (2008). Molecular diversity and evolution of cystine knot toxins of the tarantula Chilobrachys jingzhao. *Cell Mol Life Sci* 65, 2431-2444.

Coriat, R., Alexandre, J., Nicco, C., Quinquis, L., Benoit, E., Chéreau, C., Lemaréchal, H., Mir, O., Borderie, D., Tréluyer, J.M., Weill, B., Coste, J., Goldwasser, F., & Batteux, F. (2014) Treatment of oxaliplatin-induced peripheral neuropathy by intravenous mangafodipir. *J Clin Invest* 124, 262-272.

Crofford, L.J. (2015). Chronic Pain: Where the Body Meets the Brain. *Trans Am Clin Climatol Assoc* 126, 167-183.

Crumb, W.J., Jr., Vicente, J., Johannesen, L., & Strauss, D.G. (2016). An evaluation of 30 clinical drugs against the comprehensive in vitro proarrhythmia assay (CiPA) proposed ion channel panel. *J Pharmacol Toxicol Methods* 81, 251-262.

De Lera Ruiz, M., & Kraus, R.L. (2015). Voltage-Gated Sodium Channels: Structure, Function, Pharmacology, and Clinical Indications. *J Med Chem* 58, 7093-7118.

Deuis, J.R., Dekan, Z., Inserra, M.C., Lee, T.H., Aguilar, M.I., Craik, D.J., Lewis, R.J., Alewood, P.F., Mobli, M., Schroeder, C.I., Henriques, S.T., & Vetter, I. (2016a). Development of a muO-Conotoxin Analogue with Improved Lipid Membrane Interactions and Potency for the Analgesic Sodium Channel NaV1.8. *J Biol Chem* 291, 11829-11842.

Deuis, J.R., Dekan, Z., Wingerd, J.S., Smith, J.J., Munasinghe, N.R., Bhola, R.F., Imlach, W.L., Herzig, V., Armstrong, D.A., Rosengren, K.J., Bosmans, F., Waxman, S.G., Dib-Hajj, S.D., Escoubas, P., Minett, M.S., Christie, M.J., King, G.F., Alewood, P.F., Lewis, R.J., Wood, J.N., & Vetter, I. (2017). Pharmacological characterisation of the highly NaV1.7 selective spider venom peptide Pn3a. *Sci Rep* 7, 40883.

Deuis, J.R., Wingerd, J.S., Winter, Z., Durek, T., Dekan, Z., Sousa, S.R., Zimmermann, K., Hoffmann, T., Weidner, C., Nassar, M.A., Alewood, P.F., Lewis, R.J., & Vetter, I. (2016b). Analgesic Effects of GpTx-1, PF-04856264 and CNV1014802 in a Mouse Model of NaV1.7-Mediated Pain. *Toxins (Basel)* 8.

Dib-Hajj, S.D., Black, J.A., & Waxman, S.G. (2015). NaV1.9: a sodium channel linked to human pain. *Nat Rev Neurosci* 16, 511-519.

Dib-Hajj, S.D., Fjell, J., Cummins, T.R., Zheng, Z., Fried, K., Lamotte, R., Black, J.A., & Waxman, S.G. (1999). Plasticity of sodium channel expression in DRG neurons in the chronic constriction injury model of neuropathic pain. *Pain* 83, 591-600.

Dick, O.E., Krylov, B.V., & Nozdrachev, A.D. (2017). Possible mechanism of bursting suppression in nociceptive neurons. *Dokl Biochem Biophys* 473, 137-140.

Diochot, S., Baron, A., Salinas, M., Douguet, D., Scarzello, S., Dabert-Gay, A.S., Debayle, D., Friend, V., Alloui, A., Lazdunski, M., & Lingueglia, E. (2012). Black mamba venom peptides target acid-sensing ion channels to abolish pain. *Nature* 490, 552-555.

Dupoiron D, Bore F, Lefebvre-Kuntz D, Brenet O, Debourmont S, Dixmerias F, Buisset N, Lebrec N, & Monnin D. (2012) Pain Ziconotide adverse events in patients with cancer pain: a multicenter observational study of a slow titration, multidrug protocol. *Physician* 15, 395-403.

Dutertre S., Jin A.H., Vetter I., Hamilton B., Sunagar K., Lavergne V., Dutertre V., Fry B.G., Antunes A., Venter D.J., Alewood P.F., & Lewis R.J. (2014) Evolution of separate predation- and defence-evoked venoms in carnivorous cone snails. *Nature Communications* 5:3521.

Dutra, A.A., Sousa, L.O., Resende, R.R., Brandao, R.L., Kalapothakis, E., & Castro, I.M. (2008). Expression and characterization of LTx2, a neurotoxin from Lasiodora sp. effecting on calcium channels. *Peptides* 29, 1505-1513.

Emery, E.C., Luiz, A.P., & Wood, J.N. (2016). Nav1.7 and other voltage-gated sodium channels as drug targets for pain relief. *Expert Opin Ther Targets* 20, 975-983.

Escoubas, P., Bosmans, F., Cuypers, E., Diochot, S., Mebs, D., Craik, D., Hill, J., Nakajima, T., Lazdunski M., & Tytgat, J. (2006). Phlotoxin-1, a toxin from tarantula venom, is a potent modulator of $Na_V1.7$ sodium channels and a potential analgesic. In: 15^{th} World congress on Animal, plant & microbial toxins organized by the International Society on Toxinology, Glasgow, Scotland, 23-28 July 2006. *Abstract book*, p. 220.

Field, M.J., Cox, P.J., Stott, E., Melrose, H., Offord, J., Su, T.Z., Bramwell, S., Corradini, L., England, S., Winks, J., Kinloch, R.A., Hendrich, J., Dolphin, A.C., Webb, T., & Williams, D. (2006). Identification of the alpha2-delta-1 subunit of voltage-dependent calcium channels as a molecular target for pain mediating the analgesic actions of pregabalin. *Proc Natl Acad Sci U S A* 103, 17537-17542.

Flinspach, M., Xu, Q., Piekarz, A.D., Fellows, R., Hagan, R., Gibbs, A., Liu, Y., Neff, R.A., Freedman, J., Eckert, W.A., Zhou, M., Bonesteel, R., Pennington, M.W., Eddinger, K.A., Yaksh, T.L., Hunter, M., Swanson, R.V., & Wickenden, A.D. (2017). Insensitivity to pain induced by a potent selective closed-state Nav1.7 inhibitor. *Sci Rep* 7, 39662.

Francois, A., Laffray, S., Pizzoccaro, A., Eschalier, A., & Bourinet, E. (2014). T-type calcium channels in chronic pain: mouse models and specific blockers. *Pflugers Arch* 466, 707-717.

Fry, B.G., Roelants, K., Champagne, D.E., Scheib, H., Tyndall, J.D., King, G.F., Nevalainen, T.J., Norman, J.A., Lewis, R.J., Norton, R.S., Renjifo, C., & De La Vega, R.C. (2009). The toxicogenomic multiverse: convergent recruitment of proteins into animal venoms. *Annu Rev Genomics Hum Genet* 10, 483-511.

Gajewiak, J., Azam, L., Imperial, J., Walewska, A., Green, B.R., Bandyopadhyay, P.K., Raghuraman, S., Ueberheide, B., Bern, M., Zhou, H.M., Minassian, N.A., Hagan, R.H., Flinspach, M., Liu, Y., Bulaj, G., Wickenden, A.D., Olivera, B.M., Yoshikami, D., & Zhang, M.M. (2014). A disulfide tether stabilizes the block of sodium channels by the conotoxin muO section sign-GVIIJ. *Proc Natl Acad Sci U S A* 111, 2758-2763.

Gandini, M.A., Sandoval, A., & Felix, R. (2015). Toxins targeting voltage-activated Ca2+ channels and their potential biomedical applications. *Curr Top Med Chem* 15, 604-616.

Gilchrist, J., Olivera, B.M., & Bosmans, F. (2014). Animal toxins influence voltage-gated sodium channel function. *Handb Exp Pharmacol* 221, 203-229.

Gilles, N., & Servent, D. (2014). The European FP7 Venomics Project. *Future Med Chem* 6, 1611-1612.

Goldberg, D.S., & Mcgee, S.J. (2011). Pain as a global public health priority. *BMC Public Health* 11, 770.

Goldin, A.L. (2001). Resurgence of sodium channel research. *Annu Rev Physiol* 63, 871-894.

Gonçalves, T.C., Benoit, E., Partiseti, M., & Servent, D. (2018a). The NaV1.7 Channel Subtype as an Antinociceptive Target for Spider Toxins in Adult Dorsal Root Ganglia Neurons. *Front Pharmacol* 9, 1000.

Gonçalves, T.C., Boukaiba, R., Molgo, J., Amar, M., Partiseti, M., Servent, D., & Benoit, E. (2018b). Direct evidence for high affinity blockade of NaV1.6 channel subtype by huwentoxin-IV spider peptide, using multiscale functional approaches. *Neuropharmacology* 133, 404-414.

Hagen, N.A., Cantin, L., Constant, J., Haller, T., Blaise, G., Ong-Lam, M., Du Souich, P., Korz, W., & Lapointe, B. (2017). Tetrodotoxin for Moderate to Severe Cancer-Related Pain: A Multicentre, Randomized, Double-Blind, Placebo-Controlled, Parallel-Design Trial. *Pain Res Manag* 2017, 7212713.

Hamad, M.K., He, K., Abdulrazeq, H.F., Mustafa, A.M., Luceri, R., Kamal, N., Ali, M., Nakhla, J., Herzallah, M.M., & Mammis, A. (2018). Potential Uses of Isolated Toxin Peptides in Neuropathic Pain Relief: A Literature Review. *World Neurosurg* 113, 333-347 e335.

Harding, S.D., Sharman, J.L., Faccenda, E., Southan, C., Pawson, A.J., Ireland, S., Gray, A.J.G., Bruce, L., Alexander, S.P.H., Anderton, S., Bryant, C., Davenport, A.P., Doerig, C., Fabbro, D., Levi-Schaffer, F., Spedding, M., Davies, J.A., & Nc, I. (2018). The IUPHAR/BPS Guide to PHARMACOLOGY in 2018: updates and expansion to encompass the new guide to IMMUNOPHARMACOLOGY. Nucleic Acids Res 46, D1091-D1106.

Hardy, M.C., Daly, N.L., Mobli, M., Morales, R.A., & King, G.F. (2013). Isolation of an orally active insecticidal toxin from the venom of an Australian tarantula. *PLoS One* 8, e73136.

Hernandez-Plata, E., Ortiz, C.S., Marquina-Castillo, B., Medina-Martinez, I., Alfaro, A., Berumen, J., Rivera, M., & Gomora, J.C. (2012). Overexpression of NaV 1.6 channels is associated with the invasion capacity of human cervical cancer. *Int J Cancer* 130, 2013-2023.

Hiyama, T.Y., Watanabe, E., Ono, K., Inenaga, K., Tamkun, M.M., Yoshida, S., & Noda, M. (2002). Na(x) channel involved in CNS sodium-level sensing. *Nat Neurosci* 5, 511-512.

Ho, C., & O'leary, M.E. (2011). Single-cell analysis of sodium channel expression in dorsal root ganglion neurons. *Mol Cell Neurosci* 46, 159-166.

Ho, C., Zhao, J., Malinowski, S., Chahine, M., & O'leary, M.E. (2012). Differential expression of sodium channel beta subunits in dorsal root ganglion sensory neurons. *J Biol Chem* 287, 15044-15053.

Hopkins, A.L., & Groom, C.R. (2002). The druggable genome. Nat Rev Drug Discov 1, 727-730.

Huo, R., Sheng, Y., Guo, W.T., & Dong, D.L. (2014). The potential role of Kv4.3 K+ channel in heart hypertrophy. *Channels (Austin)* 8, 203-209.

Imbrici, P., Nicolotti, O., Leonetti, F., Conte, D., & Liantonio, A. (2018). Ion Channels in Drug Discovery and Safety Pharmacology. *Methods Mol Biol* 1800, 313-326.

Inserra, M.C., Israel, M.R., Caldwell, A., Castro, J., Deuis, J.R., Harrington, A.M., Keramidas, A., Garcia-Caraballo, S., Maddern, J., Erickson, A., Grundy, L., Rychkov, G.Y., Zimmermann, K., Lewis, R.J.,

Brierley, S.M., & Vetter, I. (2017). Multiple sodium channel isoforms mediate the pathological effects of Pacific ciguatoxin-1. *Sci Rep* 7, 42810.

Isensee, J., Krahé, L., Moeller, K., Pereira, V., Sexton, J.E., Sun, X., Emery, E., Wood, J.N., & Hucho, T. (2017) Synergistic regulation of serotonin and opioid signaling contributes to pain insensitivity in Nav1.7 knockout mice. *Sci Signal* 10(461).

Isom, L.L. (2001). Sodium channel beta subunits: anything but auxiliary. *Neuroscientist* 7, 42-54.

Israel, M.R., Tay, B., Deuis, J.R., & Vetter, I. (2017). Sodium Channels and Venom Peptide Pharmacology. *Adv Pharmacol* 79, 67-116.

Jami, S., Erickson, A., Brierley, S.M., & Vetter, I. (2017). Pain-Causing Venom Peptides: Insights into Sensory Neuron Pharmacology. *Toxins (Basel)* 10.

Jones, C.M., Mack, K.A., & Paulozzi, L.J. (2013). Pharmaceutical overdose deaths, United States, 2010. *JAMA* 309, 657-659.

Kalia, J., Milescu, M., Salvatierra, J., Wagner, J., Klint, J.K., King, G.F., Olivera, B.M., & Bosmans, F. (2015). From foe to friend: using animal toxins to investigate ion channel function. *J Mol Biol* 427, 158-175.

Kim, C.H., Oh, Y., Chung, J.M., & Chung, K. (2001). The changes in expression of three subtypes of TTX sensitive sodium channels in sensory neurons after spinal nerve ligation. *Brain Res Mol Brain Res* 95, 153-161.

King, G.F. (2011). Venoms as a platform for human drugs: translating toxins into therapeutics. *Expert Opin Biol Ther* 11, 1469-1484.

King, G.F., Gentz, M.C., Escoubas, P., & Nicholson, G.M. (2008). A rational nomenclature for naming peptide toxins from spiders and other venomous animals. *Toxicon* 52, 264-276.

Klint J.K., Smith J.J., Vetter I., Rupasinghe D.B., Er S.Y., Senff S., Herzig V., Mobli M., Lewis R.J., Bosmans F., & King G.F.(2015) Seven novel modulators of the analgesic target NaV 1.7 uncovered using a high-throughput venom-based discovery approach. *Br J Pharmacol.* 172, 2445–2458.

Klint, J.K., Berecki, G., Durek, T., Mobli, M., Knapp, O., King, G.F., Adams, D.J., Alewood, P.F., & Rash, L.D. (2014). Isolation, synthesis and characterization of omega-TRTX-Cc1a, a novel tarantula venom peptide that selectively targets L-type Cav channels. *Biochem Pharmacol* 89, 276-286.

Klint, J.K., Senff, S., Rupasinghe, D.B., Er, S.Y., Herzig, V., Nicholson, G.M., & King, G.F. (2012). Spider-venom peptides that target voltage-gated sodium channels: pharmacological tools and potential therapeutic leads. *Toxicon* 60, 478-491.

Koh, W.U., Choi, S.S., Lee, J.H., Lee, S.H., Lee, S.K., Lee, Y.K., Leem, J.G., Song, J.G., & Shin, J.W. (2014). Perineural pretreatment of bee venom attenuated the development of allodynia in the spinal nerve ligation injured neuropathic pain model; an experimental study. *BMC Complement Altern Med* 14, 431.

Kraus, R.L., Warren, V.A., Smith, M.M., Middleton, R.E., & Cohen, C.J. (2000). Modulation of R1G and R1C calcium channels by the spider toxin ProTx-II. *Soc. Neurosci. Abstr.* 26, 623.

Kraus, R.L., Warren, V.A., Smith, M.M., Middleton, R.E., Blumenthal, K.M., & Cohen, C.J. (2002) A spider toxin that inhibits activation of voltage-gated sodium channels. *Biophys. J.* 82, 85a.

Kubista, H., Mafra, R.A., Chong, Y., Nicholson, G.M., Beirao, P.S., Cruz, J.S., Boehm, S., Nentwig, W., & Kuhn-Nentwig, L. (2007). CSTX-1, a toxin from the venom of the hunting spider Cupiennius salei, is a selective blocker of L-type calcium channels in mammalian neurons. *Neuropharmacology* 52, 1650-1662.

Lee, J.H., Park, C.K., Chen, G., Han, Q., Xie, R.G., Liu, T., Ji, R.R., & Lee, S.Y. (2014). A monoclonal antibody that targets a NaV1.7 channel voltage sensor for pain and itch relief. *Cell* 157, 1393-1404.

Liu, D., Tseng, M., Epstein, L.F., Green, L., Chan, B., Soriano, B., Lim, D., Pan, O., Murawsky, C.M., King, C.T., & Moyer, B.D. (2016). Evaluation of recombinant monoclonal antibody SVmab1 binding to Na V1.7 target sequences and block of human Na V1.7 currents. *F1000Res* 5, 2764.

Liu, X., Li, C., Chen, J., Du, J., Zhang, J., Li, G., Jin, X., & Wu, C. (2014a). AGAP, a new recombinant neurotoxic polypeptide, targets the voltage-gated calcium channels in rat small diameter DRG neurons. *Biochem Biophys Res Commun* 452, 60-65.

Liu, Y., Tang, J., Zhang, Y., Xun, X., Tang, D., Peng, D., Yi, J., Liu, Z., & Shi, X. (2014b). Synthesis and analgesic effects of mu-TRTX-Hhn1b on models of inflammatory and neuropathic pain. *Toxins (Basel)* 6, 2363-2378.

Liu, Y., Wu, Z., Tang, D., Xun, X., Liu, L., Li, X., Nie, D., Xiang, Y., Yi, J., & Yi, J. (2014c). Analgesic effects of Huwentoxin-IV on animal models of inflammatory and neuropathic pain. *Protein Pept Lett* 21, 153-158.

Lopez-Santiago, L.F., Pertin, M., Morisod, X., Chen, C., Hong, S., Wiley, J., Decosterd, I., & Isom, L.L. (2006). Sodium channel beta2 subunits regulate tetrodotoxin-sensitive sodium channels in small dorsal root ganglion neurons and modulate the response to pain. *J Neurosci* 26, 7984-7994.

Lory, P., Bidaud, I., Mezghrani, A., & Monteil, A. (2006). [Calcium channelopathies: the current challenges]. *Med Sci (Paris)* 22, 1028-1031.

Lotarski, S., Hain, H., Peterson, J., Galvin, S., Strenkowski, B., Donevan, S., & Offord, J. (2014). Anticonvulsant activity of pregabalin in the maximal electroshock-induced seizure assay in alpha2delta1 (R217A) and alpha2delta2 (R279A) mouse mutants. *Epilepsy Res* 108, 833-842.

Lotarski, S.M., Donevan, S., El-Kattan, A., Osgood, S., Poe, J., Taylor, C.P., & Offord, J. (2011). Anxiolytic-like activity of pregabalin in the Vogel conflict test in alpha2delta-1 (R217A) and alpha2delta-2 (R279A) mouse mutants. *J Pharmacol Exp Ther* 338, 615-621.

Luo, Z.D., Calcutt, N.A., Higuera, E.S., Valder, C.R., Song, Y.H., Svensson, C.I., & Myers, R.R. (2002). Injury type-specific calcium channel alpha 2 delta-1 subunit up-regulation in rat neuropathic pain models correlates with antiallodynic effects of gabapentin. *J Pharmacol Exp Ther* 303, 1199-1205.

Luo, Z.D., Chaplan, S.R., Higuera, E.S., Sorkin, L.S., Stauderman, K.A., Williams, M.E., & Yaksh, T.L. (2001). Upregulation of dorsal root ganglion (alpha)2(delta) calcium channel subunit and its correlation with allodynia in spinal nerve-injured rats. *J Neurosci* 21, 1868-1875.

Manglik, A., Lin, H., Aryal, D.K., Mccorvy, J.D., Dengler, D., Corder, G., Levit, A., Kling, R.C., Bernat, V., Hubner, H., Huang, X.P., Sassano, M.F., Giguere, P.M., Lober, S., Da, D., Scherrer, G., Kobilka, B.K., Gmeiner, P., Roth, B.L., & Shoichet, B.K. (2016). Structure-based discovery of opioid analgesics with reduced side effects. *Nature* 537, 185-190.

Marionneau, C., Carrasquillo, Y., Norris, A.J., Townsend, R.R., Isom, L.L., Link, A.J., & Nerbonne, J.M. (2012) The sodium channel accessory subunit Navβ1 regulates neuronal excitability through modulation of repolarizing voltage-gated K^+ channels. *J Neurosci* 32, 5716-5527.

Martin-Eauclaire M.F., Abbas N., Sauze N., Mercier L., Berge-Lefranc J.L., Condo J., Bougis P.E., & Guieu R. (2010) Involvement of endogenous opioid system in scorpion toxin-induced antinociception in mice. *Neurosci Lett.* 482, 45-50.

Mattei, C. (2018). Tetrodotoxin, a Candidate Drug for Nav1.1-Induced Mechanical Pain? *Mar Drugs* 16.

Matthies, D., Bae, C., Toombes, G.E., Fox, T., Bartesaghi, A., Subramaniam, S., & Swartz, K.J. (2018). Single-particle cryo-EM structure of a voltage-activated potassium channel in lipid nanodiscs. *Elife* 7.

Mccormack, K., Santos, S., Chapman, M.L., Krafte, D.S., Marron, B.E., West, C.W., Krambis, M.J., Antonio, B.M., Zellmer, S.G., Printzenhoff, D., Padilla, K.M., Lin, Z., Wagoner, P.K., Swain, N.A., Stupple, P.A., De Groot, M., Butt, R.P., & Castle, N.A. (2013). Voltage sensor interaction site for selective small molecule inhibitors of voltage-gated sodium channels. *Proc Natl Acad Sci U S A* 110, E2724-2732.

Meir, A., Cherki, R.S., Kolb, E., Langut, Y., & Bajayo, N. (2012). Novel peptides isolated from spider venom, and uses thereof. *Submitted to UniProtKB*.

Meng, X., Xu, Y., Zhao, M., Wang, F., Ma, Y., Jin, Y., Liu, Y., Song, Y., & Zhang, J. (2015). The Functional Property Changes of Muscular Na(v)1.4 and Cardiac Na(v)1.5 Induced by Scorpion Toxin BmK AGP-SYPU1 Mutants Y42F and Y5F. *Biochemistry* 54, 2988-2996.

Middleton, R.E., Warren, V.A., Kraus, R.L., Hwang, J.C., Liu, C.J., Dai, G., Brochu, R.M., Kohler, M.G., Gao, Y.D., Garsky, V.M., Bogusky, M.J., Mehl, J.T., Cohen, C.J., & Smith, M.M. (2002). Two tarantula peptides inhibit activation of multiple sodium channels. *Biochemistry* 41, 14734-14747.

Molinski, T.F., Dalisay, D.S., Lievens, S.L., & Saludes, J.P. (2009). Drug development from marine natural products. Nat Rev Drug Discov 8, 69-85.

Murray, J.K., Biswas, K., Holder, J.R., Zou, A., Ligutti, J., Liu, D., Poppe, L., Andrews, K.L., Lin, F.F., Meng, S.Y., Moyer, B.D., Mcdonough, S.I., & Miranda, L.P. (2015a). Sustained inhibition of the NaV1.7 sodium channel by engineered dimers of the domain II binding peptide GpTx-1. *Bioorg Med Chem Lett* 25, 4866-4871.

Murray, J.K., Ligutti, J., Liu, D., Zou, A., Poppe, L., Li, H., Andrews, K.L., Moyer, B.D., Mcdonough, S.I., Favreau, P., Stocklin, R., & Miranda, L.P. (2015b). Engineering potent and selective analogues of GpTx-1, a tarantula venom peptide antagonist of the Na(V)1.7 sodium channel. *J Med Chem* 58, 2299-2314.

Murray, J.K., Long, J., Zou, A., Ligutti, J., Andrews, K.L., Poppe, L., Biswas, K., Moyer, B.D., Mcdonough, S.I., & Miranda, L.P. (2016). Single Residue Substitutions That Confer Voltage-Gated Sodium Ion Channel Subtype Selectivity in the NaV1.7 Inhibitory Peptide GpTx-1. *J Med Chem* 59, 2704-2717.

Namadurai, S., Yereddi, N.R., Cusdin, F.S., Huang, C.L., Chirgadze, D.Y., & Jackson, A.P. (2015). A new look at sodium channel beta subunits. *Open Biol* 5, 140192.

Nguyen H.M., Miyazaki H., Hoshi N., Smith B.J., Nukina N., Goldin A.L., & Chandy K.G. (2012). Modulation of voltage-gated K+ channels by the sodium channel beta1 subunit. *Proc. Natl. Acad. Sci. U. S. A.*109, 18577-18582.

Nerbonne, J.M., & Kass, R.S. (2005). Molecular physiology of cardiac repolarization. *Physiol Rev* 85, 1205-1253.

Norton, R.S., & Chandy, K.G. (2017). Venom-derived peptide inhibitors of voltage-gated potassium channels. *Neuropharmacology* 127, 124-138.

Ono, S., Kimura, T., & Kubo, T. (2011). Characterization of voltage-dependent calcium channel blocking peptides from the venom of the tarantula Grammostola rosea. *Toxicon* 58, 265-276.

Osteen, J.D., Herzig, V., Gilchrist, J., Emrick, J.J., Zhang, C., Wang, X., Castro, J., Garcia-Caraballo, S., Grundy, L., Rychkov, G.Y., Weyer, A.D., Dekan, Z., Undheim, E.A., Alewood, P., Stucky, C.L., Brierley, S.M., Basbaum, A.I., Bosmans, F., King, G.F., & Julius, D. (2016). Selective spider toxins reveal a role for the Nav1.1 channel in mechanical pain. *Nature* 534, 494-499.

Pan, H.L., Wu, Z.Z., Zhou, H.Y., Chen, S.R., Zhang, H.M., & Li, D.P. (2008). Modulation of pain transmission by G-protein-coupled receptors. *Pharmacol Ther* 117, 141-161.

Pan, X., Li, Z., Zhou, Q., Shen, H., Wu, K., Huang, X., Chen, J., Zhang, J., Zhu, X., Lei, J., Xiong, W., Gong, H., Xiao, B., & Yan, N. (2018). Structure of the human voltage-gated sodium channel Nav1.4 in complex with beta1. *Science* 362.

Payandeh, J., & Minor, D.L., Jr. (2015). Bacterial voltage-gated sodium channels (BacNa(V)s) from the soil, sea, and salt lakes enlighten molecular mechanisms of electrical signaling and pharmacology in the brain and heart. *J Mol Biol* 427, 3-30.

Payandeh, J., Scheuer, T., Zheng, N., & Catterall, W.A. (2011). The crystal structure of a voltage-gated sodium channel. *Nature* 475, 353-358.

Peng, K., Shu, Q., Liu, Z., & Liang, S. (2002). Function and solution structure of huwentoxin-IV, a potent neuronal tetrodotoxin (TTX)-sensitive sodium channel antagonist from Chinese bird spider Selenocosmia huwena. *J Biol Chem* 277, 47564-47571.

Pennington, M.W., Czerwinski, A., & Norton, R.S. (2018). Peptide therapeutics from venom: Current status and potential. *Bioorg Med Chem* 26, 2738-2758.

Penzotti, J.L., Fozzard, H.A., Lipkind, G.M., & Dudley, S.C., Jr. (1998). Differences in saxitoxin and tetrodotoxin binding revealed by mutagenesis of the Na+ channel outer vestibule. *Biophys J* 75, 2647-2657.

Pineda, S.S., Chaumeil, P.A., Kunert, A., Kaas, Q., Thang, M.W.C., Le, L., Nuhn, M., Herzig, V., Saez, N.J., Cristofori-Armstrong, B., Anangi, R., Senff, S., Gorse, D., & King, G.F. (2018). ArachnoServer 3.0: an online resource for automated discovery, analysis and annotation of spider toxins. *Bioinformatics* 34, 1074-1076.

Priest, B.T., Blumenthal, K.M., Smith, J.J., Warren, V.A., & Smith, M.M. (2007). ProTx-I and ProTx-II: gating modifiers of voltage-gated sodium channels. *Toxicon* 49, 194-201.

Pringos, E., Vignes, M., Martinez, J., & Rolland, V. (2011). Peptide neurotoxins that affect voltage-gated calcium channels: a close-up on omega-agatoxins. *Toxins (Basel)* 3, 17-42.

Raffaeli W., Sarti D., Demartini L., Sotgiu A., & Bonezzi C.(2011) Italian registry on long-term intrathecal ziconotide treatment. *Pain Physician* 14, 15-24.

Rahnama, S., Deuis, J.R., Cardoso, F.C., Ramanujam, V., Lewis, R.J., Rash, L.D., King, G.F., Vetter, I., & Mobli, M. (2017). The structure, dynamics and selectivity profile of a NaV1.7 potency-optimised huwentoxin-IV variant. *PLoS One* 12, e0173551.

Revell, J.D., Lund, P.E., Linley, J.E., Metcalfe, J., Burmeister, N., Sridharan, S., Jones, C., Jermutus, L., & Bednarek, M.A. (2013). Potency optimization of Huwentoxin-IV on hNav1.7: a neurotoxin TTX-S sodium-channel antagonist from the venom of the Chinese bird-eating spider Selenocosmia huwena. *Peptides* 44, 40-46.

Rigo, F.K., Trevisan, G., De Pra, S.D., Cordeiro, M.N., Borges, M.H., Silva, J.F., Santa Cecilia, F.V., De Souza, A.H., De Oliveira Adamante, G., Milioli, A.M., De Castro Junior, C.J., Ferreira, J., & Gomez, M.V. (2017). The spider toxin Phalpha1beta recombinant possesses strong analgesic activity. *Toxicon* 133, 145-152.

Rostaing-Rigattieri, S., & Guerin, J. (2014). [Cancer pain management: good clinical practices, use of strong opioids]. *Presse Med* 43, 252-262.

Rush, A.M., Cummins, T.R., & Waxman, S.G. (2007). Multiple sodium channels and their roles in electrogenesis within dorsal root ganglion neurons. *J. Physiol.* 579, 1-14.

Saegusa, H., Kurihara, T., Zong, S., Kazuno, A., Matsuda, Y., Nonaka, T., Han, W., Toriyama, H., & Tanabe, T. (2001). Suppression of inflammatory and neuropathic pain symptoms in mice lacking the N-type Ca2+ channel. *EMBO J* 20, 2349-2356.

Saez, N.J., Senff, S., Jensen, J.E., Er, S.Y., Herzig, V., Rash, L.D., & King, G.F. (2010). Spider-venom peptides as therapeutics. *Toxins (Basel)* 2, 2851-2871.

Safavi-Hemami, H., Brogan, S.E., & Olivera, B.M. (2018). Pain therapeutics from cone snail venoms: From Ziconotide to novel non-opioid pathways. *J Proteomics*.

Santana R.C., Perez D., Dobson J., Panagides N., Raven R.J., Nouwens A., Jones A., King G.F., & Fry B.G. (2017) Venom Profiling of a Population of the Theraphosid Spider Phlogius crassipes Reveals Continuous Ontogenetic Changes from Juveniles through Adulthood. *Toxins (Basel)* 9.

Saucedo, A.L., Del Rio-Portilla, F., Picco, C., Estrada, G., Prestipino, G., Possani, L.D., Delepierre, M., & Corzo, G. (2012). Solution structure of native and recombinant expressed toxin CssII from the venom of the scorpion Centruroides suffusus suffusus, and their effects on Nav1.5 sodium channels. *Biochim Biophys Acta* 1824, 478-487.

Schmidt, G. (2010). Wie lautet der korrekte Name von Selenocosmia huwena Wang, Peng & Xie, 1993?. *Tarantulas World* 142, 23e27.

Sekiguchi, F., Tsubota, M., & Kawabata, A. (2018). Involvement of Voltage-Gated Calcium Channels in Inflammation and Inflammatory Pain. *Biol Pharm Bull* 41, 1127-1134.

Sevenet, T. (2006). [Toxines toxiques, toxines utiles chez les plantes]. *Biofutur*, 272, 30-34.

Shen, H., Zhou, Q., Pan, X., Li, Z., Wu, J., & Yan, N. (2017). Structure of a eukaryotic voltage-gated sodium channel at near-atomic resolution. *Science* 355.

Snutch, T.P., &Monteil, A. (2007) The sodium "leak" has finally been plugged. *Neuron* 54, 505-507.

Sousa, S.R., Vetter, I., & Lewis, R.J. (2013). Venom peptides as a rich source of cav2.2 channel blockers. *Toxins (Basel)* 5, 286-314.

Sousa, S.R., Wingerd, J.S., Brust, A., Bladen, C., Ragnarsson, L., Herzig, V., Deuis, J.R., Dutertre, S., Vetter, I., Zamponi, G.W., King, G.F., Alewood, P.F., & Lewis, R.J. (2017). Discovery and mode of action of a novel analgesic beta-toxin from the African spider Ceratogyrus darlingi. *PLoS One* 12, e0182848.

Staats P.S., Yearwood T., Charapata S.G., Presley R.W., Wallace M.S., Byas-Smith M., Fisher R., Bryce D.A., Mangieri E.A., Luther R.R., Mayo M., McGuire D., & Ellis D. (2004) Intrathecal ziconotide in the treatment of refractory pain in patients with cancer or AIDS: a randomized controlled trial. *JAMA* 291, 63-70.

Sun, S., Jia, Q., Zenova, A.Y., Chafeev, M., Zhang, Z., Lin, S., Kwan, R., Grimwood, M.E., Chowdhury, S., Young, C., Cohen, C.J., & Oballa, R.M. (2014). The discovery of benzenesulfonamide-based potent and selective inhibitors of voltage-gated sodium channel Na(v)1.7. *Bioorg Med Chem Lett* 24, 4397-4401.

Sutton, K.G., Siok, C., Stea, A., Zamponi, G.W., Heck, S.D., Volkmann, R.A., Ahlijanian, M.K., & Snutch, T.P. (1998). Inhibition of neuronal calcium channels by a novel peptide spider toxin, DW13.3. *Mol Pharmacol* 54, 407-418.

Tan, A.M., Samad, O.A., Dib-Hajj, S.D., & Waxman, S.G. (2015). Virus-Mediated Knockdown of Nav1.3 in Dorsal Root Ganglia of STZ-Induced Diabetic Rats Alleviates Tactile Allodynia. *Mol Med* 21, 544-552.

Templin, C., Ghadri, J.R., Rougier, J.S., Baumer, A., Kaplan, V., Albesa, M., Sticht, H., Rauch, A., Puleo, C., Hu, D., Barajas-Martinez, H., Antzelevitch, C., Luscher, T.F., Abriel, H., & Duru, F. (2011).

Identification of a novel loss-of-function calcium channel gene mutation in short QT syndrome (SQTS6). *Eur Heart J* 32, 1077-1088.

Tibbs, G.R., Posson, D.J., & Goldstein, P.A. (2016). Voltage-Gated Ion Channels in the PNS: Novel Therapies for Neuropathic Pain? *Trends Pharmacol Sci* 37, 522-542.

Tobassum S., Tahir H.M., Zahid M.T., Gardner Q.A., & Ahsan M.M. (2018). Effect of Milking Method, Diet, and Temperature on Venom Production in Scorpions. *J Insect Sci* 18.

Trimmer, J.S., & Rhodes, K.J. (2004). Localization of voltage-gated ion channels in mammalian brain. *Annu Rev Physiol* 66, 477-519.

Veeresham, C. (2012). Natural products derived from plants as a source of drugs. *J Adv Pharm Technol Res* 3, 200-201.

Vetter, I., Deuis, J.R., Mueller, A., Israel, M.R., Starobova, H., Zhang, A., Rash, L.D., & Mobli, M. (2017). NaV1.7 as a pain target - From gene to pharmacology. *Pharmacol Ther* 172, 73-100.

Villanueva, M.T. (2017). Analgesia: Designing out opioid side effects. *Nat Rev Drug Discov* 16, 311.

Villegas, E., Adachi-Akahane, S., Bosmans, F., Tytgat, J., Nakajima, T., & Corzo, G. (2008). Biochemical characterization of cysteine-rich peptides from Oxyopes sp. venom that block calcium ion channels. *Toxicon* 52, 228-236.

Wang, C., Shan, B., Wang, Q., Xu, Q., Zhang, H., & Lei, H. (2017a). Fusion of Ssm6a with a protein scaffold retains selectivity on NaV 1.7 and improves its therapeutic potential against chronic pain. *Chem Biol Drug Des* 89, 825-833.

Wang, F., Yan, Z., Liu, Z., Wang, S., Wu, Q., Yu, S., Ding, J., & Dai, Q. (2016). Molecular basis of toxicity of N-type calcium channel inhibitor MVIIA. *Neuropharmacology* 101, 137-145.

Wang, Y., Li, X., Yang, M., Wu, C., Zou, Z., Tang, J., & Yang, X. (2017b). Centipede venom peptide SsmTX-I with two intramolecular disulfide bonds shows analgesic activities in animal models. *J Pept Sci* 23, 384-391.

Waxman, S.G., Kocsis, J.D., & Black, J.A. (1994). Type III sodium channel mRNA is expressed in embryonic but not adult spinal sensory neurons, and is reexpressed following axotomy. *J Neurophysiol* 72, 466-470.

Waxman, S.G., & Zamponi, G.W. (2014). Regulating excitability of peripheral afferents: emerging ion channel targets. *Nat Neurosci* 17, 153-163.

Wilson, D., & Daly, N.L. (2018). Venomics: A Mini-Review. *High Throughput* 7.

Winters, S., Martin, C., Murphy, D., & Shokar, N.K. (2017). Breast Cancer Epidemiology, Prevention, and Screening. *Prog Mol Biol Transl Sci* 151, 1-32.

Wong, E.S., Hardy, M.C., Wood, D., Bailey, T., & King, G.F. (2013). SVM-based prediction of propeptide cleavage sites in spider toxins identifies toxin innovation in an Australian tarantula. *PLoS One* 8, e66279.

Wright, Z.V.F., Mccarthy, S., Dickman, R., Reyes, F.E., Sanchez-Martinez, S., Cryar, A., Kilford, I., Hall, A., Takle, A.K., Topf, M., Gonen, T., Thalassinos, K., & Tabor, A.B. (2017). The Role of Disulfide Bond Replacements in Analogues of the Tarantula Toxin ProTx-II and Their Effects on Inhibition of the Voltage-Gated Sodium Ion Channel Nav1.7. *J Am Chem Soc* 139, 13063-13075.

Wu, J., Yan, Z., Li, Z., Qian, X., Lu, S., Dong, M., Zhou, Q., & Yan, N. (2016). Structure of the voltage-gated calcium channel Ca(v)1.1 at 3.6 A resolution. *Nature* 537, 191-196.

Wulff, H., Castle, N.A., & Pardo, L.A. (2009). Voltage-gated potassium channels as therapeutic targets. *Nat Rev Drug Discov* 8, 982-1001.

Xiao, Y., Luo, X., Kuang, F., Deng, M., Wang, M., Zeng, X., & Liang, S. (2008). Synthesis and characterization of huwentoxin-IV, a neurotoxin inhibiting central neuronal sodium channels. *Toxicon* 51, 230-239.

Xie, W., Tan, Z.Y., Barbosa, C., Strong, J.A., Cummins, T.R., & Zhang, J.M. (2016). Upregulation of the sodium channel NaVbeta4 subunit and its contributions to mechanical hypersensitivity and neuronal hyperexcitability in a rat model of radicular pain induced by local dorsal root ganglion inflammation. *Pain* 157, 879-891.

Yang, L., Li, Q., Liu, X., & Liu, S. (2016). Roles of Voltage-Gated Tetrodotoxin-Sensitive Sodium Channels NaV1.3 and NaV1.7 in Diabetes and Painful Diabetic Neuropathy. *Int J Mol Sci* 17.

Yan Z., Zhou Q., Wang L., Wu J., Zhao Y., Huang G., Peng W., Shen H., Lei J., & Yan N. (2017) Structure of the Nav1.4-b1 Complex from Electric Eel. *Cell* 170, 470–482.

Yang, S., Xiao, Y., Kang, D., Liu, J., Li, Y., Undheim, E.A., Klint, J.K., Rong, M., Lai, R., & King, G.F. (2013). Discovery of a selective NaV1.7 inhibitor from centipede venom with analgesic efficacy exceeding morphine in rodent pain models. *Proc Natl Acad Sci U S A* 110, 17534-17539.

Yasuda, O., Morimoto, S., Jiang, B., Kuroda, H., Kimura, T., Sakakibara, S., Fukuo, K., Chen, S., Tamatani, M., & Ogihara, T. (1994). FS2. a mamba venom toxin, is a specific blocker of the L-type calcium channels. *Artery* 21, 287-302.

Yekkirala, A.S., Roberson, D.P., Bean, B.P., & Woolf, C.J. (2017). Breaking barriers to novel analgesic drug development. *Nat Rev Drug Discov* 16, 810.

Young, K., Lin, S., Sun, L., Lee, E., Modi, M., Hellings, S., Husbands, M., Ozenberger, B., & Franco, R. (1998). Identification of a calcium channel modulator using a high throughput yeast two-hybrid screen. *Nat Biotechnol* 16, 946-950.

Yu, F. H., & Catterall.W. A. (2004). The VGL-chanome: a protein superfamily specialized for electrical signaling and ionic homeostasis. *Sci STKE*, 2004: re15.

Zambelli, V.O., Pasqualoto, K.F., Picolo, G., Chudzinski-Tavassi, A.M., & Cury, Y. (2016). Harnessing the knowledge of animal toxins to generate drugs. *Pharmacol Res* 112, 30-36.

Zamponi, G.W., Striessnig, J., Koschak, A., & Dolphin, A.C. (2015). The Physiology, Pathology, and Pharmacology of Voltage-Gated Calcium Channels and Their Future Therapeutic Potential. *Pharmacol Rev* 67, 821-870.

Zemel, B.M., Ritter, D.M., Covarrubias, M., & Muqeem, T. (2018). A-Type KV Channels in Dorsal Root Ganglion Neurons: Diversity, Function, and Dysfunction. *Front Mol Neurosci* 11, 253.

ANNEXES

A1. Liste des publications, des participations à des congrès et des formations

A1.1. Publications

Articles

1. **GONÇALVES T.C.**, BOUKAIBA R., MOLGO J., AMAR M., PARTISETI M., SERVENT D. & BENOIT E. (2018) Direct evidence for high affinity blockade of $Na_V1.6$ channel subtype by huwentoxin-IV spider peptide, using multiscale functional approaches. Neuropharmacology, 133: 404-414.
2. **GONÇALVES T.C.**, BENOIT E., PARTISETI M. & SERVENT D. (2018) The $Na_V1.7$ channel subtype as an antinociceptive target for spider toxins in adult dorsal root ganglia neurons. Frontiers in Pharmacology, 9:1000. doi: 10.3389/fphar.2018.01000.
3. **GONÇALVES T.C.**, BENOIT E., KURZ M., LUCARAIN L., FOUCONNIER S., COMBEMALE S., JAQUILLARD L., SCHOMBERT B., CHAMBARD J.-M., BOUKAIBA R., HESSLER G., BOHME A., BIALY L., HOURCADE S., BÉROUD R., DE WAARD M., SERVENT D. & PARTISETI M. (2018) Cyriotoxin-1a, the first toxin from *Cyriopagopus schioedtei* spider with antinociceptive properties: from identification to functional characterization. British Journal of Pharmacology (en révision).
4. CERLES O., **GONÇALVES T.C.**, CHOUZENOUX S., BENOIT E., SCHMITT A., BENETT SAIDU N.E., KAVIAN N., CHÉREAU C., GOBEAUX C., WEILL B., CORIAT R., NICCO C. & BATTEUX F. (2018) Blocking muscarinic receptors by benztropine prevents platinum-induced peripheral neuropathies and tumor growth. Acta Neuropathologica Communications (en révision).

Abstracts

1. **GONÇALVES T.C.**, AMAR A., BOUKAIBA R., PARTISETI M., SERVENT D. & BENOIT E. (2018) D peptide, a promising toxin as potential antinociceptive agent targeting the $Na_V1.7$ subtype of voltage-gated sodium channels. Toxicon, 149: 89.
2. **GONÇALVES T.C.**, PARTISETI M., SERVENT D. & BENOIT E. (2018) A non-invasive method to appraise time-dependent effects of venom toxins on the mouse neuromuscular excitability *in vivo*. Toxicon, 149: 104.
3. **GONÇALVES T.C.**, BOUKAIBA R., MOLGO J., AMAR A., PARTISETI M., SERVENT D. & BENOIT E. (2018) A multiscale functional approach to assess pharmacological interactions between huwentoxin-IV spider peptide and sodium channel subtypes. Toxicon, 149: 105-106.

A1.2. Participations à des congrès

Conférence invitée

1. **GONÇALVES T.C.**, BENOIT E., SERVENT D. & PARTISETI M. (septembre 2018) Antinociceptive evaluation of cyriotoxin-1a and huwentoxin-IV, two spider toxins that block with high affinity the $Na_V1.7$ subtype of voltage-gated sodium channels. 29^{th} Ion Channel Meeting, Sète.

Communications orales

1. **GONÇALVES T.C.**, AMAR M., BOUKAIBA R., PARTISETI M., SERVENT D. & BENOIT E. (décembre 2016) D peptide, a promising toxin as potential antinociceptive agent targeting the $Na_V1.7$ subtype of voltage-gated sodium channels. 23èmes Rencontres en Toxinologie "Toxins: Immunity, Inflammation and Pain" organisées par la Société Française pour l'Etude des Toxines (SFET), Institut Pasteur, Paris.
2. **GONÇALVES T.C.** (juillet 2017) Evaluation multi-échelle de toxines de venins comme agents thérapeutiques potentiels ou marqueurs diagnostiques (180 secondes). Journées des doctorants de l'Institut des Sciences de la Vie Frédéric Joliot, CEA de Saclay, Gif-sur-Yvette.
3. **GONÇALVES T.C.**, AMAR M., BOUKAIBA R., PARTISETI M., SERVENT D. & BENOIT E. (août 2017) Comparison of D peptide and Huwentoxin-IV as potential antinociceptive agents targeting the $Na_V1.7$ subtype of voltage-gated sodium channels. 4th International Symposium "Venoms 2017: Evolutionary diversity of natural toxins: implications for antivenom development and drug discovery", Oxford, Angleterre.

Posters (le présentateur est souligné)

1. **GONÇALVES T.C.**, AMAR M., MOLGO J., PARTISETI M., SERVENT D. & BENOIT E. (mai 2016) Multiscale evaluation of venom toxins as potential antinociceptive agents. Journées des doctorants de l'Institut de Biologie et de Technologies de Saclay (IBITEC-S), CEA de Saclay, Gif-sur-Yvette.
2. **GONÇALVES T.C.**, AMAR M., MOLGO J., PARTISETI M., SERVENT D. & BENOIT E. (juin 2016) Multi-scale evaluation of venom toxins as potential antinociceptive agents. Journées de l'Ecole Doctorale "Innovation Thérapeutique: du fondamental à l'appliqué", Châtenay-Malabry.
3. **GONÇALVES T.C.**, AMAR M., BOUKAIBA R., PARTISETI M., SERVENT D. & BENOIT E. (juin 2017) Cyriotoxin-1a, a promising toxin as potential antinociceptive agent targeting the $Na_V1.7$ subtype of voltage-gated sodium channels. 15ème Symposium ICSN "Substances Naturelles ICSN-UPSay", Gif-sur-Yvette.
4. **GONÇALVES T.C.**, BOUKAIBA R., MOLGO J., AMAR M., PARTISETI M., SERVENT D. & BENOIT E. (décembre 2017) A multiscale functional approach to assess the pharmacological interactions between Huwentoxin-IV spider peptide and sodium channel subtypes. 24èmes Rencontres en Toxinologie "Toxins: Biodiversity, Environment and Evolution" organisées par la SFET, Institut Pasteur, Paris.
5. **GONÇALVES T.C.**, PARTISETI M., SERVENT D. & BENOIT E. (décembre 2017) A non-invasive method to appraise time-dependent effects of venom toxins on the mouse neuromuscular excitability *in vivo*. 24èmes Rencontres en Toxinologie "Toxins: Biodiversity, Environment and Evolution" organisées par la SFET, Institut Pasteur, Paris.
6. **GONÇALVES T.C.**, BOUKAIBA R., MOLGO J., AMAR M., PARTISETI M., SERVENT D. & BENOIT E. (décembre 2017) A multiscale functional approach to evidence high affinity blockade of $Na_V1.6$ channel subtype by huwentoxin-IV spider peptide. 7ème colloque annuel du LabEx LERMIT, LAL, Orsay.
7. **GONÇALVES T.C.**, PARTISETI M., SERVENT D. & BENOIT E. (janvier 2018) A non-invasive method to appraise time-dependent effects of venom toxins on the mouse neuromuscular excitability *in vivo*. Journées Scientifiques organisées dans le cadre du programme national de la lutte contre le terrorisme (projet NRBC-E), CEA de Saclay, Gif-sur-Yvette.
8. **GONÇALVES T.C.**, BENOIT E., BOUKAIBA R., HESSLER G., SERVENT D. & PARTISETI M. (avril 2018) *In vivo* evaluation of antinociceptive effects of cyriotoxin-1a, the first toxin purified from *Cyriopagopus schioedtei* spider venom. 1st international symposium of Paris-Saclay University "Drug Discovery and New Therapeutics", Orsay.

9. GILLES N., MOURIER M., KESSLER P., DROCTOVE L., **GONÇALVES T.C.**, BENOIT E. & SERVENT D. (avril 2018) Therapeutic potential of venom peptides interacting with GPCRs and ion channels. 1st international symposium of Paris-Saclay University "Drug Discovery and New Therapeutics", Orsay.
10. **GONÇALVES T.C.**, PARTISETI M., SERVENT D. & BENOIT E. (avril 2018) A non-invasive method to appraise time-dependent effects of venom toxin-based therapeutics on the mouse neuromuscular excitability *in vivo*. 1st international symposium of Paris-Saclay University "Drug Discovery and New Therapeutics", Orsay.
11. **GONÇALVES T.C.**, PARTISETI M., SERVENT D. & BENOIT E. (mai 2018) A multiscale functional approach to appraise the pharmacological interactions between spider venom peptides and $Na_V1.7$, a genetically validated analgesic target. 9th Young Researchers in Life Science (YRLS), Campus ENS Jourdan, Paris.
12. **GONÇALVES T.C.**, BENOIT E., KURZ M., LUCARAIN L., FOUCONNIER S., COMBEMALE S., JAQUILLARD L., SCHOMBERT B., CHAMBARD J.-M., BOUKAIBA R., HESSLER G., BOHME A., BIALY L., HOURCADE S., BÉROUD R., DE WAARD M., SERVENT D. & PARTISETI M. (août 2018) Cyriotoxin-1a, the first toxin with antinociceptive properties purified from *Cyriopagopus schioedtei* spider venom: from identification to structural and functional characterization. Gordon Research Conference "Venom Evolution, Function and Biomedical Applications", Mount Snow, West Dover, Vermont, USA.
13. **GONÇALVES T.C.**, BOUKAIBA R., MOLGO J., AMAR M., PARTISETI M., SERVENT D. & BENOIT E. (septembre 2018) Multiscale functional approaches to evidence high affinity blockade of $Na_V1.6$ channel subtype by huwentoxin-IV spider peptide. 29th Ion Channel Meeting, Sète.
14. **GONÇALVES T.C.**, BENOIT E., PARTISETI M. & SERVENT D. (novembre 2018) Antinociceptive targets for spider toxins in adult dorsal root ganglia neurons. 25èmes Rencontres en Toxinologie "Toxins and Health: From molecules to organisms" organisées par la SFET, Institut Pasteur, Paris.

A1.3. Formations

1. Technique de dissociation et de mise en culture primaire de neurones des ganglions de la racine dorsale (DRG) de souris adultes. SANOFI Aventis, Chilly-Mazarin (novembre 2015).
2. UE de Master II: Protéines solubles et membranaires: expression, purification et caractérisation. INSTN, CEA de Saclay, Gif-sur-Yvette (décembre 2015).
3. Formation spécifique destinée aux personnes concevant ou réalisant des procédures expérimentales sur modèle rongeur (ancien niveau 1). Ecole vétérinaire, Maisons-Alfort (mai 2016).
4. Formation en Neurosciences sur l'imagerie optique et l'électrophysiologie. École des Neurosciences de Paris (ENP) – Université Paris Descartes – École Normale Supérieure (ENS), Paris (juin 2017).
5. Formation sur la chaîne du médicament: point de vue des industriels par le LabEx LERMIT. Montigny-le-Bretonneux (juillet 2017).
6. Cours d'anglais général et de communication scientifique en anglais (niveau intermédiaire) par l'Université Paris-Sud. Campus d'Orsay (octobre 2017).
7. "How to improve your scientific presentations" par la Fondation Estève, en collaboration avec le GDR 3545, le CNRS et le Collège de France. Paris (novembre 2017).
8. Séminaire DRF Animal et Société par le Comité d'Ethique pour l'Expérimentation Animale du CEA. CEA de Fontenay aux Roses (novembre 2017).

9. "Les impacts de la diversité et de la mixité sur les métiers de la recherche et de l'innovation" par l'ANRT (Association Nationale Recherche Technologie). Paris (mars 2018).
10. E-learning SANOFI "Lutte contre la corruption" (mai 2018).
11. E-learning SANOFI "Code éthique" (juin 2018).
12. E-learning SANOFI "Essentiels sur la protection des données personnelles" (juillet 2018).
13. E-learning SANOFI "L'essentiel de la confidentialité" (septembre 2018).

A2. Publication n°6

Contexte de l'étude

L'oxaliplatine est l'une des principales molécules utilisées en oncologie digestive ayant prouvé sa capacité à traiter certaines tumeurs solides dont le cancer colorectal en situation métastatique et le cancer gastrique. Cependant, la neuropathie périphérique induite par cet agent anticancéreux conduit fréquemment à l'arrêt de son administration. Depuis 2014, notre équipe, en collaboration avec celle du Pr. Frédéric Batteux (Hôpital Cochin, Paris), explore les mécanismes de cette neuropathie en utilisant un modèle murin de neurotoxicité induite chimiquement par l'oxaliplatine. En particulier, les effets thérapeutiques du mangafodipir et du niclosamide, molécules dotées de propriétés anti-oxydantes, ont été évalués chez ce modèle murin et certains des résultats obtenus ont été confirmés chez l'homme (Coriat et al., 2014; Cerles et al., 2017).

La neurotoxicité induite chimiquement peut être due, entre autres, aux interactions de l'agent anticancéreux avec l'ADN, à des perturbations mitochondriales, à des dérégulations des canaux ioniques ou encore à des dysfonctionnements de la neurotransmission glutaminergique. Des lésions peuvent survenir au niveau des neurones sensoriels, incluant les neurones de DRG, associées à des défauts de transport axonal ou à la dégénérescence de l'axone. Les cellules de Schwann sont connues pour être les principaux effecteurs de la régénération axonale dans une variété de 94 affections neuropathiques périphériques (notamment héréditaires, inflammatoires et toxiques) et dans le cas de lésions traumatiques des fibres nerveuses périphériques.

La benztropine est un inhibiteur des récepteurs muscariniques M1-M3 de l'acétylcholine. Ce médicament est connu pour favoriser la différenciation de cellules précurseurs d'oligodendrocytes tout en permettant une remyélinisation axonale avec une puissance supérieure à celle des molécules actuellement prescrites aux patients atteints de sclérose en plaques. Par ailleurs, lors de traitements à l'oxaliplatine, des croissances tumorales induites par l'acétylcholine, et impliquant principalement

une surexpression du récepteur muscarinique M3 de l'acétylcholine, ont été détectées dans plusieurs organes. De plus, plusieurs études ont mis en évidence une prévention de la croissance tumorale et des métastases par le blocage des récepteurs muscariniques.

C'est dans ce contexte que nous avons évalué les effets de la benztropine non seulement sur les neuropathies périphériques induites par l'oxaliplatine mais également sur celles apparaissant dans les cas de diabète, *in vivo* chez des modèles expérimentaux de souris, *ex vivo* sur les nerfs sciatiques isolés de souris et *in vitro* sur des cultures primaires de neurones de DRG de souris.

Acta Neuropathologica Communications (publication en révision)

"Blocking muscarinic receptors by benztropine prevents platinum-induced peripheral neuropathies and tumor growth"

Olivier Cerles, **Tânia C. Gonçalves**, Sandrine Chouzenoux, Evelyne Benoit, Alain Schmitt, Nathaniel Edward Benett Saidu, Niloufar Kavian, Christiane Chéreau, Camille Gobeaux, Bernard Weill, Romain Coriat, Carole Nicco & Frédéric Batteux

Blocking muscarinic receptors by benztropine prevents platinum-induced peripheral neuropathies and tumor growth

Olivier Cerles[1], Tânia Cristina Gonçalves[2,3], Sandrine Chouzenoux[1], Evelyne Benoit[2], Alain Schmitt[4], Nathaniel Edward Bennett Saidu[1], Niloufar Kavian[1,5], Christiane Chéreau[1], Camille Gobeaux[6], Bernard Weill[1,5], Romain Coriat[1,7], Carole Nicco[§1], Frédéric Batteux[§1, 5*]

Author Affiliations: [1]Department "Development, Reproduction and Cancer", Institut Cochin, Paris Descartes University, Sorbonne Paris City, INSERM U1016, Paris, France; [2]Molecular engineering of proteins unit (SIMOPRO), CEA of Saclay, and Paris-Saclay Institute of Neuroscience (Neuro-PSI), UMR CNRS 9197, Paris-Saclay University, Gif-sur-Yvette, France; [3]Sanofi R & D, Integrated Drug Discovery – High Content Biology, Vitry-sur-Seine, France; [4]Plateforme imagerie : microscopie électronique, Institut Cochin, INSERM U1016, Paris, France; [5]Department of Immunology, Cochin Teaching Hospital, AP-HP, Paris, France; [6]Service de diagnostic biologique automatisé, Cochin Teaching Hospital, Paris, France; [7]Department of Gastroenterology, Cochin Teaching Hospital, Paris Descartes University, Paris, France.

§ Frédéric Batteux and Carole Nicco contributed equally to this article.

***Corresponding Author**: Frédéric Batteux, Cochin Teaching Hospital, 27 rue du faubourg Saint-Jacques, Paris F75014, France; Phone: +33 (1) 5841 2141; Fax: +33 (1) 4441 2546
Email: frederic.batteux@cch.aphp.fr

Conflicts of Interest: The authors declare no competing financial interests.

Keywords: Benztropine, Oxaliplatin, Peripheral neuropathies, Muscarinic receptors, Myelin.

Abstract

The endogenous cholinergic system plays a key role in neuronal cells, by suppressing neurite outgrowth and myelination and, in some cancer cells, favoring tumor growth. Platinum compounds are widely used as part of first line conventional cancer chemotherapy but their efficacy is however limited by peripheral neuropathy as a major side-effect. We have evaluated whether blocking muscarinic receptors M1 and M3 with benztropine can increase anti-tumoral efficacy of oxaliplatin, while preventing its neurotoxicity.

Benztropine ameliorates acute and chronic clinical symptoms of oxaliplatin-induced peripheral neuropathies in mice. Sensory alterations detected by electrophysiology in oxaliplatin-treated mice were consistent with a decreased nerve conduction velocity and membrane hyperexcitability due to alterations in the density and/or functioning of both sodium and potassium channels, confirmed by action potential analysis from *ex-vivo* cultures of mouse dorsal root ganglion sensory neurons using whole-cell patch-clamp. These alterations were all prevented by benztropine. In oxaliplatin-treated mice, MBP expression, confocal and electronic microscopy of the sciatic nerves revealed a demyelination and confirmed the alteration of the myelinated axons morphology when compared to animals injected with oxaliplatin plus benztropine. Benztropine also prevented the decrease in neuronal density in the paws of mice injected with oxaliplatin. The neuroprotection conferred by benztropine against chemotherapeutic drugs was associated with a lower expression of inflammatory cytokines and extended to diabetic-induced peripheral neuropathy in mice.

Mice receiving benztropine alone presented a lower tumor growth when compared to untreated

animals and synergized the anti-tumoral effect of oxaliplatin, a phenomenon explained at least in part by benztropine-induced ROS imbalance in tumor cells.

This report shows that blocking muscarinic receptors with benztropine prevents peripheral neuropathies and increases the therapeutic index of oxaliplatin. These results can be rapidly transposable to patients as benztropine is currently indicated in Parkinson's disease in the United States.

Introduction

Chemotherapy-induced peripheral neuropathy (CIPN) is a severe and long lasting side effect caused by diverse anticancer agents that damage sensory and/or motor nerves. CIPN occurs in 30–70% of patients treated with specific categories of anticancer agents [1]. Symptoms of CIPN include numbness, pain, burning, tingling, heat/cold hyperalgesia, and mechanical allodynia, as well as reduced motor function. CIPN commonly presents a "stocking-glove" distribution with the most distal portions of the limb exhibiting the greatest deficits [2]. These symptoms usually begin after multiple doses of the chemotherapeutic agents, and progress as treatment continues. After the treatments end, they can resolve in a short time period, or persist as an after-effect of cancer therapy.

Oxaliplatin-associated CIPN is the most frequent cause of interruption of an otherwise successful therapy [3]. About 12% to 18% of patients experience the highest grade 3 CIPN evaluated on the National Cancer Institute's Common Terminology Criteria for Adverse Events (NCI-CTCAE) scale [4,5], when persistent neuropathy graded more than 2 usually results in complete discontinuation of the chemotherapy.

Oxaliplatin is a platinum compound indicated in solid tumor cancers [6,7], which induces peripheral neuropathies of two forms: an acute but reversible form [8] which manifests within hours following the first infusion and a chronic form that occurs following cumulative high doses of the drug and is non-reversible [9]. Several clinical manifestations characterize this condition, but hallmark symptoms include persistent distal chronic paresthesia, allodynia and thermoalgesia. Indeed, the severity of the pain endured by some patients may require treatment arrest, rendering this neuropathy a limiting-factor for this chemotherapy.

The mechanisms behind the neurotoxicity of chemotherapy are complex and are not fully understood [10,11]. Neurotoxicity may be due to chemotherapy interactions with DNA, mitochondrial perturbations, ion channel dysregulations, reactive oxygen balance modifications, kinases and / or glutamatergic neurotransmission dysfunction. The lesions can occur at the level of the dorsal root ganglia (DRG), at the level of the sensory neurons, associated with defects of axonal transport related to the microtubules or to degeneration of the axon. They may also affect Schwann cells by inducing dedifferentiation and mitochondrial [12] and satellite cell [13] dysfunction. The complexity of the involved mechanisms partly explains the lack of effective treatments to prevent CIPN.

Diabetic neuropathies (DN) are similar in their anatomo-pathological features to oxaliplatin-induced peripheral neuropathies, as they involve demyelination, axonal swelling and reduced cutaneous nerve fiber density [14,15]. A progressive development with sensory loss, pain and autonomic dysfunction are common symptoms [16]. Pathologically, DN is characterized by interrelated metabolic abnormalities with insulin deficiency and hyperglycemia as the initiating culprits [16]. The neuropathy accompanying type 2 DM (insulin resistance) and type 1 DM (insulin deficiency)

appears to differ, the former showing a milder axonal involvement and segmental myelin breakdown, whereas the latter shows a more severe axonal atrophy and axonal loss. The disorder does not only involve somatic peripheral nerves but also autonomic and central nerve tracts. Today no successful therapy exists for DN.

In both CIPN [13] and DN [16], myelin-forming Schwann cells of the peripheral nervous system are crucial for the proper function and maintenance of peripheral nerves. Schwann cells wrap around axons and thereby provide insulation, acceleration of electric signal propagation, and axonal protection and maintenance. Schwann cells are the main effectors for regeneration in a variety of peripheral neuropathic conditions [17–19], including inherited, inflammatory, toxic (e.g. CIPN), and DN, as well as traumatic injuries to peripheral nerve fibers.

Over the last two decades, fundamental progress have been made in understanding the molecular basis of Schwann cells biology with potential clinical applications in peripheral nerve disorders. Benztropine, an inhibitor of acetylcholine (ACh) muscarinic M1 and M3 receptors (mAChR), has been shown to promote oligodendrocyte precursor cells differentiation while allowing greater axonal remyelination than molecules currently prescribed to multiple sclerosis patients [20]. Interestingly, M3 and M1 mAChR are also expressed on peripheral myelin forming Schwann cells but their roles in the myelination process remain unclear.

Muscarinic acetylcholine receptors are widely expressed both in the central and peripheral nervous system, and are involved in relevant physiological processes like myelination and modulation of nociceptive stimuli [21,22]. Indeed, M1 and M3 muscarinic receptors agonist can block M channels thus increasing neuronal excitability, by contrast muscarinic M1 and M3 receptor antagonists can activate M channels and attenuate the discharge of sensory Aδ or C-fibers induced by heat stimulation. Interestingly, flupirtine, an M channel enhancer has been shown to reduce oxaliplatin-induced peripheral nerve hyperexcitability [23]. Morever the expression of muscarinic receptors in leucocytes has been known since early 1970s, their activation can modulate the inflammatory responses [24,25].

Targeting a particular pathway to prevent CIPN must be considered with caution, since additional treatments may directly or indirectly favor tumor growth or dissemination. Interestingly, in the case of muscarinic receptor blockade, several studies have highlighted the potential of targeting M3 muscarinic receptors to prevent tumor growth and metastases [26,27]. Furthermore, ACh-induced tumorigenesis has been reported in several organs that are commonly treated with oxaliplatin [26,28]. In addition, the differential distribution between mAChR subtypes could allow the specific targeting of tumor cells.

These observations of potential for both preventing neurotoxicity by promoting axonal protection as well as increasing the efficacy profile of neurotoxic chemotherapies, prompted us to investigate the effects of the mAChRs inhibitor, benztropine, associated with oxaliplatin, in vitro and in vivo on CIPN, DN and tumor growth.

Results

In vivo effects of oxaliplatin and benztropine on mouse cold hyperalgesia

To determine whether benztropine could abrogate oxaliplatin-induced peripheral neuropathy, cold hyperalgesia was evaluated in oxaliplatin-exposed mice treated or not with benztropine. After oxaliplatin cycle 1, the mean number of brisk lifts was over twice as high in oxaliplatin-treated mice

than in animals injected with vehicle alone (26.57 ± 2.45 with oxaliplatin *versus* 11.43 ± 1.13 with vehicle, $p = 0.0001$). The same changes were observed after the second injection of oxaliplatin (17.43 ± 1.70 with oxaliplatin *versus* 11.29 ± 0.84 with vehicle, $p = 0.0071$). Association with benztropine rescued this hyperalgesia from the first injection of oxaliplatin (17.71 ± 2.76 with oxaliplatin plus benztropine *versus* 11.43 ± 1.13 with vehicle, $p = 0.0566$) (Fig. 1).

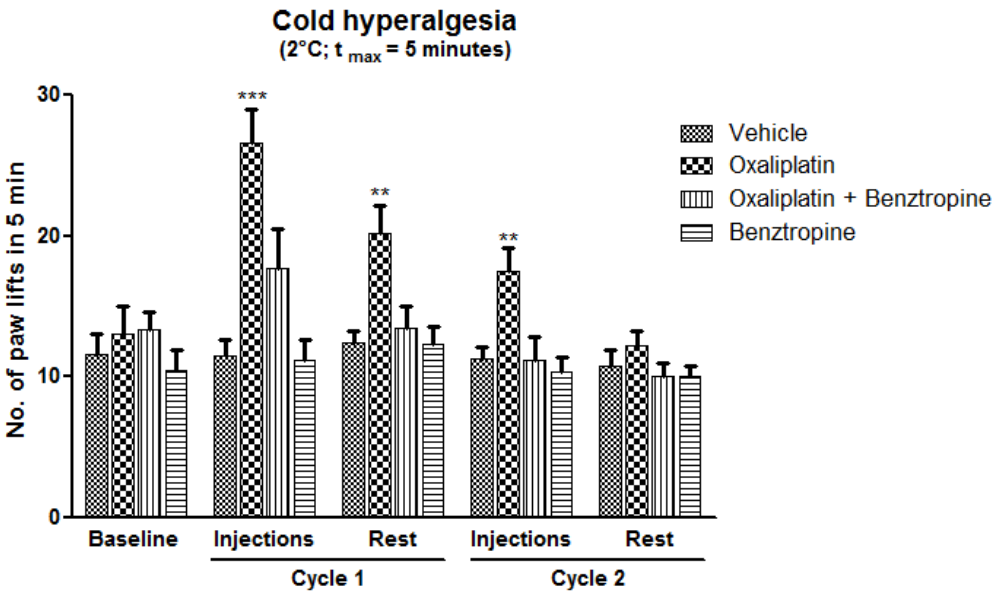

Figure 1. *In vivo* effects of oxaliplatin and benztropine on mouse cold hyperalgesia. Evaluation of hyperalgesia required two 5-day cycles of daily oxaliplatin (3 mg/kg). Control mice received either oxaliplatin or vehicle alone. Cold hyperalgesia was evaluated using a cold plate set at +2°C. Data are expressed as means ± SEM of 7 different mice under each condition. *$p < 0.05$, **$p < 0.01$, ***$p < 0.001$ *versus* vehicle.

In vivo effects of oxaliplatin and benztropine on mouse cold and tactile hypoesthesia

In addition to acute cold hyperalgesia, patients treated with oxaliplatin also suffer from permanent pathological thermal and tactile perception at their extremities. Mice injected with 10 mg/kg oxaliplatin developed diminished tactile perception from week 3 of treatment (0.2419 ± 0.0687 with oxaliplatin *versus* 0.0625 ± 0.0107 with vehicle, $p = 0.0151$) with a peak tactile hypoesthesia observed at the end of the testing period (at week 6, 0.7225 ± 0.0973 with oxaliplatin *versus* 0.1188 ± 0.0348 with vehicle, $p < 0.0001$). Mice treated with benztropine associated with the chemotherapy did not display these symptoms of altered tactile hypoesthesia at week 3 (0.1515 ± 0.0704 with oxaliplatin plus benztropine *versus* 0.0625 ± 0.0107 with vehicle, $p = 0.2212$) nor at any time point during the experiment (at week 6, 0.1575 ± 0.0458 with oxaliplatin plus benztropine *versus* 0.1188 ± 0.0348 with vehicle, $p = 0.5054$) (Fig. 2a). Mice injected with 10 mg/kg oxaliplatin developed reduced cold hypoesthesia from week 3 of treatment (13.13 ± 1.11 with oxaliplatin *versus* 17.25 ± 0.87 with vehicle, $p = 0.0066$). The most severe cold hypoesthesia in oxaliplatin-treated mice was observed at the end of the testing period (at week 6, 5.44 ± 0.36 with oxaliplatin *versus* 16.19 ± 0.81 with vehicle, $p < 0.0001$). Mice treated with benztropine associated with the chemotherapy did not display these symptoms of altered cold hypoesthesia at week 3 (15.56 ± 1.00 with oxaliplatin plus benztropine *versus* 17.25 ± 0.87 with vehicle, $p = 0.2145$) nor at any time point during the experiment (at week 6, 13.75 ± 0.99 with oxaliplatin plus benztropine *versus* 16.19 ± 0.81 with vehicle, $p = 0.0659$) (Fig. 2b).

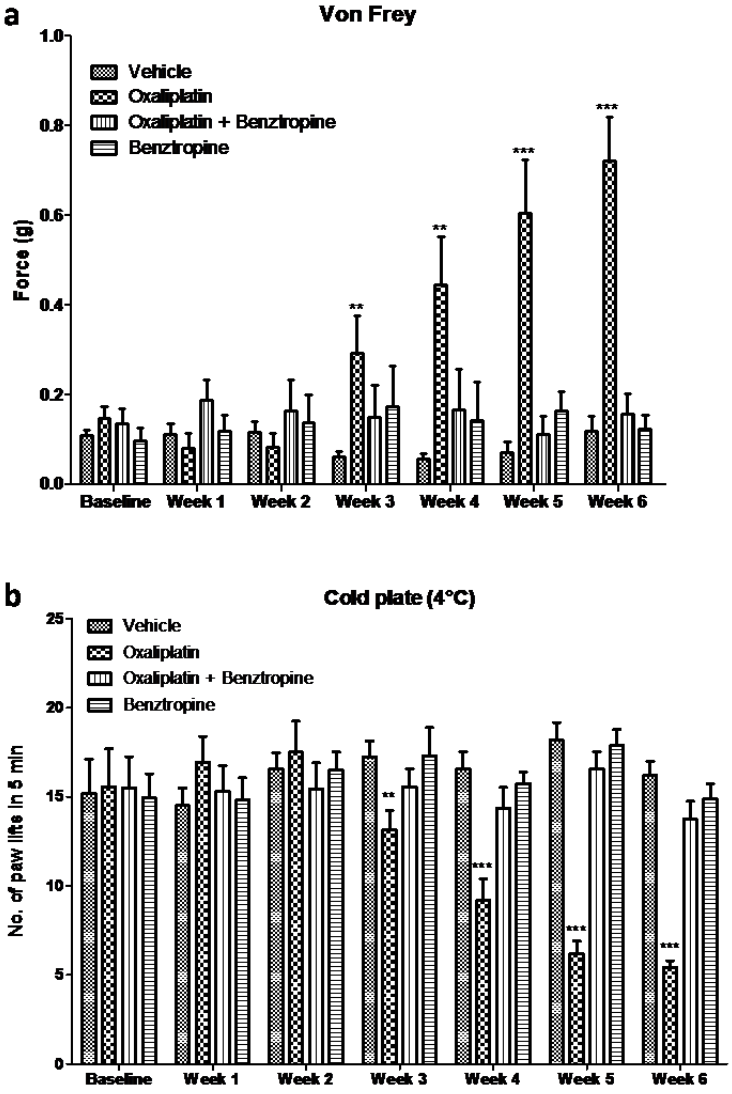

Figure 2. *In vivo* effects of oxaliplatin and benztropine on oxaliplatin peripheral neuropathies. (a) von Frey test and (b) cold-plate test. Experimental mice received oxaliplatin (10 mg/kg) weekly and benztropine (10 mg/kg) daily for 6 weeks. Control mice received either oxaliplatin or vehicle alone. Both the von Frey and the cold-plate tests were performed on a weekly basis. Data are expressed as means ± SEM of 8 different mice under each condition. *$p < 0.05$, **$p < 0.01$, ***$p < 0.001$ *versus* vehicle.

In vivo effects of benztropine on diabetic mouse tactile hypoesthesia and hot hyperesthesia

Since peripheral neuropathies can result from causes other than oxaliplatin infusions, we sought to investigate whether benztropine could alleviate painful symptoms brought about by other etiologies. Mice models of streptozotocin (STZ)-induced diabetes are robust and well-documented [29]. These mice develop peripheral neuropathies similar to those witnessed in diabetic patients. Diabetic mice developed diminished tactile perception from week 1 (0.1780 ± 0.0398 in diabetic mice *versus* 0.0636 ± 0.0173 in non-diabetic mice, $p = 0.0168$). Peak tactile hypoesthesia in diabetic mice was observed at the end of the testing period (week 6, 1.0800 ± 0.0800 in diabetic mice *versus* 0.1950 ± 0.0481 in non-diabetic mice, $p < 0.0001$). Diabetic mice treated with benztropine did not display these symptoms of altered tactile hypoesthesia at week 1 (0.0768 ± 0.0191 in benztropine-treated diabetic mice *versus* 0.0636 ± 0.0173 in non-diabetic mice, $p = 0.6153$) nor at any time point during the experiment (at week 6, 0.1200 ± 0.0355 in benztropine-treated diabetic mice *versus* 0.1950 ± 0.0481 in non-diabetic mice, $p = 0.2253$) (Fig. 3a). Diabetic mice developed transient heat hyperalgesia from week 1 (7.70 ± 0.68 in diabetic mice *versus* 11.00 ± 0.75 in non-diabetic mice, $p = 0.0043$). Diabetic mice treated with benztropine did not display these symptoms of exacerbated

pain to the hot plate at week 1 (10.00 ± 0.97 in benztropine-treated diabetic mice *versus* 11.00 ± 0.75 in non-diabetic mice, $p = 0.4232$) or symptoms of hot hypoalgesia at week 6 (9.90 ± 0.85 in benztropine-treated diabetic mice *versus* 9.20 ± 0.93 in non-diabetic mice, $p = 0.5849$), at which it peaked in diabetic mice (17.20 ± 1.36 in diabetic mice *versus* 9.20 ± 0.93 in non-diabetic mice, $p = 0.0001$) (Fig. 3b). Benztropine corrected both thermal perception abnormalities, namely transient hot hyperalgesia and persistent hot hypoalgesia, as well as tactile hypoesthesia in diabetic mice.

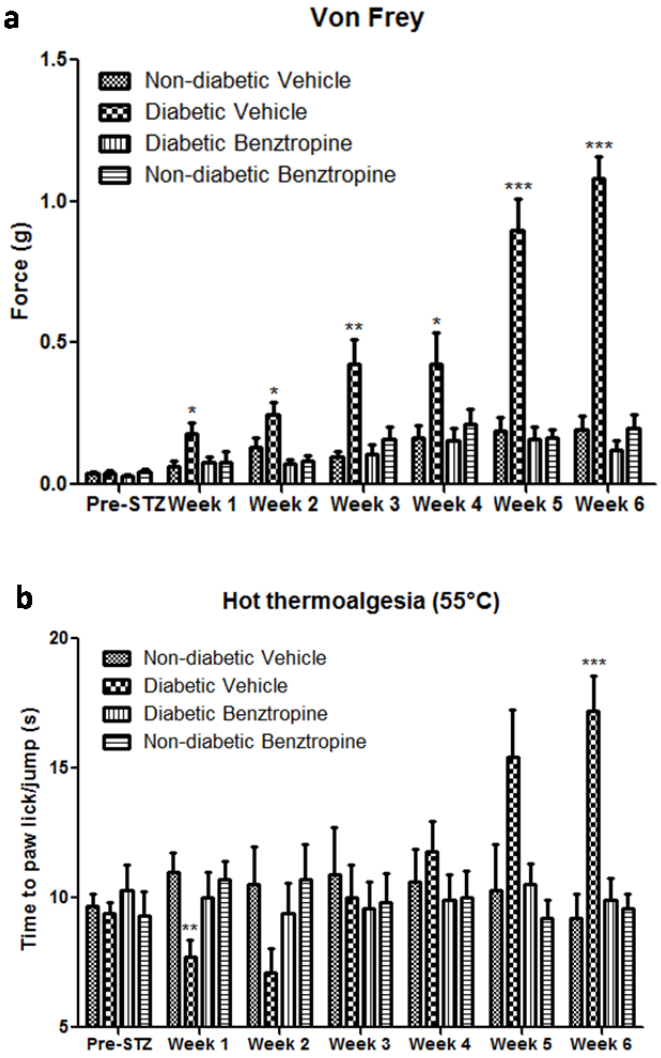

Figure 3. *In vivo* effects of oxaliplatin and benztropine on diabetes-induced peripheral neuropathies. (a) von Frey test and (b) hot-plate test. Experimental diabetic mice received benztropine (10 mg/kg) daily for 6 weeks. Control mice received either benztropine or vehicle alone. Both, the von Frey as well as the hot-plate tests were performed on a weekly basis. Data are expressed as means ± SEM of 8 different mice under each condition. *$p < 0.05$, **$p < 0.01$, ***$p < 0.001$ *versus* vehicle.

In vivo effects of benztropine on sensory and neuromuscular excitability of oxaliplatin-treated and diabetic mice

Oxaliplatin-treated mice presented significant alterations, consistent with membrane hyperexcitability, in sensory excitability variables, compared with control animals (*i.e.*, mice injected with vehicle). In particular, the maximal CNAP amplitude was significantly reduced in oxaliplatin-treated mice compared to control mice (0.026 ± 0.012 with oxaliplatin *versus* 0.041 ± 0.012 with vehicle, $p = 0.0137$). Associating benztropine to the chemotherapy abrogated this reduction (0.037 ± 0.009 with oxaliplatin plus benztropine *versus* 0.041 ± 0.012 with vehicle, $p =$

0.4060), while benztropine alone did not alter maximal CNAP (0.040 ± 0.009 with benztropine *versus* 0.041 ± 0.012 with vehicle, $p = 0.8096$) (Fig. 4a). The stimulus intensity required to give 50% of maximal CNAP amplitude was also altered in mice treated with oxaliplatin (0.179 ± 0.059 with oxaliplatin *versus* 0.259 ± 0.038 with vehicle, $p = 0.0041$). Associating benztropine to the chemotherapy abrogated this reduction (0.256 ± 0.024 with oxaliplatin plus benztropine *versus* 0.259 ± 0.038 with vehicle, $p = 0.8090$), while benztropine alone did not alter this variable (0.290 ± 0.033 with benztropine *versus* 0.259 ± 0.038 with vehicle, $p = 0.0909$) (Fig. 4b). Finally, an increased latency was observed in oxaliplatin-treated mice (3.552 ± 0.202 with oxaliplatin *versus* 3.163 ± 0.218 with vehicle, $p = 0.0014$). This increase was not observed when mice treated with the chemotherapy also received benztropine (3.187 ± 0.220 with oxaliplatin plus benztropine *versus* 3.163 ± 0.218 with vehicle, $p = 0.8284$) or when mice received benztropine alone (3.137 ± 0.261 with benztropine *versus* 3.163 ± 0.218 with vehicle, $p = 0.8230$) (Fig. 4c). It is worth noting that the

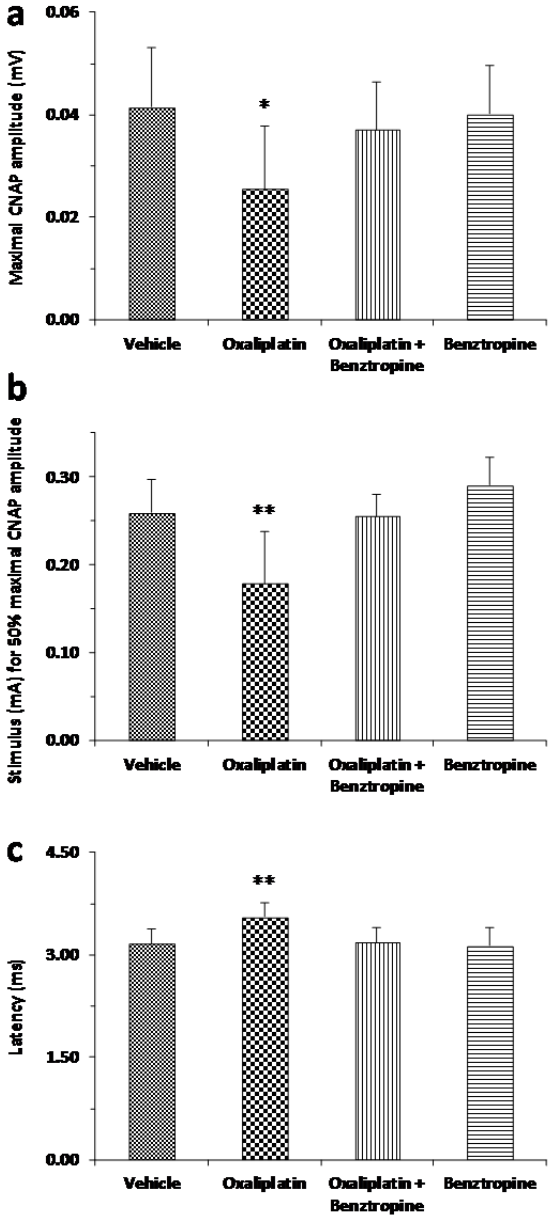

Figure 4. *In vivo* effects of oxaliplatin and benztropine on mouse sensory excitability variables. Histograms of mean values ± SD of maximal CNAP peak amplitude (a), stimulus intensity necessary to evoke 50% of maximal CNAP amplitude (b), and latency (c) determined from recordings at the tail base in response to caudal nerve stimulation in mice treated for 6 weeks with vehicle (n = 9), oxaliplatin (n = 10), oxaliplatin plus benztropine (n = 10) or benztropine alone (n = 10). *$p < 0.05$, **$p < 0.01$ *versus* vehicle.

sensory alterations detected in oxaliplatin-treated mice were consistent with a decreased nerve conduction velocity, suggesting an apparent reduction in the number of fast-conducting fibers or decrease of density and/or functioning of transient sodium channels, and a modification in the voltage dependence of these channels.

Oxaliplatin-treated and diabetic mice also presented significant alterations, consistent with membrane hyperexcitability, in neuromuscular (motor) excitability waveforms and derived variables, compared with animals injected with vehicle (Supplementary Fig. 1 and 2; Supplementary Table 1). These alterations mainly consisted of *(i)* an enhanced CMAP amplitude and a reduced stimulus intensity to evoke 50% of maximal CMAP amplitude, suggesting an apparent decreased density and/or functioning of fast potassium channels and modification in the voltage dependence of transient sodium channels, respectively, with no change in the latency, *i.e.*, no modification in the neurotransmission velocity; *(ii)* reduced minimum and hyperpolarizing slopes of the current–threshold relationship, indicating decreased density and/or functioning of cyclic nucleotide-gated channels; *(iii)* increased threshold changes in response to depolarizing and/or hyperpolarizing currents (threshold electrotonus), likely caused by reduced density and/or functioning of potassium channels; and *(iv)* lower superexcitability (recovery cycle), reflecting again fast potassium channel dysfunction. These alterations were not detected, or were greatly reduced, in oxaliplatin-treated and diabetic mice injected with benztropine, or in animals administered with benztropine alone.

In vitro effects of oxaliplatin and benztropine on excitability of mouse DRG sensory neurons

The *in vitro* effects of oxaliplatin, associated or not with benztropine, were assessed on the resting membrane and action potentials recorded from primary cultures of mouse DRG sensory neurons, using whole-cell patch-clamp technique (Fig. 5).

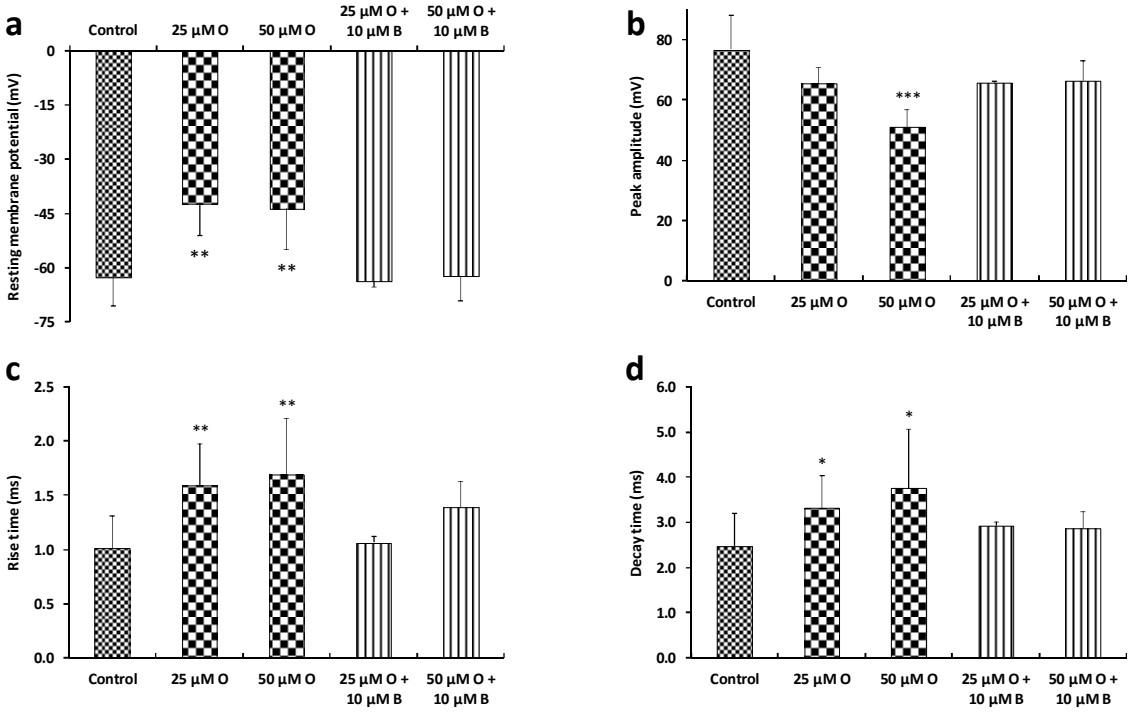

Figure 5. *In vitro* effects of oxaliplatin, associated or not with benztropine, on excitability of mouse DRG sensory neurons, using whole-cell patch-clamp technique. Resting membrane potential (a), and action potential peak amplitude (b), rise time (c) and decay time (d) measured from recordings performed on DRG neurons before (control) and 10-20 min after addition of first 25-50 µM oxaliplatin (O) and then 25-50 µM oxaliplatin plus 10 µM benztropine (B) to the standard physiological medium. Mean ± SD of 5-18 neurons. *p = 0.010-0.014, **p = 0.002-0.005 and ***p < 0.001 *versus* control.

Recordings were performed on relatively small neurons since their mean ± SD cell diameter (determined from their membrane capacity) was 21.6 ± 4.5 µm (n = 18). Under control conditions, two types of responses were recorded from neurons stimulated by 100-ms current test-pulses: a single action potential (tonic response) from 39% (7/18) of cells, and more than one action potential (phasic response) from 61% (11/18) of cells. The mean ± SD ratio of the number of action potentials on the current intensity necessary to evoke action potentials was 0.007 ± 0.001 pA^{-1} (n = 18). This ratio was significantly increased ($p = 0.024$) to 0.011 ± 0.002 pA^{-1} (n = 11) in the presence of 50 µM oxaliplatin, due to both an increased number of action potentials in response to 100-ms current test-pulses and a decreased current intensity necessary to evoke action potentials, indicating membrane hyperexcitability of these neurons. When oxaliplatin (50 µM) was added together with benztropine (10 µM) to the standard external medium, the ratio returned to 0.005 ± 0.002 pA^{-1} (n = 9), *i.e.*, mean ± SD values were not statistically different ($p = 0.148$) from those determined under control conditions. The addition of oxaliplatin (25 or 50 µM) to the external medium bathing the neurons produced *(i)* about 20-mV membrane depolarization identified by a reduced resting membrane potential, *(ii)* a significant decreased peak amplitude, and *(iii)* significant increased rise and decay times of action potentials, compared to control conditions. These modifications, indicating alterations in the density and/or functioning of both sodium and potassium channels, were greatly reduced, if not completely reversed, when oxaliplatin was added together with benztropine (10 µM) to the external standard medium.

Ex vivo effects of oxaliplatin and benztropine on mouse sciatic nerve fiber morphology and myelin content

The morphology of myelinated axons of mouse sciatic nerves was assessed using confocal microscopy. Quantification of morphometric parameters of single myelinated axons revealed a significant increase in the nodal diameter, length and volume, as functions of the internodal diameter, in mice injected for 6 weeks with oxaliplatin, compared to vehicle-treated animals (Fig. 6, left panels; Supplementary Table 2). These results are likely the consequence of oxaliplatin-induced

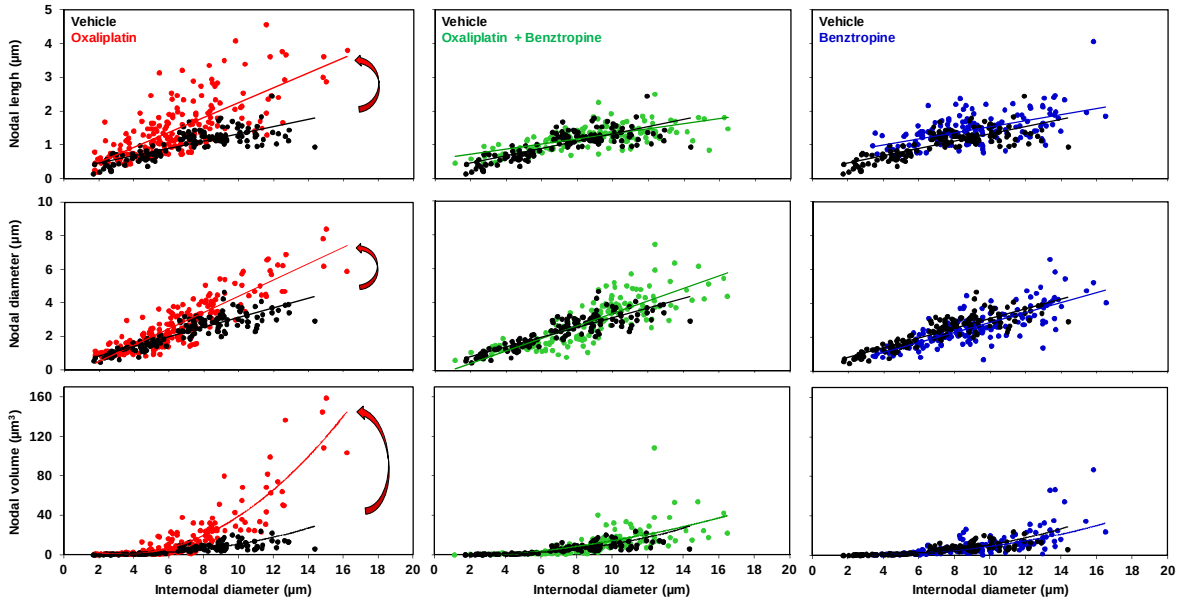

Figure 6. *Ex vivo* effects of oxaliplatin and benztropine on the morphology of myelinated axons isolated from mouse sciatic nerves, using confocal microscopy. Representations of nodal length, diameter and volume, as functions of internodal diameter, of myelinated axons isolated from mice (n = 4 in each group) injected with vehicle (black closed circles, n = 137), oxaliplatin (red closed circles, n = 206), oxaliplatin plus benztropine (green closed circles, n = 150) or benztropine alone (blue closed circles, n = 160) for 6 weeks. The curves represent the linear (upper and middle panels) or non-linear (lower panels) fits of data points with R^2 (correlation coefficients) between 0.441 and 0.877. In left panels, the arrows underline the effects of oxaliplatin.

membrane hyperexcitability. In these animals, a reduction of the internodal diameter was also observed, which may reflect either a preferential loss of large myelinated nerve fibers or an alteration in myelin sheath layers surrounding the axons. These alterations of morphometric parameters were greatly reduced, if not absent, in mice injected for 6 weeks with oxaliplatin plus benztropine (Fig. 6, middle panels; Supplementary Table 2) or benztropine alone (Fig. 6, right panels; Supplementary Table 2).

The myelin sheaths of sciatic nerves from experimental and control groups of mice were also assessed using electronic microscopy. Analyses revealed a demyelination in oxaliplatin-treated mice compared to animals injected with vehicle, oxaliplatin plus benztropine or benztropine alone (Fig. 7).

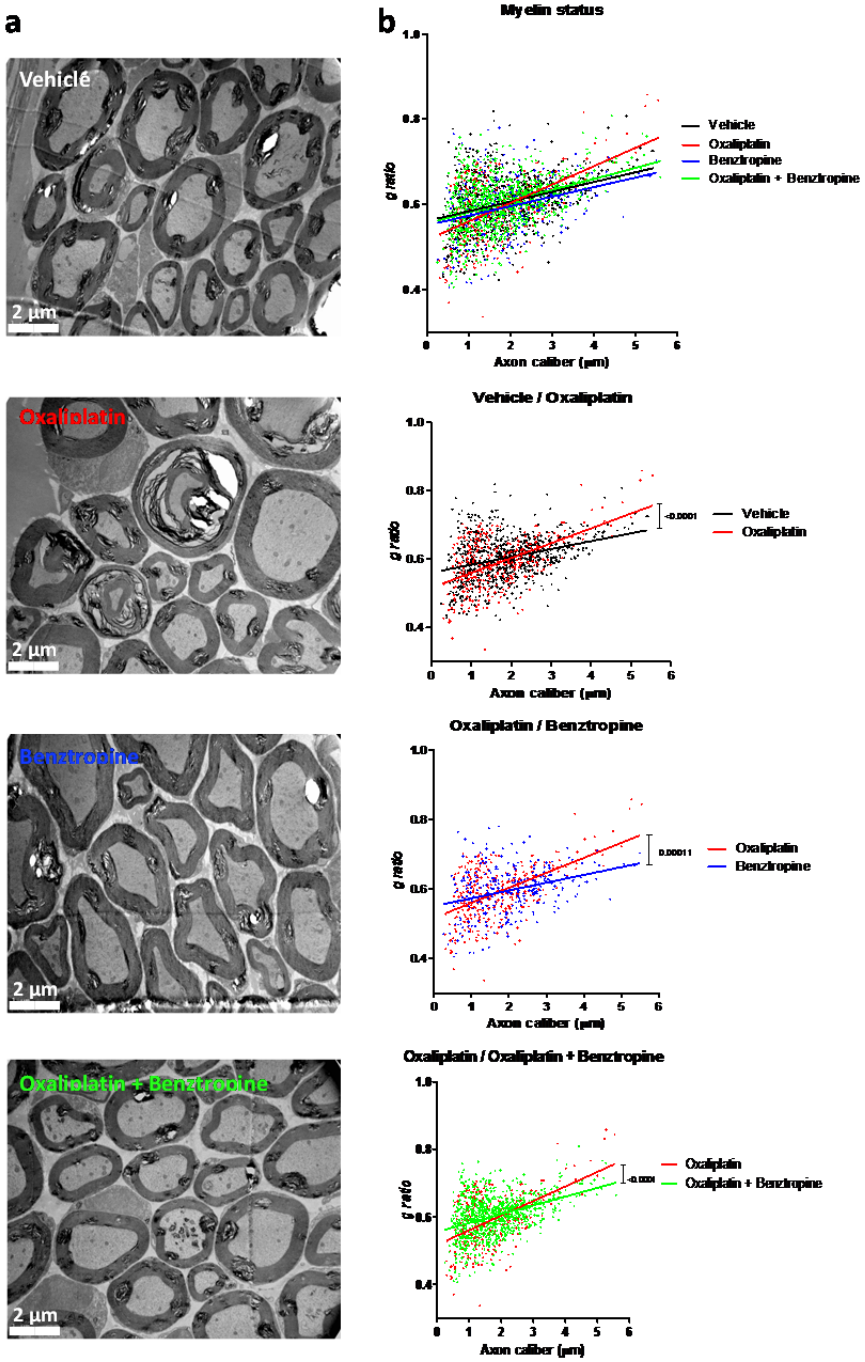

Figure 7. Effect of benztropine on demyelination and axonal atrophy in oxaliplatin-treated mice. (a) Representative images of EM micrographs of ultrathin cross-sections of sciatic nerves from vehicle, oxaliplatin, benztropine and oxaliplatin plus benztropine animals at 6 weeks. (b) Quantification of myelin state though g-ratio analysis reported to axonal caliber. At least 200 axons per animal (n = 2-3) were analyzed. The curves are linear regression fits of data points. *$p < 0.05$, **$p < 0.01$.

Semi-automated computerized measurement of myelin thickness allowed the quantification of the profound demyelination in sciatic nerves from oxaliplatin mice (0.0344 ± 0.0037 with oxaliplatin *versus* 0.0233 ± 0.0023 with vehicle, $p = 0.007$). Associating benztropine to the chemotherapy abrogated the reduction in myelin sheath thickness observed in oxaliplatin mice (0.0261 ± 0.0019 with oxaliplatin plus benztropine *versus* 0.0233 ± 0.0023 with vehicle, $p = 0.346$). Benztropine did not impair myelin formation nor did it lead to excessive myelination (0.0224 ± 0.0038 with benztropine *versus* 0.0233 ± 0.0023 with vehicle, $p = 0.842$).

Ex vivo study of myelin protein content in sciatic nerves

The myelin basic protein (MBP) expression was reduced in oxaliplatin-treated mice (0.5825 ± 0.1014 with oxaliplatin *versus* 0.7125 ± 0.1409 with vehicle, $p = 0.4823$), while co-administration of benztropine with the chemotherapy rescued this reduced expression of this key myelin protein (0.6767 ± 0.1172 with oxaliplatin plus benztropine *versus* 0.7125 ± 0.1409 with vehicle, $p = 0.8603$). It is worth nothing that MBP expression was identical in mice receiving benztropine alone and control animals (0.7075 ± 0.2781 with benztropine *versus* 0.7125 ± 0.1409 with vehicle, $p = 0.8603$) (Fig. 8).

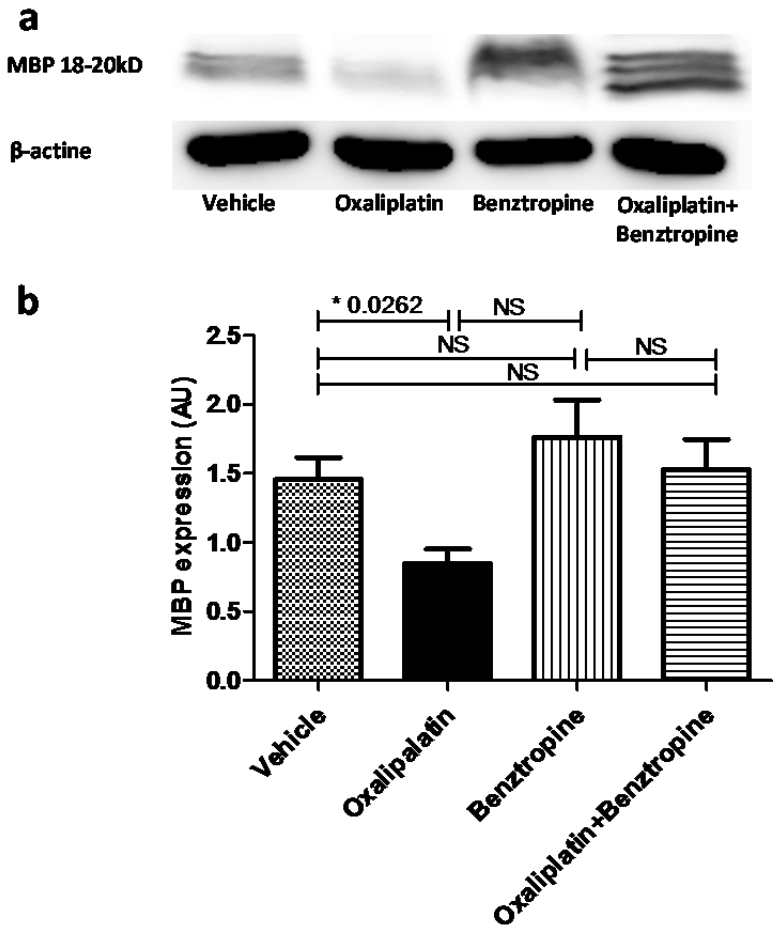

Figure 8. Effect of benztropine on MBP expression in the sciatic nerves of oxaliplatin-treated mice. Western blot analyses of total protein lysates from brain sciatic nerves of control, and treated mice. (a) panel shows detection of MBP and (b) panel shows anti-β-actin for loading control. NS: non-significant.

Ex vivo effects of oxaliplatin and benztropine on mouse cutaneous nerve fiber density

The density of cutaneous nerve fibers was examined in the paws of mice injected with vehicle, oxaliplatin, oxaliplatin plus benztropine or benztropine alone for 6-8 weeks (Fig. 9). Staining of the nerve fibers with PGP9.5 antibody revealed a reduced cutaneous nerve fiber density in paw skin of

oxaliplatin-treated mice (7.67 ± 0.99 with oxaliplatin *versus* 16.33 ± 1.87 with vehicle, $p = 0.0022$). Benztropine abrogated this alteration in oxaliplatin-treated mice since the density of PGP9.5-stained nerves was maintained in these animals (13.50 ± 1.56 with oxaliplatin plus benztropine *versus* 16.33 ± 1.87 with vehicle, $p = 0.2728$). Benztropine alone did not alter cutaneous nerve fiber's integrity (15.00 ± 2.85 with benztropine *versus* 16.33 ± 1.87 with vehicle, $p = 0.7042$).

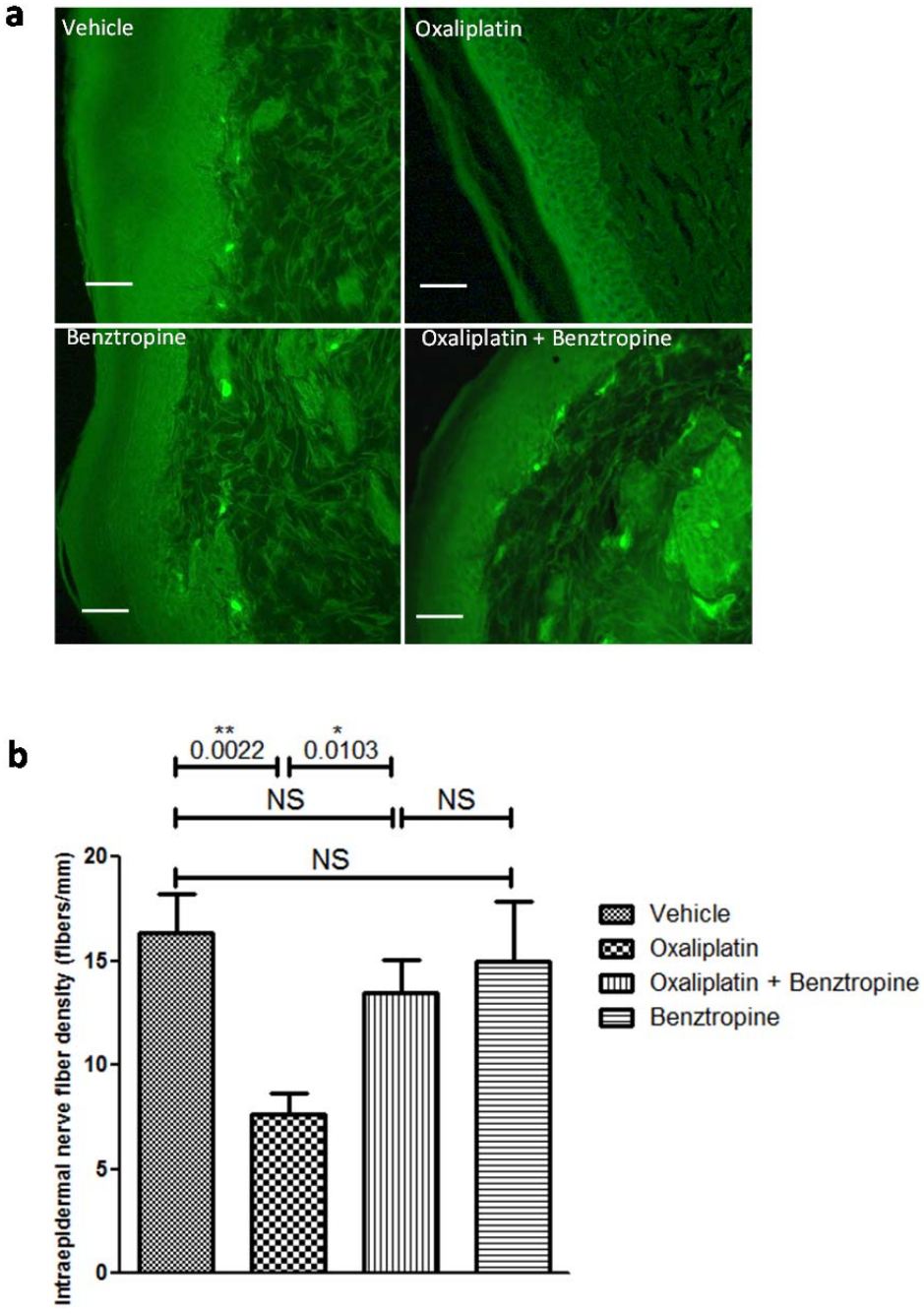

Figure 9. Effect of benztropine cutaneous nerve fiber density reduction induced by oxaliplatin. (a) Representative images of staining with PGP9.5 of cutaneous nerve fibers. (b) Analysis of cutaneous nerve fiber density from paw skin samples (6 µm) of mice treated for 6 weeks with vehicle, oxaliplatin, oxaliplatin plus benztropine or benztropine alone. Mean ± SEM of 8 mice. *$p < 0.05$, **$p < 0.01$. NS: non-significant. Scale bar = 50 µm.

Ex vivo effects of oxaliplatin and benztropine on systemic inflammatory markers

In order to evaluate the systemic effects of benztropine on pro-inflammatory cytokine levels, serum samples were analyzed (Fig. 10). Sera IL-6 levels were significantly increased in the oxaliplatin-

treated group (21.14 ± 1.07 ng/mL with oxaliplatin *versus* 15.87 ± 1.27 ng/mL with vehicle, p = 0.0034). Associating benztropine to the chemotherapy prevented this systemic inflammation (16.97 ± 0.81 ng/mL with oxaliplatin plus benztropine *versus* 15.87 ± 1.27 ng/mL with vehicle, p = 0.4674, and *versus* 21.14 ± 1.07 ng/mL with oxaliplatin, p = 0.0042). Benztropine alone did not induce any changes in IL-6 levels (15.12 ± 1.28 ng/mL with benztropine *versus* 15.87 ± 1.27 ng/mL with vehicle, p = 0.6829) (Fig. 10a). Sera TNF-α levels were also significantly increased in the oxaliplatin-treated group compared to the control group (84.18 ± 6.86 pg/mL with oxaliplatin *versus* 58.36 ± 7.27 pg/mL with vehicle, p = 0.0150). Similar to its effects on IL-6 levels, benztropine also prevented the significant increase in TNF-α levels observed in oxaliplatin-treated-animals (54.36 ± 5.17 pg/mL with oxaliplatin plus benztropine *versus* 58.36 ± 7.27 pg/mL with vehicle, p = 0.6570, and *versus* 84.18 ± 6.86 pg/mL with oxaliplatin, p = 0.0016). Benztropine on its own induced a slight, but non-significant, decrease in TNF-α levels (47.30 ± 5.17 pg/mL with benztropine *versus* 58.36 ± 7.27 pg/mL with vehicle, p = 0.2246) (Fig. 10b).

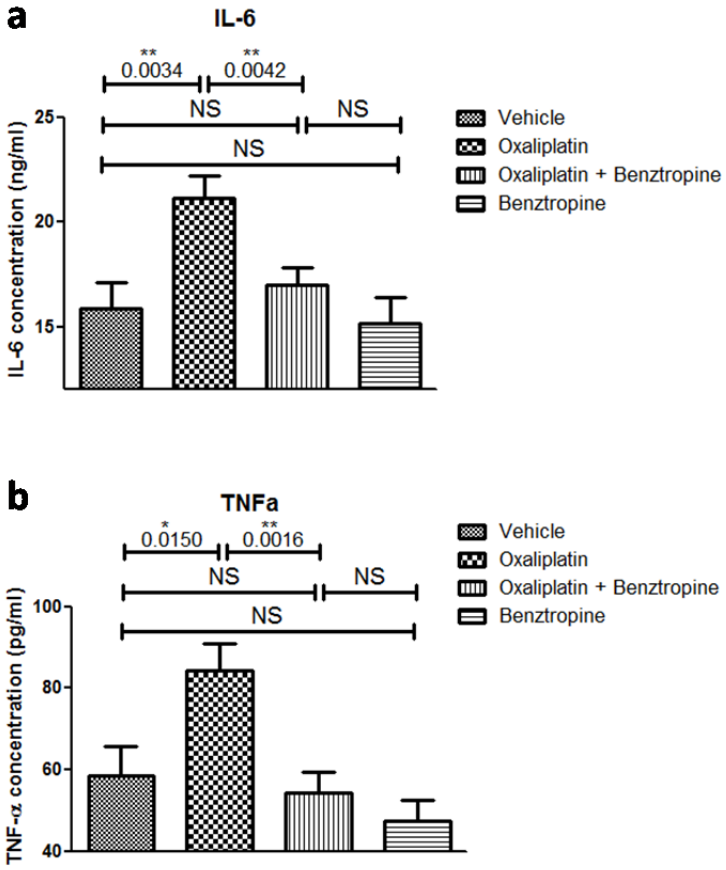

Figure 10. Sera inflammatory markers. (a) ELISA-quantified levels of IL-6 in sera from mice treated for 6 weeks with vehicle, oxaliplatin, oxaliplatin plus benztropine or benztropine alone. (b) ELISA-quantified levels of TNF-α in sera from mice treated for 6 weeks with vehicle, oxaliplatin, oxaliplatin plus /benztropine or benztropine alone. Data are mean ± SEM of 8 mice. *p < 0.05, **p < 0.01, ***p < 0.001 *versus* vehicle. NS: non-significant.

In vivo effects of benztropine on oxaliplatin-induced tumor growth in mice

Results obtained from neurological tests provided a rationale to use benztropine as a neuroprotective drug. However, further data regarding its effect on oxaliplatin efficacy had to be gathered to guarantee its safety in addressing the primary aspect of the condition which is tumor growth (Fig. 11). From day 6 of treatment, benztropine displayed antitumor efficacy upon

association with oxaliplatin (tumor size of 333.5 ± 42.3 mm^3 with oxaliplatin plus benztropine *versus* 832.1 ± 105.8 mm^3 with vehicle, $p = 0.0009$). Moreover, from day 6 treatment, benztropine potentiated the chemotherapy response (tumor size of 333.5 ± 42.3 mm^3 with oxaliplatin plus benztropine *versus* 624.8 ± 69.8 mm^3 with oxaliplatin, $p = 0.0039$), while oxaliplatin alone had not yet demonstrated antitumor efficacy (tumor size of 624.8 ± 69.8 mm^3 with oxaliplatin *versus* 832.1 ± 105.8 mm^3 with vehicle, $p = 0.1279$). At the end of the experiment, when the largest tumors had reached ethical guidelines' endpoint, mice which received benztropine associated with oxaliplatin presented the lowest tumor burden (687.5 ± 103.3 mm^3 with oxaliplatin plus benztropine *versus* 4721.0 ± 560.0 mm^3 with vehicle, $p < 0.0001$). In addition, mice which received benztropine alone displayed smaller, although non-significant, tumors compared to control mice (4132.0 ± 522.8 mm^3 with benztropine *versus* 4721.0 ± 560.0 mm^3 with vehicle, $p = 0.4571$).

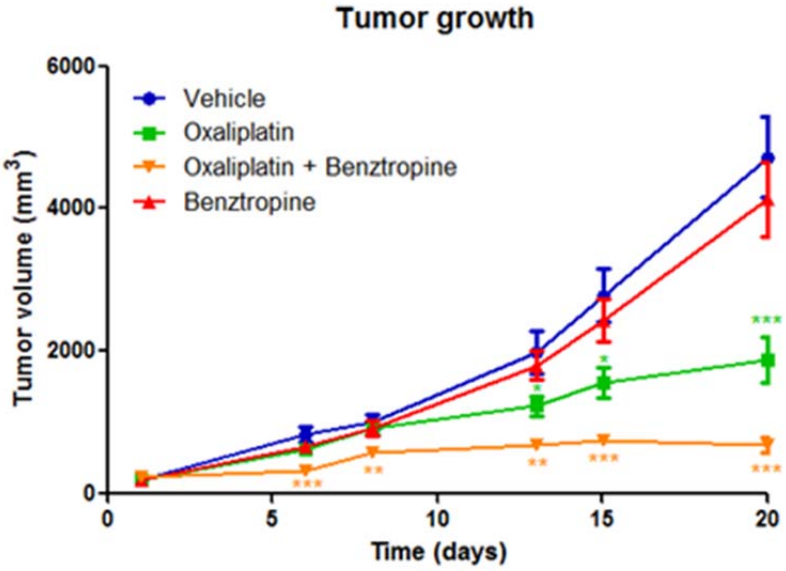

Figure 11. Benztropine prevents tumor growth and displays a synergistic antitumoral effect when associated with oxaliplatin in an ectopic model of colorectal cancer. Tumor size in mice injected subcutaneously into the back with 106 CT26 cells and treated with vehicle, oxaliplatin, oxaliplatin associated with benztropine or benztropine alone. Data are mean ± SEM of 8 tumor volume under each condition. *$p < 0.05$, **$p < 0.01$, ***$p < 0.001$ *versus* vehicle.

In vitro effects of oxaliplatin associated or not with benztropine on cultured cell viability

The *in vitro* neuroprotective potential of benztropine on oxaliplatin-induced peripheral neuropathies was assessed on N2a neuron-like cells. The effects of benztropine on oxaliplatin-induced anti-tumor effect were also evaluated *in vitro* on CT26 colon carcinoma cell lines. Our results indicate that oxaliplatin has a cytotoxic effect on both N2a and CT26 cells. Benztropine modulates cell viability in a cell-type-dependent manner. Benztropine potentiated oxaliplatin cytotoxicity on CT26 cells (Fig. 12a). Inversely, in benztropine-treated neuron-like N2a cells, the cytotoxicity of oxaliplatin was reduced with a viability increased from 56% without benztropine to 70% with benztropine (Fig. 12b). Moreover, in cells treated with 6.25µM oxaliplatin, co-incubation with 15 µM of benztropine induced a significant decrease of GSH in CT26 cells (2141±120 *versus* 2931±142 in untreated cells, $p<0.05$, Fig. 12c) but a significant increase of GSH in N2a (18344±634 *versus* 11355±934 in untreated cells, $p<0.001$, Fig. 12d). ROS production evidenced by H2DCFDA staining was stimulated in both cell types treated with oxaliplatin. However, benztropine at a concentration of 7.5 and 15 µM decreased oxaliplatin-induced ROS production in N2a cells ($p<0.05$) (Fig. 12f) and, in

contrast, 15 µM of benztropine increased oxaliplatin-induced ROS production in CT26 cells ($p<0.05$ to $p<0.01$) (Fig. 12e).

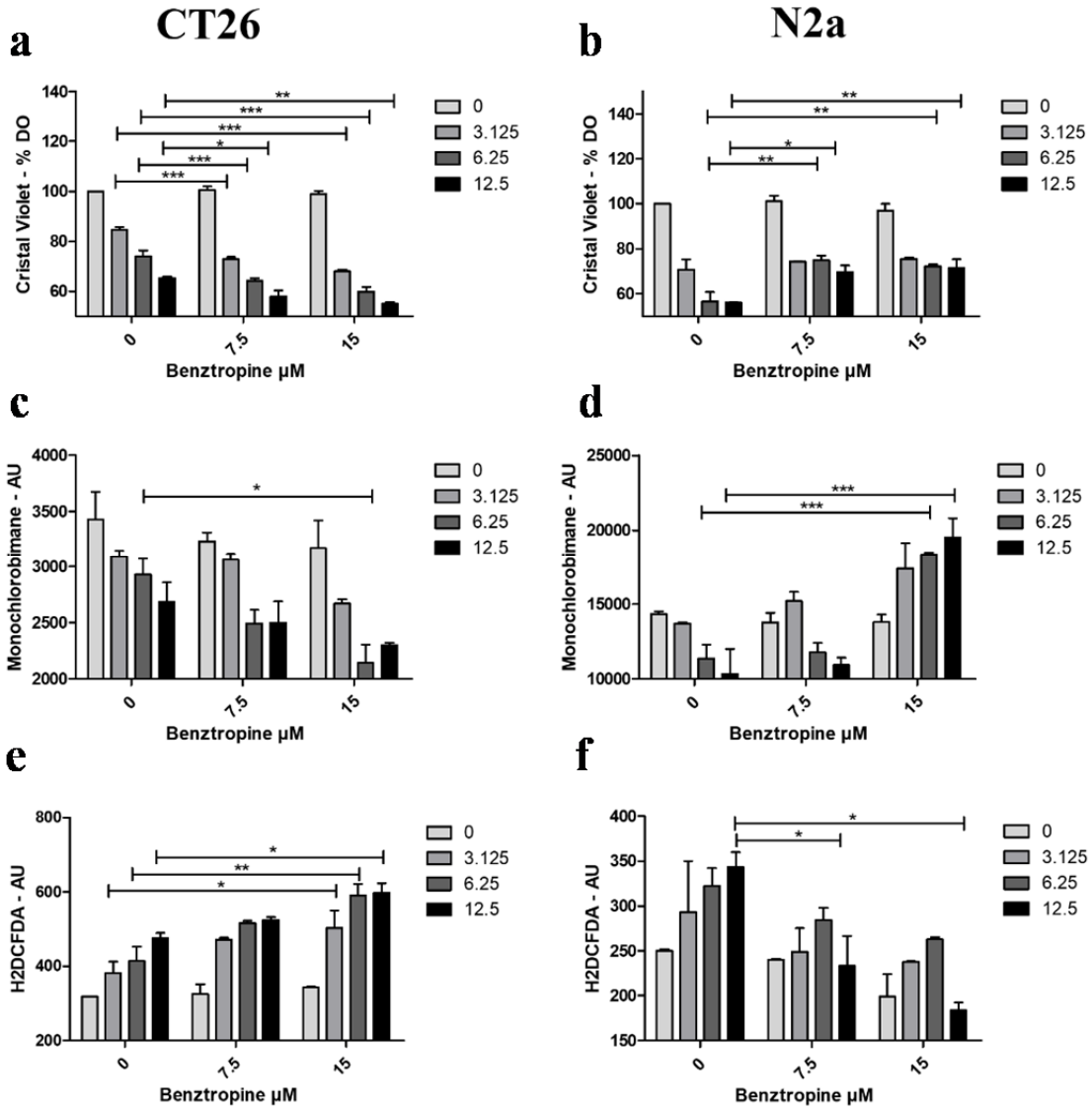

Figure 12. *In vitro* effects of oxaliplatin associated or not with benztropine on cell viability, GSH and ROS production. Viability was expressed as percent ± SEM *versus* cells in culture medium alone (100% viability) in CT26 cells (a) and N2a cells (b). GSH was measured using the monochlorobimane dye in CT26 cells (c) and N2a cells (d). ROS generation was measured using H2DCFDA fluorescent emission when converted to the highly fluorescent DCF in CT26 cells (e) and N2a cells (f). Data from at least 4 independent experiments have been pooled and were expressed as means ± SEM of triplicates. $*p < 0.05$, $**p < 0.01$ *versus* oxaliplatin.

Discussion

Peripheral neuropathy is one of the most prevalent neurologic conditions encountered by physicians of all specialties [30] and is frequently associated with viral, toxic or metabolic etiologies [31]. Despite its high prevalence, no efficient curative treatment is available to decrease peripheral neuropathic pain and disability [32]. In this report, we demonstrate that benztropine, an inhibitor of acetylcholine (ACh) muscarinic M1, M2 and M3 receptors (mAChR) [20], improves both acute and chronic clinical symptoms of experimental peripheral neuropathies in mice induced either by treatment with the chemotherapeutic drug oxaliplatin {Citation}or with streptozotocin (STZ) in a model of diabetes-induced peripheral neuropathy [29,33].

In order to better understand the mechanisms of this protection at neuronal levels, we performed electrophysiological tests to evaluate sensory and neuromuscular excitability. Oxaliplatin-treated mice presented significant reductions of the maximal CNAP amplitude and of the stimulus intensity required to give 50% of maximal CNAP as well as an increase in latency, both these signs being associated with membrane hyperexcitability. The sensory alterations detected in oxaliplatin-treated mice were consistent with a decreased nerve conduction velocity, suggesting an apparent reduction in the number of fast-conducting fibers or a decrease of density and/or functioning of transient sodium channels, and a modification in the voltage dependence of these channels. These alterations were all prevented by treatment with benztropine. The *in vitro* effects of oxaliplatin on the resting membrane and action potentials recorded from primary cultures of mouse DRG sensory neurons using whole-cell patch-clamp showed modifications characteristic of alterations in the density and/or functioning of both sodium and potassium channels. These alterations were greatly reduced, if not completely reversed, when the anticancer agent was added together with benztropine (10 µM) to the external standard medium.

Oxaliplatin is known to exhibit a tetrodotoxin-like inhibitory effect on neuronal voltage-gated sodium (Na+) channels [34–36]. It remarkably slows their inactivation and reduces the peak Na+ current, leading to an increase in the duration of the relative refractory period of sensory neurons that become hyperexcitable. Oxaliplatin may also affect the Na+ channels indirectly *via* the chelation of extracellular calcium ions by its metabolite oxalate (diaminocyclohexane-platinum-C2O4) [34]. Peripheral nerve axonal excitability studies performed after oxaliplatin administration *in vivo* have revealed acute abnormalities in sensory nerve function related to Na+ channel dysfunction, including decreased refractoriness and increased superexcitability [37]. The effects of oxaliplatin on the Nav1.6 voltage-gated Na+ channel isoforms have been associated with the development of unique neuropathy symptoms such as cold-aggravated peripheral pain [38,39]. In rat hippocampal neurons, muscarinic receptor agonists modulate Na+ channel activity through activation of PKC [40]. In the periphery, the implication of PKC activation in nociceptive neurons has been largely studied and linked to hyperexcitability and hyperalgesia through upregulation of both Nav1.8 and Nav1.9 [41,42]. Blocking PKC by muscarinic antagonists could be relevant to prevent peripheral neuropathies, as PKC inhibition has been shown to prevent hyperalgesia in an *in vivo* model of diabetic neuropathy [43].

Kagiava et al [44] suggested that altered voltage-gated potassium channel activity may also be involved in oxaliplatin-induced neurotoxicity. Oxaliplatin was found to cause broadening of action potentials and repetitive firing, suggesting its antagonistic effect on fast and slow neuronal potassium channels. Many sensory neurons in rat dorsal root ganglia express Kv7.2, Kv7.3 and Kv7.5. These channels are known as M channels and are closed by receptors coupled to Gq such as M1 and M3 muscarinic receptors. This blockade increases neuronal excitability and underlies some forms of cholinergic excitation. By contrast, their activation attenuates sensory Aδ and C-fiber discharges induced by heat stimulation when applied to the *peripheral* endings of sensory fibers in the isolated rat skin nerve preparation [45], and increases the threshold for C-fiber stimulation in human sural nerves [46]. These experiments clearly demonstrate the presence of Kv7/M-channels at various sites along the sensory neuraxis and also indicate the therapeutic potential of enhancing their activity [47]. Interestingly, Sittl et al [23] showed that enhancement of axonal potassium conductance by flupirtine, a Kv7/M-channel enhancer could reduce oxaliplatin-induced peripheral nerve hyperexcitability, supporting our findings that blockade of muscarinic receptor M1 and M3 by benztropine can produce the same effects.

Oxaliplatin-treated and diabetic mice also presented significant alterations, consistent with

membrane hyperexcitability, in neuromuscular (motor) excitability waveforms and derived variables, compared with animals injected with vehicle, suggesting an apparent decreased density and/or functioning of fast potassium channels and modification in the voltage dependence of transient sodium channels, respectively; decreased density and/or functioning of cyclic nucleotide-gated channels; reduced density and/or functioning of potassium channels. These alterations were not detected, or were greatly reduced, in oxaliplatin-treated and diabetic mice injected with benztropine, or in animals administered with benztropine alone. At the neuromuscular levels, oxaliplatin has been shown to increase both evoked and spontaneous neurotransmitter release in the motor nerve terminal of a phrenic nerve hemidiaphragm preparation [35]. The hyperexcitability effects of oxaliplatin on the mammalian neuromuscular junction appear related to a mechanism which delays entry of Na+ channels into an inactivated state and, to a lesser extent, to a reduced K+ channel activity, both of which can be prevented by benztropine.

Electronic microscopy of the myelin sheaths of the sciatic nerves revealed a demyelination in oxaliplatin-treated mice compared to animals injected with vehicle alone, oxaliplatin plus benztropine or benztropine alone. Confocal microscopy of mouse sciatic nerves confirms the alteration of the morphology of myelinated axons with a significant increase in the nodal diameter, length and volume, as functions of the internodal diameter, in oxaliplatin-treated mice compared to vehicle-treated animals. These results are likely the consequence of oxaliplatin-induced membrane hyperexcitability as previously described [36]. In these animals, a reduction of the internodal diameter was also observed, which may reflect either a preferential loss of large myelinated nerve fibers or an alteration in myelin sheath layers surrounding the axons. The drop in MBP expression in oxaliplatin-treated animals confirmed the severe reduction of neuron myelination in DRG and sciatic nerves. These alterations of morphometric parameters were greatly reduced, if not absent, in mice co-injected with oxaliplatin and benztropine. In a recent study, Imai and coworkers [12] showed that treatment with oxaliplatin induced cytotoxicity of myelin-forming Schwann cells accompanied by mitochondrial dysfunction at concentrations lower than those impairing DRG neurons. These direct effects of oxaliplatin on Schwann cells might be an underlying cause of CIPN in addition to its direct toxicity in peripheral neurons. Schwann cells express muscarinic receptors M1, M2, M3, and M4 [48,49] and localize to the axon□Schwann cell boundary [50]. Activation of AChR on Schwann cells modified the myelin sheet by altering the viscosity of the myelin membrane [51] that can be prevented by muscarinic receptor antagonists.

A severe reduction in the number of cutaneous nerve fibers is frequently observed in humans and mice treated with oxaliplatin as a result of neuronal toxicity of the platinum compound. Interestingly, benztropine also prevented the drop in neuronal density in the paws of mice injected with oxaliplatin. It has recently been demonstrated that neurite outgrowth is controlled by muscarinic receptors through regulation of mitochondrial function. M1R-deficient mice rended diabetic with STZ are protected from physiological and structural indices of sensory neuropathy and pharmacological blockade of M1R using antimuscarinic drugs prevented or reversed indices of diabetic or chemotherapy-induced peripheral neuropathy [52].

Proinflammatory cytokines like TNFα or IL-6 contribute to axonal damage, alteration of the myelin structure and voltage dependent channel integrity but also modulate spontaneous nociceptor sensitivity and activity by increasing Na+ and Ca2+ currents at the nociceptor peripheral terminals, which results in an increased membrane excitability, and a reduction in pain threshold and peripheral sensitization [53,54,55]. The pain sensation in distal extremities has been attributed to dysfunction of small myelinated Aδ or unmyelinated C-fibers [56,57]. Sensitizing uninjured adjacent

nerve fibers (nociceptors) or sensory neurons by proinflammatory cytokines plays a critical role in the development of the chemotherapy- and diabetic-induced painful peripheral neuropathy as evidenced by numerous clinical and experimental studies [55,58]. Indeed, following intravenous administration of chemotherapy drugs, an important activation of Schwann cells along with a massive infiltration of activated macrophages in the DRG and in peripheral nerves leads to a subsequent production and secretion of inflammatory cytokines like TNFα, IL-1β and IL-6; promoting neuroinflammation with allodynia and hyperalgesia [59]. Injection of an anti-IL-6 neutralizing antibody alleviated pain-related behaviors [60,61] and a recent clinical study reported that IL-6 levels were significantly higher after the conclusion of chemotherapy in breast cancer patients with CIPN than in those without CIPN, providing the first clinical evidence of the involvement of IL-6 in CIPN [62]. In diabetes, an enhanced expression of the NF-κB-derived cytokine TNFα in the sciatic nerve of diabetic rats and mice was associated with decreased expression of myelin basic protein and with both large and small nerve fiber dysfunction, as documented by reductions in the motor and sensory nerve conduction velocities and in the intraepidermal nerve fiber density in the diabetic animals [63]. These neuronal dysfunctions were all reverted by blocking TNF with a recombinant human TNF receptor–antibody fusion protein [64]. Interestingly, neurons and immune cells, especially macrophages, express all five muscarinic [25]receptors and their stimulation promotes a pro-inflammatory reaction while blocking the M1, M2 and M3 receptors has been shown to reduce the synthesis of the pro-inflammatory cytokines IL-6 and TNFα [24].

In addressing the primary aspect of the condition, which is tumor growth, we found that mice receiving benztropine alone had a reduced size of tumors compared to untreated animals and when associated with oxaliplatin presented the lowest tumor burden compared to mice treated with oxaliplatin alone. These data are in line with the role of muscarinic receptors on tumor growth and especially on colon cancer progression. Indeed, the levels of expression and activation of M3 muscarinic receptors in colon cancer cells are very high and associated with increased tumor cell proliferation by activation of the MAPKinase pathways and invasiveness by increasing MMP1 release. All of these effects are reduced by M3R antagonists [65].

Benztropine exerts an original effect on neuronal cells by increasing the level of reduced glutathione thus reducing ROS levels induced by oxaliplatin and cell death. Blocking muscarinic receptors has already been associated with a reduction in ROS release, prevention of glutathione depletion and enhanced viability in various normal non tumoral cell types [66]. By contrast, benztropine potentiates the cytotoxic effect of oxaliplatin on tumor cells via a drop in GSH level and an increase in H_2O_2 production, in line with the capacity of benztropine to reduce neuronal toxicity while maintaining the anti-tumor efficacy of oxaliplatin. Activation of the M1 muscarinic receptor by various agonists decreases SOD activities and induces superoxide anion production in neuronal cells [67]. Interestingly, superoxide anions have been shown to be particularly cytotoxic for neurons upon exposure to oxaliplatin, as superoxide dismutase mimics prevent oxaliplatin-induced neuropathies while increasing the anti-tumoral effect of the chemotherapy on colon cancer cells [68]. SOD increase by M1 blockade leads to superoxide anions dismutation into H_2O_2, whose cytotoxicity towards tumor cells adds up to that of oxaliplatin. The differences observed between normal and tumor cells fate upon oxaliplatin and benztropin exposure can be related to their different basal levels of GSH and responses towards a H_2O_2-mediated stress [69–72]. Tumor cells are more sensitive to ROS-induced cell death than normal cells due to increased metabolism of tumor cells and antioxidant defense exhaustion. Indeed, in normal cells, similar levels of H_2O_2 that kill tumor cells favor cellular viability and proliferation through adaptation and mobilization of antioxidant defenses, usually through NRF2 induction[73]. Furthermore, GSH homeostasis is of prime

importance for neurons as their depletion in this antioxidant molecule ultimately leads to their senescence mediated by oxidative stress [74]. Several studies concur with the observation that GSH-mediated detoxification of H_2O_2 is paramount to address neurologic disorders, may they be central or peripheral [75,76]. In clinical settings, GSH infusions significantly reduce the severity of the neurodegenerative side effects of oxaliplatin [77].

A limitation of this study is that results have been gained in animals only. However, the literature indicates that murine models of peripheral neuropathies are robust models for modeling human neuropathy [38,78]. Indeed, the components of this murine neurodegeneration are also observed in humans and the neuroprotection conferred by molecules on these models is also observed in humans [68,79]. This observation leads us to believe that the neuroprotection conferred by benztropine, which is currently indicated in Parkinson's disease in the United States, could be transposable to patients suffering from peripheral neuropathies. These very encouraging results for benztropine deserve to lead to a study in humans in order to be able to address a problematic with clinical relevance. The results of this clinical trial could lead to the exploration of benztropine as a potentially neuroprotective agent in other pathologies of the PNS.

Competing interests: Tânia Cristina Gonçalves was an employee of Sanofi (and a Sanofi shareholder via participation/profit-sharing) when these studies were conducted. All other co-authors declare no conflict of interest.

Acknowledgments: The authors would like to thank Dr. Pierre Billuart for his expertise in perfusing the mice and kind advice. The authors are also very grateful to Dr. Thomas Guilbert for having created a macro allowing us to systematically measure the G-ratios on the sections of electron microscopy.

Materials and Methods

Cell culture and treatments

CT26 (mouse colon carcinoma) cells, purchased from the ATCC (CRL-2638), were grown in Dulbecco's Modified Eagle Medium (Gibco, Sigma-Aldrich) with 10% FBS (Gibco, Sigma-Aldrich), penicillin/streptomycin, and L-glutamine supplementation. N2a (mouse brain neuroblastoma) cells, purchased from the ATCC (CCL-131), were grown in Eagle Minimum Essential Medium supplemented with 10% FBS, penicillin/streptomycin, 2% sodium pyruvate, 1% ciprofloxacin, non-essential amino acids, and L-glutamine supplementation.

Animal models and treatments

Five-week-old male BALB/cJRj mice were purchased from Janvier Laboratory (Le Genest Saint Isle, France). All mice were housed in ventilated cages (n = 7 to 10 animals per cage) with sterile food and water *ad libitum* and were exposed to a standard light cycle of 12 h on and 12 h off. All experiments were performed in accordance with European and French institutional guidelines (Directive 2010/63/EU, Ethics committee CEEA 34 – APAFIS authorization #8394).

Model of oxaliplatin-induced peripheral neuropathies

Both models of oxaliplatin-induced peripheral neuropathies, namely, the acute form and the chronic form were induced by protocols with timeframes that were analogous to the clinical protocols which results in the induction of either of these forms in patients, and were previously used in mice.

The acute form of oxaliplatin peripheral neuropathy was induced by daily low doses intraperitoneal injections of oxaliplatin [Accord, 5 mg/mL IV solution, 3 mg/kg diluted in phosphate-buffered saline (PBS 1X)] for 5 days followed by 5 days of rest, for 2 cycles [68,80]. The chronic form of oxaliplatin peripheral neuropathy mice was induced by intraperitoneal injections of first, oxaliplatin (10 mg/kg diluted in PBS) once a week for 6-8 weeks [68,81]. In both models of oxaliplatin-induced peripheral neuropathies, benztropine was administered 5 days a week intraperitoneal injections (10 mg/kg diluted in PBS) [20], 6h after oxaliplatin injections.

Model of streptozotocin-induced diabetic peripheral neuropathies

Poor survival over the course of preliminary tests was observed with a 3-h food withdrawal before and after a single dose of 200 mg/kg of Streptozotocin (STZ) [82]. This dose was therefore lowered to 180 mg/kg (dissolved in 10 mmol/L sodium citrate buffer, pH 4.5) with 3-h food fasting before and after the injection. STZ was diluted to allow a final volume of 0.1 mL/10 g body weight for intraperitoneal injections. One week after STZ injection, diabetes was confirmed by blood glucose levels using a Cobas 8000 modular analyzer (Roche) in blood samples taken under isoflurane 2,5% (Isovet, #ISO005, Centravet, Plancoët, France) from mice retro-orbital sinus. Mice with blood glucose levels $\geq$ 12 mM were considered diabetic and included in the study [29]. Benztropine was administered 5 days a week intraperitoneal injections (10 mg/kg diluted in PBS) [20], 6h after oxaliplatin injections.

Behavioral studies

Prior to baseline measurements for every behavioral test, mice underwent 2 weeks of acclimation sessions with the specific training protocols to familiarize them with the experimental environments and testing procedures, without probing with plastic fibers nor temperature setting. Before each behavioral test, mice were allowed to acclimate to the experimental room for 10 minutes in their home cages. Mice were only tested once on any given test day to avoid any possible stress, anesthetic or tissue damage effects that could result from repeated exposure to the cold surface.

***In vivo* cold hyperalgesia**

Mice from the acute model of oxaliplatin-induced peripheral neuropathies were subjected to weekly tests for cold hyperalgesia. Mice were put on a cold/hot plate (Ugo Basile, Comerio, Italy) set at the temperature of 2°C ± 0.2°C [83]. The total number of brisk lifts from either hind paw or jumps, considered as a painful response to cold, was counted simultaneously by two observers to ensure accuracy and averaged for the two observers' counts. A maximal cut-off time of 5 minutes was imposed to prevent tissue damage. Results are expressed as the mean ± SEM of the observers' counts.

***In vivo* cold hypoesthesia**

Mice from the chronic model of oxaliplatin-induced peripheral neuropathies were subjected to weekly tests for cold hypoesthesia which was evaluated using temperature settings previously described [68]. Briefly, mice were put on the cold/hot plate set at 4°C ± 0.2°C for 5 minutes. Similar, to the test assessing cold hyperalgesia, the total number of brisk lifts from either hind paw or jumps was counted simultaneously by two observers to ensure accuracy and averaged for the two observers' counts. Results are expressed as the mean ± SEM of the observers' counts.

***In vivo* tactile hypoesthesia**

Mice from both the chronic oxaliplatin-induced and the diabetic models underwent weekly tests for mechanical allodynia with the von Frey method [84], a standardized protocol assessing tactile

sensitivity [85]. A set of 20 monofilaments based on the Semmes Weinstein monofilament set was used (Model: Bio-VF-M, Bioseb, USA/Canada). The Semmes Weinstein set of monofilaments provides an approximate logarithmic scale of actual force, and a linear scale of perceived intensity. Briefly, mice were put on a mesh grid, an enclosed by a clear plexiglass barrier with a top cover and left to calm down for 5 minutes. After the settling phase, mice are motionless allowing the experimenter to touch their hind paws with a flexible plastic fiber of a fixed diameter. The fiber is pressed through the mesh against the plantar surface at a right angle. The force of application increases as long as the investigator pushes the probe and until the fiber bends. The scale of force used ranged from 0.008 to 1.400 g. The threshold to perception of probing was asserted to the movement of pulling back of either hind paw. Based on observations on control animals (vehicle-injected or non-diabetic mice), the end-point for testing was set when a fiber tended to raise the entire limb rather than to buckle.

In vivo hot hyperesthesia

Mice from the diabetic model of peripheral neuropathies underwent a weekly assessment of thermal hyperalgesia according to a previously published study protocol [29]. The same equipment as for cold sensitivity was used for this experiment. The plate was set at 55°C ± 0.2°C. Latency to hind paw licking or jumping was recorded simultaneously by two observers with a timer and time to response was averaged for the two counts. To prevent tissue damage a cutoff time of 30 seconds was implemented.

In vivo electrophysiological exploration of neuromuscular and sensory excitability

The sensory and/or neuromuscular excitability was assessed *in vivo* on mice under isoflurane (AErrane®) anesthesia by minimally invasive electrophysiological methods using the Qtrac© software (Prof. H. Bostock, Institute of Neurology, London, England), as previously described [83]. Briefly, an anaesthetized mouse was placed on a heating pad to maintain body temperature (from 36.02 ± 0.06 to 36.13 ± 0.04, n = 85) throughout the experiments to avoid non-specific modifications of excitability variables.

For neuromuscular excitability exploration, electrical stimulation was delivered to the sciatic motor nerve by means of surface electrodes, and the compound muscle action potential (CMAP) was recorded using needle electrodes inserted into the plantar muscle. Each mouse was systematically submitted to one session of excitability measurements (TRONDE protocol), which consisted of five different excitability tests performed together: (C0) The stimulus-response relationship (*i.e.* the CMAP amplitude as a function of the intensity of a 1-ms stimulation) evaluated notably both the CMAP maximal amplitude and the stimulation intensity that had to be applied to evoke a CMAP of 50% maximal amplitude, giving information on the global neuromuscular excitability state. (C1) The current-threshold relationship evaluated the threshold changes at the end of 200-ms conditioning subthreshold depolarizing and hyperpolarizing currents ranging from 50 to 100% thresholds, giving information on axonal accommodation capacities to depolarizations and hyperpolarizations. (C2) The strength-duration relationship (*i.e.,* the intensity in relation to the duration of a stimulus necessary to evoke a given amplitude of CMAP) evaluated the minimal intensity of infinitely long duration stimulation necessary to evoke a CMAP (rheobase) and the intensity duration of twice the rheobase stimulation necessary to evoke a CMAP (chronaxis), giving information on the axonal resting potential at the nodal membrane. (C3) The threshold electrotonus (*i.e.,* the threshold changes during and after 100-ms conditioning subthreshold depolarizing and hyperpolarizing currents applied at ±40% thresholds) evaluated the electrotonic changes in membrane potential, giving also information on axonal accommodation capacities to

depolarizations and hyperpolarizations. (C4) The recovery cycle (*i.e.,* the excitability changes that occur following a CMAP) evaluated the refractory periods (during which membrane excitability is either nil or markedly decreased) followed by the supernormal and late subnormal periods (during which membrane excitability is increased and decreased, respectively). As a whole, more than thirty variables were determined from these excitability tests and analyzed. Most of them provide specific and complementary information on the density and functional state of ion channels, receptors and pumps, as well as on the passive membrane properties of the neuromuscular system [86,87].

For sensory excitability exploration, the compound nerve action potential (CNAP) was recorded using needle electrodes inserted into the base of the tail, in response to stimulation of the caudal nerve applied at the distal part of the tail by means of surface electrodes. Each mouse was systematically and only submitted to the first session of excitability measurements (TRONDE protocol) to establish the stimulus-response relationship (*i.e.,* the CNAP amplitude as a function of the intensity of a 1-ms stimulation) and thus, evaluate notably the CNAP maximal amplitude, the stimulation intensity that had to be applied to evoke a CNAP of 50% maximal amplitude and the latency measured from stimulation onset to peak amplitude, giving information on the global sensory excitability state.

***In vitro* electrophysiological exploration of sensory excitability**

In vitro electrophysiological exploration of sensory excitability was performed by recording the action potential from primary cultures of mouse dorsal root ganglia (DRG) sensory neurons, using the patch-clamp technique. After being removed from the spinal cord of euthanized adult female Swiss mice (10-12 weeks of age and 28-32 g body weight, purchased from Janvier Elevage and housed at the CEA animal facility), DRG were placed in iced-Ham's F-12 medium (Sigma-Aldrich, Saint-Quentin Fallavier, France) and enzymatically dissociated with collagenase type IA (2 mg/mL; Sigma-Aldrich) and dispase (5 mg/mL; Gibco, Thermo Fisher Scientific, Villebon-sur-Yvette, France). Neurons were then plated on 12-mm glass coverslips placed in a 24-wells plate coated with 10 µg/mL of poly-D-lysine and 100 µg/mL of murin laminin (Sigma-Aldrich). The cells were maintained in culture at 37°C (in 95% air and 5% CO_2) in Neurobasal A medium (Gibco) containing horse serum (5%; Gibco), penicillin/streptomycin (47.64 U/mL; Gibco), nerve growth factor (83.33 ng/mL; Sigma-Aldrich), N2 supplement (3.18x; Gibco), Dulbecco's PBS (1X) w/o $CaCl_2$ and $MgCl_2$ (1.68%; Gibco), bovine serum albumin (16.83 µg/mL; Sigma-Aldrich), corticosteron (214.85 nM; Sigma-Aldrich), T3 hormone (56.06 nM; Sigma-Aldrich) and L-glutamine (1.90 mM; Sigma-Aldrich). Cytosine β-D-arabinofuranoside (2 µM; Sigma-Aldrich) was added to the culture medium, 24 h later, to stop proliferation of satellite glial cells. Experiments were carried out within 2 to 6 days after cell plating. The day of their use, the neurons plated on coverslips were transferred, for a minimum of 30 min at 37°C prior to patch-clamp recordings, in 35-mm Petri dishes filled with a standard physiological medium of the following composition (in mM): NaCl 134, KCl 3, $CaCl_2$ 1, $MgCl_2$ 1, D-glucose 20, and HEPES 20 (pH 7.35, adjusted with NaOH), and then in the recording bath filled with the standard physiological medium.

Whole-cell patch-clamp experiments were performed under current-clamp condition, by using a MultiClamp 700B integrating patch-clamp amplifier and the pClamp10.6 software (Molecular Devices, Sunnyvale, CA, USA), as previously described [88]. The signals, acquired at a 4-kHz sample rate, were filtered at 2 kHz with a low-pass Bessel filter and digitized with the aid of a computer equipped with an analog-to-digital converter (Digidata-1440A model; Molecular Devices). The patch-clamp pipettes were filled with a medium composed of (in mM): KCl 134, NaCl 10, $MgCl_2$ 2,

EGTA 2, ATP-Na_2 4, and HEPES 20 (pH 7.32, adjusted with KOH), and had 2.71 ± 0.25 MΩ resistance (n = 18) in the standard physiological medium. A fast superfusion system allowed changing the solution [standard physiological medium without or with oxaliplatin (25-50 µM) alone or oxaliplatin (25-50 µM) plus benztropine (10 µM)] around the recorded cell within a few seconds. The experiments were carried out at constant room temperature (22°C). Action potentials were elicited, at a frequency of 0.5 Hz, by 100-ms current test-pulses of -0.2 to 1 nA (in 0.1-nA increments) applied 200 ms after 200-ms current pre-pulses of -0.1 nA (to check the membrane passive properties of neurons, mainly membrane capacitance).

Ex vivo confocal microscopy morphological study of sciatic nerves

The experiments were carried out on single myelinated axons isolated from the sciatic nerves of euthanized mice, as previously detailed [83]. Briefly, sciatic nerve sections of about 2 cm in length were removed from their sheaths, dissected, and fixed for 1h in PBS 1X with 2% paraformaldehyde, then rinsed three times with PBS. Sciatic nerves were deposited on microscope slides, myelinated axons were gently teased apart from the main trunk, and preparations were kept at -20°C until use. Just before the experiments, sciatic nerves were rehydrated for about 1 h with a standard physiological solution containing (in mM): NaCl 154, KCl 5, $CaCl_2$ 2, $MgCl_2$ 1, glucose 11, and HEPES 5 (pH 7.4, adjusted with NaOH. Preparations were then exposed for 30 min to the fluorescent dye FM1-43 (Molecular Probes) dissolved in a standard physiological solution to stain the plasma membranes of the myelinated axons, and washed with dye-free solution before imaging. A Zeiss LSM 510 META (Carl Zeiss) multiphoton scanning confocal microscope, mounted on an upright microscope and controlled with the manufacturer's software and workstation, was used for optical sectioning of myelinated axons and subsequent 3D high-resolution digital reconstruction of their structure. Images were collected using a 63x oil-immersion objective with a 1.40 numerical aperture (Zeiss Plan-Apochromat); following excitation of FM1-43 with the 488 nm wavelength line of an Argon ion laser, and then digitized at 12-bit resolution into a 512 x 512 pixel array. Images were then analyzed using the ImageJ software (National Institutes of Health - NIH). Quantification of morphometric parameters of myelinated axons were performed by measuring the internodal diameter, nodal diameter (D) and nodal length (L). Assuming the simplest geometry in which a node of Ranvier approaches a cylinder, the nodal volume (V) was then determined as $V = \pi L(D/2)^2$.

Ex vivo electronic microscopy morphological study of sciatic nerves

Mice were anesthetized by intraperitoneal injections of 100 mg/kg ketamine and 10 mg/kg xylazine and then intracardially perfused with first, 0.1 M PBS, pH 7.4, for 8 min and then 4% paraformaldehyde, 2.5% glutaraldehyde, and 0.1 M PBS, pH 7.4. Mice were euthanized after complete rigidity of the lower limbs and liver (endpoint of the perfusion). Tissues were dissected 24h later and immersed in the fixative solution at 4°C for 72h, washed in PBS, post-fixed in 2% osmium tetroxide, dehydrated in graded ethanol, and embedded in epoxy resin. Ultrathin sections (50–90 nm) were cut on an ultramicrotome (8800 Ultrotome III; LKB Bromma) and collected on 300-mesh nickel grids. Staining was performed on drops of 4% aqueous uranyl acetate, followed by Reynolds lead citrate. Ultrastructural analyses were performed in a JEOL JEM-1011 electron microscope and digitalized with Digital Micrograph software. G-ratios and axon diameters were calculated with the ImageJ software (National Institutes of Health) and the plugin *g*-ratio version 3.2 (Plug-in and source code available online at http://gratio.efil.de) according to previously published material [89]. Diameters were calculated from enclosed areas, considering first, the diameter of the axon without the myelin and dividing it by the diameter of the axon plus the myelin

sheaths surrounding it. The plugin allows for semi-automated analysis of randomly selected fibers with both diameters being considered and automatically processed through the algorithm to calculate the g-ratio. A minimum of 500 randomly selected axons were analyzed per experimental group, with at least 3 mice per group.

Ex vivo study of myelin protein content in sciatic nerves

Nerves were extracted in lysis buffer containing a cocktail of proteinase and phosphatase inhibitors using a glass homogenizer. Protein lysate samples (40g) were resolved on 10% SDS-PAGE gels and transferred by electrophoresis to nitrocellulose membranes. The membranes were blocked for non-specific binding sites at room temperature in TBS buffer containing 0.1% Tween 20 and 5% nonfat dried milk for 1 h. The membranes were then incubated overnight at 4°C with a primary antibody against MBP (1:500; Merck). Subsequently, the membranes were incubated with an anti-rabbit IgG, horseradish peroxidase linked whole antibody from donkey (1:1000; GE Healthcare Life Sciences NA934, Little Chalfont, UK) and subjected to ECL reagent treatment. After film exposure, all membranes were washed and then incubated with a 1:50,000 dilution of mouse monoclonal anti-actin-peroxidase antibody (Sigma Aldrich; Saint Louis, Missouri, USA) as previously described [90].The images were captured using a CCD camera (LAS3000 from Fujifilm), and the bands were quantified using MultiGauge software from Fujifilm.

Ex vivo study of cutaneous nerve fiber density

Sections of skin from the hind paws of mice were preserved in buffered 4% formol (VWR Chemicals, Labonord SAS, France) and immersed in successive baths of increasing concentrations of ethanol (50%, 70%, 90%, 100%). Samples were then immersed in histosol before being fixed in paraffin, kept at 4°C and cut into 6 µm-thick slices. Samples were then unwaxed in three successive baths of histosol for 3 min and rehydrated in ethanol baths for 1 min each, starting with two baths of pure ethanol followed with baths of 90%, 70% and 30% ethanol and two baths of H_2O. Slides were then washed in PBS for 2 min before being immersed in citrate buffer at 95°C for 10 min. Samples were washed in 3 baths of PBS of 5 min each. Samples were then permeabilized (PBS, 0.25% Triton X-100) for 10 min before being rinsed in PBS in 3 baths of 5 min each and immersed in a blocking solution (PBS, 10% goat serum, 1% BSA) for at least 180 min. Samples were further incubated at 4°C overnight in the primary antibody (Abcam, ab10404, rabbit polyclonal to PGP9.5**,** 1:1000) before being rinsed in PBS in 3 baths of 5 min each before incubating in the secondary antibody (Sigma, F9887, anti-rabbit IgG FITC-conjugate, 1:1000) at room temperature in the dark. Prior to mounting (Thermo Scientific, Shandon Immuno-Mount), slides were washed with PBS in 3 baths of 5 min each. Images were collected using a Nikon Eclipse 80i microscope with a Nikon PlanFluor 100x/1.30 oil-immersion DIC H/N2 objective.

Ex vivo study of systemic inflammatory markers

Blood samples were taken under isoflurane from the retro-orbital sinus immediately before sacrifice, centrifuged at 10.000 rpm and 2°C. Sera were diluted (1:4) in ELISA/ELISPOT diluent 1X before being distributed on ELISA 96-well plates specific of IL-6 and Tumor necrosis factor alpha (TNF-α; Mouse IL-6 ELISA Ready-SET-Go!® and Mouse TNF ELISA Ready-SET-Go!® - eBioscience, San Diego, CA, USA). Concentrations were calculated from a standard curve according to the manufacturer's protocol.

In vivo study of antitumor activity of benztropine upon association with chemotherapy

A total of 1.10^6 viable CT26 cells, as determined by trypan blue staining, and resuspended in DMEM were injected subcutaneously into the back of the mice. When tumors reached a mean size

of 200 to 500 mm^3, animals were randomized and received a single weekly injection of either oxaliplatin (10 mg/kg) or vehicle. Concomitantly, mice received vehicle or benztropine (10 mg/kg) every day. Following randomization, tumor size was measured with a numeric caliper twice a week for 3 weeks. In order to comply with ethical guidelines, tumor growth experiments were stopped three weeks after the first oxaliplatin injection. Tumor volume was calculated as follows: TV (mm^3) = (L x W^2)/2, where L is the longest and W the shortest radius of the tumor in millimeters. Results are expressed as mean ± SD of tumor volumes (n = 7 in each group).

Viability and ROS assays

All cells (2×10^4 per well) were seeded in 96-well plates (Sigma-Aldrich, Saint-Quentin Fallavier France) and incubated for 24 h with 7.5 to 30 µM of benztropin (Sigma-Aldrich, Saint-Quentin Fallavier France) and treated with 0 to 100 µM of oxaliplatin (Accord Healthcare Limited, Lille, France). Cell viability was assessed by a crystal violet assay, and results are expressed as the mean percentage of viable cells ± SEM versus cells not exposed to oxaliplatin (100% viability). Cellular production of ROS and reduced glutathione (GSH) were assessed by spectrofluorimetry with 2′,7′-dichlorodihydrofluorescein diacetate (H2DCFDA, #6883 Sigma-Aldrich, Saint-Quentin Fallavier France) and monochlorobimane (#69899 Sigma-Aldrich), respectively[69].

Statistical analysis

Statistical analysis was performed using GraphPad Prism 5. Artwork, was also created using GraphPad Prism 5, except for electrophysiological study artwork which was created using the Qtrac© software. Differences between values were tested using the unpaired Student's *t*-test, two-way ANOVA, or the nonparametric Mann-Whitney *U* test, depending on the equality of variances estimated using Lilliefors test. They were considered significant when $p < 0.05$, p values being denoted as follows: $*p < 0.05$, $**p < 0.01$, $***p < 0.001$, $****p < 0.0001$; NS: non-significant.

References

1. Seretny, M. *et al.* Incidence, prevalence, and predictors of chemotherapy-induced peripheral neuropathy: A systematic review and meta-analysis. *Pain* **155,** 2461–2470 (2014).
2. Brewer, J. R., Morrison, G., Dolan, M. E. & Fleming, G. F. Chemotherapy-induced peripheral neuropathy: Current status and progress. *Gynecol. Oncol.* **140,** 176–183 (2016).
3. Grisold, W., Cavaletti, G. & Windebank, A. J. Peripheral neuropathies from chemotherapeutics and targeted agents: diagnosis, treatment, and prevention. *Neuro-Oncol.* **14 Suppl 4,** iv45-54 (2012).
4. de Gramont, A. *et al.* Leucovorin and fluorouracil with or without oxaliplatin as first-line treatment in advanced colorectal cancer. *J. Clin. Oncol. Off. J. Am. Soc. Clin. Oncol.* **18,** 2938–2947 (2000).
5. André, T. *et al.* Oxaliplatin, fluorouracil, and leucovorin as adjuvant treatment for colon cancer. *N. Engl. J. Med.* **350,** 2343–2351 (2004).
6. Wagner, A. D. *et al.* Chemotherapy for advanced gastric cancer. *Cochrane Database Syst. Rev.* **8,** CD004064 (2017).
7. Iqbal, A. & George, T. J. Randomized Clinical Trials in Colon and Rectal Cancer. *Surg. Oncol. Clin. N. Am.* **26,** 689–704 (2017).
8. Loprinzi, C. L. *et al.* Phase III randomized, placebo-controlled, double-blind study of intravenous calcium and magnesium to prevent oxaliplatin-induced sensory neurotoxicity (N08CB/Alliance). *J. Clin. Oncol. Off. J. Am. Soc. Clin. Oncol.* **32,** 997–1005 (2014).
9. Pulvers, J. N. & Marx, G. Factors associated with the development and severity of oxaliplatin-induced peripheral neuropathy: a systematic review. *Asia Pac. J. Clin. Oncol.* (2017). doi:10.1111/ajco.12694
10. Cavaletti, G., Alberti, P. & Marmiroli, P. Chemotherapy-induced peripheral neurotoxicity in the era of pharmacogenomics. *Lancet Oncol.* **12,** 1151–1161 (2011).
11. Bakogeorgos, M. & Georgoulias, V. Risk-reduction and treatment of chemotherapy-induced peripheral neuropathy. *Expert Rev. Anticancer Ther.* **17,** 1045–1060 (2017).

12. Imai, S. *et al.* Taxanes and platinum derivatives impair Schwann cells via distinct mechanisms. *Sci. Rep.* **7,** 5947 (2017).
13. Carozzi, V. A., Canta, A. & Chiorazzi, A. Chemotherapy-induced peripheral neuropathy: What do we know about mechanisms? *Neurosci. Lett.* **596,** 90–107 (2015).
14. Sima, A. A. F. & Zhang, W. Mechanisms of diabetic neuropathy: axon dysfunction. *Handb. Clin. Neurol.* **126,** 429–442 (2014).
15. Heinen, A., Lehmann, H. C. & Küry, P. Negative regulators of schwann cell differentiation-novel targets for peripheral nerve therapies? *J. Clin. Immunol.* **33 Suppl 1,** S18-26 (2013).
16. Feldman, E. L., Bennett, D. L. H., Nave, K.-A. & Jensen, T. S. New Horizons in Diabetic Neuropathy: Mechanisms, Bioenergetics, and Pain. *Neuron* **93,** 1296–1313 (2017).
17. Gonçalves, N. P. *et al.* Schwann cell interactions with axons and microvessels in diabetic neuropathy. *Nat. Rev. Neurol.* **13,** 135–147 (2017).
18. Lehmann, H. C. & Höke, A. Schwann cells as a therapeutic target for peripheral neuropathies. *CNS Neurol. Disord. Drug Targets* **9,** 801–806 (2010).
19. Gonçalves, N. P., Vægter, C. B. & Pallesen, L. T. Peripheral Glial Cells in the Development of Diabetic Neuropathy. *Front. Neurol.* **9,** (2018).
20. Deshmukh, V. A. *et al.* A regenerative approach to the treatment of multiple sclerosis. *Nature* **502,** 327–332 (2013).
21. Caulfield, M. P. Muscarinic receptors--characterization, coupling and function. *Pharmacol. Ther.* **58,** 319–379 (1993).
22. Wess, J. *et al.* Muscarinic receptor subtypes mediating central and peripheral antinociception studied with muscarinic receptor knockout mice: a review. *Life Sci.* **72,** 2047–2054 (2003).
23. Sittl, R., Carr, R. W., Schwarz, J. R. & Grafe, P. The Kv7 potassium channel activator flupirtine affects clinical excitability parameters of myelinated axons in isolated rat sural nerve. *J. Peripher. Nerv. Syst. JPNS* **15,** 63–72 (2010).
24. Fujii, T. Expression and Function of the Cholinergic System in Immune Cells. - PubMed - NCBI. 6;8:1085 (2017).
25. Kawashima, K. & Fujii, T. Extraneuronal cholinergic system in lymphocytes. *Pharmacol. Ther.* **86,** 29–48 (2000).
26. Cheng, K., Shang, A. C., Drachenberg, C. B., Zhan, M. & Raufman, J.-P. Differential expression of M3 muscarinic receptors in progressive colon neoplasia and metastasis. *Oncotarget* **8,** 21106–21114 (2017).
27. Spindel, E. R. Muscarinic Receptor Agonists and Antagonists: Effects on Cancer. *Handb. Exp. Pharmacol.* 451–468 (2012). doi:10.1007/978-3-642-23274-9_19
28. Yu, H. *et al.* Acetylcholine acts through M3 muscarinic receptor to activate the EGFR signaling and promotes gastric cancer cell proliferation. *Sci. Rep.* **7,** 40802 (2017).
29. Ulugol, A. *et al.* 5-HT7 receptor activation attenuates thermal hyperalgesia in streptozocin-induced diabetic mice. *Pharmacol. Biochem. Behav.* **102,** 344–348 (2012).
30. Watson, J. C. & Dyck, P. J. B. Peripheral Neuropathy: A Practical Approach to Diagnosis and Symptom Management. *Mayo Clin. Proc.* **90,** 940–951 (2015).
31. Mendell, J. Painful Sensory Neuropathy. *N. Engl. J. Med.* **Volume: 348 Issue 13 (2003),** 13 (2003).
32. Doughty, C. T. & Seyedsadjadi, R. Approach to Peripheral Neuropathy for the Primary Care Clinician. *Am. J. Med.* (2018). doi:10.1016/j.amjmed.2017.12.042
33. Vinik, A. I., Casellini, C. & Névoret, M.-L. Alternative Quantitative Tools in the Assessment of Diabetic Peripheral and Autonomic Neuropathy. in *International Review of Neurobiology* (eds. Calcutt, N. A. & Fernyhough, P.) **127,** 235–285 (Academic Press, 2016).
34. Adelsberger, H. *et al.* The chemotherapeutic oxaliplatin alters voltage-gated Na(+) channel kinetics on rat sensory neurons. *Eur. J. Pharmacol.* **406,** 25–32 (2000).
35. Webster, R. G., Brain, K. L., Wilson, R. H., Grem, J. L. & Vincent, A. Oxaliplatin induces hyperexcitability at motor and autonomic neuromuscular junctions through effects on voltage-gated sodium channels. *Br. J. Pharmacol.* **146,** 1027–1039 (2005).
36. Benoit, E., Brienza, S. & Dubois, J. M. Oxaliplatin, an anticancer agent that affects both Na+ and K+ channels in frog peripheral myelinated axons. *Gen. Physiol. Biophys.* **25,** 263–276 (2006).
37. Park, B., Kim, K., Rhee, D. & Pyo, S. The apoptotic effect of allicin in MCF-7 human breast cancer cells: role for ATF3. *FASEB J.* **26,** lb367–lb367 (2012).
38. Sittl, R. *et al.* Anticancer drug oxaliplatin induces acute cooling-aggravated neuropathy via sodium channel subtype Na(V)1.6-resurgent and persistent current. *Proc. Natl. Acad. Sci. U. S. A.* **109,** 6704–6709 (2012).

39. Deuis, J. R. *et al.* An animal model of oxaliplatin-induced cold allodynia reveals a crucial role for Nav1.6 in peripheral pain pathways. *Pain* **154,** 1749–1757 (2013).
40. Cantrell, A. R., Ma, J. Y., Scheuer, T. & Catterall, W. A. Muscarinic modulation of sodium current by activation of protein kinase C in rat hippocampal neurons. *Neuron* **16,** 1019–1026 (1996).
41. Wu, D.-F. *et al.* PKCε phosphorylation of the sodium channel NaV1.8 increases channel function and produces mechanical hyperalgesia in mice. *J. Clin. Invest.* **122,** 1306–1315 (2012).
42. Laedermann, C. J., Abriel, H. & Decosterd, I. Post-translational modifications of voltage-gated sodium channels in chronic pain syndromes. *Front. Pharmacol.* **6,** (2015).
43. Kamei, N. *et al.* Overexpression of monocyte chemoattractant protein-1 in adipose tissues causes macrophage recruitment and insulin resistance. *J. Biol. Chem.* **281,** 26602–26614 (2006).
44. Kagiava, A., Tsingotjidou, A., Emmanouilides, C. & Theophilidis, G. The effects of oxaliplatin, an anticancer drug, on potassium channels of the peripheral myelinated nerve fibres of the adult rat. *Neurotoxicology* **29,** 1100–1106 (2008).
45. Passmore, G. & Brown, D. Effects of M-channel mod-ulators on peripheral excitability inrat hairy skin. *Soc. Neurosci. Abstr* 681.8 (2007).
46. Lang, P. M., Fleckenstein, J., Passmore, G. M., Brown, D. A. & Grafe, P. Retigabine reduces the excitability of unmyelinated peripheral human axons. *Neuropharmacology* **54,** 1271–1278 (2008).
47. Brown, D. A. & Passmore, G. M. Neural KCNQ (Kv7) channels. *Br. J. Pharmacol.* **156,** 1185–1195 (2009).
48. Loreti, S. *et al.* Rat Schwann cells express M1-M4 muscarinic receptor subtypes. *J. Neurosci. Res.* **84,** 97–105 (2006).
49. Fields, R. D., Dutta, D. J., Belgrad, J. & Robnett, M. Cholinergic signaling in myelination. *Glia* **65,** 687–698 (2017).
50. Rawlins, F. A. & Villegas, J. Autoradiographic localization of acetylcholine receptors in the Schwann cell membrane of the squid nerve fiber. *J. Cell Biol.* **77,** 371–376 (1978).
51. Verdiyan, E. E., Allakhverdiev, E. S. & Maksimov, G. V. Study of the Peripheral Nerve Fibers Myelin Structure Changes during Activation of Schwann Cell Acetylcholine Receptors. *PloS One* **11,** e0158083 (2016).
52. Calcutt, N. A. *et al.* Selective antagonism of muscarinic receptors is neuroprotective in peripheral neuropathy. *J. Clin. Invest.* **127,** 608–622 (2017).
53. Keswani, S. C. *et al.* Schwann cell chemokine receptors mediate HIV-1 gp120 toxicity to sensory neurons. *Ann. Neurol.* **54,** 287–296 (2003).
54. Cunha, T. A cascade of cytokines mediates mechanical inflammatory hypernociception in mice. - PubMed - NCBI. 1;102(5):1755-60 (2005).
55. Scholz, J. & Woolf, C. J. The neuropathic pain triad: neurons, immune cells and glia. *Nat. Neurosci.* **10,** 1361–1368 (2007).
56. Flatters, S. J. L. & Bennett, G. J. Studies of peripheral sensory nerves in paclitaxel-induced painful peripheral neuropathy: evidence for mitochondrial dysfunction. *Pain* **122,** 245–257 (2006).
57. Verstappen, C. C. P., Heimans, J. J., Hoekman, K. & Postma, T. J. Neurotoxic complications of chemotherapy in patients with cancer: clinical signs and optimal management. *Drugs* **63,** 1549–1563 (2003).
58. Marchand, F., Perretti, M. & McMahon, S. B. Role of the immune system in chronic pain. *Nat. Rev. Neurosci.* **6,** 521–532 (2005).
59. Peters, C. M. *et al.* Intravenous paclitaxel administration in the rat induces a peripheral sensory neuropathy characterized by macrophage infiltration and injury to sensory neurons and their supporting cells. *Exp. Neurol.* **203,** 42–54 (2007).
60. Melemedjian, O. K. *et al.* Local translation and retrograde axonal transport of CREB regulates IL-6-induced nociceptive plasticity. *Mol. Pain* **10,** 45 (2014).
61. Vazquez, E. *et al.* Spinal interleukin-6 is an amplifier of arthritic pain in the rat. *Arthritis Rheum.* **64,** 2233–2242 (2012).
62. Starkweather, A. Increased interleukin-6 activity associated with painful chemotherapy-induced peripheral neuropathy in women after breast cancer treatment. *Nurs. Res. Pract.* **2010,** 281531 (2010).
63. Kellogg, A. P. *et al.* Protective effects of cyclooxygenase-2 gene inactivation against peripheral nerve dysfunction and intraepidermal nerve fiber loss in experimental diabetes. *Diabetes* **56,** 2997–3005 (2007).
64. Shi, X., Chen, Y., Nadeem, L. & Xu, G. Beneficial effect of TNF-α inhibition on diabetic peripheral neuropathy. *J. Neuroinflammation* **10,** 69 (2013).
65. Felton, J., Hu, S. & Raufman, J.-P. Targeting M3 Muscarinic Receptors for Colon Cancer Therapy. *Curr. Mol. Pharmacol.* (2018). doi:10.2174/1874467211666180119115828

66. Urrunaga, N. H. *et al.* M1 muscarinic receptors modify oxidative stress response to acetaminophen-induced acute liver injury. *Free Radic. Biol. Med.* **78,** 66–81 (2015).
67. Mangelus, M., Kroyter, A., Galron, R. & Sokolovsky, M. Reactive oxygen species regulate signaling pathways induced by M1 muscarinic receptors in PC12M1 cells. *J. Neurochem.* **76,** 1701–1711 (2001).
68. Coriat, R. *et al.* Treatment of oxaliplatin-induced peripheral neuropathy by intravenous mangafodipir. *J. Clin. Invest.* **124,** 262–272 (2014).
69. Laurent, A. *et al.* Controlling tumor growth by modulating endogenous production of reactive oxygen species. *Cancer Res.* **65,** 948–956 (2005).
70. Alexandre, J. *et al.* Improvement of the therapeutic index of anticancer drugs by the superoxide dismutase mimic mangafodipir. *J. Natl. Cancer Inst.* **98,** 236–244 (2006).
71. Morales, M.-C. *et al.* Intracellular glutathione levels determine cell sensitivity to apoptosis induced by the antineoplasic agent N-(4-hydroxyphenyl) retinamide. *Anticancer Res.* **25,** 1945–1951 (2005).
72. Trachootham, D., Alexandre, J. & Huang, P. Targeting cancer cells by ROS-mediated mechanisms: a radical therapeutic approach? *Nat. Rev. Drug Discov.* **8,** 579–591 (2009).
73. González-Reyes, S., Guzmán-Beltrán, S., Medina-Campos, O. N. & Pedraza-Chaverri, J. Curcumin pretreatment induces Nrf2 and an antioxidant response and prevents hemin-induced toxicity in primary cultures of cerebellar granule neurons of rats. *Oxid. Med. Cell. Longev.* **2013,** 801418 (2013).
74. Belrose, J. C., Xie, Y.-F., Gierszewski, L. J., MacDonald, J. F. & Jackson, M. F. Loss of glutathione homeostasis associated with neuronal senescence facilitates TRPM2 channel activation in cultured hippocampal pyramidal neurons. *Mol. Brain* **5,** 11 (2012).
75. Bains, J. S. & Shaw, C. A. Neurodegenerative disorders in humans: the role of glutathione in oxidative stress-mediated neuronal death. *Brain Res. Brain Res. Rev.* **25,** 335–358 (1997).
76. Sagara, M. *et al.* Inhibition of development of peripheral neuropathy in streptozotocin-induced diabetic rats with N-acetylcysteine. *Diabetologia* **39,** 263–269 (1996).
77. Cascinu, S. *et al.* Neuroprotective effect of reduced glutathione on oxaliplatin-based chemotherapy in advanced colorectal cancer: a randomized, double-blind, placebo-controlled trial. *J. Clin. Oncol. Off. J. Am. Soc. Clin. Oncol.* **20,** 3478–3483 (2002).
78. Lehky, T. J., Leonard, G. D., Wilson, R. H., Grem, J. L. & Floeter, M. K. Oxaliplatin-induced neurotoxicity: acute hyperexcitability and chronic neuropathy. *Muscle Nerve* **29,** 387–392 (2004).
79. Renn, C. L. *et al.* Multimodal assessment of painful peripheral neuropathy induced by chronic oxaliplatin-based chemotherapy in mice. *Mol. Pain* **7,** 29 (2011).
80. Ta, L. E., Low, P. A. & Windebank, A. J. Mice with cisplatin and oxaliplatin-induced painful neuropathy develop distinct early responses to thermal stimuli. *Mol. Pain* **5,** 9 (2009).
81. Toyama, S. *et al.* Characterization of acute and chronic neuropathies induced by oxaliplatin in mice and differential effects of a novel mitochondria-targeted antioxidant on the neuropathies. *Anesthesiology* **120,** 459–473 (2014).
82. Jack, M. M., Ryals, J. M. & Wright, D. E. Protection from diabetes-induced peripheral sensory neuropathy--a role for elevated glyoxalase I? *Exp. Neurol.* **234,** 62–69 (2012).
83. Cerles, O. *et al.* Niclosamide Inhibits Oxaliplatin Neurotoxicity while Improving Colorectal Cancer Therapeutic Response. *Mol. Cancer Ther.* **16,** 300–311 (2017).
84. Lopes, L. C. G. *et al.* Beyond weakness: Characterization of pain, sensory profile and conditioned pain modulation in patients with motor neuron disease: A controlled study. *Eur. J. Pain Lond. Engl.* **22,** 72–83 (2018).
85. Miraucourt, L. S., Moisset, X., Dallel, R. & Voisin, D. L. Glycine Inhibitory Dysfunction Induces a Selectively Dynamic, Morphine-Resistant, and Neurokinin 1 Receptor- Independent Mechanical Allodynia. *J. Neurosci.* **29,** 2519–2527 (2009).
86. Kiernan, M. C., Burke, D., Andersen, K. V. & Bostock, H. Multiple measures of axonal excitability: a new approach in clinical testing. *Muscle Nerve* **23,** 399–409 (2000).
87. Krishnan, A. V., Lin, C. S.-Y., Park, S. B. & Kiernan, M. C. Assessment of nerve excitability in toxic and metabolic neuropathies. *J. Peripher. Nerv. Syst. JPNS* **13,** 7–26 (2008).
88. Schlumberger, S. *et al.* Permeability characteristics of cell-membrane pores induced by ostreolysin A/pleurotolysin B, binary pore-forming proteins from the oyster mushroom. *FEBS Lett.* **588,** 35–40 (2014).
89. Goebbels, S. *et al.* Elevated Phosphatidylinositol 3,4,5-Trisphosphate in Glia Triggers Cell-Autonomous Membrane Wrapping and Myelination. *J. Neurosci.* **30,** 8953–8964 (2010).
90. Liu, Z. *et al.* Specific marker expression and cell state of Schwann cells during culture in vitro. *PloS One* **10,** e0123278 (2015).

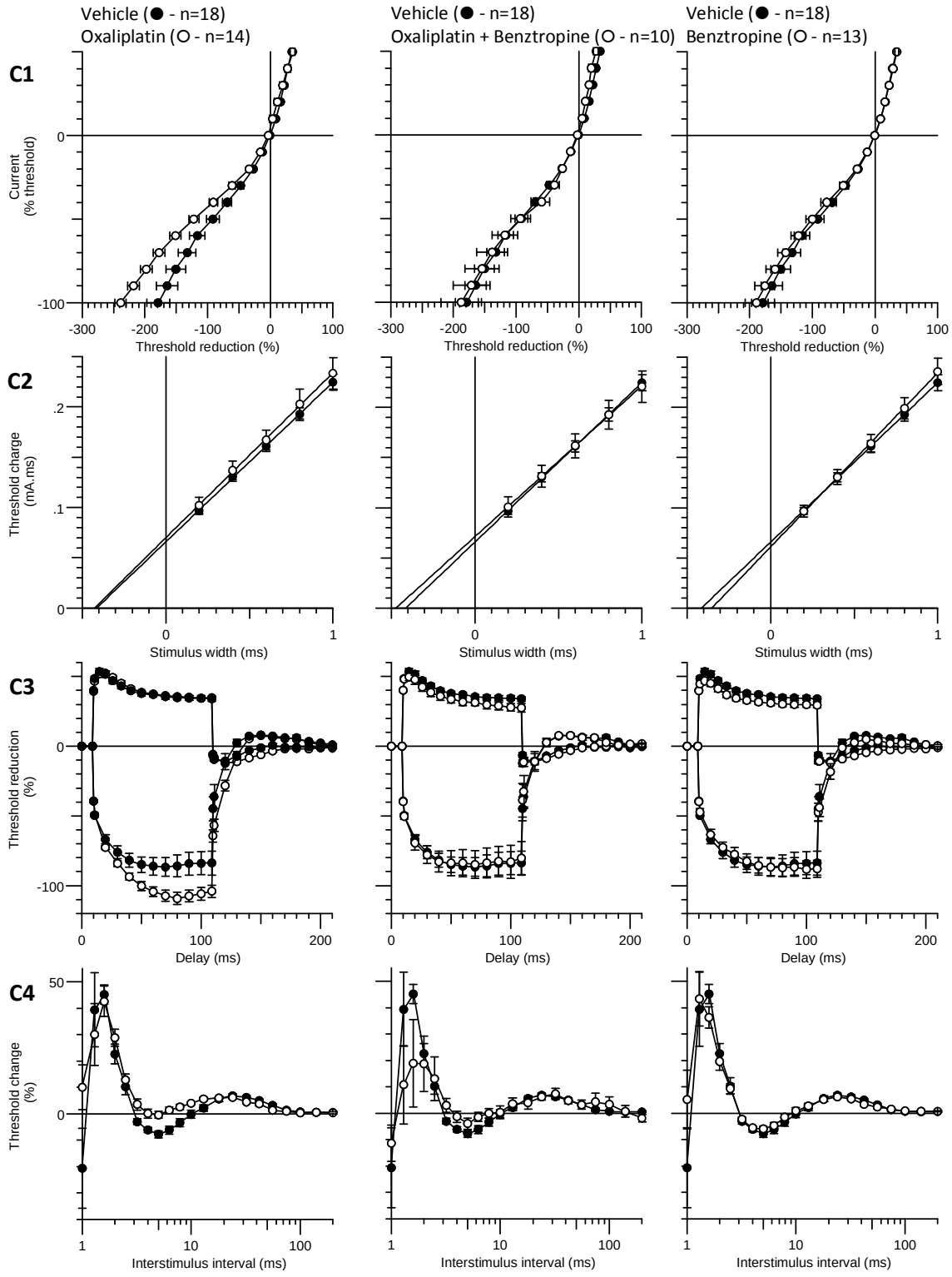

Supplementary Figure 1. Benztropine prevents the *in vivo* effects induced by oxaliplatin on mouse neuromuscular excitability curves. Excitability curves (means ± SD) were recorded at the plantar muscle in response to sciatic motor nerve stimulation of mice treated for 6 weeks with vehicle (black circles, n = 18), oxaliplatin (white circles, n = 14, left panels), oxaliplatin plus benztropine (white circles, n = 10, middle panels) or benztropine alone (white circles, n = 13, right panels). (C1) Current-threshold relationship [excitability modifications in response to depolarizing (up) and hyperpolarizing (down) currents], (C2) strength-duration relationship, (C3) threshold electrotonus in response to constant depolarizing (up) and hyperpolarizing (down) long-duration currents applied at sub-threshold intensity (± 40%), and (C4) recovery cycle. Note the absence of effect of oxaliplatin plus benztropine and benztropine alone, *versus* vehicle, on excitability waveforms.

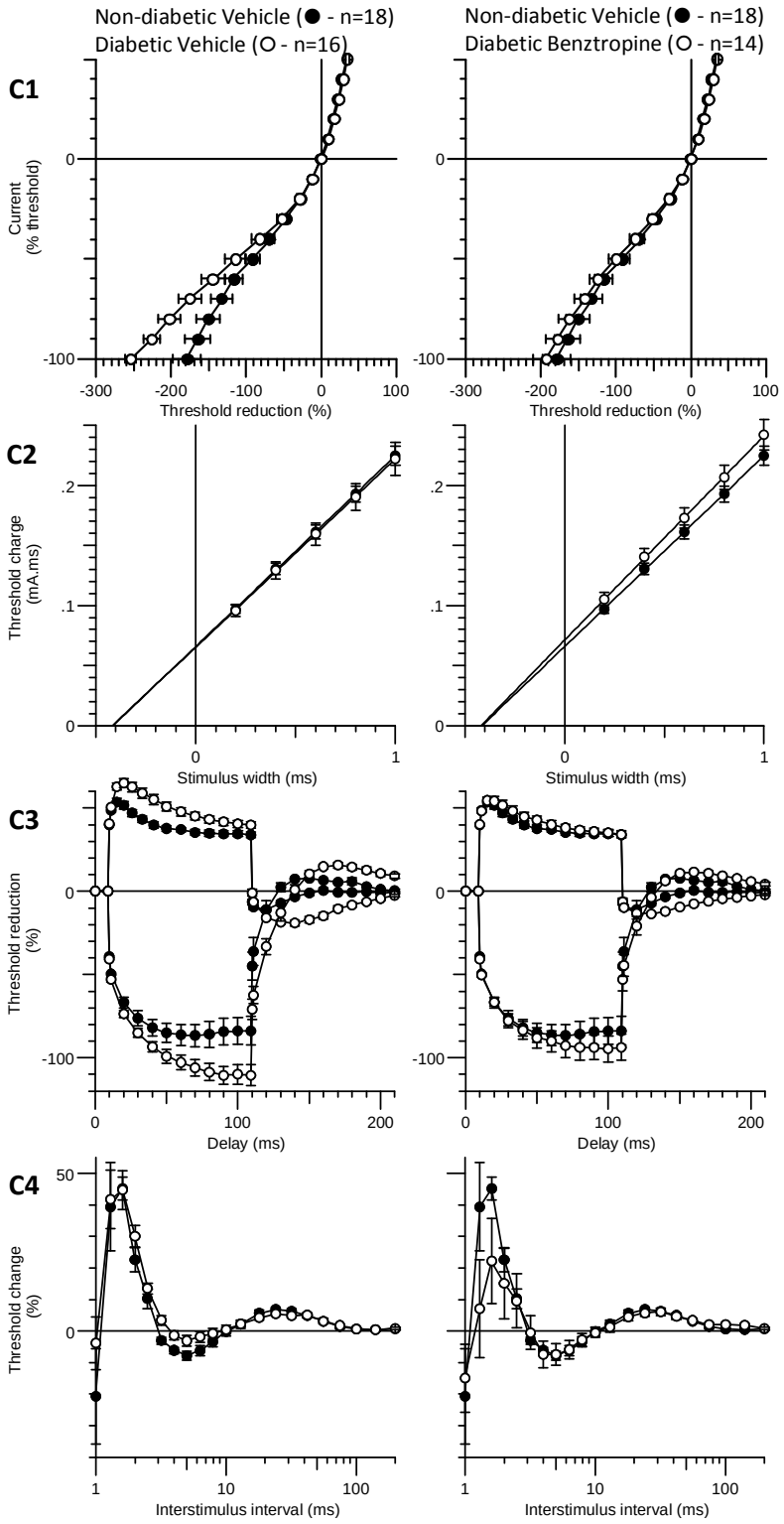

Supplementary Figure 2. Benztropine prevents the *in vivo* effects induced by diabetes on mouse neuromuscular excitability curves. Excitability curves (means ± SD) were recorded at the plantar muscle in response to sciatic motor nerve stimulation of mice treated for 6 weeks with non-diabetic vehicle (black circles, n = 18), diabetic vehicle (white circles, n = 16, left panels), and diabetic benztropine (white circles, n = 14, right panels). (C1) Current-threshold relationship [excitability modifications in response to depolarizing (up) and hyperpolarizing (down) currents], (C2) strength-duration relationship, (C3) threshold electrotonus in response to constant depolarizing (up) and hyperpolarizing (down) long-duration currents applied at sub-threshold intensity (± 40%), and (C4) recovery cycle. Note the absence of effect of diabetic benztropine, *versus* non-diabetic vehicle, on excitability waveforms.

Supplementary Table 1. Benztropine prevents the *in vivo* effects induced by oxaliplatin and diabetes on mouse neuromuscular excitability variables. Variables (means ± SD) derived from excitability curves established from plantar muscle recordings in response to sciatic motor nerve stimulation of mice treated with vehicle (n = 18), oxaliplatin (n = 14), oxaliplatin plus benztropine (n = 10), diabetic vehicle (n = 16), diabetic benztropine (n = 14) or benztropine alone (n = 13) for 6 weeks.

	Vehicle	Oxaliplatin	Oxaliplatin + Benztropine	Diabetic Vehicle	Diabetic Benztropine	Benztropine
C0 **06.** Peak response (mV)	3.21 ± 1.11	4.24 ± 1.12*	2.87 ± 1.18	5.57 ± 1.10**	3.40 ± 1.19	2.85 ± 1.18
C0 **19.** Latency (ms)	3.07 ± 0.10	3.01 ± 0.12	3.16 ± 0.17	3.38 ± 0.08	3.06 ± 0.11	2.75 ± 0.08
C0 **01.** Stimulus (mA) for 50% max response	0.25 ± 0.05	0.18 ± 0.04***	0.22 ± 0.09	0.20 ± 0.06*	0.24 ± 0.04	0.32 ± 0.08
C0 **05.** Stimulus-response slope	3.23 ± 1.09	3.25 ± 1.15	3.30 ± 1.31	2.84 ± 1.12	3.06 ± 1.10	4.24 ± 1.17
C1 **07.** Resting slope	0.95 ± 0.05	0.96 ± 0.03	1.03 ± 0.18	0.95 ± 0.09	0.91 ± 0.05	1.15 ± 0.23
C1 **08.** Minimum slope	0.51 ± 0.03	0.30 ± 0.01*	0.63 ± 0.17	0.27 ± 0.01*	0.46 ± 0.07	0.37 ± 0.03
C1 **28.** Hyperpolarizing slope	1.63 ± 0.08	0.50 ± 0.03**	2.08 ± 1.06	0.44 ± 0.06**	1.62 ± 0.07	1.09 ± 1.00
C2 **03.** Strength-duration time constant (ms)	0.43 ± 0.02	0.45 ± 0.04	0.49 ± 0.06	0.43 ± 0.04	0.43 ± 0.03	0.37 ± 0.03
C2 **04.** Rheobase (mA)	0.16 ± 1.04	0.16 ± 1.07	0.14 ± 1.08	0.15 ± 1.08	0.17 ± 1.05	0.17 ± 1.07
C3 **12.** TEd (10-20 ms)	47.97 ± 2.17	49.87 ± 1.52	43.66 ± 3.15	62.88 ± 2.86***	52.04 ± 2.97	41.98 ± 2.30
C3 **25.** TEd (peak)	49.48 ± 2.05	50.15 ± 1.38	45.87 ± 2.79	62.49 ± 2.68**	52.52 ± 2.56	44.66 ± 1.78
C3 **20.** TEd (40-60 ms)	36.81 ± 1.56	37.45 ± 1.06	32.17 ± 2.48	47.97 ± 2.39**	40.24 ± 2.30	31.77 ± 1.96
C3 **21.** TEd (90-100 ms)	34.24 ± 1.63	34.68 ± 1.09	28.06 ± 3.22	40.16 ± 2.07*	34.65 ± 2.08	29.66 ± 1.83
C3 **26.** S2 accommodation	15.25 ± 1.20	15.48 ± 0.79	18.14 ± 1.71	22.33 ± 0.88***	17.87 ± 1.11	14.00 ± 0.93
C3 **23.** TEd (undershoot)	-9.53 ± 1.03	-11.74 ± 0.78	-11.38 ± 1.29	-19.15 ± 1.39****	-13.61 ± 0.76**	-11.05 ± 0.89
C3 **22.** TEh (10-20 ms)	-71.52 ± 3.91	-78.37 ± 1.77*	-73.64 ± 5.76	-79.42 ± 2.17	-72.19 ± 3.41	-67.96 ± 3.62
C3 **30.** TEh (20-40 ms)	-81.21 ± 5.06	-92.88 ± 2.60*	-81.81 ± 7.49	-92.71 ± 3.07	-83.18 ± 5.18	-77.66 ± 4.64
C3 **11.** TEh (90-100 ms)	-83.88 ± 8.32	-104.90 ± 4.42*	-81.59 ± 11.90	-110.20 ± 6.13*	-94.17 ± 7.78	-88.14 ± 6.24
C3 **24.** TEh (overshoot)	9.16 ± 0.91	8.09 ± 0.76	9.25 ± 1.07	16.26 ± 1.50***	11.09 ± 1.07	6.34 ± 0.98
C4 **32.** Refractoriness at 2 ms (%)	22.60 ± 3.77	28.84 ± 3.25	18.69 ± 10.40	30.07 ± 3.44	15.07 ± 11.20	19.60 ± 3.27
C4 **29.** Refractoriness at 2.5 ms (%)	10.24 ± 3.13	12.77 ± 2.32	13.09 ± 8.23	13.47 ± 1.65	9.55 ± 8.56	9.31 ± 1.94
C4 **34.** Superexcitability at 5 ms (%)	-7.78 ± 1.35	-0.43 ± 1.33**	-3.95 ± 2.11	-3.10 ± 1.63*	-7.39 ± 3.46	-5.99 ± 1.02
C4 **33.** Superexcitability at 7 ms (%)	-4.81 ± 1.54	1.96 ± 0.99**	-0.74 ± 1.70	-1.31 ± 1.03*	-4.37 ± 2.38	-3.08 ± 1.14
C4 **14.** Subexcitability (%)	6.75 ± 0.72	6.30 ± 0.33	8.35 ± 1.93	6.19 ± 0.33	6.45 ± 0.82	6.09 ± 0.67

(C0) Stimulus-response relationship, (C1) current-threshold relationship, (C2) strength-duration relationship, (C3) threshold electrotonus in response to constant depolarizing (TEd) and hyperpolarizing (TEh) long-duration currents applied at sub-threshold intensity (± 40%), and (C4) recovery cycle. *$p < 0.05$, **$p < 0.01$, ***$p < 0.001$, and ****$p < 0.0001$ *versus* vehicle (highlighted in grey). Note that, compared to vehicle; most if not all variables modified with oxaliplatin and diabetic vehicle remain unchanged with oxaliplatin plus benztropine, diabetic benztropine or benztropine alone.

Supplementary Table 2. Comparison of morphometric parameters. Mean values ± SD of morphometric parameters of single myelinated axons isolated from sciatic nerves of mice injected with vehicle, oxaliplatin, oxaliplatin plus benztropine or benztropine alone, for 6 weeks (137-206 axons from 4 different mice under each condition). *P = 0.011-0.049, **P = 0.006 and ***$P < 0.0001$ *versus* vehicle (highlighted in grey).

Morphometric parameters	Vehicle	Oxaliplatin	Oxaliplatin + Benztropine	Benztropine
Internodal diameter (Di, in µm)	7.19 ± 0.25	6.33 ± 0.20 **	7.71 ± 0.23	7.85 ± 0.21
Nodal diameter (D, in µm)	2.32 ± 0.08	2.62 ± 0.11 *	2.49 ± 0.11	2.49 ± 0.08
Nodal length (L, in µm)	1.03 ± 0.03	1.44 ± 0.06 ***	1.12 ± 0.03 *	1.16 ± 0.04 *
Nodal volume (V, in μm^3)	6.07 ± 0.44	15.06 ± 1.77 ***	8.51 ± 0.92 *	7.98 ± 0.82
D/Di	0.33 ± 0.01	0.40 ± 0.01 ***	0.33 ± 0.01	0.32 ± 0.01
L/Di	0.15 ± 0.01	0.23 ± 0.01 ***	0.18 ± 0.01	0.16 ± 0.01
V/Di	0.70 ± 0.04	1.67 ± 0.14 ***	0.89 ± 0.08 *	0.86 ± 0.06 *

Résumé des résultats obtenus

L'évaluation multimodale des propriétés d'excitabilité sensorielle, *in vivo* chez des souris anesthésiées ayant reçu des injections intrapéritonéales hebdomadaires d'oxaliplatine (10 mg/kg) pendant 6 semaines, révèle des modifications traduisant une hyperexcitabilité membranaire et une diminution de la vitesse de conduction nerveuse, ce qui suggère une réduction du nombre de fibres à conduction rapide ou une diminution de la densité et/ou du fonctionnement des canaux Na_V, et une modification de la dépendance vis-à-vis du potentiel de ces canaux. L'évaluation multimodale des propriétés d'excitabilité neuromusculaire, *in vivo* chez ces mêmes souris et chez des souris diabétiques (*i.e.* ayant subi une injection de 180 mg/kg de streptozotocine), révèle également des modifications compatibles avec une hyperexcitabilité membranaire et suggérant une modification de la dépendance vis-à-vis du potentiel des canaux Na_V ainsi qu'une diminution de la densité et/ou du fonctionnement des canaux K_V, sans que la vitesse de transmission neuromusculaire ne soit affectée. Ces modifications n'apparaissent pas chez des souris ayant subi des administrations conjointes d'oxaliplatine (10 mg/kg) et de benztropine (10 mg/kg) et sont considérablement réduites chez des souris diabétiques ayant subi des administrations de benztropine (10 mg/kg).

De plus, l'étude morphologique *ex vivo* des nerfs sciatiques isolés de souris ayant subi les injections d'oxaliplatine, par une exploration au microscope confocal, met en évidence une diminution du diamètre internodal des axones myélinisés, ce qui suggère fortement une perte préférentielle des fibres de gros diamètre, *i.e.* à conduction rapide (voir ci-dessus). Cette diminution du diamètre internodal est associée notamment à une augmentation de la longueur nodale, ce qui traduit une démyélinisation axonale. Cette démyélinisation axonale est confirmée par l'exploration au microscope électronique des nerfs sciatiques et par l'étude de l'expression de la protéine basique de la myéline (MBP pour "myelin basic protein") réalisées par l'équipe du Pr. Batteux. Ces altérations n'apparaissent pas ou sont considérablement réduites chez les souris ayant subi des administrations conjointes d'oxaliplatine et de benztropine.

Finalement, les effets de l'oxaliplatine et de la benztropine ont été également évalués *in vitro* sur les potentiels d'action enregistrés à partir de cultures primaires de neurones sensoriels de DRG de souris, à l'aide de la technique de patch clamp en configuration "cellule entière". Les modifications détectées en présence d'oxaliplatine (25-50 µM) traduisent, là encore, une hyperexcitabilité membranaire: *(i)* un potentiel de repos membranaire moins négatif d'environ 20 mV (dépolarisation membranaire), *(ii)* une diminution de l'intensité du courant nécessaire pour évoquer un nombre accru de potentiels d'action répétitifs, et *(iii)* une diminution de l'amplitude maximale et une augmentation de la durée des phases ascendante et descendante des potentiels d'action. Ces

modifications, indiquant des altérations de la densité et/ou du fonctionnement des canaux Na_V et K_V, n'apparaissent pas en présence d'oxaliplatine (50 µM) et de benztropine (10 µM).

La neuroprotection conférée par la benztropine est associée à une expression plus faible de cytokines inflammatoires et à une diminution de la croissance tumorale expliquée, au moins en partie, par un déséquilibre des espèces réactives de l'oxygène dans les cellules tumorales (études réalisées par l'équipe du Pr. Batteux).

Conclusion

La benztropine, un inhibiteur des récepteurs muscariniques M1-M3 de l'acétylcholine, améliore les symptômes de neuropathies périphériques dues à la chimiothérapie (oxaliplatine) et au diabète, chez des modèles expérimentaux de souris, et augmente l'effet antitumoral de l'oxaliplatine. Ces résultats pourraient être à court terme transposables aux patients puisque la benztropine est actuellement indiquée pour traiter la maladie de Parkinson aux États-Unis et a donc déjà obtenu une autorisation de mise sur le marché par la FDA.

Titre : Evaluation multi-échelle de toxines de venins comme agents antinociceptifs potentiels

Mots clés : toxines de venins, antinociception, canaux sodium dépendants du potentiel, électrophysiologie

Résumé: L'objectif de ma thèse était d'identifier, comme agents antinociceptifs potentiels, des toxines de venins originales par leur séquence et/ou leur provenance. Dans cette optique, un criblage à haut débit de deux banques de venins a été réalisé par des méthodes électrophysiologiques de "patch-clamp" automatique, sur des lignées cellulaires exprimant le sous-type neuronal $hNa_V1.7$ de canaux sodium (*versus* celles exprimant le sous-type cardiaque $hNa_V1.5$), une cible antidouleur validée génétiquement et fortement exprimée au niveau des neurones sensoriels primaires des ganglions de la racine dorsale, premier support de la transmission du message nociceptif.
Le criblage de la première banque de venins (appartenant à Smartox Biotechnology) a permis l'identification et la caractérisation, par des approches structurales et fonctionnelles multi-échelles (de la cellule *in vitro* à l'organisme *in vivo*), de 2 peptides de venins d'araignées ayant des propriétés potentiellement antinociceptives : *(1)* la cyriotoxine-1a du venin de *Cyriopagopus schioedtei*, dont les propriétés fonctionnelles sont proches de celles des peptides appartenant à la famille 1 des toxines d'araignées inhibant les canaux sodium, et *(2)* la poecitoxine-1a du venin de *Poecilotheria subfusca*, qui présente une meilleure affinité pour le sous-type $hCa_V1.2$ de canaux calcium que pour le sous-type $hNa_V1.7$. Nous avons également mené une étude de "structure-activité" afin d'améliorer le profil de sélectivité *de* la phlotoxine-1 d'une araignée *Phlogiellus*, connue pour son activité antinocieptive. Finalement, nous avons mis en évidence une interaction directe entre l'huwentoxine-IV, déjà connue comme agent antinociceptif potentiel, et le sous-type neuronal $Na_V1.6$, responsable d'effets neuromusculaires indésirables. Le criblage de la deuxième banque de venins (appartenant à SANOFI) a permis d'identifier des *hits* intéressants provenant de venins d'araignées et de scorpions non étudiés jusqu'à présent et ayant une séquence originale présentant peu d'homologie avec les séquences déjà connues.

Title : Multiscale evaluation of venom toxins as potential antinociceptive agents

Keywords : venom toxins, antinociception, voltage-dependent sodium channels, electrophysiology

Abstract: The aim of my thesis was to identify original venom toxins, by their sequence and/or origin, as potential antinociceptive agents. In this context, a high-throughput screening of two venom libraries was performed, by automated patch-clamp electrophysiology, on cell lines expressing the $hNa_V1.7$ neuronal subtype of sodium channels (*versus* those expressing the $hNa_V1.5$ cardiac subtype), a genetically-validated and strongly expressed pain target in the primary sensory neurons of dorsal root ganglia, the first support of nociceptive message transmission.
The screening of the first venom library (belonging to Smartox Biotechnology) allowed the identification and characterization, by structural and multiscale functional approaches (from the cell *in vitro* to the organism *in vivo*), of 2 peptides from spider venoms having potential antinociceptive properties : *(1)* cyriotoxin-1a from *Cyriopagopus schioedtei* venom, whose functional properties are close to those of peptides belonging to family 1 of spider toxins inhibiting sodium channels, and *(2)* poecitoxin-1a from *Poecilotheria subfusca* venom, which has a better affinity for the $hCa_V1.2$ subtype of calcium channels than for the $hNa_V1.7$ subtype. We also conducted a "structure-activity" study to improve the selectivity profile of phlotoxin-1 from a *Phlogiellus* spider, known for its antinociceptive activity. Finally, we evidenced a direct interaction between huwentoxin-IV, already known as a potential antinociceptive agent, and the $Na_V1.6$ neuronal subtype which is the main cause of undesirable neuromuscular effects. The screening of the second venom library (belonging to SANOFI) allowed to identify interesting hits from spider and scorpion venoms, not studied until now, having an original sequence with little homology with already known sequences.

Université Paris-Saclay
Espace Technologique / Immeuble Discovery
Route de l'Orme aux Merisiers RD 128 / 91190 Saint-Aubin, France